Hari Vasudevan
Vijaya Kumar N. Kottur
Amool A. Raina *Editors*

Proceedings of International Conference on Intelligent Manufacturing and Automation

ICIMA 2018

Springer

Lecture Notes in Mechanical Engineering

Lecture Notes in Mechanical Engineering (LNME) publishes the latest developments in Mechanical Engineering—quickly, informally and with high quality. Original research reported in proceedings and post-proceedings represents the core of LNME. Also considered for publication are monographs, contributed volumes and lecture notes of exceptionally high quality and interest. Volumes published in LNME embrace all aspects, subfields and new challenges of mechanical engineering. Topics in the series include:

- Engineering Design
- Machinery and Machine Elements
- Mechanical Structures and Stress Analysis
- Automotive Engineering
- Engine Technology
- Aerospace Technology and Astronautics
- Nanotechnology and Microengineering
- Control, Robotics, Mechatronics
- MEMS
- Theoretical and Applied Mechanics
- Dynamical Systems, Control
- Fluid Mechanics
- Engineering Thermodynamics, Heat and Mass Transfer
- Manufacturing
- Precision Engineering, Instrumentation, Measurement
- Materials Engineering
- Tribology and Surface Technology

Hari Vasudevan · Vijaya Kumar N. Kottur
Amool A. Raina
Editors

Proceedings of International Conference on Intelligent Manufacturing and Automation

ICIMA 2018

Springer

Editors
Hari Vasudevan
Department of Production Engineering
Dwarkadas J. Sanghvi College
  of Engineering
Mumbai, Maharashtra, India

Amool A. Raina
Aerospace Group, Institute of Textile
  Technology
RWTH Aachen University
Aachen, Germany

Vijaya Kumar N. Kottur
Department of Mechanical Engineering
Dwarkadas J. Sanghvi College
  of Engineering
Mumbai, Maharashtra, India

Preface

This is an exciting time for business and wealth creation in the fields of manufacturing and automation. It is the time when industries are looking up to manufacturing and automation engineers for their assistance in increasing the overall productivity in their organisation. It is also the time when the governments across the globe have started to focus more on the manufacturing sector. The International Conference on Intelligent Manufacturing and Automation 2018 (ICIMA 2018) was therefore designed to encourage discussions and research on advancements and applications in the areas of manufacturing and automation. The primary focus of this conference was to bring together academicians, researchers and scientists for knowledge sharing in various areas of manufacturing, automation and other allied domains. The conference covered topics encompassing automation, mechatronics, robotics, manufacturing processes, management and other related areas such as product design and development, green manufacturing and smart materials with the objective of brainstorming and emphasising upon the applications in the field of intelligent manufacturing and automation. The response to call for papers was overwhelming with 109 full papers being submitted, covering a wide spectrum of topics related to the theme of the conference. We express our sincere appreciation to the authors for their contribution to this book. We would also like to express our sincere gratitude to all the experts and referees for their valuable comments and support extended during the review process.

Mumbai, India   Hari Vasudevan
Mumbai, India   Vijaya Kumar N. Kottur
Aachen, Germany   Amool A. Raina

ICIMA 2018

Patrons

Shri Amrish R. Patel, Chief Patron, President, SVKM
Shri Bhupesh R. Patel, Joint President, SVKM
Shri Bharat M. Sanghvi, Vice President and Trustee, SVKM, and Chairman, Governing Council, DJSCE
Shri Sunandan R. Divatia, Hon. Secretary, SVKM
Shri Utpal H. Bhayani, Hon. Treasurer, SVKM
Shri Shalin S. Divatia, Hon. Joint Secretary, SVKM
Shri Jayant P. Gandhi, Hon. Joint Secretary, SVKM
Shri Harshad H. Shah, Hon. Joint Treasurer, SVKM
Shri Harit H. Chitalia, Hon. Joint Treasurer, SVKM

International Advisory Committee

Dr. Amit S. Jariwala, Georgia Institute of Technology, USA
Dr. Huynh T. Luong, Asian Institute of Technology, Thailand
Dr. Raghu Echempati, Kettering University, USA
Dr. Amool Raina, RWTH Aachen University, Germany
Dr. Rohan A. Shirwaiker, North Carolina State University, USA
Dr. Iris V. Rivero, Iowa State University, USA

National Advisory Committee

Dr. S. K. Ukarande, Dean, Faculty of Science and Technology, University of Mumbai
Dr. S. S. Mantha, Former Chairman, AICTE, New Delhi
Dr. S. K. Mahajan, Joint Director, DTE, Maharashtra
Dr. S. M. Khot, FCRIT, Navi Mumbai
Dr. L. Ganapathy, NITIE, Mumbai
Dr. S. G. Deshmukh, ABV-IIITM, Gwalior
Dr. K. P. Karunakaran, IIT Bombay
Dr. K. Maddulety, NITIE, Mumbai

Dr. Suhas S. Joshi, IIT Bombay
Dr. Tushar Desai, NIT Surat
Dr. V. R. Kalamkar, VNIT Nagpur
Dr. P. Sakthivel, VIT Vellore
Mr. C. M. Venkateswaran, Aker Solutions

Organising Committee

Dr. Hari Vasudevan, General Chair, Convener and Principal, DJSCE
Dr. A. C. Daptardar, General Co-Chair, Vice Principal (Admin.), DJSCE
Dr. M. J. Godse, General Co-Chair, Vice Principal (Acad.), DJSCE
Dr. Vijaya Kumar N. Kottur, Joint Convener, Professor and Head, Department of Mechanical Engineering, DJSCE
Mr. Rajendra S. Khavekar, Co-Convener, Training and Placement Officer, DJSCE

Members

Dr. Atul Dhale
Dr. Sanjeev Thool
Mr. E. Narayanan
Mr. Sandeep R. Vaity
Mr. Prasad S. Shirodkar
Mr. Vyankatesh U. Bagal
Mr. P. Frank Crasta
Mr. Prashant P. Patankar
Mr. Rajnarayan M. Yadav
Mr. Bronin Cyriac
Mr. Greegory Mathew
Mr. Dharam V. Ranka
Mrs. Meeta N. Gandhi
Mr. Amit Chaudhari
Mr. Ramesh Rajguru
Mrs. Trupti Markose
Mr. Rohit K. Chaurasia
Mr. Mehul S. Prajapati
Mr. Vinit R. Katira
Mr. Pavan R. Rayar
Mr. Kartik M. Ajugia
Mr. Dhaval J. Birajdar
Mr. Sandip H. Mane
Mr. Sanket D. Parab
Mr. Shashikant M. Auti
Mr. Dhananjay Shukla
Mr. Ravikant Hattale

About This Book

This volume comprises the best-selected papers presented at the International Conference on Intelligent Manufacturing and Automation, which was organised by the Departments of Mechanical Engineering and Production Engineering of Dwarkadas J. Sanghvi College of Engineering. The volume focuses on narrowed topics of automation, mechatronics, robotics, CAD/CAM/CAE/CIM/FMS in manufacturing, product design and development, DFM/DFA/FMEA, MEMS and nanotechnology, rapid prototyping, computational techniques, industrial engineering, manufacturing process management, modelling and optimisation techniques, CRM, MRP and ERP, logistics and supply chain management, quality assurance and environment protection, advanced materials processing and characterisation and composites and smart materials. The papers are divided into four main domains like design, advanced materials, manufacturing and automation. We expect the articles, being published in the book, would contribute to and reinvigorate the overall efforts in enhancing manufacturing productivity across various sectors. The content of the book is also expected to be helpful for postgraduate and doctoral students in their efforts to enhance the research outcome of their studies.

Contents

Part IV   Automation

About the Editors

Dr. Hari Vasudevan has his master's degree in production engineering and postgraduate diploma in industrial engineering from VJTI (University of Mumbai) and Ph.D. from IIT Bombay. He has also done a 3-month full-time certificate programme (ERP-BaaN) from S.P. Jain Institute of Management and Research, Mumbai, under the University Synergy Programme of the BaaN Institute, Netherlands. His areas of interest include manufacturing engineering, manufacturing systems and strategy, market orientation of manufacturing firms and world-class manufacturing. He is an approved Ph.D. guide at the University of Mumbai and NMIMS (Deemed to be University) and has so far guided three Ph.D. students. He is the president of Indian Society of Manufacturing Engineering (ISME); life member of ISTE, New Delhi; fellow of the Institution of Engineers (India); fellow of ISME and senior member of IEDRC. He has 26 years of experience in teaching and 2 years of experience in the industry. Presently, he is working as the principal of Dwarkadas J. Sanghvi College of Engineering, Mumbai. He has published over 82 papers in international and national conferences and journals.

Dr. Vijaya Kumar N. Kottur heads the Department of Mechanical Engineering at Dwarkadas J. Sanghvi College of Engineering, Mumbai. He completed his master's degree in engineering management from SJCE Mysore, master's degree in mechanical engineering with machine design as specialisation from SPCE Mumbai and Ph.D. from the University of Mumbai. He has 28 years of teaching experience and published 48 papers in national and international journals and conferences. He is an approved Ph.D. guide at the University of Mumbai, Pune University and JJTU University and has so far guided two Ph.D. students. He worked as a guest faculty at NITIE Mumbai. His areas of interest are quality engineering, world-class manufacturing, supply chain management and system dynamics. He is the life member of professional bodies like ISNDT, IIIE, ISTE and ISME.

Dr. Amool A. Raina currently coordinates and heads the aerospace programme at the Institut für Textiltechnik (ITA) of RWTH Aachen University. His doctoral thesis (highest distinction received) majoring in aerospace engineering at the University of Kansas presented solutions for the improvement in wind turbine design and manufacturing. He is considered as an expert in wind turbine design and engineering and has a work experience of over 6 years in the aerospace and renewable industry prior to joining ITA. He has designed and engineered over 35 wind turbine blades ranging from 2 to 105 m in length with over 16,000 blades successfully flying worldwide. He has also been involved in projects relating to design and optimisation of aircraft engines and other components. He is currently developing and promoting textile-based solutions for several sectors including aerospace, automotive, traditional textiles and digital solutions as per Industry 4.0 norms for the above industries. Apart from his technical responsibilities, he also heads all affairs and activities pertaining to the European Union and European Space Agency at ITA.

Part I
Design

Mathematical Modeling and Optimization of Process Parameters for Tensile Strength and Nugget Diameter in Resistance Spot Welding of HR E-34 Steel Sheet Joint

B. S. Gawai, R. L. Karwande, Md. Irfan and Prafull S. Thakare

Abstract   In the present investigation, HR E-34 steel sheets are welded by resistance spot welding. The welding current, welding cycle, and pressure are the principal variables that are controlled in order to provide the necessary combination of heat and pressure to form the weld. The effect of various parameters on weld strength of Hot Rolled E-34 material is determined by using Minitab 16 software and using design of experiment. Response surface methodology (Box-Behnken Design) is chosen to design the experiments. The highly significant factor was determined by analysis of variance. In the analysis, it was observed that predicted and experimental results were in good agreement and the coefficient of determination was found to be 0.967 and 0.955 for tensile strength and nugget diameter implies adequacy of derived model. The aim of the research is to find out improvement in welds strength and also reduces various welding defects.

Keywords   Response surface method (RSM) · Tensile strength · Nugget diameter Analysis of variance (ANOVA) · Resistance spot welding (RSW)

B. S. Gawai
MSS'S, College of Engineering and Technology, Jalna,
Maharashtra, India
e-mail: bimbisargawai@gmail.com

R. L. Karwande (✉) · Md. Irfan · P. S. Thakare
Department of Mechanical Engineering, MSS'S,
College of Engineering and Technology, Jalna, Maharashtra, India
e-mail: ravindrakarwande@yahoo.com

Md. Irfan
e-mail: irfanmohd777@gmail.com

P. S. Thakare
e-mail: prafull.thakare16@gmail.com

1   Introduction

Resistance welding is one of the oldest of the electric welding processes in use by industry today. Resistance welding is group of welding processes which produce coalescence of metals with the heat obtained from resistance offered by the workpiece to the flow of electrical current through the parts being joined. In this process, heavy electric current is passed through the metals to be joined. This causes local heating to increase temperature to plastic state over limited area of contact. Mechanical pressure is applied to join them completely. No additional filler metal is required. The current is passed through the electrodes which incorporate very low resistance in the circuit and the resistance at the joints of metals is very high. Thus, maximum heating is produced at the point of contact where weld is to be made. Resistance welding is use to weld sheet metals of all engineering metals in Steel cabinets, boxes, cans and furniture automobile industry, air craft industry, and pipe and tubing production. It is an efficient joining process widely used for the fabrication of sheet metal assemblies.

2   Literature Review

The review present in this section is related to mathematical modeling and optimization of process parameters of resistance spot welding machine. The present literature review investigates various techniques and methods for improvement in parameters like nugget diameter and tensile Strength. The survey is given as:

Kahraman [1] has carried out outcome of experimental investigations to assess the performance of commercially pure (CP) titanium sheets (ASTM Grade 2) were welded by resistance spot welding at different welding parameters and under different welding environments. Aslanlar [2] has experimentally studied the change in Nucleus size ratio for tensile peel strength and Tensile shear strength were investigate and optimum welding condition for parameters like weld current and time were find out. Vural et al. [3] have aimed to analyze the effect of welding nugget diameter on the fatigue strength of the resistance spot welded joints of different steel sheets. Han et al. [4] concluded experimental correlation study of mechanical strength of resistance spot welding of AA5754 aluminium alloy.

Hamidinejad et al. [5] carried out the modeling and process analysis of resistance spot welding on galvanized steel sheets used in car body manufacturing. Zhao et al. [6] investigated and optimized process parameter like welding time, welding current, and electrode force for improvement in failure energy and spot weld quality of spot welded titanium alloy. Mathematical model of input parameter and output parameter was prepared by using response surface methodology.

2.1 Material

Material used in this study is Hot rolled E-34 steel sheet. Material is cut in samples of dimensions $100 \times 20 \times 2$ mm (Table 1).

3 DOE

DOE (Design of experiment) is used to know the nature of any system. Experiments were carried out with the help of DOE method. By using DOE, it can predict the result of output maximum or output minimum. In DOE, response surface methodology is used for mathematical modeling. Box–Behnken design was used to set experimental runs. The input process parameters were weld current, weld time, pressure for research work. Nugget diameter and tensile strength were output parameters. For each experimental run the parameter were fit and alter with respect to the design table. Parameter ranges are decided on the basis of literature review recommended and machine feasibility and specifications given by BAJAJ Materials department Bajaj auto Ltd, Akrudi.

3.1 Resistance Spot Welding Machine Specifications

75 KVA spot welding machine is employed for experimentation. Weld, current, and pressure are used for responses like nugget diameter and strength of weld. Following Fig. 1 shows setup of resistance spot welding.
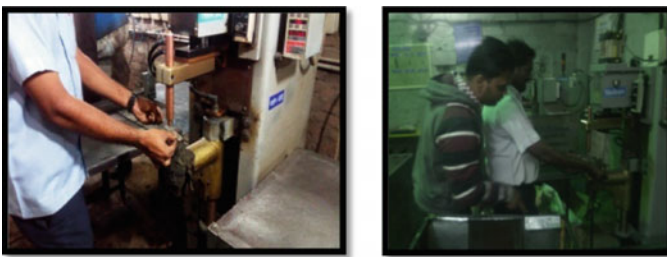
Fig. 1 Resistance spot welding machine setup

Table 1 Chemical composition of HR E-34

Element	%C	%Mn	%S	%P	%Si	%Al	%Nb	%Ti	%V	Iron
Composition (wt%)	0.1	0.7	0.03	0.03	0.2	0.02–0.06	0.055	0.045	0.095	Balance

3.2 Experimentation

Welding is carried out with resistance spot welding machine with supply 415 V, frequency 50 Hz with water-cooled chromium copper electrodes. Specimens are prepared of size $100 \times 20 \times 2$ mm and trial taken by spot welding process with above-mentioned parameters. Later on same specimens are tested for tensile strength on UTM machine.

$$\text{Weld strength} = \text{Breaking Load}/\text{Nugget shearing Area} = P/2\pi\,Dt$$

where D is Nugget diameter and $t = $ Thickness of specimen, $P = $ Breaking Load

4 Results and Discussion

4.1 Regression Analysis of Nugget Diameter

The mathematical model depicted by equation x is obtained by performing regression analysis on generated data during experimentation. The regression equation is

$$\text{Nugget diameter} = 2.56 + 0.0075\,\text{Weld Cycle} + 0.330\,\text{Current} - 0.390\,\text{Pressure}$$

4.2 Model Adequacy Test for Nugget Diameter

(See Tables 2 and 3).

$$S = 0.0983377\ R - Sq = 95.5\%\ R - Sq\,(\text{adj}) = 94.3\%\ R - Sq\,(\text{pred}) = 92.98\%$$

Table 2 Pre ANOVA model summary statics of nugget diameter

Predictor	Coef	SE coef	T	P
Constant	2.5603	0.4761	5.38	0.000*
Weld cycle	0.0075	0.01738	0.43	0.674*
Current	0.33	0.02318	14.24	0.000*
Pressure	−0.39	0.06954	−5.61	0.000*

*Denotes significant terms

Table 3 ANOVA model summary statics of nugget diameter

Source	DF	Contribution (%)	Adj SS	Adj MS	F-value	P-value	Remark
Model	3	95.52	2.2662	0.7554	78.12	0	
Linear	3	95.52	2.2662	0.7554	78.12	0	
Weld cycle	1	0.08	0.0018	0.0018	0.19	0.674	Less significant
Current	1	82.62	1.9602	1.9602	202.7	0	Most significant
Pressure	1	12.82	0.3042	0.3042	31.46	0	More significant
Error	11	4.48	0.10637	0.00967			
Lack-of-fit	9	2.54	0.06031	0.0067	0.29	0.922	
Pure error	2	1.94	0.04607	0.02303			
Total	14	100.00					
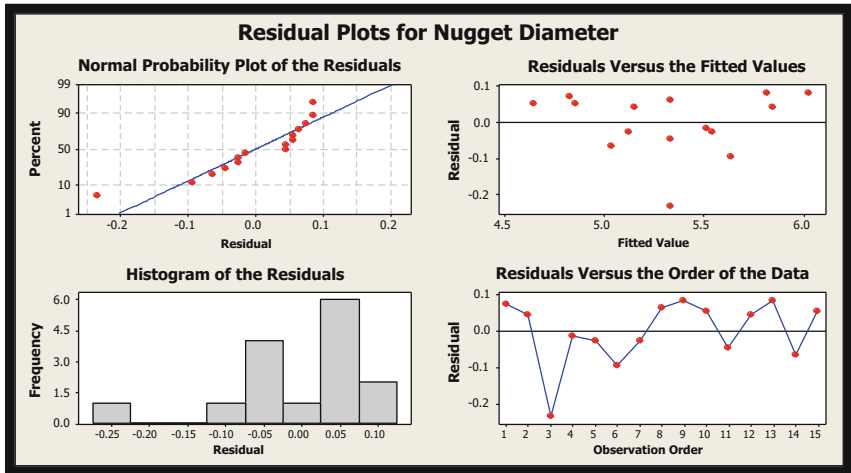
Graph 1 Residual plots for nugget diameter

4.2.1 Interpretation of Residual Graph

(See Graph 1).
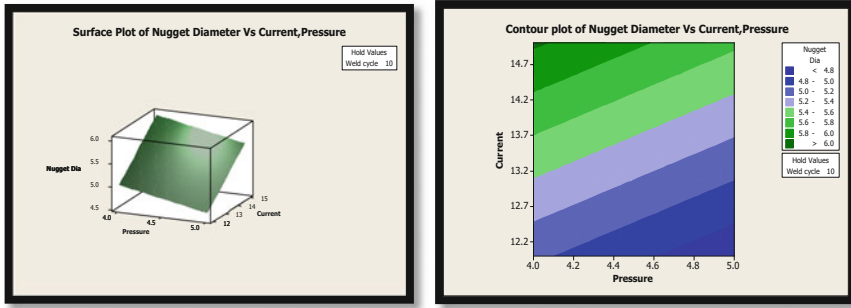
Fig. 2 Surface plot showing effect of current and pressure on nugget diameter

Table 4 Pre ANOVA model summary statics of tensile strength

Predictor	Coef	SE coef	T	P
Constant	159.63	12.11	13.18	0*
Weld cycle	3.9069	0.4421	8.84	0*
Current	−6.5855	0.5895	−11.17	0*
Pressure	19.481	1.769	11.01	0*

*Denotes significant term

4.3 Analysis of Nugget Diameter

The responses can be expressed graphically called surface plot or contour plots. Surface and contour plot can be obtained by taking responses in suitable plane against variables. Figure 2 depicts a 3-dimensional surface which shows the effect of current and weld cycle time on the value of nugget diameter under the pressure 4.5.

4.4 Regression Analysis of Tensile Strength

The mathematical model depicted by equation x is obtained by performing regression analysis on generated data during experimentation. The generated regression equation for tensile strength is given by

Tensile Strength = 160 + 3.91 Weld Cycle − 6.59 Current + 9.5 Pressure

4.5 Model Adequacy Test for Tensile Strength

(See Tables 4 and 5).

Table 5 ANOVA model summary statics of tensile strength

Source	DF	Contribution (%)	Adj SS	Adj MS	F-value	P-value	Remark
Model	3	96.72	2028.06	676.019	108.06	0	
Linear	3	96.72	2028.06	676.019	108.06	0	
Weld cycle	1	23.29	488.44	488.438	78.08	0	Less significant
Current	1	37.23	780.64	780.639	124.79	0	Most significant
Pressure	1	36.20	758.98	758.98	121.33	0	More significant
Error	11	3.28	68.81	6.256			
Lack-of-fit	9	3.14	65.78	7.309	4.82	0.184	
Pure error	2	0.14	3.04	1.518			
Total	14	100.00	2096.87				
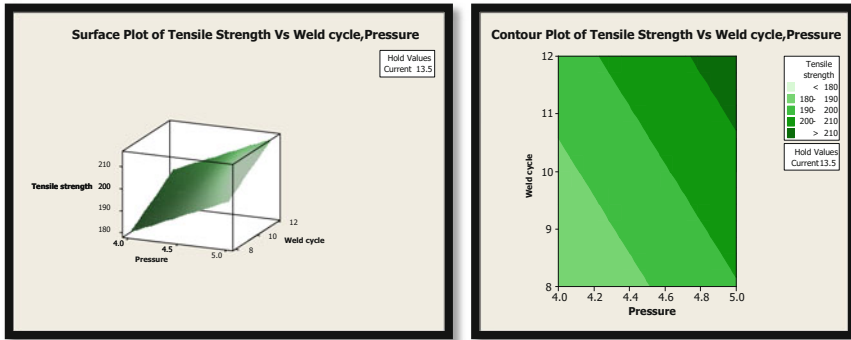
Fig. 3 Surface plot and contour plot showing effect of pressure and weld cycle on tensile strength

$$S = 2.50113 \ R - Sq = 96.7\% \ R - Sq\,(\text{adj}) = 95.8\%$$
$$R - Sq\,(\text{pred}) = 93.12\%$$

4.6 Analysis of Tensile Strength

(See Figs. 3 and 4).
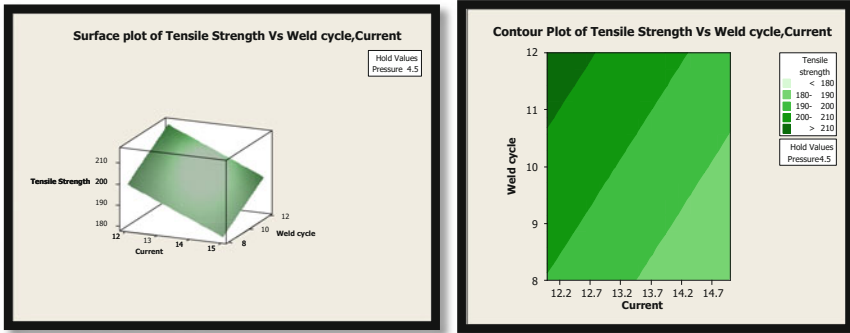
Fig. 4 Surface plot showing effect of current and weld cycle on tensile strength
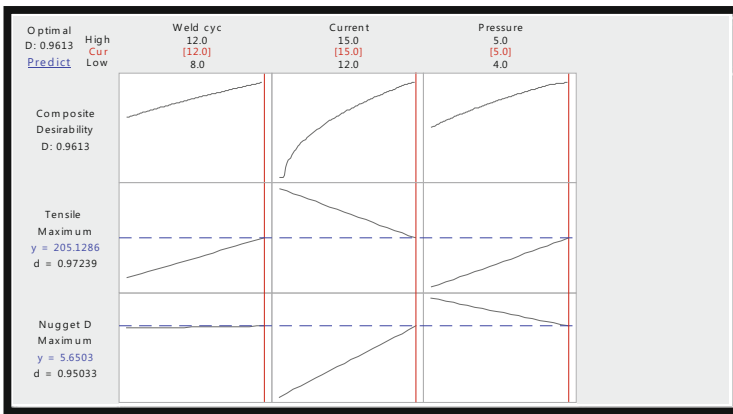
Graph 2 Optimization plot for nugget diameter and tensile strength

5   Confirmation Test

Confirmation test is performed in order to verify the difference between optimized values predicted by RSM's D-optimization Method and the values obtained through conducting experiment by using parameters level setting for optimal performance of both the responses. Table 6 shows the results obtained through experimentation and prediction by model, also prediction error in terms of % is calculated. It is observed that experimentally obtained values are in close proximity with predicted values of both the responses (Graph 2).

The feasible solution obtained is accepted for production trial on the resistance spot welding machine. Trial done on successive product lot and survey done regarding qualitative issues of weld obtained by resistance spot welding.

Table 6 Result of the confirmation experiment

S. No.	Actual factors			Nugget dia. (mm)		Pred. error %	Tensile Strength (N/mm^2)		Pred. error %
	Weld cycle	Current	Pressure	Predicted	Actual		Predicted	Actual	
1	12	15	5	5.65	5.68	0.53	205.12	206.62	0.73

6   Conclusions

In this Investigation, tensile strength and nugget diameter were optimized in the resistance spot welding process of hot rolled E-34 material. The generated empirical models yield to the following conclusions:

(1) The outcomes of analysis of variance and coefficient of determination for nugget diameter $= 0.95$ and for tensile strength $= 0.96$ represent that the fitted regression models moderately determine the responses.

(2) Optimum results have been found by using response surface method for tensile strength and nugget diameter are at weld cycle of 12 cycles, current of 15 KA, and pressure of 5 kg/cm^2, so by using this combination of input parameter we can reduce various types of defects and error produced during resistance spot welding operation.

(3) Rationalization of machining parameters is done for the responses in the resistance spot welding machine process of Hot Rolled E-34 material. Since by using proper combinations of input parameter values we can overcome various defects in welding and process is improved.

(4) The percentage contribution of weld strength and nugget diameter for weld current, pressure, and weld cycle is found as 37.23, 36.2, 23.29% and 82.62, 12.82, 0.08%, respectively.

References

1. Nizamettin Kahraman, "The influence of welding parameters on the joint strength of resistance spot-welded titanium sheets", Materials and Design, 28 (2007). 420–427.
2. S. Aslanlar, "The effect of nucleus size on mechanical properties in electrical resistance spot welding of sheets used in automotive industry", Materials and Design, 27 (2006), 125–131.
3. Vural, A. Akkus, B. Ery¨urek," Effect of welding nugget diameter on the fatigue strength of the resistance spot welded joints of different steel sheets", Journal of Materials Processing Technology 176 (2006), 127–132.
4. L. Han, M. Thornton, D. Boomer, M. Shergoldc, "A Correlation Study of Mechanical Strength of Resistance Spot Welding Of AA5754 Aluminium Alloy", Journal of Materials Processing Technology 211 (2011), 513–521.
5. S. M. Hamidinejad, F. Kolahan, A. H. Kokabi, " The modeling and process analysis of resistance spot welding on galvanized steel sheets used in car body manufacturing", Materials and Design 34 (2012), 759–767.
6. Zhao D, Yuanxun Wang, Xiaodong Wang, Xuenong Wang, Fa Chen, Dongjie Liang, "Process analysis and optimization for failure energy of spot welded titanium alloy", Materials and Design 60 (2014), 479–489.

Numerical Simulation Over Conical Aerospike at Mach 6

Rahul S. Pawar, N. R. Gilke and Vivek P. Warade

Abstract Hypersonic missiles unite the speed of ballistic missiles together with the precision and maneuverability of cruise missiles. By cruising at hypersonic speed in the atmosphere, the blunt nose of missile encounters large surface heating and a great amount of drag. This drag force can be reduced by employing a structure known as aerospike. This spike is connected in front of the body that changes the flow field and influences aerodynamic drag at hypersonic speeds. In the current paper, the performance of conical aerospike for various L/D (Length to Diameter) ratios is examined by using computational fluid dynamics (CFD) approach. The CFD analysis is executed to analyze the effect of drag, lift, and pitching moment coefficient onto the blunt body with and without implementation of an aerospike. However, the addition of a conical aerospike in front of the blunt body has an advantage for the reduction in drag subjected to the angle of attack, but increase in pitching moment has to be taken into consideration.

Keywords Conical aerospike · L/D ratios · Angles of attack

1 Introduction

Vehicles traveling at hypersonic speeds need to be constructed to run at the given aerodynamic conditions. The vehicles like space plane, missiles, launch vehicles, etc. usually have a blunt nose bodies traveling at supersonic and hypersonic speeds. Due to this, a huge amount of aerodynamic drag is levied onto these vehicles, thus leading to the malfunctioning of the vehicle due to the presence of strong bow shock wave in the vicinity of the blunt nose. This aerodynamic drag, in turn, leads to material damage to nose body. So, it is worthwhile to have a vehicle with a lesser drag in

R. S. Pawar (✉) · N. R. Gilke
K. J. Somaiya College of Engineering, Mumbai 400 077, India
e-mail: pawar.rs@somaiya.edu

V. P. Warade
Zeus Numerix Pvt. Ltd., Pune 411 057, India

order to decrease the requirement of thrust from the propulsive system. It is reliable to implement an aerospike for the reduction of the drag, since it alters the strong bow shock wave into weaker conical shock waves and thereby forming a low-pressure region which shields the blunt body from aerodynamic drag [1]. Investigations are still in process to analyze the effects of an aerospike by varying its shape, size, and blunt nose arrangements.

An oblique shock wave is emitted from the front portion of aerospike which relocates itself from the blunt nose of the body. This occurs due to the shape of the aerospike, thereby generating a recirculation region next at the origin of aerospike up to the reattachment point at the shoulder of the blunt body [2]. If this reattachment point is transferred backward or expelled from the blunt body shoulder, it results in the reduction of drag [3].

Various investigations are processed till date to improve the utility of an aerospike for reduction of drag. Jackson R. Stalder and Helmer V. Nielsen executed the examination with the conical-nosed spikes of semi-apex 10° and L/D ratio of 0.5–2.0 [4]. Davis H. Crawford reported the flow field over a hemispherical spike which was scrutinized at a Mach number of 6.8 and at a Re range (established on flow conditions and the diameter of the model). He also described about the pressure circulation in the locality of the blunt body related to the region of separation and the region of reattachment for shock waves [5]. Noboru Motoyama et al. explained the effects related to the spike length, form, and nose arrangement at various angles of attack for reduction of drag, which was experimentally studied with the employment of a hypersonic wind tunnel at the Department of Aeronautics and Astronautics, University of Tokyo [3].

R. Kalimuthu, et al. carried out the results for the spike length, form, and nose arrangement at various angles of attack on account for the reduction of drag. This was examined experimentally by use of the hypersonic wind tunnel. The effects of these parameters onto spike at various angles of incidence onto the aerodynamic coefficients were inspected using schlieren pictures and measuring aerodynamic forces [2]. G. d'Humières and J. L. Stollery enlightened about a simple model built for reduction of pressure drag generated at blunt cone and showed good settlement with experimental data. They studied about conical aerospike in their research work [6]. M. Barzegar Gerdroodbary and S. M. Hosseinalipour described the different shapes and lengths employed onto aerospike to inspect the effect of the flow field on the blunt nose of the body [7].

M. Y. M. Ahmed and N. Qin explained that aerospikes were efficient for minimizing drag and heating onto the blunt nose of the body. In their survey, the numerical examination was directed onto the hemispherical body which was equipped with a conical aerospike and the hemispherical aerodisk of various sizes in hypersonic freestream conditions for diverse L/D ratios and angles of incidences [1]. M. Y. M. Ahmed and N. Qin in another paper discussed that the aerospike substitutes the bow shock with the organization of conical shocks by creating a zone of recirculation flow in the front portion of the blunt body, thereby reducing both drag and aeroheating by performing numerical simulations for various L/D ratios and angles of incidences [8].

The primary objectives of the current study are to visualize the shock wave structure around the blunt nose with aerospike and to study the influence of different *L/D* ratios as well as angles of attack for aerospike on account of drag reduction. These objectives are discussed in the succeeding sections.

2 Geometric Modeling and Grid Generation

While executing any CFD simulation, there are many constraints needed to be taken into account. Development of the model is the first stage to be considered. In the second stage, the mesh is to be generated, which is either structured or unstructured mesh type. In the next stage, the boundary conditions for each surface need to be defined.

To safeguard the accuracy of the solution, an accurate boundary condition setup is important. The meshing process is completed by exporting the mesh file into solver software. In solver, the turbulence model and fluid properties need to be carefully picked out to calculate the fluid behavior in the organization.

2.1 Geometry Details

The blunt body diameter (D) is considered to be 0.04 m, length of the body ($L0$) is considered to be 1.25D, and the Reynolds number is considered as 9.79×10^6 [2]. Details of blunt geometry and conical aerospike geometry relations are illustrated in Figs. 1 and 2, respectively.

The shape of fluid domain is considered as cylindrical in shape and length of the domain is 17D and diameter is 10D. The diameter of the domain is considered long enough for visualization shock wave phenomenon in front of the body and to reduce the backward flow of the velocity.

Fig. 1 Blunt body geometry relations [2]
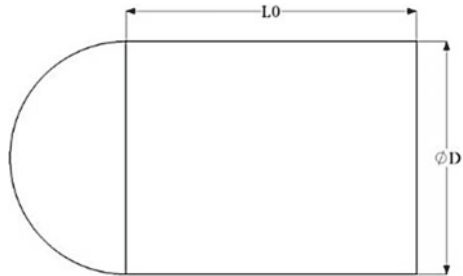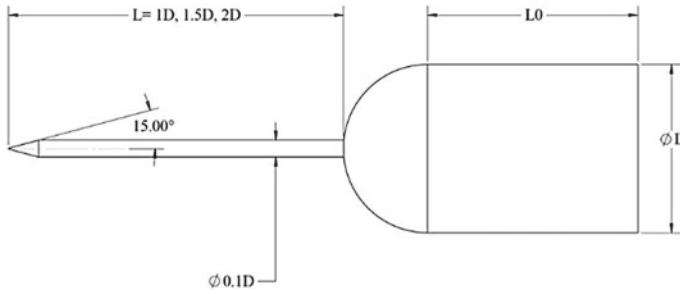
Fig. 2 Conical aerospike geometry relations [2]

Fig. 3 Surface mesh of
blunt body
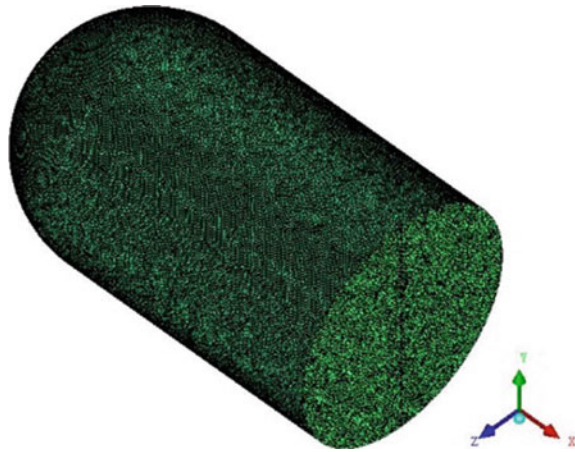
2.2 Mesh Generation

Referable to the presence of complexities in the geometry, the unstructured mesh is
chosen. But to get the behavior of fluid near the wall, prism-layered mesh is used.
Prism-layered mesh has been employed for generating the boundary layer elements
around the whole body. Its primary function is to capture the key variables such as
pressure, velocity, or temperature which experiences a quick change in the flow field.
Hence, the mesh type generated is hybrid mesh. The $y+$ value for generation of prism
layer is treated as 1 (as required by the turbulence model [7]), along with growth
ratio of 1.2 and number of layers as 18. Tetrahedral and pyramid meshes are usually
used for generating nodes and components in the fluid domain. The surface mesh
and volume mesh for the blunt body are as shown in Figs. 3 and 4.

Fig. 4 Prism layer over the blunt body
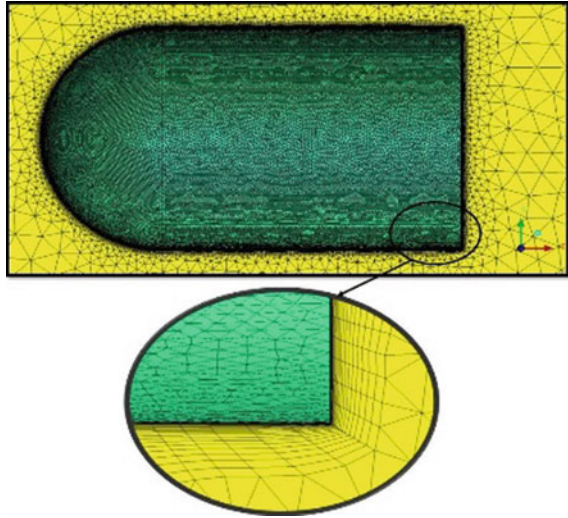
Table 1 Solver parameters of the body

Solver	Density-based
Analysis type	3D
Turbulence model	Spalart-Allmaras
Fluid type	Air
Time	Steady state

2.3 Flow Field Conditions

The computational results are reliant on the boundary conditions imposed. The flow of velocity is taking place in positive X-direction and is flowing through the inlet face of the domain, then impinged onto the blunt body or aerospike body, and finally coming out of the outlet face. The boundary conditions required for the current study are: the inlet face as velocity inlet, the cylindrical face and outlet face as pressure far field and body along with spike are given as no-slip wall boundary condition. The solver parameters used for numerical simulations are presented in Table 1.

3 Grid Independence Test and Validation

After simulations, the solutions obtained are having residuals of order three for mass, momentum, and energy equations. Also, the pressure and friction forces acting on the models were monitored and converged. Coefficients of drag, lift, and pitching moment are calculated using these equations [9].

Table 2 CFD results of grid independence test

Mesh type	Number of elements	CFD simulation C_d	Literature experimental C_d	% |Error|
Coarse	1,528,373	0.8690	0.89	2.35
Medium	3,242,393	0.8907	0.89	0.07
Fine	6,395,146	0.8904	0.89	0.04

$$F_x = \frac{1}{2} \times C_x \times \rho \times A \times V^2 \tag{1}$$

$$F_y = \frac{1}{2} \times C_y \times \rho \times A \times V^2 \tag{2}$$

$$C_d = C_x \times \cos\alpha + C_y \times \sin\alpha \tag{3}$$

$$C_\mathrm{l} = C_y \times \cos\alpha - C_x \times \sin\alpha \tag{4}$$

$$F_m = \frac{1}{2} \times C_m \times \rho \times A \times V^2 \times l \tag{5}$$

where F_x and F_y are forces acting in X and Y direction (N); F_m is pitching moment (Nm); ρ, A, and V are density (kg/m^3); area of cross-section (m^2) and velocity of an object (m/s); l is the reference length of model (m); C_x and C_y are coefficient of forces along X and Y direction; C_d, C_l, and C_m are coefficients of drag, lift, and pitching moment; α is angle of attack/incidence (in degrees).

3.1 Grid Independence Test

The grid independence test is done to study the consequences of mesh size over the computation results obtained. The grid independence test is implemented on the same body, same domain, and same boundary conditions. Generally, three different kinds of mesh are used for studying the grid independence, i.e., coarse, medium, and fine mesh. The usual CFD practices start with the coarse mesh and gradually refines it till the fine mesh by changing the element sizing. The size of the mesh is refined until the results for coefficient of drag approaches the literature experimental value for the coefficient of drag. This computational study is carried out using CFD Expert-Lite™ solver (developed by M/s Zeus Numerix Pvt. Ltd.) The CFD simulation results for three types of mesh are shown in Table 2. It can be observed that the obtained value of the coefficient of drag for the medium and fine mesh is nearly similar. So medium mesh is preferred for further analysis. If the fine mesh is selected, it will increase the number of elements which in turn increases the computational time.
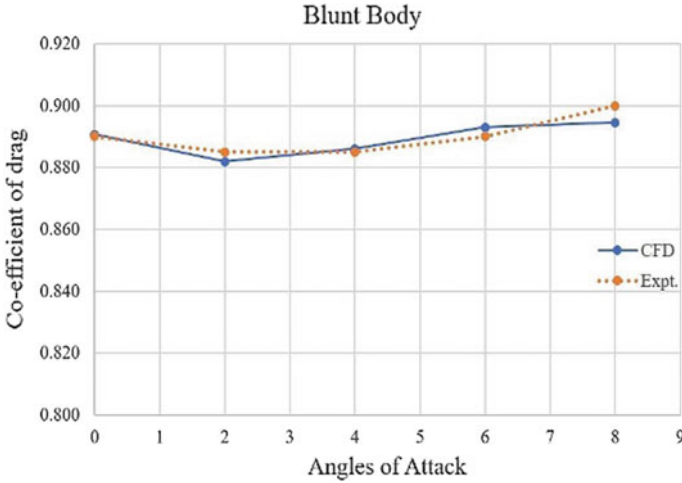
Blunt Body

Fig. 5   Validation of CFD result with experimental result

3.2   *Validation*

The validation is done by comparing the present computational result with the literature experimental result for the blunt body at different angles of incidence. It is observed that the coefficient of drag (C_d) of the computed result and experimental result [2] for different angles of attack are near to each other as shown in Fig. 5.

4   Results and Discussion

4.1   *Flow Field Visualization*

In this section, the numerical flow pattern is validated with the experimental flow pattern. In conical aerospike case, the conical shock wave is generated at the tip of conical aerospike. The conical shock wave produced from aerospike is mainly reliant on the angle of incidence. The blunt body is completely enclosed within the zone of recirculation. The phenomenon for the shaping of the shock wave is due to the geometry of the aerospike, which generates an oblique shock wave at the tip of aerospike and thereby generating a recirculation region in between the origin of aerospike up to the point of reattachment at the shoulder of the nose of blunt body. Hence, if this reattachment point can be shifted backward or expelled from the shoulder of the nose body, there are chances for the reduction in drag.

The contour plots describe for reduction of drag due to increase in the separation region in front of the conical aerospike. The oblique shock wave which is generated

Fig. 6 Comparison between CFD and Experimental Mach plot
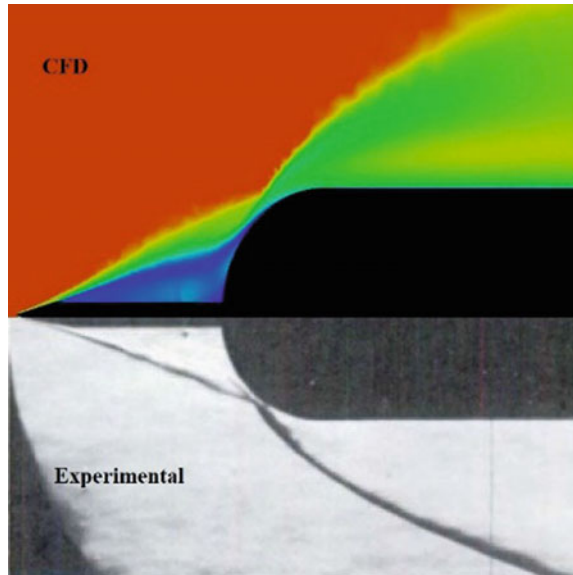
in front of the conical aerospike will reduce the drag. Motoyama et al. [3] also experimentally witnessed that a conical shock wave is produced due to the conical aerospike and a large recirculation zone developed at the origin of the aerospike. The comparison between the CFD and Experimental Mach plot for conical aerospike at an *L/D* ratio of 1.5 and zero angle of incidence is illustrated in Fig. 6.

Surface flow contours for Pressure and Mach number over blunt body and conical aerospike were obtained for the *L/D* ratios of 1, 1.5, and 2, at zero angle of incidence and Mach 6, as illustrated in Figs. 7 and 8. Figure 7 represents pressure distribution over blunt body and conical aerospike at midplane of body. For blunt body, there is a sudden increase in pressure at stagnant point which affects the velocity of the body. This indicates, there is development of bow shock wave in front of the blunt body. In conical aerospike case, the conical shock wave is generated from the tip of aerospike. The pressure acting onto tip of nose body for conical aerospike is lower as compared to the pressure acting directly on blunt body due to the presence of conical shock wave and the recirculation region formed due to the shape of aerospike.

Figure 8 represents Mach contour over blunt body and conical aerospike at midplane of body. For blunt body, there is formation of bow shock wave due to the presence of stagnant point in front of the blunt body. Whereas in case of conical aerospike, the oblique shock wave generated due to the shape of aerospike which shields the nose of body and as *L/D* ratio increases, the reattachment point is shifted away from the shoulder of the nose body, thereby reducing drag.
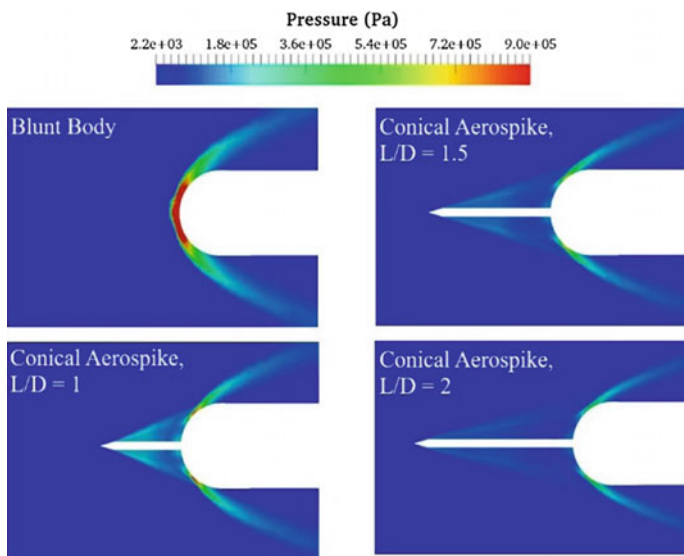
Fig. 7 Pressure contour for blunt body and Conical aerospike at angle of attack = 0°
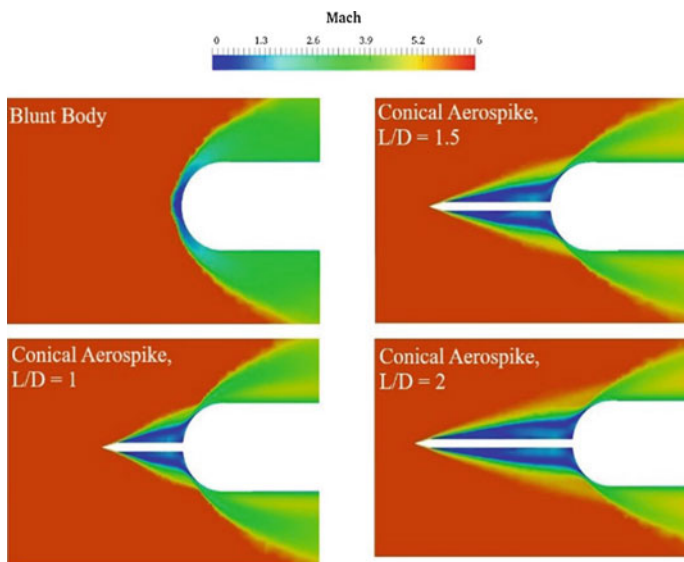
Fig. 8 Mach contour for blunt body and Conical aerospike at angle of attack = 0°
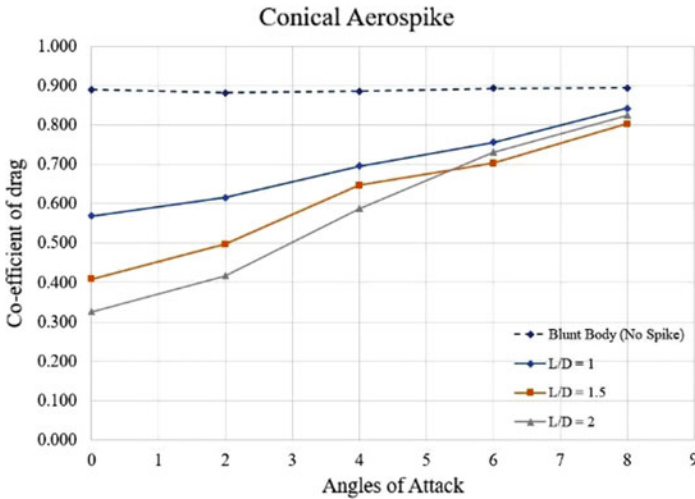
Fig. 9 Comparison between the coefficient of drag versus angles of attack

4.2 Effect of Conical Aerospike on Angle of Attack

A comparative study of drag onto the blunt body and aerospike implemented body configurations for angles of attack ranging from 0° to 8° can be observed in Fig. 9. An important inference can be made that the implementation of aerospike is beneficial for the reduction in drag when the body is subjected to an angle of incidence. It is observed that the implementation of aerospike has a smaller coefficient of drag as compared to the blunt body. This is caused due to the existence of recirculation region in between the origin of aerospike up to the point of reattachment at the shoulder of the nose body. As the angle of attack increases, the flow over the aerospike becomes uneven and hence changes the intensity of recirculation region.

The coefficient of lift tends to rise as angle of attack increases, as shown in Fig. 10. Also, a comparative study is performed on pitching moment coefficient on the blunt body and aerospike implemented body configurations for angles of incidence ranging from 0° to 8°. It can be observed from Fig. 11 that when the blunt body with conical aerospike is at angle of incidence, it is subjected to large pitching moment raised from the aerospike. Hence, as the angle of attack increases, the pitching moment coefficient further increases. It is a vital point to be considered for counterbalancing the added pitching moment for utilization of the aerospike as the angle of attack increases [6].
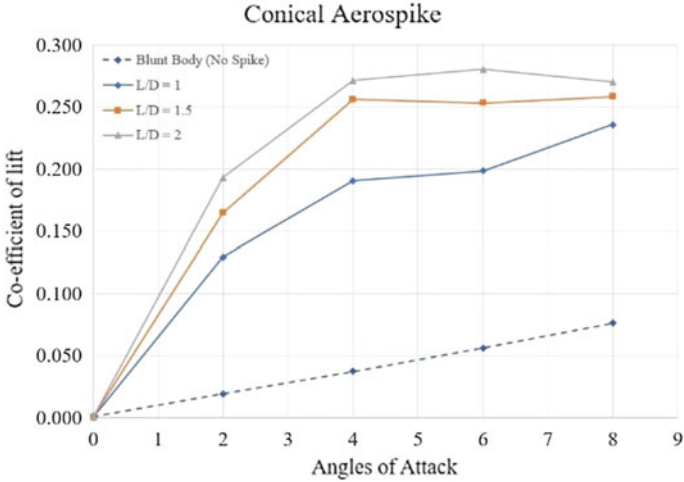
Fig. 10 Comparison between the coefficient of lift versus angles of attack
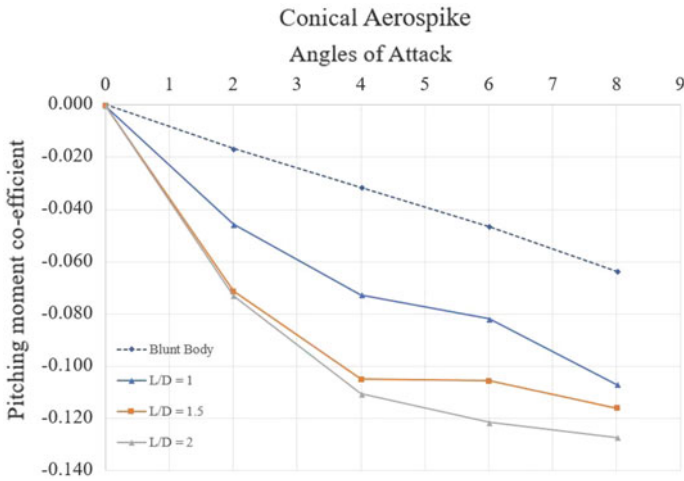
Fig. 11 Comparison between pitching moment coefficient versus angles of attack

5 Conclusion

The study shows that there is formation of zone of recirculation immediately behind the conical aerospike. Also, if the reattachment point is shifted backward or expelled from the shoulder of the blunt body, there are chances for the reduction in drag. Hence, the aerodynamic drag imposed onto the blunt body is greatly affected by choosing the optimal aerospike length. From CFD results, it can be observed that the aerospike produces 36.1%, 54%, and 63.4% reduction in drag for the *L/D* ratios of 1,

1.5, and 2, respectively (which is maximum at zero angle of attack). Also, considering the effects for drag reduction and lift increment without considering aerodynamic stability, the conical aerospike with an *L/D* ratio of 2 is more effective as compared to *L/D* ratios of 1 and 1.5, respectively. But, increase in pitching moment due to aerospike attached needs to be taken into account for study.

References

1. M. Y. M. Ahmed and N. Qin. Drag Reduction Using Aerodisks for Hypersonic Hemispherical Bodies. Journal of Spacecraft and Rockets, Vol. 47, No. 1, January–February 2010.
2. R. Kalimuthu, R. C. Mehta, E. Rathakrishnan. Experimental investigation on spiked body in hypersonic flow. The Aeronautical Journal, Vol. 112, No. 1136, October 2008.
3. Noboru Motoyama, Ken Mihara, Ryo Miyajima, Tadaharu Watanuki and Hirotoshi Kubota. Thermal protection and drag reduction with use of spike in hypersonic flow. American Institute of Aeronautics & Astronautics, Kyoto, Japan, AIAA 2001-1828, April 2001.
4. Jackson R. Stalder and Helmer V. Nielsen. Heat transfer from a hemisphere cylinder equipped with flow-separation spikes. National Advisory Committee for Aeronautics, Technical Note 3287, September 1954.
5. Davis H. Crawford. Investigation of the flow over a spiked nose hemisphere cylinder at M = 6.8. National Aeronautics and Space Administration, Washington, NASA TN-118, December 1959.
6. G. d'Humières, J. L. Stollery. Drag reduction on a spiked body at hypersonic speed. The Aeronautical Journal, Vol. 114, No. 1152, February 2010.
7. M. Barzegar Gerdroodbary, S. M. Hosseinalipour. Numerical simulation of hypersonic flow over highly blunted cones with spike. ACTA Astronautica 67, pp. 425–449, 2010.
8. M. Y. M. Ahmed, N. Qin. Recent advances in the aero-thermodynamics of spiked hypersonic vehicles. Progress in Aerospace Sciences 47, pp. 425–449, 2011.
9. John D. Anderson Jr. Computational Fluid Dynamics – The basics with Applications. McGraw-Hill Inc., 1995.

Multi-characteristics Optimization in the Turning of GFRP Composites Based on Grey-Taguchi Method

Hari Vasudevan, Ramesh Rajguru and Kalpesh Tank

Abstract Glass fibre reinforced polymer (GFRP) composites possess lightweight, high strength, high stiffness, good fatigues resistance and good corrosion resistance and are proven successful substitutes over traditional reinforcement methods. Due to the increasing demand of alternative materials in the industry, an in-depth research in the machining of GFRP is found necessary. Turning is the most practical machining operation for removing excess material to produce a well-defined and high-quality surface, and this study has used a glass fibre reinforced epoxy composite as material for the experimentation. In this study, a Taguchi's L_{27} orthogonal array was used for the experimental design. The turning parameters, such as tool nose radius, cutting speed, feed rate and depth of cut at three levels, were optimized with multiple performance considerations, such as force, material removal rate and surface roughness. Grey-Taguchi method enables the determination of the optimal combination of turning parameters for multiple process responses. Based on the analyses, the optimal cutting force, surface roughness and material removal rate were achieved, with the tool nose radius 1.2 mm, cutting speed 200 m/min, feed rate 0.05 mm/rev and depth of cut 1 mm (A3B3C1D2) for lesser cutting force and improved surface finish.

Keywords Grey relational analysis · CNC turning · Taguchi methodology
Woven fabric · GFRP

1 Introduction

Glass fibre reinforced polymer (GFRP) composites are extensively used in a variety of industrial applications, such as aerospace and automotive sectors, electrical

H. Vasudevan
D. J. Sanghvi College of Engineering, Vile Parle (w), Mumbai, India

R. Rajguru (✉) · K. Tank
Mechanical Engineering Department,
D. J. Sanghvi College of Engineering, Vile Parle (w), Mumbai, India
e-mail: ramesh.rajguru@djsce.ac.in

power generation and distribution systems. Composite materials have lightweight, high strength, high stiffness, good fatigues resistance and good corrosion resistance. With the forthcoming usage of glass fibre reinforced polymer (GFRP) composites in various areas of applications for making structural parts, machining of these materials has become a main concern for the manufacturing industries.

Vasudevan et al. [1] presented an overview of the various aspects, such as cutting mechanism, influence of tool material, tool geometry, surface quality and health and safety aspects in machining FRPS, involved in the conventional machining of GFRP types of composite material. Gupta and Kumar et al. [2] investigated turning of a unidirectional GFRP composite material using polycrystalline diamond tool (PCD). Three input variables were selected in the study to optimize the machining parameters involved in the process of turning for determining the minimum radial cutting force, the simulated annealing, and a meta-heuristic optimization technique was used. The results of this study revealed that the most significant machining parameters for radial cutting force are the depth of cut, followed by feed rate.

Altin et al. [3] presented the review article on machinability properties of GFRP and CFRP composite materials during conventional machining (turning, drilling, milling, etc.) and nonconventional machining. They stated that in the conventional machining of GFRP and CFRP composite materials higher compressive forces could be obtained as a result of increasing feed rate. In a review on the machinability of glass fibre reinforced polymer composite by Alessandra Caggiano, problems related with the conventional and unconventional machining process of composite materials such as delamination, uncut fibres, cracking are pointed out. Moreover, they proposed hybrid machining method to reduce machining defects [4]. Hussain et al. [5] investigated the machinability aspects such as surface roughness and cutting force of turning operation on glass fibre reinforced polymer composite tubes manufactured by filament winding process with altered fibre orientation using three different types of cutting inserts such as carbide, cubic boron nitride and poly-crystalline diamond. They concluded that better surface finish and lower cutting force are achieved by poly-crystalline diamond tool inserts followed by cubic boron nitride inserts.

Sivasankaran et al. [6] investigated on the influence of cutting parameters and workpiece type GFRP composite pipes with PCD tool during turning operation. The results revealed that good quality machinability was obtained at lower feed rate, cutting speed and depth of cut for E-Glass mat fibre reinforced GFRP pipe. Rajguru et al. [7] investigated the optimization of the drilling operation, using grey relational analysis coupled with Taguchi method to achieve minimum delamination and cutting force. They found that the optimal process parameters were achieved at spindle speed 1500 rpm, feed rate 75 mm/min, thickness 8 mm and drill size 6 mm. Vasudevan et al. [8] used Taguchi method with GRA for the optimization of turning operations with multiple performance characteristics. From the above studies, it has been found that the GRA is one of the important optimization techniques, and it could be successfully applied in machining processes, such as turning.

Quality and productivity are two important aspects, but often providing a trade-off in results, while performing machining operations. Hence, it becomes essential to evaluate the optimal cutting parameters setting in order to satisfy contradicting

requirements of quality and productivity. In this context, the aim of this research study was to analyze the problem of optimization of process parameters in CNC turning of woven fabric based glass fibre reinforced polymer (GFRP) composites using Grey Relational Analysis coupled with Taguchi method.

2 Experimental Details

2.1 Work Material and Cutting Tool

The specimen material used in conducting this experiment was GFRP/E composite as shown in Fig. 1. The work specimens were in tubular form with the dimensions of 50 mm long, inner diameter of 20 mm and outer diameter of 55 mm. Carbide inserts of fine grade were used as cutting tool for turning GFRP/E composite, manufactured by SANDVIK Coronmant.

2.2 Experimental Details

The experiments were planned using Taguchi's design of experiments (DOE) [9], and the input variable parameters for the experiment chosen were feed rate (mm/rev) 0.05, 0.15, 0.25, depth of cut (mm) 0.6, 1, 1.6, tool nose radius 0.4, 0.8, 1.2 and cutting speed (m/min) 120, 160, 200. The responses chosen were cutting force, surface roughness parameters (Ra) and MRR. The process of turning was done on an Ace Jobber XL CNC machine, as shown in Fig. 2.

The cutting force generated during the turning operation was measured with Kistler dynamometer. The surface roughness measurement of the machined components was done on Taylor Hobson Talysurf-5, machine set up with data acquisition by Se-surf software and the results are given in Table 1. Material removal rate (MRR)

Fig. 1 GFRP/E composite

Fig. 2 Experimental setup

could be calculated from the difference in weights of the workpieces before and after the experiment.

3 Multi-response Parametric Optimization

The grey system theory was proposed by Deng in 1982. This theory is suitable for handling various problems with meagre, inadequate and ambiguous information. The grey relational analysis (GRA) based on this theory can be productively adopted for solving multi-objective optimization problems. Grey relational grade (GRG) calculated using this analysis is treated as the composite objective function for simultaneous optimization of multiple responses.

Three different equations are used for this normalization procedure, depending upon the type of quality characteristics. If the original sequence data has a quality characteristic as "larger-the-better", then it is pre-processed by using the following equation.

$$x_i^*(k) = \frac{x_i^0(k) - \min x_i^0(k)}{\max x_i^0(k) - \min x_i^0(k)} \tag{1}$$

$$x_i^*(k) = \frac{\max x_i^0(k) - x_i^0(k)}{\max x_i^0(k) - \min x_i^0(k)} \tag{2}$$

$$\gamma\left(x_0^*(k), x_i^*(k)\right) = \frac{\Delta\min + \xi\,\Delta\max}{\Delta_{ik} + \xi\,\Delta\max} \tag{3}$$

Table 1 Taguchi's L_{27} OA and the measured mean values of the responses

Experiment No.	Design of experiments				Force (N)	Ra (μm)	M.R.R.
	A	B	C	D			
1	1	1	1	1	30.72	3.411	236.80
2	1	1	2	2	47.94	2.619	1173.33
3	1	1	3	3	94.88	3.039	3086.22
4	1	2	1	2	34.84	2.925	521.48
5	1	2	2	3	66.41	2.516	2468.98
6	1	2	3	1	36.6	3.662	1578.67
7	1	3	1	3	35.91	3.023	1028.74
8	1	3	2	1	31.37	3.064	1184.00
9	1	3	3	2	62.4	3.566	3259.26
10	2	1	1	1	29.02	2.832	236.80
11	2	1	2	2	42.18	2.075	1173.33
12	2	1	3	3	86.57	3.956	3086.22
13	2	2	1	2	32.62	3.514	521.48
14	2	2	2	3	64.22	3.525	2468.98
15	2	2	3	1	30.8	2.921	1578.67
16	2	3	1	3	37.23	2.213	1028.74
17	2	3	2	1	27.85	2.692	1184.00
18	2	3	3	2	55.18	3.108	3259.26
19	3	1	1	1	24.8	2.321	236.80
20	3	1	2	2	39.56	3.621	1173.33
21	3	1	3	3	76.29	3.177	3086.22
22	3	2	1	2	29.54	1.785	521.48
23	3	2	2	3	54.83	4.543	2468.98
24	3	2	3	1	31.63	2.839	1578.67
25	3	3	1	3	36.82	2.247	1028.74
26	3	3	2	1	26.28	2.244	1184.00
27	3	3	3	2	46.43	3.186	3259.26

where, max $x_i^0(k)$ and min $x_i^0(k)$ are the maximum and minimum values, respectively of the original sequence $x_i^0(k)$. Comparable sequence $x_i^*(k)$ is the normalized sequence of original data. ξ is the distinguishing coefficient and $\xi \in (0, 1)$.

$$0 < \gamma\left(x_0^*(k), x_i^*(k)\right) \leq 1 \qquad (4)$$

$$\Gamma\left(x_0^*, x_i^*\right) = \sum_{k=1}^{n} W_k \gamma\left(x_0^*(k), x_i^*(k)\right); \qquad (5)$$

W_k is the weightage assigned by the experimenter to the quality attribute K. Equations 1 and 2 are used for normalization of MRR and surface roughness, respectively,

Table 2 Grey relational coefficient values of the responses and grade

Experiment No.	GRC values of responses			Grey relational grade	Rank
	(Force)	(Ra)	(M.R.R.)		
1	0.841	0.459	1.000	0.7665	5
2	0.597	0.623	0.617	0.6125	16
3	0.333	0.524	0.347	0.4012	26
4	0.766	0.547	0.841	0.7182	6
5	0.455	0.654	0.404	0.5042	19
6	0.738	0.424	0.530	0.5636	18
7	0.748	0.527	0.656	0.6439	13
8	0.828	0.519	0.615	0.6538	12
9	0.480	0.436	0.333	0.4166	24
10	0.876	0.568	1.000	0.8148	3
11	0.661	0.826	0.617	0.7015	10
12	0.362	0.388	0.347	0.3655	27
13	0.804	0.444	0.841	0.6965	11
14	0.468	0.442	0.404	0.4381	22
15	0.839	0.548	0.530	0.6390	15
16	0.728	0.763	0.656	0.7158	7
17	0.902	0.603	0.615	0.7067	9
18	0.532	0.510	0.333	0.4586	21
19	0.978	0.720	1.000	0.8993	2
20	0.695	0.429	0.617	0.5804	17
21	0.404	0.498	0.347	0.4161	25
22	0.865	1.000	0.841	0.9021	1
23	0.535	0.333	0.404	0.4239	23
24	0.823	0.567	0.530	0.6398	14
25	0.734	0.749	0.656	0.7132	8
26	0.940	0.750	0.615	0.7682	4
27	0.612	0.496	0.333	0.4806	20

and Eqs. 3–5 are used to calculate the grey relation coefficient and grey relation grade and recorded in Table 2 (Source: Deng [10]).

4 Results and Discussion

The analysis was conducted with the help of Minitab-17 to aggregate the influence of the machining parameters on surface roughness and material removal rate. It is

Table 3 Response table for GRG

	Level 1	Level 2	Level 3	Max–min (Δ)	Rank
A	0.5726	0.6010	**0.6320**	0.0594	2
B	0.6073	0.5835	**0.6158**	0.0323	4
C	**0.6420**	0.5818	0.5827	0.0602	1
D	0.6150	**0.6167**	0.5748	0.0419	3

concluded from Table 3 that the input variable setting of test number 22 has the highest GRG. Thus, the 22nd test gave the excellent multi-objective performance amongst the 27 experiments.

It is observed from the response table; the feed rate has the strongest effect on the multiple performance characteristics from amongst the other turning parameters, followed by nose radius. Based on the analyses, the optimal cutting force, surface roughness and material removal rate were achieved, with the tool nose radius 1.2 mm, cutting speed 200 m/min, feed rate 0.05 mm/rev and depth of cut 1 mm (A3B3C1D2) for lesser cutting force and improved surface finish.

5 Confirmation Tests

The overall mean of GRG (η) could be computed by using the following equations (Source: Madhav [11]).

$$\eta_{\text{opt}} = \bar{\eta} + (A_2 - \bar{\eta}) + (B_2 - \bar{\eta}) + (C_3 - \bar{\eta}) + (D_1 - \bar{\eta}) \tag{6}$$

where $\bar{\eta}$ = overall mean of GRG (η) = 0.61631; A_2 = average value of GRG (η) at third level of tool nose radius = 0.6320; B_2 = average value of GRG (η) at third level of cutting speed = 0.6158; C_3 = average value of GRG (η) for at first level of feed rate = 0.6420 and D_1 = average value of GRG (η) for a second level of depth of cut = 0.6167. Hence, the overall predicted value of mean was 0.65757. The average value of GRG was found to be 0.70486. This value is more than the predicted value of 0.65757. Hence, the optimal settings of the process parameters, as found by the investigation, could be implemented.

6 Conclusion

In this study, experimental investigation into the turning of GFRP epoxy based was conducted in order to optimize settings of the process parameters on surface roughness and material removal rate.

It is concluded from the response table that the feed rate has the strongest effect on the surface roughness and material removal rate amongst the other turning parameters, followed by nose radius. Based on the analyses, the optimal cutting force, surface roughness and material removal rate were achieved, with the tool nose radius 1.2 mm, cutting speed 200 m/min, feed rate 0.05 mm/rev and depth of cut 1 mm (A3B3C1D2) for lesser cutting force and improved surface finish.

References

1. Hari Vasudevan, Ramesh Rajguru, "A Review of Machining Processes and Machinability in the case of GFRP Composite Materials" in IPI journal (The official publication of Indian Plastics Institute), August/September 2013, Vol. 18, issue 3.
2. Gupta Meenu, S. Kumar "Prediction of cutting force in turning of UD-GFRP using mathematical model and simulated annealing" Front. Mech. Eng., 7 (4) (2012), pp. 417–426.
3. Altin Karatas M., Gokkaya H., "A review on machinability of carbon fiber reinforced polymer (CFRP) and glass fiber reinforced polymer (GFRP) composite materials" Defence Technology (2018).
4. Alessandra Caggiano "ReviewMachining of Fibre Reinforced PlasticComposite Materials" Materials 2018, 11, 442.
5. Syed AltafHussain, V. Pandurangadu, K. Palani Kumar "Machinability of glass fiber reinforced plastic (GFRP) composite materials" International Journal of Engineering, Science and Technology Vol. 3, No. 4, 2011, pp. 103–118.
6. S. Sivasankaran, P.T. Harisagar, E. Saminathan, S. Siddharth, P. Sasikumar, Effect of process parameters in surface roughness during turning of GFRP pipes using PCD insert tool, Procedia Engineering 97 (2014) 64–71.
7. Ramesh Rajguru, Hari Vasudevan and Naresh Deshpande "Multi-criteria optimization using Taguchi and Grey relational analysis in CNC drilling of GFRP/E composite material" in the International Conference on Advanced Manufacturing and Automation (INCAMA-2013, ISBN 978-93-80686-50-9) organised by the Department of Mechanical Engineering (DST-FIST Sponsored) Kalasalingam University, Madurai, Tamil Nadu from the 28th-30th March 2013.
8. Hari Vasudevan, Kalpesh and Mandar "Optimization of Material Removal Rate and Cutting Forces in Turning of GFRP composites" in the 6th International & 27th All India Manufacturing Technology, Design & Research Conference (AIMTDR–2016) held at College of Engineering, Pune during 16–18 December 2016.
9. Genichi Taguchi, Subir Chowdhury, Yuin Wu (2005) Taguchi's Quality Engineering Handbook, John Wiley & Sons, New Jersey.
10. Deng, J.L. (1989). Introduction to Grey system. Journal of Grey System, 1: 1–24.
11. Madhav S. Phadke (1989) Quality Engineering Using Robust Design, P T R Prentice-Hall, New Jersey.

Vibrational Analysis of Single-Point Cutting Tool for Different Tool Material and Nose Radius Using Design of Experiment

C. M. Choudhari, I. A. Bhisti, M. G. Choudhary and A. H. Mistry

Abstract The main objective of the paper is to study the vibrational analysis of a single-point cutting tool by varying the materials and nose radius. In this work, simulation-based experiments were performed through finite element analysis done by using ANSYS Workbench 18.2 software. Three different tool materials such as high-speed steel (HSS), stainless steel (SS) and cubic boron nitride (CBN) along with three tool nose radius such as 0.4, 0.6 and 0.8 mm have been selected as a significant process parameters affecting the performance of machining process. Cutting tool 3D model is prepared by taking existing cutting tool dimensions. Simulation is carried out in ANSYS 18.2 for suitable permutation and combination of material and nose radius for evaluating respective frequency. The results of the total deformation and frequency obtained through ANSYS software were further analyzed by using design of experiments on Minitab software, thereby generating a regression equation and resulting graphs were obtained.

Keywords ANSYS software · Design of experiments · Vibration analysis
Cutting tool · Nose radius

1 Introduction

In the modern world, manufacturing industries aim at manufacturing high quality, cost-effective products and heading towards automation. An essential part of a machining system is to control the tool wear or damage. Chatter and tool wear continue to be a problem, which in turn limit the productivity. In this project, FEM simulation technique is utilized to investigate the physical cutting process for predicting—vibration analysis of single-point cutting tool. There are various researches and great deal on single-point cutting tool analysis. FEM-based simulation helps us

C. M. Choudhari · I. A. Bhisti (✉) · M. G. Choudhary · A. H. Mistry
Department of Mechanical Engineering, Dwarkadas J. Sanghvi College of Engineering,
Mumbai 400056, India
e-mail: ankitmistry001@gmail.com
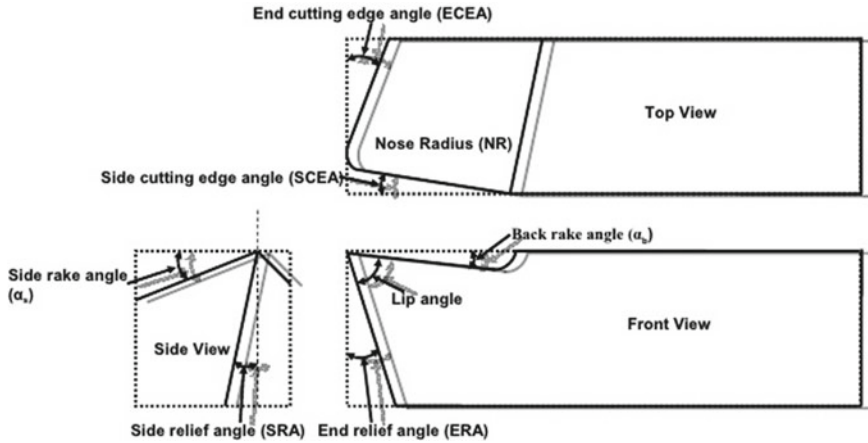
Fig. 1 Nomenclature of single-point cutting tool

with better understanding for deflection and vibration in cutting zones also provides with resulting stress and temperature fields.

1.1 Overview of Single-Point Cutting Tool

Cutting tool used for turning, boring, shaping and planning on lathes, etc., is a single-point cutting tool. Single-point cutting tool is shown in Fig. 1. Framework used for designating the cutting tool is nose radius back rake angle, side rake angle, end relief angle, end cutting angle, side cutting angle. Performance and life of cutting tool depend on above-mentioned parameters.

1.2 Literature Review

Geometry, orientation and material of the cutting tool are the three important factors that determine ease and performance of machining (machinability). There are various types of material available for cutting tool, such as stainless steels, alloy of cast cobalt, cemented cast, and coated carbides. The point of intersection of three surfaces such as rake surface, principal flank surface, auxiliary flank surface gives rise to the tooltip. Since tooltip is subjected to the severe cutting force during machining, so any sharp point may break quickly. By definition, nose radius is the radius value at the tip of the turning tool, measured on reference plane. Many research papers have been proposed related to the topic. Sinha et al. [1] have performed the vibrational analysis on mechanical component to improve the efficiency machine and to reduce

down time and mechanical failure. Patil [2] has consisted temperatures measured by experimental set-up during machining and calculated forces analytically for the same condition. Kumar et al. [3] have involved tool deflection and tool failure due to vibration while turning on lathe. Jadhav et al. [4] have identified the cutting forces and feed forces in turning process. Experiments were conducted on lathe machines and were studied with help of (ANOVA) based on adjusted approach. Özel et al. [5] have studied the effects of cutting edge geometry, *w/p* hardness, feed rate and cutting speed on surface roughness and result of forces in the finish hard turning of AISI H13 steel. Liu et al. [6] have represented a cutting forces prediction model in the end milling of GH4169, super alloy carbide tools by orthogonal experiment. Rao et al. [7] have included study of deflection and tool failure due to vibrations while turning on lathe. Experiments were performed with mild steel as workpiece and different tool material for which various machining forces have been measured. Rodrigues L. L. R et al. taking into reference to the aforementioned papers, this paper has been proposed about the difference in the techniques used to evaluate frequencies. The research is carried out by varying two parameters of tool and analyzing the achieved results by using the DOE. Vibration analysis on single-point cutting tool is done in various papers to find the critical frequency, but in this paper, we changed some crucial parameters such as materials and nose radius. By combination and permutation of different material with consistent change in nose radius, we analyzed virtually the change in the critical frequency for each nine combinations and finally find out the best combination of material and nose radius for critical frequency. This will let us know the optimum parameter which affects the critical frequency and threshold values which should be maintained in order to get the best results out of this experiment. Simulation has been performed using ANSYS 18.2 and Minitab18 software.

2 Methodology

In this study, methodology adopted is represented in following flow chart (Fig. 2)

2.1 *Geometric Model*

The cutting tool is modelled with the help of solid works software with the actual dimensions of existing cutting tool. Tool is made up of three different materials such as stainless steel (SS), high speed steel (HSS) and cubic boron nitride (CBN). Also, three different nose radius of tool has been followed viz. 0.6, 0.8, 1 mm. This will develop the nine numbers of permutation and combination to carry out simulating experiment.

```
┌──────────────┐      ┌──────────────┐      ┌──────────────┐
│  Geometric   │─────▶│  Analysis in │─────▶│Data collected│
│   Modeling   │      │    ANSYS     │      │ from ANSYS   │
└──────────────┘      └──────────────┘      └──────────────┘
                                                    │
                                                    ▼
┌──────────────┐      ┌──────────────┐      ┌──────────────┐
│   Minitab    │◀─────│Identification│◀─────│  Design of   │
│   Software   │      │  of factors  │      │  Experiment  │
└──────────────┘      └──────────────┘      └──────────────┘
       │
       ▼
┌──────────────┐            ┌──────────────────────┐
│   Results    │───────────▶│     Factor plots     │
└──────────────┘            └──────────────────────┘
                            ┌──────────────────────┐
                            │ Regression Equation  │
                            └──────────────────────┘
```
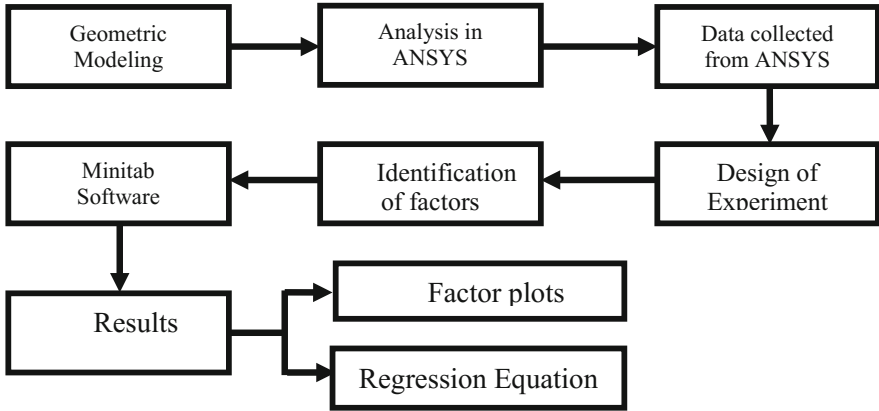
Fig. 2 Methodology for obtaining frequency and factor plots regression equation

Fig. 3 Meshing
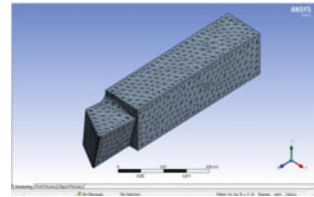
Fig. 4 Applying constraint
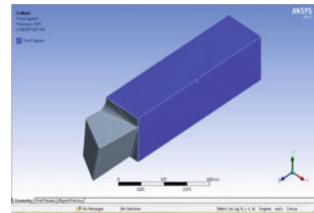
2.2 Analysis in ANSYS

Single-point cutting tool model was imported from the SolidWorks to ANSYS software. Body is divided into finite number of elements as shown in Fig. 3. Constraints are applied to tool in such a way that how it is inserted in tool post during turning operation as shown in Fig. 4. Results are obtained by doing vibration analysis. Frequency at different modes and deformation was obtained as shown in Fig. 5a large deformation was observed at the tip of the tool. Figure 5b shows deformation and frequency for all nine combinations.

(1) **Data collected from ANSYS**

(a)
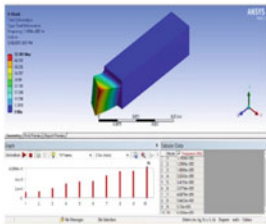
(b)

Stainless Steel		
Nose Radius 0.4mm Frequency – 4848 Hz	Nose Radius 0.6mm Frequency - 4855.5 Hz	Nose Radius 0.8mm Frequency -4855.6 Hz
High Speed Steel		
Nose Radius 0.4mm Frequency - 4848 Hz	Nose Radius 0.6mm Frequency - 4693.6 Hz	Nose Radius 0.8mm frequency- 4693.7 Hz
Cubic Boron Nitride		
Nose Radius 0.4mm Frequency – 4848 Hz	Nose Radius 0.6mm Frequency - 3189.2 Hz	Nose Radius 0.8mm Frequency - 3189.5 Hz

Fig. 5 a Results, **b** deformation and frequency for all nine combinations of materials and nose radius

Vibration analysis was performed on ANSYS Workbench18.2 software. Highest value of frequency observed is highlighted in table below corresponding to combination of tool materials and nose radius.

Above figure shows simulation of three different materials (SS, CBN, HSS) for corresponding nose radius of 0.4, 0.6 and 0.8 is carried out. Result shows that frequency is different three materials and their nose radius.

2.3 Design of Experiment (DOE)

Design of experiments (DOE) is a systematic method to determine the relationship between factors affecting a process and the output of that process. In other words, it is used to find cause-and-effect relationship. It enables us for multiple input factors to be manipulated determining their effect on a desired output.

Identification of factors

As mentioned in previous section, three different tool materials such as stainless steel (SS), high-speed steel (HSS) and cubic boron nitride (CBN) along with three tool nose radius such as 0.4, 0.6 and 0.8 mm have been selected as a significant process parameters affecting the performance of machining process. Table 1a shows the input factors and their levels. Based on simulation result, frequency of vibration was obtained as mentioned in Table 1b for different combination of tool material and nose radius. The selection of a particular orthogonal array is based on the number of levels of various factors. Here, L9 orthogonal array is selected.

2.4 Minitab18 Statistical Software

Minitab is statistics software that often combined with the implementation of six sigma, Capability Maturity Model Integration (CMMI) and other statistics-based process improvement methods. Minitab can perform several function such as computation function, calculator function, generating data function, probability distribution function, matrix operation, design of experiments, data analysis function, statistic, regression analysis, Variance analysis, multivariable analysis and non-parametric estimation.

2.5 Results

a. Factor plot

In statistics, a full factorial experiment is an experiment whose design consists of two or more factors, each with discrete possible values or levels, and whose experimental units take on all possible combinations of these levels across all such

Table 1 a Levels of machining parameters, b combination of tool material and nose radius

Machining parameters	Code	Stage 1	Stage 2	Stage 3
(a)				
Tool materials	A	SS	HSS	CBN
Nose radius [mm]	B	0.4	0.6	0.8
(b)				

Expt. No.	Material	Nose radius (mm)	Response: frequency (Hz)
1	Stainless steel	0.4	4848
2	Stainless steel	0.6	4855.5
3	Stainless steel	0.8	4858.6
4	High-speed steel	0.4	4848
5	High-speed steel	0.6	4693.6
6	High-speed steel	0.8	4693.7
7	Cubic boron nitride	0.4	4848
8	Cubic boron nitride	0.6	3189.2
9	Cubic boron nitride	0.8	3189.5

Fig. 6 Response plot
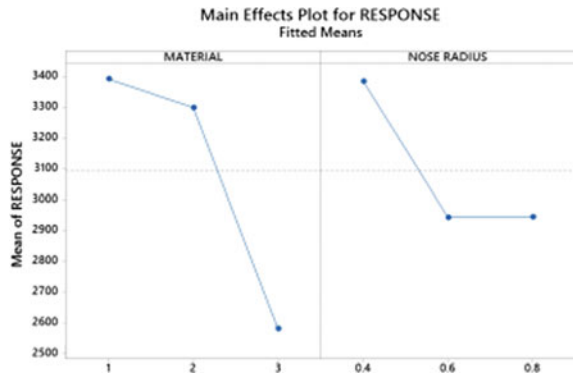
factors. Based on previous experiments and using Minitab software, following results are obtained as shown in Figs. 6 and 7.

b. Regression equation

Multiple regressions are a statistical tool used to drive the value of a criterion from several other independent, or predictor, variables. It is simultaneous combination of multiple factors to assess how and what extent they affect a certain outcome. The regression analysis is performed using statistical analysis software Minitab 14. It

Fig. 7 Interaction plot
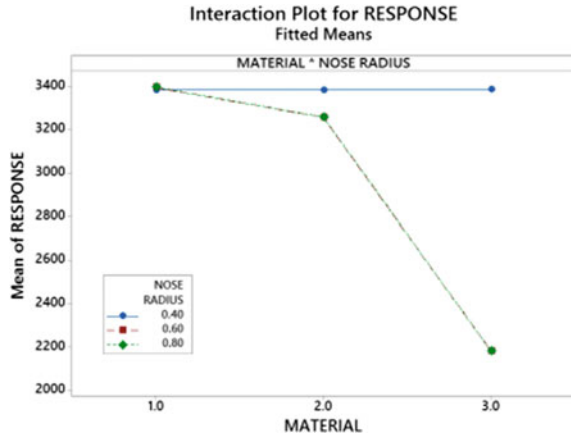
gives the relationship between ultimate tensile strength and hardness with mild chill size and pouring temperature.

Regression Equation (Response) = 4447 + 406.9 A_1 + 298.0 A_2-704.9 A_3 + 400.9 $B\_0.4$ − 201.0 $B\_0.6$ − 199.9 $B\_0.8$ − 406.9 $A*B\_1$ 0.4 + 202.5 $A*B\_1$ 0.6 + 204.4 $A*B\_1$ 0.8 − 298.0 $A*B\_2$ 0.4 + 149.5 $A*B\_2$ 0.6 + 148.5 $A*B\_2$ 0.8 + 704.9 $A*B\_3$ 0.4 − 352.0 $A*B\_3$ 0.6 − 352.9 $A*B\_3$ 0.

Regression equation indicates different coefficients for all variables used. Variable '406.9 A_1' needs to control primarily as it produces significant effect on desired result.

3   Results and Discussion

3.1   ANSYS Results

The aforementioned graph shows that there is not much effect of change in nose radius even though the materials are changed as shown in Figs. 8, 9 and 10.

3.2   Minitab Results

This is the main response plot obtained from the experiment performed. Figure 11 indicates the variation of the material and nose radius at different frequencies. Material 1 (SS) has been found to be more significant as compared to other two materials, and nose radius (0.4 mm) has been found to be more significant as compared to

Fig. 8 Stainless steel
frequency versus nose radius
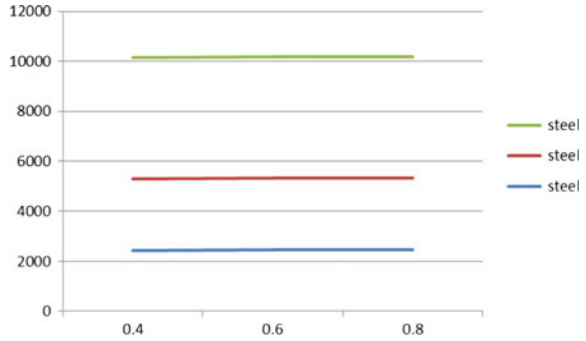
Fig. 9 High-speed steel
frequency versus nose radius
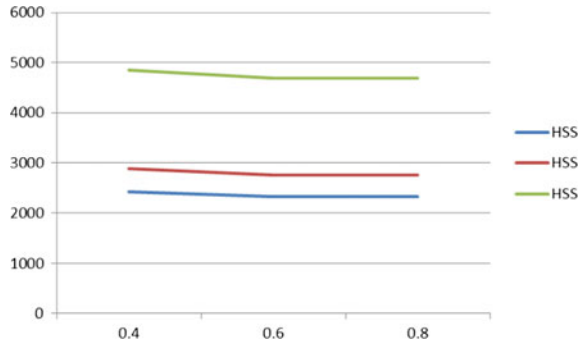
Fig. 10 Boron nitride
frequency versus nose radius
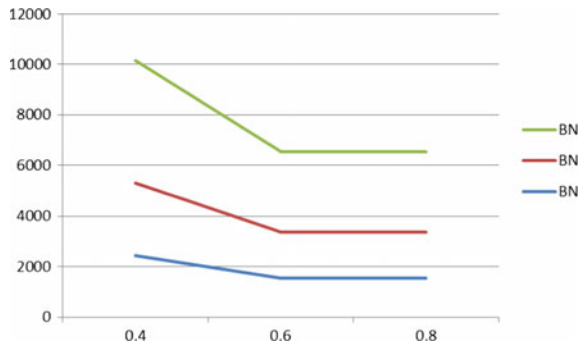
other two nose radius. Hence, material 1 and smaller nose radius is required to be
controlled.

Figure 12 shows the combined effect of material and nose radius on frequency. It
can be concluded that frequency of vibration remains constant for all three materials
at nose radius of '0.4 mm', and vibration frequency decreases with increase in nose
radius for selected materials. It is response data from DOE; hence, finding is taken
into account to identify critical parameter.

Fig. 11 Response plot

Main Effects Plot for response

Fig. 12 Interaction plot

Interaction Plot for response
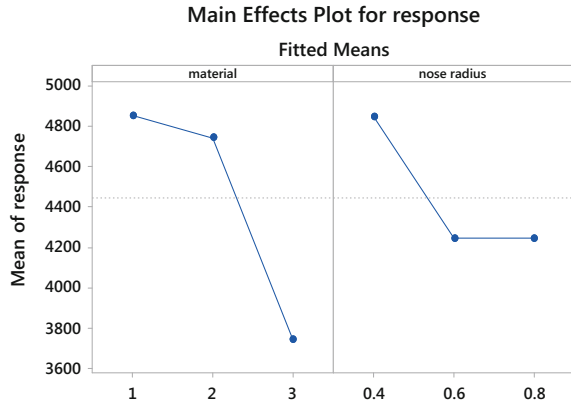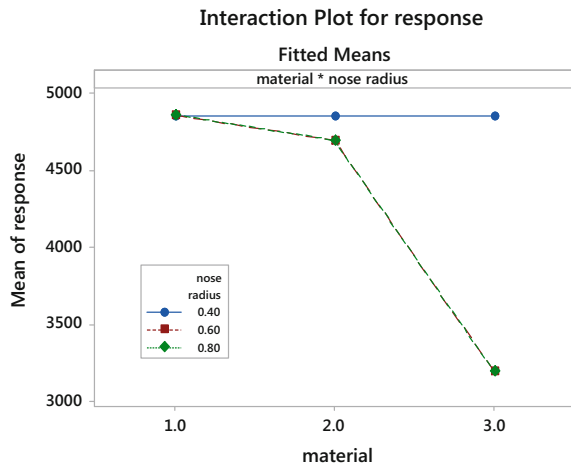
4   Conclusion

Vibration analysis on single-point cutting tool is done in various papers to find the critical frequency, but in this paper, we changed some crucial parameters such as materials and nose radius at different modes in the tool and find out the critical frequency. By combination and permutation of different material with consistent change in nose radius, we analyzed virtually the change in the critical frequency for each nine combinations and finally find out the best combination of material and nose radius for critical frequency. This will let us know the optimum parameters which effects the critical frequency the most as well as the threshold values which should be maintained in order to get the best results out of these experiments. The above experiments are performed using ANSYS Workbench18.2 and design of experiments under Minitab software. Since this study is based simulation approach using ANSYS, software has been observed to be less time-consuming and cost saving. Otherwise,

constitution of nine experiments in physical form would have been time consuming and costly. But in order to validate, we required the optimum configuration to be checked, and hence, one trial as resulted from above finding will be sufficient. Significance of statistical data as DOE is well explained.

In all cited literature and hence performing statistical experiments are cost effective at the same. As per literature, it has been observed results given by DOE are almost similar. Experimental investigation which is costly and time-consuming.

References

1. Prabhat Kumar Sinha, Rajneesh Pandey, Vijay Kumar Yadav, Analysis and modeling of single point cutting (HSS material) tool with help of ANSYS for optimization of (transient) vibration parameters, IJMET, 5, 14–27 Volume, 2014.
2. Maheshwari N Patil, Shreepad Sarange Finite Element Analysis of Von Misses Stresses and Deformation at Tip of Cutting Tool, IJIRAE, 1, 211–217, 2014.
3. Pramod Kumar N,Avinash NV,Sudheer K and Umashankar K, Modeling and Harmonic Analysis of Turning Operation, IJR, 1, Issue-8, 77–86, 2014.
4. Jadhav J.S., Jadhav B.R., Experimental study of Effect of Cutting Parameters on Cutting Force in Turning Process, IJIRAE, 1, Issue 6, 240–248, 2014.
5. Tugrul O zel, Tsu-Kong Hsu, Erol Zeren, Effects of cutting edge geometry, workpiece hardness, feed rate and cutting speed on surface roughness and forces in finish turning of hardened AISI H13 steel, The International Journal of Advanced Manufacturing Technology, 25, Issue 3–4, 262–269, 2005.
6. Wei-Wei Liu Li-Jian Zhu Chen-Wei Shan Feng Li "Effect of cutting parameters on the cutting force in the end milling of GH4169 super alloy" Key Laboratory of Contemporary Design and Integrated Manufacturing Technology, Ministry of Education Northwestern Polytechnical University Xi'an, Shaanxi, China, Issue-6, Volume 1, July 2014.
7. T. Eswara Rao, G. Bala Murali, Vibration Analysis for Different Materials of Single Point Cutting Tool during Turning, Journal of Engineering, 5, Issue 11, 16–24, 2015.

Design of Automated Two-Wheeled Forklift with Retracting Third Wheel and Dynamic Counterbalance Mechanism

Abhinav Kshirsagar, Neha Kesarkar and N. S. Chandrashekhar

Abstract The material handling equipments are an integral part of any industry, whatever maybe the size of the industry. The material handling equipment industry offers a variety of products depending upon the particular requirements in the industry. This paper mentions the designing of a two-wheeled forklift having a lifting capacity of 4000 lbs. (1814.37 kg) up to a height of 7 m. This forklift has an overall length of 1.7 m so as to comfortably maneuver in narrow aisle space of less than 2.1 m. The possible design of forklift in the narrow aisle is obtained with the application of an innovative mechanical counterbalancing mechanism.

Keywords Dynamic transfer · Retracting mechanism · Sensors · Actuators

1 Introduction

The material handling equipments can be broadly classified into two types depending upon the need of handling capacity—unit load handling and bulk load handling. The requirements of unit load handling are fulfilled by equipments like forklifts, scissor lifts, goods lifts, pick and place robots, walking beam conveyors cranes, roller conveyors, hoists, pallet trucks, and trolleys, and for bulk load handling, equipment like belt conveyors, bucket elevators, stacker reclaimers, wheel loaders, screw conveyors, and grabbing cranes are widely used.

The most common trend nowadays in the material handling industry is to increase the level of automation, increase efficiency, and hence enhance productivity and to maximize safety. The equipments available today are highly superior in terms

A. Kshirsagar (✉) · N. Kesarkar
L.Y.B-Tech Mechanical, K. J. Somaiya College of Engineering, Mumbai, India
e-mail: a.kshirsagar@somaiya.edu

N. S. Chandrashekhar
Department of Mechanical Engineering, K. J. Somaiya College of Engineering,
Mumbai 400077, India

of safety, accuracy, quality, etc., and the use of electronic sensors, actuators, and inverters guarantees safety, reducing the human interference.

Catering to the need of fitting a forklift in an ever-decreasing aisle space so as to make the warehouse smaller in size, we have developed a forklift that can easily maneuver through the narrow aisle (typically an aisle space of about 1.7 m). In the present scenario, narrow aisle is dimensioned as 1.9 m aisle space. So this forklift can easily maneuver through the present-day narrow aisle but can also move with ease in the aisles dimensioned to some smaller dimension in the near future. This paper emphasizes on the mechanism that enables this concept of retracting third wheel mechanism with dynamic mass transfer so as to decrease the overall length and width of the already existing forklift.

2 Literature Review

The current trend in forklift manufacturing is to provide the four-wheeled and three-wheeled forklifts with paradigm shifting from the use of conventional fuel sources to electrically operated, equipped with advanced automation. However, the two-wheeled forklift design is in its primitive stage with low lift capacity requiring manual efforts for its motion. Large research and review is done to improve the three-wheeled and four-wheeled forklifts.

Many research papers are available on the topics related to design optimization and product analysis [1] and dynamic simulation of forklift [2]; like to lift a load of irregular surface, the individual movement of the fork was achieved through pneumatic actuation [3]. Also one of the crucial operations in any forklift is lifting the heavy loads at high heights for which hydraulic system is designed [4]. Some of the major findings with regard to safety standards are the development of the system of active stability (SAS), which was designed by Toyota Engineers that makes use of series of sensors to detect instability to avoid tipping during its operation. To check for the safety of the forklift, there are various tests in order to ensure safety from sideward tilt and forward tilt as per international standards [5]. To ensure the stability of the forklift, the center of forklift must always lie within the stability triangle. The stability triangle is defined by the pivot axis and the center of the rear wheel shaft. The pivot axis is the line joining the center of the two front wheels of the forklift. [5]

By analyzing the literature available in the field, we concluded that there is a lack of research relating to optimizing the size along with efficient maneuverability and ensuring safety at high speeds by devising a counterbalance mechanism. So we devised a counterbalance mechanism with retracting third wheel so as to perform dynamic mass transfer.

3   Designing the Counterbalance Mechanism

This paper concentrates on developing a retracting third wheel mechanism; since during the design of entire forklift, it was one of the most critical components to ensure stability. A very agile and quick response mechanism was required to dynamically balance the forklift in all its operating conditions. Also in order to increase the maneuverability and increase the operational speed, we decided to make a two-wheeled forklift. However, in the loaded condition the stability could not be achieved so we decided to include a retracting third wheel which will be in operation when the forklift is loaded forming the base of the stability triangle.

The size of standard narrow aisle space is 2.1 m so subtracting the clearance of about 0.15 m from each side the forklift needed to be of 1.8 m from fork end to rear tire. With standard Industrial Truck Association (ITA) forks, the space available for mechanism was 0.580 m, so to lift the load of 1814.4 kg (4000 lbs) at a lift height of 7 m (23 feet), the dead weight required is 2000 kg.

Some of the major components of this retracting third wheel mechanism are as follows:

(1) Falling element (2) Retracting wheel (3) Rack and pinion.

3.1   Calculation for Cross Section of Frame

Considering it as cantilever with UDL
    Mass of load $= 1200$ kg
    Since, 2400 kg divided into 2 bars
    Considering material steel 50C4

$$\sigma_{yt} = 720 \text{ N/mm}^2$$

$$E = 2.1 \times 10^5 \text{ N/mm}^2$$

$$\text{FoS} = 6$$

Using bending moment equation:

$$\frac{\sigma_b}{y_{max}} = \frac{M_{max}}{I}$$

where $M_{max} = \frac{wl^2}{2}$, $I = \frac{bd^3}{12}$ and $y_{max} = \frac{wl^4}{8EI}$.

After iterations, we get the cross section to be 30 mm $\times$ 50 m.

3.2   Calculation for Rollers

Three rollers are considered of material: steel 50C4 mass of load $= 800$ kg.

$$\frac{\sigma_b}{y_{max}} = \frac{M_{max}}{I}$$

where $M_{max} = \frac{wl^2}{2}$, $I = \frac{\pi d^4}{64}$ and $y_{max} = \frac{wl^4}{8EI}$

We get diameter as 46 mm after iterations.

3.3   Calculation for Rack and Pinion

Required speed $= 1.3$ m/s
m $= 50$ kg
Power $= 52.25$ W
we get module $= 4$ and pinion diameter as 68 mm
length of rack required $= 260$ mm.

4   Techniques of Enhancing the Mechanism by Sensors and Actuators

Various types of sensors would be required to execute the retracting motion to place the retracting third wheel exactly in its place. The load cells placed on the fork surface help us to measure the load placed on the forks. This measurement is of utmost importance as the motion of the dead weight so as to maintain the stability of the forklift depends on the weight measured by the load cells. But even before the load cells come into the picture, the proximity sensors guide the entire vehicle to the required location so that the forks would exactly align with the pallet opening (Fig. 1).

High precision load cells are used to exactly get the required output voltage which is further processed as shown in the following charts (Figs. 2, 3).

5   Illustration of Working Conditions

5.1   Case 1

Initially, the dead weight is at a distance of 213.5 mm from the pivot point. Therefore, in the unloaded condition the torque provided by the dead weight and the rear platform

Fig. 1 Rack and pinion mechanism for retracting third wheel motion

Load cell generates voltage signal	Signal to Arduino	Signal to motor driver	The motor enables the motion of the dead weight
• The load cells measure the weight of the load placed on the forks and produces an equivalent electric signal	• The voltage signal is interpreted by the arduino circuit • Also the exact value of weight is known from the voltage. • The exact distance to which the dead must translate is determined	• The voltage signal is received by the motor driver and accordingly the voltage and current modifications are made to drive the motor	• The dead weight is shifted to the exact position to provide the required counter balance torque. This position is predetermined by the arduino programme.

Fig. 2 Flowchart of working of the load cell circuit

is just enough to counterbalance the weight of the assembly in front of the pivot, i.e., the weight of the forks and a part of the mast. At this point of time, as there is no load on the forks the dead weight remains in its initial position.

When the pallet on which the load is placed is at a distance of 1228 mm (1028 mm fork length + 200 mm clearance), from the face of the mast, an IR sensor actuates the motor to move the retracting third wheel from its initial position to final position. This retracting motion of the third wheel is possible via the conversion of rotational motion of the actuated motor shaft into the linear motion with the help of a rack and pinion assembly.

In the same time (0.2757 s assuming the forklift speed to be 15 kmph*), the falling platform rotated by an angle of 90° gets aligned with the other half of the platform to form an exactly horizontal surface on which the dead mass would translate.

Now by this time (0.2757 s), the forklift has moved forward and the forks are in position to lift the load.

5.2 Case 2

When the forks are just about to come in contact with the pallet surface, at this point of time the load cells placed on the fork surface sense the load and accordingly
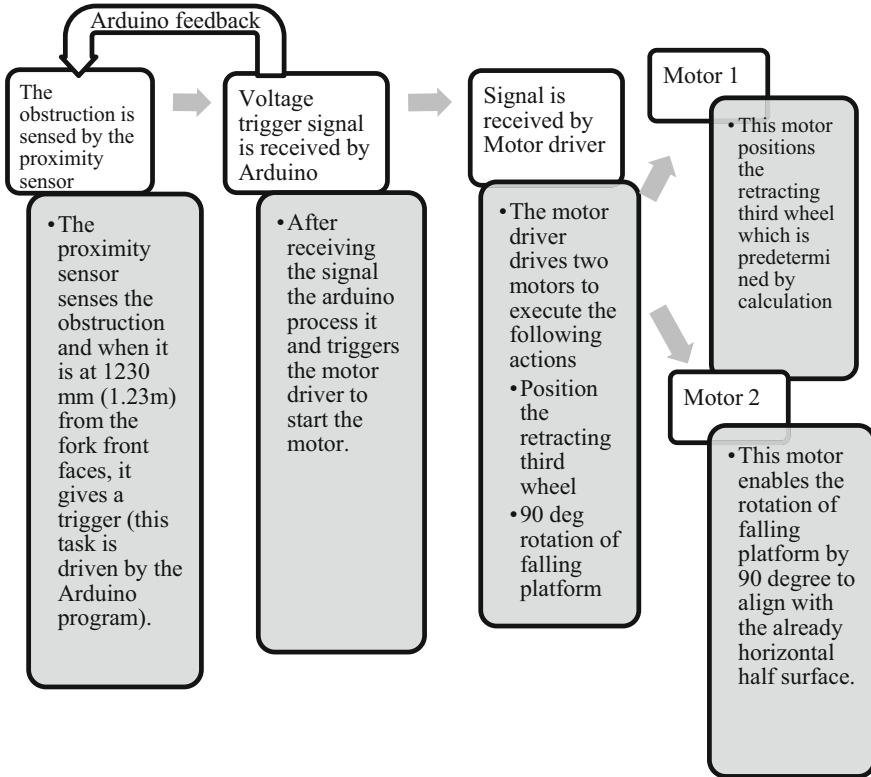
Fig. 3 Flowchart of working of the proximity sensor

actuate the motor driver to provide the required motion to the dead weight so as to translate it in accordance with the weight to lift.

The distance moved by the dead weight over the roller assembly is a function of the mass of the load to be lifted. These two quantities are directly proportional. More the weight of the load to be lifted, more would be the distance the dead weight has to travel.

5.3   Case 3

When the forks have lifted the load to a particular height, the center of gravity (C.G.) moves upward and there is a greater possibility of it moving outside the stability triangle as it is broader at the base and converges to a point at 3092 mm plus vertical height of C.G of load. So in order to compensate this shift in C.G., the position of the dead weight needs to be set accordingly.

5.4 Case 4

At this point of time, the forks have placed the load on the shelves and are about to lose contact with the pallet. The load cells give feedback to the various motors to move the mass back to its initial position. Succeeding this task, inputs are given to motors to bring the retracting wheel to its initial position and the falling platform is rotated by 90° in the opposite direction of its first rotation.

6 Results

The simulation results at the topmost position of the forks in the loaded condition which is the most probable zone of toppling of the forklift illustrated that the C.G. lies within the stability triangle and thus the forklift is stable in all the situations. Also, the quick response of the electronic systems ensured that the forklift remains stable, by appropriately displacing the dead weight to provide required counterbalance torque.

7 Conclusion

It was concluded that it is possible to have a narrow aisled forklift more efficient than the present-day two-wheeled and three-wheeled forklifts. The retracting third wheel comes into action only when the forklift is in the loaded condition thus ensuring stability and agility in the non-loaded condition. Thus, in the non-loaded condition the forklift is only 1.7 m in length, perfectly designed for the futuristic narrow aisle. Not only does this forklift reduce the space requirements but also saves the non-value added time owing to its higher speed of operation.

8 Future Scope

As of now, no dynamic feedback is given if the stability of the forklift is not maintained due to any unforeseen situations, so in future with the help of gyroscope, we plan to implement a dynamic feedback mechanism that would make simultaneous motions of the dead weight as soon as some tilt is observed from the vertical. This tilt would be measured by a gyroscope which would act as an input to trigger the motor driver which in turn would drive the motor to position the dead weight at the required location.

References

1. Design and Analysis of New Flexible and Safe Forklifts. Northeastern Library
2. Ilir Doçi, Vegim Imerib: Dynamic Analysis of Forklift during Load Lifting using Modeling and Simulations, 2013
3. K Nanthakumar, M Arun, K Ranjith kumar, R Sabarinathan, K Yuvaraj: Design And Fabricated Pneumatic Operated Forklift. 2015
4. Liai Pan, Qiulei Du, Chunshan He: Design Research on Hydraulic System of Working Device of a Forklift. 2015
5. J Lambert & Associates: Forklift Stability and Other Technical Safety Issues. 2003
6. Leopoldo Armesto, Josep Tomero, Juan Carlos Torres: Transport Process Automation With Industrial Forklifts. 2003
7. Raymond A. Kulwiec. Materials Handling handbook, John Wiley & Sons. 1985

Design and Analysis of Piercing and Extrusion Tool

Gopal B. Mudholkar, Girish M. Lonare and Sadhana R. Hivre

Abstract Design and analysis of press tool for piercing and extrusion operation of an automobile part is carried out in this endeavor. This paper deals about press tool to be used in sheet metal extrusion process which consists of forming an integral collar around the periphery of hole in a sheet metal part on a single stroke. The design and material selection of piercing and extrusion press tool elements is finalized by ensuring standard press tool die design approach and analysis methods. Autodesk Inventor, AutoCAD software has been used for modeling and detailing. Solid works software is adopted as a reference to analyze the feasibility of the proposed processes.

Keywords Press tool · Piercing punch · Extrusion punch · Extrusion die design

1 Introduction

The most appropriate materials and manufacturing methods under specified conditions should be preferred consciously by considering total manufacturing cost into account. Components manufactured from sheet material have various qualities including good dimensional accuracy, lightweight, substantial strength and manufacture in a broad range size is possible [1]. Various techniques are possible to adopt, and therefore before starting a manufacturing, it is important to understand which forming method is most suitable to manufacture a given product with a required qual-

G. B. Mudholkar (✉) · G. M. Lonare
Bharati Vidyapeeth College of Engineering, Kharghar, Navi Mumbai 400614,
Maharashtra, India
e-mail: gopal.mudholkar@gmail.com

G. M. Lonare
e-mail: girishlonare1977@gmail.com

S. R. Hivre
Dr. Babasaheb Ambedkar Technological University, Vidyavihar, Lonere,
Raigad 402103, Maharashtra, India
e-mail: srhivre@dbatu.ac.in

ity and minimum manufacturing cost [2]. This work adopts piercing and extrusion operation on sheet metal part and pursues to obtain flange with a more significant lip and greater height.

2 Design of Piercing and Extrusion Press Tool

Piercing and extrusion process is normally carried out by first piercing a hole of a predetermined size into a sheet metal part with the help of piercing punch and extrusion punch, and then, this sheet metal part is rigidly clamped around its periphery between a stripper plate and extrusion die. Then, this extrusion die block which is subjected to counter pressure holds the sheet metal part and moves downward with the piercing punch together. Finally, extrusion punch which is fixed, after moving a certain distance of extrusion die, deformation zone of sheet metal part is entirely extruded to move into the extrusion die thereby forming a cylindrical collar as shown in Fig. 1.

The steps in the designing of piercing and extrusion press tool are as follows.

2.1 Component Details

The part shown in Fig. 2 is made up of cold rolled low-carbon steel sheet of 1.2 mm thickness. The detailed chemical composition of the material and the identified mechanical properties are presented in Tables 1 and 2 respectively.
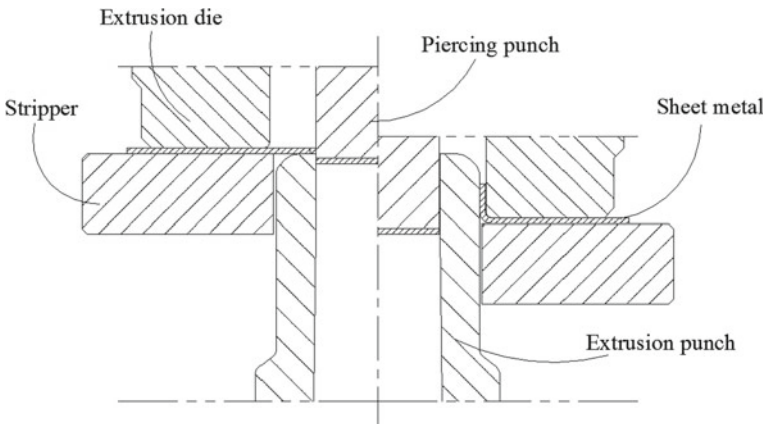
Fig. 1 Piercing and extrusion tool setup
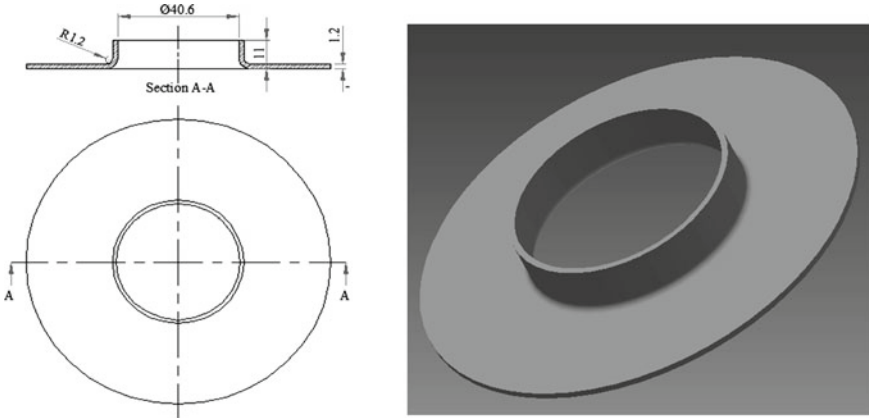
Fig. 2 Sheet metal component details

Table 1 Chemical composition of the material

Elements	C	Mn	S	P
%	0.063	0.228	0.007	0.010

Table 2 Mechanical properties of the material

Mechanical properties	Yield stress, N/mm^2	Ultimate tensile stress, N/mm^2	Elongation (%)	Hardness HRB
Value	213	314	42	52

2.2 Tool Steel Material Selection

High carbon, high chromium D2 tool steel alloyed with molybdenum and vanadium distinguished by high wear resistance, compressive strength, stability, good through hardening, and good resistance to tempering back is selected for extrusion punch, piercing punch and extrusion die block.

2.3 Determination of Cutting Clearance

Maximum and minimum value of die clearance for particular carbon steel of thickness 1.2 mm is ranging from 2.5 to 5% [3].

$$\text{Optimum clearance} = (0.06 + 0.03)/2$$
$$= 0.045 \text{ mm}$$

Piercing punch size $=24.7$ mm (calculated from the theory of equal line length [4])

$$\text{Extrusion punch bore size} = \text{punch size} + 2(\text{clearances/side})$$
$$= 24.7 + 2 \times 0.045$$
$$= 24.8 \text{ mm}$$

$$\text{Cutting land} = 3t \text{ or 3 mm, whichever is greater.}$$
$$= 3 \times 1.2$$
$$= 3.6 \text{ mm. where, } t = \text{material thickness in mm.} \tag{1}$$

In extrusion operation, initially the clearance between extrusion punch and die becomes equal to the material thickness and a full contact between the material and the extrusion die is established.

2.4 Press Tonnage Requirement

Calculating the total force is important for checking whether the machine has enough tonnage to do the sheet metal part or workpiece without damaging the machine itself.

$$\text{Vertical shear force}(V) = P \times t \times T_s$$
$$= (24.7 \times 3.14) \times 1.2 \times 251$$
$$= 23361 \text{ N} = 2.38 \text{ ton} \tag{2}$$

where $P =$ cut length in mm, $T_s =$ shear strength in N/mm^2 (shear strength is considered as 80% of tensile strength).

Horizontal force depends upon die cutting clearance and vertical shear force.

$$\text{Horizontal force}(H) = \text{clearance \% with thickness} \times V$$
$$= 0.045 \times 21965 \text{ N}$$
$$= 988.42 \text{ N} = 0.1 \text{ ton} \tag{3}$$

Then, resultant shear (piercing) force R_{pierce} is given by,

$$R_{\text{pierce}} = \sqrt{V^2 + H^2}$$
$$= \sqrt{(2.38)^2 + (0.1)^2} = 2.38 \text{ ton} \tag{4}$$

Extrusion force depends on the thickness of sheet metal part, length of bend, and tensile strength. Extrusion force ($F_{\text{extrision}}$) required for this particular steel sheet is [5]

$$\begin{aligned} F_{\text{extrision}} &= 1.5\pi(d - d_{\text{o}})t(\sigma_{\text{B}}) \\ &= 1.5 \times 3.14 \times (43{-}24.7) \times 1.2 \times 314 = 3.33 \,\text{ton} \end{aligned} \tag{5}$$

where $d =$ hole size after extrusion in mm, $d_{\text{o}} =$ hole size before extrusion (piercing size) in mm, $\sigma_{\text{B}} =$ ultimate tensile strength in N/mm^2.

Piercing and extrusion force

$$(F_{\text{p\&e}}) = R_{\text{pierce}} + F_{\text{extrusion}} = 2.38 + 3.33 = 5.71 \,\text{ton} \tag{6}$$

$$\text{Stripping force} = 10\% \text{ of piercing and extrusion force}$$

$$= 10/100 \times 5.71 = 0.57 \,\text{ton} \tag{7}$$

The capacity of press machine should be 20% more force than that required for consistent performance [5, 6].

Press tonnage requirement

$$(F_{\text{total}}) = 1.2 \times F_{\text{combine}} = 1.2 \times 6.28 \,\text{ton} = 7.54 \,\text{ton} \tag{8}$$

Tonnage requirement is less than the capacity of available mechanical press machine of 10 ton.

2.5 Extrusion Die Block Calculation

Basically, die block design depends on the strip or component thickness and size, the shape of the component, and the tool steel material [3].

$$\text{Die thickness}(t_{\text{D}}) = \sqrt[3]{F_{\text{combine}}} = \sqrt[3]{6.28} = 1.8 \text{ cm} = 18 \text{ mm} \tag{9}$$

where

t_{D} Minimum thickness of die plate in cm,
F_{combine} Required tonnage for piercing and extrusion operation in ton

So final thickness (t_{Ds}) in addition to reshaping allowance will be $(18{+}3) = 21$ mm.

$$\begin{aligned} \text{Margin}(M) &= (1 \text{ to } 1.5) \times t_{\text{D}} \\ &= 1.2 \times 21 = 25.2 \,\text{mm} \end{aligned}$$

Diameter of die block (d_{D}) can be found using margin (M) and die cavity slot (A).

$$d_{\mathrm{D}} = A + 2M = 43 + 2(25.2) = 93.4 = 94 \text{ mm} \qquad (10)$$

Similarly to the die block, the punch holder is designed and dimensioned.

$$t_{\mathrm{Ph}} = t_{\mathrm{D}} = 21 \text{ mm where, } t_{\mathrm{Ph}} = \text{thickness of punch holder} \qquad (11)$$

$$d_{\mathrm{Ph}} = d_{\mathrm{D}} = 94 \text{ mm} \qquad (12)$$

In piercing and extrusion operation, combine die block and punch holder design, for manufacturing and assembly point of view, and maintain geometric characteristics.

2.5.1 Deflection and Stress Calculation

Assume that the extrusion die is considered as one of the ends is fixed and force acting on other end is compressive. Here, for extrusion operation, 80% of extrusion and stripping force is acting on die block as compressive nature [7].

$$\begin{aligned}
\text{Deflection}(\delta) &= FL/AE \\
&= 30607.2 \times 42/5484.8 \times 210 \times 103 = 0.0011 < 0.025 \text{ mm} \quad (13)
\end{aligned}$$

where

F 80% of ($F_{\mathrm{extrision}}$ + stripping force)
   $= 0.8 \times 38{,}259 = 30{,}607.2$ N.
L length of extrusion die in mm,
A punch cross-sectional area in mm^2

$$\begin{aligned}
\text{Stress} &= \text{Force}(F)/\text{Area} \\
&= 30607.2/5484.8 = 5.58 \text{ N/mm}^2 \qquad (14)
\end{aligned}$$

Stress induced is 5.58 N/mm^2 which is less than the allowable strength 2200 N/mm^2 [3].

2.6 Piercing Punch Calculation

$$\begin{aligned}
\text{Overall punch length} &= \text{Extrusion die thk.} + \text{material thk.} + \text{grinding allowance} \\
&= 42 + 1.2 + 0.8 = 44 \qquad (15)
\end{aligned}$$

2.6.1 Critical Bucking Force

Now to calculate critical buckling load, Euler's equation will be used [3].

$$P_{cr} = (\pi^2 E I_{min})/L^2$$
$$= 7.8 \times 106 > 23347.8 \text{ N} \tag{16}$$

where

I_{min} minimum moment of inertia $= 18{,}261.54 \text{ mm}^4$,
L unsupported punch length $= 22$ mm

Applying load 23,347.8 N is less than buckling load 7.8×10^6 N, it is safe load.

2.6.2 Deflection and Stress Calculation

Assuming one end of punch is fixed and on the other end compressive force is acting.

$$\text{Deflection}(\delta) = FL/AE$$
$$= 0.0082 \text{ mm} < 0.025 \text{ mm} \tag{17}$$

where

F 80% of piercing force $(F_{pierce}) = 18{,}678.24$ N,
L length of pierce punch $= 44$ mm,
A cross-sectional area of punch $= 478.92 \text{ mm}^2$

$$\text{Stress} = \text{Force}(F)/\text{Area}$$
$$= 18678.24/478.92 = 39 \text{ N/mm}^2 \tag{18}$$

The stress induced is 39 N/mm^2, which is very much less than the allowable stress 2200 N/mm^2 [3].

2.7 Stripper Plate Calculation

The minimum thickness of the stripper plate (h_{St}) can be estimated by using following formula [1].

$$h_{St} = 0.033 W_S + 2t$$
$$= 0.033(86) + 2(1.2) = 5.27 \text{ mm.} \tag{19}$$

where $W_S = $ width of stock.

2.8 Extrusion Punch Calculation

Extrusion punch length = Extrusion punch entry radius + component flange height

+ stripper thickness + compressed spring length

$$= 5 + 8 + 16 + 46 = 75 \text{ mm} \tag{20}$$

2.8.1 Deflection and Stress Calculation

Assuming extrusion punch, consider one end is fixed and compressive force is acting on the other end. We know that the extrusion force and stripping force are acting on extrusion punch.

$$\text{Deflection}(\delta) = FL/AE$$
$$= 30607.2 \times 75/817.54 \times 210 \times 103$$
$$= 0.013 \text{ mm} < 0.025 \text{ mm} \tag{21}$$

where

F 80% of ($F_{\text{extrusion}}$ + stripping force)
    $= 0.8 \times 38{,}259 = 30{,}607.2 \text{ N}$,
L length of the extrusion die block in mm,
A cross-sectional area of the punch

$$\text{Stress} = \text{Force}(F)/\text{Area}$$
$$= 30607.2/817.54 = 37.44 \text{ N/mm}^2 \tag{22}$$

Stress induced is 37.44 N/mm^2 which is less than the allowable strength 2200 N/mm^2 [3].

2.9 Bottom Plate Thickness Calculation

The bottom plate gives cushioning effect to the extrusion punch and provides enough space for the tool to be clamped to the press bed. Bottom and upper plate thickness can be calculated as [3],

$$T_{\text{base}} = (1.5 \text{ to } 2) \times t_{\text{Ds}}$$
$$= 1.8 \times 21 = 38 \text{ mm} \tag{23}$$
$$T_{\text{upper}} = (1.25 \text{ to } 1.5) \times t_{\text{Ds}}$$
$$= 1.5 \times 21 = 32 \text{ mm} \tag{24}$$

2.9.1 Deflection and Stress Calculation for Bottom Plate

Bottom plate is considered to be on two parallel linear.

$$\text{Deflection}(\delta) = 5FL^3/354EI \tag{25}$$

where,

F	80% of combine force ($F_{combine}$) = 49,285.44 N,
L	distance between parallel block in mm,
Moment of inertia (I)	$bh^3/12 = 140 \times (42)^3/12 = 864{,}360$ mm^4
Deflection (δ)	$5 \times 49{,}285.4 \times (102)^3/354 \times 210 \times 10^3 \times 864{,}360$
	$= 0.0041$ mm < 0.025 m

This value of deflection shows that bottom plate is sufficient to be 42 mm thick.

$$\text{Stress} = \text{Force}(F)/\text{Area}$$
$$= 49285.44/140 \times 38 = 9.26 \text{ N/mm}^2 \tag{26}$$

Stress induced is 8.38 N/mm^2 which is less than allowable strength 240 N/mm^2 [3].

2.9.2 Deflection and Stress Calculation for Top Plate

Assuming that the upper plate is considered as simply supported beam subjected to force concentrated at the center of the top plate.

$$\text{Deflection}(\delta) = FL^3/48EI \tag{27}$$

where

F	80% of combine force ($F_{combine}$)
	$= 0.8 \times 61{,}606.8 = 49{,}285.44$ N
L	distance between successive bolts or dowels in mm,
Moment of inertia (I)	$bh^3/12 = 140 \times (32)^3/12 = 382{,}293.33$ mm^4
Deflection (δ)	$49{,}285.44 \times (60)^3/48 \times 210 \times 10^3 \times 382{,}293.33$
	$= 0.0028 < 0.025$ mm

This value of deflection shows that the upper plate is safe to be 32 mm thick.

$$\text{Stress} = \text{Force}(F)/\text{Area}$$
$$= 49285.44/140 \times 32 = 11 \text{ N/mm}^2 \tag{28}$$

The stress induced in the upper plate is 11 N/mm^2 which is much less than the allowable strength of 240 N/mm^2 [3].

3 FEM Analysis of Critical Components

3.1 Upper Plate

Material type: Structural steel (St-42),
Modules of elasticity $= 210 \times 10^3$ N/mm^2,
Poisson's ratio $= 0.3$,
Load: Simply supported beam subjected to concentrated force at the center with 49285.44 N,
Compressive strength $(\sigma_y) = 240$ N/mm^2 (Fig. 3).

3.2 Bottom Plate

Material type: Structural steel (St-42),
Modules of elasticity $= 210 \times 10^3$ N/mm^2,
Poisson's ratio $= 0.3$,
Load: Simply supported beam with a uniformly distributed load with 49285.44 N,
Compressive strength $(\sigma_y) = 240$ N/mm^2 (Fig. 4).

3.3 Extrusion Die Block

Material type: Tool steel (D2),
Modules of elasticity $= 210 \times 10^3$ N/mm^2,
Poisson's ratio $= 0.3$,
Load: Uniformly distributed force 30607.2 N,
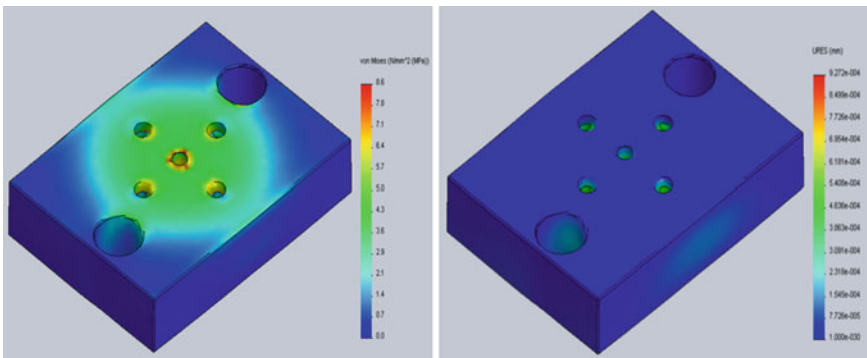
Fig. 3 Upper plate Von mises stress and resultant displacement
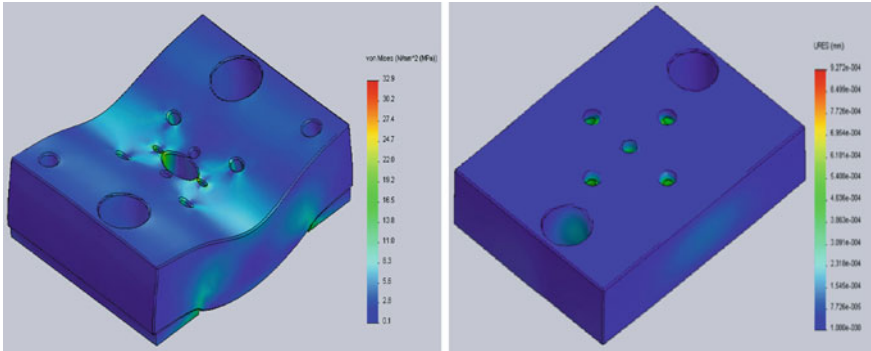
Fig. 4 Bottom plate Von mises stress and resultant displacement
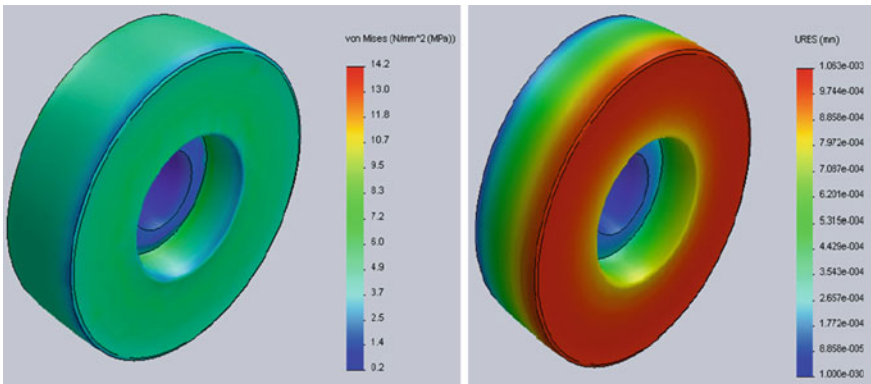
Fig. 5 Extrusion die block Von mises stress and resultant displacement

Compressive strength (σ_y) = 2200 N/mm^2 (Fig. 5).

3.4 Extrusion Punch

Material type: Tool steel (D2),
Modules of elasticity = 210×10^3 N/mm^2,
Poisson's ratio = 0.3,
Load: Uniformly distributed force 30607.2 N,
Compressive strength (σ_y) = 2200 N/mm^2 (Fig. 6).
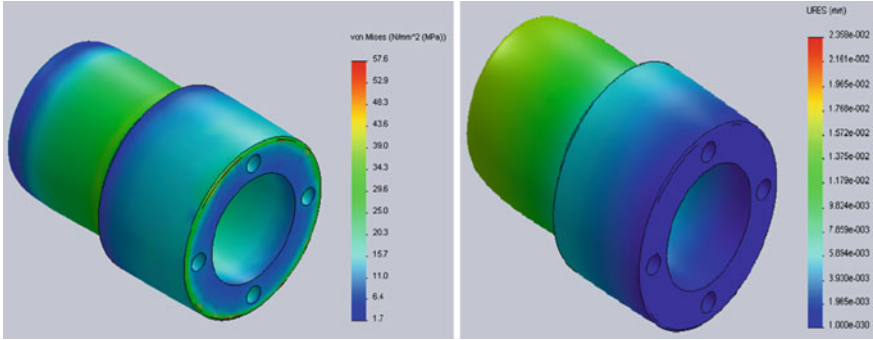
Fig. 6 Extrusion punch Von mises stress and resultant displacement
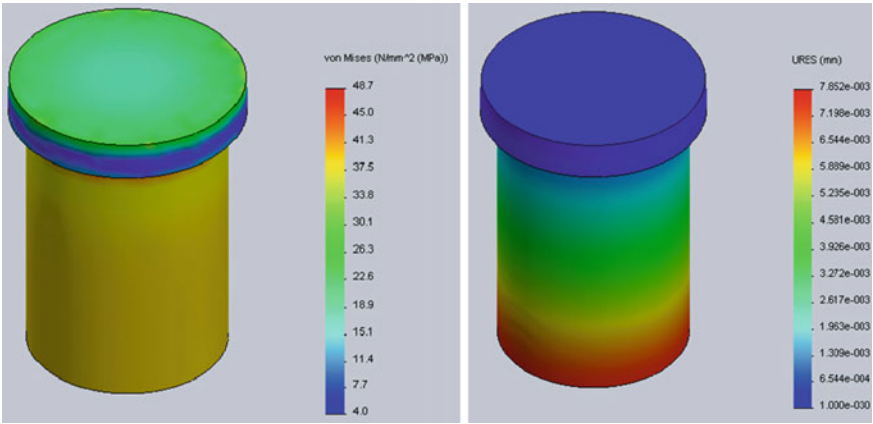
Fig. 7 Piercing punch Von mises stress and resultant displacement

3.5 Piercing Punch

Material type: Tool steel (D2),
Modules of elasticity = 210×10^3 N/mm^2,
Poisson's ratio = 0.3,
Load: Uniformly distributed force 30607.2 N,
Compressive strength (σ_y) = 2200 N/mm^2 (Fig. 7).

4 Results

See Table 3

Table 3 Comparison between analytical and FEM results

Press tool elements	Allowable stress (N/mm^2)	Analytical results		FEM results	
		Stress (N/mm^2)	Deflection (mm)	Stress (N/mm^2)	Deflection (mm)
Bottom plate	240	09.26	0.0041	13.80	0.0037
Upper plate	240	11.00	0.0028	08.55	0.0010
Extrusion punch	2200	37.44	0.0130	39.00	0.0093
Piercing punch	2200	39.00	0.0082	45.00	0.0078
Extrusion die	2200	05.58	0.0011	08.30	0.0011

5 Conclusion

Analytical and FEM results of critical elements of the piercing and extrusion tool are sound, and all the results of displacement and stress were used as a parameter to check the acceptability of the design of each press tool elements which shows that it is within the allowable limit. Results obtained from solid works simulation software show that the stress values for press tool elements are less than the respective allowable yield stress value of the material. As per the recommendation of tool manufacturers, deflections of press tool elements during operation are kept below 0.025 mm. So, the designed piercing and extrusion press tool elements are safe under the given loading conditions.

References

1. Ivana Suchy: Hand Book of Die Design, 2nd edition, McGraw-Hill 2006. (1998)
2. Fissha B. Teshome, Yonas M. Degu: Design of combined press tool for the manufacturing of rice thresher blade. The International Journal of Engineering and Science (IJES). (2014)
3. Gashaw Desie, Yonas Mitiku: Progressive Die Design for Self Explosive Reactive Armor Holder (Case Study at Bishoftu Motorization Industry, Ethiopia). International Journal of Engineering and Science (IJES), Volume 3. Issue 3 (2014) 75–86
4. Yang Li, Zhonglei Wang, Xiao Li, Gang Cheng: Optimization Design Method of the Pre-Manufactured Hole of Flanging. Applied Mechanics and Materials, Vols. 395. (2013)
5. Prakash H. Joshi: Press tools design and construction, New Delhi.
6. G.R. Nagpal: Tool Engineering and design. Khanna Publishers. 2002
7. Ch. Mastanamma, K. Prasada Rao, Dr. M. Venkateswara Rao: Design and Analysis of Progressive Tool. International Journal of Engineering Research & Technology (IJERT), Vol 1. Issue 6 (2012)

Design and Analysis of Coaxial Rotor Wind Turbine

Sachin Manohar Shinde, Mohit Chaudhari, Tejas Jeurkar, Sanket Kadam and Kiran B. Salunkhe

Abstract Wind turbine is one of the booming technologies to generate optimum electricity from renewable source at a most economical cost; the extraction of energy in the present era is already established and further enhanced to improve its efficiency. Coaxial wind turbine is a great rise in the technology of the wind rotor motors when trying to obtain additional power of a unit and, therefore, the most practical use of the kinetic energy of the wind of an equivalent air flow that operates the standard turbine. The concept to which this is often analogous to is the composition of the turbine. The main objective of the paper is to employ the concept of capitalization in turbine technology to obtain as much potential energy from an equivalent current. The objective is to further expand the generation of energy per unit, and this assembly accepts other structural benefits, such as a better dynamic balance and noise suppression.

Keywords Renewable energy sources · Coaxial rotor · Compounding
Kinetic energy

1 Introduction

Coaxial rotor wind turbine is to chain the advantages of the coaxial rotor assembly with the design of conventional wind turbine. The rotor may be controlled in both

S. M. Shinde
Department of Mechanical Engineering, K. J. Somaiya College of Engineering, Vidyavihar, Mumbai 400077, India
e-mail: shindes_82@yahoo.co.in

M. Chaudhari · T. Jeurkar (✉) · S. Kadam
Department of Mechanical Engineering,
Datta Meghe College of Engineering, Airoli, Navi Mumbai, India
e-mail: tjeurkar@gmail.com

K. B. Salunkhe
Department of Mechanical Engineering,
Government Polytechnic Mumbai, Bandra, Mumbai, India

directions with respect to the wind flow. Theoretical literature reveals that the wind turbine should develop twice as much as power than the conventional single rotor windmill can generate. This assembly is expected to generate additional power from the single unit of windmill. The concept which is implemented in the design is originated from Russian helicopters which are not used till date in wind turbine technology. The aim of this design was to investigate the possibility of integration of coaxial rotor assembly with wind turbine or in other words to use coaxial rotor assembly as wind turbine. Further, in the design process, analysis is done using CFD technique to investigate the practicability of the idea of coaxial wind turbine.

2 Literature Survey

Cycon et al. [1] have designed simple assembly with a single-stage gearbox with gear on a rotor and another pinion engaged. Next to the gearbox, the assembly holds the housing of the gearbox and the central hub. In the transfer unit, the pinion is toothed on both sides with spiral bevel gears to counteract this. Pair of bevel gears is fixedly connected to the rotor shafts attached to the hoist housing. The intermediate housing is transported in the middle of the hub. The thermal stresses and vibrations are transmitted to the carrier through the central housing, and the bending stresses caused due to the rotation are absorbed within the central housing itself. For the purpose of splash lubrication, gearbox is internally designed. The basic goal behind the creation of the coaxial rotor assembly was to enhance the transfer rate and impart greater rotor power and minimize energy loss. Putman et al. [2] have focused on the conversion of kinetic energy from wind to electricity earlier than the actual development of wind turbines, and power generators operated with propeller rotors were managed to generate electricity, but these were not cost-effective enough to obtain an adequate amount of energy. This development was primarily designed to overcome the memory problem by relating the power generation units directly to the high voltage transmission lines. For this type of turbine, there is a fundamental requirement that the wind turbine can be operated in wide speed ranges, so that the wind energy varies directly with the cube of their speed. Brody et al. [3] have explained the application of the coaxial rotor assembly; the coaxial rotorcraft was first designed. In fact, the coaxial arrangement is the reformation of the standard rotor arrangement. This set accelerated the lifting of the ship and enhanced the power transmission to the rotor. The differential thrust generated by the fans provides control of the ejector, and the forward thrust is given by the tail rotors. Sarangi et al. [4] Department of Mechanical Engineering NIT Rourkela has proposed dynamic analysis of a wind turbine in which geometric blade is designed and validation of it is carried out by CFD analysis and frequencies are compared with other reference papers. McGugan et al. [5] has presented and explained the design of wind turbine blades. The technological development work focuses on reliability and maintenance describe fluid structure for rotor blade. Daut et al. [6] has studied the wind as a renewable energy in Perlis Northern Malaysia. Their study showed the development

possibilities of wind energy in Perlis. Pannase et al. [7] has done optimization on design modeling and structural analysis of windmill blade in which he compared and evaluated the performance of 18 bladed HAWT trapezoidal and rectangular blades. Chehouriet et al. [8] have given the wind turbine design and multi-objective optimization; the blade is designed based on multi-objective principles using generic algorithm. Joseph et al. [9] have presented magnetically levitated vertical axis wind turbine using effect of magnetic repulsion. Schubel et al. [10] have designed load on wind turbine blades describing aerodynamic gravitational centrifugal gyroscopic and operation conditions.

The above literature focuses only on the design and optimization of wind turbine blade, but not much focuses on the compounding of blade of the wind turbine. This loophole is further filled from the proposed design and calculations explained in the research paper.

3 Nomenclatures for Windmill

A_b	Area of blade
A	area of rotor
B_P	width of profile = 0.106 m
C_D	Drag co-efficient
C_{DO}	Profile drags coefficient
D	diameter of rotor
(L/D)	Lift to drag ratio
P	Power output = 36,000 W
R	Radius of rotor
TM	Torque speed characteristics
TSR	Tip speed ratio
U	Airfoil velocity
V	Volume of blade
V_2	Exit velocity of wind
V_∞	Wind speed = 10 m/s
W	Relative velocity
i	Angle attack
n	Number of blades = 3
α	Pitch angle = 25°
η_E	efficiency of electrical generator

4 Construction Details

In the prototype, a pair of rotors are used, one mounted on the outer hollow shaft and the other on the inner solid shaft. In the area of the two mutually parallel axes, a

much smaller distance must be maintained. The angle of attack of the wind against the rotor blade is exactly opposite to the angle of attack of the rotor blade on the surface, i.e., we can say that the aerodynamic shapes of the two sheets are reflected vertically.

The torque generated by the kinetic energy by the wind on the rotor blades of the engine is transmitted through the axles to the gears. To assemble the turbine wheel, the power generation unit is also implemented in two ways, either by coupling each axle to the generator separately or first by combining the two axles and then coupling that single axle to the single generator. In the first approach, the investment price could increase due to the use of the two generators of identical capacity within the single unit; however, the losses that occur during the transfer are actually reduced during this possibility. To mix the two axes, a combination of bevel gears is used; however, this arrangement will increase the mechanical elements within the power generation unit, which may decrease the net power due to the losses that occur in it, the conical gears. In a gear combination, the force generated by the rotor is additionally used to rotate the gear combination, whereby the force achievable in the generator is reduced.

5   Working Principles

The wind speed in the vicinity of the turbine blades is less than the speed of the free stream. The particular resistance and resistance generated by the turbine blades depend on the relative wind speed. The resistance tends to the leaves toward the edge. The aerodynamic wind flow over the aerodynamic blade reduces air resistance and increases lift, which is responsible for the increased efficiency of the turbine. The coaxial rotor assembly desires the largest amount of kinetic energy of the wind stream.

The torque is transmitted by turning the shaft to the gearbox and then to the generator shaft. The mechanism of rotation of the head is through the gear. Increasing the speed of generator shaft will result in the generation of additional power. One equivalent occurs in the same way because of the K.E. In fact, it helps to extract more and more wind flow performance at low linear velocities.

6   Design of Windmill

This design methodology is to increase the efficiency of the windmill; at first, the designing steps start with the design of windmill blades, because these blades will mainly affect the overall efficiency of the windmill. For a particular application, the windmill blade should be in required size. Before this, getting knowledge about the aerodynamic style of windmill blade in order to get the full efficiency is very much important.

The design is based on four steps as follows:

1. Design of wind turbine rotor
2. Design of tower
3. Design of gear
4. Selection or Design of generator (Fig. 1)

6.1 Design of Wind Turbine Rotor

Specifications of Turbine Blades

Blade Diameter	14 m
Density of Air	1.225 Kg/m^2
Range of Wind Speed	4–10 m/s
Blade Efficiency	30%
Reduction in Wind Speed Over First Rotor	40%
Tip Speed Ratio	7
Wind Speed	10 m/s
Power 1	28.272 kW
Power 2	6.107 kW
Total Power	34.378 kW
Reduced Wind Speed	6 m/s
% Increase in Power	21.6%
Speed of Rotation	10 rad/s
Torque 1	282.718 N-m
Torque 2	61.068 N-m

6.2 Airfoil Specification

Airfoil type	NACA 4412
(L/d)	20
C_1	1
C_d	0.2
Angle of attack	5.5°

6.3 Design of Tower

From the Table 1, required power is 3.6 kW. So, height is selected as 20 m.
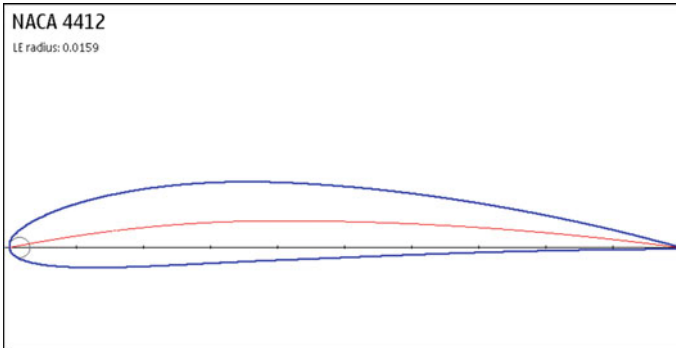
Fig. 1 Blade specification (*Source* www.airfoiltools.com)

Table 1 Tower height selection

Power	Tower height
Up to 100 kW	Up to 30 m
100–300 kW	30–35 m
300–500 kW	35–40 m
Above 500 kW	Above 40 m

6.4 Design of Turbine Shaft

Swept area	153.86 m²
Weight of air packet per m of flow	188.47 kg/m
Maximum mass flow rate through blades	1884.7 kg/s
For 3 blades, mass flow rate	5654.1 kg/s
Material of shaft	C-45
Ultimate strength	38 MPa
Factor of safety	2.5

Equivalent Twisting moment on shaft,

$$T_e = \sqrt{T^2 + M^2}$$

which implies that

$$T_e = 28.82 \times 10^6 \text{ N-mm}$$

$$T_e = \frac{\pi}{32} \times d^3 \times \tau$$

$$28.82 \times 10^6 = \frac{\pi}{32} \times d^3 \times 76$$

Fig. 2 Gearbox layout
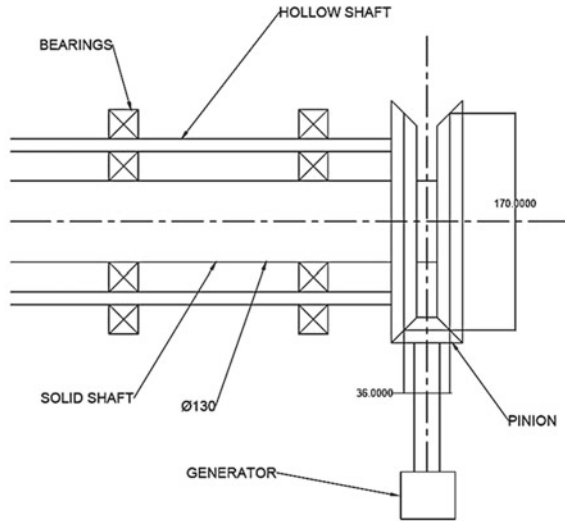
Therefore,

$$d = 130\,\text{mm}.$$

Selecting the bearing, *DGBB—6026* and *No of bearings*=4.

6.5 Design of Gear and Gearbox

Transverse module, M_t	2 mm
No. of teeth, Z_1	18
No. of teeth, Z_2	85, $\Delta 2 = 12°$
Face width (b)	20 mm
Pitch angle $\delta 1$	78°
Pitch circle diameter, $d1$	36 mm

See Fig. 2.

6.6 Design/Selection of Generator

Generators in the turbine are the simple alternators which convert the rotational energy to the electrical energy. The alternators simply work on the principle of Faraday's Law of Electromagnetic Induction. The energy generated can be stored in

the batteries using inverter circuits or can be attached directly to the electrical circuit. Keeping in mind the maximum power that need to be generated, the two types of alternators are available in the market, i.e., induction type and permanent magnet type. The speed range of the induction type generators is of the order 1500 rpm, and the speed range of the permanent magnet generators is of the order 450–480 rpm. The gearing system that is needed to increase the speed from 80 to 1500 rpm will be quite bulky. Therefore, permanent magnet alternators will be suitable for the desired application. The alternator selected for the application is of the model 500STK6M with rated power capacity of 41.219 kW at 450 rpm.

7 Calculations

See Table 2.

8 CFD Results

The purpose to perform the CFD analysis on the airfoils is to decide the velocity reduction from one blade to the other blade. The airfoil, used in the blade design,

Table 2 Estimation of power available

	Estimation of theoretical power available				Estimation of actual power available			
Wind	1st power	2nd power	Total	% Increase				
Speed (Kmph)	(kW)	(kW)	Power (kW)	In power	1st power (kW)	2nd power (kW)	Total power (kW)	% Increase in power
14	1.662	0.359	2.021	21.6	1.6627	0.6468	2.3096	38.9
16	2.482	0.536	3.018	21.6	2.4820	0.9655	3.4475	38.9
18	3.533	0.763	4.297	21.6	3.5339	1.3747	4.9087	38.9
20	4.847	1.047	5.894	21.6	4.8476	1.8858	6.7335	38.9
22	6.452	1.393	7.845	21.6	6.4522	2.5100	8.9623	38.9
24	8.376	1.809	10.186	21.6	8.3768	3.2587	11.635	38.9
26	10.65	2.300	12.950	21.6	10.650	4.1431	14.793	38.9
28	13.302	2.873	16.175	21.6	13.302	5.1747	18.476	38.9
30	16.360	3.533	19.894	21.6	16.360	6.3646	22.725	38.9
32	19.856	4.288	24.145	21.6	19.856	7.7243	27.580	38.9
34	23.816	5.144	28.961	21.6	23.816	9.2651	33.081	38.9
36	28.271	6.106	34.378	21.6	28.271	10.998	39.269	38.9

Fig. 3 2-D geometry of airfoil NACA-4412
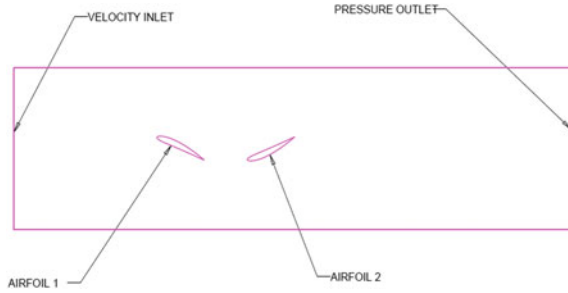
Table 3 Input parameters for simulation

Parameters	Values
Input wind velocity	10 m/s
Airfoil walls	Adiabatic walls
Atmospheric temperature	300 K
Outlet	Pressure outlet
Analysis type	Steady-state analysis
Viscosity and turbulence model	K-epsilon (2 equation) turbulence model
Turbulence intensity	5%
Surface roughness	0.05 mm

is NACA-4412. In the theoretical analysis, we have considered that the reduction in the wind velocity after passing over the first set of rotor is about 40%. This assumption was based on the empirical relations regarding the wind turbine blade design. Simulation of wind velocity which is flown over the set of blades is calculated using ANSYS Fluent. The parameters used in the analysis are as follows (Fig. 3; Table 3).

Streamlines displayed in the Figs. 4 and 5 start from the velocity inlet and are used to show the flow of air over the set of blades. Streamlines show that, though there is reduction in the wind speed over the first set of blades, the wind still enters the second set of blades without considerable turbulence and low velocity that the power cannot be further extracted. The pressure contours, in Fig. 7, explain that the pressure gradient required for the airfoils to generate the lift is sufficient. The pressure on the lower side of airfoil is approximately 1.014454 bar, and the same pressure above the airfoil is 1.01233 bars. These gradients are enough to produce the lift force over the airfoil which in turn generates the torque. The above-generated CFD results are clearly showing that the velocity reduction over the first blade is not as high as considered in the theoretical design. The simulated results show that the average reduction in the velocity of wind over the first blade is only about 27% where in the basic design it was considered to be 40%. The pressure gradients across and over the airfoils also show that it is possible to generate the torque from the wind flowing over the second blade. In Fig. 6, the compounded velocity of wind at second
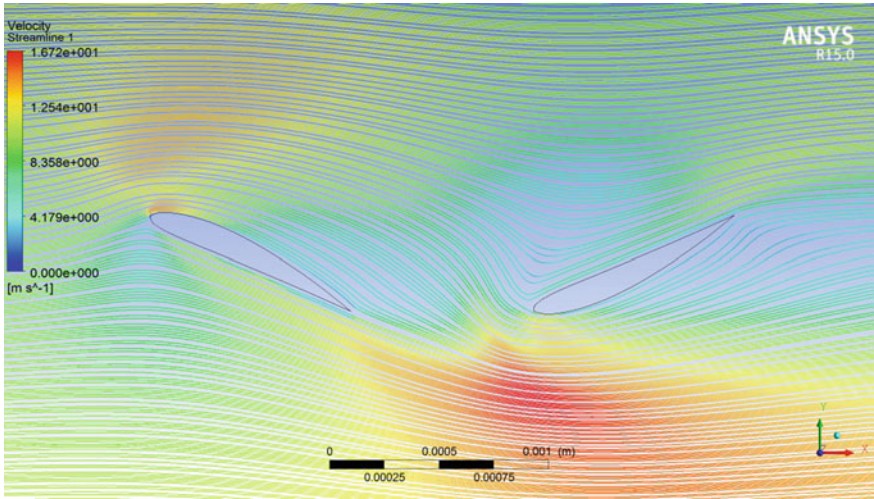
Fig. 4 Streamlines showing velocity contours
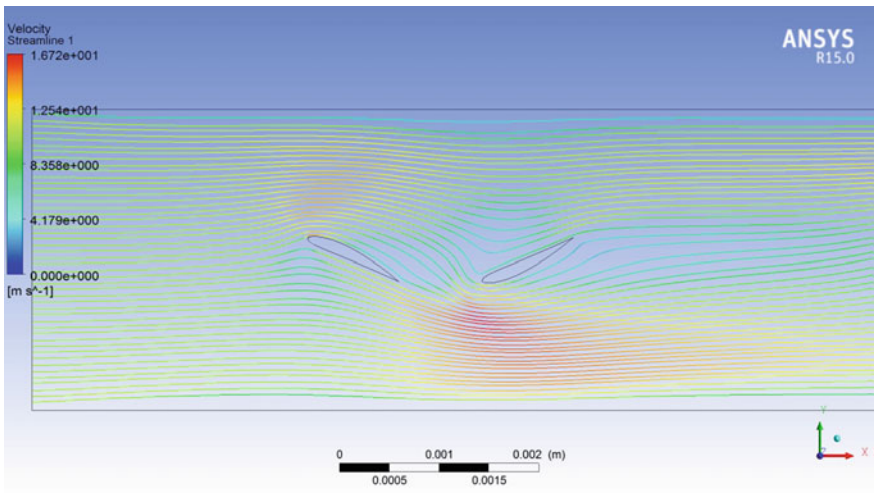
Fig. 5 Complete view of streamlines

stage is less than as compared to the first stage, which can be used to generate the torque again using the second set of blades.
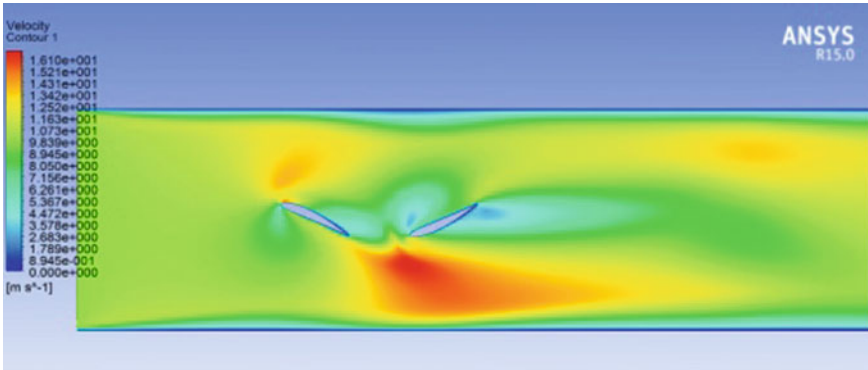
Fig. 6 Contours of velocity
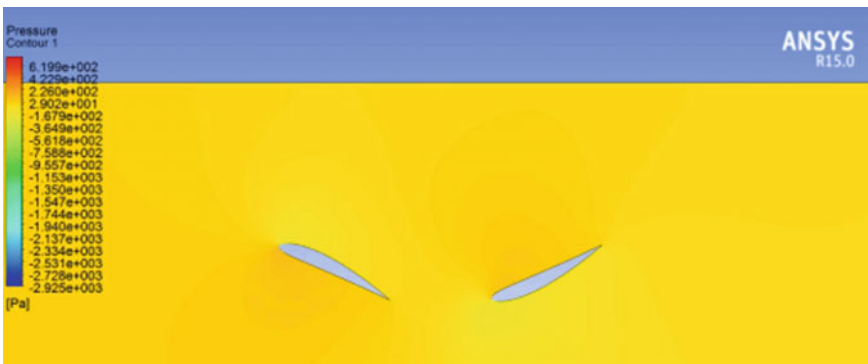
Fig. 7 Pressure contours

9 Conclusions

The result has implemented the new methodology. The basic design represents the methodology to generate additional power from the single wind turbine assembly. In the basic design using the empirical relations, the increase in power generation was expected to be 21.08%. Further, the detailed CFD analysis showed that, in practice, the actual power generation because of second rotor is quite high as expected from the theoretical design. The modified calculations of the available power available revealed that the increase in power generation is nearly equal to 38%.

References

1. James p. Cycon, fred w. Kohlhepp, vincent f. Millea, 1994, "coaxial transmission/center hub subassembly for a rotor assembly having, coaxial counter-rotating rotors", patent number: 5,351,913.
2. Putman p. C., 1941, "wind turbine", patent number: 2,360,791.
3. Brody, D. E. (2012). (12) United States Patent (45) Date of Paten: U. S. Patent, 2(12).
4. Sarangi, Dynamic Analysis of a Wind Turbine Blade.
5. Ostachowicz, W., McGugan, M., Schröder-Hinrichs, J. U., & Luczak, M. (2016). MARE-WINT: New materials and reliability in offshore wind turbine technology. MARE-WINT: New Materials and Reliability in Offshore Wind Turbine Technology, 1–432. https://doi.org/10.1007/978-3-319-39095-6.
6. Daut, I., Razliana, A. R. N., Irwan, Y. M., & Farhana, Z. (2012). A study on the wind as renewable energy in Perlis, northern Malaysia. Energy Procedia, 18, 1428–1433. https://doi.org/10.1016/j.egypro.2012.05.159.
7. Vaibhav R. Pannase, A. M. S. (2013). Optimization design, modeling and structural analysis of wind mill blade. Ijmerr, 2(3), 379–384.
8. Chehouri A., Younes, R., Ilinca, A., Perron, J., & Lakiss, H. (2015). Optimal design for a composite wind turbine blade with fatigue and failure constraints.
9. Joseph, A. P., Chavhan, S. P., Sahare, P. K., Arif, A., & Hussain, T. A. (2016). Review Paper on Wind Turbine using Magnetic Levitation 1, 5762, 87–90.
10. Schubel, P. J., & Crossley, R. J. (2012). Wind turbine blade design. Energies, 5(9), 3425–3449. https://doi.org/10.3390/en5093425 (Schubel&Crossley, 2012).

Parametric Optimization of MIG Welding on IS 1079 HR 2 by Taguchi Method

Mayur D. Jagtap and Niyati Raut

Abstract The hot-rolled low-carbon (IS 1079 HR 2) steel is widely used material in automobile industry. Joining of metal for different parts is done by GMAW. Process parameter greatly affects the welded joint strength. This paper presents the case study to investigate the ongoing MIG welding process carried out by industrial firm in its welding protocol, by suggesting alternative effective method to achieve better strength with improved process parameters. These suggestions are achieved by investigating parameters like welding voltage, current, and shielding gas. Research is designed by Taguchi method to get required data and further analyzed by *S/N* ratio with interaction plot. The optimum process parameters 150 A, 30 V, and 25 L/min gas flow rate are suggested. This research also suggests that Taguchi method has successfully improved the existing welding protocol of the firm.

Keywords IS 1079 HR 2 · Hot-rolled low-carbon steel · *S/N* ratio
Visual inspection · Tension test · UTM

1 Introduction

The IS 1079 HR 2 is hot-rolled low-carbon steel, which contains carbon of 0.12%. It is also called GRADE-D material which is specifically used for automobile industry. This particular material has properties like drawing, severe forming, and welding [1]. The weld ability of this steel and alloy is of great importance to manufacturing and automobile fields. The failure of such welding part in automobile can be life threatening. There is a lot of scope for setting parameters on an appropriate level to boost the strength of joint. However, most industrial firms stick to their old set of parameters, and this could happen because of lack of research on such material or on joining process. The value of each parameter affects greatly on the welded joint. Parameters for MIG welding are voltage, welding current, shielding gas flow rate,

M. D. Jagtap (✉) · N. Raut
University of Mumbai, Mumbai, Maharashtra, India
e-mail: mayur.mdj94@gmail.com

speed of welding, feed rate of filler wire. In most GMAW research, welding quality is judged by strength of joint and depth of weld bead.

Some of the researchers have been made investigation on GMAW for different materials with Taguchi techniques, those are as follows. Talabi et al. [2] investigated to find out tensile strength, hardness, and yield strength on low-carbon steel. His findings are if current and voltage increases it causes to increase heat input which would create room for defect formation, thereby reducing mechanical properties and yield strength. Karadeniz [3] investigated the process parameter on penetration on Erdemir 6842 steel. Welding current, speed, and welding voltage were selected parameters. Result shows that depth of penetration increases by increasing welding current (from 95–115 A) and increase in welding voltage does not show that much of difference in penetration depth. It was found that high-welding current causes high penetration depth, and for thin plates, it should be well determined. Haken Ates et al. [4] optimize parameter by ANN. Low-carbon steel (15*150*450) mm welded under 180 A and 28 V, CO_2 and Ar as shielding gas with flow rate 15 L/min and contact tip to workpiece distance 15 mm. ANN conducted to optimize parameter for mechanical properties. Gas mixture and welding current show significant effects on tensile strength and impact strength. Thakur et al. [5] investigated that Taguchi technique was used on RSW of AISI 3040 for finding out the effect made by input parameters on elastic quality. Hirato in 2004 [6] evaluated the performance of MIG by concluding that one pulse makes one drop transfer and its process was very effective for spatter reduction. He also states that stable and spatter-free welding was achieved by only controlling welding current from last 10 years. Size and shape of the welding depends on the detachment of metal drop. The author thinks that welding torch should have visual sensor for autoadjustment of feed rate and current for better penetration. Long et al. [7] used GMAW on thin plates of butt joints for distortion and residual stress investigation. During welding of plates, mechanical and thermal behavior model studied by using thermo-elastic plastic finite element simulation method. Welding distortions and residual stresses are greatly affected by welding thickness and welding speed. Heat transferred to the welding pool is traveled in the thickness direction of the plate and then in width and longitudinal directions to reach uniformed distributions. Juang et al. [8] adopted Taguchi method to study the effect of welding input parameters which are gas flow rate, supply current, welding speed, and arc voltage on the weld pool geometry. Juang also states that geometry was improved by using Taguchi method and smaller the better approach on S304 stainless steel of 1.5 mm thick. Sheshnk et al. [9] studied effect of pulse current GTAW parameters on bead geometry of aluminum checked by Taguchi approach and artificial neural network Tarng et al. [10] considered the Taguchi technique to examine the procedure parameters for ideal weld pool geometry in GTAW welding of treated. Yilmaz et al. [11] used MIG and TIG weldings for exploring the mechanical properties of AISI 304L and 316L. Filler used for GTAW was ER 308L and for GMAW was ER 316L. Joseph et al. [12] showed by his work that on selecting input parameters such as current, voltage, speed, and time against response of ultimate tensile strength of steel, and optimization was achieved by Taguchi method. Optimum process parameters current 240 A, welding time 2.0 min, speed 0.062 m/s, voltage

33 V were suggested. Shaha et al. [13] studied process parameters for MIG welding using L6 orthogonal array. Shielding gas used for this process was CO_2 and butt joint combination. Significance of factors on overall output features of weldments is carried out by ANOVA, and he also concludes that welding voltage has maximum influence. MIG Handbook [14] shows that carbon and low alloy steels are welded with CO_2 as shielding gas. Excess of CO_2 produces high level of spatter and low voltage is used to maintain short buried arc to minimize spatter. Ghazvinloo [15] studied Taguchi method on AA6061 joints with input parameters as welding current, welding voltage, and welding speed on fatigue life, bead penetration, and impact energy.

2 Taguchi Approach

This method is invented by Dr. Genichi Taguchi, a Japanese QA consultant. It is an integration of design of experiment (DOE) and parametric optimization of process with the help of orthogonal array. It provides well-reduce experiment of variance resulting in different level of process parameters with optimal setting [16]. To get the optimal parameter setting *S/N* ratio is used. It is meant to deviation ratio that means signal to noise. The *S/N* ratios are:

$$S/N \text{ ratio for smaller the best: } \eta = -10 \log[(\Sigma Yi2)/n] \qquad (1)$$

$$S/N \text{ ratio for larger the best: } \eta = -10 \log[(\Sigma 1/Yi2)/n] \qquad (2)$$

where

Yi *i*th observed value of response
η signal-to-noise ratio,
y average of observed response
n no of observations in a trial.

For this research, *S/N* ratio larger the best is selected as maximum tensile strength is needed which will give the optimum result.

3 Experimental Setup

In this, experiments are done according to L_9 orthogonal array (OA) design available on Minitab 18. Welding voltage, welding current, and shielding gas flow rate are the selected parameters. The base metal is hot-rolled low-carbon steel with a dimension 100 mm × 50 mm × 3 mm is joined by GMAW welding. No edge preparation required for low-carbon steel as it is less than 3-mm thick. ER 70S-60 is a mild steel solid wire formulated to provide high strength required dimension for 3-mm-thick

Table 1 Chemical composition of IS 1079 HR 2

Carbon %	Manganese %	Silicon %	Sulfur %	Phosphorus %	Nitrogen %
0.1200	0.500	0.150	0.040	0.040	90

Table 2 Chemical composition of ER 70S-6

Chemical composition requirement	
C = 0.06–0.15%	Ni = 0.15 max
Mn = 1.40–1.85%	Cr = 0.15% max
Si = 0.80–1.15%	Mo = 0.15% max
P = 0.025% max	V = 0.03% max
S = 0.035% max	Cu = 0.50% max

Table 3 Process parameters and their levels

Factors	Unit	Levels of factor		
		0	1	2
Welding current	Ampere	75	100	150
Welding voltage	Volt	24	27	30
Gas flow rate	l/mm	12	20	25

Table 4 Data collected as per L_9

Sr. no	Welding current (A)	Welding voltage (V)	Gas flow rate (L/min)	Tensile strength (kN)	*S/N* ratio
1	75	24	12	23.95	27.58
2	75	27	20	41.75	32.413
3	75	30	25	47.00	33.44
4	100	24	20	36.25	31.18
5	100	27	25	34.15	30.66
6	100	30	12	37.00	31.36
7	150	24	25	37.9	31.57
8	150	27	12	36.75	31.30
9	150	30	20	40.15	32.073

plate is 0.8 mm copper-coated as per AISI (American Iron and Steel Institute). The base metal (IS 1079 HR 2) and filler rod (ER 70S-60) compositions are shown in Tables 1 and 2, respectively.

Selected parameters are shown in Table 3 with their levels. Minitab 18 suggested orthogonal array that was used for data collection shown in Table 4. For this, base metal is joined by MIG welding process and it is done on MANDAR MW-MIG 300 welding machine. Varied input parameters were used to make butt-welded joints. After visual inspection, tensile test carried out on specimen is shown in Fig. 1. For tensile test, small size specimen is made in the workshop and it is tested on UTM.

Model no of UTM   UTE-100,

Serial no   1/2016-5644
Maximum capacity   1000 kN

3.1 Results

The result of the optimization process is shown in Table 4. *S/N* ratio and the main effect plot were utilized to understand the relation between these input parameters like current, welding voltage, and gas flow rate. First of all, the input parameters are defined in the software as per their corresponding value and then give the response data to optimize.

3.2 Analysis of Tensile Strength

After conducting all run-order, Taguchi method is applied on the result using Minitab 18. Following Figures (Figs. 2 and 3) describe the *S/N* ratio and mean for the tensile strength.

For this research, *S/N* ratio larger the best is selected as we need maximum tensile strength which will give the optimum result that shown in Table 5.

From the above figures, we can conclude as follows:
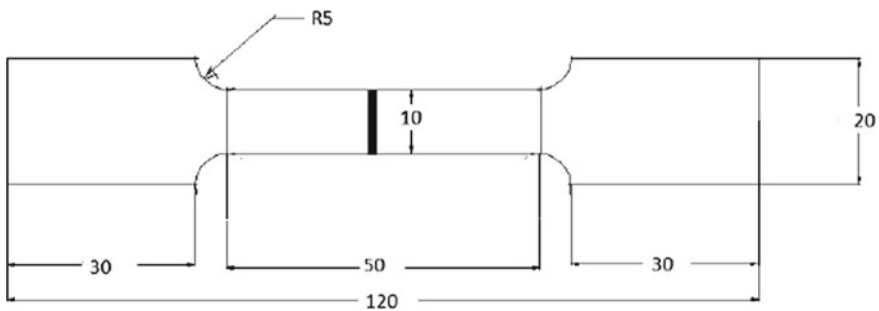
Fig. 1 Tensile test specimen

Table 5 Response Table for *S/N* ratio

Level	Welding current	Welding voltage	Gas flow rate
1	29.84	29.56	29.55
2	29.85	29.95	30.07
3	30.01	30.18	30.07
Delta	0.17	0.62	0.52
Rank	3	1	2

Main Effects Plot for Ultimate Strength
Data Means
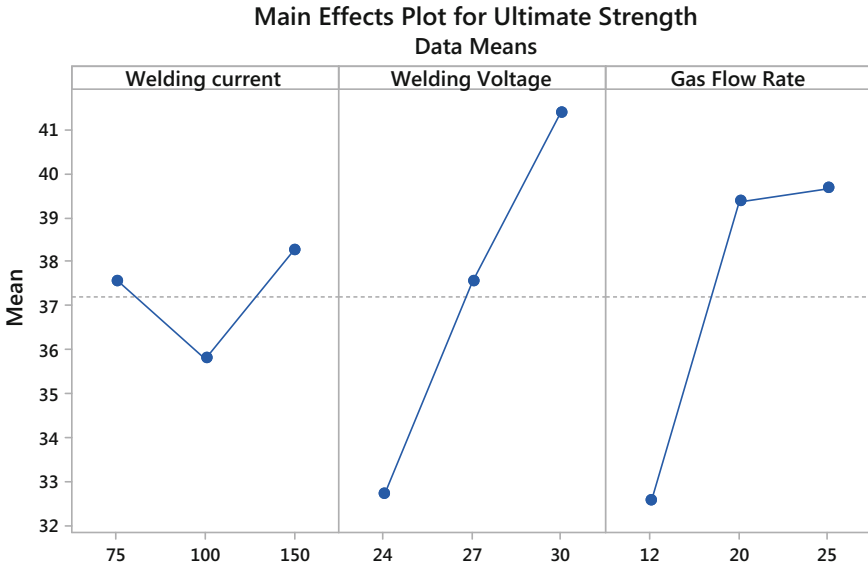
Fig. 2 Process parameter versus mean of tensile strength

Interaction Plot for Ultimate Strength
Data Means
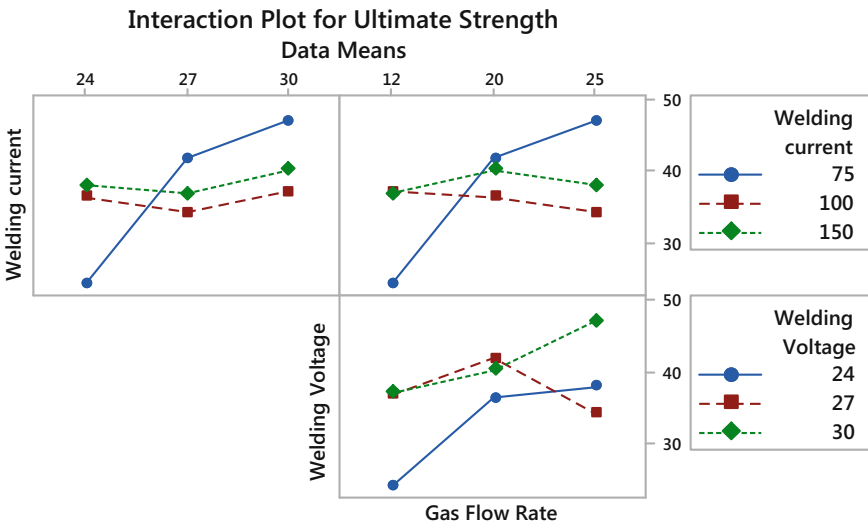
Fig. 3 Interaction plot for ultimate strength

1. **Effect of welding current on tensile strength:** We observe that tensile strength shows pattern on the range from 75 to 150 A. We get maximum strength of welding joint at 150 A. From the *S/N* ratio, we see that the value increases gradually at the range of 100–150. It lies in between 31 and 32.

2. **Effect of welding voltage on tensile strength:** We observe that voltage plays vital role in strength. As voltage increases from 24 to 30 V, tensile strength also increases. From *S/N* ratio table, we can see that values of mean of *S/N* ratio increases with increasing in voltage in a range of 24–32.5.

3. **Effect of gas flow rate on tensile strength:** We observe that gas flow rate affects the strength up to certain level as strength value does slightly increases with increasing gas flow rate.

4   Conclusion

The Taguchi method has been applied on IS 1079 HR 2 product which is widely used for reverse gear shifter of auto-rickshaw parts. The result gives the best and improved combination for existing welding parameters of industrial firm. The suggested values for optimize combination obtained from the *S/N* ratio and main effect plot are welding current 150 A, welding voltage 30 V, and CO_2 gas flow rate 25 L/min for the 0.8 ER 70S-6 copper-coated electrode. It is also found that voltage has a great influence on welding quality of joint.

References

1. Bureau Of Indian Standards. http://www.bis.org.in/mtd/mtd4(4730).
2. Talabi S.I., Oqolabi O.B.: Effect of welding Variable on Mechanical Properties of Low Carbon Steel Advances in production Engg. & Management. DEC 2014. Vol. 9. 181–186.
3. Karadeniz, Erdal, The effect of process parameters on penetration in gas metal arc welding processes. Turkey: Material & design, 28(2007). 649–656.
4. Haken Ates, Prediction Of Gas Metal Arc Welding Parameter Based On ANN Tarkey: AI-Department Of Metallurgy, FEB(2007).
5. A. G. Thakur and V. M. Nandedkar. Application of Taguchi method to determine resistance spot welding conditions of austenitic stainless steel AISI 304, Journal of Scientific & Industrial Research, 69 (2010) 680–683.
6. Hirato, Yoshinari, Recent Progress Of GMAW Processes In Japan. Suita, Osaka: Material & Manufacturing Science. 565–871.
7. H. Long, D. Grey. Prediction of welding distortion in butt joint of thin plates Material & Design, 30(2009). 4126–4135.
8. S.C. Juang, Y.S. Tang. Process Parameter Selection For Optimizing The Weld Pool Geometry In The Tungsten Inert Gas Welding Of Stainless Steel: Journal Of Material Processing Technology, 2002. 1233–37.
9. Sheshnk,K., Prediction Of Bead Geometry In Pulsed Current Gas Tungsten Arc Welding Of Aluminum Using Artificial Neural Network. Proceeding Of International Conference On Information And Knowledge Engineering, IKE; June 23–26, Las Vegas [NV], USA: 149–53(2003).
10. Tarng YS, Yang WH, The Use Of Fuzzy Logic In The Taguchi Method For The Optimization Of The Submerged Arc Welding Process. Inter J Adv Manuf Technology 16:688–694(2000).
11. Yilmaz R., and Uzun H., Mechanical Properties Of Austenite Stainless Steel Welded By GMAW And GTAW. Journal Of Marmara For Pure And Applied Science 18(2002): pp. 97–113.

12. I. Joseph, Optimization Of GMAW Protocols & Parameters For Improving Weld Strength Quality Applying The Taguchi Method july 6–8 2011, UK: Proceeding Of The World Congress On Engineering, 2011, Vol. I.
13. M.K. Shaha, Santanu Das. Researchgate.Net. [Online] 2012. https://www.researchgate.net/publication/278026692.
14. K. Weman and G. Lindén, MIG Welding Guide, Woodhead Publishing Limited, 2006.
15. Ghazvinloo H. Effect Of Arc Voltage, Welding Current & Welding Speed On Fatigue Life, Impact Energy & Bead Penetration Of AA6061 Joint Indian Journal Of Science & Technology, 2010, Vol. 3.
16. R.K. Keshwani, S.K. Panda. S.K. Pal, Multi Objective Optimization of Friction Stir welding Parameters for joining of Two Dissimilar Thin Aluminum Sheets, Procedia Material Science, 6(2014) 178–187.

Design and Prototype of Wireless Robot for Condition Monitoring of Coal Conveyor Roller Bearings

Vikesh P. Kumawat, Nikhil S. Divate, Sangeeta Bansode, Amit Kumar Patel and Kailas S. Jagtap

Abstract Belt conveyors are a critical part which plays an important role in the mining, processing, and transportation of coal in thermal power plant. It is necessary that the conveyor system must operate maximum efficiency without any major breakdown. The project consists of an implementation of sensor, hardware and software platform which measures temperature and noise level of each bearing of roller with frame number and generates the report cum warning system and live video output of maintenance carried by robot in controlling computer. The implementation of robot with real-time online condition monitoring of roller in conveyor system of thermal power plant will reduce the overall maintenance cost of thermal power plant and it will also save the man power and improve the safety which requires during maintenance personnel.

V. P. Kumawat (✉) · N. S. Divate · K. S. Jagtap
CAD CAM and Robotics, K J Somaiya College of Engineering,
Mumbai 400 077, India
e-mail: vikesh.k@somaiya.edu

N. S. Divate
e-mail: n.divate@somaiya.edu

K. S. Jagtap
e-mail: kailas.jagtap@somaiya.edu

S. Bansode
Department of Mechanical Engineering, K J Somaiya College of Engineering,
Mumbai 400 077, India
e-mail: sangeetabansode@somaiya.edu

A. K. Patel
Tata Power, Mumbai, India
e-mail: amitkumar.patel@tatapower.com

1 Introduction

In an industrial revolution, material handling performs a key role in product development and company growth for that several transportation systems get used like cranes, industrial trucks, and conveyors, manual handling, etc. When the material needs to move frequently between specific points and in a fixed path with sufficient flow, then conveyor system is considered to be the best option. Belt conveyor is the best out of all conveyors types which provides a smooth and fast transportation of material especially in powder form like coal in thermal power plant.

The initial cost of coal conveyor is not so high, and power consumption for system is also less. The belt conveyor is successfully used mostly which has an inclination angle of roller 25°–140° to the horizontal. The load carrying capacity of conveyors may vary from 60 to 120 tones/h.

1.1 Structure of Belt Conveyor and Operating Condition

The belt conveyor consists of driving unit which includes a motor for conversion of electrical energy to mechanical energy, gear for power transmission, belt for carrying coal, idlers for support of belt and several auxiliary parts like which acts as support and control in the coal conveyor system. The performance of coal conveyor system is totally dependent on its operating condition. The main operating component of conveyor is roller (Idler) that consists of parts shown in Fig. 1.

Most of the thermal power plants are always located at the remote location like near seashore. As coal conveyor system works openly that needs to face the all environmental condition on a coastal area like a dusty environment with high moisture and differential temperature condition.

As the environment is very dusty and rusty that affects the parts of conveyor like outer and inner body parts of roller which include bearing, seal working conditions.
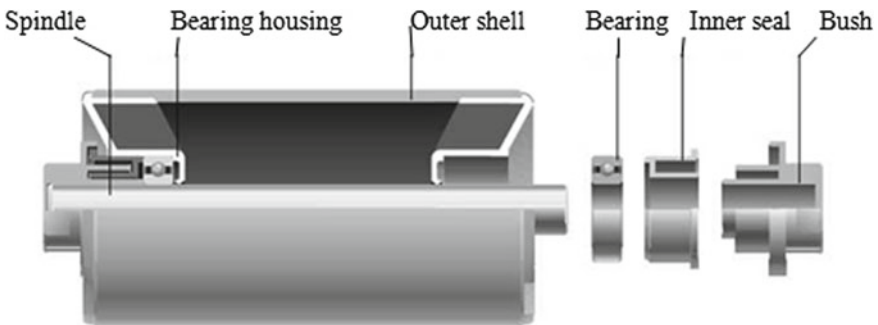
Fig. 1 Solidworks model of assembly parts of roller (Idlers)

The defect in any single part leads to disturbances in rotary motion further which causes the vibration and rise in temperature due to high friction.

Belt conveyor system generally designed to work continuously for longer time, Due to continue working and at variable load acting on parts the misalignments of rollers shaft leads which to major failure in the conveyor system which causes to carry out the maintenance after particular interval. The maintenance is an important issues in a conveyor system which can be viewed in two ways: first kind is that replacement of part done when sudden breakdown occurs and second is replacement of part done during pre-scheduled maintenance.

1.2 Objectives of Project

The coal conveyor system is basically used to transport the coal from one place to other, as the plant is located near seashore that causes the dust particles to enter to the open conveyor system along with the coal dust particles. As a result of that rollers may get jammed due to dust contamination on bearings, if the rollers still go on rotating continuously that causes extra vibrations in it that further produces the noise. If noise increases that increases the chances of bearing failure. To minimize that noise data must be calculated and to do that the following project objectives must be satisfied to ensure and deliver the proper solution:

1. Design and construct of robot which will carry whole sensor and other useful devices which are required for monitoring of rollers.
2. To build up sensor platform this will detect the noise level of bearings.
3. To develop simple wireless communication system to make robot.
4. To generate report cum warning system for the maintenance personnel.

2 Literature

The literature represents the investigation done by various authors in the different field of belt conveyor which include the various sources which are responsible for breakdown of belt conveyor and importance of roller monitoring and sources of roller failure in conveyor.

Reciks [1] defines the role of idler in conveyor system that also includes the design parameters of the rollers along with material selection which decides the life of rollers. Author also focuses on the bearings as it is an important component of the roller, selection criteria also implies the smooth and continued operation of the conveyor system. Watson [2] states for high-speed conveyor systems, design parameters become most critical part due to high precision requirement. In this paper, author tried to find out the failure cause due to design and manufacturing parameters.

In that same description failure due to end cap deflection, loose base holding and roller imbalance are discussed.

Zimroz [3] defines failure analysis for condition monitoring and the estimation of problem which most frequently occurs with their location on system. The paper also deals with the method which requires for each part of system. The most frequent failure is due to bearings, shells, gearbox, and shaft. According to author, vibration test can be used for gearbox and pulley testing, and model analysis for pulley shell damage detection, idler condition by thermography, belt condition by nondestructive testing like magnetic field measurement can be used. Akula [4] discussed about the principle of thermal imaging and use of thermal image in different application. The studies elaborate thermography to capture hot spots; the hot spots are the area on roller where the temperature is significantly higher than surrounding areas which can be captured by non-contact way.

Smith [5] proposed the system for continuous monitoring of the sound level (Noise). Author also states the reasons for the noise generations from the mining machines under load and unloads conditions. Noise created due to dust contamination on the hydraulic machines and mining machines was calculated and compared with the noise of the rollers of the conveyor system as a part of result. To calculate the noise or sound level, Jiang [6] made an audio detection system which is actually based on neural network using wavelet transform system. In the wavelet method, Fourier transformation is used to observe a sound signal in time domain and frequency domain by attending this author manages to state the importance of automatic fault detection system.

3   Methodology

Figure 2 shows that literature reviews clear all basic parts which are needed for fabrication of robot. Selection of sensor for noise and temperature, it's coding and interfacing with microcontroller provides the data which is required for analysis.

4   Proposed Work

4.1   Basic Concept

The block diagram of basic concept is shown in Fig. 3, which represents sensor platform along with components. Microprocessor performs major part as it controls the microcontroller along with all sensors. RFID defines the location of the roller stage. As a part of working when RFID reads the card located at the roller frame stage running motor receives command to stop for particular time (5 s) at the same time both the sensors (temperature and sound) get turned on and started getting live
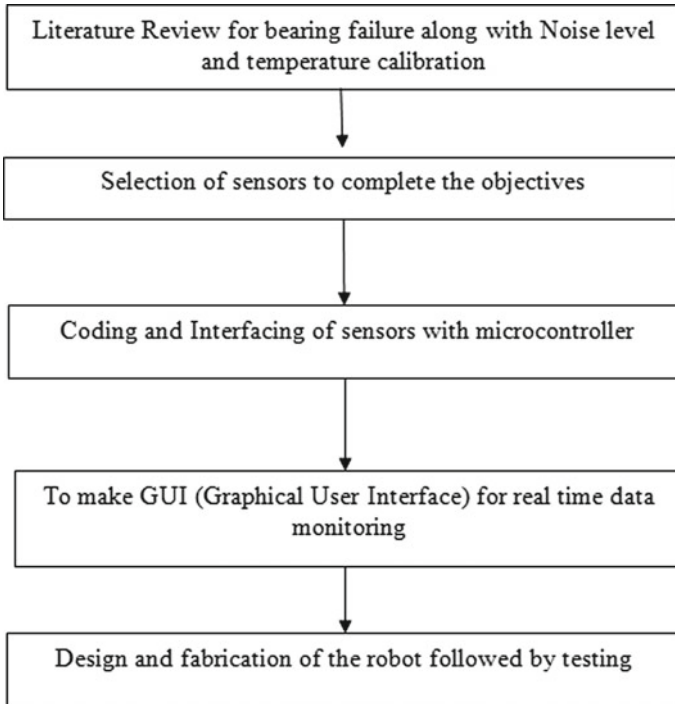
Fig. 2 Flowchart of approach to fulfill the inspection requirements

data which can be stored in the text file then the data transfer to .CSV file for further analysis. The camera interface with microprocessor provides live video streaming which can be tracked on graphical user interface in which sensor data can also be viewed. The microprocessor is connected to a WIFI which helps to send data live wirelessly.

4.2 Hardware Requirement

a. **Temperature sensor**

To measure hot spot on roller's bearing, the infrared non-contact temperature sensor is selected. Due to high vibration, misalignment of shaft rollers and high friction at the bearing cause increase in temperature of bearing, so to find the temperature of bearing becomes necessary part. Figure 4 shows the working and connection of sensor with microcontroller.

b. **Sound sensor**

Conveyor system works continuously for longer time, due to contamination of dust particle in bearing amplitude of vibration started increasing that leads to increase in
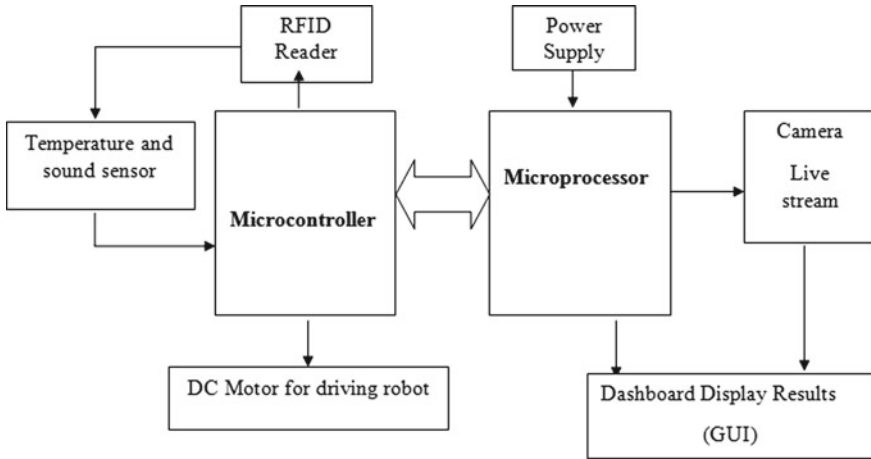
Fig. 3 Block diagram of system components
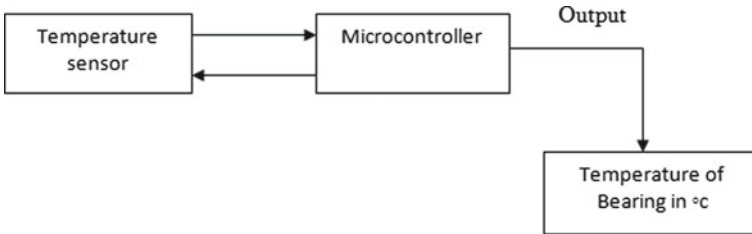
Fig. 4 Working of temperature sensor
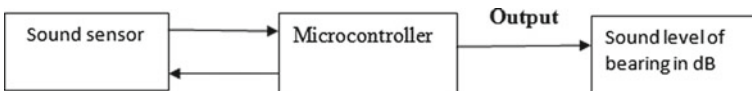
Fig. 5 Working of sound sensor

noise. Sound level meter is selected which gives sound level in decibel (dB) which is controlled by microcontroller, Fig. 5 shows the working and connection of it.

c. **Motor**

A planetary geared DC motor is selected for requirement of high torque and high load carrying capacity. This motor is also suitable for inclined angle path at conveyor system and it is controlled by microcontroller.

d. **RFID reader**

125 kHz (low frequency) receiving capacity RFID reader is used which has 1 ft of tag treading range. It is controlled through the microcontroller and its signals are responsible for movement of motor.
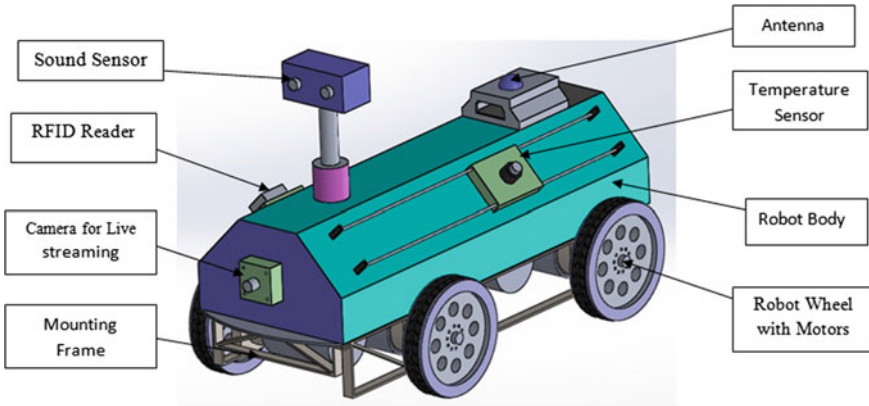
Fig. 6 Solidworks design of robot
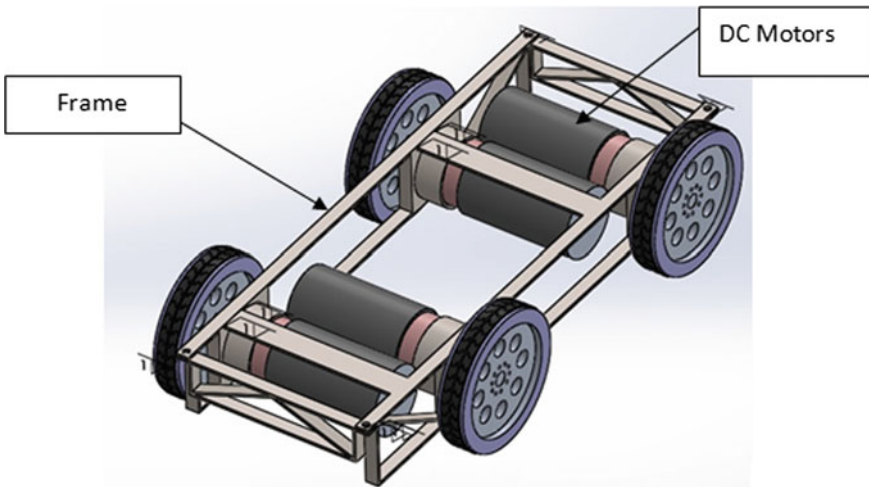
Fig. 7 Solidworks model of motor mounting

4.3 *Robot Design with Sensor Adjustment*

The proposed design of robot after interfacing of all sensors with microcontroller and microprocessor can be viewed in Figs. 6, 7 and 8.

Fig. 8 Internal hardware of robot
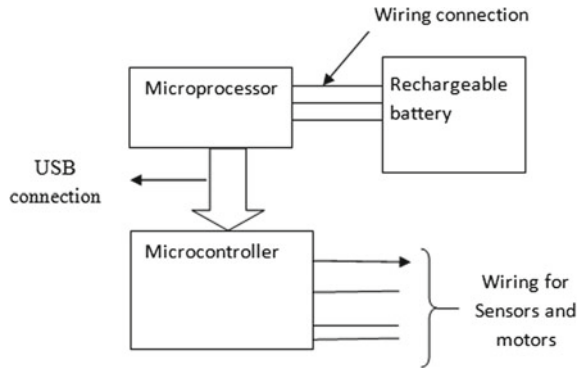
	A	B	C	D	E
1	**Date and Time**	**Roller Frame Number**	**Sound Level (dB)**	**Temperature of Hot spot (°c)**	**Ambient temperature (°c)**
2	16/03/2018 14:31	Frame 1	75	100	32
3	16/03/2018 14:32	Frame 2	70	95	32
4	16/03/2018 14:33	Frame 3	72	98	32
5	16/03/2018 14:34	Frame 4	73	102	32
6	16/03/2018 14:35	Frame 5	73	102	32
7	16/03/2018 14:36	Frame 6	74	105	32
8	16/03/2018 14:37	Frame 7	75	107	32
9	16/03/2018 14:38	Frame 8	75	107	32
10	16/03/2018 14:39	Frame 9	73	98	32

Fig. 9 Live Sensor data in excel

5 Results

At a conveyor system, roller stages are located at 2 m apart from each other. So, the robot stops at each stage take the data of sound and temperature along with ambient temperature which is live and stored in text file by serial communications of microcontroller with an software this text file is imported in excel sheet for better visualization. Figure 9 shows the sensor report in excel format, and Fig. 10 shows the data in graphical format.

6 Future Work

1. NVH and thermal analysis of bearings of roller to calculate vibrational amplitude and variation in temperature.
2. Comparing the sensor data with the analysis results.
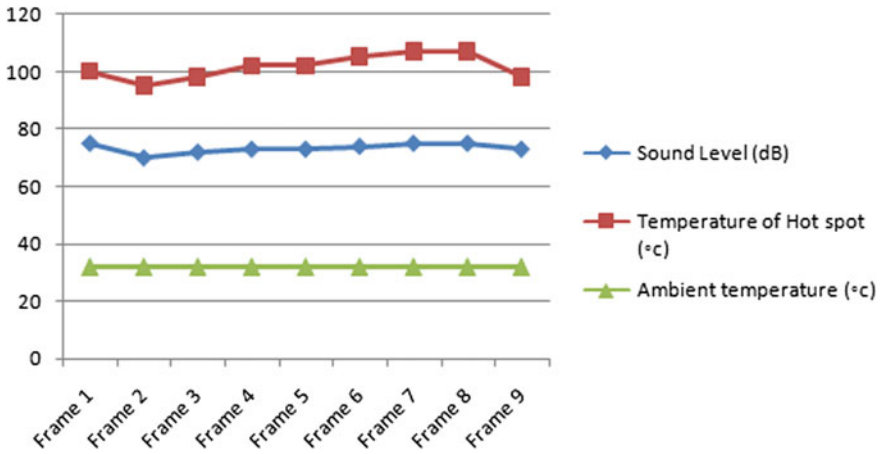
Fig. 10 Sensor data in graphical format

3. Implementation of graphical user interface for sensor data visualization.

References

1. Allen V. Reciks, A. Belt conveyor idler roll behaviors (2008).
2. D.R. Watson High speed conveyor idlers (2010).
3. Radoslaw Zimroz. Failure analysis of Belt conveyor systems for conditionmonitoring purposes. (2009).
4. Aparna Akula. Thermal imaging and its application in defense systems. AIPconference proc.1391, 333–335(2011) American institute of physics 978-0-7354-0960-6.
5. Adam K Smith. Continuous Mining Machine Conveyor System Sound Power Levels.
6. Xiao-ping Jiang. Belt conveyor roller fault audio detection based onWavelet neural network. IEEE (2015).

Design, Analysis and Modification of 3 Stage Helical Gearbox Casing Using Finite Element Method Considering Different Materials

Ronak D. Gandhi and Nimeshchandra S. Patel

Abstract   An effort was made to design and analyse triple deduction helical gearbox housing. To start with, the investigations were carried out to examine and interpret the structural performance of gearbox casing. After surveying literature, it was found that majorities of companies nowadays are facing problems of total weight and strength of their existing gearbox. Thus, design and analysis of gearbox cover have evolved a prominent field of exploration to diminish the failures and for optimal model. Hence, modal analysis, vibration analysis, harmonic analysis and response spectrum analysis were performed for existing helical gearbox casing (structural steel A36) and modified design (high carbon steel and structural steel A36) to predict behaviour of gearbox casing subjected to respective loading and no loading conditions. From design and analysis perspective, lastly it was safely concluded that, modified design having material high carbon steel is best suited as compared to existing model in regard to resilience, weight, vibrations, durability, material and cost.

Keywords   Triple deduction gearbox housing · Permanence · Prominence
Finite element approach and optimization

1   Introduction

Gears are one of the most critical components in mechanical power transmitting devices and in most of the industrial rotating machinery. These gears systems are encircled in a rigid closed cover called as gearbox casing or housing. Arrays of forces are acting on gearbox cover which must be managed precariously while modelling the gearbox casing. In the gearbox covering design, main reasons for the dereliction of the gearbox casing are bending stress, surface strength of the gear tooth's and vibrations. Hence, stress analysis is very essential which can help designer to find out

R. D. Gandhi (✉) · N. S. Patel
Department of Mechanical Engineering, Faculty of Technology,
Dharmsinh Desai University, Nadiad 387001, Gujarat, India
e-mail: ronakgandhi401@gmail.com

how much is stress acting and also to predict behaviour of casing and its components subjected to actual stagnant and vigorous loads. There were several people who are associated with this study and design modification of the helical gearbox casing. The details of some of the persons and their contributed work are further discussed.

Emmanuel et al. [1] studied the impact of mechanical properties for different elements on the crucial rotating speeds of gearbox using finite element method. The computation of the vibrational reverberation revealed that the maximum dynamic mesh forces equivalent to a resonant excitation of modes which have an utmost potential energy relevant with the mesh clumsiness. Further, numerical simulations showed that a realistic forecast of vital rotational speeds should consider the entire constituent in the gearbox.

Sekar et al. [2] analysed thermal and equivalent von misses stress pursuing on inward and outward gearbox casing employing numerical method like finite element analysis. Moreover, convection effect linking the internal surface of casing and circulating oil is also discussed. This issue was found trivial and thus neglected. Furthermore, results obtained showed that thermal stress acting on the gearbox cover was 68.866 MPa along with deformation of 0.15434 mm considering the impact of both force and heat.

Chhabra et al. [3] discussed their work on modelling and analysis of composite material gearbox. In this paper, computer-aided methodology to create and analyse stress and deformation acting on 3D model of gear box was used. In addition, expedition of composite material gearbox was done to restore the existing metallic gearbox for specific weight minimization to acquire enhanced energy efficiency, corrosion resistance, noise curtailment, prominent inherent frequency and more stabilized model.

Hazry et al. [4] studied vibration diagnosis for gearbox housing using finite element approach. The primary purpose of this work was to execute analysis for evaluating the recurrences and harmonic frequency response in order to intercept resonance of gearbox casing. Moreover, it was found that the vital component was the design of the fastened couplings within the uppermost and lowermost casing and the modelling of the attachments to the support. Furthermore, results acquired exhibited the extent of the frequency that was preferable for gearbox cover to intercept maximum amplitude.

After surveying various literature [1–5], it can be concluded that majority of the work have already been done on 2 stage helical gearbox casing. From the study [6–8], it was further found that very few investigators have worked in field of 3 stage gearbox casing. Furthermore, it was terminated that most of organizations are facing problems of total weight and strength of existing gearbox [9–12]. So, present work was carried out with prime objectives to minimize the weight and improve strength of casing.

2   Gearbox Specifications

Triple stage helical gearbox is connected to one leaf of the bridge utilizing leading drive pinion. This gearbox weights nearly 900 kg and is compelled by the differential gearbox. The material of the housing is ASTM Steel A36 with a modulus of resilience (E) of 29 * 10^6 psi or 200 GPA and Poisson's ratio (μ) of 0.26 [13]. This housing is linked together by a consolidation of welding and bolted joints. This gearbox is outlined to impart 112.5 h.p. at 174 rpm with a gear ratio of 71.0521. The summaries of shaft and gear specifications are revealed in Tables 1 and 2, respectively. The dimensions and specifications were provided by Finstern Engineering Private Limited Company, Vadodara [15].

Table 1   Shaft informations for triple stage helical gearbox [15]

Shaft	Diameter (mm)	Length across bearing ends (mm)
Input shaft	65.0	552.0
First intermediate shaft	62.0	
Second intermediate shaft	90.0	
Output shaft	130.0	

Table 2   Pinion and gear specifications for the triple reduction helical gearbox [15]

Name	No. of teeth	Diametric pitch	Helix angle (°)	Pressure angle (°)
Input shaft pinion	16	3	15	20
First intermediate shaft pinion	16	2	20.24	20
First intermediate shaft gear	72	3	15	20
Second intermediate shaft pinion	19	1.5	15	20
Second intermediate shaft gear	60	2	20.24	20
Output shaft gear	80	1.5	15	20

3 Finite Element Modelling and Analysis

3.1 Finite Element Modelling

3D CAD Modelling. Computer Aided Design (CAD) is described as adoption of computing devices for modelling, refinement, investigation and optimization of designs. It usually contains all design data such as geometry, dimensions, tolerances and manufacturing related details. Modelling software that can be used is Creo 2.0, CATIA V5R20, NX, SolidWorks, etc. Thus, as per company specifications and dimensions, 3D CAD model was prepared in CATIA V5R20 modelling software.

   Meshing. Meshing feature in ANSYS workbench 14.5 imparts designer with a distinctive involuntary mesh generation technology. Generally, meshing should be more dense and sparse near to the load and little load area, respectively. Existing and modified geometric model after meshing with proper mesh size of 5 mm is presented below (Figs. 1 and 2).

   Applying Material Properties. This engineering data workspace is outlined to admit creator to produce, preserve and recover material properties. Here, the material which was used for existing gearbox casing is structural steel A36 having modulus of elasticity (E) of $29 * 10^6$ psi or 200 GPa and Poisson's ratio (μ) of 0.26 [13]. Whereas, material selected for modified design was high carbon steel with a modulus of elasticity (E) of $30.45 * 10^6$ psi or 210 GPa and Poisson's ratio (μ) of 0.26 and structural steel A36 with a modulus of elasticity (E) of $29 * 10^6$ psi or 200 GPa and Poisson's ratio (μ) of 0.26 [13].
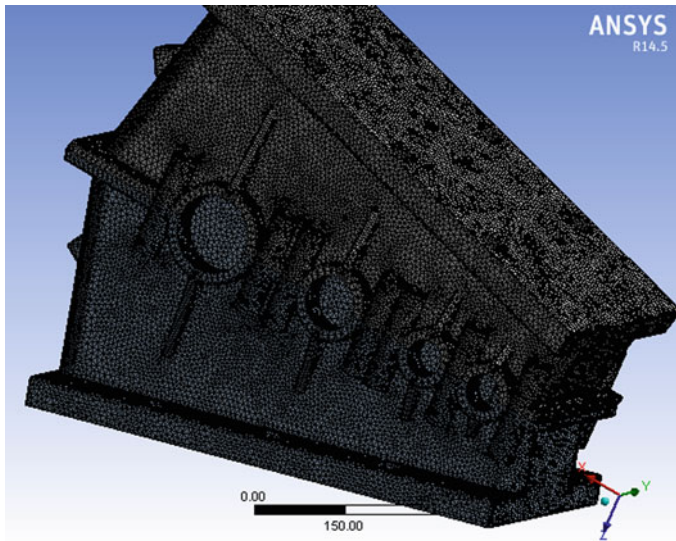
Fig. 1 Meshed model of existing helical gearbox casing
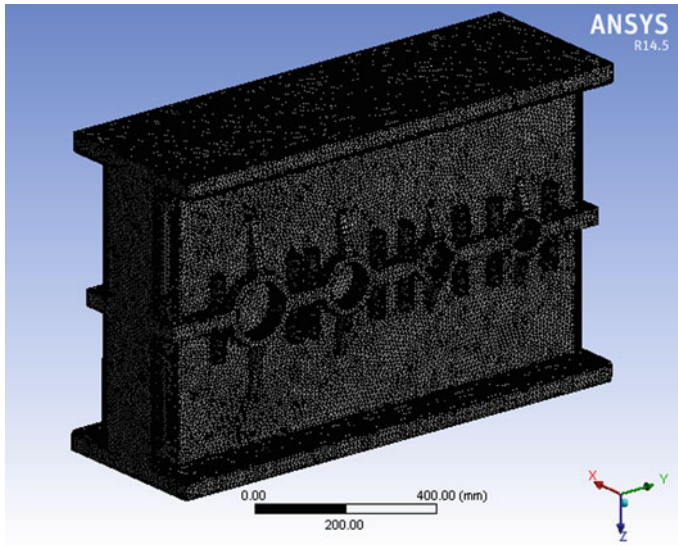
Fig. 2 Meshed model of modified design helical gearbox casing

Applying Loading and Boundary Conditions. Gearbox support casing is fixed attached to the foundation through six bolted connections. Reposing surface of housing is also restrained in all degree of freedom. There are several forms of payloads pertinent over gearbox cover. The stagnant pressure of transmitting gear and drive shank pursuing on bearing hole splits into two parts, namely radial and axial thrust [14]. These loads are employed to ascertain the literal effect of stress and deformations acting on gearbox case. Thus, loading and boundary conditions were utilized on casing based upon application endowed by the company [15].

3.2 Finite Element Analysis

This analysis phase generally depends upon type of problem defined earlier or type of analysis like Modal, Vibration, Harmonic, Spectrum and Static structural analysis.

Modal Analysis. Modal analysis is a technique utilized for assuring the vibration peculiarities (inherent recurrences and mode configurations) of a design or an element while it is being modelled. Hence, analysing the inherent oscillations and mode profiles are very essential parameters in the modelling of a component. This modal analysis can further be served as a beginning point for more detailed analysis like transitory strenuous analysis, frequency response analysis and spectrum analysis. Total deformations which were obtained after performing modal analysis at few frequencies for modified model (H.C.S) are depicted in Figs. 3 and 4, respectively. Analogously, results which were procured after doing modal analysis for transformed
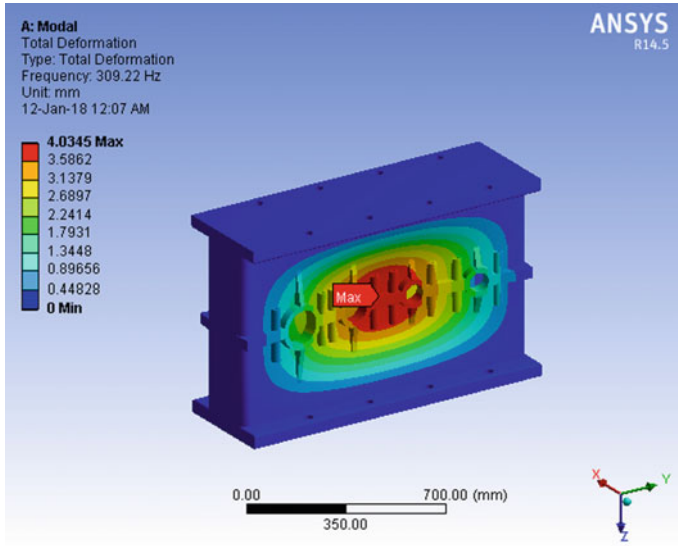
Fig. 3 Total deformation for modified design (H.C.S) at frequency of 309.22 Hz
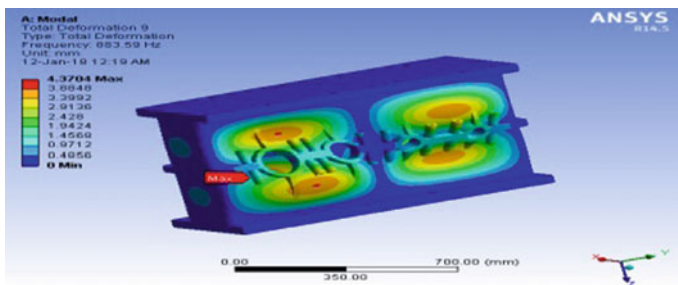
Fig. 4 Total deformation for modified design (H.C.S) at frequency of 883.59 Hz

design considering structural steel A36 and high carbon steel materials are outlined in Table 3.

Vibration Analysis. Vibration analysis is a method employed for predicting vibration that is occurring on the components during loading conditions. This vibration can be due to poor product design or the surroundings in which the product is operating. Sometimes, it can have a substantial influence on endurance and drowsiness, emineting to a curtailed service life. In industries, vibration analysis is mainly preferred to recognize any premature ancestors of machine deterioration, allowing equipment to be refurbished prior to an expensive breakdown happens which can relieve immense sustenance expense and equipment interruption significantly. Results which were achieved after carrying out vibration analysis for modified model (H.C.S) are exposed in Figs. 5 and 6, respectively.

Table 3 Comparison of modal analysis results between existing model and modified design

Name	Existing model (structural steel A36)			Design modification (high carbon steel)			Design modification (structural steel A36)		
	Freq. (Hz)	Min. value (mm)	Max. value (mm)	Freq. (Hz)	Min. value (mm)	Max. value (mm)	Freq. (Hz)	Min. value (mm)	Max. value (mm)
Total deformation	731.5	0	6.1273	309.22	0	4.0345	303.21	0	4.0344
Total deformation	734.5	0	6.2085	311.89	0	4.0823	305.83	0	4.0822
Total deformation	1103.3	0	4.5778	434.09	0	3.8982	425.66	0	3.8983
Total deformation	1181.8	0	5.5360	441.81	0	3.8751	433.23	0	3.8752
Total deformation	1357.0	0	4.7364	654.44	0	3.9034	641.73	0	3.9034
Total deformation	1507.0	0	6.6006	660.11	0	3.8506	647.29	0	3.8507
Total deformation	1512.0	0	6.6346	751.91	0	4.3978	737.91	0	4.4005
Total deformation	1587.2	0	5.1187	752.98	0	4.4153	738.36	0	4.4179
Total deformation	1715.4	0	5.3091	883.59	0	4.3704	866.44	0	4.3709
Total deformation	1918.4	0	4.6402	886.94	0	4.3927	869.41	0	4.3924
Total deformation	2078.4	0	6.8004	905.64	0	3.7859	888.05	0	3.7860
Total deformation	2109.6	0	6.9264	926.56	0	3.7988	908.57	0	3.7989
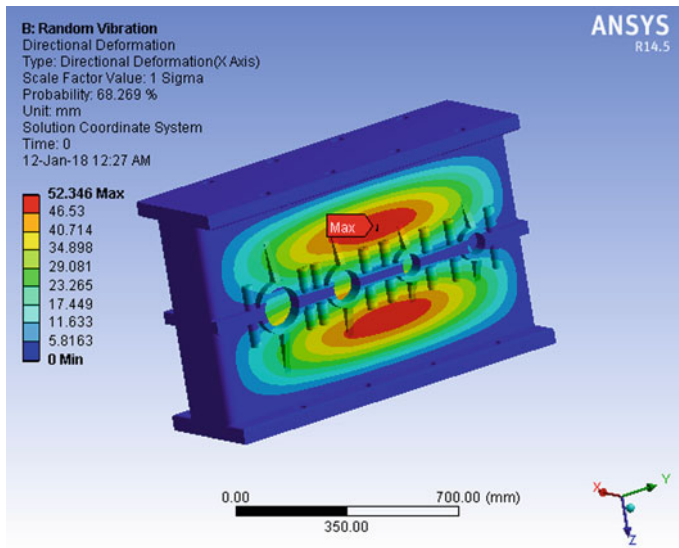
Fig. 5 *X* direction deformation obtained for modified design (H.C.S)
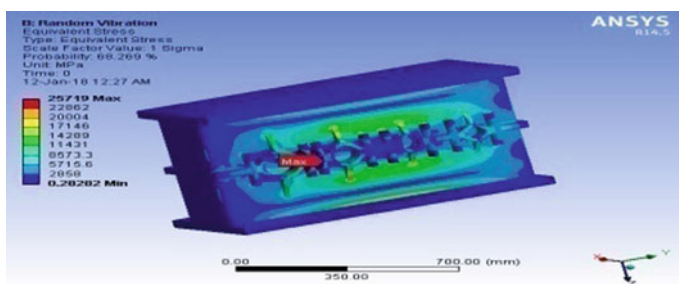
Fig. 6 Equivalent stress obtained for modified design (H.C.S)

Likewise, vibration analysis for altered design was accomplished using material structural steel A36. Results which were acquired after operating vibration analysis for refined model adopting structural steel A36 and high carbon steel materials are summarized in Table 4.

Harmonic Analysis (Frequency Response Analysis). Harmonic response analysis is an approach facilitated for computing the behaviour of elements enthralled to loads that differ sinusoidally (harmonically) in regard to time. Harmonic response analysis bestows designer the capability to anticipate the sustained dynamic response of their model, thus permitting designer to authenticate whether or not their model will favourably conquer reverberance, debilitation and other detrimental outcomes of forced oscillations. Hence, intension is to reckon the structure's behaviour at certain frequencies and thus acquire a profile of few response quantities versus frequencies.

Table 4 Comparison of vibration analysis results between existing model and modified design

Name	Existing model (structural steel A36)		Design Modification (high carbon steel)		Design modification (structural steel A36)	
	Min. value	Max. value	Min. value	Max. value	Min. value	Max. value
X direction deformation (mm)	0	12.135	0	25.346	0	51.852
Y direction deformation (mm)	0	91.416	0	4.5838	0	4.5400
Z direction deformation (mm)	0	41.625	0	17.949	0	16.506
Stress (MPa)	0.55757	$2.685\ e^5$	0.28282	25719.0	3.7002	29497.0
Strain	$2.7878\ e^{-6}$	1.3425	$1.3467\ e^{-6}$	0.122471	$1.5805\ e^{-6}$	0.14748
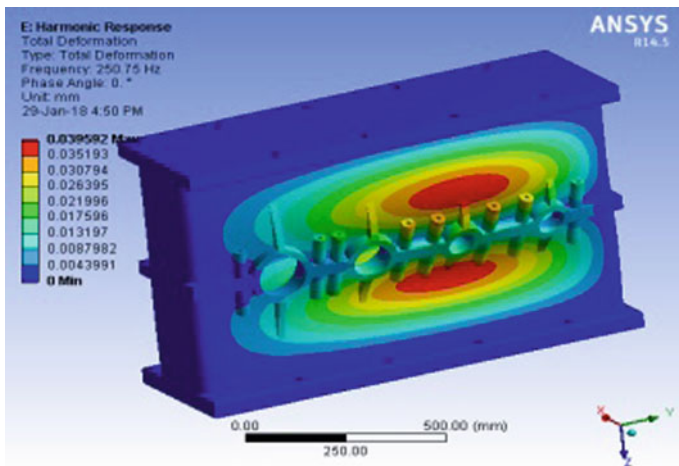
Fig. 7 Total deformation for modified design (H.C.S) at frequency 250.0 Hz

Total deformations and Equivalent stress gained after conducting analysis for modified design (H.C.S) at various frequencies are shown in Figs. 7, 8, 9, 10, 11 and 12, respectively.

Similarly, frequency response analysis was performed for reformed model utilizing material structural steel A36. Results which were secured after evaluating harmonic analysis for improved design taking both materials at different respective frequencies are epitomized in Table 5.

Table 5 Comparison of harmonic analysis results between existing model and modified design

Name	Existing model (structural steel A36)			Design modification (high carbon steel)			Design modification (structural steel A36)		
	Freq. (Hz)	Min. value	Max. value	Freq. (Hz)	Min. value	Max. value	Freq. (Hz)	Min. value	Max. value
Stress (MPa)	500	$2.2\,e^{-5}$	14.648	250.75	$4.2\,e^{-6}$	13.094	100.00	$3.6\,e^{-5}$	17.146
Total deformation (mm)	500	0	0.0720	250.75	0	0.0121	100.00	0	0.0373
Stress (MPa)	731.5	$2.5\,e^{-5}$	16.947	309.22	$5.7\,e^{-6}$	15.938	303.21	$8.6\,e^{-5}$	20.187
Total deformation (mm)	731.5	0	0.0837	309.22	0	0.0149	303.21	0	0.0443
Stress (MPa)	1000	$3.3\,e^{-5}$	22.634	750.00	$3.1\,e^{-6}$	18.397	500.00	$1.1\,e^{-5}$	30.545
Total deformation (mm)	1000	0	0.1115	750.00	0	0.0173	500.00	0	0.0665

Fig. 8 Total deformation for modified design (H.C.S) at resonance frequency 309.2 Hz

Fig. 9 Total deformation for modified design (H.C.S) at frequency 750.0 Hz

4   Results and Discussion

In the present work, detailed investigations were carried out to design and analyse behaviour of 3 stage helical gearbox casing. Table 3 shows correlation between results acquired after performing modal analysis for existing model and numerical ensues gained for modified design deliberating both materials. After comparing outgrowths of modal analysis, it clearly shows that good agreement is found between the results. Total deformations obtained for modified design contemplating both materials are almost nearly same. It may be due to possibilities that, there are no loading conditions
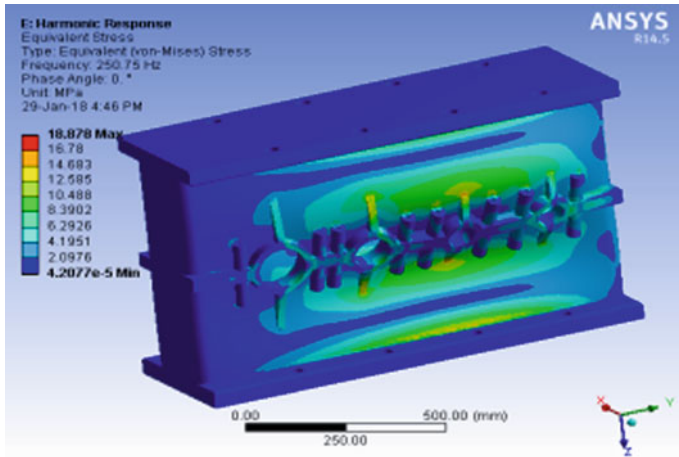
Fig. 10 Equivalent stress for modified design (H.C.S) at frequency 250.0 Hz
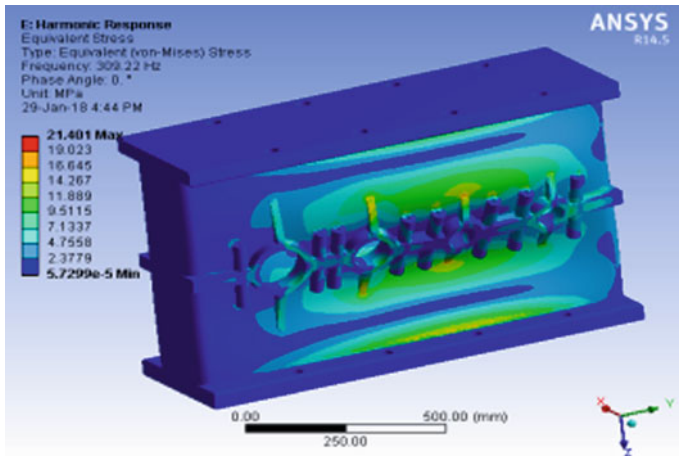
Fig. 11 Equivalent stress for modified design (H.C.S) at resonance frequency 309.2 Hz

applied in modal analysis or perhaps because of different materials used for analysis. Thus, from perceptive of strength, weight, vibrations, stress and material cost, modified design having material high carbon steel may exhibit good performance in correlation with existing model.

Further, these frequencies were used to accomplish random vibration analysis for various alternatives to predict vibrations that are occurring on the gearbox housing. Repercussions which were seized after exercising vibration analysis are summarized in Table 4. After matching results of vibration analysis, it clearly reveals that good concurrence is observed between the results. Additionally, it was also observed that
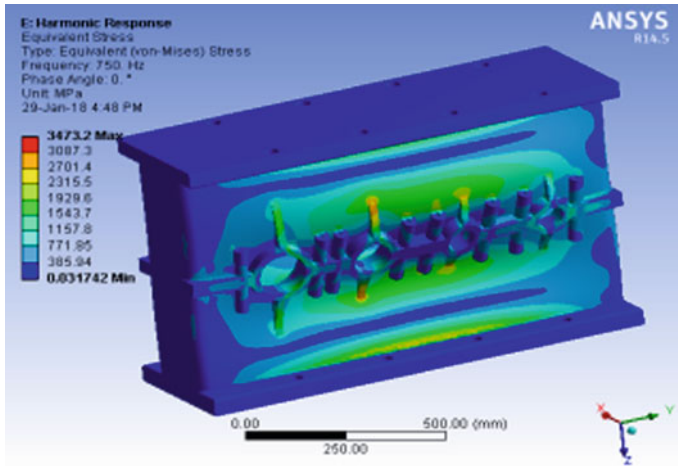
Fig. 12 Equivalent stress for modified design (H.C.S) at frequency 750.0 Hz

deformation values in 2 different directions are less in contrast to other direction. It may be due to fact that, loading conditions are applied in that particular direction where distortion is more. Moreover, stress value for modified design having material high carbon steel is very less in resemblance with existing model because of liability that, high carbon steel material is having more proportion of alloying elements like carbon, copper, iron, phosphorous, manganese and sulphur.

Furthermore, harmonic analysis was endeavoured for all choices to predict structure's responses subjected to forces that vary harmonically in respect to time. This frequency response analysis was fulfilled preferably at resonance frequency, frequency greater or lesser than resonance frequency to validate whether design would be able to overcome resonance, fatigue and other harmful effects of forced vibrations. Graph which were obtained while executing harmonic analysis contemplating materials high carbon steel and structural steel are manifested in Figs. 13 and 14 respectively. Results which were attainted after enacting frequency response analysis at certain natural frequencies are encapsulated in Table 5. After correlating outcomes of frequency response analysis, it precisely indicates that agreeable concordance is perceived within the outgrowths.

5   Conclusion

After comparing various finite element analysis results for design modification (H.C.S and S.S.A36) with the numerical results retrieved from existing model (S.S.A36), following conclusions were drawn:
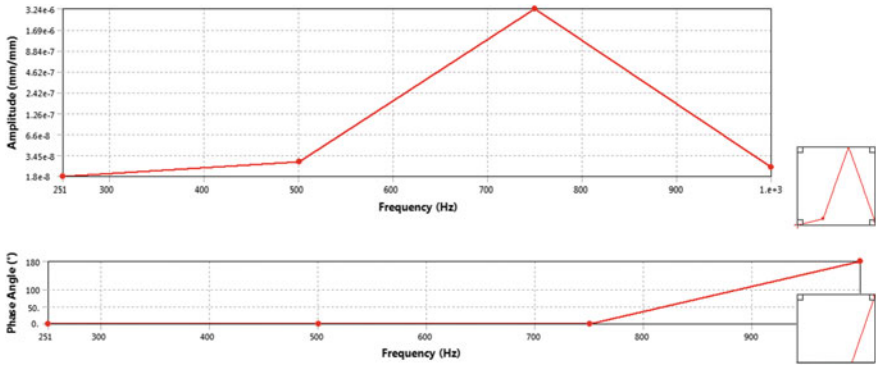
Fig. 13 Frequency response deformation graph obtained for modified design (H.C.S)
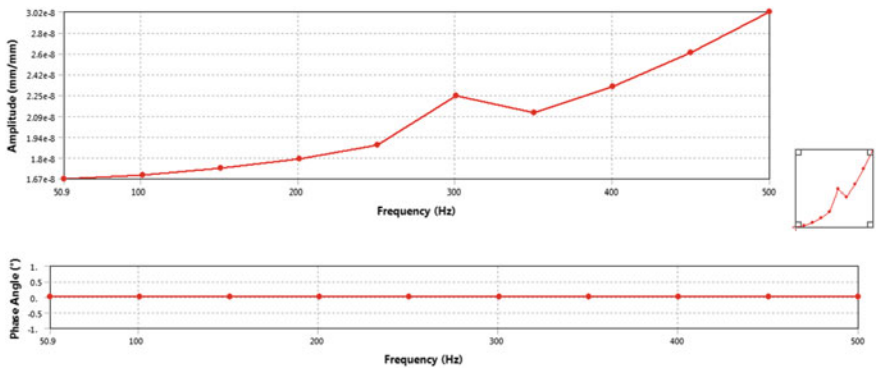
Fig. 14 Frequency response deformation graph obtained for modified design (S.S.A36)

- After correlating results of modal analysis, it can be concluded that for design modification having material high carbon steel and structural steel, maximum value of deformations is reduced by 36.46 and 35.25%, respectively, in comparison with existing model.
- After matching outcomes of vibration analysis, it can be said that for modified design having material high carbon steel and structural steel, utmost value of stress is diminished by 90.42 and 89.01%, respectively, in accordance with actual model.
- After analysing values of harmonic analysis, it was come to end that, highest value of stress for modified design having material high carbon steel and structural steel at respective resonance frequencies is proportionally depleted and increased by 5.95 and 16.04% in correlation with existing model. Moreover, after performing same analysis for some lower and higher value of frequency than resonance, it was observed that abundant value of stress is appropriately dropped by 10.60 and

18.71% for high carbon steel material and intensified correspondingly by 14.56 and 25.89% for structural steel material in agreement with actual design.

From design and analysis point of view, it can be safely concluded that, modified design having material high carbon steel is best suited for casing as compared to existing casing design in terms of strength, weight, vibration, durability, material and cost.

Future Scope

In any gearbox, possibilities of better options are present. Always chances of better things selection or say optimizing gearbox need to be done after its completion. In this 3 stage helical gearbox also, there are several things that can be optimized with software and theories best combinations. After complete understanding of requirements and components used into this 3 stage helical gearbox, one should focus on optimizing each and every component used in existing gearbox. In future, there are large scopes for further optimization of existing or modified gearbox casing. Hence, researchers can make an effort to explore all appropriate alternatives and try to give best possible solutions for stated problems.

References

1. Emanuel B., Sabot S.: Study to Analyze the Impact of the Mechanical Properties for Different Elements on the Crucial Rotational Speeds of Gearbox. Recent Trends in Engineering and Material Sciences. 5(3), (2010) 388–391
2. Sekar P., Utpat A.: Steady State Thermal Stress Analysis of Gearbox Casing by Finite Element Method. Finite Element in Analysis and Design. 97, (2011) 1097–1106
3. Chhabra P., Bhatia A.: Modelling and Analysis of Composite Material Gearbox. Advances in Manufacturing and Material Engineering. 5, (2012) 40–49
4. Hazry S., Kumar A., Patil P.: Study about the Vibration Analysis for Gearbox Cover Utilizing Finite Element Analysis. In: Proceeding of International Conference on Advances in Manufacturing and Material Engineering (AMME 2014), Germany (2014) 140–149
5. Ramesh, Renuka D., Jyothirmai S.: Study on the Vibration Analysis of Gearbox Top Casing. In: Proceeding of 2nd International Conference on Materials Processing and Charac-terisation (ICMPC 2013), Russia (2013) 907–918
6. Patel M., Patil A.: Study about Stress and Deformation of 3 Stage Helical Gearbox Casing. International Journal of Advance Research in Engineering, Science & Technology (IJAREST). 02(07), (2015) 65–71
7. Setty R., Gulam I., Totar D., Naik S.: Designing and Dynamic Analysis of Gearbox Housing Using Finite Element Analysis. Journals of Computational Design & Engineering. 192, (2015) 953–960
8. Babu M., Reddy Y.: Stress Analysis of Gearbox Casing Using ANSYS Workbench. Journal of Applied Research and Technology. 8, (2016) 1397–1405

9. Zdziennicki Z., Maciejczyk I.: Design Calculation and Modification of Industrial Gearbox. Journal of Mechanical Science and Technology. 26(3), (2016) 575–589

10. Hessen J., Vanhollebeke F., Mirant S.: Multibody Modelling of Varying Complexity for Modal Behaviour Analysis of Gearboxes. Journal of Mechanical Transmission. 36(11), (2017) 184–196

11. Xue Q., Wang D., Zhang X.: Study on Modal Analysis and Structure Optimization Method of Gearbox. ASME Journal of Mechanical Design. 117, (2017) 241–247

12. Abauel S., Mohammed E.: Analysis for Dynamic Characteristics of the Automobile Transmission Gearbox. Research Journal of Applied Sciences, Engineering & Technology. 5(15), (2017) 1449–1453

13. PSG College of Technology: PSG Design Data Book. Kalaikathir Achchagam, Coimbatore, (2016) 861–862

14. Shigley J.E.: Mechanical System Design. Tata McGraw Hill Publication Limited, Newdelhi, (2016) 392

15. Finstern Engineering Private Limited Information, http://www.finstern.in

Analysis of Cyclone Separator Used for Liquid-Gas Mixing

Gayatri Malekar and Niyati Raut

Abstract The present study deals with the evaluating the performance of liquid and gas separation cyclone separator with the pleated filter. The study is carried out by comparing the results from experimental and theoretical processes. The parameters of comparison are the pressure, velocity and the flow rate. After the evaluation, comparison of the various parameters and their effects on the performance would be studied. The main objective of this paper is to study the effect of filter on the performance of cyclone separator. The cyclone separator is studied using an experimental set-up which contains vacuum pump connected at the outlet and a mixing tank connected at the inlet of cyclone separator.

Keywords Cyclone separator · Pleated filter · Vortex length · Vortex finder

1 Introduction

Cyclone separators are devices that separate the two immiscible liquids through centrifugal vortex formation. The liquid and gas mixture enters the inlet of cyclone separator tangentially at high speed. This inertia force is transformed to centrifugal force forming vortex in the cyclone separator. The centrifugal force causes the liquid and gas to get separated. The liquid settles down at the bottom and can be discharged from bottom. The separated gas flows radially inwards and then goes upwards towards the top. The vortex flow formed in the cyclone separator depends on the densities of gas and liquids. The liquid due to high density settles at the bottom due to gravity and the gas after separation flows upwards due to low density. The efficiency of cyclone separator can be improved by the changing in design parameters.

The liquid and gas cyclone separators designs have been developed recently due to its variety of potential applications. Alexander [1] have studied about the vortex

G. Malekar (✉) · N. Raut
Department of Mechanical Engineering, Viva Institute of Technology,
Virar, Maharashtra, India
e-mail: malekar.gayatri@gmail.com

length and found the effects of inlet dimensions on the performance of cyclone separator. Stairmand [2] studied on the design of cyclone separator and suggested that the shell height of should be 1.5 times the cyclone shell diameter for improving the performance of cyclone separator. Ito [3] studied on the velocity flow and indicated that there is forced vortex near the centre of cyclone and free vortex near the wall of cyclone separator. Lun [4] presented on the pressure and the radial distribution. This pressure loss is studied by various researchers. Leith and Dirgo [5] studied on the effects of cone opening on the collection efficiency and pressure loss. The dimensions of shell and cone have influence on the performance of cyclone separator. The effect of cone dimensions on the performance of cyclone separator was also investigated by Xiang [6]. Researches of Chuah [7] also show that when the cone size is more than the outlet nozzle then it is observed that there is high collection efficiency without significant increase in pressure drop. Raoufi [8] also found the effect of shape and diameter of vortex finder on the performance of cyclone separator. Square cyclone separator designs and their performances were studied by Mao [9]. Iozia [10] studied the effects of vortex diameter on cyclone separator performances. Zhu and Lee [11] conducted experiments on different shell diameter and different vortex length and found that these parameters have considerable influence on the collection efficiency. Movafaghian [12] studied the effect of inlet geometry on the hydrodynamics of gas-liquid cyclone separator. Rongbiao and Xiang [13] suggested that flow rate has strong influence on the performance of cyclone separator. Zhao [14] reported that improving the inlet geometry will improve the collection efficiency. Wang [15] used the full Reynolds stress model in conjunction with the stochastic Lagrangian multiphase model to improve the accuracy of CFD models. Zhao [16] investigated the effects of cyclone inlet on the flow field and performance of cyclone separator. Erdal and Shirazi [17] investigated the effect of three different inlet geometries (one inclined inlet, two inclined inlets and a gradually reduced inlet nozzle) on the flow behaviour. They reported that the gradually reduced inlet nozzle geometry is the preferred geometry. Zhang [18] studied computationally the effect of inlet angle. He found that if the angle is 45°, pressure loss decreases up to 30% lower than the conventional design. The effects of shell height of cyclone on the performance of cyclone separator were studied by Safikhani [19] and Hoffmann [20]. Chen and Shi [21] established a 'universal' model to calculate cyclone pressure drop. The cone dimensions effects on the bottom of cyclone separator were studied by [22–24]. Karagoz [25] presented new design of cyclone separator by increasing the vortex length to improve the performance of cyclone separator.

1.1 Basic Design of Cyclone Separator

Cyclone separators are utilized for isolating scattered strong particles from liquid gas stage. These devices have basic design and simple in construction for fabrication. Also, these devices are less expensive. Therefore, they are used in many industries such as petroleum and chemical industries. Despite being inexpensive and easy to

operate, its flow structure and analysis is very complex. The gas particles and liquid enters the cyclone tangentially. The tangent flow produces the swirling motion on the inside of the wall of cyclone. The swirling motion produces centrifugal force, causing the liquid to settle down and gas to flow radially towards the centre and then discharges towards top of the cyclone.

Separation processes are based on centrifugation and filtration. These processes are discussed below:

(a) Mechanical Separation by Filtration: Filtration is the process in which the separation is carried out using the filter. Cyclone separator consists of filter inside which separates the liquid and gas and filters the gas to flow outside. The liquids and gas filtration is carried out using the pleated filters while the solid–liquid filtration is carried out using the pleated filters. Pleated filters have the advantage of being low cost, easy to install, use no electricity and generate no waste water. However, the disadvantages of pleated filters are that eventually sediment will plug up the pores of the pleated membrane, cause pressure drop and result in a loss of pressure.

(b) Mechanical Separation by Centrifugation: Centrifugation separation is the process wherein the separation process is carried out using the momentum principle. Different liquid-gas mixtures have different momentum. This difference in momentum is utilized to separate the mixtures. The liquid-gas mixture flows at high speed at particular velocity through the tangential inlet nozzle of the cyclone separator. As it flows, greater momentum force won't enable the particles of heavier stage to turn as quickly as the lighter liquid, so the separation happens. The difference in the densities of fluids causes the heavier fluid to impact on walls of cyclone separator and gradually get separated and settle down due to gravity while the gaseous particles being lighter remains in centre of cyclone separator moving the particles axially upwards.

The performance of cyclone separator is measured in terms of collection efficiency which is the ratio of liquid separated and pressure drop. The collection efficiency and pressure drop performance of the cyclone separator are a direct result of the flow patterns of gas and solid and pressure field inside the cyclone. The cyclone separator uses the centrifugal and gravitational forces the separate the liquid and gas particles. Figure 1 shows the basic construction of cyclone separator. The cyclone separator consists of shell, cone, inlet, outlet and discharge nozzle and pleated filter (Table 1).

2   Experimental Procedure and Methodology

The test set-up is as shown in Fig. 2. In this, the cyclone separator is connected between the mixing tank and the vacuum pump. The main purpose of the cyclone separator is to separate the liquid from gas and send to the vacuum pump.

The experimental set-up shown below consists of mixing tank, cyclone separator, product can and the vacuum pump. The main purpose of this set-up is to create

Fig. 1 Cyclone separator nomenclature
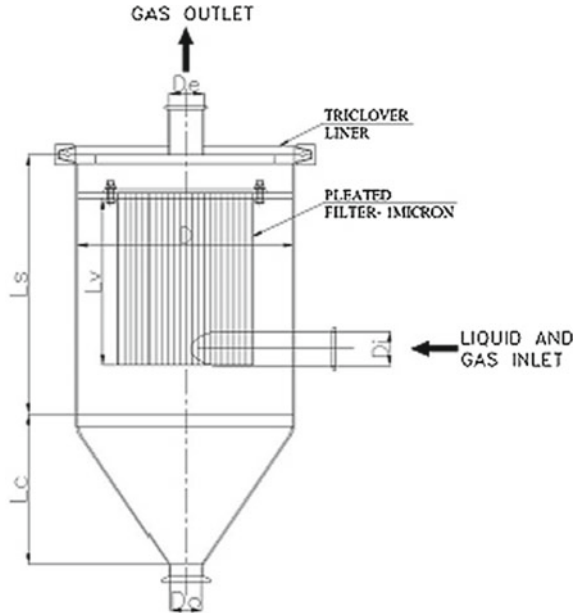
Table 1 Cyclone dimensions

S. No.	Cyclone parameters	Cyclone dimensions	Dimension values (mm)
1	Diameter of cyclone main body	D	200
2	Length of shell	L_s	300
3	Length of cone	L_c	175
4	Diameter of inlet nozzle	D_i	38
5	Diameter of gas exit	D_e	38
6	Diameter of outlet nozzle	D_o	38
7	Length of vortex finder	L_v	200

vacuum in the mixing tank. The vacuum pump capacity selected is 2 Hp. This vacuum pump creates vacuum in pipeline as well as in mixing tank. Due to vacuum created in tank, the product suction takes place, causing product from product can to fill in the mixing tank. The flow rate (of gas) at which the whole system works is 60 m³/h. This is the required flow rate of the product filling in the tank. The product is filled to the mixing tank from the product tank. The capacity of vacuum pump is calculated as per the flow rate required. The tank capacity is 1000 L and the time required to fill the product in tank is 1 min. Thus, the flow rate calculated is 1000 L/min. The vacuum
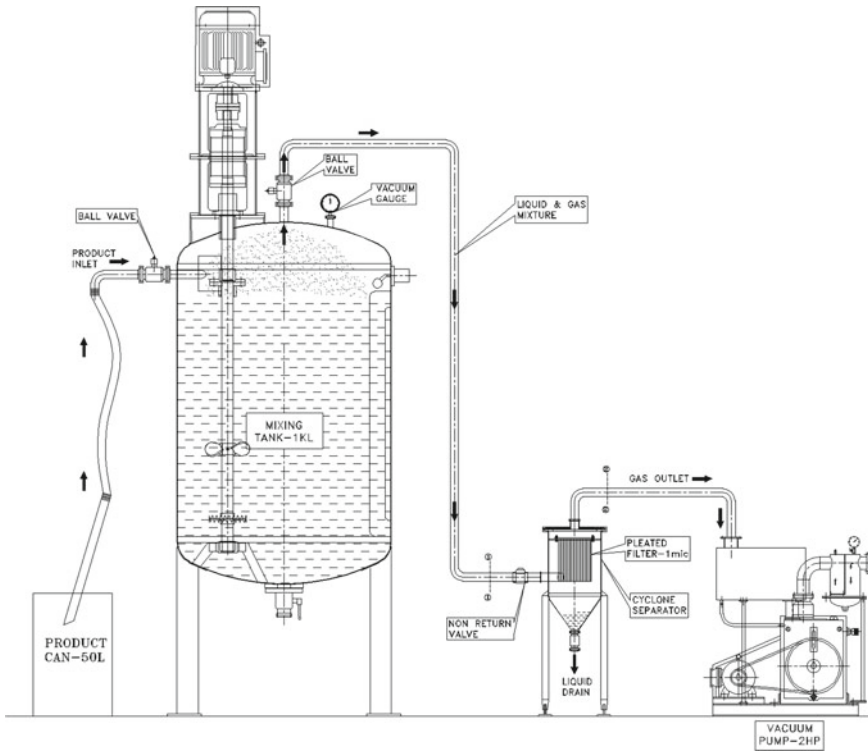
Fig. 2 Experimental set-up for cyclone separator

is lost in the working process. Also, the design and volume have a considerable difference since all factors have significant effects on the working conditions.

The principle function of the cyclone separator is to separate the liquid and gas mixture and send only the separated gas to the vacuum pump. The high velocity gas and liquid flows through the inlet of cyclone separator. The flow is tangential at the inlet. The tangent flow produces the swirling motion on the inside of the wall of cyclone. The swirling motion produces centrifugal force, causing the liquid to settle down and gas to flow radially towards the centre and then discharges towards top of the cyclone. The outlet gas flows towards the vacuum pump and gets exhausted.

In this experiment, the mixing tank is filled with the suction generated by the vacuum pump. Initially, when the vacuum pump is started, the vacuum is generated in the mixing tank. The vacuum generated causes the product to flow through the pipe to the mixing tank. Here one condition is to be fulfilled i.e. $P < W$, where P—internal pressure in tank and W—weight of liquid. During mixing the gas and liquid mixture is formed which gets discharge from the upper nozzle of tank. This liquid and gas mixtures formed are forced to flow towards the vacuum pump through cyclone separator. The set-up was designed to fill the mixing tank at 1000 L/min.

Table 2 The ISHVP-1000 model vacuum pump was selected

Single stage vacuum pump			
Model	Free air displacement (L/min)	Motor (hp)	Oil charge (L)
ISHVP-500	500	1.5	10
ISHVP-1000	1000	2	20
ISHVP-1500	1500	3	35

This states that the mixing tank which is of 1000 L capacity is to be fulfilled in 60 s. Accordingly, the vacuum pump was selected as per the catalogue (Table 2).

1. The velocity of flow in cyclone separator inlet pipe is measured through the fluid flow probe mounted at the inlet and air flow metre mounted at the outlet pipe
2. Now the vacuum generated in tank due to vacuum pump has design capacity to work at 670 mmHg. The trial was taken to hold the vacuum in the tank to find any drop in vacuum pressure.

3 Results and Discussions

3.1 Theoretical Results

The theoretical results were compared with the trail reports. The set-up was designed to fill the mixing tank at 1000 L/min. The vacuum pump selected was 2 Hp. The results obtained from the calculations are as follows:

1. The velocity of flow in tank during suction is calculated as

$$Q = A \times V \tag{1}$$

where, Q—flow rate, m³/s
A—area of tank, diameter of tank $= 1.1$ m, height of tank $= 1.1$ m
V—velocity of flow, m/s
∴ As per Eq. (1)

$$0.0167 = 0.785 * 1.1^2 * V$$
$$V = 0.0175 \text{ m/s}.$$

The velocity found is 0.0175 m/s and the tank height is 1.1 m so the time required to fill the tank is 62 s.
2. The velocity of flow in cyclone separator outlet pipe is calculated as
Here, Diameter of tank $= 0.038$ m

∴ As per Eq. (1)

$$0.0167 = 0.785 * 0.038^2 * V$$
$$V = 15 \text{ m/s.}$$

3. The Pressure at the inlet and the outlet of cyclone separator is calculated using the Bernoulli's equation;

$$P1/\delta g + V1^2/2g + Z1 = P2/\delta g + V2^2/2g + Z2 \qquad (2)$$

where, $P1$—pressure at inlet

$$P1 = \text{POWER}(P)/\text{FLOWRATE}(Q)$$
$$= 1492/0.0167$$
$$= 89341 \text{ Pa}$$

Δ—density of Air-1.27 kg/m^3
$V1$—velocity at inlet $= 15$ m/s
$Z1$—head at inlet
$P2$—pressure at outlet
$V2$—velocity at outlet/Starting Vel $= 0$
$Z2$—head at outlet

$$P2 = P1/\delta g + Z1 - Z2 + V1^2/2g$$
$$= -89341/(1.27 * 9.81) - 0.25 + 15^2/(2 * 9.81)$$
$$= -89195 \text{ Pa}$$

∴ The Pressure at the tank is $P2 = 669$ mm of Hg.

3.2 Experimental Results

The tests and trials were performed in the company, and these results were compared with the theoretical values obtained from calculations. The set-up was designed to fill the mixing tank at 1000 L/min. The vacuum pump selected was 2 Hp.

As per the requirements, the following observations were made.

1. The mixing tank is filled with the product within 66 s.

The following results after vacuum test were observed.

2. The velocity observed is 15.36 m/s at inlet nozzle and 15.12 m/s at the outlet nozzle.
3. The loss of pressure at the cyclone separator is 146 Pa.

4 Conclusion

The detailed study of work done in the synopsis about cyclone separator specifies that the swirling motion caused due to high velocity liquid and gas causes the separation of the liquid from the gas. The vortex is formed which causes the impact of liquid and gas on the wall of the cyclone. Due to different viscosities of the gas and the liquids, the liquid gets separated and settles due to gravity while the gas flows through the outlet pipe. The velocity at the inlet and the outlet pipe is approximately same. The flow rate is same.

The vacuum hold at the mixing tank is 669 mmHg. The suction causes the product to flow through the suction pipe towards the tank. As the product is drawn into the tank, it is observed the vacuum pressure decreases. As the product occupies the volume of tank, the vacuum drops. The filter causes the pressure drop in the cyclone, so this can be tested in the experiment and analysis of cyclone without the filter. The efficiency of cyclone separator with filter needs to be compared with the one without it. The cyclone separator efficiency can be increased by removal of the filter from its main body. This filter not only decreases the efficiency but also increases the cost of operation and maintenance. Filter requires the timely replacement since the liquid particles stuck on the filter. The enhancement of the efficiency can be improved through the changes in the design by changing the height of vortex finder and the filter removal.

References

1. R.M. Alexander, Fundamentals of cyclone design and operation, in: Proceedings of the Australian Institute of Mineral and Metallurgy. 152, 1949. pp. 203–228.
2. Stairmand, C.J.: The Design and Performance of Cyclone Separators. Trans. Inst. Chem. Eng., vol. 29, 1951, p. 356–383.
3. Ito, S., Ogawa, K. and Kuroda, C.: Decay Process of Swirling Flow in a Circular Pipe. International Chemical Engineering. Vol. 19, No. 4, 1979, pp. 600–611.
4. C. K. K. Lun: Kinetic theories for granular flow: inelastic particles in Couette flow and slightly inelastic particles in a general flow field. Journal of Fluid Mechanics, vol. 140, 1984. pp. 223–256.
5. Dirgo, J. and Leith, D.: Performance of Theoretically Optimized Cyclones. Filtration and Separation. March/April, 1985. p. 119.
6. R. Xiang, S.H. Park, K.W. Lee: Effects on cone dimension on cyclone performance, J. Aerosol Sci. 32 (2011) 549–561.
7. T.G. Chuah, J. Gimbun, T.S.Y. Choong: A CFD study of the effect of cone dimensions on sampling aerocyclones performance and hydrodynamics. Powder Technol. 162 (2006) 126–132.
8. A. Raoufi, M. Shams, M. Farzaneh, R. Ebrahimi: Numerical simulation and optimization of fluid flow in cyclone vortex finder. Chem. Eng. Process. 47 (2008) 128–137.
9. Y. Mao: Experimental study on the gas–solid suspension flow in a square cyclone separator. Chem. Eng. J. 121 (2006) 51–58.
10. D.L. Iozia, D. Leith: Effect of cyclone dimensions on gas flow pattern and collection efficiency, Aerosol Science and Technology. 10, 1989. pp. 491–500.
11. Zhu, Y., & Lee, K. W.: Experimental study on small cyclones operating at high flow rates. Journal of Aerosol Science. 30, 1999. pp. 1303–1315.

12. S. Movafaghian, J.A. Jaua-Marturet, R. Mohan, O. Shoham, G. Kouba: The effects of geometry, fluid properties and pressure on the hydrodynamics of gas–liquid cylindrical cyclone separators. International Journal of Multiphase Flow 26 (6), 2000, pp 999–1018.
13. Rongbiao, S. H., Xiang, K. W., Park, K. W., & Lee, K. W: Effects of cone dimension on cyclone performance. Aerosol Science. 32, 2001, pp. 549–561.
14. B. Zhao: Experimental investigation of flow patterns in cyclones with conventional and symmetrical inlet geometries. Chemical Engineering & Technology 28, 2005, pp. 969–972.
15. B. Wang, D. L. Xu, K. W. Chu, and A. B. Yu, "Numerical study of gas-solid flow in a cyclone separator". Applied Mathematical Modelling. vol. 30, no. 11. 2006, pp. 1326–134.
16. B. Zhao, Y. Su, J. Zhang: Simulation of gas flow pattern and separation efficiency in cyclone with conventional single and spiral double inlet configuration. Chemical Engineering Research and Design. 84, 2006. pp. 1158–1165.
17. F.M. Erdal, S.A. Shirazi: Effect of the inlet geometry on the flow in a cylindrical cyclone separator. Journal of Energy Resources Technology 128, 2006, pp. 62–69.
18. B. Zhang, S. Hui: Numerical simulation and PIV study of the turbulent flow in a cyclonic separator. International Conference on Power Engineering. Hangzhou. China. 2007.
19. H. Safikhani, M. Shams, S., Dashti: Numerical simulation of square cyclones in small sizes. Adv. Powder Technol. 22 (3) (2011) 359–365.
20. A.C. Hoffmann, M. de Groot, W. Peng, H.W.A. Dries, J. Kater: Advantages and risks in increasing cyclone separator length, AIChE J. 47 (11) (2001) 2452–2460.
21. Chen, J., Shi, M., 2007: A universal model to calculate cyclone pressure drop. Powder Technology 171 (3), 184–191.
22. H. Yoshida, S. Akiyama, K. Fukui, S. Taniguchi: Effect of apex cone height on particle classification performance of a cyclone separator, Adv. Powder Technol. 14 (3) (2003) 263–278.
23. H. Yoshida, Y. Nishimura, K. Fukui, T. Yamamoto: Effect of apex cone shape on fine particle classification of gas-cyclone. Powder Technol. 204 (2010) 54–62.
24. A. Kepa: The effect of a counter-cone position on cyclone performance, Separ. Sci. Technol. 47 (2012) 2250–2255.
25. Shalaby, K. Wozniak, and G. Wozniak: Numerical calculation of particle-laden cyclone separator flow using LES, Engineering Applications of Computational Fluid Mechanics. vol. 2. 2008. pp. 382–392.

Development of Mathematical Model for Top Roller Displacement of Three-Roller Bending Machine Using Dimensional Analysis

Prafull S. Thakare, Sandip M. Salodkar and C. C. Handa

Abstract   Roll bending or roll forming is one of the metal forming processes used in manufacturing industries. Various products having cylindrical, conical or elliptical profiles are manufactured using roller bending process. Trial and error method is generally used to achieve desired curvature or shape of final products. Prediction of top roller displacement of three-roller bending machine in downward direction to obtain desired radius of curvature is utmost concern. A generalized mathematical model is developed using dimensional analysis. Dimensional analysis is simplest tool for mathematical modeling when relationship among variables is unknown. Dimensional analysis is used to make the independent and dependent variables dimensionless and to get dimensionless equation. Multiple regression analysis is applied to this dimensionless equation to obtain the index values based on the least square method. Developed model is validated with experimental data and root mean square error between computed and estimated values are calculated.

Keywords   Roll bending · Mathematical model · Dimensional analysis
MATLAB · Regression analysis · Buckingham pi theorem

1   Introduction

Roll bending or roll forming is one of the metal forming processes in which a long, straight metal strip is passed through a set of rollers to transform it into desired curved cross-sectional profile. The plates to be bent are cut for required shape and size. Roll bending is a continuous forming process, produces higher dimensional accuracy of the finished products without loss of material. Cylindrical, conical, elliptical,

P. S. Thakare (✉) · C. C. Handa
Department of Mechanical Engineering, KDKCE, Nagpur 440009, India
e-mail: prafull.thakare16@gmail.com

S. M. Salodkar
A. P. J. Abdul Kalam University, Indore, India

oval shells are widely used in process industries like power plants, food processing, dairy equipment manufacturing. Various products like cylindrical tanks, drums, boilers, pressure vessels, tunnels, containers, chimneys, towers, structural components are manufactured using roller bending process. Pyramid type three-roller bending machine is widely used in industries because of its peculiar configuration and ease of operation [1]. Though roller bending is widely used in metal forming industries, its process is quite complex to understand. Normal practice of the roller bending still heavily depends upon experience and skill of operators. Position of top roller is explicit function of desired radius of curvature, which needs to be formulated. An attempt is made in this paper, to develop a mathematical model for the prediction of top roller displacement of three-roller bending machine in downward direction to achieve desired curved shape or profile of products.

2 Literature Review

Many researchers and academicians conducted research on three as well as four-roller bending process over last few decades. Complex mechanics of the process has been discussed through various models. Gandhi and Raval [2] reported the analytical and empirical models of the top roller position as a function of desired radius for single pass three-roller cylindrical bending machine. Yang and Shima [3] have discussed the distribution of curvature and calculated bending moment in accordance with displacement and rotation of rolls by simulating the deformation of work piece. Hua et al. [4–7] have extensively worked over the analysis of four-roller bending process. Hua et al. [4] have proposed a mathematical model for determining plate internal bending resistance at the top roller contact for multi pass four-roll thin plate bending operation. Hua and Lin [4] proposed a mathematical model to simulate the mechanics for four-roll thin plate bending process considering varying radius of curvature of the plate between the rollers. Hua and Baines [5, 6] proposed an analytical model for continuous single pass four-roll thin plate bending process considering the equilibrium of the internal and external bending moment. Hua and Lin [7] also investigated influence of material strain hardening on the mechanics of four-roll bending process. Hua and Lin [7] presented a mathematical model to simulate the mechanics in a steady continuous bending mode for four-roll thin plate bending process. A lot of research work has been reported in the area of analytical modeling of conical bending process for single as well as multipass bending operation. Chudasama and Raval [8, 9] have developed analytical models for the prediction of bending force during static as well as dynamic roll bending. They concluded that force required for dynamic bending is very less as compared to that of static bending stage. Hardt et al. [10] presented a scheme for closed loop shape control of the three-roller bending process. A series of experiments were performed to test this scheme by bending thin sheets of different materials to constant radii, specifying only the desired radius. Shakil Kagzi et al. made an attempt to simulate the three-roller bending process in Abaqus (FEA) software and results of simulation are compared with reported

analytical model for prediction of spring back. It is seen that, spring back results of the simulation and reported analytical model are in agreement with each other within reasonable range. Shin and Lee [11] explained a logical procedure to determine the center roller displacement in the three-roller bending process using finite element methodology. Ktari et al. [12] presented a two dimensional finite element model of the three-roller bending process using Abaqus based on boundary conditions, material properties, meshing techniques and so on. Desired curvature radii are generated by varying the distance between bottom rollers and position of top roller and results are validated with experimental and numerical model. Feng et al. [13–15] established a finite element model for a non-kinematical roll bending process with cylindrical rolls. Established model is then simulated to achieve desired cone. Feng [15] also developed a numerical model to predict the position of lateral rolls in case of asymmetrical three-roller bending process, numerical simulation is validated with experiments.

3   Experimental Approach and Design of Experimentation

The approach adopted for development of mathematical model suggested by Schenck [16] is detailed below

1. Identification of independent, dependent, and independent extraneous variables.
2. Reduction of independent variables adopting dimensional analysis.
3. Determination of test envelope, test points, test sequence, and experimentation plan.
4. Physical design of an experimental set up.
5. Execution of experimentation for data collection.
6. Purification of experimentation data.
7. Formulation of the field data based model.
8. Model optimization.
9. Sensitivity analysis and reliability of the model.

The presented research work in this paper is limited to formulation of field data-based model only. Total 108 experiments based on full factorial mixed-level design of experiment approach for different combinations of input parameters were conducted on three-roller bending machine and corresponding response is measured for further analysis. Effect of various geometrical and process parameters on the top roller displacement is also investigated. Experiments were performed on structural steel of different grades.

4 Formulation of Mathematical Model Using Dimensional Analysis

The main objective of this section is to formulate a mathematical model to predict top roller displacement of three-roller bending machine using dimensional analysis. A mathematical model is a description of a system or a process in mathematical forms. A model helps to explain a system or a process and to study the effects of different parameters influencing the response. Dimensional analysis is a powerful tool for understanding and analyzing engineering problems. Dimensional analysis computes dimensionless groups of parameters and provides information to what group of parameters affects the response. To formulate the mathematical model, Buckingham pi theorem is used. Buckingham's Pi Theorem [17] states that if there is a physically meaningful equation involving a certain number n of physical variables, then the original equation can be rewritten in terms of a set of $p = n - k$ dimensionless parameters $\pi 1$, $\pi 2$, …, πp constructed from the original variables. To calculate dimensionless pi terms, all dependent and independent parameters are expressed in terms of fundamental [MLT] physical quantities.

For three-roller bending process, total 10 parameters are selected, out of which 03 are selected as repeating variables (E, x, G). Hence, 05 independent pi groups and 02 dependent pi groups are formed. This paper is restricted to the development of mathematical model for top roller displacement only. So, for model development, 05 independent pi groups and 01 dependent pi groups are used. Description of parameters with fundamental form and dimensionless pi groups are as shown in Tables 1 and 2.

Each dependent pi term is the function of the available independent Pi terms [17]. Hence,

$$\pi_R = f(\pi_1, \pi_2, \pi_3, \pi_4, \pi_5) \tag{1}$$

A probable exact mathematical form for the dimensional equations of the phenomenon could be assumed to be of exponential form as

$$\pi_R = k_1 \times \pi_1^{a_1} \times \pi_2^{a_2} \times \pi_3^{a_3} \times \pi_4^{a_4} \times \pi_5^{a_5} \tag{2}$$

Here, K_1 is curve fitting constant and a_1 to a_5 be indices which needs to be calculated using matrix method.

For the solution of Eq. (2), taking log on both sides of Eq. (2),

$$\log \pi_R = \log k_1 + a_1 \log \pi_1 + a_2 \log \pi_2 \\ + a_3 \log \pi_3 + a_4 \log \pi_4 + a_5 \log \pi_5$$

Above equation is valid for all the readings collected during experimentation. Hence putting summation on both the sides

Table 1 Fundamental dimensions of input and output parameters

S. No.	Description of variables	Symbol	Unit	Dimensions	Type of variable	Nature
1	Top roller diameter	D_1	mm	$[M^0L^1T^0]$	Independent	Varying
2	Bottom rollers diameter	D_2	mm	$[M^0L^1T^0]$	Independent	Varying
3	Span of bottom rollers	X	mm	$[M^0L^1T^0]$	Independent	Varying
4	Yield strength of material	σ	MPa	$[M^1L^{-1}T^{-2}]$	Independent	Varying
5	Young's modulus of material	E	MPa	$[M^1L^{-1}T^{-2}]$	Independent	Constant
6	Thickness of plate	T	mm	$[M^0L^1T^0]$	Independent	Varying
7	Desired radius	R	mm	$[M^0L^1T^0]$	Independent	Varying
8	Acceleration due to gravity	G	m/s^2	$[M^0L^1T^{-2}]$	Independent	Constant
9	Top roller displacement	Y	mm	$[M^0L^1T^0]$	Dependent	Response
10	Number of passes	N	–	$[M^0L^0T^0]$	Dependent	Response

Table 2 Dimensionless pi groups

S. No.	Dimensionless groups (pi terms)	Type of variables
1	$\pi_R = \frac{Y}{x}$	Dependent
2	$\pi_1 = \frac{D_1}{x}$	Independent
3	$\pi_2 = \frac{D_2}{x}$	Independent
4	$\pi_3 = \frac{\sigma}{E}$	Independent
5	$\pi_4 = \frac{t}{x}$	Independent
6	$\pi_5 = \frac{R}{x}$	Independent

$$\sum_{i=1}^{i=n} \log \pi_R = \sum_{i=1}^{i=n} (\log k_1 + a_1 \log \pi_{1i} + a_2 \log \pi_{2i}$$

$$+ a_3 \log \pi_{3i} + a_4 \log \pi_{4i} + a_5 \log \pi_{5i})$$

Let, $Z = \log \pi_R$, $K = \log k1$, $A = \log \pi_1$, $B = \log \pi_2$, $C = \log \pi_3$, $D = \log \pi_4$, and $E = \log \pi_5$

$$Z = K_1 + a_1 A + a_2 B + a_3 C + a_4 D + a_5 E \tag{3}$$

Equation (3) is a regression equation of Z on A, B, C, D, and E.

Multiply Eq. (3) by A, B, C, D, and E separately to obtain a set of simultaneous equations.

$$ZA = K_1 A + a_1 A^2 + a_2 AB + a_3 AC + a_4 AD + a_5 AE \tag{4}$$

$$ZB = K_1 B + a_1 AB + a_2 B^2 + a_3 BC + a_4 BD + a_5 BE \tag{5}$$

$$ZC = K_1 C + a_1 AC + a_2 BC + a_3 C^2 + a_4 CD + a_5 CE \tag{6}$$

$$ZD = K_1 D + a_1 AD + a_2 BD + a_3 CD + a_4 D^2 + a_5 DE \tag{7}$$

$$ZE = K_1 E + a_1 AE + a_2 BE + a_3 CE + a_4 DE + a_5 E^2 \tag{8}$$

Equations (3)–(8) are simultaneously solved for unknowns using matrix method in "MATLAB" and values of Z, A, B, C, D, and E are obtained from experimental data. After obtaining the unknowns, Eq. (9) is used as a mathematical model to investigate top roller displacement of three-roller bending machine in terms of pi groups. The same can be written as follows:

$$\pi_R = 0.0518 \times \pi_1^{-0.7068} \times \pi_2^{-0.9934} \times \pi_3^{0.2820} \times \pi_4^{-0.5384} \times \pi_5^{-0.8016} \tag{9}$$

5 Analysis of Model

Developed model for π_R related to top roller displacement of three-roller bending machine is analyzed by calculating percentage error between experimental values and values obtained from mathematical model. Values of dependent parameter π_R from mathematical model are obtained by putting the experimental values of independent variables in mathematical model formed. Deviation of the values obtained from mathematical model from actual experimental values of dependent parameters shows closeness of the mathematical model with real-life process. Deviation of the values can be obtained in terms of percentage error. Following mathematical relationship will give percentage error between actual values and mathematical values.

$$\text{Percentage Error} = \frac{\text{Experimental values} - \text{Model values}}{\text{Experimental values}} \times 100 \tag{10}$$

Percentage error for π_R related to top roller displacement is found to be 1.237%. Percentage error obtained is less than 10%. It shows that values obtained from mathematical model are close with actual experimental values.

6 Results and Discussion

Indices of Pi Terms for π_R

	π3	π4	π1	π5	π2
■ Indices	0.282	-0.5384	-0.7068	-0.8016	-0.9934
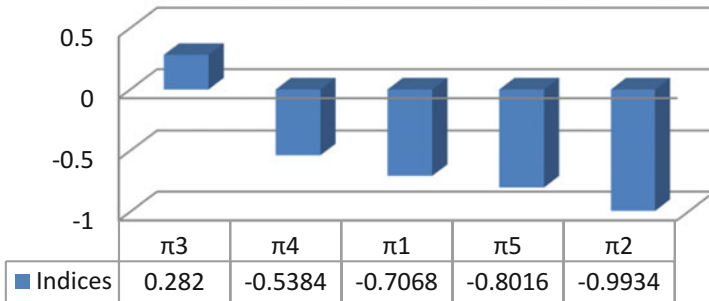
In this paper, a generalized field data-based model is developed to predict top roller displacement of three-roller bending machine to obtain desired radius of curvature. Methodology of dimensional analysis is used. Graph shows the independent pi terms influencing the dependent pi term π_R in descending order. The following primary conclusions appear to be justified from the above model.

1. The absolute index value of π_3 is highest and is equal to 0.2820. Thus, terms used in π_3 group are most influencing. The value of the index is positive indicating π_R directly varying with respect to π_3.
2. The absolute index value of π_2 is lowest and is equal to -0.9934. Thus, terms used in π_2 group are least influencing. The value of the index is negative indicating π_R inversely varying with respect to π_2.
3. The sequence of influence of the other independent pi terms present in the model are π_4, π_1, and π_5 having absolute indices -0.5384, -0.7068, and -0.8016 respectively.
4. The curve fitting constant in the model is 0.0518. This value represents the effect of clearances and other factors which affect the phenomena.
5. Percentage error for top roller displacement is found to be 1.237%. Percentage error obtained is less than 10%. It shows that values obtained from mathematical model are close with actual experimental values.
6. This paper presented a new methodology of dimensional analysis to develop relationship of various parameters of bending process. It is concluded that dimensional analysis is simple and excellent when functional relationship among variables is unknown.

References

1. P. S. Thakare, Dr. C. C. Handa et. al, "Productivity analysis of manually operated and power operated sheet bending machine: A comparative study", IJERA, vol. 2, 2012, pp 111–114.
2. A. H. Gandhi, H. K. Raval, "Analytical and Empirical of top roller position for three roller cylindrical bending of plates and its experimental verification", Journal of Material Processing Technology, 2008, pp 268–278.
3. Ming Yang, Susumu Shima," Simulation of Pyramid type three roller bending process", International Journal of Mechanical Science", 1988, Vol. 30, pp 877–886.
4. M. Hua, K. Baines, I. M. Cole, "Bending Mechanisms, Experimental Techniques and Preliminary Tests for the Continuous Four Roll Plate Process", Journal of Material Processing Technology, 1995, pp 159–172.
5. M. Hua, D. H. Sansme, K. Baines, "Mathematical modelling of the internal bending moment at the top roll contact in multi pass four roll thin plate bending", Journal of Material Processing Technology, 1995, pp 425–459.
6. M. Hua, I.M. Cole, K. Baines, "A formulation for determining the single-pass mechanics of the continuous four-roll thin plate bending process", Journal of Materials Processing Technology, 1997, pp 189–194.
7. M. Hua, Y. H. Lin, "Effect of strain hardening on the continuous four roll plate edge bending process", Journal of Material Processing Technology, 1999, pp 12–18.
8. M. K. Chudasama, H. K. Raval, "An approximate bending force prediction for 3 – roller conical bending process", Int J Mater Form, Springer, 2011.
9. M. K. Chudasama, H. K. Raval, "Comparative study of static and dynamic bending forces during 3-roller cone frustum bending process", International Journal of Mechanical, Aerospace, Industrial, Mechatronics and Manufacturing Engineering, vol. 9, 2015, pp 1081–1084.
10. D. E. Hardt, M. A. Roberts, K. A. Stelson, "Closed Loop Shape Control of a Roll Bending Process", Journal of Dynamic Systems, Measurements and Control, 1982, vol. 104, pp 317–322.
11. Jong Gye Shin, Jang Hyun Lee, You II Kim, Hyunjune Yim, "Mechanics-Based Determination of the Center Roller Displacement in Three-Roll Bending for Smoothly Curved Rectangular Plates", KSME International Journal Vol 15. No. 12, 2001, pp. 1655–1663.
12. Ahmed Ktari, Zied Antar, Nader Haddar and Khaled Elleuch, "Modeling and Computation of the three-roller bending process of steel sheets", Journal of Mechanical Science and Technology, 2012 pp 123–12.
13. Z. Feng, "Numerical Study of non-kinematical conical bending with cylindrical rolls", Simulation Modelling Practice and Theory, 2009, pp 1710–1722.
14. Z. Feng, "Three stage process for improving roll bending quality", Simulation Modelling Practice and Theory, 2011, pp 887–898.
15. Z. Feng, "Modelling and Simulation of asymmetrical three roll bending process", Simulation Modelling Practice and Theory, 2011, pp 1913–1917.
16. Hilbert Schenck Jr, (1968). Theories of Engineering Experimentation, McGraw Hill, New York.
17. G. Maheedhara Reddy, V. Diwakar Reddy, "Theoretical Investigation on Dimensional Analysis of Ball Bearing Parameters by Using Buckingham Pi-Theorem", 12th Global Congress on Manufacturing and Management, GCMM 2014, Procedia Engineering (97), Elsevier, pp 1305–1311, 2014.
18. I. M. Jamadar, Dr. D. P. Vakharia, "Model Development for Investigation of Localized Defects in Taper Roller Bearings Using Matrix Method of Dimensional Analysis", 12th International Conference on Vibration Problems, ICOVP 2015, Procedia Engineering (144), Elsevier, pp 751–758, 2016.
19. R. S. Kadu, G. K. Awari, C. N. Sakhale, J. P. Modak, "Formulation of Mathematical Model for the Investigation of Tool Wears in Boaring Machining Operation on Cast Iron Using Carbide and CBN Tools", Procedia Material Science (6), Elsevier, 2014, pp 1710–1724.

Design and Analysis of Vertical Vacuum Fryer

Abhishek Gupta, Amit Choudhari, Taha Kadaka and Pavan Rayar

Abstract Since last few decades, people have been highly reliable on conventional deep fat fried products due to their unique texture–flavor combination. However, they are least aware about the harmful effects of consuming these products. When any food product is fried in an open atmosphere and at high-temperature condition (160–170 °C), a carcinogenic substance acrylamide is produced. With too much of emphasis given on awareness of health in today's generation, vacuum frying is the key to most of the health-related problems. Horizontal vacuum frying machine is available in market, but due to its low productivity and higher processing cost, it is not economical to use. The purpose of this research paper is to compare the conventional less-productive horizontal vacuum frying machine with more productive vertical vacuum frying machine. This paper includes the design and manufacturing of vertical vacuum frying machine along with different inner chamber configurations and working mechanisms.

Keywords Deep fat frying · Acrylamide · Health awareness
Horizontal vacuum frying · Vertical vacuum frying · Design · Analysis
Outer chamber · Inner chamber configurations · Working mechanisms
Productivity

1   Introduction

Frying has been one of the most important cooking methods around world of which deep fat frying is most common of all. Deep fat frying is a method of cooking food in an open atmospheric condition and at temperatures around 170–190 °C [1]. Since past few decades, there has been pervasive love for deep fat fried food products due to their unique flavor–texture combination. However, with increase in awareness

A. Gupta (✉) · A. Choudhari · T. Kadaka · P. Rayar
Department of Mechanical Engineering, D.J. Sanghvi College of Engineering,
Mumbai, India
e-mail: guptaabhishek755@gmail.com

of various heart diseases and health-conscious programs, there has been a constant
need to limit the oil consumption and cholesterol levels in human body. Deep fat
frying leads to production of undesirable flavor compounds, excessive darkening,
and scorching of products, destroys all valuable nutrition, and thereby deteriorates
the quality of oil due to hydrolysis and oxidation. Also, it has been proved that Frying
at high temperatures leads to formation of acrylamide which a carcinogen is, i.e.,
found to have toxic effects on nervous system and cause cancer ([2]: As per June 2002
report by the Food and Agriculture Organization of the United Nations and the World
Health Organization). Hence, vacuum frying is the answer to all questions. Vacuum
frying is an efficient method wherein the food is cooked in an enclosed chamber
at pressure range of 0.01–0.25 bar and temperature range of around 80–120 °C. It
reduces the oil content in fried snacks, maintains product nutritional quality, better
color–flavor combination, and reduces oil deterioration. Vacuum frying reduces the
acrylamide content (micrograms per kg) in food products by 94% as compared to
atmospheric fried products [2].

2   Schematic Representation of Vertical Vacuum Fryer

As shown in Fig. 1, vertical vacuum frying machine consists of following parts:
    (a) Outer chamber, (b) inner chamber, (c) vacuum pump, (d) oil separator, (e)
motor (f) Vacuum gauge, (g) piping, (h) temperature transducer, (i) heating element.
    Outer chamber (a) is connected to the vacuum pump (c) with oil separator (d)
in between them. It also consists of inner chamber (b) which is initially placed in
the uppermost part of the outer chamber (a) just above the oil level. Temperature
transducer (h) and vacuum gauge (f) are also attached to the outer chamber so as to
monitor working condition inside the chamber. Motor (e) is connected with inner

Fig. 1 Schematic
representation of vertical
vacuum fryer
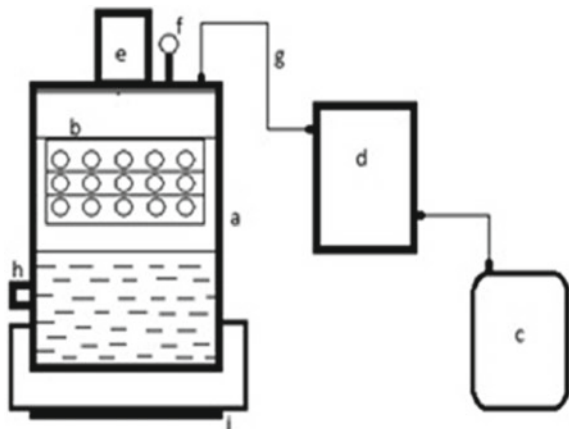
chamber (b) and heating element (i) is used for heating the oil inside the outer chamber (a).

3 Horizontal Vacuum Fryer

The schematic representation of horizontal vacuum fryer remains the same. Figure 2 represents horizontal vacuum frying machine, and it consists of a cylindrical outer chamber made of food-grade material which placed horizontally using supporting structures with oil being filled in the lower half of this chamber. The inner chamber is a half-cylindrical section placed initially in the upper half of the outer chamber. Once vacuum is created inside the outer chamber and oil is preheated to about 80–120 °C, the inner chamber is rotated about its axis driven by a motor and is dipped in the oil. This process is carried out till the products are evenly cooked. The major disadvantage of this type of vacuum fryer is its low productivity since only half-cylindrical section is used for frying purpose, which in turn means less quantity of food chips placed; hence, each batch produces less quantity of vacuum fried products as compared to vertical vacuum fryer. Also, horizontal vacuum fryer creates rotation difficulties due to uneven distribution of mass. The leakage problem associated with this machine is also much higher as compared to the vertical vacuum frying machine. Due to poor engineering design of the horizontal machine, centering of the inner chamber in the bush is very difficult and there is no provision for storing of oil for cyclic process [3].

Fig. 2 Horizontal vacuum fryer

Table 1 Vacuum frying conditions for different products

Product	Temp. (°C)	Time (min.)	Pressure (kPa)	Reference
Apple	98	4.5	6.48	Dueik and Bouchon [5]
Banana	90	90	9.33	Apintanapong et al. [6]
Carrot	98	5	6.48	Dueik and Bouchon [5]
Jackfruit	90	135	6.76	Diamante (2009)
Potato	98	6.5	6.48	Dueik and Bouchon [5]

4 Vacuum Frying Methodology

(See Fig. 3).

4.1 Vacuum Frying Conditions for Different Products

(See Table 1).

Fig. 3 Vacuum frying methodology [4]
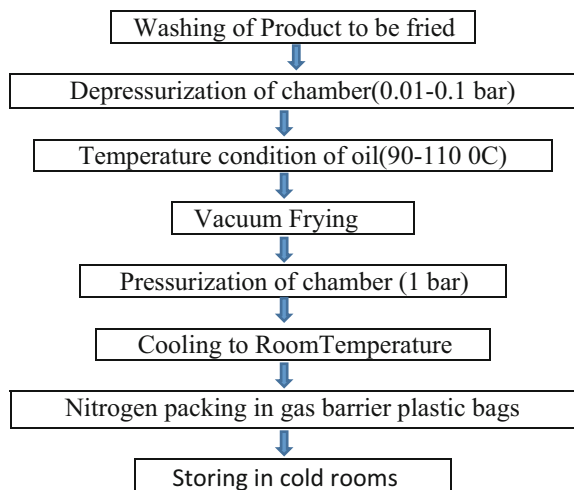
Table 2 Material selection

Properties	SS-316L	SS-410
Tensile strength (MPa)	485	480
Yield strength (MPa)	170	275 min
Thermal conductivity (W/mK)	16.3	24.9

5 Design and Analysis

5.1 Selection of Material

Among several materials available, the food industry utilizes stainless steel for the construction and manufacturing of almost all food processing and storage apparatus. Different grades of stainless steels are extensively used for storage, transportation, and preparation purpose in food industries. Various food-grade materials of stainless steel are available in the market as per the range of temperature required, pressure, strength, etc. Some of them which can be used for the manufacturing of the vacuum frying machine are as follows;

1. Stainless Steel-304; 2. Stainless Steel-316; 3. Stainless Steel-316L; 4. Stainless Steel-410.

Table 2 shows the different properties of SS-316l and SS-410. Base plate of outer chamber is made up of SS-410 due to excellent mechanical and thermal properties that prevent deformation of the material due to direct heating. Rest of the equipments are made up of SS-316L that prevents contamination and maintains freshness of food items and possesses excellent heat resistant properties.

5.2 Outer Chamber

Thickness Calculation:

Design of outer chamber includes pre-defining the inner diameter and height of the cylinder, so as to calculate the minimum thickness that is required to prevent the collapsing of cylinder walls when required vacuum is created inside the chamber. From Lloyd Brownell–Wiley Inter-science Handbook page no. 144 Article 8.43 [7].

$$\text{Allowable Pressure} = \frac{K}{n} \times E \times \left(\frac{t}{d}\right)^3$$

where

$P =$ max. allowable pressure difference $= 0.099$ bar, $K =$ constant $= 22$, $E =$ Young's Modulus $= 200$ GPa……..material (stainless steel 316L), $H =$ height (mm) $= 609.6$ mm, $d =$ diameter (mm) $= 355.6$ mm, $n =$ factor of safety $= 4$.
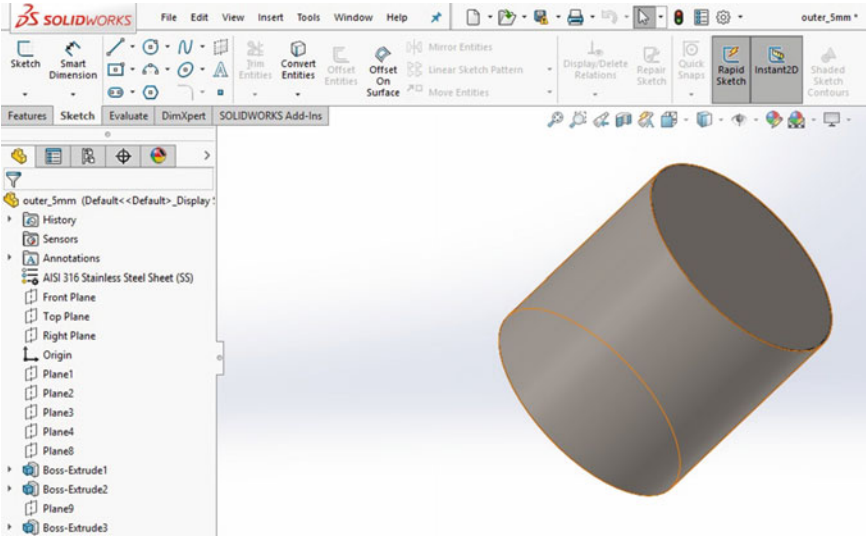
Fig. 4 Solid works model of outer chamber

Fig. 5 TIME versus CFM graph that shows as we increase the CFM of pump, time required for creation of the vacuum inside the chamber reduces
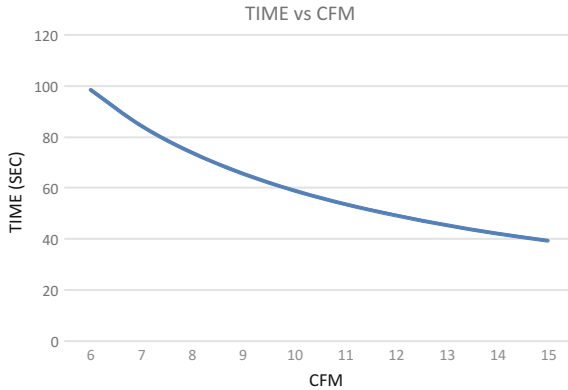
The minimum thickness that is required to prevent the collapsing of cylindrical walls is 1.59 mm, considering $t = 2$ mm.

Taking thermal consideration into account to prevent failing due to thermal effect, $t = 3$ mm (Figs. 4 and 5).

Time required to create the required pressure inside the outer chamber:

From Lloyd Brownell–Wiley Inter-science Handbook of Vacuum Science (Page no. 67), we get [8].

Table 3 CFM versus TIME

CFM	6	7	8	9	10
Time (s)	98.4	84.3	73.8	65.6	59.04
CFM	11	12	13	14	15
Time (s)	53.67	49.41	45.41	42.17	39.36

Table 4 Analysis of outer chamber

Thickness (mm)	Total deformation (m)	Equivalent stress (MPa)
3	1.6827e-5	10.283
4	1.255e-5	7.746

$$\frac{-st}{v} = \ln\left(\frac{P}{Po}\right)$$

where

P = required absolute pressure in chamber (bar),
P_0 = atmospheric pressure in bar = 1 bar,
V = volume of outer chamber = 2.138 ft^3,
S = CFM of motor, t = time in seconds

Time required to reduce pressure from 1 bar to 0.01 bar, with different pump specifications (CFM), is shown in Table 3.

Analysis of outer Chamber:

Analysis of different thickness of outer chamber is being carried out, and the results of deformation and equivalent stress are plotted in tabular format (Table 4). Outer chamber with thickness equal to 3 mm is selected for manufacturing purpose (Figs. 6, 7, 8 and 9).

5.3 Inner Chamber

Different configurations of Inner Chamber: Inner chamber of different shape and design, having their own benefits and limitations, can be used to carry the frying products when placed inside the outer chamber.

Diameter = 12 in.
Total height = 12 in.
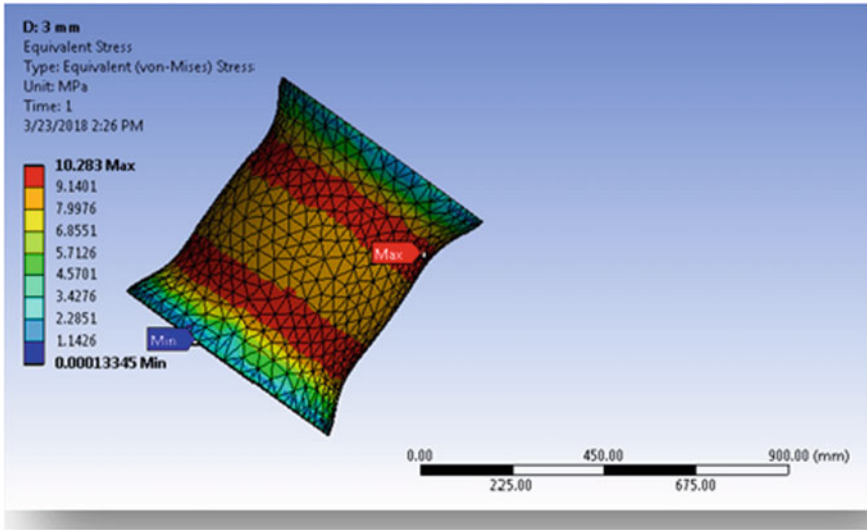
Fig. 6 Equivalent stress and deformation of 3 mm outer chamber, respectively
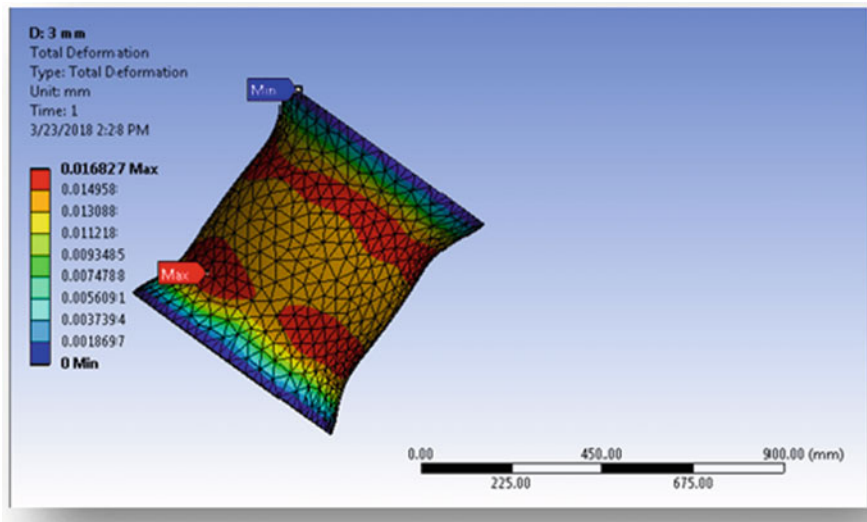
Fig. 7 Equivalent stress and deformation of 3 mm outer chamber, respectively

5.3.1 Tiffin Box Arrangement

Figure 10 shows circular inner chamber with four separable stacks. Basic idea behind this configuration can be related to a tiffin box. It consists of four separable stacks which can be easily assembled and disassembled for loading and unloading of the
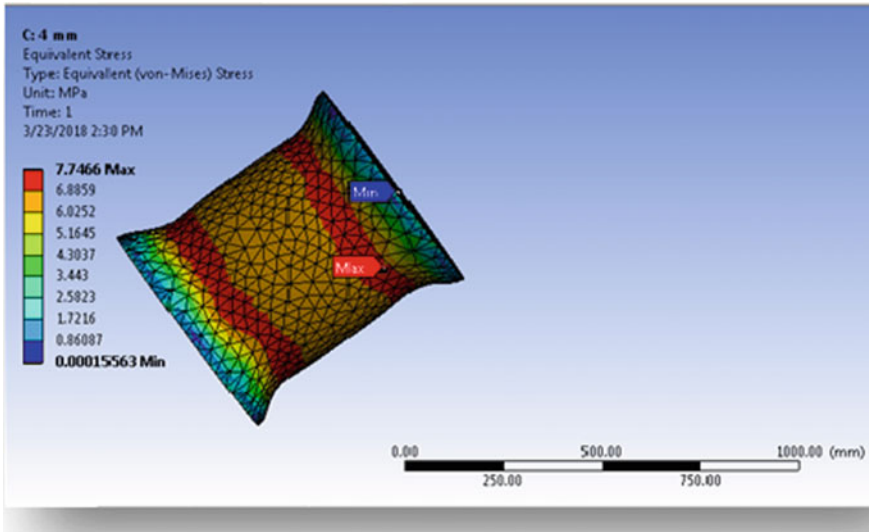
Fig. 8 Equivalent stress and deformation of 4 mm outer chamber, respectively
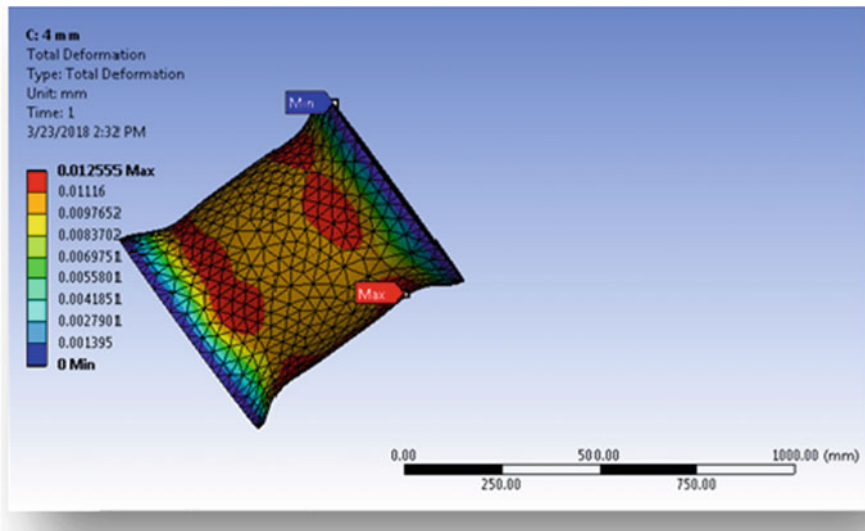
Fig. 9 Equivalent stress and deformation of 4 mm outer chamber, respectively

raw materials like banana, carrot, potato, jackfruit, apple, etc. The main limitation with this arrangement is that the loading and unloading of the materials are a time-consuming process.

5.3.2   Rectangular Arrangement

Figure 11 shows rectangular inner chamber with three fixed stacks. This design was
created to overcome the limitation of tiffin box arrangement, i.e., the time required for
loading and unloading of material. Rectangular inner chamber arrangement consists
of three fixed stacks and a rectangular door provided with hinge for its easy opening
and closing during loading and unloading of the raw material (potato, banana, jack-
fruit, apple, etc.). The main limitation of this arrangement is the space available for
carrying the raw material which is less as compared to the cylindrical arrangement.

5.3.3   Combined Cylindrical and Rectangular Arrangement

Figure 12 shows circular inner chamber with rectangular opening and three fixed
stacks. Basically, this design is the combination of the above two designs, to overcome
the limitations arrived. It consists of partial cylindrical portion with a rectangular door
and three fixed stacks so that loading and unloading of the material are easy. The
main problem with this design is that during the rotation of the inner chamber the raw
material (i.e., chips) will follow a circular path along the curvature of the chamber
but while coming in contact with the rectangular door, the product tends to change
its path along the door, thereby leading to breaking of chips.

Fig. 11 Rectangular arrangement
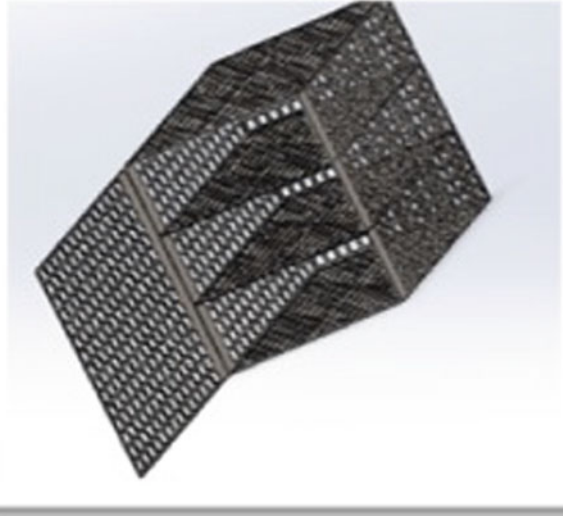
Fig. 12 Combined cylindrical and rectangular arrangement
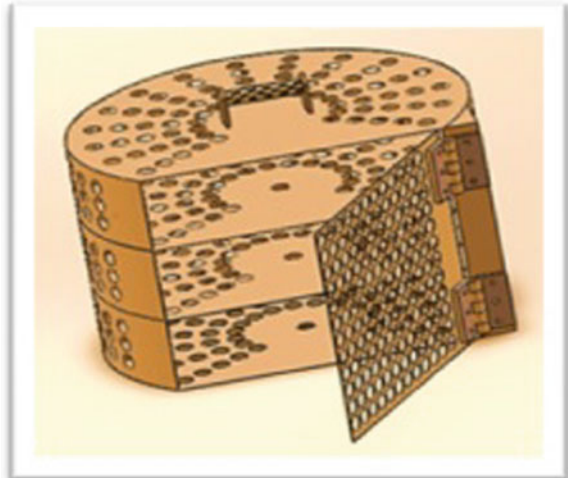
5.3.4 Cage-Type Arrangement

Figure 13 shows circular inner chamber with two fixed stacks. This design basically consists of an inner chamber that is attached to circumferentially threaded top plate permitting up–down motion during working when placed inside the outer chamber. It is similar to above design (Fig. 12), but the only difference is that the rectangular door is replaced with quarter-circular door. This design consists of only two fixed stacks made for mechanism I (6.1 Mechanism I).

Fig. 13 Cage-type
arrangement

5.4 Vacuum Pump

Figure 14 shows a vacuum pump. Vacuum pump will be used for production of
vacuum in the outer chamber. The pump will be connected to outer chamber through
oil separator. Vacuum pump is the only device for creation of vacuum. Vacuum pump
will remove gas molecules from an enclosed space of outer chamber; therefore, a
partial vacuum of about 0.01–0.25 bar will be created (Fig. 15).

5.5 Vacuum Gauge

Figure 16 shows vacuum gauge. Vacuum gauge is used for measuring the pressure
inside the outer chamber. It is fitted on the lid of the outer chamber with the help
of a valve and gasket. It is fitted on the lid by making a hole on it. The range of
measurement of this gauge varies from 0 to 760 mm of mercury vacuum pressure.

5.6 Vacuum Seals

Figure 15 shows a vacuum seal. During creation of vacuum inside the outer chamber,
there are chances of leakage of air from atmosphere to inside of chamber since inside
pressure is less than the atmospheric pressure. To prevent this, we need a vacuum

Fig. 14 Vacuum pump

Fig. 15 Vacuum seals

seal which will not allow the air to enter inside the outer chamber during vacuum creation and ongoing process. For ultra-vacuum to be maintained inside the chamber, we generally require a high-quality seal which is arranged in series to maintain ultra-vacuum. Our application is of medium vacuum with temperature of about 90–110 °C. Therefore, we will use O-ring seals for our application made up of silicon which can sustain temperature up to 400 °F.

5.7 Temperature Transducer

For continuous measurement of the temperature of oil in the outer chamber, we are using a digital temperature transducer which will convert the thermal signal into some

digital form which can be directly observed and read by the operator. It is connected to the outer chamber at just above the bottom plate, so that the temperature of oil can be easily measured by thermocouple.

5.8 Oil Separator

Figure 17 shows an oil separator. It is connected between outer chamber and vacuum pump with the help of vacuum hoses. It will separate the oil from oil–vapor mixture, and only oil-free vapor will be allowed to enter vacuum pump. The separated oil can be reused after the filtration process.

6 Working Mechanisms

The inner chamber cannot be directly placed inside the oil before creating the required frying parameters inside the outer chamber. If the chips were dipped in the oil before creating the working conditions, this would lead to increase in oil content, thereby producing soggy chips which are undesirable. This leads to the need of developing a mechanism that would hold the inner chamber above the oil level in the outer chamber until the required working conditions are created.

Fig. 17 Oil separator

6.1 Mechanism I

Figure 18 shows mechanism I. In this mechanism, the inner chamber is provided with a supporting plate of thickness equal to 25.4 mm at the top with external threading being provided around the circumference of the plate. Internal threading is also provided in the outer chamber for a distance of 1 ft in the uppermost portion. This mechanism is based on nut and bolt arrangement for up–down motion of the inner chamber inside the outer chamber driven by motor shaft. This motor shaft is connected to a simple motor placed on the outside of the chamber at the center of lid. This motor is enclosed inside in another chamber to prevent further leakage of air into the chamber, thereby increasing the overall efficiency of the system.

6.2 Mechanism II

Figure 19 shows mechanism II. This mechanism works on the principle of nut and stud arrangement driven by an epicyclic gear train held at the inside of the lid of outer chamber with a spider lock arrangement on the respective shafts transmitting motion from planet gear to inner chamber.

Fig. 18 Mechanism I
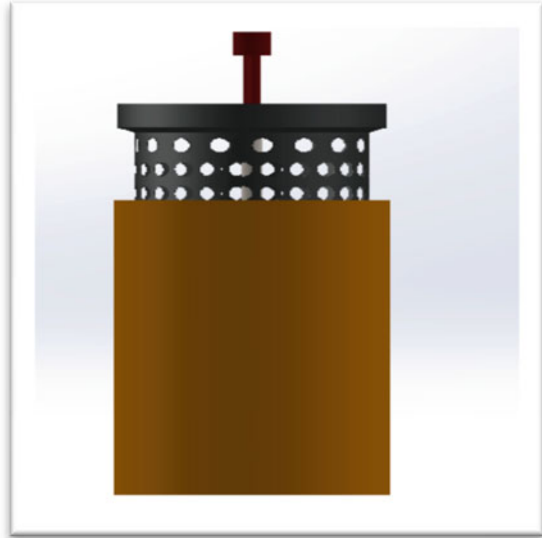
Fig. 19 Mechanism II

7   Conclusion

Vacuum frying is a promising technique because it makes possible to fry at a lower oxygen concentration and at a lower frying temperature because of the decrease in

the water boiling point. This process can therefore preserve natural colors and flavors of foods and limit oil degradation.

The main purpose behind working on this project:

i. To make this design available to small-scale industries in India (Make in India).
ii. To try and introduce vacuum fried products in food market at comparatively reasonable cost taking into consideration health consciousness.
iii. To use simple production techniques for manufacturing of this project.
iv. To improve the overall productivity of the system.

References

1. Chao Inprasit, VACUUM FRYING, Ph.D. Department of Food Engineering Kasetsart University.
2. Vacuum frying foods: products, process and optimization. Diamante, L.M., 1Shi, S., 2Hellmann, A. and 1Busch, J. International Food Research Journal 22(1): 15–22 (2015).
3. Vacuum frying: An alternative to obtain high quality potato chips and fried oil. Amany M. Basuny1, Shaker, M. Arafat, Azza, A. Ahmed. Global Advanced Research Journal of Microbiology Vol. 1(2) pp. 019–026.
4. Analysis Frying Constant of Pineapples Vacuum Frying. Lastriyanto, S. Soeparman, R. Soenoko and H.S. Sumardi. World Applied Sciences Journal 23.
5. Vacuum frying as a route to produce novel snacks with desired quality attributes according to new health trends. Dueik, V., & Bouchon, P. Journal of Food Science, 76(2), E188–E195 (2011).
6. Effect of antibrowning agents on banana slices and vacuum-fried slices. Apintanapong, M., Cheachumluang, K., Suansawan, P., & Thongprasert, N. Journal of Food Agriculture and Environment, 5(3/4), 151 (2007).
7. Lloyd Brownell- Wiley, Inter science Handbook page no. 144 Article 8.43.
8. From Lloyd Brownell- Wiley Inter science Handbook of Vacuum science (Page no. 67).
9. Vacuum frying of potato chips. Jagoba Garayo, Rosana Moreira. ELSEVIER Journal of food engineering 55 (2002).

Design, Manufacture and Testing of an Impact Attenuator for a FSAE Car

Parth Thakar, Suyash Ail, Jayraj Ranade and Parshva Mehta

Abstract All the vehicles need to be equipped with a safety device because for safety of the driver and passenger. The sole purpose of the project is to focus on a very important aspect of the vehicle which is the impact attenuator. This project deals with building of crash-protective device for an FSAE car. The rules for the following state that the mounted device on the car device must absorb enough energy such that the driver walks away without sustaining any serious injuries and also damage to the frame is minimized. After completing an extensive research on previously done designs and physics of a collision, preliminary design concepts were formulated. These designs were further compared against each other based on the rules which are being put up by the FSAE community. The specimen was further analysed using an explicit dynamic analysis software, and the results obtained were post-processed for the evaluation. Manufacturing of the product was done using some advanced manufacturing techniques like vacuum bagging, autoclave which would eventually save the cost and time and provide better finish to the product. After the software analysis part was done and after manufacturing the product, physical experiments were conducted which used the same set-up as that of software. At last, the software and the physical experiment set-up were compared and hence concluded.

Keywords Impact attenuator · FSAE · Vacuum bagging · Autoclave

P. Thakar · S. Ail (✉)
Electronics and Telecommunication Department, DJSCE, Vile Parle (W),
Mumbai 400056, India
e-mail: suyashaila@gmail.com

P. Thakar
e-mail: truelier03@gmail.com

J. Ranade · P. Mehta
Mechanical Department, DJSCE, Vile Parle (W), Mumbai 400056, India
e-mail: ranade.jayraj@gmail.com

P. Mehta
e-mail: parshvamehta007@gmail.com

1   Introduction

Motorsport is all about speed, but that often comes at the expense of driver's safety. This thesis is about the design, manufacture and testing of an impact attenuator which is mounted on the frontal area of the car. There have been several injuries in Formula One which were often fatal. Hence, the FIA community has set some rules for all the teams pertaining to the driver's safety. Measures have been implemented to safeguard the driver during a rollover condition, side impact as well as the frontal impact. Similarly, FSAE community, which was developed to apply student's engineering knowledge practically, in the year 1980, by Texas SAE students, has also set-up certain guidelines following FIA pattern. The aim of the project is to implement a custom impact attenuator (IA) for the FSAE race car. Earlier the team used a SAE certified standard impact attenuator. The custom IA has a scope in terms of weight reduction, compactness in the design and better energy absorption on the impact and design grades. This project includes the designing as well as the physical testing of the specimen as both the results need to converge according to the rules of FSAE [1].

2   Survey

Before proceeding to the initial design phase, the group conducted extensive study on the previous designs and materials used for the impact attenuator [2–5]. Designs of universities like Polytechnic di Torino, Worchester Polytechnic Institute, California Polytechnic State University and many more were studied, and all of them used different materials, software and also methods for physical testing. The final outcome after the literature review which we obtained was:

Material: Considering the above research on other teams and papers, we selected various materials. Every material chosen here has their own pros and cons. Aluminium sheet, aluminium honeycomb, carbon fibre reinforced plastic and glass fibre were the materials to be analysed for the final selection.

Software: There are various software that could be used in the course of the project starting from the basic designing software to dynamic analysis software [2, 3, 6, 7]. The two dynamic analysis software used above most commonly were LS DYNA and ABAQUS. ABAQUS will be used in this project as it has easy user interface and requires less computer memory to conduct a test.

Experiment: It is essential to conduct a physical test for the conformation of the design goals. There are various experiments that can be performed to conduct the test. A further detailed description would be provided later in this document. Also, there were some design goals which were set initially, and they were:

- In FSAE, the primary goal of every team is to get the overall vehicle mass down at every step. They have several reasons to do so, ranging from vehicle dynamics to increasing the power/weight ratio.

Table 1 Comparison table for material selection

Material	Cost (₹)	Weight (g)	Availability	Strength	Ease of manu-facturing
Aluminium	3000	900	Easily available	Low	Easy
High-density foam	15,000	500	Not available	High	Easy
Carbon fibre	13,000	600	Available	High	Difficult
Aluminium honeycomb	5,000	1200	Not easily available	Moderate	Difficult
Glass fibre	8000	1100	Available	Moderate	Difficult

- Lesser the mass of the part, less is the mass moment of inertia causing easy steering in the car, and also, weight reduction in the car helps the car go faster.
- The front part of the car should be compact and so should the impact attenuator for better aerodynamic effect and streamline the air around the bodywork.
- This thesis will be focused on reducing the mass of the attenuator as compared to the standard IA.
- Along with the reduced mass, it should have enough strength and energy absorption property such that it meets the FSAE requirements [1].

3 Calculations

By conservation of energy: $K_E = P_E$
Calculating the desired drop height: $P_E = m * g *$ Hd
Time of impact: $t = V_{impact}/Ac$
Impulse and force: $Im = M(V_{impact} - V_{final})$

4 Material Selection

It is a wide and the most critical part of this project as the selection of the material will implicitly depend on the design goals. A huge amount of time is invested in this phase in the project as the final result is based on this. Every material has its own advantages and disadvantages. We need to pick the right one considering all the advantages that can converge with our design goals (Table 1).

Outcome of Material: Our goal was to reduce mass and increase the strength. From the above comparison, it was evident that carbon fibre had the least mass among all the materials without compromising on its strength. Also, the material was available within the country. Besides our design goals, the manufacturing of the
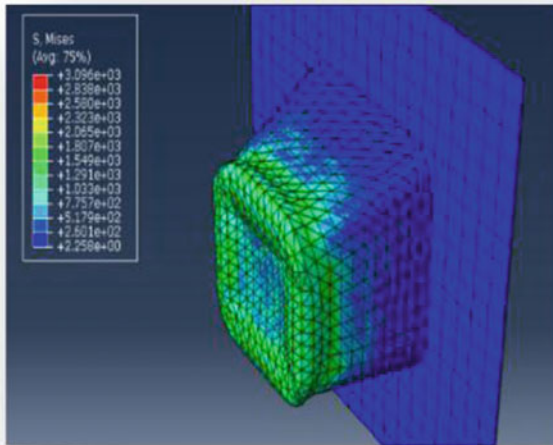
Fig. 1 Analysis of IA during impact

component with CFRP is difficult, and the cost is also high. But it is overshadowed when more importance is given to the goals.

5 Design and Analysis

All the designs were modelled in SolidWorks and were put to dynamic analysis on ABAQUS. The different structures were dynamically analysed taking into account similar cross-sectional areas. Force versus displacement graph was obtained for each material. Also, energy absorption was calculated using the above graph, and some other values like deceleration and AIP deflection on the application of the impact were also evaluated. These were compared, and the structure was selected for the modelling of the final specimen. The shape of the sample is very important as it decides the strength and energy absorption of the model. For determining the ideal shape of the sample, the group conducted a study and listed down the most common shapes which gave better strength when subjected to impact (Figs. 1, 2 and 3; Table 2).

The following shapes were finalized for analysis of the software, and after analysing, specimen 3 was selected whose analysis is shown below.
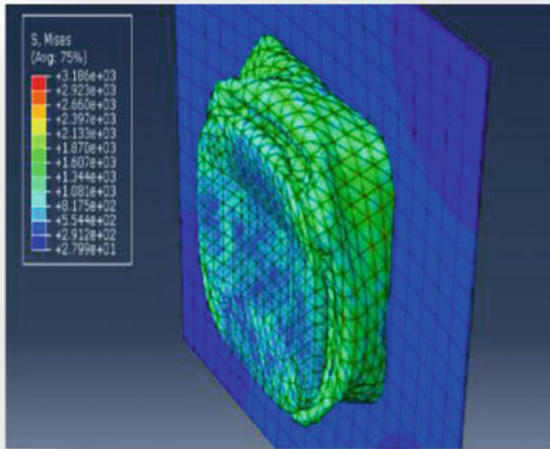
Fig. 2 Analysis of IA after impact
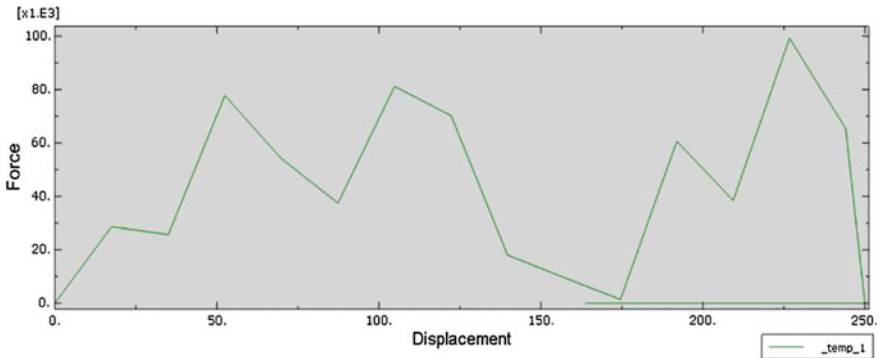
Fig. 3 Force versus displacement graph for square frustum structure

6 Manufacturing

Vacuum Bagging: It is a technique which creates mechanical pressure on a laminate during its cure cycle. Initially, it removes trapped air between layers. Further, it compacts the fibre layers for efficient force transmission amongst fibre bundles and prevents shifting of fibre orientation during cure. Later, it reduces humidity. At last, the vacuum bagging technique optimizes the fibre-to-resin ratio in the composite part.

Table 2 Comparison between all the different impact attenuator specimens

Specimen	Energy absorption (J)	Peak deceleration (m/s^2)	AIP deflection (mm)
1	7380	36	21
2	5239.49	39.93	32
3	9835.5	36.2	19.32

Fig. 4 Manufactured mould

Hand lay-up: In this process, the fibres are laid upon each other with epoxy in between in order to attain a required shape and bond the fibres intact. This process is done manually, and, hence there is a great possibility of excess epoxy getting used, thereby increasing the weight. Also, the surface finish is not good.

Vacuum Infusion: The vacuum infusion process or VIP is one of many closed mould processes. It differentiates itself by being the only process that utilizes only atmospheric pressure to push the resin into the mould cavity. The mould cavity can be a one-sided mould with bagging film being utilized for the 'B' side, a two-sided mould, or even a soft 'envelope' bag. The process is controlled easily.

Autoclave: These are widely used to cure composites and in the vulcanization of rubber. The high heat and pressure that autoclaves allow help to ensure that the best possible physical properties are repeatable. The industries like Aerospace and spar makers (for sailboats to be precise) have autoclaves well over 50 feet (15 m) long, some over 10 feet (3.0 m) wide.

Out of all the above, we have used vacuum bagging method for manufacturing our impact attenuator (Figs. 4 and 5).

Fig. 5 Vacuum bagging
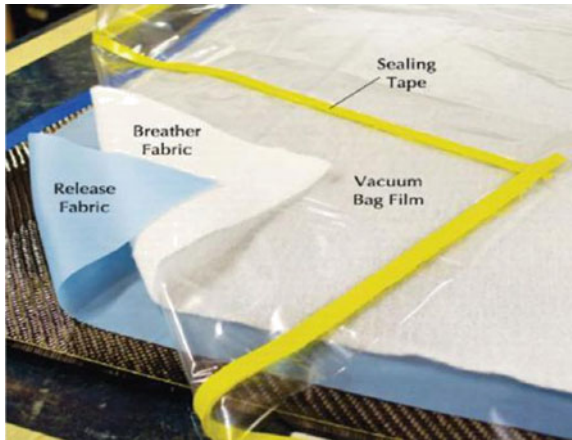
Fig. 6 IA before testing
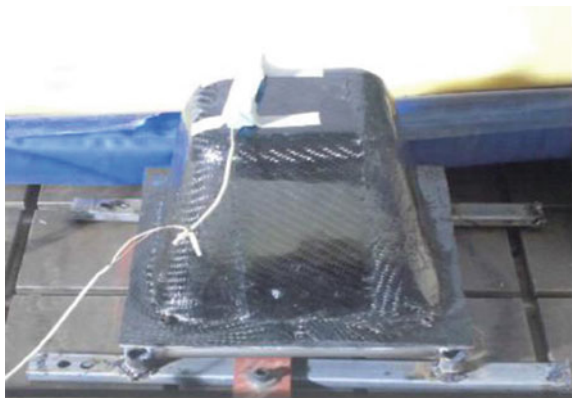
7   Testing and Comparison

Physical testing of the impact attenuator is essential to prove that the impact attenuator meets the functional requirements. A drop test was performed for the physical validation of this sample as it was the cheapest and easily available facility. The impact attenuator before and after testing with its related graphs is shown in Figs. 6, 7, 8 and 9.

Standard impact attenuator provided by SAE, although met with all the SAE rules, as it was pretested and then mass manufactured, had a mass of 850 g. The energy absorption of that structure was close to 7350 J which is the minimum requirement, while the customized IA absorbed over 10,000 J of energy. Also, a weight reduction of almost 30% was achieved by using the custom IA (Table 3).

It is clear that the actual results are in agreement with the software results. Though there was a deviation in the peak deceleration value, the energy absorption was close to the software values. The AIP deflection value is almost the same (Table 4).

Fig. 7 IA after testing
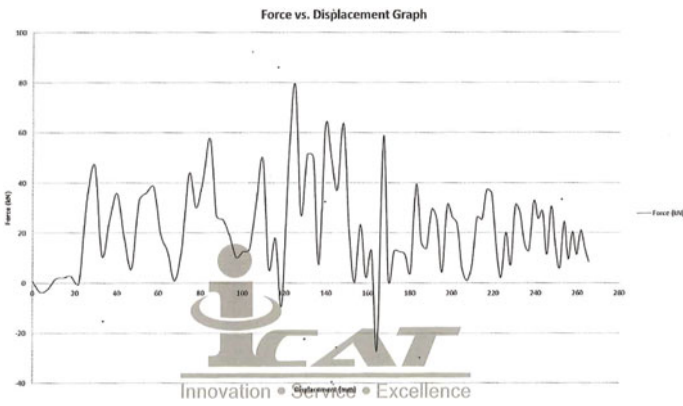
Fig. 8 Force versus displacement graph
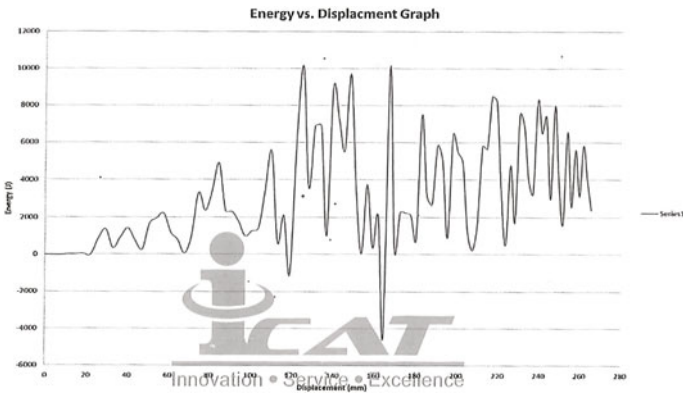
Fig. 9 Energy versus displacement graph

Table 3 Comparison between the standard IA and the customized IA

Parameter	Standard IA	Customized IA	% Improvement
Weight	850 g	600 g	29.41
Energy absorption	7350 J	10,129 J	37.8
Max c/s area	0.1225 m^2	0.0841 m^2	31.35

Table 4 Comparison between the software and physical testing results

Parameter	Software result	Physical testing result
Peak deceleration	33.33 g	26.86 g
Energy absorption	10,825 J	10,129 J
AIP deformation	16 mm	19 mm

8 Conclusion

According to the results obtained from the drop test, it is clear that the impact attenuator design successfully passed the test. The peak deceleration of the mass was 26.89 g's which is well within the maximum deceleration limit. The energy absorbed was 10,129 J. The value of energy absorption is quite close to that obtained in the software results. We managed to achieve our goals and reduced the weight by almost 30%. Also, we have reduced the overall dimensions of the sample as compared to the standard impact attenuator, which further enables compact design of the front part of the car and in turn reduces more weight.

References

1. "2017 Formula SAE Rules." SAE International https://www.formulastudent.de/uploads/media/FS-Rules_2017_V1.1.pdf.
2. "Design of the Impact Attenuator for a Formula Student Racing Car: Numerical Simulation of the Impact Crash Test" by Giovanni Belingardi and Jovan Obradovic.
3. "FSAE Impact Attenuator" by Jon Hart Craig Kennedy Todd LeClerc Justin Pollard, 2009–2010 for Worcester Polytechnic Institute (WPI), USA.
4. "Anaysis of Carbon Fiber Reinforced Impact attenuator for Formula SAE Vehicle using Finite Element Analysis" by John Thomas Rappolt, June 2015.
5. "Behaviour of an Impact Attenuator for Formula SAE Car under Dynamic Loading" by Simonetta Boria.
6. "FSAE News." Western Washington University FSAE. Western Washington University, 24 Now 2009.
7. Hiroshi Enomoto, Yusuke Miyazaki, Hiroshi Mizuno, Eiji Hirano, Satoshi Kitayama, Koetsu Yamazaki and Naoki Uota. "Development of CFRP Monocoque Front Impact." ISCBC. Kanazawa University, KADO Corporation, 2007.

Application of Steady State and Transient Modeling for Characterization of Vortex in Vertical Pump Intake for Single Phase

Rahul Paliwal, Bhola Nagelia, Hrishikesh Pangarkar, Anant Jhaveri and Channamallikarjun S. Mathpati

Abstract Non-uniform flow caused due to a vortex in the pump intake is considered undesirable for highly efficient and low maintenance operation. Sometime due to improper design or complex flow condition, this problem becomes unavoidable. Hence, there is a need to characterize such condition. Performing experiment is not feasible on conventional setup; hence, experiments with scale models have been done to assess the performance of the pump. Such tests are expensive and time consuming and thus there is a need of alternative computation fluid dynamics (CFD) methods. By referring to some of the benchmark experimental results [1], we have analyzed the performance of different turbulent models available with fluent 15.0 for steady state and transient state single-phase operation. Results of $k-\omega$, LES (Large eddy simulation), and DES (Detached eddy simulation) models have been generated and compared with the benchmark result [1].

Keywords Vortex · Turbulent model · Single phase · Large eddy simulation Detached eddy simulation

R. Paliwal (✉) · B. Nagelia · H. Pangarkar · A. Jhaveri
Mukesh Patel School of Technology Management & Engineering, NMIMS,
Ville Parle (W), Mumbai 400056, India
e-mail: rahul.paliwal@nmims.edu

B. Nagelia
e-mail: bnagelia4@gmail.com

H. Pangarkar
e-mail: hpangarkar82@gmail.com

A. Jhaveri
e-mail: asjhari42@gmail.com

C. S. Mathpati
Institute of Chemical Technology, Matunga, Mumbai 400019, India
e-mail: cs.mathpati@ictmumbai.edu.in

1 Introduction

For efficient pumping operation, uniform flow of water in the pump intake is a desirable property. This requirement becomes essential if we are dealing with high capacity pumps at power plants, dams, and water treatment sites for high efficiency and low maintenance operation. Many standards are available for designing a sump which is used to maintain water at a specific level for the pump intake. However, non-uniform vortex flow disturbs both operation and life of the pump. Inlet section from river or reservoir (in large-scale application) to one or multiple pumps consists of an approach channel. It is commonly known as pump bay or sump which consists of various devices to bring the uniformity in the flow toward the pump inlet region. Generally, baffles like structures are used to split and to divide the flow in the pump bay. These structures can be attached on the bottom surface, on the side wall, and near the inlet of pump inlet.

Usually, vortexes are observed in the inlet section near the pump inlet pipe. Depending on the region of occurrence, vortexes can be classified as free surface (on the top surface of the water) or subsurface vortex (under the water) near pump inlet pipe. Various problems related to pump maintenance and operation can be occurred due to entrance of air parcel with free surface and debris with floor attached vortexes. Major problems are vibration and cavitation due to which pump may suffer significant efficiency loss [2] and large maintenance cost.

Two main reasons for the generation of these vortexes are poor design of the intake bay and the level of non-uniformity of the approach flow [3]. Free surface vortex has a tapering hollow core which pulls the air into the suction inlet causing irregular orbital motion [4], Fig. 1 shows different types of surface vortex. A small depth of water above an intake structure can lead to air entrainment causing vortex formation. Free surface vortex can cause damage and energy losses to intake structure, pipelines, and pumps [5, 2] reduce pump's performance and discharging capacity creating vibration, cavitation, and noise problems. Subsurface vortex results in reduction of pump efficiency by causing vibrations and high bearing loads, thereby increasing operational and maintenance cost.

The very first numerical study of pump intake was approached using steady Reynolds-Averaged Navier-Stroke (RANS) with $k-\varepsilon$ turbulence models [6, 7]. The next study of Constantinescu and Patel was based on near-wall two-equation turbulence model ($k-\varepsilon$ and $k-\omega$) with conditions of high and low Reynolds numbers using 3D multiblock Reynolds-averaged Navier-Stokes(RANS) approach. In recent times, the numerical studies for analyzing the pump intakes are done using commercial solvers with steady and unsteady RANS approaches [8, 1, 9] or with LES solvers [10, 11].

The benchmark experiment [1] was performed at different flow rate to study the effect of flow rate and water level in the sump. In order to study air-entrained free surface vortex, we have tried to predict the results for flow rate of 1 m^3/min with 230 mm of water level in the tank. Simulations have been done by using different models under $k - \omega$ turbulent model for steady state with $k - \omega$ standard and $k-\omega$
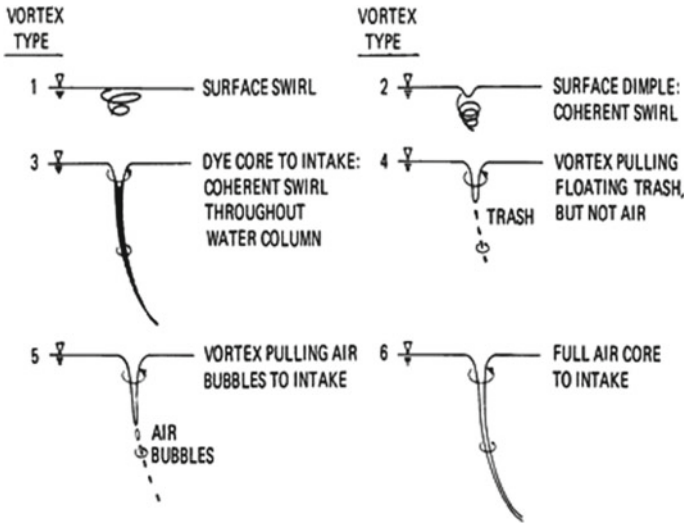
Fig. 1 Types of surface vortex [4]

Table 1 Different numerical models in benchmark study [1]

S. No.	A	B	C	D	E	F
Models	$k - \varepsilon$/RNG non-structured mesh	$k - \varepsilon$ non-structured mesh	$k - \varepsilon$ structured mesh	$k - \varepsilon$/reliable	Vortex method	Shear stress transport

standard with low Re. Further by using the steady-state results, we have done the transient state simulation with LES and DES models. Results from the numerical model have been compared with results of the experimental and numerical models of the benchmark study [1]. Different models used in the benchmark study are given in Table 1.

2 Mesh Details, Boundary Conditions, and Numerical Method

Figure 2 shows the geometrical values of the scale model for the sump, used by [1] in experimental studies. Free surface vortex, i.e., the air-entrained vortex and subsurface vortex, i.e., submerged vortexes are mainly observed in this sump. The pipe center location is a little off-center to generate asymmetry in the flow.

Mesh Detail: For analyzing the case geometrical dimensions were kept the same as that of experimental model used in the benchmark study [1]. A uniform mesh was generated by using cut cell assembly meshing with inflation at tank wall. Figure 3

Fig. 2 Geometrical details for experiment and numerical setup in benchmark study [1]
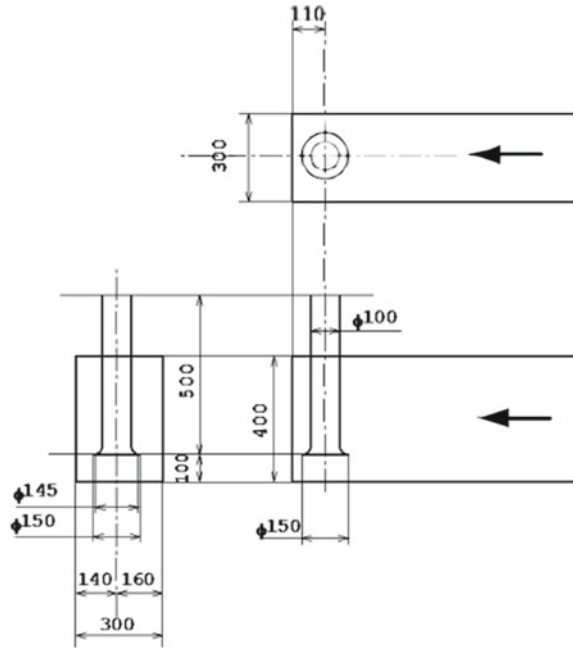
Fig. 3 Cut section of the mesh in the geometry
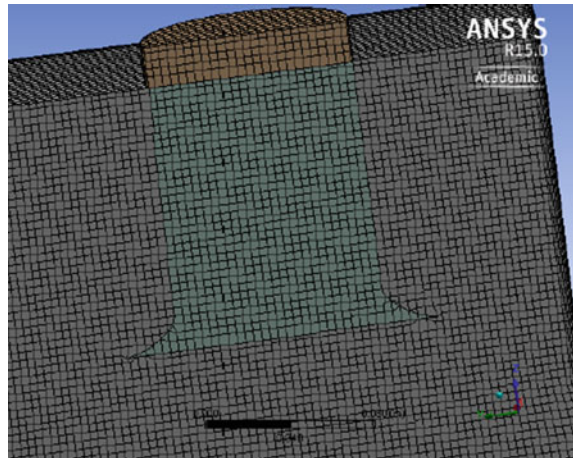
shows the mesh generated for the geometry. Hexagonal mesh with 11.12 Lac nodes and $y+$ value of 0.65 was used.

Boundary Condition: The hydrostatic pressure is assumed constant in the entrance plane and the upstream boundary is assumed to have a uniform velocity distribution with small turbulence. Concerning other boundary condition, the free surface is given symmetry condition. Outlet was given fixed flow rate condition.

Fig. 4 Measured location of vortex through PIV at top surface of tank [1]
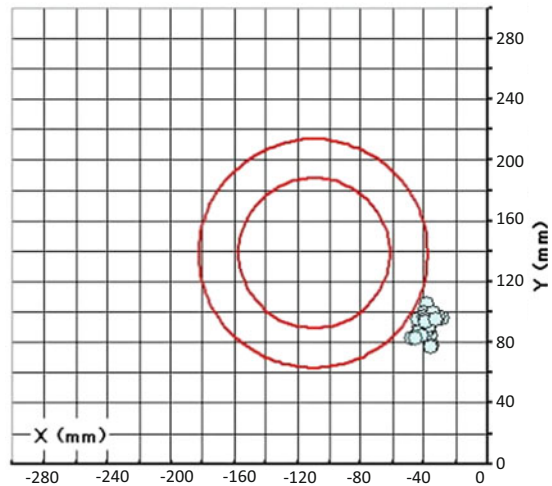
The criteria for evaluating a vortex during the experiment depend on the number of time a vortex appears at certain location. Thus, the CFD technique should be able to predict whether the vortex will be appearing or not at the location observed during experiment, i.e., whether the vortex core is in the gas or liquid state. Prediction of critical submergence is not in the scope of present work and all the models treat a single-phase flow in the calculation, hence, the gas phase is not directly predictable.

Numerical method adopted by previous study is given in Table 1. Also, in the present paper we have simulated $k - \omega$ standard and $k - \omega$ standard with low Re correction. Further, by using the converged steady-state results of $k - \omega$ standard we have simulated it for unsteady state condition for 30 s with LES and DES.

2.1 Numerical Results

Figures 4 and 5 show the locations of the center core of air-entrained vortex on the free surface obtained by experiments and computational methods used in the previous work [1]. Almost all the models predicted the location of the air-entraining vortex well. They also predicted that the other vortex will occur in the upper area behind the suction pipe. However, only one visible air-entrained vortex was observed experimentally. Figure 6 shows the location of vortex obtained by $k - \omega$, LES, and DES model. It can be seen that our results are in complete agreement with the previous study.

Table 2 shows the velocity vectors obtained numerically and experimentally at section Z220 [1]. This section is located just under the water-free surface 220 mm above the floor of the sump. The photograph of streamlines is obtained during the

Fig. 5 Predicted locations of vortex by numerical model [1]
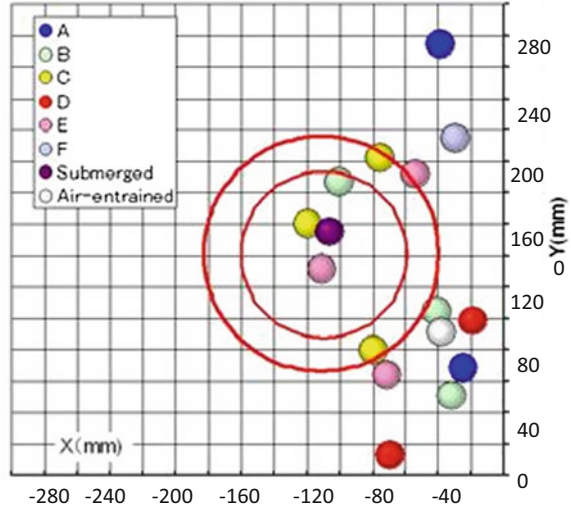
Fig. 6 Predicted location of vortex by $k - \omega$, LES, and DES models in present study
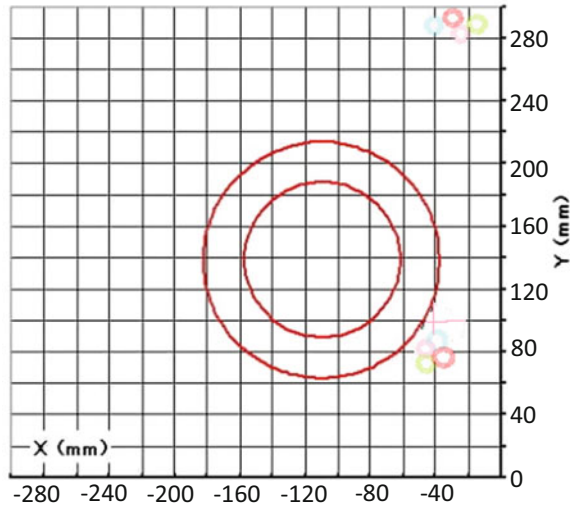
experiment by laser light sheet method and PIV results are also listed. The color scale is kept constant with velocity range from 0 to 1.5 m/s. An air-entrained vortex can be observed in the LLS and PIV result which can be seen in code A, D, E, and F. Figure 7 shows the velocity vector for the same plane developed by $k - \omega$, LES, and DES models. All the codes can be used to predict the velocity vector of air-entrained core.

Table 2 Predicted and measured velocity vector at plane Z 220
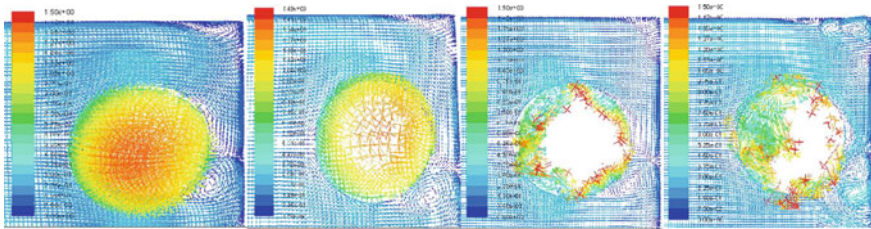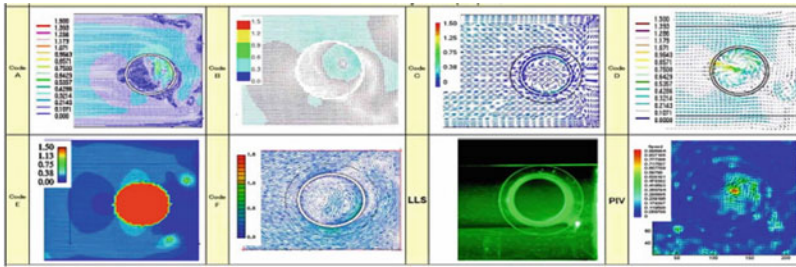
Fig. 7 Velocity vector by $k - \omega$ standard, $k - \omega$ with low Re, LES, and DES models at Z220 plane

Fig. 8 v velocity at line Z085 [1]
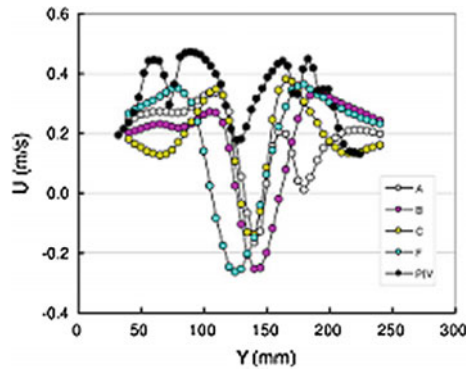
Figures 8, 10, and 12 show the velocity distribution under the bell entrance at line (Z085) [1] in the y direction above 85 mm from the bottom surface of the tank. w, v, and u mean the velocity components in z, y, and x directions. Figures 9, 11, and 13 show the velocity distribution at the same line for $k - \omega$, LES, and DES model and we can see the LES model is able to predict the results in large agreement with the experimental results. It can be seen that predicted results were well matched with the experimental results for w and v velocity. But for the u velocity, it can be seen that the results predicted were in agreement with experimental results only qualitatively. The major reason of this mismatched was explained in the original paper [1] that there was lack of accuracy during the measurement of the results.

Fig. 9 *v* velocity at line
Z085 in present work
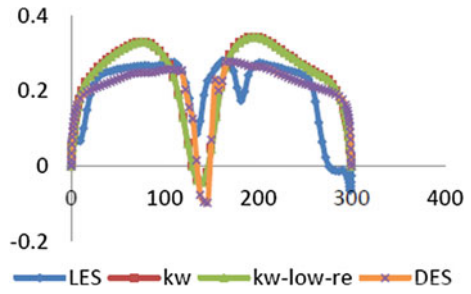
Fig. 10 *v* velocity at line
Z085 [1]
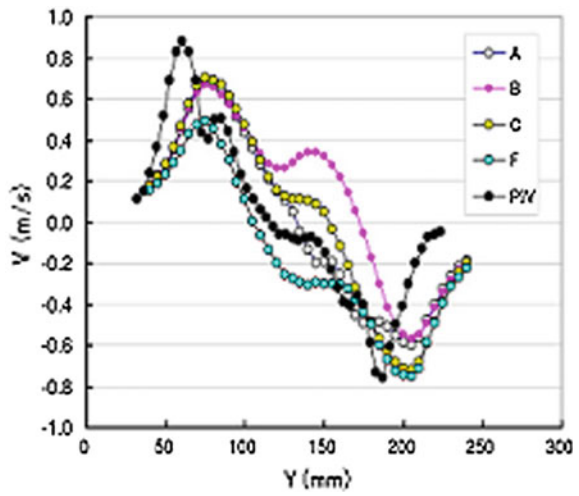
Fig. 11 *v* velocity at line
Z085 in present work
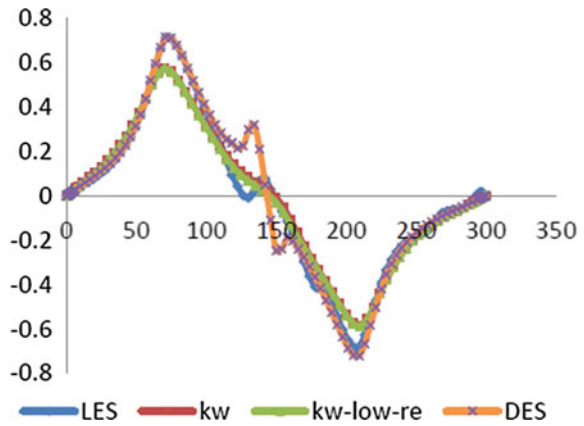
Fig. 12 *w* velocity at line Z085 [1]
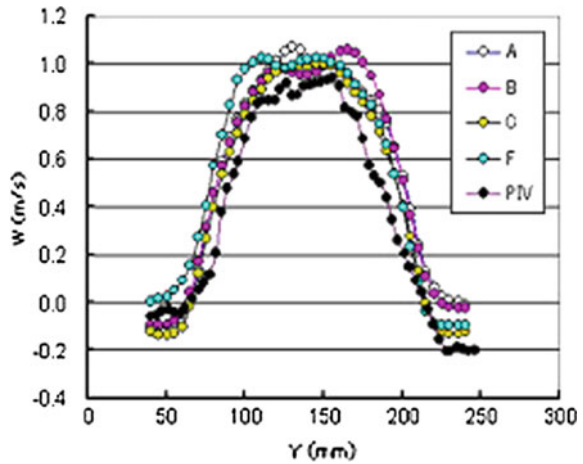
Fig. 13 *w* velocity at line Z085 in present work
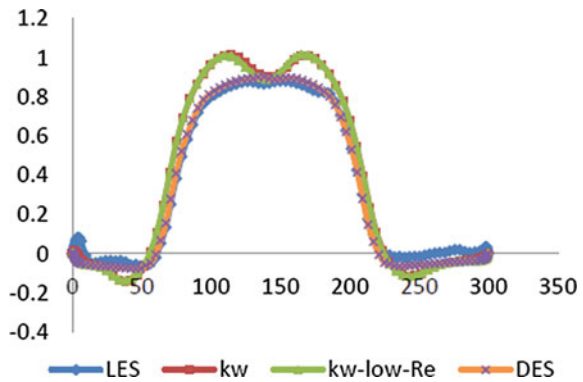
3 Conclusion

It can be found that the location and velocity vector for the air-entrained vortex can be predicted by using $k - \varepsilon$ model, which had been shown by various researchers in their studies. However, results obtained by using $k - \varepsilon$ model cannot be used in further analysis as it fails to consider the swirl and eddy conditions. These factors can be included only if the $k - \omega$ model is considered but for complete characterization of the vortex we need transient data which can be obtained by using LES and DES models. It can be further shown that both LES and DES can be used to predict the experimental results. In the future, we can use either LES or DES model for further analysis of air-entrained and submerged vortex. Also we found that air pockets can entered into the pump inlet along with free surface vortex in pump bay it reflects that we can also carry out an analysis by considering two-phase flow condition into our simulation.

References

1. Okamura, T., Kamemoto K., Matsui J.: CFD prediction and model experiment on suction vortices in pump sump.: In The 9th Asian International Conference on Fluid Machinery, Jeju Korea, AICFM9-053 1-10 (2007)
2. Messina J. P.: Periodic Noise in Circulating Water Pumps Traced to Underwater Vortices at Inlet.: In Power, p. 70 September, (1971)
3. S. A. Shabayek: Improving Approach Flow Hydraulics at Pump Intakes. In International Journal of Civil & Environmental Engineering IJCEE-IJENS Vol: 10 No: 06, 23–31. (2010)
4. Igor J. Karassik, Joseph P. Messina, Paul Cooper, Charles C. Heald: Pumps Handbook, MC Graw- Hill, Third Edition, (2001)
5. Denny D. F. and Young G. A. J.: The Prevention of Vortices and Swirl at Intakes. Paper No. C1 in Proceedings of IAHR 7th Congress, Lisbon, (1957)
6. Constantinescu, G., and Patel, V.: Numerical Model for Simulation of Pump-Intake Flow and Vortices, In J. Hydraul. Eng., 124(2), pp. 123–134. (1998)
7. Tagomori, M., and Gotoch, M.: Flow Patterns and Vortices in Pump-Sumps. In Proceedings of the International Symposium on Large Hydraulic Machinery, China Press, Beijing, China, May 28–31, pp. 13–22. (1989)
8. Kirst, K., and Hellmann, D.H.: Optimization of Approach Flow Conditions of Vertical Pumping Systems by Computational Analysis and Physical Model Investigation. In ASME 2010 3rd Joint U.S.-European Fluids. (2010) Engineering Summer Meeting Collocated with 8th International Conference on Nanochannels, Microchannels, and Minichannels, Montreal, QC, Canada, Aug. 1–5, pp. 249–258
9. Tang, X. L., Wang, F. J., Li, Y. J., Cong, G. H., Shi, X. Y., Wu, Y. L., and Qi, L. Y.: Numerical Investigations of Vortex Flows and Vortex Suppression Schemes in a Large Pumping-Station Sump. In Proc. Inst. Mech. Eng., Part C, 225(6), pp. 1459–1480. (2011)
10. Lucino, C. and Gonzalo Dur, S.: Vortex Detection in Pump Sumps by Means of CFD. In XXIV Latin American Congress on Hydraulics, Punta Del Este, Uruguay, Nov. 21–25. (2010)
11. Tokyay, T., and Constantinescu, S., 2006: Validation of a Large-Eddy Simulation Model to Simulate Flow in Pump Intakes of Realistic Geometry. In J. Hydraul. Eng., 132(12), pp. 1303–1315. (2006)

Design of Feedstock and Liquefier for Printing Aluminium Parts by Fused Deposition Modeling

Pravin S. Misal and N. S. Chandrashekhar

Abstract Growth of any additive manufacturing technology always depends on the market, make, metrology and material. Fused deposition modelling technology which mostly uses thermoplastic feedstock in filament form has gain large market since it developed. However, a demand for developing new material for FDM process to make its applications in metal printing has always been there. The operation of FDM is similar to extrusion process where the filament above the liquefier acts as the plunger and filament in the liquefier acts as the billet to be extruded. Many efforts have been made to develop the FDM process for low-melting point solder materials. It is difficult to handle the high-melting point metal having dendritic microstructure in semi-solid range. Thixo-extrusion process gives us the ability to extrude the metal in mushy like thermoplastics. In this work, the process for preparation of aluminium alloy feedstock having non-dendritic micro-structure has been presented. And the liquefier for semi-solid extrusion of aluminium alloy filament has been designed referring conventional FDM liquefier.

Keywords Additive manufacturing · Fused deposition modelling
Liquefier design · Thixo-extrusion · Feedstock preparation
Aluminium printing etc.

1 Introduction

After developing various additive manufacturing processes since 1980, this technology is trying to shift its applications to rapid tooling from rapid prototyping. AM is an exception for the concept that the design complexity increases the production cost. According to Wohler's reports, majority of the end products will be produced

P. S. Misal (✉) · N. S. Chandrashekhar
K J Somaiya College of Engineering, Mumbai 400077, India
e-mail: pravin.misal@somaiya.edu

N. S. Chandrashekhar
e-mail: nschandrashekhar@somaiya.edu

by AM in future [1]. AM techniques are classified as binder jetting, vat photopoly-merisation, sheet lamination, powder bed fusion, material jetting, material extrusion and directed energy deposition according to ISO/ASTM 529000:2015 [2] .

1.1 Fused Deposition Modelling

Among the seven AM processes, extrusion based is one of the majorly accepted pro-cesses [3]. FDM having the less cost than professional AM machines is very popular in the desktop 3-D printers and FDM machines from Stratasys, Inc are currently dom-inating the commercial extrusion-based AM systems market with 3.5 times market share at 41.5% of all systems sold. Entry-level 3-D printers are predominantly based on FDM [4].

In spite of numerous advantages of AM over subtractive manufacturing, it is still not accepted by most of the industries. Lots of designs, materials, new processes and machines, modelling and control in processes, applications in biomedical field and energy are to be researched and developed to increase the applicability of AM processes and bring it to mainstream. Materials and metrology are thus the two key enabling technologies that have to progress beyond its current state of the art to translate AM from rapid functional prototyping to genuine industrial manufacturing [4]. To develop the FDM process for rapid tooling and rapid manufacturing, new materials are needed. The operating principle of FDM process offers us the oppor-tunity to develop the feedstock of metals and composites of required size, strength and properties [5].

In this paper, we are going to discuss the method to design the feedstock filament and liquefier for FDM for printing aluminium parts.

2 Literature Review

Many efforts are made to develop the FDM system for printing metal parts. Like electrically heating the fusible alloy and depositing through a blunt needle applicable for printing electronic circuitry [6]. FDM 3000 was modified and used for deposition of low melting temperature solder alloys filament [7]. But these methods were not possible for high-melting point metals because high-melting point metals have a narrow range of non-eutectic region. Direct molten aluminium was deposited for free-form fabrication by Cao and Miyamoto [8]. Metal polymer composite filament was developed with different ratios and particle sizes and injection moulding inserts were successfully printed [9]. Semi-solid metal extrusion principle was used to print the solder metals. In their work, the liquefier was developed by using the thixo-extrusion principle and the filament feedstock having microstructure necessary for thixo-extrusion was developed. The printed parts were having high strength than the cast parts [10].

2.1 Thixo-Extrusion

Thixo-extrusion is an extrusion of metal in semi-solid state. The feedstock having non-dendritic microstructure is used in this process which allows us to form the metal in viscous state. Thixo-extrusion is different than conventional extrusion process. It can be done at various solid fractions. The solid fraction decreases with increase in temperature and viscosity of slug decreases. Thixo-extrusion, one of the thixo-forming processes, has advantages of high productivity, reduction of the extrusion pressure, extension of the die life and cost saving due to low-energy consumption compared with conventional extrusion processes.

Y. Birol thixo-extruded EN AW 2014 $Si_{0.6}$ $Fe_{0.5}$ $Cu_{4.618}$ $Mn_{0.932}$ $Mg_{0.265}$ $Zn_{0.18}$ $Ti_{0.03}$ $Al_{92.80}$ at extrusion ratio of 2.56 and solid fraction of 0.8 [11]. Kapranos et al. [12] thixo-extruded Al_{5182} ($Mg_{4.5}$ $Mn_{0.25}$ $Cu < 0.15Al$) with an extrusion ratio of 2.77 and solid fraction 0.5. He used alumina ceramic die because it has the operating temperature of 1650 °C and good mechanical properties. Shiomi et al. thixo-extruded an aluminium alloy (Al–7%Si–0.3%Mg, AC4CH) which is similar to A356 to an extrusion ratio 3.75 in 2002 [13]. In 2013, Abolhasani et al. thixo-extruded AL6061 ($Si_{0.475}$ $Fe_{0.218}$ $Cu_{0.172}$ $Mn_{0.137}$ $Mg_{0.844}$ $Cr_{0.159}$ $Zn_{0.035}$ $Ti_{0.026}$) with extrusion ratio 1.56 and 2.04. The solid fraction was from 0.1 to 0.9 [14]. A357 in 2010 was thixo-extruded at solid fraction of 0.85 and extrusion ratio of 8.5 [15].

All this literature proofs that aluminium alloy can be thixo-extruded at any solid fraction. The working of FDM liquefier is same as the extrusion process where the filament above the liquefier acts as the plunger and filament in the liquefier acts as the billet to be extruded [16]. Hence using this thixo-extrusion principle of aluminium, a liquefier for FDM system is designed in this paper. Following sections includes the topics like material selection of feedstock, material selection for liquefier, thermal design of liquefier and modifications in liquefier design.

3 Feedstock and Liquefier Design

Operation of any FDM system depends on the rheological behaviour of filament material and liquefier geometry. In this section, the material for feedstock is selected and feedstock development process is designed. Liquefier for printing aluminium parts is designed along with its material selection.

3.1 Feedstock Material Selection

In FDM 3-D Printer, the rheological properties of filament material are very important. The thermoplastic polymers behaviours in viscous manner and hence their deposition rate can be controlled easier way.

The extrusion and material deposition in FDM process is same as the normal billet extrusion in which a filament above liquefier act as plunger and below liquefier after heating acts as the billet to be extruded. The nozzle of FDM acts as a die of extrusion diameter. The aluminium alloys having more silica content can be easily thixo-extruded. Hence some aluminium cast alloys were reviewed for feedstock material selection.

From the Table 1, we can see that the alloys A356, A357 and A390 are having good silica content. A390 is having the highest silica content, but the copper percentage is also more i.e. 4.5%. Al alloys having higher copper percentage are difficult to form. Hence out of A356 and A357, we selected the A357 because the Mg content in A357 is more than the A356 hence will have more strength [17].

3.2 Feedstock Preparation Process

Feedstock preparation process is done for converting the dendritic microstructure into non-dendritic form (Fig. 1).

The metal should have globular microstructure for any thixo-extrusion process. Spheroid solid surround by the liquid matrix is a requirement for semisolid processing

Table 1 Composition of aluminium cast alloys [18]

Aluminium alloy	Composition (% mass)
A296	Al–4.5Cu–2.5Si
A356	Al–7Si–0.3Mg
A357	Al–7Si–0.5Mg
A390	Al–17Si–4.5Cu–0.6Mg
A520	Al–10Mg
A771	Al–7Zn–0.9Mg–0.13Cr
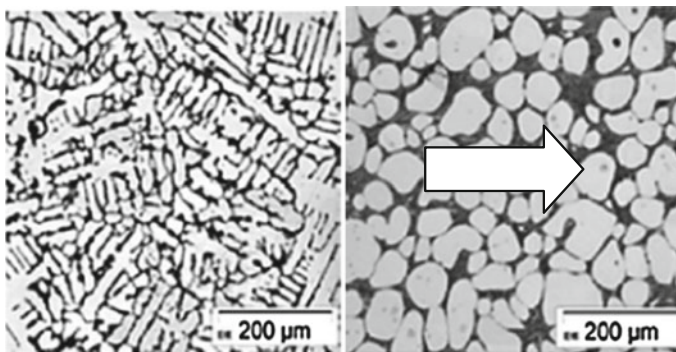
Fig. 1 Preparation of feedstock from dendritic to non-dendritic microstructure [19]

Fig. 2 Temperature time graph of SIMA process [19]
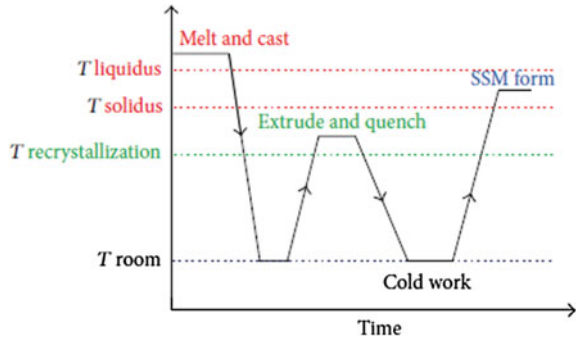
and thixotropic condition [19]. For extrusion of feedstock having small diameters, strain induced melt activated (SIMA) process is recommended [10]. SIMA is the process in which deformed material is again heated into the semi-solid form. The first deformation takes place at the temperature above the recrystallisation temperature followed by cold working at room temperature. This is a critical step in storing the energy flow as result of partial remelting. The uniform, globular and non-dendritic solid particles get placed in a liquid matrix as shown in Fig. 2 and semi-solid state of material is reached [19].

3.3 Material of Liquefier

As we are designing the FDM liquefier for printing aluminium parts, we need the material for liquefier which can sustain temperature more than the 650 °C. The high thermal conductivity, high oxidation resistance, non-reactivity with metals and low thermal stresses are the important desirable properties for selection of material. For this requirement, the ceramics are better candidates than any metal. After reviewing oxides-based and non-oxide-based ceramics like alumina, zirconia, aluminum titanate (Al TiO) SiAlON, silicon carbide, aluminium nitride, silicon nitride and alumina-based ceramic were found to be suitable for our requirement. As in thixo-extrusion of aluminium alloy Al5182 done by Kapranos et al., an alumina ceramic die was used [12]. We referred various grades of alumina ceramic and studied their properties. Alumina ceramic with purity 82–86 and 99% was evaluated for designing our liquefier.

3.4 Thermal Design of Liquefier

The FDM liquefier is like a metal block through which a filament or melt flows. A channel is machined in it to occupy the filament or melt flow. In the systems like

Stratasys, the channel is surrounded by a liquefier and connected to a disposable print head. A liquefier chamber is surrounded by resistive heater which is coil type. The design of system is such that the uniform temperature is maintained throughout the length of the liquefier. A thermocouple with a controller is used along with the heater for maintaining the temperature.

Normally, the filament diameter used in FDM is from 1.5 to 3 mm. The heat emitted by liquefier chamber is used by feedstock filament for melting. Heat transfer should bring the feedstock material to the semi-solid state. The heat flux and feed rate decide the semi-solid amount in the liquefier [16]. For designing the liquefier for extreme difficult case, we considered the feedstock filament diameter of 3 mm. Just to start and take trials we considered the liquefier temperature as 800 °C and feed rate of minimum 1 mm/s and maximum 5 mm/s.

From transient thermal FEM analysis, we get that for feedstock of maximum 3 mm diameter, and liquefier temperature of 800 °C, it took 27.6 s to achieve 650 °C. Hence for feed rate of 1 mm/s, the sleeve of length 27.6 mm is required. And considering maximum feed rate of 5 mm/s the sleeve length required is 138 mm (Fig. 3).

For trying less length of liquefier, we can increase the temperature of liquefier as alumina ceramic has operating temperature of 1650 °C. Hence for liquefier temperature of 1200 °C, it took 12 s to achieve 650 °C. Hence for feed rate of 5 mm/s 60 mm length is sufficient.
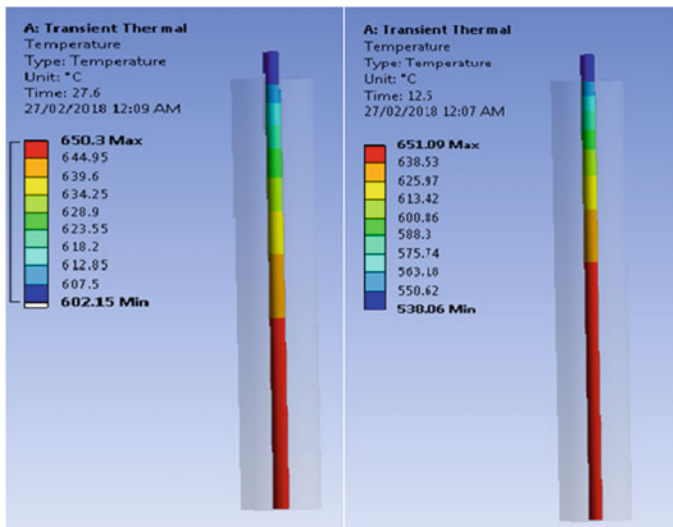
Fig. 3 Time taken by filament to reach 650 °C for sleeve temperature 800 and 1200 °C

3.5 Mechanical Design and Modifications

After thermal design of liquefier we decided to design the liquefier for 1200. A cylindrical sleeve of length 60 mm was designed first and fixed support was applied at its upper face. Many stresses were induced in the upper face showing that the design was unsafe. The reason behind that was the thermal stress due to thermal coefficient of expansion (Fig. 4).

(a) **Modification 1**

Hence to avoid thermal stresses, heat dissipation was necessary. Referring the design of conventional FDM liquefier, the heat sink fins were added and safe design with respect to stresses were achieved by applying fixed support at above face. But the large amount of deformation was induced at the nozzle end which is undesirable.

(b) **Modification 2**

Hence to restrict the vertical movement at nozzle end, the support at nozzle end was applied and fixed support from the upper face was removed (Fig. 5).

Hence alumina ceramic job with 82–86% purity is suitable for our application (Figs. 6 and 7).

After modifications in liquefier design, again time required to achieve the temperature of 650 °C was checked and it was found that the filament achieves 650 °C much before the time the filament is extruded from the nozzle.

Fig. 4 Stresses induced in liquefier
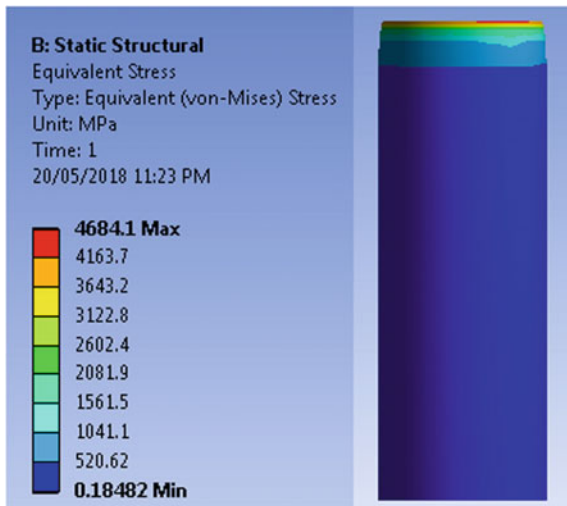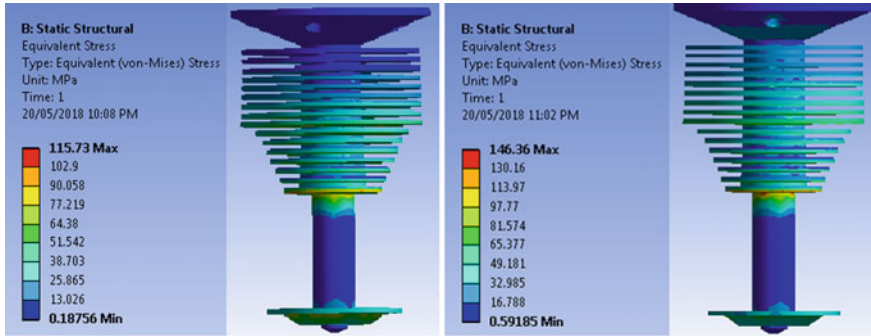
Fig. 5 Maximum stress for 82–86% purity alumina ceramic was 115 MPa and for 99% Purity Alumina ceramic was 146 MPa

Fig. 6 Model of liquefier after modifications
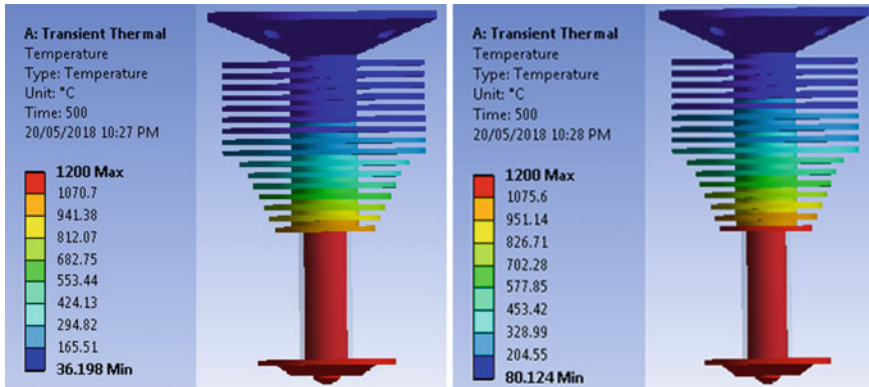
Fig. 7 Temperature Distribution for Alunina ceramic 82–86% and Alumina ceramic 99% purity

4 Conclusion

Material limitation of FDM AM technique was identified and solutions tried by the researchers to overcome this limitation were studied. The limitations of those solutions were also identified and by taking reference of their methodology and more literature survey thixo-extrusion principle is used to design the liquefier and feedstock preparation process for the FDM AM technique which will able to print aluminium parts. Thixo-extrusion is the promising technology which can be used for designing the FDM liquefier. The liquefier for printing aluminium parts by FDM system is designed. The feedstock preparation process is also proposed in our work. After this testing of our design is the main step. Hence future work includes the simulation and validation of optimized design. Future work also includes modelling the process parameters like temperature, solid fraction, feed rate and deposition speed and heat dissipation. Pressure drop along the liquefier is necessary to be calculated for designing the feeding mechanism. Cooling system also needs to be designed for our liquefier as large amount of heat is emitted by the heat sink. For validation of process parameters, experimental trials will also be taken by installing the liquefier on the Cartesian guiding mechanism like typical FDM 3-D Printers.

References

1. Weller, Christian, Robin Kleer, and Frank T. Piller. "Economic implications of 3D printing: Market structure models in light of additive manufacturing revisited." *International Journal of Production Economics* 164 (2015): 43–56.
2. Lee, Jian-Yuan, Jia An, and Chee Kai Chua. "Fundamentals and applications of 3D printing for novel materials." *Applied Materials Today* 7 (2017): 120–133.
3. Gardan, Julien. "Additive manufacturing technologies: state of the art and trends." *International Journal of Production Research* 54.10 (2016): 3118–3132.

4. Tofail, Syed AM, et al. "Additive manufacturing: scientific and technological challenges, market uptake and opportunities." *Materials Today* (2017).
5. Masood, S. H., and W. Q. Song. "Development of new metal/polymer materials for rapid tooling using fused deposition modelling." *Materials & design* 25.7 (2004): 587–594.
6. Yu, Yongze, Fujun Liu, and Jing Liu. "Direct 3D printing of low melting point alloy via adhesion mechanism." *Rapid Prototyping Journal* 23.3 (2017): 642–650.
7. Mireles, Jorge, et al. "Development of a fused deposition modeling system for low melting temperature metal alloys." *Journal of Electronic Packaging* 135.1 (2013): 011008.
8. Cao, Wenbin, and Yoshinari Miyamoto. "Freeform fabrication of aluminum parts by direct deposition of molten aluminum." *Journal of Materials Processing Technology* 173.2 (2006): 209–212.
9. Masood, S. H., and W. Q. Song. "Development of new metal/polymer materials for rapid tooling using fused deposition modelling." *Materials & design* 25.7 (2004): 587–594.
10. Jabbari, Amin, and Karen Abrinia. "A metal additive manufacturing method: semi-solid metal extrusion and deposition." *The International Journal of Advanced Manufacturing Technology* 94.9–12 (2018): 3819-3828.
11. Birol, Yucel. "Thixoforming of EN AW-2014 alloy at high solid fraction." *Journal of Materials Processing Technology* 211.11 (2011): 1749–1756.
12. Kapranos, Plato, et al. "Thixo-extrusion of 5182 aluminium alloy." *Solid State Phenomena*. Vol. 141. Trans Tech Publications, 2008.
13. Shiomi, M., et al. "Forming of aluminium alloy at temperatures just below melting point." *International Journal of Machine Tools and Manufacture* 43.3 (2003): 229–235.
14. Abolhasani, D., et al. "Microstructure and mechanical properties evolution of 6061 aluminum alloy formed by forward thixoextrusion process." *Materials & Design* 49 (2013): 784–790.
15. Forn, Antonio, et al. "Thixoextrusion of A357 aluminium alloy." *Transactions of Nonferrous Metals Society of China* 20 (2010): s1005–s1009.
16. N. Turner, Brian, Robert Strong, and Scott A. Gold. "A review of melt extrusion additive manufacturing processes: I. Process design and modeling." *Rapid Prototyping Journal* 20.3 (2014): 192–204.
17. Alhawari, K. S., et al. "Microstructural evolution during semisolid processing of Al–Si–Cu alloy with different Mg contents." *Transactions of Nonferrous Metals Society of China* 27.7 (2017): 1483–1497.
18. Z. Fan, (2013) Semisolid metal processing. International Materials Reviews 47 (2):49–85.
19. Mohammed, M. N., et al. "Semisolid metal processing techniques for non-dendritic feedstock production." The Scientific World Journal 2013 (2013).

Static Structural Analysis of Car Rim by Finite Element Method

Suraj L. Gondhali, Atul D. Dhale and Sunil Pagare

Abstract This paper includes the comparison of equivalent stress values and total deformation in Maruti Eeco wheel rim by finite element method. In this work, the rim is disc wheel category (Akbulut in Finite elements in analysis and design. Elsevier Ltd, pp. 433–443, 2003 [1]; Bhavikutti and Ramkrushnana in CAS. Pergamon Press Ltd, pp. 397–401, 1980 [2]). CAD modelling of disc wheel rim was done using SolidWorks software, whereas static structural analysis of disc wheel rim was done using FEM software (ANSYS 15.0). Static structural analysis is carried out for tyre inflation pressure, bearing load and bending moment condition. First, the dimensions of the existing Maruti Eeco car rim are obtained using reverse engineering approach. Modelling is done using SolidWorks, and analysis is done using ANSYS software. After that, new modified design is created based on the material reduction approach so that total weight will reduce substantially to increase the fuel economy (mileage) of the car and to improve the tractive effort of the vehicle without compromising its strength and stability (Sunil Kumar Nakka in Int J Res Eng Technol. 2016 [3]; Chia-Lung Chang in Eng Fail Anal. Elsevier Ltd, pp. 1711–1719, 2009 [4]). The analysis is done for three different materials, namely structural steel, aluminium alloy and magnesium alloy, respectively, and results are compared for different boundary conditions. By analysing the results, suitable material rim design is proposed which gives optimum results based on strength, weight, cost and durability criteria.

Keywords Static structural analysis · Car rim · Modelling · ANSYS

S. L. Gondhali (✉) · S. Pagare
Department of Mechanical Engineering, B. R. Harne College of Engineering and Technology (BRHCET), Thane, Maharashtra, India
e-mail: surajgondhali@gmail.com

A. D. Dhale
Department of Mechanical Engineering, D. J. Sanghvi College of Engineering and Technology (DJSCOE), Mumbai, Maharashtra, India

1 Introduction

The wheel rim bents due to excessive radial load. Damages such as rust, cracks and dentsetc may create damage to the vehicle in the form of instability, excessive vibration, loss of air pressure and even structure can be completely failed. So, the need of hour is to provide weight/cost-effective products without compromising the stringent safety requirements [5]. This analysis helps to predict the best optimized wheel design for the stated vehicle without compromising its performance parameters.

2 Modelling of Car Rim

Automobile rim specifications of existing Maruti Eeco car which is used for analysis are shown in Table 1.

Figure 1 the actual view of the Maruti Eeco car rim model when viewing from both sides.

Table 1 Specifications of Maruti Eeco car rim

S. No.	Specification	Value
1	Width of the rim	0.124 m
2	Diameter of the rim	0.354 m
3	Offset	0.041 m
4	Central hole diameter	0.054 m
5	Thickness of the rim	0.002 m
6	Diameter of stud hole	0.015 m
7	Diameter of stud hole circle	0.100 m
8	Number of stud holes	04 no's

Fig. 1 Actual model of Maruti Eeco car rim

Table 2 Selection of material for the analysis of Maruti Eeco car rim

S. No.	Material name	Density (ρ) Kg/m^3	Young's modulus (E) Pa	Poisson's ratio (1/m)
1	Structural steel	7850	2×10^{11}	0.3
2	Aluminium alloy	2770	7.1×10^{10}	0.33
3	Magnesium alloy	1800	4.5×10^{10}	0.35

3 Material Selection

Materials were chosen for analysis of car rim with their properties as shown in Table 2.

4 Finite Element Analysis of Car Rim

4.1 Boundary Conditions

After import into ANSYS, car rim is being applied by boundary conditions as follows:

- Fixed support is given to the four bolt holes because the rim is fixed by bolts at the stated location [6].
- Bearing load is calculated analytically by considering the total weight acting on the rim and acceleration test factor [7]. Total bearing load of 7769.5 N is applied at the hub centre in '-Y' direction because hub is fixed in the central hole and applies load on the rim like bearing [8, 9].
- The vehicle rims' circumferential tread and flange portion are applied by average pressure in the tube of tyre which is taken as 0.241 MPa [10].
- The rotational velocity of car rim is taken as 100 Kmph, i.e. 965 RPM obtained by considering diameter of tyre as 0.550 m [11].
- The moment acting on the rim because of axle and uneven road profile is calculated analytically by considering the acceleration factor and coefficient of friction between tyre and road surface [12] as stated in annexures of AIS-073 (Part 2) Automotive Vehicles [13].
- Frictionless support is given to the inner chamfered portion of hub central hole [14].

The loading conditions applied in ANSYS for the existing car rim design and modified car rim design are as shown in Figs. 2 and 3, respectively. *A* denotes fixed support, *B* denotes bearing load, *C* denotes internal pressure, *D* denotes rotational velocity, *E* denotes bending moment and *F* denotes frictionless support applied on the rim, respectively.
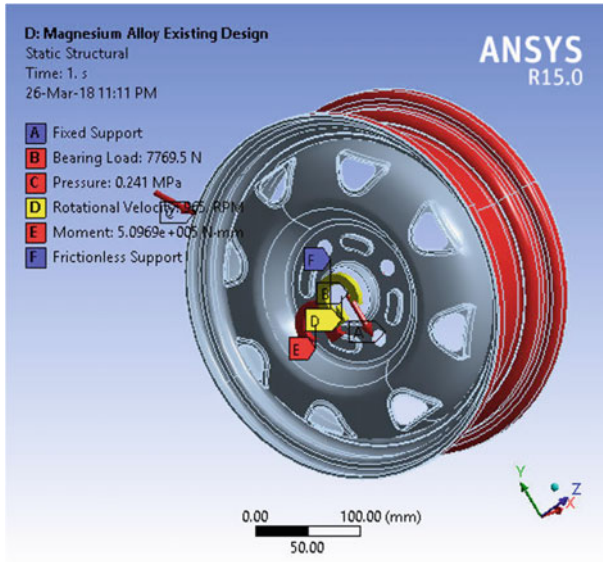
Fig. 2 Combination of loading conditions—existing design
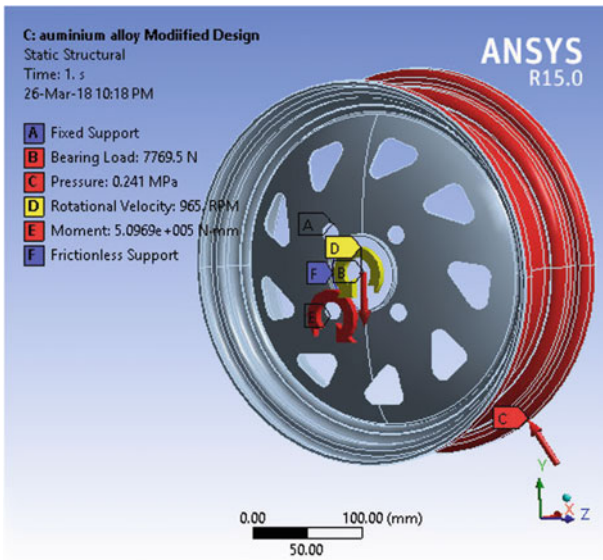
Fig. 3 Combination of loading conditions—modified design
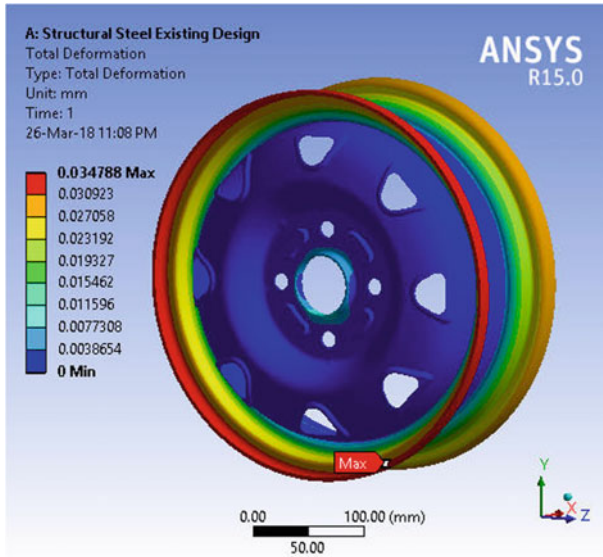
Fig. 4 Total deformation for structural steel existing rim design

5   Results and Discussion

5.1   *Results*

After applying the loading conditions on the car rim models of the existing design and modified designs for different materials, following results are obtained for total deformation in mm as shown in Table 3.

Maximum deformation for structural steel existing rim design is 0.034788 mm as shown in Fig. 4 and maximum deformation for structural steel modified rim design is 0.042381 mm as shown in Fig. 5. In both the cases, maximum deformation is occurred at flange portion of the rim whereas minimum deformation is occurred at the bolt circle portion.

Maximum deformation for aluminium alloy existing rim design is 0.097809 mm as shown in Fig. 6 and maximum deformation for aluminium alloy modified rim design is 0.10225 mm as shown in Fig. 7. In both the cases, maximum deformation is occurred at flange portion of the rim whereas minimum deformation is occurred at the bolt circle portion.

Maximum deformation for magnesium alloy existing rim design is 0.21516 mm as shown in Fig. 8, and maximum deformation for magnesium alloy modified rim design is 0.20694 mm as shown in Fig. 9. In both the cases, maximum deformation is occurred at flange portion of the rim whereas minimum deformation is occurred at the bolt circle portion.
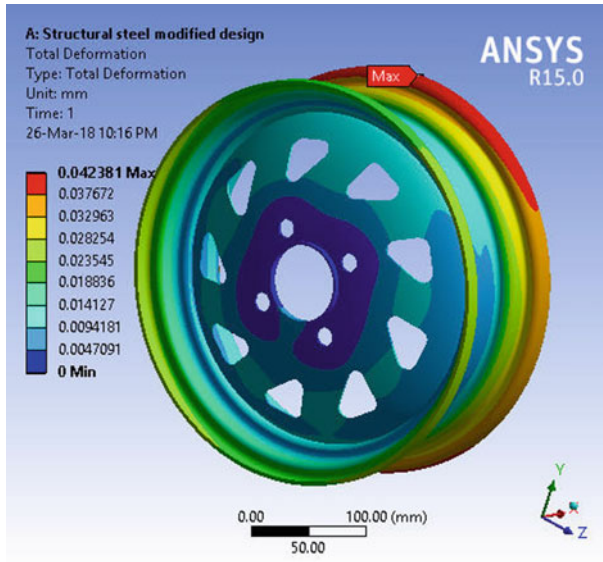
Fig. 5 Total deformation for structural steel modified rim design
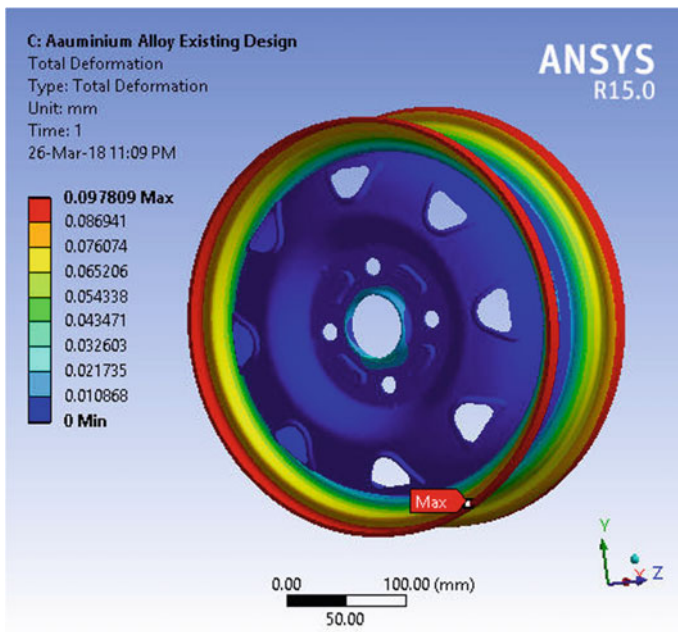
Fig. 6 Total deformation for aluminium alloy existing rim design
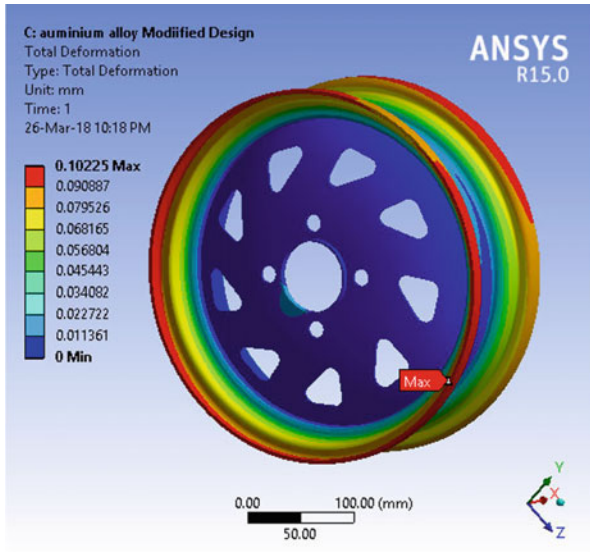
Fig. 7 Total deformation for aluminium alloy modified rim design
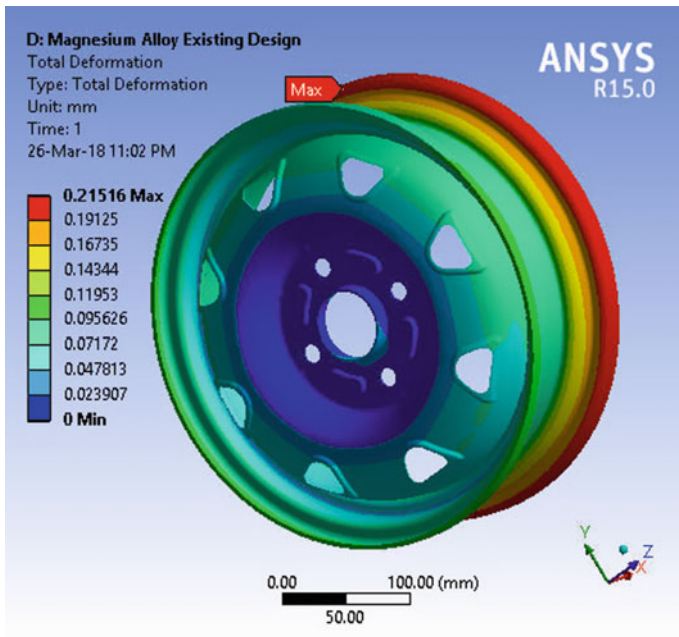
Fig. 8 Total deformation for magnesium alloy existing rim design
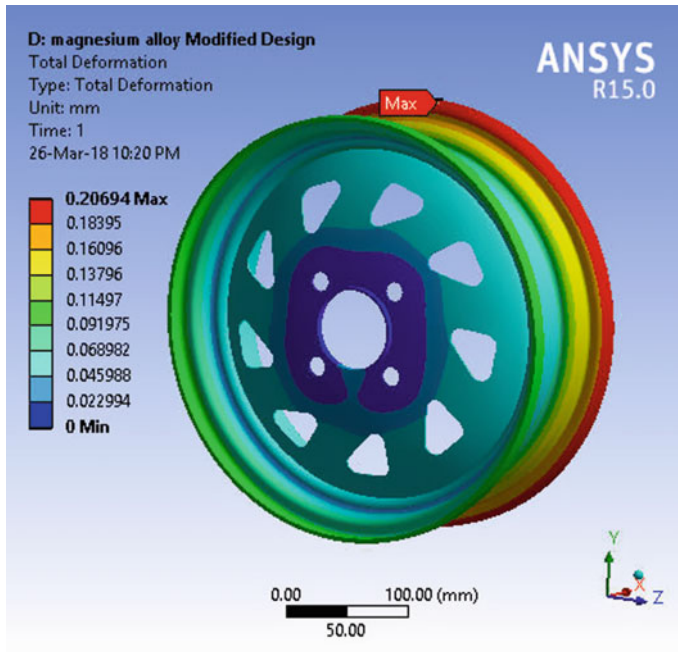
Fig. 9 Total deformation for magnesium alloy modified rim design

Table 3 Result for total deformation due to all loading conditions

S. No.	Material	Total deformation (mm)	
		Existing car rim design	Modified car rim design
1	Structural steel	0.03478	0.04238
2	Aluminium alloy	0.0978	0.10225
3	Magnesium alloy	0.2151	0.20694

Equivalent (von Mises) stress values after analysis are as shown in Table 4.

Table 4 Result for equivalent stresses in MPa due to all loading conditions

S. No.	Material	Equivalent stress MPa	
		Existing car rim design	Modified car rim design
1	Structural steel	70.05	52.98
2	Aluminium alloy	70.524	51.88
3	Magnesium alloy	70.14	52.744
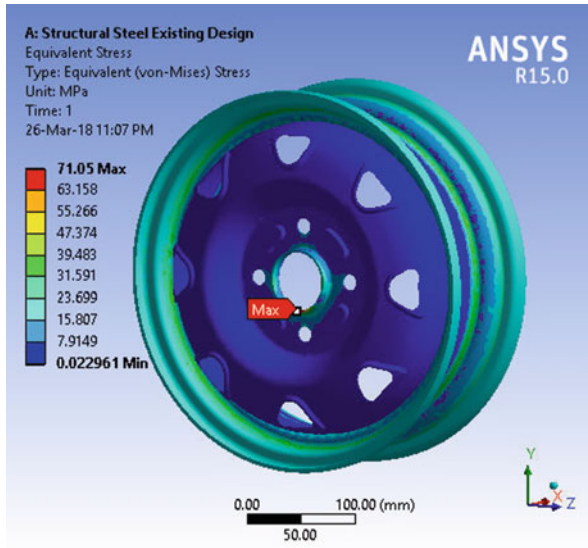
Fig. 10 Equivalent stresses for structural steel existing rim design

Table 5 Reduced weight table for existing and modified rim designs

S. No.	Material	Weight kg	
		Existing car rim design	Modified car rim design
1	Structural steel	4.2846	3.7780
2	Aluminium alloy	1.5119	1.3335
3	Magnesium alloy	0.98245	0.8665

Maximum equivalent stress for structural steel existing rim design is 71.05 MPa as shown in Fig. 10, and maximum equivalent stress for structural steel modified rim design is 52.99 MPa as shown in Fig. 11.

Maximum equivalent stress for aluminium alloy existing rim design is 70.524 MPa as shown in Fig. 12, and maximum equivalent stress for aluminium alloy modified rim design is 51.886 MPa as shown in Fig. 13.

Maximum equivalent stress for magnesium alloy existing rim design is 70.145 MPa as shown in Fig. 14, and maximum equivalent stress for magnesium alloy modified rim design is 52.744 MPa as shown in Fig. 15.

The detailed analysis shows the results for both existing car rim design and modified car rim design, which is well below allowable values. It depicts that the weight optimization is successfully carried out. Reduced weight after modification is as shown in Table 5.
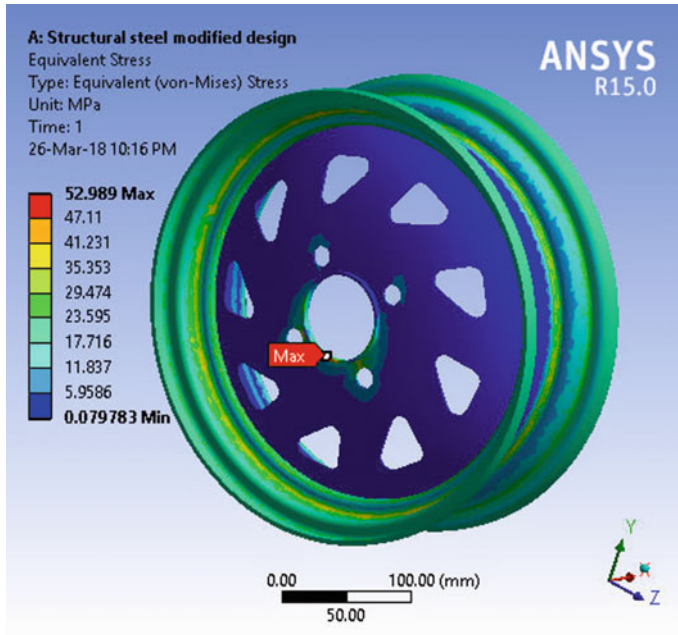
Fig. 11 Equivalent stresses for structural steel modified rim design

6 Conclusion

By comparing the above results, since in all the cases equivalent (von Mises) stresses are less than the allowable stress values for ultimate strength. Taking deflections into account, structural steel is preferred as the best material for design of wheel rim with least deflection. We can conclude that the modified design of the car rim with structural steel material is proven to be the best and optimized design that can be proposed with highest weight reduction. Reduced weight of the car rim will also positively affect the steering effort and the tractive effort of the vehicle [8]. Structural steel is having the best strength and rigidity as compared to aluminium alloy and magnesium alloy. Hence, by evaluating and analysing the results obtained from the analysis for the existing and modified designs, we propose structural steel as the best material for modified design of the wheel rim of Maruti Eeco vehicle.
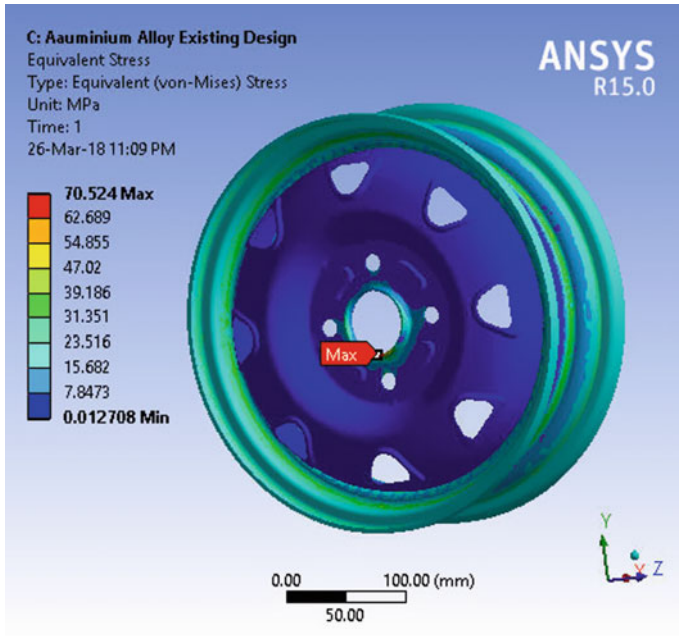
Fig. 12 Equivalent stresses for aluminium alloy existing rim design
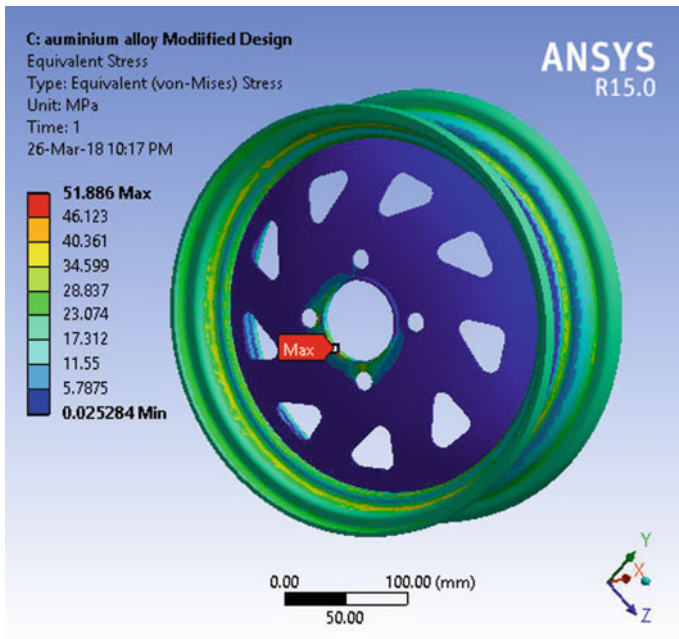
Fig. 13 Equivalent stresses for aluminium alloy modified rim design
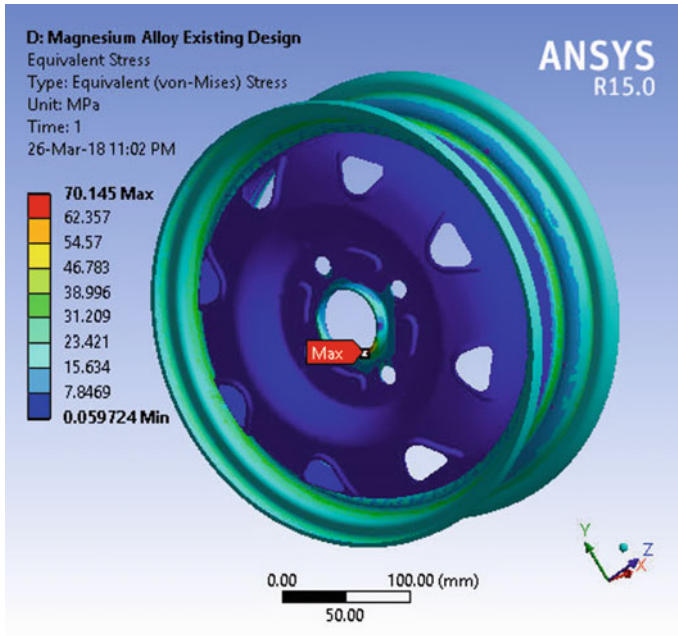
Fig. 14 Equivalent stresses for magnesium alloy existing rim design
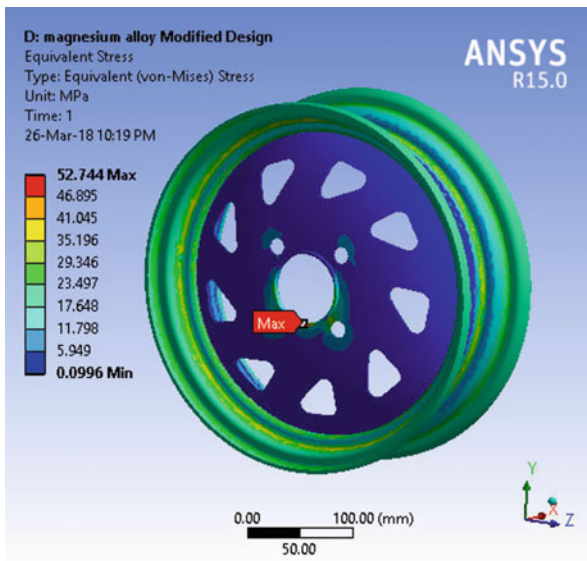
Fig. 15 Equivalent stresses for magnesium alloy modified rim design

References

1. H. Akbulut "On optimization of a car rim using nite element method" Finite Elements in Analysis and Design 39 (2003) 433–443: Elsevier Ltd.
2. S.S. Bhavikutti, C.V. Ramkrushnana "Optimum shape Design of Disc" CAS Vol II No. 5-C pp. 397–401 Pergamon Press Ltd. (1980).
3. Sunil Kumar Nakka et al. "Structural Analysis of Car alloy wheel using Aluminum and magnesium Alloys" International Journal for Development of Computer Science and Technology (IJDCST) Issue- V-4, I-2, SW-09, March 2016.
4. Chia-Lung Chang et al. "Simulation of wheel impact test using finite element method", Engineering Failure Analysis 16 (2009) 1711–1719: Elsevier Ltd.
5. Muhammet Cerit "Numerical simulation of dynamic side impact test for an aluminium alloy wheel" Scientific Research and Essays (SRE) Volume 5, ISSN 1992-2248 (Sept. 2010), Page No. 2694–2701.
6. B Raghupathi et al. "Design and analysis of car wheel rim using fem technique" International Journal of Computer Science information and Engg Technologies (IJCSIET) Vol. 3, Series 4, Issue. 4, Dec. 2014.
7. Indian Standard for Automotive Vehicles Rims-General requirements, IS10694(1): 1993.
8. T. SivaPrasad et al. "A Review on Modeling and Analysis of Car Wheel Rim using CATIA and ANSYS" International Journal of Innovative Science and Modern Engineering (IJISME) ISSN: 2319-6386, Volume-2, Issue-6, May 2014.
9. M.M. Topaç et al. "Fatigue life prediction of a heavy vehicle steel wheel under radial loads by using finite element analysis" Engineering Failure Analysis 20 (2012) 67–79: Elsevier Ltd.
10. J. Stearns et al. "Understanding the Influence of Pressure and Radial Loads on Stress and Displacement Response of a Rotating Body: The Automobile Wheel" International Journal of Rotating Machinery Volume 2006, Article ID 60193, Pages 1–8 https://doi.org/10.1155/ijrm/2006/60193.
11. Jaspreet Singh et al. "Static analysis of alloy wheel using ANSYS15.0" International Journal of Research in Engineering and Technology (IJRET). ISSN No. 2319-1163, Volume 4, Issue 7 (July 2015).
12. Liangmo Wang et al. "Fatigue Life Analysis of Aluminum Wheels by Simulation of Rotary Fatigue Test" Journal of Mechanical Engineering Volume 1 Pages 31–39 (2011).
13. AIS—073 (Part 2) Automotive Vehicles—Wheel Rims for Two and Three Wheeled Vehicles—Sheet Metal Wheel Rims—Method of Test and Requirements.
14. Sunil N. Yadav et al. "Analyze the Effect of Camber Angle on Fatigue Life of Wheel Rim of Passenger Car by Using Radial Fatigue Testing' International Journal of Engineering Science and Innovative Technology (IJESIT) Volume 2, Issue 5, September 2013.

Comparative Thermal Analysis of Fins

H. A. Patel, V. S. Kale, S. U. Joshi, S. D. Jadhav and S. N. Teli

Abstract In several engineering applications, heat dissipation is an important factor which if not taken care of might result in high-thermal stresses and mechanical failures. The amount of heat dissipated depends on the heat transfer coefficient and surface area which can be increased by the use of extended surfaces, i.e., fins. Thermal analysis of three fins, namely rectangular, inclined non-uniform perforated, twin extension, is performed. The models were designed in Creo 4.0 and the analysis was carried out using ANSYS 15.0. The fins were analyzed for forced convection. The fins were compared on the basis of non-dimensional Nusselt number (Nu) and Reynolds number (Re), which proved that twin extension fin was the most effective among all the three. It was followed by inclined non-uniform perforated fin.

Keywords Twin extension fin · Rectangular fin
Inclined non-uniform perforated fin · Heat transfer coefficient · Nusselt number
Reynolds number

1   Introduction

The increase of heat transfer is a subject of concern in thermal engineering as the removal of excessive heat from system is necessary to avoid the problem of over-heating. The heat transfer from the surface could also be increased by increasing the heat transfer surface or by increasing the heat transfer coefficient between surface and surrounding or by both. Extended surfaces additionally referred as fins are commonly used for increasing the area exposed to surroundings and enhancing heat transfer coefficient in several industries [1]. The heat generated or conducted through

H. A. Patel · V. S. Kale · S. U. Joshi · S. D. Jadhav · S. N. Teli (✉)
Department of Mechanical Engineering, Bharati Vidyapeeth College of Engineering,
Navi Mumbai, India
e-mail: shivanandteli@yahoo.com

H. A. Patel
e-mail: hhiren1997@gmail.com

solids, walls, or boundaries ought to be unendingly dissipated to the surrounding to maintain steady condition of the system. In several engineering applications, the areas for dissipation of large quantities heat are very small. Heat dissipation by convection between a surface and fluid surrounding it can be enhanced by attaching to the surface thin melts strips called "Fins" [2].

A fin is a solid within which one directional heat transfer is assumed to be done by conduction along its length while heat is also transferred from the surface in a direction perpendicular to that of conduction by means of convection. The temperature difference diminishes as one moves out along the fin which is sticking out from the primary heat transfer surface. Fins are classified according to the following criteria: geometrical design, arrangement, and number of fluid reservoirs in contact, location, and composition. The fins are often found in industry, particularly in heat exchanger industries as in finned tubes of double pipe shell and tube and compact heat exchangers. Moreover, the fins are also used in cooling of gas turbine blades as well as in cooling of large heat flux electronic devices.

The geometry and cross-sectional area play a significant role in determining the effectiveness and efficiency of fin [3]. The heat transfer coefficient increases with increase in turbulence effect which may be increased by notching the surface of fin [4]. Creation of holes, i.e., perforation additionally increases turbulence effect, thus increasing heat transfer coefficient [5]. Making grooves also increase the turbulence effect which in turn increases the heat transfer coefficient [6].

Changing materials also may increase or decrease heat transfer. Alloy steel gives more heat dissipation than aluminum and steel [7]. The heat transfer can also be increased by the use of composite materials. More heat transfer can be achieved in non-metallic radial fins than metallic fin. Non-metallic fins are also easy to manufacture [8]. Thermal flux for Beryllium material was more than other materials like aluminum alloy and magnesium alloy and also thickness plays an important role in heat dissipation [9].

Nusselt number (Nu) is the ratio of heat flow by convection under a unit temperature difference to the heat flow by conduction under a unit temperature difference and a stationary thickness.

$$Nu = \frac{\text{Convective Heat Transfer}}{\text{Conductive Heat Transfer}} = \frac{hD}{k} \tag{1}$$

h Heat transfer coefficient (W/m^2 k);
D Hydraulic diameter (m);
k Thermal conductivity (W/m k).

The Reynolds number signifies the relative predominance of inertia to the viscous force. It is a convenient parameter for predicting if a flow is laminar or turbulent.

$$Re = \frac{\text{Inertia Forces}}{\text{Viscous Forces}} = \frac{\rho \cdot V \cdot D}{\mu} \tag{2}$$

ρ Density (kg/m^3);

V   Velocity of air (m/s);
D   Hydraulic diameter (m);
μ Absolute viscosity (Pa s).

The most important parameter affecting the heat transfer was Reynolds number and secondly the perforation geometry. Utilization of perforated fins increases the heat dissipation rate, simultaneously reducing the fin's weight, thus saving the material [1]. As the size of the perforation increase, the area for convection increases which eventually leads to an increase in heat transfer [10]. Increasing the size of perforation increases the heat transfer up to a certain limit and then decreases [3]. Increasing the eccentricity of perforation decreases the value of heat transfer coefficient thus the eccentricity of perforation should be as low as possible. At higher values of the Reynolds number, heat transfer coefficient becomes almost constant for all the shapes of perforation [11]. The heat transfer rate is more in fins with two perforations in both natural and in forced convection compared to solid fins and fins with one perforation. Staggered perforations showed more heat transfer than inline perforation [12].

Fin with extensions provided near about 5–13% more enhancement of heat transfer as compared to fin without extensions. Heat transfer through fin with rectangular extension was higher than that of fin with other types of extensions. It was found that heat transfer rate was higher for the copper trapezoidal rod than that of circular copper rod and rectangular copper rod [13]. The efficiency of fin varied to change in shape even if the fins had same surface area. Parabolic fin was found to be more effective over conical and cylindrical fins [2]. The wavy surface increases the length of air flow and also mixes the air flow, which leads to increase in heat transfer.

2   Modeling of Fins

The 3-D modeling of rectangular, inclined non-uniform perforated, and twin extension fins were done using Creo 4.0 as shown in Fig. 1. The dimensions of base plate are 200 m × 55 mm × 3 mm. The size of fin was 25.4 mm × 200 mm × 3 mm, and the fin spacing was 5 mm. The size of perforation was 8 mm in diameter and the length of extension was 2 and 1 mm at a length of 20 and 16 mm from the tip of fin, respectively. The thickness of extensions is 3 mm.

3   Thermal Analysis of Fins

ANSYS 15.0 was selected as the software for analysis. Fluid flow (Fluent) was selected as the analysis consisted of a solid surface surrounded by a fluid medium. The thermal analysis of fin has done in three steps:

Step 1: Design of duct
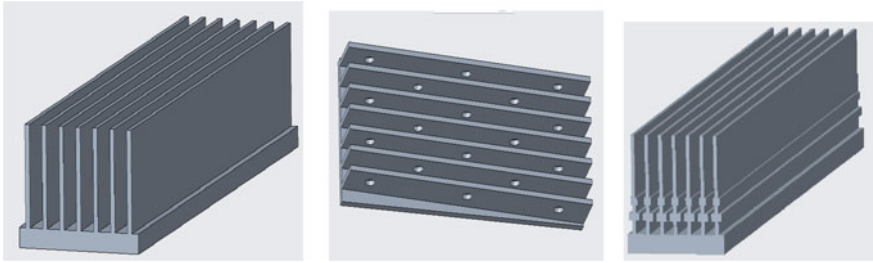
Fig. 1 Rectangular, inclined non-uniform perforated and twin extension fins
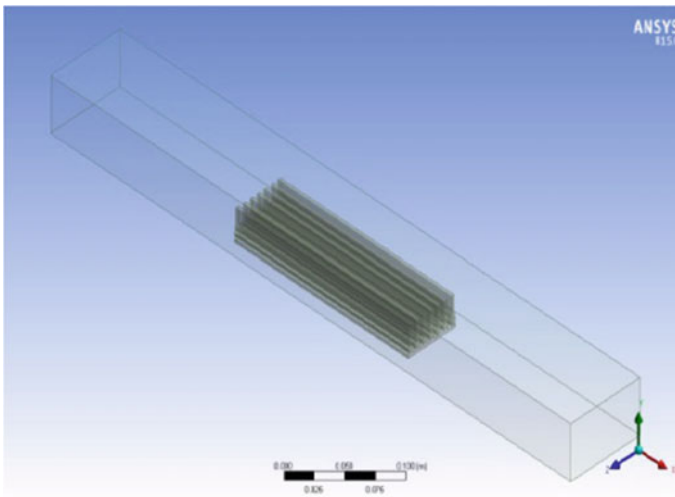
Fig. 2 Enclosure

An enclosure was created around the fin of dimension 600 mm × 80 mm × 50 mm as shown in Fig. 2. This enclosure will act as a duct. The fin model will be placed in the enclosure and air will be flown over it. The hydraulic diameter of the enclosure was 62.53 mm. The enclosure created of same dimension for all three fins.

Step 2: Mesh generation

The fine meshing was done to get accurate and precise results. The mesh element was tetrahedral because it covers the entire volume of specimen and leaves behind minimal voids as shown in Fig. 3. The mesh is generated and the number of nodes and elements for all fins are mentioned in Table 1. The specific sections required for boundary conditions such as inlet, outlet, fin surface, and heat flux are defined.

Step 3: Applying input parameters

The input parameters for analysis of all the three types of fins are Inlet air velocity, temperature of base plate, temperature of inlet air, and heat flux. The analysis was
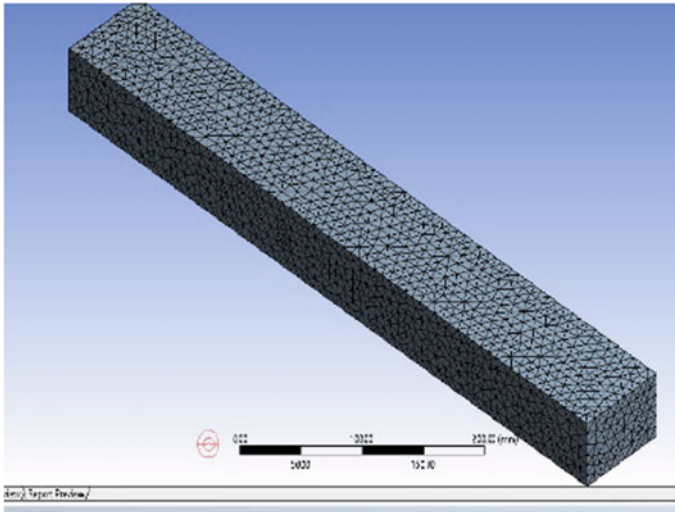
Fig. 3 Mesh generation

Table 1 Number of nodes and elements

Type of fin	Number of nodes	Number of elements
Rectangular	8048	27,299
Inclined non-uniform perforated	53,348	236,255
Twin extension	14,066	38,744

Table 2 Boundary conditions

Inlet air velocity (m/s)	Temperature of inlet air (K)	Base plate temperature (K)	Heat flux (W/m^2)
1, 3, 5, 7,8	300	450	5000

Table 3 Properties of aluminum and air

Property →	Density (kg/m^3)	Specific heat (J/kg K)	Thermal conductivity (W/mk)	Viscosity (Pa s)
Aluminum	2719	871	202.4	–
Air	1.225	1006.4	0.0242	1.7849×10^{-5}

carried out selecting energy model and K-epsilon model into take into consideration the turbulence effect. Table 2 shows the input parameters (boundary conditions).

The material of fin was chosen to be aluminum and the fluid flowing through the duct is air. The properties of aluminum and air are given in Table 3.

The solution was using hybrid initialization as there was no phase change taking place in air from inlet to outlet of the duct.

4   Results and Discussion

After carrying out thermal analysis of the three types (rectangular, inclined non-uniform perforated, and twin extension fins) using ANSYS 15.0, the results areas follows.

Case 1: Rectangular fin

The results (h, Nu, and Re) are obtained from ANSYS 15.0 as shown in Table 4. Figures 4 and 5 are illustrated, heat transfer coefficient (h), and Nu versus Re.

Case 2: Inclined non-uniform perforated fin

The results (h, Nu, and Re) are obtained from ANSYS 15.0 as shown in Table 5. Figures 6 and 7 are illustrated, heat transfer coefficient (h), and Nu versus Re.

Case 3: Twin extension fin

Table 4 Rectangular fin

Velocity (V)	Heat transfer coefficient (h)	Nusselt number (Nu)	Reynolds number (Re)
1	18	46.728	5681.7
3	40	103.84	17045.1
5	59	153.164	28408.5
7	76	197.296	39771.9
8	81	210.276	45453.6
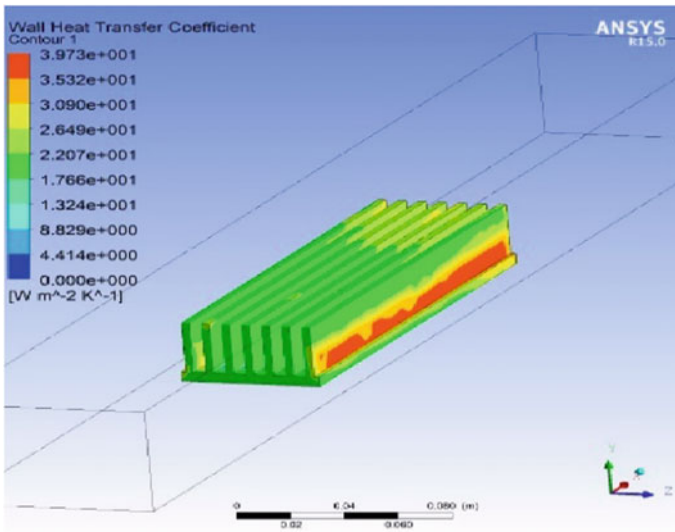
Fig. 4   Heat transfer coefficient (h) rectangular fin

Fig. 5 *Nu* versus
Re (Rectangular fin)
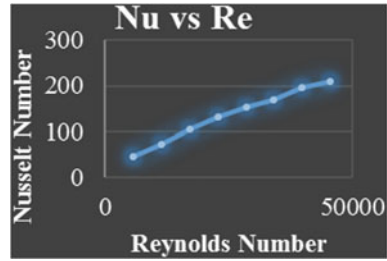
Table 5 Inclined non-uniform perforated fin

Velocity (*V*)	Heat transfer coefficient (*h*)	Nusselt number (*Nu*)	Reynolds number (*Re*)
1	41	106.436	5681.7
3	50	129.800	17045.1
5	64	166.144	28408.5
7	80	207.68	39771.9
8	91	236.36	45453.6
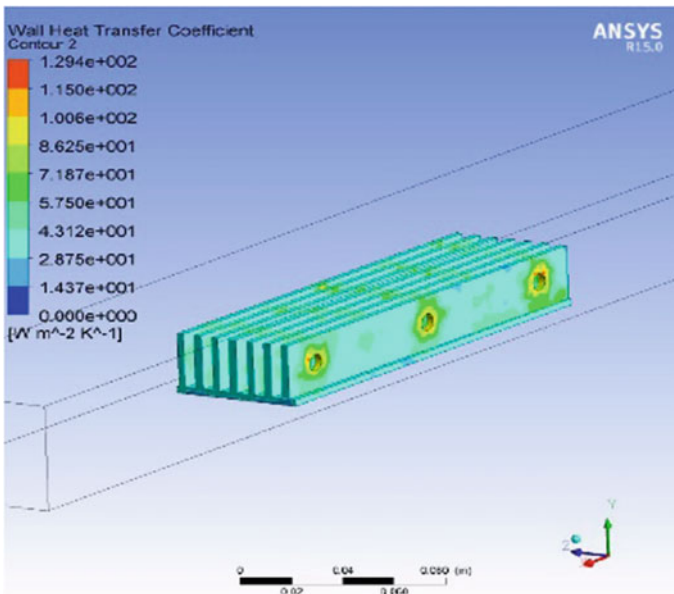
Fig. 6 Heat transfer coefficient (*h*) of inclined non-uniform perforated fin

The results (*h*, *Nu*, and *Re*) are obtained from ANSYS 15.0 of as shown in Table 6. Figures 8 and 9 are illustrated, heat transfer coefficient (*h*), and *Nu* versus *Re*.

After studying heat transfer coefficient plots, the graph of *Nu* versus *Re* depicting the combination of all the three Fins was made as shown in Fig. 10.

Fig. 7 *Nu* versus
*Re (Inclined
non-uniform perforated fin)*
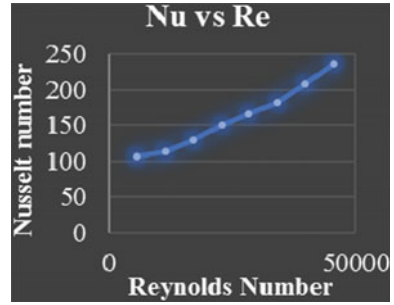
Table 6 Twin extension fin

Velocity (*V*)	Heat transfer coefficient (*h*)	Nusselt number (*Nu*)	Reynolds number (*Re*)
1	37	96.052	5681.7
3	52	134.992	17,045.1
5	75	194.700	28,408.5
7	100	259.600	39,771.9
8	37	96.052	45,453.6
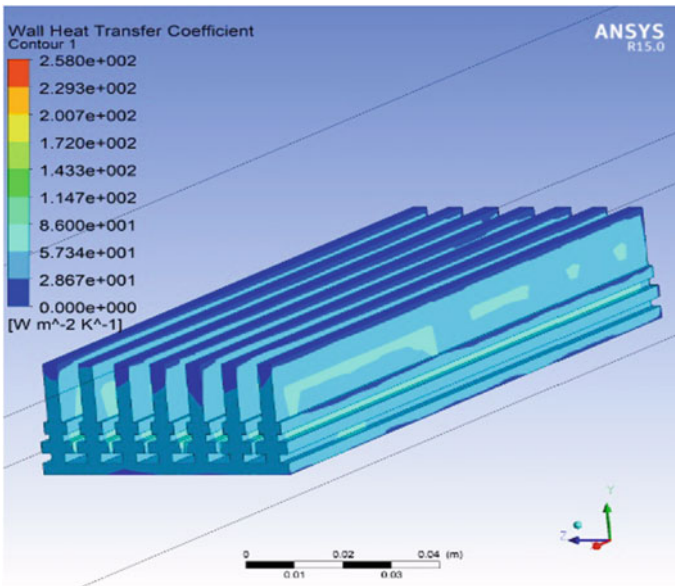
Fig. 8 Heat transfer coefficient (*h*) of twin extension fin

Fig. 9 *Nu* versus *Re (Twin extension fin)*
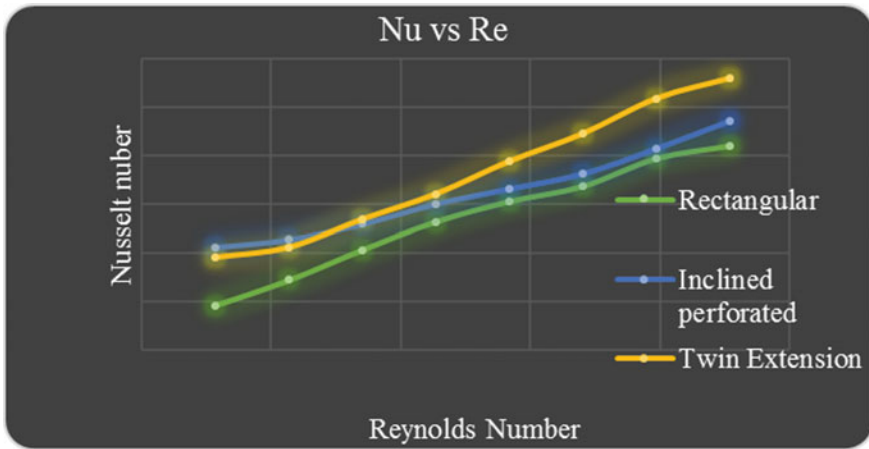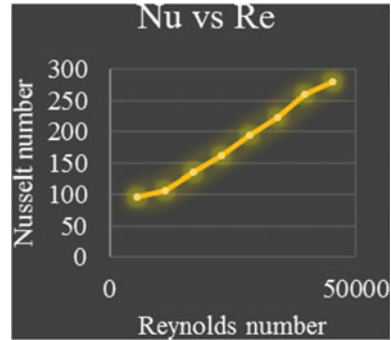
Fig. 10 *Nu* versus *Re* for all three types Fins

5   Conclusion

From Fig. 10 (*Nu* vs. *Re*) for all the three types of Fins, it is evident that:

- Both the inclined non-uniform perforated fins and twin extension fins are more effective than normal rectangular fins.
- For lower velocities, i.e., up to 2 m/s, inclined non-uniform perforated fins are superior to twin extension fins.
- For higher velocities, twin extension fins are preferable.

References

1. Dhanawade, K.H., Sunnapwar, V.K., Dhanawade, H.S.: Thermal Analysis of Square and Circular Perforated Fin Arrays by Forced Convection. International Journal of Current Engineering and Technology, Special Issue-2, pp. 110–113 (2014)
2. K, Prasad Raju., Sk.R. S. Mahaboob Ali, Sk. M.Z.M.Saqheeb Ali, k, Sunil Kumar: Thermal Analysis of Fins with Different Geometries. SSRG International Journal of Mechanical Engineering, Vol. 4(6), pp. 6–9 (2017)
3. Tekhre, D., Saini, J.: Design Modification and Thermal Analysis of IC Engine Fin – A Review. IJIRST –International Journal for Innovative Research in Science & Technology, Vol. 4 (1), pp. 57–59, (2017)
4. Singh, B., Singh, S.: A Research Paper on Heat Transfer in Notch Fin and UN Notch Fin. International Journal for Research in Applied Science & Engineering Technology, Vol. 4(9), pp. 12–18, (2016)
5. Sajesh, K.M., Soni, N., Kosti, S.: Design Modification and Heat Transfer Analysis of Air Cooled Rectangular Fin Engine. International Journal of Recent Scientific Research Vol. 7, Issue 3, pp. 9653–9656, (2016)
6. Dixit, A.: Review on Heat Transfer Enhancement Through Fins Using Surface Modifications. International Journal for Research in Applied Science & Engineering Technology, Vol. 3 (3), pp. 344–349, (2015)
7. Pathak, S., Parkash, O., Ravikant.: Thermal Analysis of Fins with varying Geometry of Different Materials. International Journal for Scientific Research & Development Vol. 4 (3), pp. 1763–1765, (2016)
8. Kanthimathi, T., Naga, S.R.G.: Heat Transfer Through Annular Composite Fins. Journal of Mechanical Engineering and Technology Vol. 4 (1) 1, pp. 1–10, (2016)
9. Thammala, P., P.Sampath, R.: Analyze The Thermal Properties By varying Geometry, Material and Thickness of Cylinder Fins, Vol. 6 (6), pp. 95–118, (2015)
10. Dhanawade, H., K.N. Vijaykumar., Dhanawade, K.: Natural Convection Heat Transfer Flow Visualiation of Perforated Fin Arrays by CFD Stimulation. International Journal of Research in Engineering and Technology, Vol. 2 (12), pp. 483–490, (2013)
11. Vyas, A., Gupta, S., Gupta, S.: Determining relation among Shape of Perforation and Convective Heat transfer from the Lateral Fin arrangement using Simulation by Computational Fluid Dynamics. International Referred Journal of Engineering and Science, Vol. 5(4), pp. 24–31, (2016)
12. Prakash, S., Chethan, D.: Experimental Investigation of the Heat Transfer Rate in Perforated Fins. International Journal of Mechanical and Industrial Technology, Vol. 3(2), pp. 68–72, (2016)
13. Khalasi, Bharathbhai, K.: Experimental Study of Extended Surfaces (Fins) with Forced Convection. International Journal of Engineering Research & Technology, Vol. 3(5), pp. 2386–2390, (2014)

Design and Development of Small-Capacity Mango Process Plant

Nandu Durge, Shankar Mantha and Vikas Phalle

Abstract Mango is one of the most important tropical and subtropical fruits of the world and is popular both in fresh and the processed forms. It is called as king of fruits on account of its nutritive value, taste, and attractive fragrance. India is the largest producer of mangoes. 'Alphonso' is one of the best-rated mangoes in the world, which is cultivated in Konkan region of Maharashtra. Mango being a highly perishable fruit, it is necessary to perform various post-harvest processes like de-sapping, cleaning, washing, hot water treatment, hydro-cooling, sorting/grading, and packing to improve its shelf life and as well as quality. But it becomes difficult for farmers to carry out various post-harvest processes in farm due to limited quantity of mangoes and have to depend on other agencies like middleman/intermediaries to carry out these processes. In this paper, an attempt is made to design a small-capacity mango process plant which is cost-effective and affordable for small farmer.

Keywords Small-capacity process plant · Post-harvest process · Alphonso

1 Introduction

India is the largest producer of mangoes accounting for 42% of the total world's production [1]. The quality of the mangoes cultivated in India is good especially of the Alphonso which are produced in the Konkan region of Maharashtra; it has good nutritive value, taste, and attractive fragrance [2]. The mangoes produced in India have large demand in Global market so it is necessary to increase its shelf life and quality to attract global customer/market. But the major problem is that

N. Durge · S. Mantha (✉) · V. Phalle
Department of Mechanical Engineering, VJTI, Matunga, Mumbai 400019, India
e-mail: ssmantha@me.vjti.ac.in

N. Durge
e-mail: nandu_durge2007@yahoo.co.in

V. Phalle
e-mail: vmphalle@me.vjti.ac.in

most of the mango producers are the small and marginal land-holding capacity. As per agriculture census carried out by Government of India, the small and marginal holdings taken together constituted 92% of total number of land holding and it covers the approximately 50% of total operated area [3]. As the farmers have small land holdings, their product is less and they have to depend on processing units like packing house which are located far away from their farms and it becomes uneconomical for them to send mangoes to this unit by themselves [4]. The major intention of post-harvest treatments and management in the supply chain is to create suitable conditions or environments to extend the storage life and retain the quality attributes, nutritional and functional compositions. The general post-harvesting treatments for mangoes are de-sapping, cleaning, washing, hot water treatment, cold water treatment (hydro-cooling), sorting/grading, and packing etc.

2   Marketing of Mangoes

Marketing system helps the producer in final disposal of his produce to customer for returns of his hard work. An efficient marketing system is very important which ensuring competitive price to the producer [5]. For achieving this, it is necessary to get information about various markets, technology, and marketing linkages. Most of the producers are using traditional marketing chain because they do not want to take any risk of price and income variation due to perishability, qualities, and seasonality.

Generally, mangoes are sold through different marketing channels, and a number of intermediators are involved in it. Efficient marketing system is one which ensures higher producer's share in terms of consumer rupees. For this, reducing the number of middlemen is the only option which can be achieved if all the post-harvesting processes are carried out in the farm and direct marketing is carried out by farmer itself.

3   Post-harvesting Management

Post-harvest management means the handling of an agricultural product after harvest to increase storage life, freshness, and an attractive appearance, in order to deliver a quality product to the market.

Nearly, 20–25% of fruits are wasted due to faulty post-harvest practices during harvesting, packaging, storage, grading, etc. [6]. This wastage can be reduced to some extent by implementing latest post-harvesting technology.

Post-harvest management consists of collection of mangoes, curing in orchard, and transfer to packing house. In packing house, various processes are performed like de-sapping and washing, fungicide treatment (hot water treatment), hydro-cooling, drying, sorting and grading, packaging, low-temperature storage, and marketing [7].

Fig. 1 Mango post-harvest
process flowchart

```
┌─────────────────────────┐
│   Harvesting of Mango   │
└─────────────────────────┘
            │
            ▼
┌─────────────────────────┐
│   Transfer to Packing   │
└─────────────────────────┘
            │
            ▼
┌─────────────────────────┐
│   De-sapping & washing  │
└─────────────────────────┘
            │
            ▼
┌─────────────────────────┐
│   Hot water treatment   │
└─────────────────────────┘
            │
            ▼
┌─────────────────────────┐
│      Hydro-cooling      │
└─────────────────────────┘
            │
            ▼
┌─────────────────────────┐
│         Drying          │
└─────────────────────────┘
            │
            ▼
┌─────────────────────────┐
│    Sorting & Grading    │
└─────────────────────────┘
            │
            ▼
┌─────────────────────────┐
│  Packaging & Marketing  │
└─────────────────────────┘
```
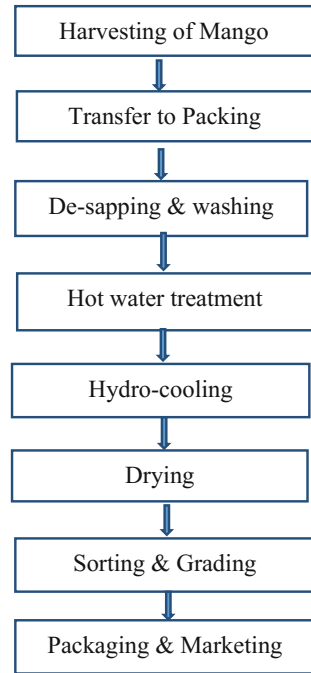
De-sapping is the process of removing latex after cutting mango stem from the shoulder of mango, and then, it is immediately washed in spray of chlorinated water to remove dust, dirt, and residue of pesticide.

Hot water treatment is carried out for removing fungus and bacterial infections like insects and fruit fly by dipping mangoes in hot water maintained at 50 °C for 15 min.

Cold water treatment is used to remove heat from the mangoes and bring it to room temperature by dipping it into normal cold water maintained at 18 °C for 15 min.

After completing all above steps, drying is carried out to remove moisture and water particles present on mango surface, and after sorting and grading, mangoes are packed in packing boxes (Fig. 1).

4   Small-Capacity Mango Post-harvesting Process Plant

In small-size plant, a batch of 1000 mangoes can be processed in one-hour cycle time. The plant is automated with one mechanical processor on a shaft. It includes a vertical shaft with screw-type helical conveyor. Microcontroller is used for controlling various processes automatically, and also various types of sensors like temperature sensor, weight sensor, and control valve are used for controlling the process. This small-capacity process plant is modeled by using SolidWorks software. The model
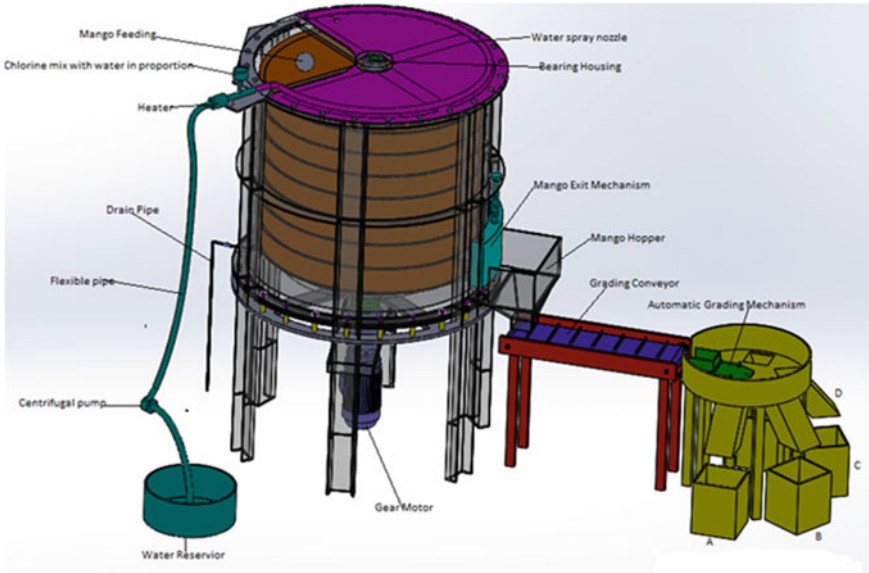
Fig. 2 Model of mango process plant using SolidWorks software

is further refined using motion simulation capabilities of the SolidWorks software (Fig. 2).

Nomenclature	Description
di	Internal diameter of process tank in mm
do	Outer diameter of tank in mm
t	Thickness of process tank in mm
ds	Diameter of conveyor shaft in mm
t_1	Thickness of conveyor plate in mm
d_1	Diameter of screw conveyor in mm
p	Pitch of screw conveyor in mm
L	Height of tank in mm
α	Helix angle of screw conveyor in degrees
P	Total power requirement in KW
P_H	Power necessary for the progress of the fruit in KW
P_N	Drive power of the screw conveyor at no load in KW
Pst	Power factor for vertical conveyor in KW
n	Number of screws (spiral) on screw conveyor
N	RPM of screw conveyor shaft
V	Volume of tank

5 Design Procedure of Plant

The complete design procedure of small-capacity plant is given below. It includes design of helical screw conveyor, selection of material, selection of different parts like gear motor, coupling, bearing, and lastly assembly of these components.

Take approximate weight of a batch of 1000 mangoes as 200 kg (Fig. 3).

Approximate Size of one mango,

$$W_{mid} = 75\% \text{ of } l_{max} \text{ and Width of mango}(W_{mid} = 90 \text{ mm})$$
$$\text{Where, } l_{max} = 120 \text{ mm}$$

5.1 Number of Mangoes Per Pitch or Screw

Internal diameter of process tank, di $= 1300$ mm

Thickness of process tank, $t = 4$ mm

Outer Diameter of tank, do $= 1308$ mm

Diameter of conveyor shaft, ds $= 70$ mm (Fig. 4)

Approximate area of one mango $120 \times 90 = 10,800$ mm^2

Shape of mango is not exactly rectangular but somewhat oval in shape

So approximate area covered by one mango is 10% less than calculated area
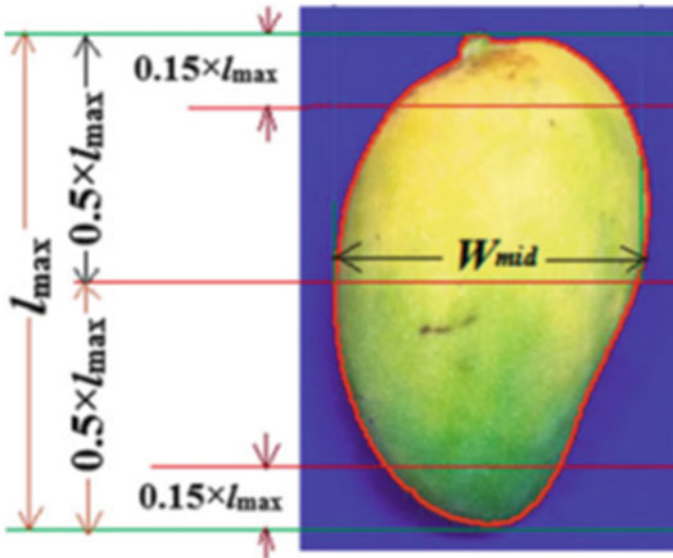
Fig. 3 Approximate dimension of Alphonso mango

$$\text{Approximate area} = 0.90 \times 10,800 = 9720 \text{ mm}^2$$

$$\text{Approximate Area of one lap of spiral} = \frac{\pi}{4} \times \left(\text{di}^2 - \text{ds}^2\right)$$
$$= \frac{\pi}{4} \times \left(1300^2 - 70^2\right)$$
$$= 1323474.445 \text{ mm}^2$$

$$\text{Number of mangoes on one lap} = \frac{1323474.445}{9720}$$
$$= 136 \text{ mangoes}$$

As there are eight screws or spirals on conveyor,

$$\text{Total capacity} = 8 \times 136 = 1088 \text{ mangoes}$$
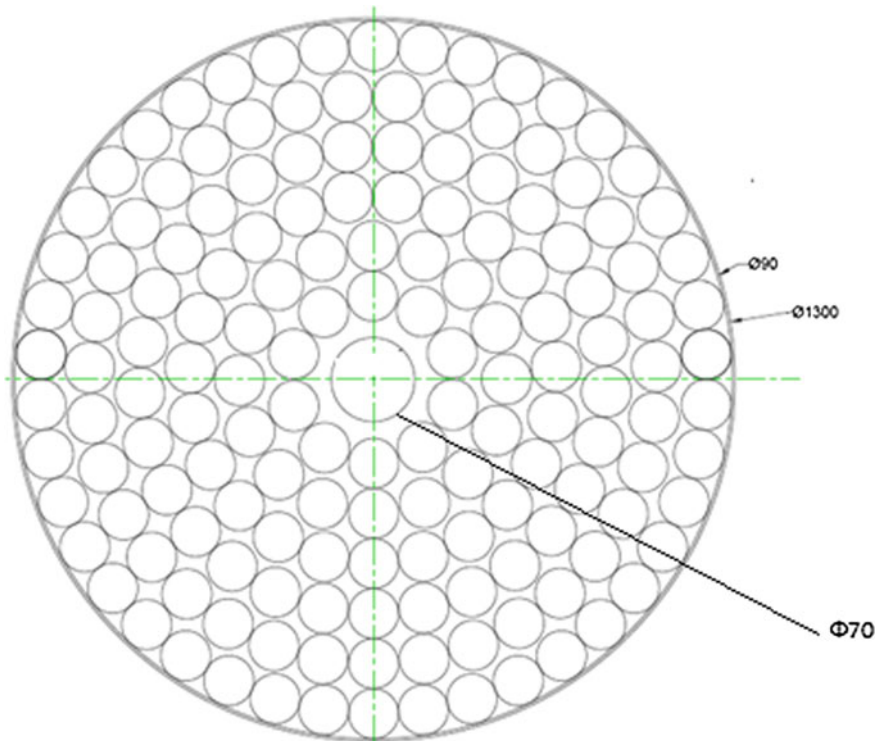
Fig. 4 AutoCAD drawing shows number of mangoes in one lap of screw conveyor

Take 5 mm clearance between tank and screw conveyor.
So diameter of screw conveyor, $d_1 = 1290$ mm.
Thickness of conveyor plate, $t_1 = 2$ mm.

5.2 Size of Screw Conveyor

The size of a screw conveyor depends on the screw diameter, screw pitch, speed of the screw, and the load on the cross-sectional area of the screw (Fig. 5).

The pitch of screw conveyor $= 120$ mm(Mango Height)

$+ 8$ mm (Gap between mango and conveyor plate)

$+ 2$ mm(Conveyor plate thickness)

Pitch, $p = 130$ mm

As there are eight screws (spirals), i.e., $(n = 8)$,
Height of screw conveyor or flight length of screw $= 130 \times 8 = 1040$ mm.
Assume 100 mm clearance on both sides of tank in screw conveyor (Fig. 6).
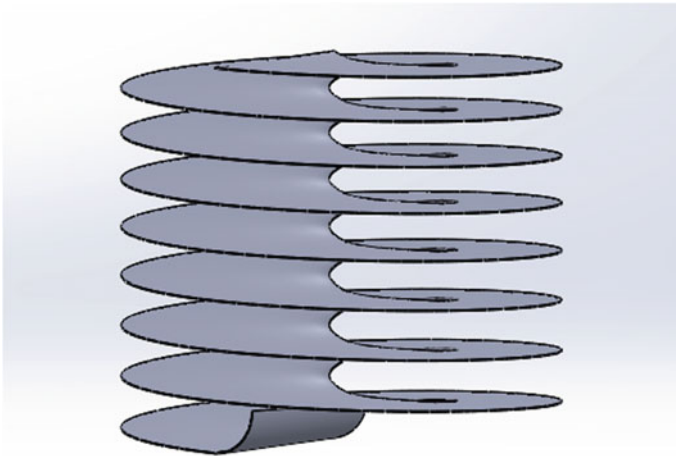
Fig. 5 Diagram of screw conveyor used in process plant
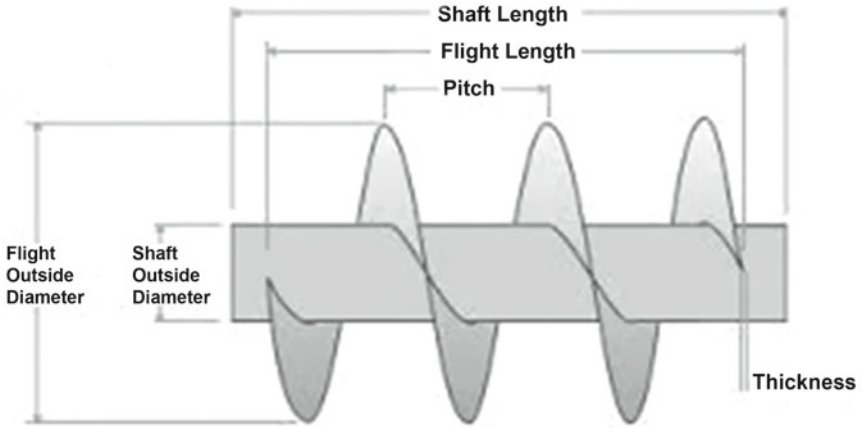
Fig. 6 General nomenclature of screw conveyor [8]

$$\text{Height of tank, } L = \text{Height of screw conveyor or flight length}$$
$$+ \text{ Clearance on both side}$$
$$= 1040 + 200 \text{ mm}$$
$$= 1240 \text{ mm}$$
$$\text{Conveyor shaft length} = \text{Height of tank} = 1240 \text{ mm}$$

By calculation, helix angle of screw, $\alpha = \tan^{-1}\left(\frac{P}{\pi D}\right)$

$$\alpha = \tan^{-1}\left(\frac{130}{\pi \times 1290}\right) = 1.84°$$

But from layout drawing, helix angle of screw $= 3°$ (approximately).

5.3 Motor Selection

Power requirement of Screw Conveyor [9]

$$P = P_{\text{H}} + P_{\text{N}} + P_{\text{st}}$$

Power necessary for the progress of the material (P_{H})

$$P_{\text{H}} = \frac{Im \times L1 \times \lambda \times g}{3600} \text{ KW}$$
$$P_{\text{H}} = \frac{200 \times 1.03 \times 1 \times 9.81}{3600} \text{ KW}$$

$$=0.56135 \text{ KW}$$

Drive power of the screw conveyor at no load, P_N.

This power requirement is very low and is proportional to the nominal diameter and length of the screw.

$$P_N = \frac{d1 \times L1}{20} \text{ KW}$$
$$= \frac{1.29 \times 1.03}{20} \text{ KW}$$
$$= 0.066435 \text{ KW}$$

Power factor for vertical conveyor: P_{st}.

This power requirement will be the product of the mass flow rate by the height H and the acceleration due to gravity g.

$$P_{st} = \frac{Im \times H \times g}{3600} \text{ KW}$$
$$= \frac{200 \times 1.03 \times 9.81}{3600} \text{ KW}$$
$$= 0.56135 \text{ KW}$$

Total power requirement.

The driving power of the loaded screw conveyor is given by:

$$P = P_H + P_N + P_{st}$$
$$= 0.56135 + 0.066435 + 0.56135$$
$$P = 1.189135 \text{ KW}/1.59 \text{ HP}$$

Select available motor of 3 HP from user manual [8].

5.4 Design of Shaft

Power required for conveyor $P = 3 \text{ HP} = 3 \times 746 = 3730 \text{ W} = 2.238 \text{ KW}$

RPM of screw conveyor shaft, $N = 20 \text{ RPM}$

$$P = \frac{2\pi NT}{60 \times 1000} \text{ KW}$$
$$2.238 = \frac{2\pi \times 20 \times T}{60 \times 1000} \text{ KW}$$
$$T = 1068.56 \text{ N-m}$$

Checking shear failure of shaft
Material of shaft as MS with zinc coating to avoid corrosion
Yield strength of material $= 250$ N/mm^2 [PSG]
Select FOS $= 3$
Torsional shear strength, $\tau = \frac{0.5 \times 250}{3} = 41.67$ N/mm^2
From Torsion Formula,
Torque, $T = \frac{\pi}{16} \tau \times ds^3$

$$1068.56 \times 10^3 = \frac{\pi}{16} \times \tau \times 70^3$$

$$\tau = 15.86 \text{ N/mm}^2 \leq \text{permissible shear stress}$$

5.5   Volume of Water Required for Filling Process Tank

Total volume of tank:

$$V = \frac{\pi}{4} \times \text{di}^2 \times L$$

$$V = \frac{\pi}{4} \times 1300^2 \times 1240$$

$$V = 1.65 \times 10^9 \text{ mm}^3$$

Volume of Shaft:

$$V_{\text{sh}} = \frac{\pi}{4} \times \text{ds}^2 \times L$$

$$= \frac{\pi}{4} \times 70^2 \times 1240$$

$$= 4.77 \times 10^6 \text{ mm}^3$$

Exact volume of the tank neglecting volume of spiral or screw conveyor,

$$V_{\text{exact}} = V_{\text{tank}} - V_{\text{shaft}}$$

$$= 1.65 \times 10^9 - 4.77 \times 10^6$$

$$= 1.64 \times 10^9 \text{ mm}^3$$

Approximate volume of mango, assume it is cylindrical.
Volume of one mango,

$$V_{\text{mango}} = \frac{\pi}{4} \times 90^2 \times 120$$

$$V_{\text{mango}} = 763.41 \times 10^3 \text{ mm}^3$$

Volume of 1088 mangoes,

$$V_{\text{mangoes}} = 763.41 \times 10^3 \times 1088 \text{ mm}^3$$
$$V_{\text{mangoes}} = 830.58 \times 10^6 \text{ mm}^3$$

Size of mango is not exactly cylindrical but somewhat oval in shape,
Actual volume of mangoes is 20% less than the volume of mango,

$$\text{Volume of mango} = 0.8 \times 830.58 \times 10^6 \text{ mm}^3$$
$$= 664.47 \times 10^6 \text{ mm}^3$$

Volume of water required for filling the tank,

$$V_{\text{water}} = 1.65 \times 10^9 \text{ mm}^3 - 664.47 \times 10^6 \text{mm}^3$$
$$= 985.53 \times 10^6 \text{ mm}^3$$

Volume of water required for filling the tank $= 985.53$ l

5.6 Selection of Gear Motor [10]

Geared motor is of make Laxmi Hydraulics Pvt. Ltd. from company user manual.
The following specifications are used to supply power from gear motor to the conveyor.
Flange mounting shaft upward (V3), FL180-100P4.
Service factor $= 1$ for light shock load with operational hours 3–10 h/day (AGMA Class I).
Rating 3 HP.
Output speed (13.5–16.5) RPM.
Rated torque 1250 N-m.

5.7 Selection of Coupling [11]

Flexible coupling is used for transmitting moderate torque, tolerating small amount of angular and lateral misalignment in shaft, and transmitting power from gear motor shaft to processor shaft.

a. First criterion: Coupling selection is based on size of driving shaft and driven shaft.

   To determine tentative coupling size.
   Output or gear motor shaft diameter $= 55$ mm and

Processor shaft diameter $= 70$ mm

b. Second criterion: Coupling selection is based on effective KW/RPM or HP/RPM or torque to be transmitted. Accordingly, select service factor from the table.

From table, take service factor SF $= 1.5$

$$\frac{KW}{RPM(effective)} = \frac{KW\ Transmitted\ \times\ Service\ factor}{RPM}$$

$$\frac{KW}{RPM(effective)} = \frac{2.2 \times 1.5}{950} = 0.00347$$

Determine torque (Nm),

$$Torque(effective) = \frac{955 \times KW\ transmitted\ \times\ SF}{RPM}$$

$$Torque(effective) = \frac{955 \times 2.2 \times 1.5}{950} = 3.31\ Nm$$

From the above calculation and selection guide, select coupling EFC 05 [11].

5.8   Selection of Spherical Roller Bearing [12]

Life of bearing is 6000 h with a reliability of 90%.

$$n = 20\ RPM$$

We can select spherical roller bearing,

$$L_{10} = \frac{Lh10 \times 60 \times n}{10^6}$$

$$L_{10} = \frac{6000 \times 60 \times 20}{10^6}$$

$$L_{10} = 7.2\ millions\ of\ revolutions$$

Select the material for spiral as galvanized steel, Density $= 7800$ kg/m^3.
Total load on conveyor $=$ Mango weight $+$ Conveyor weight $+$ Shaft weight.

$$Wt.\ of\ conveyor = 8 \times \left[Area\ of\ spiral \times thickness\ of\ plate\right]$$
$$\times\ Density \times g$$
$$= 8 \times \frac{\pi}{4} \times \left(1290^2 - 70^2\right) \times 4 \times 7800 \times 10^{-9} \times 9.81$$
$$= 3189\ N$$
$$= 3.189\ KN$$

$$\text{Wt. of shaft} = \frac{\pi}{4} \times \left(70^2 - 50^2\right) \times 1240 \times 7800 \times 10^{-9} \times 9.81$$
$$= 178.85 \text{ N}$$
$$= 0.17885 \text{ KN}$$

Total axial load acting on bearing,

$$= 200 \times 9.81 \times 10^{-3} + 3.189 + 0.17885$$
$$= 5.15138 \text{ KN}$$

Angle of conveyor bled with horizontal $= 3°$
Axial component of load $(Fa) = 5.15138 \times \cos 3° = 5.14$ KN
Radial component of load $(Fr) = 5.15138 \times \sin 3° = 0.2696$ KN
Now find out equivalent dynamic load,

$$\frac{Fa}{vFr} = \frac{6.9}{1x0.36} \geq e$$

Equivalent dynamic load,

$$Pe = (0.67 \times v \times Fr + Y_2 \times Fa) \times Ka$$

Assuming light shock, take $Ka = 1.2$
From table $Y_2 = 4.6$

$$Pe = (0.67 \times 1 \times 0.2696 + 4.6 \times 5.15138) \times 1.2$$
$$= 28.65 \text{ KN}$$

Basic dynamic load capacity,

$$L_{10} = (C/Pe)^{10/3}$$
$$7.2 = (C/28.65)^{10/3}$$
$$C = 51.79 \text{ KN}$$

Let us select bearing number BS2-2214-2CS having basic load capacity 208 KN [12].

6   Conclusions

From literature survey, various reports, and interviews with mango producers, it is found that India is a leading mango producer in the world. But it is observed that lack of utilization of new techniques has effect on crop management techniques. In spite of these issues, another major problem is marketing of mango. In India, the marketing chain is too long and so many intermediaries are involved in it. So major part of profit goes to middleman, and farmers' share in consumer market is very low. These are the major fundamental problems faced by mango grower throughout the country. These all are negatively influencing the production of mango in the country and is not proving as much profitable as it might be. In order to overcome these problems and getting more profit, mango grower must use modern tools and technology in mango cultivating and marketing may prove a real breakthrough.

A small-capacity mango process plant helps to process the mango in farm itself and get exposure for selling the mango directly to end customer. The concept of farm to home will be implemented, and in this way, mango production is more resourceful and advantageous, more economical and profitable to the mango producers. In this plant, all the processes are automatic and require one-hour cycle time. The approximate cost of this plant is Rs. 70,000 to 80,000.

References

1. "Hand Book on Horticulture Statistics - 2014" Government of India, Ministry of Agriculture, Department of Agriculture and Cooperation, New Delhi (2015)
2. E. Ravendiran Collector Sindhudurg President, R.K.V.Y District Level Committee, Sindhudurg "Comprehensive District Agriculture Plan (C-DAP)" Department of Agriculture, Sindhudurg, Government of Maharashtra
3. Satyanjai Yadav, Assistant Agricultural Marketing Adviser under overall guidance of Shri Rakesh Saxena, Dy. Agricultural Marketing Adviser, D.M.I., B.H.O., Nagpur."Post-Harvest Profile of Mango" Government of India, Ministry of Agriculture, (Department of Agriculture & Cooperation) Directorate of Marketing & Inspection, Nagpur (2013)
4. Government of Maharashtra, Department of Agriculture World Bank assisted Maharashtra Agricultural Competitiveness Project (MACP) Marketing Strategy Supplement (MSS) District - Sindhudurg
5. Dr. G. D. Banerjee, "Economics of Mango Cultivation" Department of Economic Analysis and Research, National Bank for Agriculture and Rural Development – Mumbai (2011)
6. Dharini Sivakumar, Yuming Jiang, Elhadi M. Yahia, " Maintaining mango (*Mangifera indica* L.) fruit quality during the export chain", Food Research International 44 (2011) 1254–1263
7. Dr. Jeffrey K. Brecht, "Mango post-harvest best management practices manual", The National Mango Board (NMB), U.S. Department of Agriculture, University of Florida (2010)
8. Screw conveyor catalogue and engineering manual, Continental Conveyor and Machine Works Ltd. Canada Chandra Sekhar Nandi, Bipan Tudu, and Chiranjib Koley, "Computer Vision Based Mango FruitGrading System", International conference on Innovative Engineering Technologies (ICIET' 2014) Dec. 28–29, 2014 Bangkok (Thailand)
9. Piotr Kulinowski, Screw conveyors Department of Mining, Dressing and Transport Machines AGH
10. Laxmi Hydraulics Pvt. Ltd, helical gear motor selection guide/user manual

11. Elecon flexible coupling selection guide/user manual
12. SKF rolling bearing selection guide/user manual

Analysis of Curve Fitting for Case Studies: An Appropriate or Non-appropriate Method

Rajkumar P. Narkhede and Prabha Rastogi

Abstract The data analysis is key parameter in the process optimization. The large data are generated while processes are under consideration. The e-commerce, finance accounting, industrial process planning, industrial production planning, labor planning, inventory planning, etc., are the few names of the sectors and need large data handling for required and/or targeting the final endues and/or services. The different mathematical tools have been used such as AHP, MAHP, WPM, PROMETHEE, VIKOR, Games theory, and curve fitting. However, curve fitting has been used for many industrial applications for the processes planning, inventory planning, labor resources planning, etc. Depending on the data form and ability of researcher, the different curves or lines are used for formulation of the mathematical function. These functions could be straight-line function, second-order polynomial function, third-order polynomial functions, logarithmic, exponential function, etc. This paper discusses the curve fitting technique for the US oil export payday from 1991 to 2016 and declination angle evaluation for a year. The data obtained are fitted with the fourth-, fifth-, and sixth-order polynomial curve. It is observed that the R^2 for these curves is 0.97, 0.99, and 1, respectively. However, the predicated values of the parameters deviate significantly.

Keywords Curve fitting · Polynomail function · AHP · WPM · MAHP

1 Introduction

The industrial revolution has been continuously growing, and the quest for the new products is growing which must be economical, multi-featured, with ease of operation, durable, efficient, etc. This needs the simulations and new technology inter-

R. P. Narkhede (✉)
Konkan Gyanpeeth College of Engineering, Karjat Raigad, India
e-mail: rajkumar.p.narkhede@gmail.com

P. Rastogi
Department of Mathematics, J. J. T. University, Churu, Rajasthan, India

ventions to understand various features. The past data play the significant role in the forecasting. Different methods are used for the forecasting and process optimization. The graphical representation will be the best technique to visualize the trends of various parameters under study. The large data could be arranged in a systematic way and different tools used for curve fitting. Curve fitting with the input conditions of the information is utilized for examination and understanding of the surveyed quantities. It helps in judging the quality of the connection between the free (indicator) factors and the reliant (reaction) factors and empowers expectation of ward factors for new estimations of autonomous factors. In spite of the fact, curve fitting issues were first presented just about three centuries prior [1]. There is still no single technique that can be connected generally. This is because of the decent variety of the issue territories and especially because of the computational restrictions of the different methodologies that arrange with just subsets of this degree. Straight relapse, spline fitting, and autoregressive examination are all arrangement philosophies to recognizable proof and curve fitting problems.

Multi-Criteria Decision Making (MCDM) is an arrangement of techniques which manage the assessment of an arrangement of choices regarding various, regularly clashing, choice criteria [2, 3]. In this manner, given an arrangement of (choices) various choice criteria, the objective of MCDM is to give a decision, positioning, portrayal, grouping, arranging, and in a larger part of cases a request of options, from the most wanted to the slightest favored choice [4–6]. MCDM can think about subjective and quantitative criteria. While criteria in light of quantitative factors are master autonomous, subjective criteria (factors) are master subordinate and might be subjective, since various methodologies, for example, positioning, point, or different frameworks, can be utilized to change subjective variable into quantitative units good with MCDM system. Along these lines, in basic leadership, subjective factors (criteria) are changed into quantitative factors utilizing master-planned markers and units. The paper presents a variety of MCDM procedures, each with their own attributes, fluctuating levels of complexity and various extent of use [7–14]. There are distinctive orders of MCDM issues and strategies. MCDM issues are as often as possibly arranged by the idea of the choices—either discrete or continuous [3, 15–17]. A discrete issue can be depicted as a multi-quality discrete choice, which regularly comprises of an unobtrusive accumulation of options (Multi-Attribute Decision Making (MADM)), while a constant issue as a rule comprises of a tremendous or unending measure of choice choices (Multi-Objective Decision Making (MODM)) [3, 15]. MCDM strategies may likewise be ordered relying upon their compensatory or non-compensatory nature. Compensatory techniques permit unequivocal trade-offs among criteria, though non-compensatory strategies are mainly in view of the correlation of options as for singular criteria. The target of this investigation is to evaluate distinctive lodging areas in view of a built-up set of manageable lodging moderateness appraisal criteria. The basic leadership circumstance is along these lines a positioning issue where choices should be positioned from best to worst. The issue has a discrete nature; in other words, the choices (lodging areas) will be pre-indicated, and hence, a MADM technique will be appropriate in this occurrence. Subsequently, the article deliberates around MADM strategies. For MADM issues, there are for

the most part two schools of thought—those in view of multi-characteristic esteem capacities and multi-property utility hypothesis (MAUT) (the American School) [18] and those in light of outranking techniques (the French School) [19]. The strategies in light of MAUT (e.g., WSM, WPM, AHP, TOPSIS, COPRAS) commonly have a compensatory nature and for the most part comprise of accumulating the criteria into a capacity which must be augmented [6]. Interestingly, the outranking techniques take into consideration uniqueness between alternatives and thus have a non-compensatory nature. ELECTRE [19] and PROMETHEE [20] are the most widely used outranking methods. However, it has been suggested that ELECTRE and PROMETHEE are the most broadly utilized outranking strategies. In any case, it has been proposed that ELECTRE and PROMETHEE are not generally ready to give an entire positioning of the choices [2, 20, 21]. In like manner, such strategies might be unacceptable for the kind of choice issue close by, which requires an entire requesting of options.

The present paper discusses the appropriateness of the curve fitting tool used for the data analytics. The curve fitting needs prior understanding, or otherwise, the error in the small data point is marginal, and fitting is good approximation to the actual and measured or predicted data points. However, for large data points, the error is significant and loss of information is so significant that the complete exercise is not useful at all. In this article to different standard, data points are used for the analysis and the findings are outlined.

2   Results and Discussion

The curve fitting tool is used to predict the crude oil import with the data obtained for US crude oil export from January 1, 1991, to May 1, 2016. Figure 1 shows the cured oil import from USA. The data plotted and the fourth-order polynomial fitted. The following polynomial is obtained for the data under consideration.

$$y = 2E - 09x^4 + 0.0004x^3 - 0.0841x^2 + 4.5365x + 928.48$$

where 'y' is predicted values of millions of crude oil export by USA while 'x' is the month, starting with January 1, 1991.

The R^2 for the fitted data obtained is 0.9791. The R^2 is fairly close to the 1; thus, one may conclude that the fitted function will provide the close predication over the actual data. Further, with the equation obtained the predicted value of crude oil import is evaluated and for each month the actual deviation is calculated it is observed that at 1st January 1991 the actual export of crude is 1510 thousand millions of barrel per month while the predicated oil export is 932.33 thousand millions of barrel per month, with total error in the predicted value is 38.21%. The error in the predication data and the actual data of oil exports is varying with 0.028% to maximum 38.21%. It is seen that the short range of data format the curve fitting tool work better but for the large data points the predicted values deviate significantly from the actual values.
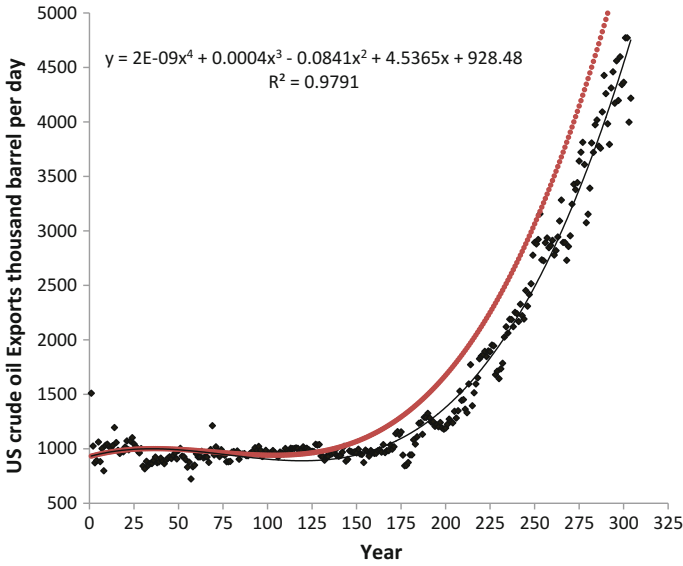
Fig. 1 Crude oil import with the data obtained for US crude oil export from January 1, 1991, to May 1, 2016 [22]

Thus, it is always important while choosing the curve fitting tool for predicting the future demand or supply. If model is not properly chosen, then it may lead to significant variation in the forecasted values.

Month starting from 1-1-1991	Oil export thousand barrels per day	Predicted oil export thousand barrels per day	Percentage error
1	1510	932.9328	38.21637
2	1025	937.2198	8.563922
3	871	941.3434	−7.47266
4	892	945.306	−5.63902
5	1062	949.11	10.62994
6	882	952.7578	−7.42663
7	1002	956.2518	4.565688
8	798	959.5944	−16.8399
9	1032	962.788	6.706588

303	3998	5726.011	−30.1783
304	4218	5790.257	−27.1535
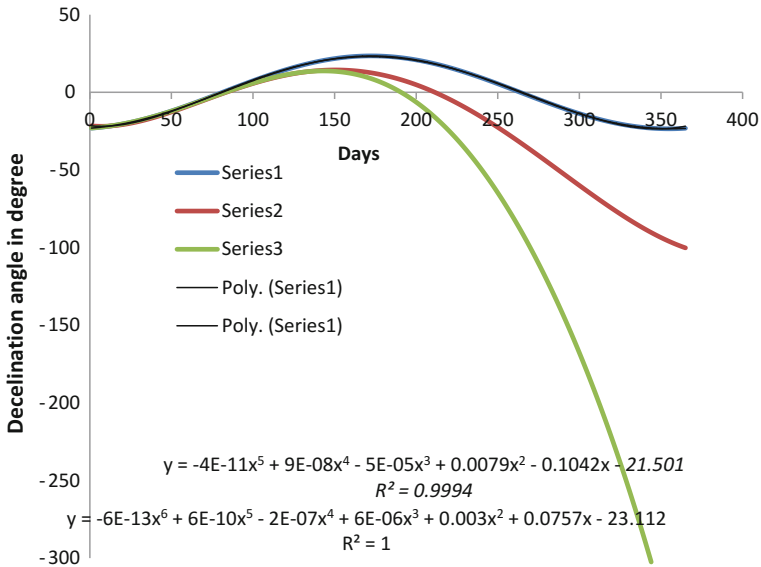
Fig. 2 Declination angle calculated for 365 days

The delineation angle is a sine function. The data generated by applying the following function of delineation:

$$\delta = 23.45 * \sin\left(\frac{360}{365} * (284 + n)\right)$$

where δ is the declination angle in degrees and 'n' is day of the year.

The systematic data generated are used for the curve fitting. The curve is fitted by fifth- and sixth-order polynomials. Then, the delineation angle is predicted for the polynomial under consideration. It observed that initially both the predicted and systematic evaluated delineation angles match very well. The percentage variation is significantly high and can go up to 10,229.35 and 27,828.28 percentages on 263th day of the year. Thus, it is evident that an order of the polynomial curve increases even the R^2 is very close to one. This is due to the region where both the curve and predicated value match and that is segment the equation suggested, and while the user used the same equation, it will deviate largely (Fig. 2; Table 1).

$$y = -4E - 11x^5 + 9E - 08x^4 - 5E - 05x^3 + 0.0079x^2 - 0.1042x$$
$$- 21.501 \text{ for fifth order function with } R^2 \text{is } 0.9994.$$

$$y = -6E - 13x^6 + 6E - 10x^5 - 2E - 07x^4 + 6E - 06x^3 + 0.003x^2 + 0.0757x$$
$$- 23.112 \text{ for sixth order function with } R^2 \text{is } 1.0.$$

Table 1 The historical oil export data and predicated values of oil exports for fourth order polynomial fit

N (day)	Delta	Delta model fifth order	Delta model sixth order	Error with fifth-order function	Error with sixth-order function
1	−23.0228	−21.5973	−23.0333	6.60007	−0.04562
2	−22.9427	−21.6782	−22.9486	5.833162	−0.02542
3	−22.8559	−21.7438	−22.8578	5.114192	−0.00827
4	−22.7622	−21.7946	−22.7609	4.439926	0.006035
5	−22.6619	−21.8307	−22.6579	3.807409	0.017674
6	−22.5548	−21.8525	−22.5488	3.213928	0.026823
7	−22.4411	−21.8602	−22.4335	2.656992	0.033642
8	−22.3207	−21.8542	−22.3121	2.134305	0.038279
9	−22.1937	−21.8348	−22.1846	1.643749	0.040873
10	−22.0601	−21.8021	−22.0509	1.183367	0.04155
–					
363	−23.2323	−99.3934	−377.019	−327.824	−1522.82
364	−23.174	−99.7751	−381.278	−330.547	−1545.28
365	−23.1089	−100.146	−385.573	−333.365	−1568.51

The error in both the polynomials used for the analysis

3   Conclusion

The curve fitting tool is used to fit the oil export data and fourth-order polynomial fit used and the values for the predicted export are calculated. It is observed that the regression R^2 provided for the fit is 0.9791. However, with the best R^2 fit, the deviation in the predicted export is around 38%. Initially, the variation is fairly close to the actual oil export values while for large data the deviation is the significantly predicted oil export value. Further, the declination angle for a day is calculated which is sine function and the systematic data are generated which then fitted. The fifth- and sixth-order polynomial data are fitted for the declination angle. For first 100 days the fitted and actual declination angle is matching but it is significantly deviates thereafter. At 263th day of the year, the deviation is almost 10,229 and 27,828% for fifth- and sixth-order polynomial, respectively. Thus, the curve fitting tool is used only useful for the short data with the straight line data.

References

1. Stigler, S. M. History of Statistics: The Measurement of Uncertainty Before 1900, Harvard University Press, Cambridge MA, 1986.
2. Triantaphyllou E. Multi-Criteria Decision Making Methods: A Comparative Study. Dordrecht: Kluwer Academic Publishers; 2000.

3. Zavadskas EK, Turskis Z, Kildienė S. State of art surveys of overviews on MCDM/MADM. Technological and Economic Development of Economy 2014;20:165–179.
4. Liou JJH, Tzeng GH. Comments on "Multiple criteria decision making (MCDM) methods in economics: an overview". Technological and Economic Development of Economy 2012;18:672–695.
5. Roy B. Multicriteria Methodology for Decision Aiding. Dordrecht: Kluwer Academic Publishers; 1996.
6. Zavadskas EK, Turskis Z. Multiple criteria decision making (MCDM) methods in economics: an overview. Technological and Economic Development of Economy 2011;17:397–427.
7. Adler N, Friedman L, Sinuany-Stern Z. Review of ranking methods in the data envelopment analysis context. European Journal of Operational Research 2002;140:249–265.
8. Maliene V. Valuation of commercial premises using a multiple criteria decision-making method. International Journal of Strategic Property Management 2001;5:87–98.
9. Maliene V. Specialised property valuation: Multiple criteria decision analysis. Journal of Retail and Leisure Property 2011;9:443–450.
10. Maliene V, Zavadskas EK, Kaklauskas A, Raslanas S. Real estate valuation by multicriteria approach. Journal of Civil Engineering and Management 1999; 5: 272–284.
11. Opricovic S, Tzeng GH. Compromise solution by MCDM methods: a comparative analysis of VIKOR and TOPSIS. European Journal of Operational Research 2004; 156: 444–5.
12. Peng Y, Kou G, Wang G, Shi Y. FAMCDM: A Fusion Approach of MCDM Methods to Rank Multiclass Classification Algorithms. Omega 2011;39:677–689.
13. Tavares LV. An acyclic outranking model to support group decision making within organizations. Omega 2012; 40: 782–790.
14. Zavadskas EK, Kaklauskas A, Maliene V. Real estate price evaluation by means of multicriteria project assessment methods. In: Zavadskas E, Sloan B, Kaklauskas A, editors. Real estate valuation and investment in central and eastern Europe during the transition to free market economy. Vilnius: Technika; 1997, 156–170.
15. Hwang C, Yoon K. Multiple Attribute Decision Making. Berlin: Springer; 1981.
16. Belton V. A comparison of the analytic hierarchy process and a simple multi- attribute value function. European Journal of Operational Research 1986;26:7–21.
17. Zanakis SH, Solomon A, Wishart N, Dublish S. Multi-attribute decision making: a simulation comparison of select methods. European Journal of Operations Research 1998; 107: 507–529.
18. Keeney R, Raiffa H. Decisions with Multiple Objectives. New York: Wiley; 1976.
19. Roy B. The outranking approach and the foundations of the ELECTRE methods. Theory and Decision 1991; 31: 49–73.
20. Brans JP, Vincke P. A Preference Ranking Organisation Method (The PROMETHEE Method for Multiple Criteria Decision Making).Management Science 1985; 31: 647–656.
21. Wang JJ, Jing YY, Zhang CF, Zhao JH. Review on multi-criteria decision analysis aid in sustainable energy decision-making. Renewable and Sustainable Energy Reviews 2009; 13: 2263–2278.
22. http://www.macrotrends.net/2563/us-crude-oil-exports-historical-chart   site   visited   on 01/03/2018.

Posture Assessment Among Waste Loading Workers in India

Francis J. Emmatty and Vinay V. Panicker

Abstract Waste collection workers are prone to occupational hazards compared to other industrial workers. Out of the various workers engaged in waste collection tasks, waste-loading workers are more susceptible to injuries. Posture analysis and method study are conducted among waste-loading workers. The posture assessment is carried out by RULA and REBA. The assessment carried out in this work pointed out the need for immediate change in the working posture of these workers. Hence, there is a definite need for the development of engineering intervention for these workers. In developing countries, low-cost tools and lifting aids will have better acceptance.

Keywords Waste collection · Loading workers · Posture analysis · Method study
RULA · REBA

1 Introduction

Waste management is one of the fastest growing job sectors in the world as solid waste and unemployment are rising at an alarming rate [1]. Waste collection workers play an essential role to reduce waste in landfills and support recycling companies. Workers involved in the waste collection are exposed to occupational risks and injury rates higher than any other industrial occupations [2, 3]. Even in developed counties, these workers are poorly paid.

The growth in the service needs together with the deficiency of sufficient facilities for municipalities is putting an enormous strain on the waste collection

F. J. Emmatty · V. V. Panicker (✉)
Department of Mechanical Engineering,
National Institute of Technology Calicut, Campus P.O., Kozhikode, Kerala, India
e-mail: vinay@nitc.ac.in

F. J. Emmatty
e-mail: fj.emmatty@gmail.com

workers [4]. The workers in developing nations are exposed to more occupational hazards compared to their counterparts in developed countries.

Waste collection tasks require frequent physical activity such as lifting, carrying, pulling, and pushing [5]. The bending and twisting of the body along with the lifting of heavy weights and repetitive tasks are associated with musculoskeletal disorders [6–9]. The most frequently occurring injury due to these tasks is in the low-back region [10].

A posture analysis study will help to identify the hazards in the waste-loading task and identification of activities which need to be mechanized and automated. There is a lack of machines and lifting equipment for handling the waste among the workers in waste collection centers [11]. Manual loading of waste containers into transport vehicles should be avoided and replaced by mechanized means of lifting and transferring [12].

Rapid Upper Limb Assessment (RULA) and Rapid Entire Body Assessment (REBA) are observational techniques for classification of body postures and force, to identify musculoskeletal risks, with action levels [13]. RULA is a postural screening method to investigate the exposure of workers to risk factors associated with upper extremity tasks [14]. REBA is a postural analysis to assess entire body for dynamic, fast-changing, or unstable postures [15].

RULA shows better results in static postures, and REBA is more suitable in the ergonomics evaluation of dynamic and unpredictable postures [16]. The profession of the workers is another factor to be considered in selecting posture analysis methods. A comparison study showed that REBA underestimated postural loads for the analyzed postures compared to RULA [17]. Many studies have applied both RULA and REBA for posture analysis and compared the results [16].

A study conducted among waste-loading workers in the USA by RULA and REBA reported that the posture of lifting and dumping tasks in waste collection tasks needs to be changed [3]. The physical workload is higher for waste loaders compared to truck drivers, solo collectors, and clerical workers who are engaged in waste collection activities [18]. MSDs were significantly higher among the waste loaders [19].

In this study, posture analysis of the waste-loading workers is assessed by RULA and REBA in the Indian scenario. A process chart for the waste-loading task is prepared to identify the different activities in waste-loading tasks. The activities identified from the process chart are further analyzed by RULA and REBA to determine the critical activities. These vital activities are also evaluated in detail.

2 Methodology

The study aims to assess waste-loading tasks to identify occupational hazards by posture analysis among the waste-loading workers in an educational institution in India. The work of waste-loading workers includes picking up of bins filled with waste and dumping into a collection vehicle and transporting to a collection yard.

Their work involves manual material handling with the lifting of heavy weights and awkward postures. These workers are susceptible to occupational injuries like back pain and joint pain in hand and legs.

Work study of the waste collection tasks are carried out by video motion analysis, and process chart is prepared to identify critical activities. The video is captured using two cameras to observe the two workers engaged in the waste-loading tasks. Video and still photographs are tremendously useful as input for the observational techniques [20].

The waste-loading activity consists of ten work elements and is recorded in process chat as given in Table 1. Process chart is a widely accepted tool to represent the activities in a work cycle for method study [21]. Two workers jointly perform the waste-loading task. The first worker (W1) transports the full waste bin and lifts the container to the second worker (W2). The worker W2 receives the bin standing inside the vehicle and dumps the waste into the vehicle and returns to the first worker. It is observed that the time taken to transport waste to and fro from the vehicle varies with the distance of the parked vehicle and the place where the bin is kept. Another observation is that the waste-dumping time by W2 depends on the quantity and type of waste in the bin.

RULA and REBA posture analysis is done to assess the difficulty of various activities in waste loading and identify the work elements that might lead to work injuries and MSDs. In this study, both RULA and REBA are considered for a comparative assessment. The standard procedures are used to calculate the RULA and REBA scores.

The procedure for calculation of RULA score is given in Table 2 [14]. The final score of the RULA assessment is classified into four ergonomic risk levels such as score 1–2 represents acceptable posture; score 3–4 suggests further investigation is needed, and changes may be required; score 5–6 shows investigation, and changes are needed soon; and score 7 means investigation, and changes are required immediately.

The procedure for calculation of RULA score is given in Table 3 [15]. The final score of the REBA assessment is divided into five ergonomic risk levels such as score 1 indicates negligible risk; score 2–3 means low risk, and change may be needed; score 4–7 suggests medium risk, change soon; score 8–10 indicates high risk, investigation, and implement change; and score 11–15 shows very high risk, implement change.

RULA and REBA analysis of waste-loading tasks is given in Table 4. Out of all the activities, lifting and dumping tasks are recognized as the most hazardous activities of the waste-loading process.

The lifting and dumping tasks are illustrated in Fig. 1. It can be observed that both the workers are working with awkward postures. In addition, the workers are engaged in lifting more than 25 kg.

Since the lifting and dumping tasks are recognized as the most hazardous activities of the waste-loading process, to analyze these tasks further, the lifting task by W1 and the dumping task by W2 are assessed three times by RULA and REBA. The RULA and REBA data sheet for lifting and dumping task is given in Table 5. Both of

Table 1 Process chart for waste-loading task

Activity description	Worker 1 (W1)	Worker 2 (W2)	Time taken (in s)
1. Transporting the bin up to the vehicle by W1 (W2 idle)	⟹		2.16
2. Aligning the bin by W1 (W2 idle)	◯		1.56
3. Opening the lid of the bin by the W1 (W2 idle)	◯		1.17
4. lifting the bin by W1 (W2 idle)	◯		2.31
5. Tilting the bin by W1 and receiving the bin by W2	◯	◯	1.35
6. Dumping and shaking the bin by W2 (W1 idle)		◯	3.34
7. Returning the bin by W2 and receiving the bin by W1	◯	◯	3.24
8. Lowering the bin by W1 (W2 idle)	◯		1.74
9. Closing the lid by W1 (W2 idle)	◯		1.20
10. Transporting the bin back to the standby W1	⟸		1.50

these activities are provided with a rating of 7 in RULA and a rating of 11 in REBA, indicating the need for immediate change in these postures.

3 Results and Discussion

A process chart is prepared for conducting a method study among the waste-loading workers. From the posture analysis, it is clear that activation of lifting and dumping

Table 2 Procedure of RULA assessment

1. Locate upper-arm position	5. Determine posture score A (1–9)	8. Find score A—arm and wrist analysis	Final RULA score (1–7)
2. Locate lower-arm position			
3. Locate wrist position			
4. Locate wrist twist position			
6. Add muscle use score (0–1)			
7. Add force/load score (0–3)			
9. Locate neck position	12. Determine posture score B (1–9)	15. Find score B—neck, trunk, and leg analysis	
10. Locate trunk position			
11. Determine legs support			
13. Add muscle use score (0–1)			
14. Add force/load score (0–3)			

Table 3 Procedure of REBA assessment

1. Locate neck position	4. Determine posture score A (1–9)	6. Find score A—neck, trunk and leg analysis	13. Find score C (1–12)	Final REBA score (1–15)
2. Locate trunk position				
3. Determine leg's support				
5. Add force/load score (0–3)				
7. Locate upper-arm position	10. Determine posture score B (1–9)	12. Find score B—arm and wrist analysis		
8. Locate lower-arm position				
9. Locate wrist position				
11. Add coupling score (0–3)				
14. Add activity score (0–3)				

Table 4 RULA and REBA analysis of waste-loading tasks

Activity	Worker 1 (W1)		Worker 2 (W2)	
	RULA score	REBA score	RULA score	REBA score
1. Transporting bin to the vehicle	2	3	1 (idle)	1 (idle)
2. Aligning the bin	4	6	1 (idle)	1 (idle)
3. Opening lid of the bin	3	4	1 (idle)	1 (idle)
4. Lifting the bin	*7*	*11*	1 (idle)	1 (idle)
5. Tilting and receiving the bin	6	8	6	11
6. Dumping waste in the bin	1 (idle)	1 (idle)	7	*11*
7. Returning and receiving bin	4	5	4	8
8. Lowering the bin	5	8	1 (idle)	1 (idle)
9. Closing lid of the bin	4	4	1 (idle)	1 (idle)
10. Transporting the bin back	3	5	1 (idle)	1 (idle)

The values in italics represents a posture score with very high risk level

Fig. 1 Lifting and dumping of waste

is the most difficult tasks as it is associated with substantial lifting and awkward bending.

Both lifting and dumping tasks are rated with a score of 7 in RULA and a score of 11 in REBA. Even though there is variation between individual workers in arm and wrist analysis (Score A) and neck, trunk and leg analysis (Score B), the overall scores are same in both the cases of RULA and REBA.

Table 5 RULA and REBA analysis of lifting and dumping tasks

		Lifting (W1)			Dumping (W2)		
		W1.1	W1.2	W1.3	W2.1	W2.2	W2.3
RULA	Arm and wrist analysis—score A	7	7	7	**9**	**8**	**9**
	Neck, trunk, and leg analysis—score B	**9**	**10**	**10**	7	7	7
	Final RULA score	7	7	7	7	7	7
REBA	Neck, trunk, and leg analysis—score A	**10**	**10**	**10**	7	8	8
	Arm and wrist analysis—score B	7	7	7	**10**	**10**	**10**
	Combined score C	11	11	11	11	11	11
	Activity score	0	0	0	0	0	0
	Final REBA score	11	11	11	11	11	11

The values in bold represents the body region that contributes to the posture score with very high risk level

From RULA and REBA scores, it can be inferred that during lifting task, worker 1 is mostly strained in neck, trunk, and leg; during dumping task, worker 2 is mostly strained in arm and wrist.

4 Conclusion

Compared to other workers in waste-related occupations, waste-loading workers are subjected to high occupational hazards. Posture analysis techniques help to identify the criticality of the various activities involved in waste-loading tasks. Understanding the waste-loading activities will help to prioritize the mechanization and automation of these critical tasks. Lifting and dumping tasks are identified as the most hazardous of the activities performed by the workers. Ergonomic interventions have to be developed to mitigate occupational hazards due to frequent lifting and dumping during the waste-loading process.

Automated equipment is available in developed countries for the lifting and dumping tasks related to waste collection. However, due to social and economic constraints, automated types of equipment are not available to workers in developing countries.

Cost-effective lifting aids and automated tools need to be developed to mitigate the burden of these unprivileged workers.

References

1. ILO: Promoting Health and Safety in a Green Economy. International Labour Organization, Geneva (2012).
2. UN-Habitat: Solid Waste Management in the World Cities. Water and Sanitation in the Worlds Cities 2010. United Nations Human Settlements Programme (2010).
3. Çakit, E.: Assessment of the physical demands of waste collection tasks. Glob. Nest J. 17, 426–438 (2015).
4. Sharholy, M., Ahmad, K., Mahmood, G., Trivedi, R.C.: Municipal solid waste management in Indian cities—A review. Waste Manag. 28, 459–467 (2008).
5. Yang, C.-Y., Chang, W.-T., Chuang, H.-Y., Tsai, S.-S., Wu, T.-N., Sung, F.-C.: Adverse health effects among household waste collectors in Taiwan. Environ. Res. 85, 195–199 (2001).
6. Engkvist, I.-L., Svensson, R., Eklund, J.: Reported occupational injuries at Swedish recycling centres—based on official statistics. Ergonomics. 54, 357–366 (2011).
7. Singh S., Chokhandre P.: Assessing the impact of waste picking on musculoskeletal disorders among waste pickers in Mumbai, India: a cross-sectional study. BMJ Open. e008474 (2015).
8. Jeong, B.Y., Lee, S., Lee, J.D.: Workplace Accidents and Work-related Illnesses of Household Waste Collectors. Saf. Health Work. 7, 138–142 (2016).
9. Zakaria, J., Sukadarin, E. H., Omar, F. A. C., & Salleh, N. F. M.: Musculoskeletal Disorder among Municipal Solid Waste Collectors. Asia Pacific Environ. Occup. Heal. J. 3, 28–32 (2017).
10. Poulsen, O.M., Breuma, N. 0, Ebbehoj, N., Hansen, M., Ivensa, U.I., Van Lelieveld, D., Matthiasen', L., Nielsena, B.H., Nielsena, E.M., Schibye, B., Skov, T., Stenbaeka, E.I., Wilkins, K.C.: Sorting and recycling of domestic waste. Review of occupational health problems and their possible causes. Sci. Total Environ. 168, 33–56 (1995).
11. Engkvist, I.-L.: Working conditions at recycling centres in Sweden—Physical and psychosocial work environment. Appl. Ergon. 41, 347–354 (2010).
12. CPCB: The National Action Plan for Municipal Solid Waste Management. Cent. Pollut. Control Board, India. (2015).
13. David, G.C.: Ergonomic methods for assessing exposure to risk factors for work-related musculoskeletal disorders. Occup. Med. 55, 190–199 (2005).
14. McAtamney, L., Corlett, E.N.: RULA: a survey method for the investigation of work-related upper limb disorders. Appl. Ergon. 24, 91–99 (1993).
15. Hignett, S., McAtamney, L.: Rapid Entire Body Assessment (REBA). Appl. Ergon. 31, 201–205 (2000).
16. Tee, K.S., Low, E., Saim, H., Zakaria, W.N.W., Khialdin, S.B.M., Isa, H., Awad, M.I., Soon, C.F.: A study on the ergonomic assessment in the workplace. AIP Conf. Proc. 1883, (2017).
17. Kee, D., Karwowski, W.: A Comparison of Three Observational Techniques for Assessing Postural Loads in Industry. Int. J. Occup. Safety Ergon. 13, 3–14 (2007).
18. Tsujimura, H., Taoda, K., Kitahara, T.: A field study on the physiological workload of garbage collectors in the Japanese summer. Ind. Health. 50, 556–566 (2012).
19. Salve, P., Chokhandre, P., Bansod, D.: Assessing musculoskeletal disorders among municipal waste loaders of Mumbai, India. Int. J. Occup. Med. Environ. Health. 30, 875–886 (2017).

20. Dempsey, P.G., Mcgorry, R.W., Maynard, W.S.: A survey of tools and methods used by certified professional ergonomists. 36, 489–503 (2005).
21. Niebel, B., Freivalds, A.: Niebel's Methods, Standards, and Work Design. McGraw-Hill higher education (2013).

Evaluation of Performance Characteristics and Bite Condition of Single Ferrule Bite Fitting by Finite Element Analysis (FEA)

Akshay Kusneniwar, Prathamesh Potdar and Santosh Rane

Abstract The leak-proof performance of ferrule is the long-standing problem for the industries. This paper proposed a systematic approach to achieve an adequate sealing condition of bite ferrule fitting by finite element analysis of swaging. The principle of contact pressure and bite of ferrule along the leak paths, also known as leak path methodology (LPM) are used for sealing. The ANSYS workbench with explicit dynamics is used for analysis with leak path methodology and validated the result by leak test and burst test experiments. The paper discussed the effect of the swaging action on the fitting. Also, identify the essential requirement to improve the performance of the ferrule at the actual operating condition. This study does not consider the effect of temperature and compatibility with different fluids on the performance of fitting. The proposed approach for swaging process reduced the dependency of experimental validation for the new or modified component. The study defines the new way of determining the seal criteria of ferrule tube fitting using finite element analysis and validates with the help of traditional experimentation.

Keywords Bite ferrule tube fitting · Hydrostatic burst test
Johnson-Cook material model · Leak path methodology

1 Introduction

Flexible tubes are used widely in the petroleum industry for the transportation of crude hydrocarbon. The tubes can be of different sizes and lengths of several hundred

A. Kusneniwar · P. Potdar (✉) · S. Rane
Department of Mechanical Engineering, Sardar Patel College of Engineering,
Munshi Nagar, Andheri-West, Mumbai 400058, India
e-mail: prathameshpotdar122@gmail.com

A. Kusneniwar
e-mail: akshaykusneniwar04@gmail.com

S. Rane
e-mail: s_rane@spce.ac.in

meters. The fittings are used to connect the tubes and to create the ancillary structures to form the necessary field infrastructure. The tubes are connected with end fitting to minimize the energy losses of fluids. The common issues faced by industries for fittings are the loss of seal due to tube grip and tube blow out of high-pressure tube connection application in industries. In today's era, industries are more focused to develop useful end fittings to minimize the leakage rate from joints. The bite ferrule fittings are extensively used as an end fitting for high-pressure tube connection due to its simple structure, adequate sealing capabilities, and availability of the metric standard. The working pressure has restricted to the maximum working pressure of the tubes. The tubes designed in such way that the tubes burst before the breakage of the joint. The seal in end fittings is usually created by swaging ferrule in between the tube and the body of the fitting. This creates two leak paths, one between the ferrule and the tube and the other at the metal-to-metal contact interface between the ferrule and the body. The essential requirements to develop a reliable high-pressure seal are the sufficient bite on the tube and contact pressure over a reasonable distance at the metal-to-metal interface Haocai Huang et al. The actual arrangement and the swaging action of cutting edges as shown in the Figs. 1 and 2 show the swaging process of bite ferrule which consists of (1) bite ferrule, (2) pressure applying nut, (3) tube connector, (4) tube rest or internal shoulder of the connector, and (5) tube.

This study used finite element model to evaluate the contact pressure at seal contact, and the results with a specifically developed leak criteria have been used to evaluate the sealing performance. The research presented a brief description of the models and some specific results. The FE model predictions are compared with the experimental burst test and leak test results.
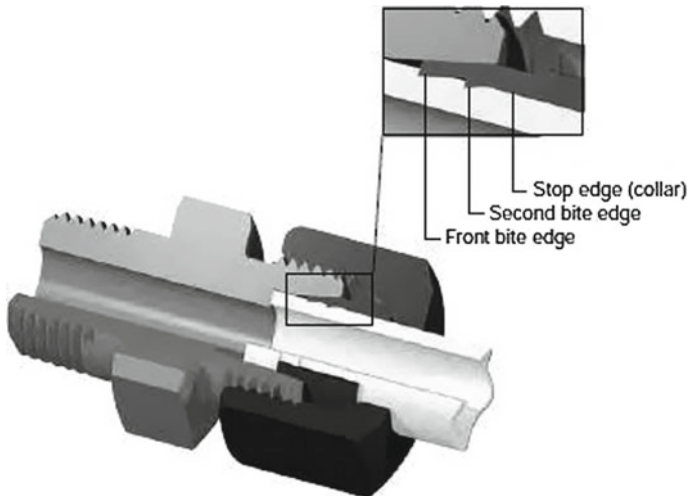
Fig. 1 Swaged assembly of the bite ferrule
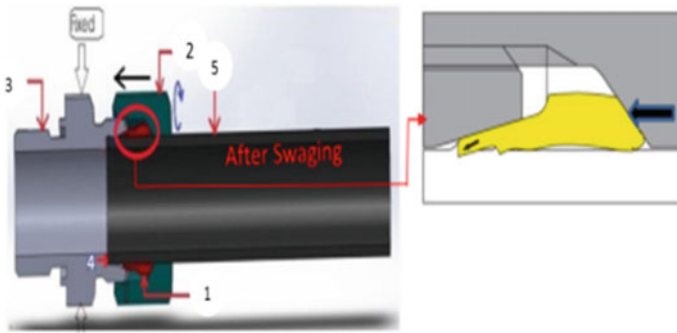
Fig. 2 Swaging process of bite ferrule fitting (Parker Catalogue 4300)

2 Literature Survey

In this research, the literature survey is performed in the domain of geometries, working mechanism, analytical approach, and metallurgy of ferrule to identify the research gap and to develop the action plan. The domains are selected to understand the ferrule mechanism and to know the existing stuff related to the ferrule. Huang and Yuan [1] analyzed the sealing performance of the tubing adapters in the gas-tight deep-sea water sampler (GTWS) by nonlinear finite element contact method with the ANSYS software. Koc et al. [2] used FEA and design of experiments to establish design guidelines for simple hydroformed parts and the effect of various parameters on the hydroformed parts. Takakuwa [3] identified the yield stress of JIS SUS316L stainless steel from the Vickers Hardness by taking account of the residual stress peening techniques and X-ray diffraction method. *ISO 8434-1* standard document provides guidelines for design and testing of bite ferrule fitting (also called as a cutting ring) for different pressure ranges and working environment. Pott et al. [4] proposed a metallic cutting ring with the annular peripheral stop edge, which projects beyond the stop face and forms an additional sealing edge. Hiszpanski [5] in his invention relates the tube fittings in particular to vibration resistant tube fittings having means for biting into the tube to provide a seal. Parker 4100-7/UK [6] Industrial Tube Fittings Europe Technical handbook provides ferrule selection procedure along with a tube of proper thickness for desired working pressure with compatible environment, and it also provides the working mechanism of ferrule specifically called as Ermeto ferrule. Parker Assembly tooling guide [7] provides detail assembly installation of Ermeto ferrule fitting by either hand swaging or machine swaging depending upon the size of the ferrule and the force required for proper swaging. It gives the standard installation procedure for Ermeto ferrule fitting currently in practice. Parker instrumentation EPR4230/4233.1 rev 2 [8] provides fitting performance report which gives the mechanical aspects of the fitting explicitly. ISO 1127 [9] tube specification guide provides detail guidelines for selection of tube for different pressure application for the different environmental condition. It gives a detailed technical specification of

such as tube hardness and the thickness of walls of tubes. A literature survey identified that there is need to develop FEA model to give the performance characteristics of bite ferrule fitting. Also, advancement in technology develops need of simulation model for assessing the difficulties arises during manufacturing and operation. The existing problem of bite ferrule for high-pressure application is the required depth of the cutting edge weakens the tube wall thickness. Therefore, it is necessary to determine the amount of penetration in the tube required for effective seal without weakening the tube strength and finding the new simulation method for determining the seal reliability.

3 Research Methodology

3.1 Working Principle

The connection has formed by applying the pressure on the threaded nut to move the ferrule into the conical surface to radially contract the front end of the ferrule. The continuous pressure applied to connector boy by threading the nut. The ferrule has to move continuously so that the front end portion is continued to be deformed inwardly with the second cutting edge biting into the outer surface of the tube to raise a ridge of material which is shaped by the curved cam surface. The transitional portion has reformed into a wedge having a trapezoidal cross-sectional shape which extends from the back surface of the cutting edge. The trapezoidal wedge-shaped of the transition portion along with the ridges supplies an indication to the operator that the formation of the connection has completed. Further, the trapezoidal cross along with the ridges provides a seal between the tube and the ferrule that cooperates with the seal formed by the pressure applied between the shoulder and the tube end to ensure a fluid-tight connection. After assembly, a visible collar of cut tube material must fill the space in front of the first cutting edge. During assembly, it is essential that the tube is held firmly against the stop in the inner conical shape of the fitting; if not, then the cutting process does not perform satisfactorily. In the actual process, the nut is moved by the effect of torque application due to its threaded arrangement, but in the simulation model the analysis of threaded arrangement is quite complicated and leads to high nonlinearity.

3.2 Development of Simulation Model

This study used the leak path methodology based on contact pressure measurement, which works on the principle of asperity deformation due to the generation of interface pressure between two contact bodies. When the bodies are in contact has asperities at the micro-scalar level, and the random asperities also form between

the contacts to form a void space of microscopic thickness. The asperities deform on the application of pressurizing medium resulting in a reduction of void space which would, in turn, reduce fluid leakage through the interface. The increase of the asperity CP above the yield stress of the material deforms the asperities plastically and completely to prevent fluid leakage from closing the leak path. Based on this hypothesis, the minimum nominal CP (*PCN*) required to prevent leakage through a surface contact is given by the yield stress σY of the weakest material on the contact. If the nominal CP falls below this line, then a leak can occur through the contact.

3.2.1 FEA Process Flow

The FEA process starts with 3-D modeling followed by simplifying the geometric model. The inputs are identified to perform finite element analysis.

3.2.2 Model Preparation

A simulation model is developed for the prediction of contact pressure, burst pressure as well as bite condition during the swaging process.

The influence of different geometrical parameters of the ferrule shape (radius of the cutting edges, cam angle, and the distance between cutting edge) and of different process parameters like displacement versus depth of bite has investigated. The complexity of swaging (biting) process, all possible effects, and parameters have to be considered and implemented in the simulation model. Bite ferrule fitting consists of body, cutting ring, and nut. The 2-D model of the component assembly has prepared and as shown in Fig. 3. Figure 4 shows schematic of bite ferrule operation. Initially, 3-D model was prepared to analyze the process. The process has complexity and needs more computing time for solving the model with an available set of resources. So the convenient way to tackle the situation is to prepare the model in a 2-D axisymmetric condition which gives nearly the same results as 3-D analysis but with less computing time.

3.2.3 Material Properties

The microscopic and macroscopic responses of the material under high strain rate loadings are affected by strain, strain rate, temperature, and microstructure of the material. Finite element analysis (FEA) is used for process analysis. The knowledge of material behavior under severe loading conditions is a prerequisite for FEA. Most of the metals model depends on deformation temperature and strain rate. Johnson and Cook using Hancock and Mackenzie experiments on the variety of metals developed an empirical relationship which states the influences of temperature, strain, and strain rate on von Mises stress. The following model is widely used in FE models to
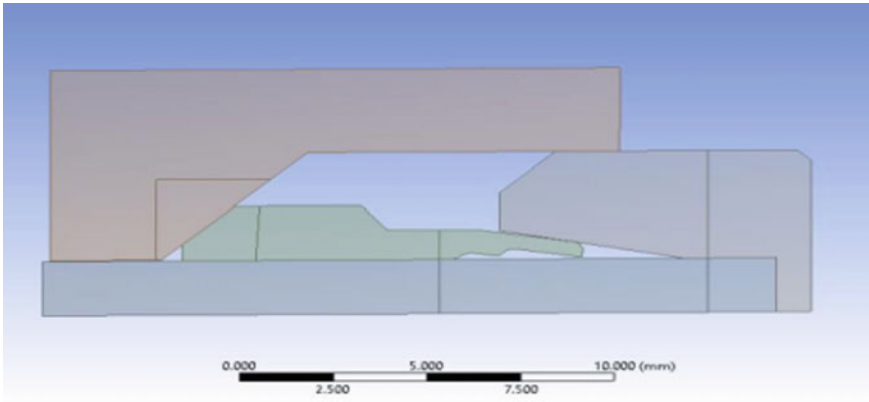
Fig. 3 Axisymmetric 2-D model of bite ferrule fitting

Fig. 4 Schematic of bite
ferrule operation
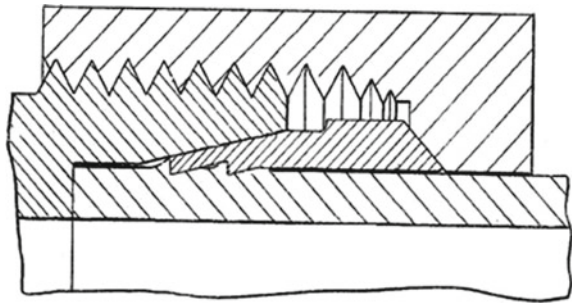
describe the constitutive behavior of metals at high strain rates over a wide range of
temperatures, its applicability over a wide range of strain (Umbrelloa et al. [10]).

$$\sigma_{\text{eq}} = \left(A + B\varepsilon_p^n\right)\left[1 + C Ln\left(\frac{\dot{\varepsilon}}{\dot{\epsilon}_0}\right)\right]\left[1 - \left(\frac{T - T_{\text{Room}}}{T_{\text{m}} - T_{\text{Room}}}\right)^m\right]$$

Here, εp is the useful plastic strain; B, C, m, n and A are five material constants
and obtained from the experiment. $\dot{\varepsilon}$ and $\dot{\varepsilon}_0$ are the current and reference strain rates.
T is the homologous temperature; T_{Room} and T_{m} are room and material melting tem-
perature, respectively. The first term at the right-hand side of the equation shows the
relation between semi-static stress and strain at the room temperature. The second
term states the effect of strain rate, and the last term illustrates the effect of temper-
ature. Tables 1, 2 and 3 represent the component standards with material, physical
properties of SS316 material, and Johnson and cook model parameters, respectively.

Table 1 Components standards and materials

Sr. No.	Components	Standard	Material
1	Tube	ASTMA269	SS316
2	Nut	ISO 8434-1	
3	Body	ISO 8434-1	
4	Cutting ring	ISO 8434-1	Hardened SS316

Table 2 Material properties of SS316

Sr. No.	Material properties	Values with unit
1	Density	7950–8000 kg/m3
2	Young's modulus	193–210 GPa
3	Poisson's ratio	0.27–0.3
4	Melting temperature	1399 °C
5	Specific heat	500 J/Kg ·°C

Table 3 Johnson and cook model parameters (Umbrelloa et al. [10])

Sr. No.	Parameters	Abbreviation	Values with unit
1	Initial yield stress	A	305 MPa
2	Hardening constant	B	1162 MPa
3	Hardening exponent	n	0.61
4	Strain rate sensitivity constant	C	0.01
5	Thermal softening coe.	m	0.517

3.2.4 Meshing

The process is nonlinear, so the elements required in that area should be fine to obtain close results. As the number of elements increase the time required for computation also increases. The selective meshing has used for meshing to overcome the problem. In selective meshing, the area where the process becomes highly nonlinear meshes with the fine elements and other parts mesh with medium size elements, this way the solution time kept as minimum as possible with best useful results. In this research, mostly all parts mesh with quadrilateral elements of the size of 0.5 mm with medium mesh and 0.1 with fine mesh. The meshing of assembly shows total 11,883 nodes and 11,367 elements have developed in static meshing.

3.2.5 Boundary Condition

The 2-D model is prepared to reduce the computation complexity of the process, and materials are highly nonlinear. In this analysis, the displacement is applied at the

end instead of torque, which has been calculated below. The standard procedure is available to find out the minimum requirement of displacement for sufficient gripping action. The standard procedure of assembly states that one and a half rotation of the nut is enough to bite the cutting ring into the tube. The adequate movement of the nut provides a sufficient grip and seal for bite ferrule fitting. Figure 5 shows the application of boundary condition, and Table 4 shows the details of boundary condition.

Displacement = No. of turns of nut × pitch of the Threads = 1.5 × 1.5 = 2.25 mm.

3.3 Experimental Setup and Procedure

The leakage test and hydraulic burst test are used to evaluate the performance of fitting. The test setup component with specification (Table 5) and procedure is explained below.

3.3.1 Leakage Test (Gas)

The gases like air, hydrogen, helium, and nitrogen are used to check the leak path of fitting. These gases are selected because of small molecules size and can escape through the minute leak path.
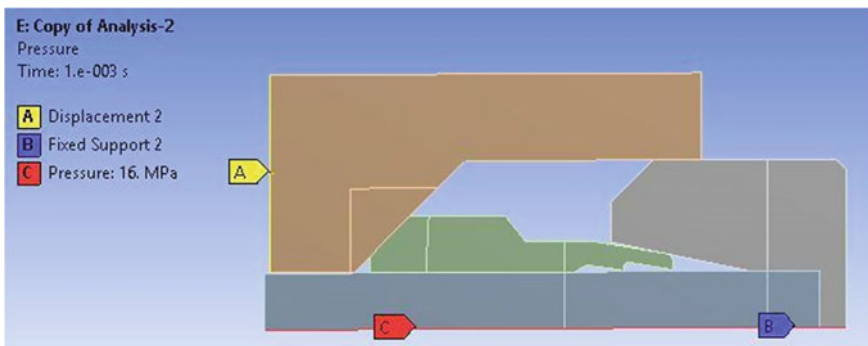
Fig. 5 Boundary condition

Table 4 Boundary condition

Sr. No.	Component	Condition	Values with unit
1	Nut	Displacement	2.25 mm
2	Body	Fixed	–
3	Tube	Internal pressure	160 Bar

Table 5 Component specification of the test ring

Sr. No.	Component	Specification
1	Nitrogen gas cylinder	9.86 kg, 2600 psi
2	Pressure gauge (max)	20,000 psi
3	Pressure control valve	Double pilot air actuated ¼″ NPT
4	Hose connector	Rubber
5	End cap	Plastic end caps
6	Bite ferrule fitted assembly	22 mm OD tube

Table 6 Component specification of burst test ring

Sr. No.	Components (Hydraulic)	Specification
1	Safety polycarbonate box	$60 \times 45 \times 30$ cm
2	Outlet pressure gauge (max)	4000 Bar
3	Hydraulic pump	8800 psi
4	Bite ferrule fitted assembly	22 mm OD tube

- **Purpose**: To identify the leak-tight performance of stainless steel bite ferrule tube fittings with thin wall.
- **Test condition**: Each sample must have one tube and two test fittings. The fitting has assembled based on the instructions given in the tube fitting installation manual.
- **Sample preparation**: The diameter of tube and wall thickness are 22 mm and 2 mm, respectively. The fittings and tube are assembled by rotating the nut by $1\frac{1}{2}$ revolution according to the instruction given in tube fitting manual.
- **Test Procedure:**

  (1) The assembly is attached to a positive pressure gas test stand and then submerged in water.
  (2) The pressurized nitrogen gas is passed through the assembly for at least 10 min to check the leakage.
  (3) If any pressure drop observed in testing, then there is leakage at the fitting, else fitting is appropriately performed.

3.3.2 Hydraulic Burst Test

The actual test ring components with specifications have shown in Table 6.

- **Purpose**: To observe the tube grip performance of 316 stainless steel bite ferrule tube fittings using heavy-wall tubing under laboratory conditions.
- **Test condition**: Each sample must have one tube and two test fittings. The fitting is assembled based on the instructions given in the tube fitting installation manual.
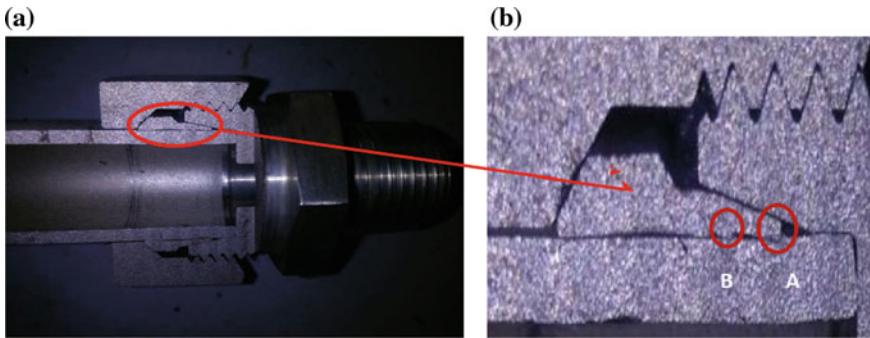
Fig. 6 a Swaged ferrule assembly. b Enlarged view of bite condition

- **Sample preparation**: The diameter of tube and wall thickness are 22 and 2 mm, respectively. The fittings and tube are assembled by rotating the nut by $1\frac{1}{2}$ revolution according to the instruction given in tube fitting manual.
- **Test Procedure:**

  (1) Place the sample on the hydraulic test stand.
  (2) The tube is held by clamping blocks to avoid the tube burst and forcing a failure at fitting to tubing engagement.
  (3) The hydraulic pressure has supplied and increased gradually up to the loss of tube grip, or leakage is observed.

4 Result and Discussion

4.1 Bite Swaging of Ferrule

1. **Experimental Swaging**
   The swaging of bite ferrule fitting the bite of the ferrule is inspected visually by confirming the formation of the collar of the material on the front cutting edge due to its cutting action and material filling the space in front of the ferrule to provide the sufficient grip and seal against the leakage. The points A and B in Fig. 6 represent the cutting action (swaging) of first and second cutting edge, respectively.
2. **FEA Swaging**
   Figures 7 and 8 show finger-tight arrangement before swaging and after swaging, respectively. The literature and experimentation suggested for successful swaging of bite ferrule have considered after the collar of material is raised at least up to 50% of front cutting edge thickness. To check the condition and for comparison between experimental results and FEA results, additional dimension
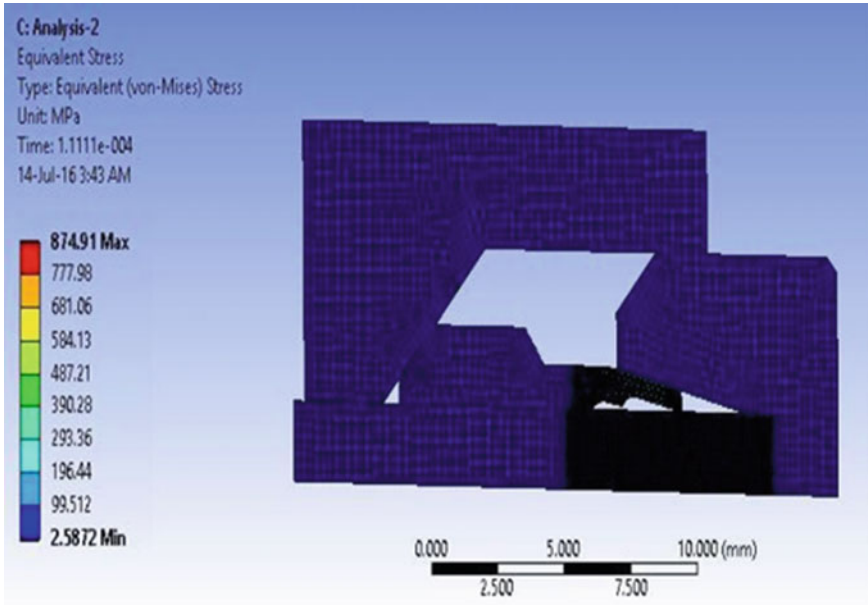
Fig. 7 Finger-tight arrangement before swaging
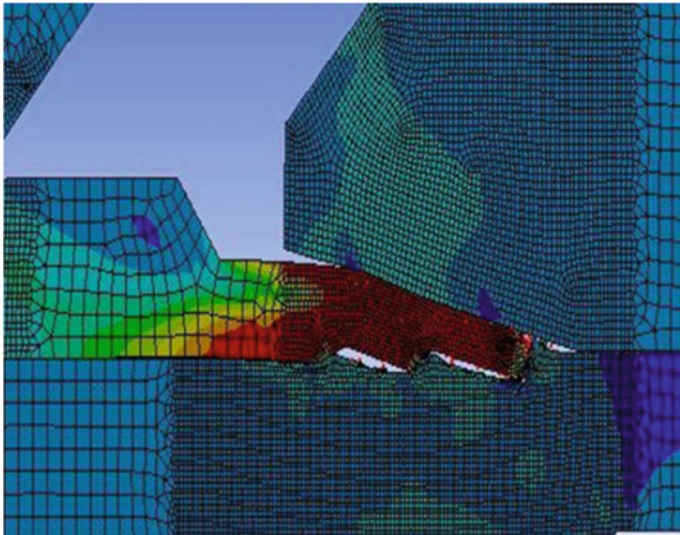
Fig. 8 Bite of the ferrule on the tube (swaging)

has measured as shown in Table 7. Figure 9 shows the condition parameters for leak tightness.

Table 7 Comparison of FEA and experimental results

Sr. No.	Parameters	FEA result (mm)	Experimental result (mm)	% Error
1	A	6.5	6	8.33
2	C	10	9	10
3	Bite depth	0.65	0.7	7.7

Fig. 9 Swage condition parameter for leak tightness
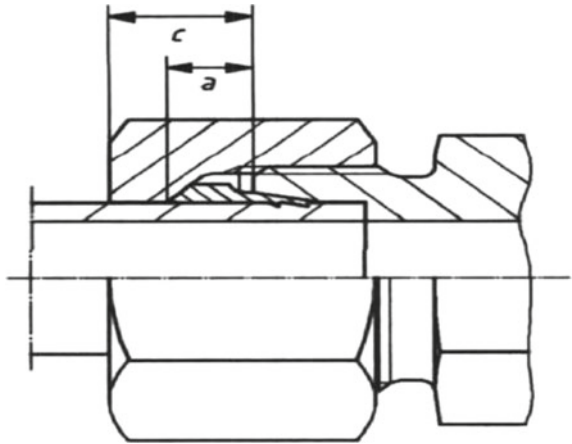
4.2 Performance Assessment

The maximum stress developed at the front cutting edge because of the deformation and cuts into the tube wall. The ferrule has designed with very stringent tolerance criteria to overcome the condition. The contact pressure and burst pressure are used in FEA and experimentation, respectively, to determine the performance of the bite ferrule assembly. The FEA gives the contact pressure along the length of two leakage path. The contact pressure along the two paths is higher than the working pressure so that leakage has sealed due to plastic deformation of the contact surfaces. The result shows that as deformation is directly proportional to displacement for some instant. Also for some instant of displacement, the deformation remains constant due to plastic flow of the tube material as it offers more resistance stain hardening property of the material. The stress generated at a point overcomes the strain hardening effect of material thus showing the steep increase deformation and completes the swaging at the end of displacement.

5   Limitations of Research

(1) This research has mainly focused on swaging process simulation and performance analysis of single ferrule bite fitting at the normal environmental condition. It does not emphasize the temperature effect on the performance of the ferrule and compatibility with different kinds of fluids.
(2) Also, the effect of surface hardness has not considered in the simulation model.
(3) This study is carried out only considering the one set of material and dimension.

6   Conclusion

This study determined the performance of the bite ferrule fitting by the contact pressure method instead of traditional experimental burst pressure test by FEA simulation. This study provides the considerations for model geometry, mesh size, geometrical constraints, material deformation models, and contact modeling approach. FEA is used to predict the contact pressure at elastic–plastic contact interface and the sealing performance of the bite ferrule in the end fittings of tubes. This research investigated the stiffness of the seal ring, and the materials in the sealing components play a significant role in the leak behavior of the sealing system since both of these factors significantly effect on contact pressure at sealing interface. The maximum contact pressure at this interface after swaging of the cutting ring is of critical importance as this initiates the leak-free contact. A subsequent change in contact pressure behavior with an increase of internal pressure determines the sealing performance of the end fitting. The future research can consider the different sets of dimensions and material aspect to check their effect on the performance of the ferrule fitting. The surface hardness effect of the ferrule on the performance can be determined in the further studies.

References

1. Haocai Huang, Zhouli Yuan. 2014. Study of the sealing performance of tubing adapters in gas-tight deep-sea water sampler. International Journal of Naval Architecture and Ocean Engineering, 6, 749–761.
2. Muammer Koc¸ Ted Allen, Suwat Jiratheranat, Taylan Altan. 2000. The use of FEA and design of experiments to establish design guidelines for simple hydroformed parts. International Journal of Machine Toolls & Manufacture, 40, 2249–2266.

3. Osamu Takakuwa. 2013 Estimation of the Yield Stress of Stainless Steel from the Vickers Hardness Taking Account of the Residual Stress. Journal of Surface Engineered Materials and Advanced Technology, 3, 262–268.
4. Harald Pott, Hickeswagen, Harald Schmldt, Wlpperlrth. 2010 Metallic cutting ring. United States Patent US 7,665,772 B2.
5. Jan A. Hiszpanski. 1972. High performance fitting. United States Patent 3,707,302.
6. Parker Industrial Tube Fittings Europe Catalogue 4100–7/UK.
7. Parker Assembly tooling- for assembly installation of bite ferrule fitting.
8. Parker instrumentation Engineering performance report, EPR4230/4233.1 rev 2.
9. ISO 1127 stainless steel pipes/tubes.
10. D. Umbrelloa, R. M'Saoubib, J.C. Outeiro. 2007. The influence of Johnson–Cook material constants on finite element simulation of machining of AISI 316L steel. International Journal of Machine Tools & Manufacture 47, 462–470.

Optimization of the Chest Geometry for the Storage and Transportation of Fruits and Vegetables

Ajinkya Netake, Rushabh Mutha, Akash Mishra, Aditya Sawant, Prathamesh Potdar and Nitin Panaskar

Abstract In today's era, there is a massive demand for E-commerce business, which is governed by the mechanism of packaging, forwarding, and transportation. The chests are commonly used in E-commerce business to transport and deliver fruits and vegetables to consumers. The present chests have not considered aesthetic and ergonomic consideration at the time of design. Due to which, some fatigue has developed in delivery person at the time of chest handling. This study aims to optimize the chest geometry for the maximum storage and transportation of fruits and vegetables and also to reduce fatigue developed in delivery person. The cost, space, and material are the factors considered in the optimization of chest geometry. The methodology includes literature survey, market research, and comparative study to optimize the chest geometry. The competitive geometries of the chest are compared based on shape, stackability, strength, ease of manufacturing, manufacturing cost, and percentage storage utilization and identified the optimal chest geometry.

Keywords Transportation and storage · Packaging · Stress analysis
Competitive geometries

1 Introduction

The transportation is one of the major drivers for successful E-commerce business. Also, the transportation industry is growing day by day to satisfy customer requirements quickly. Some of the start-ups have developed an E-commerce Web site to deliver fresh fruits and vegetables directly to the consumer. The chests are used to deliver the fruits and vegetables to consumers. There are need and scope to optimize the present chest geometry to overcome the issues faced by the industry. Optimization is achieved either by maximizing desired factors or minimizing undesired ones for the

A. Netake · R. Mutha · A. Mishra · A. Sawant · P. Potdar (✉) · N. Panaskar
Department of Mechanical Engineering, Rajiv Gandhi Institute of Technology,
Versova, Mumbai 400058, India
e-mail: prathameshpotdar122@gmail.com

most cost-effective or highest achievable performance under the given constraints. This study focuses on optimization of chest geometry in the accomplishment of cost saving and space saving and material reduction. An essential part of moving goods from producer to consumer is storage and transportation packaging. Fresh fruit and vegetables have to arrive in excellent shape regardless of where they are coming from. Storage systems play an essential part in the logistic chain such as packing, transportation, handling, protecting, and stacking. The product geometry influences the experiences the user has with a product. Geometries are unique representations with specific properties to define them. The word geometry refers to the science of properties and relations of magnitudes such as points, lines, surfaces, or solids in space and the way the parts of a particular object fit together. Geometry optimization is used to find the best solution for a design objective, such as optimizing product shape, size, minimizing weight, enhancement of strength, identifying weaker design areas, stress analysis, and life-cycle improvement. The optimization process involves performing a series of simulations while adjusting design variables based on the results of the previous iteration. The process continues until the design objective is reached and the design satisfies all specified constraints. The important role of product optimization is to differentiate the product in the market competition and contribute to successful sales results. However, its primary task is to make a particular function possible. The primary task is not only to create an attractive product but also to fulfill its functions. Athanasios Babalisa and Ioannis Ntintakisa [1] sketched out and discussed many ideas of the packaging design that are produced through brainstorming. The ideas are then assessed, and the best of them are developed using Autodesk Inventor. Also, it concluded that the design for reuse of the packaging of any product is extremely rare, but can make a difference with consumer choice if it is offered. E. J. Oude Luttikhuis and J. de Lange [2] studied the necessity of the development of packing management, the waste of raw materials reused, and effective packing management and concluded that the most important elements of packaging language that have to be learned are the functions and the life-cycle packaging. The fundamental of packaging design is a valuable addition to packing development. P. Betancur-Munoz and G. Osorio-Gómez [3] identified guidelines and the optimization algorithm for packaging design with six stages, and the material consumption is calculated. Sher Paul Singh and John Antle [4] analyzed results from a major damage assessment study that examined challenges products endure during shipping and handling in the mixed-load and less than truckload (LTL) logistics environments. Srinath Srinivasan and Wen F. Lu [5] used pairwise comparison to compute the final rating of the packaging design from eco-cost rating, material cost rating, and rating of design values. Yi Yi, Ziyi Wang, and Ronald Wennersten [6] assessed the different type of boxes and bags with different materials—life cycle of delivery packages, namely production, utilization, and waste disposal. The wooden chests, cardboard boxes, and plastic crates are most commonly used for packaging and transportation of fruit or vegetables. The existing chest used in the market is not well optimized in terms of chest capacity and material utilization for storage and transportation. From the above literature review, it is clear that there is a need for optimization of existing chest geometry.

2 Methodology

The literature survey and market research recognized the scope to optimize existing chest geometry. This study focused on optimization of chest geometry in the accomplishment of cost saving, space saving, and material reduction. The capacity of the chest is identified to carry a certain amount of goods by making some assumptions. In the next step of methodology, the critical parameters are identified for geometry optimization. The shape, stackability, strength, ease of manufacturing, cost-effectiveness, and percentage storage utilization are the selected factors for geometry optimization. The competitive chest geometries of packaging design are sketched out and discussed through brainstorming and market research. The assumptions are made to calculate dimensions of the chest. The comparative study of competitive geometries is carried out based on the selected parameters. Stress analysis is used to analyze the stress behavior and to identify weaker areas present in the chest under two different loading conditions. The effect of load on various chest geometries of different thicknesses in stacking condition and single (due to a load of weight inside) is analyzed by considering changes in displacement (mm), Factor of safety, and Von Mises Stresses (MPa). The analysis has performed in Autodesk Inventor software by simulating the models. The optimum geometry which satisfies the most of the optimization parameters is determined for packaging, forwarding, and transportation with the use of the eco-friendly raw material (Fig. 1).

3 Identify Capacity of Chest

Fruits and vegetables are irregular in shape due to which it is very difficult to compute the volume of particular fruit and vegetable. The general assumptions are made to estimate the volume of the selected organic products is as follows.

(1) Mass of products in a chest is equal to 10 kg (constant).
(2) Product assumed to resemble nearest possible geometry for ease of calculation. For example, cabbage and tomatoes have a spherical geometry.
(3) Assumed average size of the selected product.
(4) Neglected the space and overlapping between products.

Table 1 shows that the volume and weight calculation; it shows that weight/volume ratio is lowest for cabbage. It means it occupies more space (volume) per kg as compared to others. The variation in product size is neglected, shape, and considered mixed products in a container. Random close packing (RCP) is an empirical parameter used to characterize the maximum volume fraction of solid objects obtained when they are packed randomly. RCP of spheres in 3D gives a packing density of 0.64, smaller than the optimal packing density for cubic or hexagonal close packing of 0.74,048. It implies that the maximum void space is around 36%.
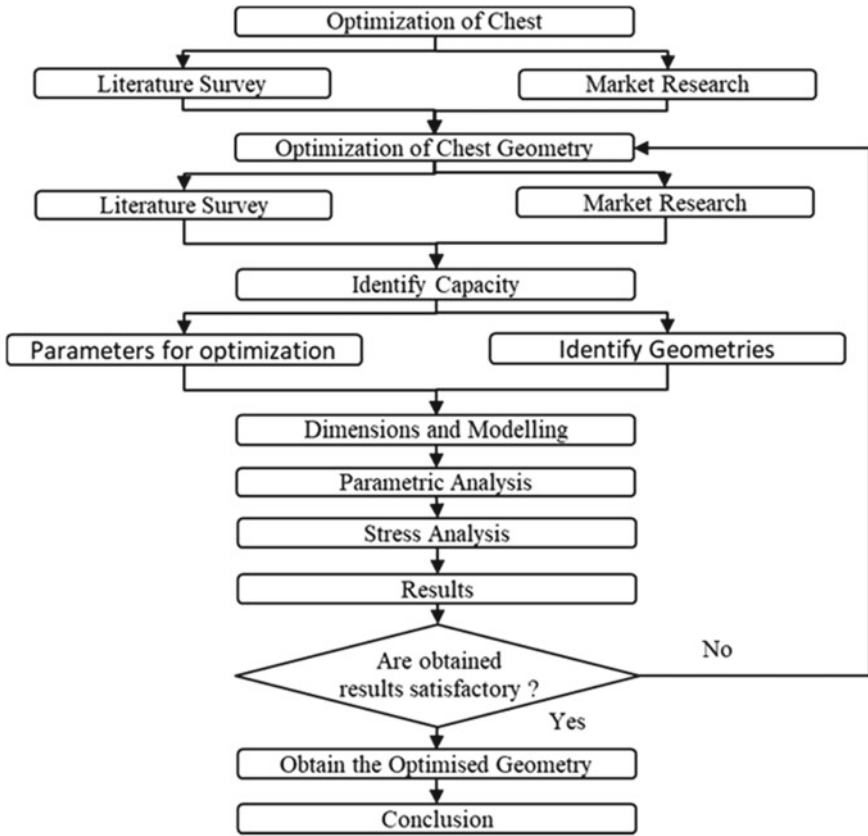
Fig. 1 Approach for chest optimization

Table 1 Volume calculation of fruits and vegetables

Sr. No.	Product	Dimension (cm)	Weight per unit (W) (gm)	Volume per unit (V) (cm^3)	Units in 10 kg	Volume of 10 kg (cm^3)	Weight/Volume (gm/cm^3)
1	Cabbage	$R = 8$	1000	2144.7	10	21.45×10^3	0.467
2	Cucumber	$14 \times 3 \times 3$	165	126	61	7.69×10^3	1.310
3	Potato	$R = 3.5$	200	179.6	50	8.98×10^3	1.114
4	Spinach	$D = 8; L = 20$	667	1005	15	15.08×10^3	0.664
5	Tomato	$R = 3$	115	113.1	87	9.84×10^3	1.017

Estimated capacity of the chest $=$ (maximum volume of the product)

$$+ \text{(Void space while packing)} + \text{(Neglected volume)}.$$
$$= \left(21.45 \times 10^3\right) + \left(0.36 \times 21.45 \times 10^3\right)$$
$$+ \left(0.3 \times 21.45 \times 10^3\right)$$
$$= 35,607 \text{ cm}^3 \tag{1}$$

However, the capacity of the chest available in the market is around $44 \times 32 \times 29 = 40{,}832$ cm^3. Hence, the volume of chest selected for maximum storage utilization is 36,000 cm^3.

3.1 Identification of Geometries

The taper angle is very important to stack the empty chests and for ease in handling. Through market research, competitive chest geometries of packaging design are sketched out and discussed. The optimization parameters are considered for the comparative study. Different shapes of chest obtained are triangular frustum, rectangular frustum, pentagonal frustum, hexagonal frustum, and circular frustum. The storage capacity of the triangular frustum is not utilized properly, due to an angle less than 90° between the walls of the chest and there is stacking problem. The pentagonal frustum is not easy to manufacture and do not show symmetry in shape. Hence, triangular and pentagonal chests are neglected. Chests selected for comparative study are rectangular frustum, hexagonal frustum, and circular frustum.

3.2 Parameters for Optimization of Chest Geometry
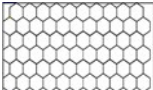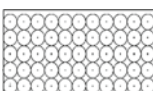
Based on the market research, critical parameters for selection are identified and discussed below:

Ease of Manufacturing: The chests which are easy to manufacture require less time and less workforce. Hence, the work aims to design the chest which is easy to manufacture.

Manufacturing cost: It includes material cost, labor cost, machine cost, and another cost. The work aims to lower the manufacturing cost of the chest and to make it more economical. Hence, the manufacturing cost for the production of the chest should be as low as possible.

Strength: Strength is the critical element in the design process. Higher the strength of chest, longer the life expectancy of the chest. Hence, the chest with good strength is selected.

Table 2 Percent storage utilization

Type of chest	Dimensions (cm)	Top view of chest arrangement	No. of chests in one layer	Total no. of chests in container	Total volume of chests (l)	Percentage utilization
Rectangular	$L = 47, B = 33$		70	490	19,600	89
Hexagonal	Diagonal dist. = 49		63	441	17,640	80
Circular	$D = 44$		55	385	15,400	70

Stackability: Stackability means how easily chests are arranged in stack/heap. Lesser the space acquired by the chest, it will provide ease in transportation and storage.

Storage utilization: Storage utilization is a measure of how efficiently the available storage space is used. Higher the percentage storage utilization, better the chest. In order to calculate percentage storage utilization of chests in transport container, consider container having length = 480 cm = 4.8 m; breadth = 231 cm = 2.31 m; height = 198 cm = 1.98 m (Table 2).

$$\text{Volume of the container} = \text{Length} \times \text{Breadth} \times \text{Height}$$
$$= a4.8 \times 2.31 \times 1.98 = 21.95 \, \text{m}^3$$
$$= 21,950 \, \text{L (approx. } 22,000 \, \text{L)} \tag{2}$$

The volume of chest becomes 40 L(considering material). Since height is constant (28 cm) for all chests,

$$\text{Max. no. of vertical layers of chest arrangement} = \frac{\text{Height of container}}{\text{Height of chest}}.$$
$$= 198/28$$
$$= 7 \, \text{(approx.)} \tag{3}$$

For rectangular chest:

$$\text{No. of chests in rows} = \frac{\text{Length of container}}{\text{Length of chest}}.$$
$$= 480/47$$
$$= 10 \text{ (approx.)} \tag{4}$$

$$\text{No. of chests in columns} = \frac{\text{Breadth of container}}{\text{Breadth of chest}}.$$
$$= 231/33$$
$$= 7 \text{ (approx.)} \tag{5}$$

$$\text{No. of chests in one layer} = 10 \times 7 = 70$$
$$\text{Total no. of chest} = 70 \times 7 = 490$$

$$\text{Percentage utilization} = \frac{\text{Total volume of chests}}{\text{Volume of container}}.$$
$$= (490 \times 40)/22000$$
$$= 89\% \tag{6}$$

Similarly, for hexagonal and circular chests, percentage utilization is 80 and 70%, respectively. From above, packing efficiency of the rectangular chest is higher than other chests.

4 Dimensioning and Modelling of Competitive Chests

Dimensions of chest are calculated by taking some assumptions, those are height = 28 cm (standard height 26 cm of FedEx box + 2 cm lid clearance); taper angle = − 5°; and volume = 36 L for maximum storage utilization (Fig. 2).
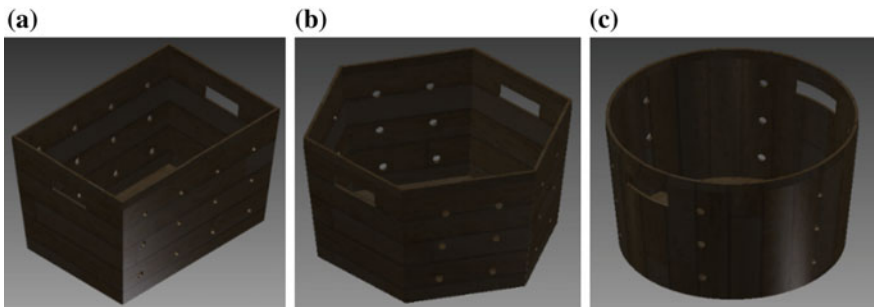
Fig. 2 Models with different chest geometries for comparison

4.1   Rectangular Chest

Rectangular geometry is one of the most basic/common structures used in day-to-day life for packaging. The reason to select the rectangular geometry is that of its ease in manufacturing, stackability, and its ability to consume less space while being stored and it is symmetric in shape. The dimensions of the rectangular chest are $L = 47$ cm; $B = 33$ cm; $H = 28$ cm.

4.2   Hexagonal Chest

From bees' honeycombs to the Gian's Causeway, hexagonal structures are prevalent in nature due to their efficiency. Hexagonal geometry resembles the strength, with more number of sides and number of corners are more in the hexagonal structure which provides good strength to the structure. The hexagonal shape is symmetric. The dimensions of the hexagonal chest are as follows: upper surface diagonal distance = 48.6 cm; height = 28 cm.

4.3   Circular Chest

The above two geometries have edges and corners. The idea of selecting the circular chest is because of its curvature geometry, hence to widen the scope of research. The dimensions of the circular chest are upper surface diameter = 44 cm and height = 28 cm. Chests are developed further through the use of CAD software like Autodesk Inventor.

5   Parametric Analysis

Comparative study of the three geometries versus the parameters is done which is shown in Table 3.

6   Stress Analysis

Structural analysis is the determination of the effects of loads on physical structure and their components. The structural analysis employs the fields of applied mechanics, material science, and applied mathematics to compute a structures deformation, internal forces, stresses, support reaction, displacement, and Von Mises Stress. The

Table 3 Comparative study of three chest geometries

Parameters	Rectangular	Hexagonal	Circular
Manufacturing cost	Low	Moderate	High
Ease of manufacturing	High	Moderate	Low
Strength	Moderate	High	Low
Stackability	High	Moderate	Low
Storage utilization	High	Moderate	Low

Applied load is 2500N

Displacement (mm)

Factor of Safety

Von Mises Stress (MPa)
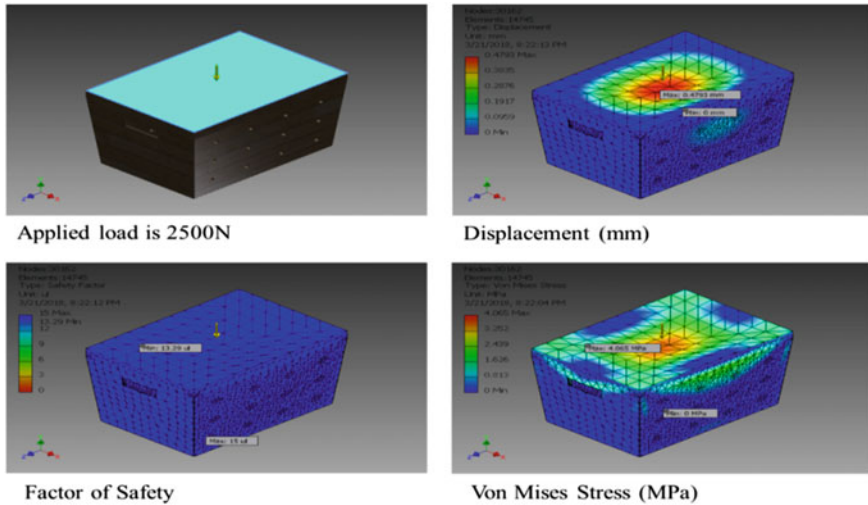
Fig. 3 Simulation of rectangular chest in stacking condition

material selected for study is maple wood. The effect of load on rectangular, hexagonal, and circular chest each of thickness 6, 8, and 12 mm in stacking condition and single (due to a load of weight inside) is analyzed by considering changes in displacement (mm), Factor of safety, and Von Mises Stresses (MPa). Structural analysis is done in Autodesk Inventor software by simulating the models as follows. From the structural analysis, chest with 12 mm thickness is found to be over-engineered, and 6-mm-thickness chest is found to be more economical, lightweight, optimum required strength for carrying goods (Figs. 3, 4 and Table 4).

Applied load is 200N

Displacement (mm)

Factor of Safety

Von Mises Stress (MPa)
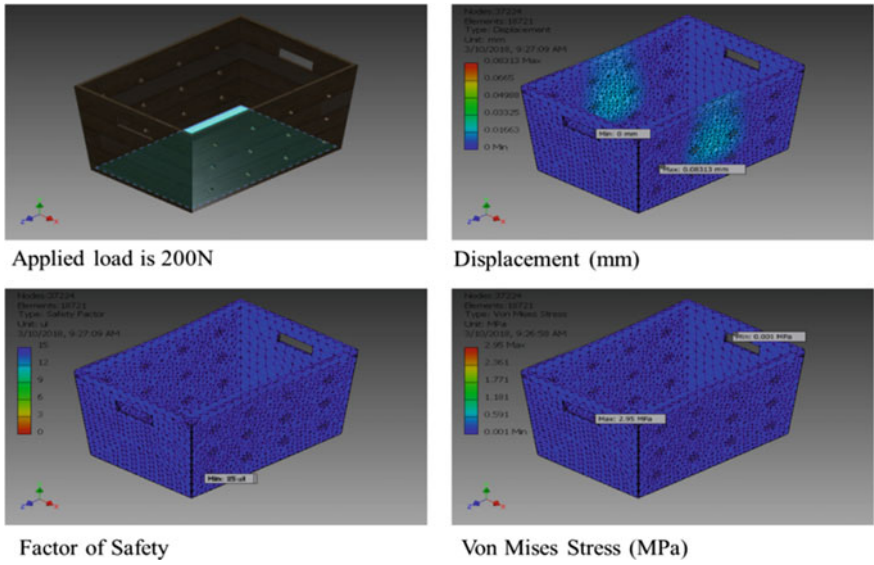
Fig. 4 Simulation of rectangular chest in single (due to load weight inside)

Table 4 Result of structural analysis of different types of chest

Type of chest	Thickness of the chest in mm	Displacement (mm)		Factor of safety		Von Mises Stresses (MPa)	
		Stack	Single	Stack	Single	Stack	Single
Rectangular	6	0–0.579	0–0.190	12.5–15	15–15	0–4.324	0–3.265
	8	0–0.479	0–0.083	13.3–15	15–15	0–4.064	0–2.950
	12	0–0.329	0–0.026	15–15	15–15	0–2.983	0–1.850
Hexagonal	6	0–0.650	0–0.222	12.1–15	12.5–15	0–4.448	0–4.334
	8	0–0.525	0–0.094	13.9–15	14.5–15	0–3.877	0–3.736
	12	0–0.377	0–0.031	15–15	15–15	0–3.088	0–2.260
Circular	6	0–0.582	0–0.206	10.7–15	15–15	0–5.046	0–2.555
	8	0–0.470	0–0.092	12.2–15	15–15	0–4.415	0–1.943
	12	0–0.358	0–0.030	15–15	15–15	0–3.060	0–1.380

7 Results

The following results obtained after comparative study:

1. Rectangular chest shows 89% of storage utilization, which is highest.
2. The strength of the rectangular chest is found to be moderate.
3. The manufacturing cost of the rectangular chest is lowest.

4. Ease of manufacturing for rectangular chest is highest.
5. Rectangular chest shows the highest stackability.
6. It found that reduced fatigue due to ease of handling in the rectangular chest.

8 Conclusion and Future Scope

In this research, the three geometries are compared based on selected optimization parameter. The result shows that the rectangular geometry is a better alternative than other geometries for chest. The displacement of the rectangular chest is less as compared to other geometries in the stack and single condition. The rectangular chest has less manufacturing cost, good stackability, high-storage utilization, ease of manufacturing as simple in geometry, and moderate strength as compared to other geometries. The geometry selection plays a very critical role in good design and to achieve design output. The final dimension of the rectangular chest is $L = 47$ cm; $B = 33$ cm; $H = 28$ cm. The identified dimension gives maximum storage capacity for selected volume, which gives the efficiency of 89%.

Future development of the work will consider the analysis of life cycle, environmental, and economic impacts. Develop the chest which can use for multi-purpose not only for carrying objects but can transform into the table, chair, etc., so that when it is not in used it should not be just lying down on floor to block space. The manufacturing processes should also be optimized for economic impact.

References

1. Athanasios B., Ioannis N., Dimitrios C.: Design and Development of Innovative Packaging for Agricultural Products. Procedia Technology 8 (2013) 575–579.
2. E.J. Oude Luttikhuis, J. de Lange, R. ten Klooster: Project-led Education in Packaging Development and Management. Procedia CIRP 21 (2014) 348–353.
3. P. Betancur, G. Osorio, J.F. Martínez, J.F. Duque: Integrating Design for Assembly Guidelines in Packaging Design with a Context-based Approach. Procedia CIRP 21 (2014) 342–347.
4. Sher P .S., John A., Jay S: Load Securement and Packaging Methods to Reduce Risk of Damage and Personal Injury for Cargo Freightin Truck, Container, and Intermodal Shipments. Journal of Applied Packaging Research 6 (2014) No.1, Article 6.
5. Srinath Srinivasan, WenF.Lu:Development of a Supporting Tool for Sustainable FMCG Packaging Designs. Procedia CIRP 15 (2014) 395–400.
6. YiYi , ZiyiWang, RonaldW., QieSun: Lifecycle Assessment of Delivery Packages in China. Energy Procedia 105 (2017) 3711–3719.

Part II
Advanced Materials

Experimental Investigations of Mechanical Properties and Microstructural Characterization of Aluminum–Silicon Alloy Castings

D. M. Wankhede, B. E Narkhede, S. K. Mahajan and C. M. Choudhari

Abstract Casting process enables the economical manufacture of products with intricate geometry to near net shape. Almost all metals and alloys are produced from liquids by solidification. The objective of the study is to find the impact of pouring temperature and chill thickness on aluminum–silicon (LM6) castings. The casting parameters such as pouring temperature and external mild steel and copper chills are considered for the experimental work. The simulation has been done using AutoCAST-X1 software to identify the hot spot and locate the shrinkage defect. The experimentation has been conducted with no chill, mild steel chills and copper chills with varying thicknesses. In this work, an attempt has been made to obtain the rapid cooling rate of aluminum–silicon (LM6) castings using external chills. It is observed that the chill has a significant effect on the properties of the castings. The design of the experiment has been set up, and experiments were conducted as per the full factorial array. Castings are made by controlling the casting process parameters at three different levels. The regression models of ultimate tensile strength and hardness have been developed with predictors. The better mechanical properties were obtained by controlling pouring temperature and the application of external chills.

D. M. Wankhede (✉)
Department of Production Engineering, Veermata Jijabai Technological Institute,
Mumbai 400019, India
e-mail: dmwankhede99@gmail.com

B. E Narkhede
Industrial Engineering and Manufacturing Systems Group, National Institute of Industrial
Engineering (NITIE), Near Vihar Lake, Powai, Mumbai 400087, India
e-mail: benarkhede@nitie.ac.in

S. K. Mahajan
Technical Education, Maharashtra State, Mumbai 400072, India
e-mail: skmahajan@dte.org.in

C. M. Choudhari
Department of Mechanical Engineering, Dwarkadas J. Sanghvi College of Engineering,
Mumbai 400756, India
e-mail: c.choudhari75@gmail.com

1 Introduction

Metal casting is one of the most ancient techniques used for manufacturing metal parts. The process consists of producing metallic objects by melting and pouring of metal into the pre-shaped cavity of a mold and allowing it to solidify. Solidification of metals continues to be a phenomenon of great interest to physicists, metallurgists, and software developers. This being a nonlinear transient phenomenon presents challenges in terms of modeling and analysis [1, 2]. The influence of various casting parameters such as pouring temperature and chill thickness has been studied to improve the mechanical properties of metal castings. Kanthavel [3] investigates the effect of mild steel chills on steel casting in the sand mold to minimize shrinkage defects. In this investigation, four parameters are considered, namely chill distance, chill thickness, pouring temperature and pouring time to minimize the shrinkage defects. Spinelli et al. [4] carried out directional solidification experiments, and the relation between the tensile properties, thermal parameters, and microstructure has been developed. The relationships between the interfacial heat transfer coefficient and ultimate tensile strength have been developed for hypoeutectic alloys. Ramesh et al. [5] studied the light alloy solidification behavior of aluminum for the casting process, mold materials used, and other casting parameters. The chill had an effect on a solidification behavior and important promoter of directional solidification. The experimental study has been done on Al 6061-SiCp alloy to find the solidification behavior of castings in a sand mold using external chills. The copper chills show the larger cooling rates during the solidification. The predicted and experimental solidification rates of the casting were in good agreement as analyzing ANSYS finite element analysis software. Ahmed et al. [6] studied an experimental investigation of Al–Si cast alloy (LM6) on green sand castings. The sand-casting quality of LM6 alloy has been affected significantly by pouring temperature. It has been observed that the less porosity defect occurred at lower pouring temperature. Chen et al. [7] studied the influence of pouring temperature on the mechanical properties and the structure of casting alloy. With the increase in pouring temperature, the tensile strength and yield strength of magnesium alloy castings are rapidly increased first and then reduced. Anantha Prasad et al. [8] studied the stir cast composites of LM13 along with carbon reinforcements. The various external chills were used to enhance the solidification. The analysis of properties such as hardness and ultimate tensile strength of casting has been done. Anilkumar et al. [9] evaluated the effect of cryogenic cooling rate on ultimate tensile strength (UTS), dendrite arm spacing, and the hardness. It has been investigated that the UTS is highly dependent on the rate of cryogenic effect and chilling which determines the dendrite arm spacing of the material. Benjuniora et al. [10] investigated that the fast cooling rate condition produced smaller grain size as compared to the slow cooling rate condition as per the results obtained in

microstructure. Chills are provided in the mold so as to increase the heat extraction capability of the sand mold. A chill normally provides a steeper temperature gradient so that directional solidification as required in a casting can be obtained. The chills are metallic objects having a higher heat absorbing capability than the sand mold. The proper use of chills helps in controlling the localized heat and cooling rate of the cast metal. The mechanical properties and microstructure of LM6 alloy castings can be improved by using the external chills. The external mild steel chills and copper chills have been used to enhance the cooling rate of castings during solidification. The input parameters such as pouring temperature and varying chill thickness have been considered for the experimental work. The design of experiment (DOE) is used to optimize the casting parameters. The rapid cooling rate gives a fine grain structure, which improves the mechanical properties of castings. By controlling the casting pouring temperature and chill size, better mechanical properties can be achieved.

2   Experimental Work

The 30-mm-square bar with 200 mm length has been selected for the experimental work. The mold was prepared with external chills. The experiments were carried out on aluminum–silicon (LM6) alloy with no chills, mild steel chills (MS), and copper chills using sand-casing method. The temperature of the casting and chill has been measured at one minute of intervals with the help of K-type thermocouple placed at the edge of casting and external chills. A data logger and millivoltmeter were used to measure the temperature with the help of thermocouple. The effect of pouring temperature, mild steel, and copper as an external chills has been considered for the experimental investigation. The design calculations for gating system have been done. The simulation work has been done using AutoCAST-X1 software. The soundness of the casting has been given the upmost priority, and then, the subsequent experiments have been performed for the improvement of mechanical properties.

The simulation has been done using AutoCAST-X and AutoCAST-X1 software to get the correct design parameters and identifying the proper placement of riser. This helps in eliminating the major casting defects such as shrinkage and porosity. Few important simulation results are shown in Fig. 1a, b.

The experimental work has been carried out on a rectangular component of Al–Si (LM6) alloy. The schematic of the node locations for temperature measurement of casting and mild steel/copper chills using thermocouple is shown in Fig. 2. The temperature readings are obtained during experimental trials at two predetermined locations (1 and 2) for the rectangular casting component as shown in Fig. 2. The temperature history has been recorded by placing the thermocouples at the right end of casting and at the edge of chill near casting chill interface.

The ultimate tensile strength (UTS) and hardness have been measured using universal testing machine (UTM) and Vickers's hardness test method, respectively. The sand-casted component has been converted as per ASTM-B557 standard for tensile test measurement [11]. The hardness test has been done on casted component as per

(a) Casting with external chills

(b) Shrinkage defect elimination
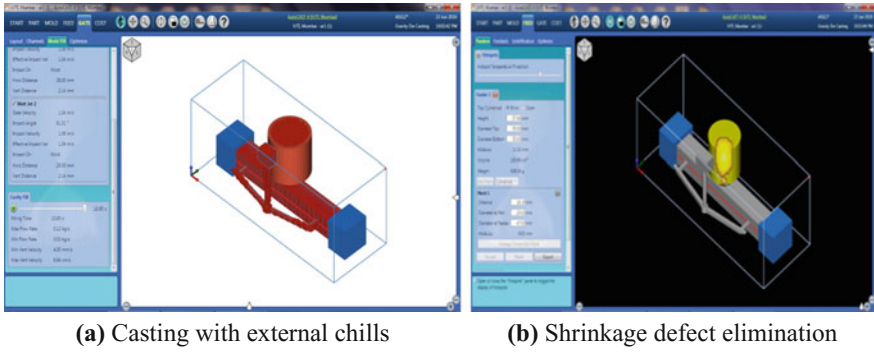
Fig. 1 **a** Casting with external chills. **b** Shrinkage defect elimination
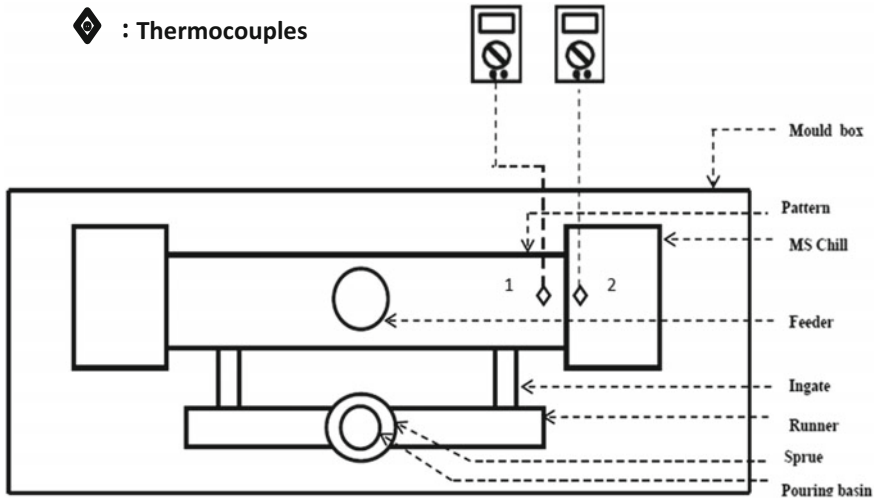
Fig. 2 Schematic for the locations of temperature measurement using thermocouple

ASTM-E384 standard. The design of experiment (DOE) has been set up at three different levels. The 30-mm-square rectangular bar of length 200 mm is cast as per simulation process. The mild steel/copper chills are used on both the ends of casting, which leads to directional solidification and helps in enhancing the mechanical properties of castings. The experiment trials have been carried out in the foundry. Total twenty-seven castings were taken out with varying pouring temperature and external chill thickness. An experiment was conducted using mild steel/copper chills with different thicknesses, i.e., 35, 45, and 55 mm. The pouring temperatures were taken as 730, 750, and 770 °C. The experimental layout is shown in Figs. 3 and 4a, b.

The levels of casting parameters have been identified for experimental investigation. Experiments have been arranged for all possible combination of these factors

(a) Casting with chills   (b) Casting with milliVoltmeter

Fig. 3 **a** Casting with chills. **b** Casting with millivoltmeter

(a) Casting samples before machining   (b) UTS test casting samples after machining
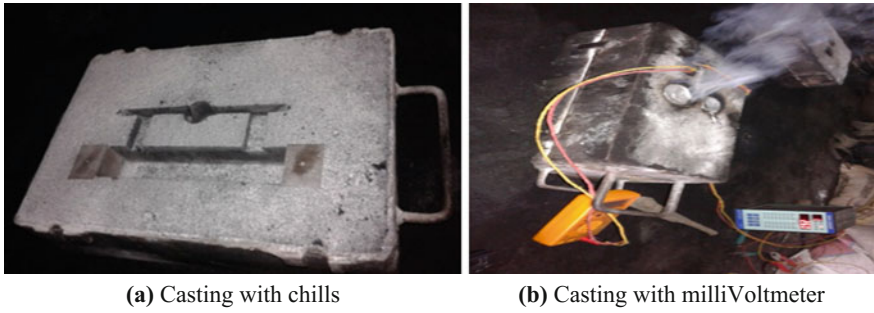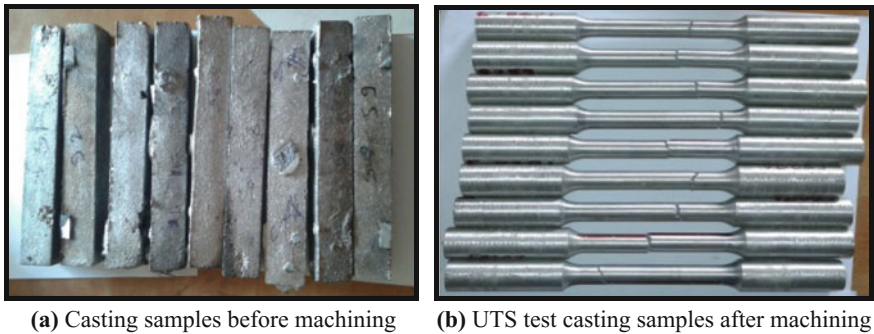
Fig. 4 **a** Casting samples before machining. **b** UTS test casting samples after machining

Table 1 Levels of casting parameters

Casting parameters	Code	Level 1	Level 2	Level 3
Pouring temperature (°C)	X_1	730	750	770
Chill thickness (mm)	X_2	35	45	55

and their levels using the design of experiment. Table 1 shows the input factors and their levels.

The selection of a particular array is depending on the number of levels and factors. The interaction graph of UTS and hardness is as shown in Fig. 5a, b using mild steel chills and Fig. 6a, b using copper chills.

The regression analysis is performed using statistical analysis software Minitab 14. It gives the relationship between ultimate tensile strength and hardness with mild chill size and pouring temperature. The regression equations for ultimate tensile strength and hardness in relation with pouring temperature and mild steel chills are shown in Eqs. 1 and 2 given below.
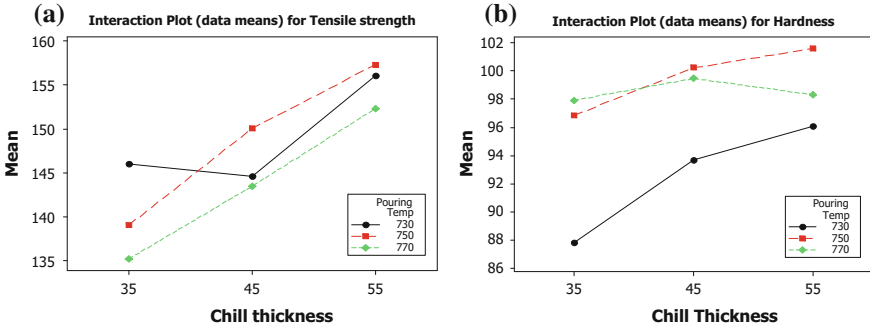
Fig. 5 **a** Interaction plot of pouring temperature, mild steel chill thickness versus UTS. **b** Interaction plot of pouring temperature, mild steel chill thickness versus hardness
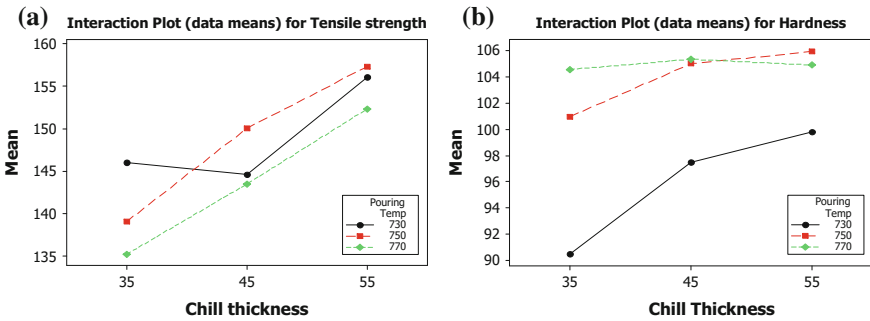
Fig. 6 **a** Interaction plot of pouring temperature, copper chill thickness versus UTS. **b** Interaction plot of pouring temp, copper chill thickness versus hardness

The regression equation of tensile strength is

$$Y_1 = 211.47 - 0.1309X_1 + 0.7517X_2 \tag{1}$$

The regression equation of hardness is

$$Y_2 = -56.95 + 0.1925X_1 + 0.222X_2. \tag{2}$$

The regression equations for ultimate tensile strength and hardness in relation with pouring temperature and copper chills are shown in Eqs. 3 and 4 given below.

The regression equation of tensile strength is

$$Y_1 = 209.64 - 0.1123X_1 + 0.6728X_2 \tag{3}$$

The regression equation of hardness is

(a)   **(b)**   **(c)**
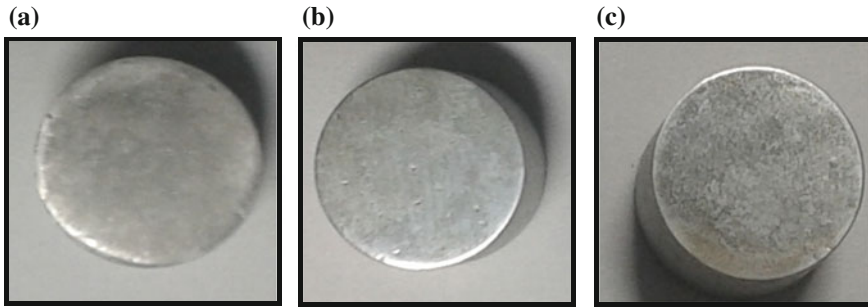
Fig. 7 a–c Casting sample with no chill, mild steel, and copper chills

(a)   **(b)**   **(c)**
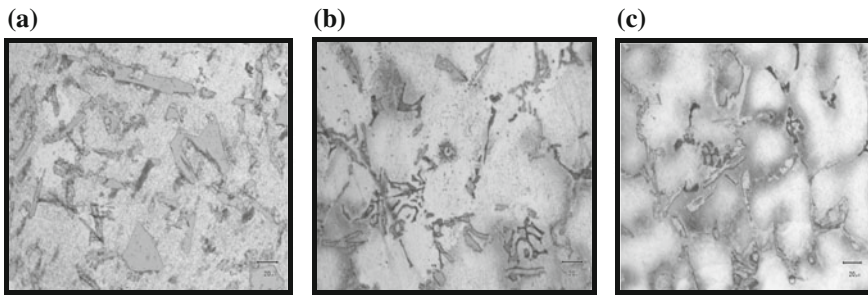
Fig. 8 a Microstructure with no chill at pouring temp 730 °C. **b** Microstructure with chill (mild steel chills) at pouring temp 730 °C. **c** Microstructure with chill (copper chills) at pouring temp 730 °C. (500× magnification)

$$Y_2 = -78.4874 + 0.2255X_1 + 0.2436X_2 \tag{4}$$

The microstructure analysis has been done on sand-casted aluminum–silicon (LM6) alloy samples at 730 °C pouring temperature. The specimens were prepared by polishing using standard metallographic techniques. The specimens were prepared by polishing using standard metallographic techniques. Keller's reagent was used to etch the samples. The Olympus GX-51 optical microscope was used for getting micrograph images. The casting specimens for microscopic analysis without and with the application of mild steel and copper chills are as shown in Fig. 7a–c. The micrographs (500× magnification) of casting samples without and with the application of mild steel and copper chills are as shown in Fig. 8a–c.

The coarse primary silicon particles have not seen in casting after the application of mild steel and copper chills. The micrograph shows very less primary coarse silicon particles. The interdendritic network of silicon particles has been observed. The fine grain structure has been obtained which lead to better microstructure as compared to casting without the application of external chills. The grain structure from the micrograph clearly indicates that the good microstructure gives better mechanical properties.

Fig. 9 Pouring temperature versus UTS
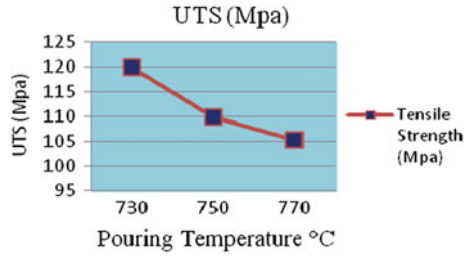
Fig. 10 Pouring temperature versus hardness
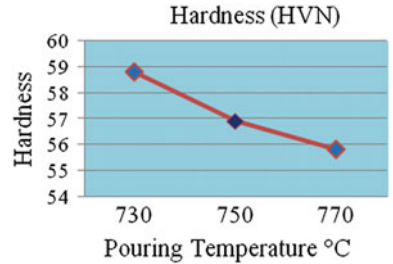
2.1 Experiment with no External Chills

The simulation work is carried out using AutoCast-X1 software without the application of external chills. The experiment trials have also been carried out in the foundry. The pouring temperature has been controlled as per the three specified levels (Table 1). The experiment has been carried out with no external chills. The graphs of pouring temperature versus mechanical properties are as shown in Figs. 9 and 10.

The pouring temperature of molten metal and temperature of casting have been measured using millivoltmeter and data logger TC 1600. The graph of pouring temperature versus cooling rate for every five minutes during casting solidification of no chills and after using mild steel and copper chills is as shown in Fig. 11a–c, respectively. The cooling rate is drastically enhanced after the application of external chills.

The comparison charts of ultimate tensile strength and hardness values of no chill, mild steel chills, and copper chills are as shown in Figs. 12 and 13.

The UTS and hardness values of castings are found better by using copper chills as compared to mild steel and no chill.

3 Results and Discussion

An experimental work has been conducted in the foundry to find out the effect of pouring temperature and no chills, mild steel, and copper chill thickness on properties of Al–Si (LM6) alloy castings. The interaction plot Fig. 6a shows that there is a combined effect of chill thickness and pouring temperature on the UTS, and it
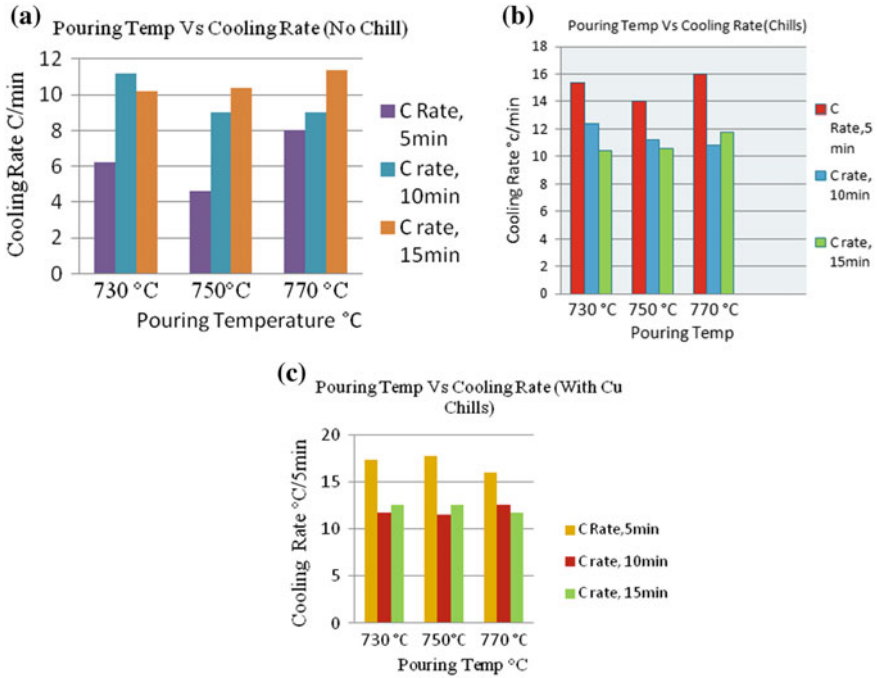
Fig. 11 Graph of pouring temperature versus cooling rate. **a** No chills. **b** With mild steel chills. **c** With copper chills
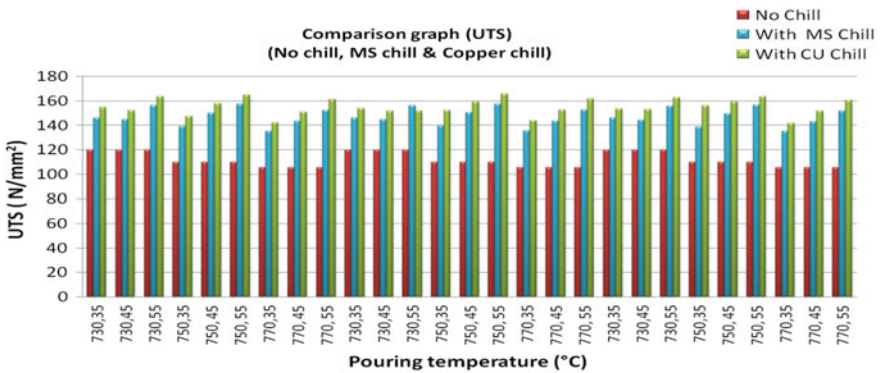
Fig. 12 Comparison graph of No chill, MS chill and Copper chill for UTS

has been found highest at 730 °C with 55 mm chill thickness. The hardness value was found highest at 750 °C with 55 mm chill thickness as shown in Fig. 6b. The micrograph of aluminum–silicon alloy with the application of mild steel and copper chills shows a better grain structure. The combined effect of controlled input parameters on UTS value was found better at lower pouring temperature with high chill
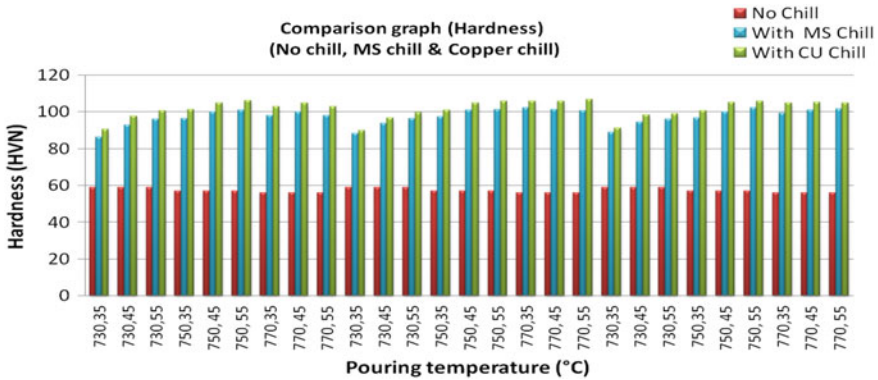
Fig. 13 Comparison graph of no chills, mild steel chills, and copper chills for hardness

thickness. The hardness value was found higher at moderate pouring temperature with high chill thickness. The cooling rate has been increased by the application of external chills. The mechanical properties and microstructures are found better by the application of copper chills compared to mild steel and no chills.

4 Conclusion

The following conclusions have been drawn from this study:

- The controlled casting process parameter and external chills help to give better mechanical properties.
- The external mild steel and copper chills help to get the directional solidification and also have a good impact on mechanical properties of aluminum alloy (LM6) castings.
- The external mild steel and copper chills help to improve the cooling rate of solidification of casting. The faster cooling rate gives a better grain structure, which improves the properties of castings.
- The ultimate tensile strength and hardness were found better with the application of external chills at 55 mm chill thickness.
- The better values of ultimate tensile strength and hardness were obtained as compared to casting without applications of external chills.
- The linear regression analysis shows that with an increase in pouring temperature, the UTS reduces and the hardness increases. The UTS and hardness increase with an increase in chill thickness.
- The castings with the application of external copper chills have found better microstructure compared to castings with mild steel chills and no chills.
- Therefore, the similar attempts can be made on any machine components which will provide improvement in its mechanical properties.

References

1. Narkhede, B.E., Choudhari, C.M., Mahajan, S.K., Modelling and Simulation for Optimum Design and Analysis of Riser in Sand Casting with Experimental Validation, Applied Mechanics and Materials: Trans Tech Publications, 465–466, 657–661 (2014)
2. Choudhari, C.M., Narkhede, B.E., Mahajan, S.K., Methoding and simulation of LM 6 sand casting for defect minimization with its experimental validation, - Procedia Eng, 97, 1145–1154 (2014)
3. Kanthavel, K., Arunkumar, K., Vivek, S., Investigation of chill performance in steel casting process using Response Surface Methodology, Procedia Eng, 97, 329–337 (2014)
4. Spinelli, J.E., Cheung, N., Goulart, P.R., José, M.V., Quaresma and Amauri, G.: Design of mechanical properties of Al-alloys chill castings based on the metal/mold interfacial heat transfer coefficient. Int J Therm Sci, 51, 145–154 (2012)
5. Ramesh, C. S., Jagdeesh, S. K., Keshavamurthy, R., Solidification studies on sand cast Al 6061-SiCp composites, J Alloys Compd, 509S, 371–374 (2011)
6. Ahmed, R., Talib, N.A., Asmael, M.B.A., Effect of pouring temperature on microstructure properties of Al-Si LM6 alloy sand casting, Applied Mechanics and Materials, 315, 856–860 (2013)
7. Chen, S., Chang, G., Huang, Y., Liu, S., Effects of melt temperature on as-cast structure and mechanical properties of AZ31B Magnesium alloy, Trans. Nonferrous Met. Soc, 23, 1602–1609 (2013)
8. Anantha Prasad, M.G., Bandekar, N., Study of Microstructure and Mechanical Behavior of Aluminum/Garnet/Carbon Hybrid Metal Matrix Composites (HMMCs) Fabricated by Chill Casting Method, Procedia Material Science, 3, 1–8 (2015)
9. Anil Kumar, B.K.., Ananthaprasad, M.G., GopalaKrishna., K. (2017). "Effect of Cryogenic Chill on Dendrite arm spacing, Ultimate tensile strength and Hardness of ASTM A494 M Grade Nickel alloy Metal Matrix Composites". Materials Today: Proceedings, Vol. 4, pp. 10769–10778
10. Benjuniora, B., Ahmada, A.H., Rashidia, M., Rezaa, M.S. (2017). "Effect of Different Cooling Rates Condition on Thermal Profile and Microstructure of Aluminium 6061". Procedia Engineering, Vol.184, pp. 298–305
11. ASTM B557-15 Standard Test Methods for Tension Testing, https://www.astm.org/standards/B557.htm

Multiobjective Optimization in Drilling of Composites

Paramjit Thakur, S. N. Teli and Siddhesh Lad

Abstract Composite laminates such as carbon fiber-reinforced polymer (CFRP) composite, glass fiber-reinforced polymer (GFRP) are attractive for many applications such as aerospace and aircraft structural components due to their superior properties. CNC drilling is the major operation which is performed on CFRP for joining these kinds of materials, due to its poor weldability. But, the major problem associated with CNC drilling of CFRP is the delamination effect which not only degrades the quality of the product but also reduces the fatigue life of the material. However, as delamination effect decreases, the material removal rate also decreases. Therefore, this work deals with the multiobjective optimization of drilling parameters in machining of CFRP considering delamination effect and material removal rate as the responses. In this work, the process parameters considered are speed, feed rate, and diameter of the drill bit. The Taguchi design of experiment was used for obtaining the setting. Out of the entire orthogonal array, L27 orthogonal array was used for the experimental setting. The delamination effect was obtained and calculated by scanning electron microscopy. Further, the fuzzy logic was applied, and the combined effects of both the responses were obtained which is called multiresponse index. The application of fuzzy logic gave an improvement of about 21% in multiresponse index.

Keywords CFRP · CNC drilling · Fuzzy · Membership function
Delamination factor

P. Thakur · S. Lad
Saraswati College of Engineering, Navi Mumbai, India
e-mail: paramjit3010@gmail.com

S. Lad
e-mail: jsiddh_10@ymail.com

S. N. Teli (✉)
Bharati Vidyapeeth College of Engineering, Navi Mumbai, India
e-mail: shivanandteli@yahoo.com

1 Introduction

CFRP has got a vast range of applications in the aviation industry due to its high strength and less weight, very less corrosion resistance, and durability. It is used in the surfaces of the aircraft and internal cabin parts [1]. The CFRP is made by hand layup method, autoclave molding techniques, and compression molding. Mostly, these materials are made to near net shape. However, they are requiring secondary machining processes like CNC drilling for joining operation due to its poor weldability. The CNC drilling with twist drill bits is the most frequent operation applied of drilling this composite [2]. But, CNC drilling operation leads to the severe damage to the composite called delamination which peels of the lamellae from the top and the bottom surface. This delamination effect not only hampers the quality of the product but also affects the fatigue life of the material to the greater extent. Many authors have worked on drilling of such composites which are explained further. Jayabal and Natarajan [3] investigated the effect of control factors, namely feed rate, drill bit diameter and speed on thrust force and tool wear in drilling holes in coir fiber composite. They also found the optimum process parameters in drilling of coir composite by the application of genetic algorithm and found the improvement in the responses. Dini [4] also predicted the delamination effect by ANN (forward propagation) and found the average error to be within the acceptable limit. Enemuoh et al. [5] applied multilayered perceptron (ANN) for the prediction of delamination effect and roughness in CNC drilling of composite. The prediction results showed good agreement with the experimental values of roughness and delamination factor. Saravanan et al. [6] performed the multiobjective optimization in drilling of CFRP composite. The authors applied a genetic algorithm and found an improvement of 10% in the multiple responses. Further, the results were compared with the results obtained by finite element analysis, which showed GA to be the better technique. Karthikayan et al. [7] applied fuzzy logic and genetic algorithm in optimization of drilling parameters in machining of Al/SiCp composite. The fuzzy logic was used for the prediction of the responses or modeling purpose, and genetic algorithm was used for finding the optimal process parameters. The optimal process parameters gave better results as compared to the previous values.

The complete literature study in drilling of fiber-reinforced composite showed that very less work is done in the area of multiobjective optimization of drilling of CFRP composite considering delamination effect and material removal rate as the responses. Further, most of the authors have used genetic algorithm, ANN, etc., as the optimization tool, and the application of fuzzy logic is yet to be reported in the literature. Hence, this work deals with the multiobjective optimization of drilling parameters in CNC machining of CFRP composite with delamination factor and material removal rate as the responses. The Taguchi design of experiment is used for getting the settings for the experimentation. Here, L27 orthogonal array is used with the control factors, namely speed, feed rate, and diameter of drill bit. Both, the responses are obtained after experimentation, and they are fed as the inputs to the fuzzy logic, and the combined effect of the responses is found as the output

which is named as multiresponse index. And, higher the value of this index, better is the combined effect. Further, the optimal process parameters are obtained, and the confirmation test is done.

2 Material and Experimentation

The CFRP material is fabricated by hand layup method. The thickness of each layer of carbon fiber used in this work is around 0.05 mm. The orientation of the fiber after every layup is kept perpendicular to each other. The fiber used for this material is continuous in nature and has uniform strength in both the directions. A bidirectional woven CFRP composite is shown in Fig. 1. The CNC drilling operation was performed on Makino vertical milling center (S33 APC) with the maximum spindle speed of 13,000 rpm. The Taguchi design of experiment is used to form the required number of settings for the experimentation. The L27 orthogonal array is used with three levels of each control factor. Here, three control factors with three level are used, namely spindle speed (1200, 1500, 1800) rpm, feed speed (0.15, 0.2, 0.25) rpm, and the diameter (8, 10, 12) mm of the drill bit. For each setting, the three sets of experiments are conducted and the average of all them is represented in table. The mechanical properties of CFRP used in this work are as follows: tensile strength (3.5 GPa), density (1.75 g/m^3), resin (epon resin 8132), viscosity of resin (5.8 poise).

2.1 Delamination Factor

Delamination is defined as the ratio of the maximum diameter (D_{max}) of the observed delamination zone (dashed black circle) to the nominal diameter (D_{min}) of the drilled hole (solid white circle).

$$F_d = D_{max}/D_{min} \tag{1}$$

where, F_d = delamination factor. The delamination is illustrated in Fig. 2.

3 Fuzzy Logic System

The fuzzy logic performs the following operation to convert the multiple inputs to single output: fuzzification, generation of fuzzy rules, application of inference engine, and defuzzification. The complete operation is shown in Fig. 3.

In fuzzification, the real-world data or crisp data is converted into fuzzy data with the help of membership functions and linguistic variables. The membership function has got the values from 0 to 1. From the literature, it is found that trapezoidal
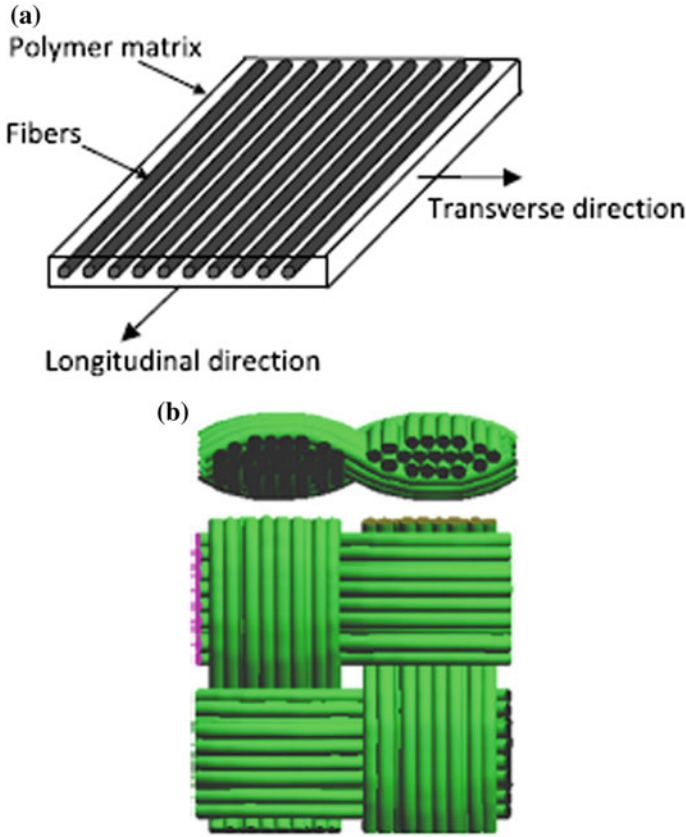
Fig. 1 **a** Unidirectional fiber orientation ply. **b** Bidirectional fiber orientation ply (woven ply)

Table 1 If-then rules formulation

MRPI	S/N ratio for MRR			
		Small	Medium	Large
S/N ratio for S/R	Small	Very small	Small	Medium
	Medium	Small	Medium	Large
	Large	Medium	Large	Very Large

membership gives better results as compared to the others, especially in machining processes. Hence, trapezoidal membership function is used in this study, which is shown in Fig. 4.

The next step is if-then rule base which generally depends on the experience of the user. The complete if-then statements for this work are given below, and it is formulated from the linguistic variable shown in Table 1.

Fig. 2 Delamination effect
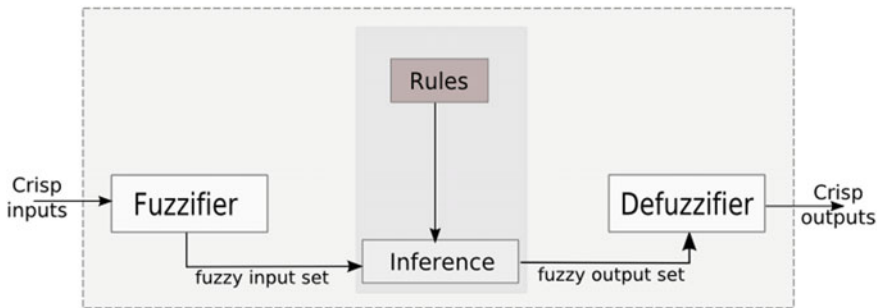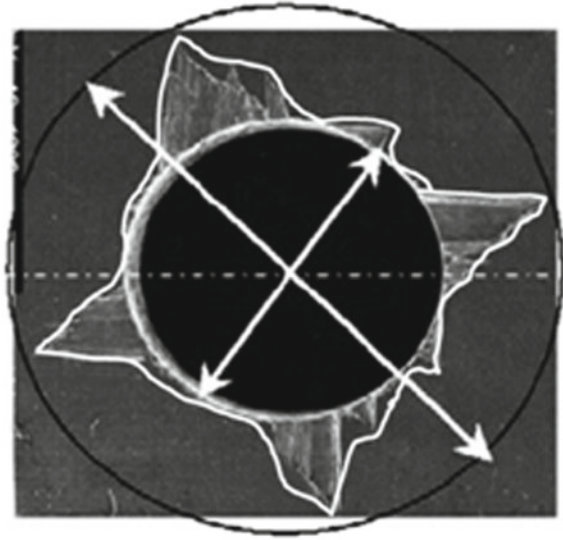
Fig. 3 Fuzzy logic system

If then rules:

- If (S/N of D_f is small) and (S/N of MRR is small), then (MRPI is very small)
- If (S/N of D_f is small) and (S/N of MRR is medium), then (MRPI is small)
- If (S/N of D_f is small) and (S/N of MRR is large), then (MRPI is medium)
- If (S/N of D_f is medium) and (S/N of MRR is small), then (MRPI is small)
- If (S/N of D_f is medium) and (S/N of MRR is medium), then (MRPI is medium)
- If (S/N of D_f is medium) and (S/N of MRR is large), then (MRPI is large)
- If (S/N of D_f is large) and (S/N of MRR is small), then (MRPI is medium)
- If (S/N of D_f is large) and (S/N of MRR is medium), then (MRPI is large)
- If (S/N of D_f is large) and (S/N of MRR is large), then (MRPI is very large).
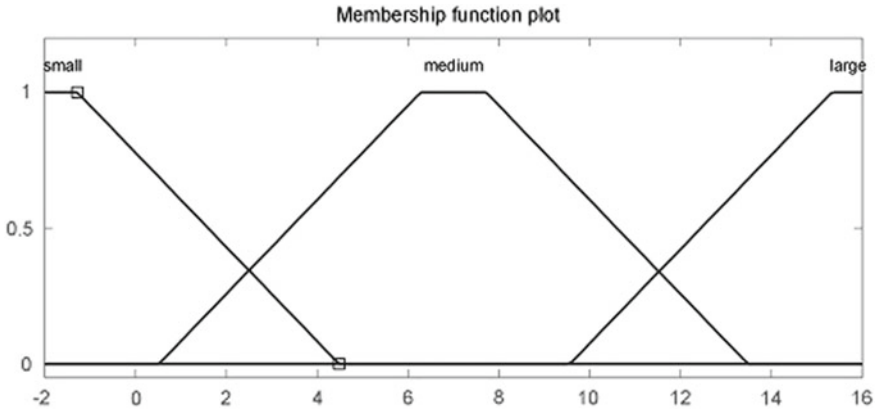
Fig. 4 Trapezoidal membership function

All the results need to be combined in a single value. This work is done by the inference engine. Finally, the combined values obtained from the inference engine are defuzzified to convert the fuzzy data into real-world data or crisp data.

4 Experimentation and Analysis

After doing drilling on the CFRP composite plate, we measured the delamination factor and material removal rate which are shown in Table 2.

Table 3 illustrates the average MRPI of all the three levels of the process parameters. The optimal process parameters for this work are selected which are diameter (012 mm), speed (1800 rpm), and feed (0.15 rev/min). The level with maximum average MRPI value is selected as the optimum level of process parameters.

Table 4 illustrates the results obtained from the confirmation test by the optimal process parameters. The comparison of the results obtained from the confirmation test and the results obtained from the use of initial parameters showed an improvement in MRPI by 0.21. The delamination factors decreased from 1.6 to 1.1, and the material removal rate increased from 14,000 to 47,000 mm^3/min.

5 Results and Discussions

The following parameter setting has been identified from Table 3 as to yield the best combination of speed 1200 rpm, feed rate 0.15 mm/rev, and drill 8 mm. The experimental results showed that there is a significant improvement in delamination and material removal rate as illustrated in Table 4. By this investigation, the optimized

Table 2 Actual run process sheet

Dia. (mm)	Feed (mm/rev)	Speed (rpm)	Nominal Dia. (D_{min})	Max. Dia. (D_{max})	Delamination factor (F_d)	MRR (m³/min)	MRPI
8	0.15	1200	7.93	12.27	1.5472	8.912	0.869
8	0.15	1500	7.99	11.89	1.4881	11.140	0.769
8	0.15	1800	8.08	10.34	1.2797	13.368	0.5
8	0.2	1200	8.05	11.83	1.4695	11.883	0.687
8	0.2	1500	7.95	9.75	1.2264	14.854	0.478
8	0.2	1800	7.98	9.56	1.1979	17.825	0.472
8	0.25	1200	7.98	12.4	1.5538	14.854	0.791
8	0.25	1500	8.16	11.02	1.3504	18.567	0.549
8	0.25	1800	8.07	11.59	1.4361	22.281	0.58
10	0.15	1200	9.52	12.96	1.3613	12.812	0.501
10	0.15	1500	9.55	11.81	1.2366	16.015	0.498
10	0.15	1800	9.55	11.29	1.1821	19.218	0.468
10	0.2	1200	9.54	12.14	1.3	17.083	0.308
10	0.2	1500	9.53	11.39	1.1951	21.354	0.515
10	0.2	1800	9.56	10.8	1.1297	25.625	0.489
10	0.25	1200	9.54	12.5	1.3102	21.354	0.597
10	0.25	1500	9.53	12.09	1.2686	26.692	0.772
10	0.25	1800	9.55	11.31	1.1842	32.031	0.573
12	0.15	1200	12.79	14.16	1.1071	22.801	0.443
12	0.15	1500	12.74	13.9	1.091	28.502	0.5
12	0.15	1800	12.76	13.62	1.0673	34.202	0.5
12	0.2	1200	12.72	15.02	1.1808	30.402	0.5
12	0.2	1500	12.74	14.4	1.1302	38.003	0.509
12	0.2	1800	12.74	14.99	1.1766	45.603	0.466
12	0.25	1200	12.73	15.15	1.19	38.003	0.584
12	0.25	1500	12.73	14.89	1.1696	47.503	0.414
12	0.25	1800	12.82	14.5	1.131	57.004	0.223

Table 3 Average MRPI of process parameters

	Initial machining parameters (industry)	Final machining parameters (fuzzy logic)
D_f	1.6	1.1
MRR (mm³/min)	14000	47,000
MRPI	0.58	0.79
Improvement in MRPI = 0.21		

Table 4 Results of confirmation test

Symbol	Machining parameters	MRPI		
		Level 1	Level 2	Level 3
A	Diameter (mm)	0.52	0.50	0.58
B	Speed (rpm)	0.41	0.51	0.59
C	Feed (mm/rev)	0.56	0.47	0.48

process parameters would solve the problems of fatigue faced by the material, by minimizing the delamination. At the same time, it will increase the productivity by maximizing the material removal rate and optimizing cutting force.

References

1. Suthar, J., Teli, S. N., Lad, S.: Review of Machining on Composite and Connected Optimisation Techniques. Int. Journal of Scientific & Engg. Research. 8 (3), 234–240 (2017).
2. Liu, D.F., Tang, Y. J., Cong, W. L. A review of mechanical drilling for composite laminates. Composite Structures. 94, 1265–1279 (2012).
3. Jayabal, S., Natarajan, U.: Optimization of thrust force, torque, and tool wear in drilling of coir fiber-reinforced composites using Nelder-Mead and genetic algorithm methods. International journal of advanced manufacturing and technology. 51, 371–381 (2010).
4. Dini, G.: online prediction of delamination in drilling of GFRP by using a neural network approach. Machining science and technology. 7, 295–314 (2003).
5. Enemuoh, E., Sherif, A., Gizawy, E., Chukwujekwu, A.: An approach for development of damage-free drilling of carbon fiber reinforced thermosets. International Journal of Machine Tools and Manufacture. 41, 1795–1814 (2001).
6. Saravanan, M., Ramalingam, D., Manikandan, G., Kaarthikeyen, R.: Multi objective optimization of drilling parameters using genetic algorithm. Procedia engineering. 38, 197–207 (2012).
7. Karthikeyan, R., Jaiganesh, S., Pai, B.C.: Optimization of drilling characteristics for Al/SiCp composites using Fuzzy/GA. International journal of metals and materials. 8(2), 163–168 (2002).

Evaluation of the Mechanical Properties of Recycled Jute Fiber–Reinforced Polymer Matrix Composites

**Pullareddy Mekala, Manohar Reddy Kunuthur
and B. Chandramohana Reddy**

Abstract This paper aims to evaluate the mechanical properties of recyclable jute fiber, without chemical treatment and applied compression load on the Recycled Jute fiber layers to be in uniform and unidirectional. To evaluate its the mechanical properties, weights of 5, 10, 15, and 20 g were taken and added to epoxy and hardener—ratio kept constant for all specimens. Specimens were prepared by hand layup technique and were cut using a manual hacksaw frame with subsequent filing to avoid sharp and uneven notches. Testing was undertaken in order to evaluate the following mechanical characteristics: tensile properties, three-point flexural strength, compression using a computerized UTM (Inston 3369).

Keywords Recycled jute fiber · Unidirectional · Hand layup technique
Mechanical properties

Nomenclature

PMC   Polymer matrix composite
NFRP   Natural fiber reinforced composites

P. Mekala (✉)
PVKK Institute of Technology, Ananthapuramu 515002, India
e-mail: pr98091@gmail.com

M. R. Kunuthur
JNTUA, Ananthapuramu 515002, India

B. Chandramohana Reddy
Department of Mechanical Engineering, JNTUA, Ananthapuramu 515002, India

1 Introduction

In modern technologies the use of natural fiber reinforced composite (NFRC) materials has gained substantial interest, especially in material science [1, 2], where these fibers may be combined with thermoplastic polymers to create natural-fiber composites having significant attributes and, therefore, applications [3, 4]. The polymer matrix composites (PMCs) [5] have properties which including being renewable and biodegradable, having short growing times (crop times), consuming CO_2 and returning O_2 to the environment, and being moldable, easy to handle, and easy to work [2].

The fiber and matrix materials, are not the form of new jute fibers, however, in this work jute fibers were used which were extracted from existing jute mate materials also the availability of jute fiber is rare, except in Bengal states. Here the jute fiber is extracted from jute mate. The jute mate is bi-directional in orientation, initially the jute fibers are extracted linearly from the jute mate [6].

The jute is unidirectional under dry conditions and is difficult to obtain [6, 7]; hackling under wet/dry conditions causes fiber defects and therefore affects the performance of the fibers. Preparation of unidirectional jute roving has become a valuable step in its production and this process is gaining in importance [8].

2 Materials and Method

2.1 Materials

2.1.1 Matrix Materials

In the present work the epoxy resin used was LY 556 [9]. It was obtained from an authorized dealer of Araldite (HY 951) Huntsman [10] (Ciba-Geigy India Ltd., Hyderabad—invoice number 10121). Table 1 gives the properties of the matrix material.

Table 1 Composition of the matrix system

Component	Molar mass (g/mol)	Supplier
Hydrochloric acid (HCl)	36.46	Hindustan Ciba-Gieg Ltd.
Sodium hydroxide (NaOH)	39.997	Hindustan Ciba-Gieg Ltd.
Sodium chloride (NaCl)	58.4	Hindustan Ciba-Gieg Ltd.

Table 2 Chemical composition of jute fiber [14]

Constituents	Percentage
Cellulose	60–62
Hemi cellulose	22–24
Lignin	12–14
Other	1–2

Table 3 Mechanical properties of jute fiber [14]

Fiber	Density (g/cm^3)	Young's modulus (GPa)	Tensile strength (MPa)	Elongation at breaking point (%)
Jute	1.3	26.5	393–773	1.5–1.8

2.1.2 Fiber Material

Jute FRC (Fiber Reinforced Compoites) possesses more strength and stiffness [11, 12]. Therefore, it is suitable as a reinforcement fiber in a polymeric resin matrix [13, 14]. The chemical composition of jute fiber is shown in Table 2.

Fiber properties depend on factors which can change fiber characteristics, such as the length of the process adopted for fiber extraction [6]. Table 3 gives the mechanical properties of jute fiber.

2.2 Method

Figure 1 shows the process of jute fiber production.

2.2.1 Fiber Orientation

Fiber orientation was unidirectional [15] with a length of 130 ($\pm$0.2) mm, as per the mold size. Fiber arrangement was undertaken using bare hands—no gloves were worn. Each individual layer was set up carefully to avoid bubble formation and gaps between fibers. Figure 1a shows a prepared mold indicating the unidirectional orientation of jute fiber.

2.2.2 Mold Preparation

The matrix (epoxy and hardener) was weighed with a jewelry weighing machine (BOLT MH Series 200 g/0.01 g); 50 g of epoxy and 5 g of hardener were mixed using an ultrasonicator. The mold was prepared [16] using an A4 wooden sheet which

was 8 mm thick. A polythene overhead projector (OHP) sheet (for easy removal) was placed on the surface [17] of the wooden sheet and nails were used to fit boarders which were 3 mm thick.

Mold Used for Tensile and Flexural Strength

The molds were in size of $130 \times 130 \times 3$ (length $\times$ breadth $\times$ height) mm [18]. To avoid minute leakages of matrix [19], liquid wax was poured across the borders of the mold [20] and the mold was then quickly rotated to close off any potential leakage points, especially at the corners—the specimen was then given a curing time of 24 h.

Mold Used for Compression Test

The compression test specimen was $10 \times 10 \times 10$ (length $\times$ breadth $\times$ height) mm [21], and was prepared using a wooden sheet. Figure 1(a) shows mold preparation. The epoxy matrix material was initially applied as a thin coat [20] so that the bottom surface of the composite specimen was smooth. Specimen curing time was 72 h. Table 2 shows the list of raw materials used in this work.

Compressing the Specimen and Finishing

The compression mold was applied to specimens which were not to the required thickness [22]. Figure 1a, b shows a mold which has been closed using a polythene sheet and the top surface of a mold closed with a wooden sheet to avoid matrix contact
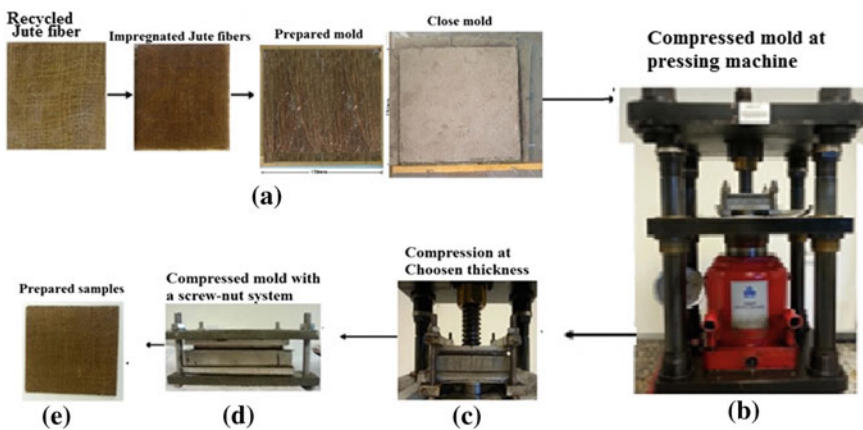
Fig. 1 **a** Processing jute fiber and molding. **b** Compressed mold at a pressing machine. **c** Compression to a chosen thickness. **d** Compressed mold using a screw–nut system. **e** Prepared samples

with the machine's jaws. Figure 1c shows the compression of a specimen in a mold to its required thickness [23]. In Fig. 1d the compression machine has stopped after the specimen has reached the required dimensions—the mold is then immediately tightened using the screw–nut system (an in-built feature of a compression machine). Figure 1e shows the samples after all the preparatory steps have been complete. The composite samples prepared with epoxy and hardener were identical for all four specimens.

The composite specimen samples were prepared with the mass of jute increasing by 5 g for each specimen, up to 20 g. The ratio of epoxy to hardener was 10:1—epoxy at 50 g and hardener at 5 g—across all samples. Table 3 provides specimen data.

3 Experimental Setup Used for Mechanical Tests

3.1 Mechanical Testing

Specimen flatness was checked with a Kemet Flatness Gauge and specimen thickness with Vernier Calipers [22]. For the compression specimens, flexural cuts were completed with a manual hacksaw, however, tensile specimens were cut using an electric switch board wire-cutting machine because the curves were difficult to achieve (dumbbell shape) using a manual hacksaw.

3.1.1 Tensile Test Setup

The tensile specimen was tested according to ASTM D3369-76 standards [24] using a UTM Inston D3339; the tensile test crosshead speed was 10 mm/min (quasistatic). Specimen dimensions are shown (ASTMD3369-76, type M-1) in Fig. 2a.

3.1.2 Three-Point Flexural Test Setup

The flexural specimen was prepared and tested according to ASTM D7264 standards [25] using a UTM Inston D3339; the flexural tests used a crosshead speed of 1 mm/min. Specimen dimensions are shown in Fig. 2b.

3.1.3 Compression Test Setup

The compression specimen was prepared and tested according to ASTM D3410 standards [26] using a UTM Inston D3339; the compression tests maintained a crosshead speed of 5 mm/min. Specimen dimensions are shown in Fig. 2c.
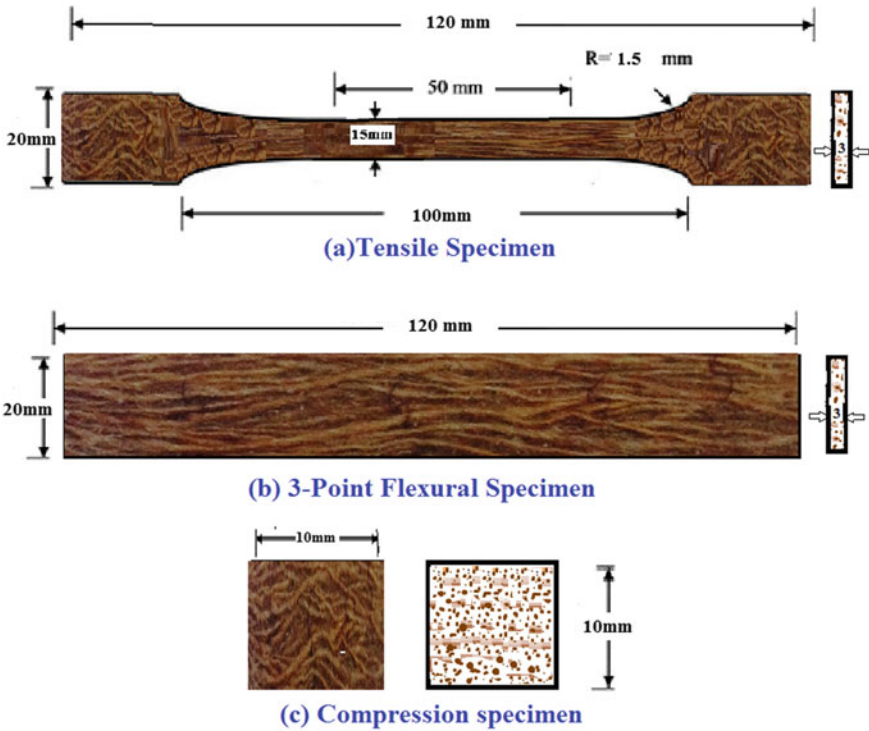
Fig. 2 Specimens and dimensions. **a** Tensile specimen. **b** Three-point flexural specimen. **c** Compression specimen

4 Results

4.1 Tensile Test

The tensile test [27, 28] specimens are shown after breakage in Fig. 3. All four specimens had the same standard dimensions (this is not clear on the image due to shaking during image capture) listed in Fig. 2a. However, the 20-g composite specimen was compressed [29].

The tensile test results are given in Table 4 for the properties of jute fiber composites reinforced with UD (Unidirectional); a gradual increase in strain was noticed in all the samples. Comparison of jute UD composites J5 and J10 showed similar tensile strengths and increased tensile strain.

Specimen J15 showed increased strength comparing with J10. Specimen J20 showed a decreased strength and increased maximum strain compared with all specimens (Table 5).

Graph 1 shows the tensile stress and tensile strain (Table 6).

Fig. 3 Tensile specimens after testing

Table 4 List of raw materials used in the work

Description	Raw materials
Matrix	Epoxy resin (LY556)
Hardener	Hardener (HV951)
Reinforcing agent	Recycled jute fiber
Mold releasing agent	Overhead projector sheet and wax
Casting	Wooden molds

Table 5 Composite sample specimen data

Specimen number	Specimen name	Jute fiber (g)	Epoxy (50 g) + hardener (5 g) (kept constant)
1	J5	5	55
2	J10	10	55
3	J15	15	55
4	J20	20	55
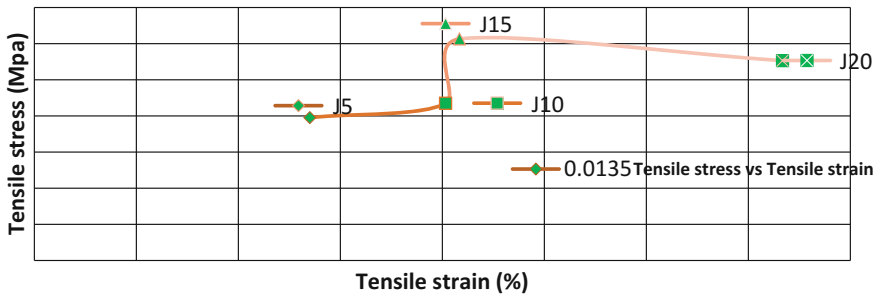
Graph 1 Tensile test graph

Table 6 Tensile test results

Specimen number	Specimen name	Tensile strain (%)	Tensile stress (Mpa)	Tensile modulus (Mpa)
1	J5	0.0135	79.07	8083.63
2	J10	0.02016	86.97	6732.71
3	J15	0.02084	122.63	8938.79
4	J20	0.03667	110.62	6122.32

Fig. 4 Three-point flexural specimen

4.2 Three-Point Flexural Test

The flexural test specimens [30] are shown after breakage in Fig. 4. All four specimens had the same standard dimensions (this is not clear on the image due to shaking during image capture) listed in Fig. 2a. However, the 20-g composite specimen was compressed (Fig. 5).

In the case of specimens J5 and J10 it was observed that both composites showed similar maximum flexural strengths [31]. However, flexural specimens in comparison of J15 and J20 indicated a decrease in strain for J15 with high stresses were reached highly in J15 but the stress and strain shown at J15 and J20 rapid increase in the flexural specimens at J15 to J20 with respect to J10 it got similar to J10. It was observed that J20 showed maximum deflection [32]. However, the flexural strain in J15 was lower compared to all other specimens (Table 7).

The flexural properties for different composites are displayed in Graph 2. Flexural stress increased with initial stage deflection and gradually moved toward failure point.
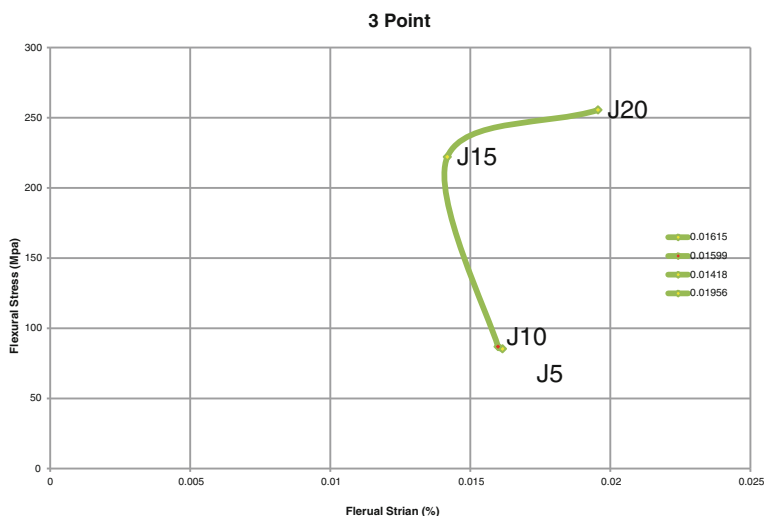
Graph 2 Three-point flexural test or three-point bending test

Fig. 5 Compression specimens after testing
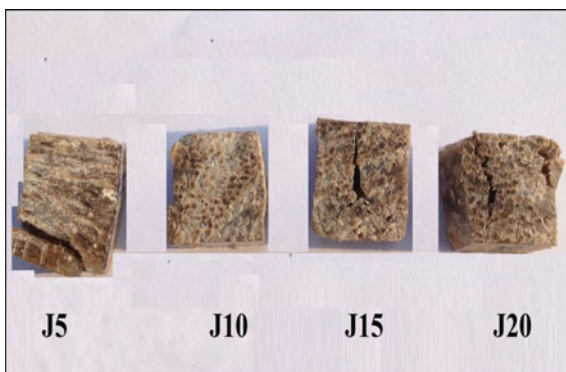
Table 7 Three-point flexural test results

Specimen number	Specimen name	Flexural strain (%)	Flexural stress (Mpa)	Flexural modulus (Mpa)
1	J5	0.01615	85.33	7740.11
2	J10	0.01599	86.91	6420.39
3	J15	0.01418	222.041	20588.53
4	J20	0.01956	255.51	21993.09
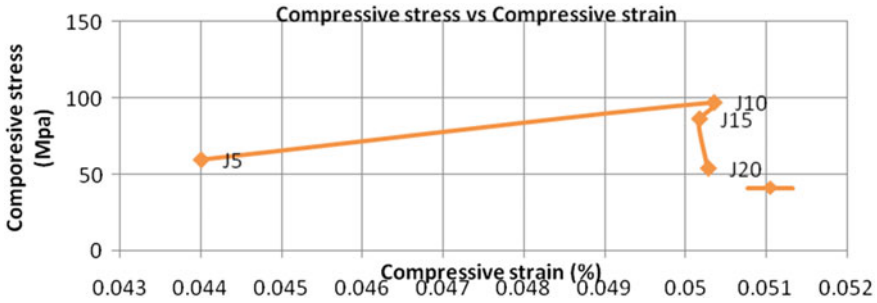
Graph 3 Compressive stress versus compressive strain

Table 8 Compressive stress versus compressive strain

Specimen number	Specimen name	Compression strain (%)	Compression stress (Mpa)	Compressive modulus (Mpa)
1	J5	0.04401	59.27	2610.51
2	J10	0.05035	96.88	4434.47
3	J15	0.05017	86.17	3706.00
4	J20	0.05028	53.7	3012.86

4.3 Compression Test

Compression properties initially were lower at J5, and specimen J10 had both good composite modulus stress and strain compared to J15 and J20; the strength of J10 decreased gradually. It was especially noted in terms of stress that there was a gradual decrease in strength in J5 compared with J20; it was observed that J5 had greater strength but was poor in terms of strain [33].

The results showed that compressive strain factor was lower in specimen J5. Compressive strain and compressive modulus factor was higher in specimen J10 (Graph 3).

The compressive stress and modulus decreased—its path followed those of J15 and J20 (Table 8).

5 Conclusion

Comparisons of reinforced jute fiber systems were explored considering their mechanical properties including compression. It was found that increased fiber content in the matrix caused poor mechanical properties.

1. Overall tensile results showed that J15 had good mechanical properties. However, strain increased in J20.

2. Flexural modulus for different composite samples showed little variation. Overall, the flexural properties shown in J15 were the best, especially its lower strain and better flexural properties.
3. The 15-g compression specimen of jute gave the best results. Specimen J10 showed a high compression modulus.

References

1. K. Pickering, Aruan efendy, m.g., le, t.m., A review of recent developments in natural fibre composites and their mechanical performance. *Composites Part A*, http://sci-hub.tw/10.1016/j.compositesa.2015.08.038.
2. Hoi-yan Cheung, Mei-po Ho, Kin-tak Lau, Francisco Cardona, David Hui, Natural fibre-reinforced composites for bioengineering and environmental engineering applications. *Composites Part B: Engineering*, Volume 40, Issue 7, 2009, 655–663, ISSN 1359-8368, http://sci-hub.tw/10.1016/j.compositesb.2009.04.014.
3. S. J. S. DA, Book: Chap.1, On the recyclability of a cyclic thermoplastic composite (2005) 1–10.
4. S. A. R. L. F. M. R. L. A. D. Alves, C., Ferrao and P.M.C, Ecodesign of automotive components making use of natural jute fiber composites, L.B, Alves, Rodrigues. http://sci-hub.tw/10.1016/j.jclepro.2009.10.022.
5. Ru-Min Wang, Shui-Rong Zheng, and Ya-Ping Zheng. Polymer Matrix Composites and Technology. Woodhead Publishing, ISBN 978-0-85709-221-2 (print).
6. S.M. Sapuan, K.F. Tamrin, Y. Nukman, Y.A. El-Shekeil, M.S.A. Hussin, and S.N.A. Aziz, 1.8 Natural Fiber-Reinforced Composites: Types, Development, Manufacturing Process, and Measurement, In: Comprehensive Materials Finishing, ed. M.S.J. Hashmi, Elsevier, Oxford, 2017, pp. 203–230, ISBN 9780128032497, http://sci-hub.tw/10.1016/B978-0-12-803581-8.09183-9.
7. Ming Cai, Hitoshi Takagi, Antonio N. Nakagaito, Yan Li, and Geoffrey I.N. Waterhouse, Effect of alkali treatment on interfacial bonding in abaca fiber-reinforced composites. *Composites Part A: Applied Science and Manufacturing*, Volume 90, 2016, pp. 589–597, ISSN 1359-835X, http://sci-hub.tw/10.1016/j.compositesa.2016.08.025.
8. S. A. R. L. F. M. R. L. A. D. Alves, C. and Ferrao, P.M.C, Ecodesign of automotive components making use of natural jute fiber composites, L.B, Alves, Rodrigues. http://sci-hub.tw/10.1016/j.jclepro.2009.10.022.
9. Araldite DBF/HY 951 Page 3, Mix Ratio, February 2005 2/6.
10. R. A. Braga and P.A.A. Magalhaes, Analysis of the mechanical and thermal properties of jute and glass fiber as reinforcement epoxy hybrid composites, Vol. 2015. http://sci-hub.tw/10.1016/j.msec.2015.06.031.
11. Sweety Shahinur, 1, 2 Mahbub Hasan, 2 Qumrul Ahsan, 3 Dilip Kumar Saha, 4 and Md. Saiful Islam, 5Characterization of the Properties of Jute Fiber at Different Portions, *International Journal of Polymer Science*, Volume 2015 (2015), http://dx.doi.org/10.1155/2015/262348.
12. Processing and Characterization of Jute Fiber Reinforced Thermoplastic Polymers, A.C. Karmaker and G. Hinrichsen, pp. 609–629, published online: September 22, 2006, http://sci-hub.tw/10.1080/03602559108019223.

13. *International Journal of Textile Science* 2012, 1(6): 84–93 DOI:http://sci-hub.tw/10.5923/j. textile.20120106.05 Jute Composites as Wood Substitute Debiprasad Gon1,*, Kousik Das2, Palash Paul2, SubhankarMaity2 1Indian Jute Industries' Research Association, 17, Taratala Road, Kolkata-88 2Panipat Institute of Engineering, Technology, Samalkha, Panipat, Haryana.

14. Ming Cai, Hitoshi Takagi, Antonio N. Nakagaito, Yan Li, and Geoffrey I.N. Waterhouse, Effect of alkali treatment on interfacial bonding in abaca fiber-reinforced composites. *Composites Part A: Applied Science and Manufacturing*, Volume 90, 2016, pp. 589–597, ISSN 1359-835X, http://sci-hub.tw/10.1016/j.compositesa.2016.08.025.

15. Processing of Polymer Matrix Composites P. K. Mallick William E. Stirton Professor of Mechanical Engineering University of Michigan-Dearborn ISBN:-13: 978-1-4665-7822-7 (Hardback) Page No 120–126 4.1 CURE CYCLE FOR THERMOSETTING POLYMERS, 5.3 LAYUP TECHNIQUES 6.8 COMPRESSION MOLDING PARAMETERS 6.9 MOLD DESIGN CONSIDERATIONS.

16. Josh Kelly and Mohsen Mohammadi, Uniaxial tensile behavior of sheet molded composite car hoods with different fibre contents under quasi-static strain rates. *Mechanics Research Communications*, Volume 87, 2018, 42–52, ISSN 0093-6413, http://sci-hub.tw/10.1016/jmechrescom. 2017.12.007.

17. R. Sothornvit, C.W. Olsen, T.H. McHugh, and J.M. Krochta, Tensile properties of compression-molded whey protein sheets: Determination of molding condition and glycerol-content effects and comparison with solution-cast films. *Journal of Food Engineering*, Volume 78, Issue 3, 2007, 855–860, ISSN 0260-8774, http://sci-hub.tw/10.1016/j.jfoodeng.2005.12.002.

18. M.V. de Sousa, S.N. Monteiro, and J.R.M. d'Almeida, Evaluation of pre-treatment, size and molding pressure on flexural mechanical behavior of chopped bagasse–polyester composites. *Polymer Testing*, Volume 23, Issue 3, 2004, 253–258, ISSN 0142-9418, http://sci-hub.tw/10. 1016/j.polymertesting.2003.09.002.

19. Ki-Taek Kim, Jin-Ho Jeong, and Yong-Taek Im, Effect of molding parameters on compression molded sheet molding compounds parts. *Journal of Materials Processing Technology*, Volume 67, Issues 1–3, 1997, 105–111, ISSN 0924-0136, http://sci-hub.tw/10.1016/S0924-0136(96)02827-0.

20. M.J. Cawood and G.A.H. Smith, A compression moulding technique for thick sheets of thermoplastics. *Polymer Testing*, Volume 1, Issue 1, 1980, 3–7, ISSN 0142-9418, http://sci-hub. tw/10.1016/0142-9418(80)90022-7.

21. Standard Practice for Compression Molding Thermoplastic Materials into Test Specimens, Plaques, or Sheets, *Annual Book of ASTM Standards*, Vol 08.01. Designation: D 4703–03.

22. ASTM D3039/D3039D-76, Standard Test Method for Tensile Properties of Polymer Matrix Composite Materials, ASTM International, West Conshohocken, PA, 2017, www.astm.org.

23. Ram Krishna Adhikari and B.S. Keerthi Gowda, Exploration of mechanical properties of banana/jute hybrid polyester composite. *Materials Today: Proceedings*, Volume 4, Issue 8, 2017, 7171–7176, ISSN 2214-7853, http://sci-hub.tw/10.1016/j.matpr.2017.07.043.

24. ASTM D7264/D7264 M-15, Standard Test Method for Flexural Properties of Polymer Matrix Composite Materials, ASTM International, West Conshohocken, PA, 2015, https://www.astm. org/Standards/D7264.htm.

25. ASTM D3410/D3410 M-16, Standard Test Method for Compressive Properties of Polymer Matrix Composite Materials with Unsupported Gage Section by Shear Loading, ASTM International, West Conshohocken, PA, 2016, www.astm.org.

26. B. D. Y. XW, Plasma treatment of sisal fibers and its effects on tensile strength and interfacial bonding. 16 703–727. http://sci-hub.tw/10.1163/156856102760099898.

27. Deng'an Cai, Guangming Zhou, and Vadim V. Silberschmidt, Effect of through-thickness compression on in-plane tensile strength of glass/epoxy composites: Experimental study. *Polymer Testing*, Volume 49, 2016, 1–7, ISSN 0142-9418, http://sci-hub.tw/10.1016/j.polymertesting. 2015.10.015.

28. R. Sothornvit, C.W. Olsen, T.H. McHugh, and J.M. Krochta, Tensile properties of compression-molded whey protein sheets: Determination of molding condition and glycerol-content effects and comparison with solution-cast films. *Journal of Food Engineering*, Volume 78, Issue 3, 2007, 855–860, ISSN 0260-8774, http://sci-hub.tw/10.1016/j.jfoodeng.2005.12.002.

29. Sudhir P. Patil and Keshav K. Sangle, Shear and flexural behaviour of prestressed and non-prestressed plain and SFRC concrete beams. *Journal of King Saud University – Engineering Sciences*, Volume 29, Issue 4, 2017, 321–328, ISSN 1018-3639, http://sci-hub.tw/10.1016/j.jksues.2016.01.005.

30. Michael I. Okereke, Flexural response of polypropylene/E-glass fibre reinforced unidirectional composites. *Composites Part B: Engineering*, Volume 89, 2016, 388–396, ISSN 1359-8368, http://sci-hub.tw/10.1016/j.compositesb.2016.01.007.

31. Hasret Aydin, Rebecca J. Gravina, and Phillip Visintin, A partial-interaction approach for extracting FRP-to-concrete bond characteristics from environmentally loaded flexural tests. *Composites Part B: Engineering*, Volume 132, 2018, 214–228, ISSN 1359-8368, http://sci-hub.tw/10.1016/j.compositesb.2017.09.018.

32. M.R. Bambach, Compression strength of natural fibre composite plates and sections of flax, jute and hemp. *Thin-Walled Structures*, Volume 119, 2017, 103–113, ISSN 0263-8231, http://sci-hub.tw/10.1016/j.tws.2017.05.034.

33. R.J. Lee, Compression strength of aligned carbon fibre-reinforced thermoplastic laminates. *Composites*, Volume 18, Issue 1, 1987, 35–39, ISSN 0010-4361, http://sci-hub.tw/10.1016/0010-4361(87)90005-X.

Predictive Modelling of Delamination Factor and Cutting Forces in the Machining of GFRP Composite Material Using ANN

Hari Vasudevan, Ramesh Rajguru and Rajnarayan Yadav

Abstract Drilling is one of the key machining operations in the hole creation processes. Compared with the machining processes, such as milling, turning, the drilling operation is largely used in the composite materials processing. Delamination is a critical problem found during drilling operation. It causes structural reliability and poor assembly tolerance as well as the potential for long-term performance decline. As a result, drilling of any material requires dimensional stability and interface quality. This study involves drilling operation in a GFRP composite material. It has selected and used the feed-forward back propagation as the algorithm with trainglm, learngdm, MSE and transig as the training, learning, performance and transfer functions, respectively. Four input parameters were taken as four nodes in the input layer and thrust force and delamination as two nodes in the output layer. 4-9-2-2 neural network structure for composite material helped in the best way to compare actual values and an artificial neural network (ANN) predictive model for thrust force and delamination in drilling operation. ANN gives very good performance for the delamination factor and the cutting force.

Keywords GFRP · Drilling · Delamination · ANN
Feed-forward back propagation

1   Introduction

Composite materials possess lightweight, high strength, high stiffness, good fatigues resistance and good corrosion resistance. They are widely used in various industrial

H. Vasudevan
D.J. Sanghvi College of Engineering, Mumbai, India
e-mail: harivasudevan@iitb.ac.in

R. Rajguru (✉) · R. Yadav
Faculty, Department of Mechanical Engineering, D.J. Sanghvi College of Engineering,
Mumbai, India
e-mail: ramesh.rajguru9@gmail.com

applications such as aerospace and automotive sectors, electrical power generation and distribution systems. There are several problems in the drilling of composite materials such as fibre pull-out, delamination and subsurface damage. With the upcoming usage of glass fibre-reinforced polymer (GFRP) composites in various areas of applications, machining of these materials has become a main concern for the manufacturing industries.

Hari Vasudevan et al. [1] presented an overview of the various aspects, such as cutting mechanism, influence of tool material, tool geometry, surface quality and health and safety aspects in machining FRPS, involved in the conventional machining of GFRP types of composite material. Ramesh Rajguru et al. [2] evaluated the best process environment to satisfy requirements of both quality and productivity during drilling operations on NEMA GFRP/E composite materials, using grey relational analysis, coupled with the Taguchi method. Twenty-seven experimental runs based on an orthogonal array of the Taguchi method were conducted to optimise the machining parameters within the experimental domain. They found that the optimal cutting force and surface roughness were achieved based on the largest value of grey relational grade, when spindle speed, feed rate, thickness of the plate and drill size were 1200 rpm, 110 mm/min 10 and 6 mm, respectively. Further, feed rate has the most dominant role in influencing the surface roughness.

Ramesh Rajguru et al. [3] investigated the multi-response optimisation of the drilling operation to achieve minimum delamination and cutting force, using grey relational analysis coupled with the Taguchi method. They found that the optimal process parameters were achieved at spindle speed 1500 rpm, feed rate 75 mm/min, thickness 8 mm and drill size 6 mm. Krishna Moorthy et al. [4] presented a delimitation factor prediction model in drilling operations, based on an artificial neural network (ANN). The input parameters were spindle speed, feed rate and the drill size, and output parameters were delamination and cutting force. Twenty-seven experiments were conducted based on Taguchi's design of experiments (DOE). They used back-propagation neural network with two hidden layers for delamination factor prediction induced in drilling of CFRP composite material. They found that 3-5-2-1 neural network architecture gave an accurate result with 0.8 and 0.03% maximum and minimum MSE error, respectively. Suman Kant [5] applied the Taguchi and the ANN models for optimising and modelling, when drilling GFRP composites. The Taguchi fractional factorial experimentation was used with three full factorials having three levels. The inputs to the models were spindle speed, feed rate and drill diameter, while the output response was delamination. The author found the prediction ANN model to be satisfactory.

Jenarthanan et al. [6] conducted end milling operations on GFRP and developed RSM and ANN models for the prediction of surface roughness. The experiments were conducted with four independent variables, namely cutting speed, fibre orientation angle, depth of cut and feed rate. They found that the ANN model is much more robust and accurate than RSM for predicting surface roughness response value. Azlan Mohd Zain et al. [7] developed an ANN predictive model for surface roughness during dry end milling operation, using three cutting parameters, namely cutting speed, feed rate (mm/tooth) and radial rake angle. The authors found that the
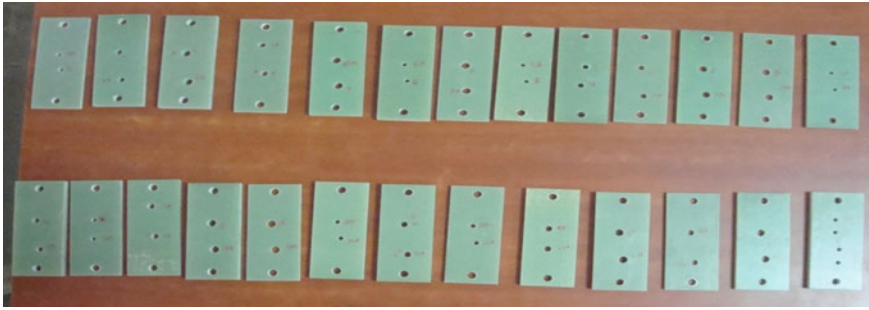
Fig. 1 GRFP/E composite materials

ANN structure 3-1-1 predicts the best performance for surface roughness. Nilesh Pohokar et al. [8] employed an ANN model for optimisation of geometric and machining parameters in tool life analysis. ANN presents a very good performance for tool life analysis.

The objective of the current study is to develop a predictive model, using ANN in order to achieve lower delamination factor and cutting force with a particular combination of cutting parameters in the drilling of GFRP composite materials.

2 Experimental Work

2.1 Work Material

The work material selected for the study was glass fibre-reinforced polymer epoxy based. The work specimens are flat plate as shown in Fig. 1. Epoxy resins are extensively used as matrix in numerous fibre-reinforced composites.

2.2 Cutting Tool

The drill bits were an ultra-fine tungsten carbide coated with titanium carbide specially designed for composite materials, drill diameter 6, 8 and 10 mm, point angle 120° and helix angle 30°, and it is shown in Fig. 2. Other specifications of drill bits are illustrated in Table 1.

Fig. 2 Drill bits

Table 1 Specification of drill bits

Drill diameter (mm)	No. of flute	Overall length (mm)	Flute length (mm)	Point angle (C)	Helix angle (C)
6	2	66	28	120	30
8	2	79	41	120	30
10	2	89	47	120	30

2.3 Experimental Procedure

The design of experiment consisted of 4: three levels machining parameters. They were spindle speed (900, 1200 and 1500 rpm), feed rate (75, 110 and 150 mm/min), material thickness (6, 8 and 10 mm) and drill size (6, 8 and 10 mm). Drilling operations were performed using HAAS TM-2 CNC machine. Workpiece was mounted on a Kistler piezoelectric dynamometer of type 5233A as shown in Fig. 3, associated with a charge amplifier to measure the cutting forces during the process.

As part of the study, the delamination was evaluated at the Institute for Design of Electrical Measuring Instruments (IDEMI) with a 2D microscope as shown in Fig. 4.

Delamination factor $= D/d$
where $D =$ maximum diameter and $d =$ actual diameter.

All measured values of delamination factor and cutting force along with L27 orthogonal array are tabulated in Table 2.

Table 2 Experimental design using orthogonal array with factors and responses

Expt. no.	A Spindle speed		B Feed rate		C Thickness		D Drill diameter		F	DF
	Actual	Coded	Actual	Coded	Actual	Coded	Actual	Coded		
1	900	1	75	1	6	1	6	1	35.19	1.086
2	900	1	75	1	8	2	8	2	50.42	1.049
3	900	1	75	1	10	3	10	3	95.61	1.036
4	900	1	110	2	6	1	8	2	46.11	1.066
5	900	1	110	2	8	2	10	3	110.11	1.035
6	900	1	110	2	10	3	6	1	48.65	1.103
7	900	1	150	3	6	1	10	3	98.6	1.05
8	900	1	150	3	8	2	6	1	36.25	1.035
9	900	1	150	3	10	3	8	2	84.35	1.242
10	1200	2	75	1	6	1	8	1	32.23	1.118
11	1200	2	75	1	8	2	10	2	65.46	1.05
12	1200	2	75	1	10	3	6	3	49.77	1.07
13	1200	2	110	2	6	1	10	2	75.07	1.029
14	1200	2	110	2	8	2	6	3	27.56	1.059
15	1200	2	110	2	10	3	8	1	71.14	1.091
16	1200	2	150	3	6	1	6	3	42.76	1.121
17	1200	2	150	3	8	2	8	1	76.93	1.056

(continued)

Table 2 (continued)

Expt. no.	A Spindle speed		B Feed rate		C Thickness		D Drill diameter		F	DF
	Actual	Coded	Actual	Coded	Actual	Coded	Actual	Coded		
18	1200	2	150	3	10	3	10	2	126.77	1.112
19	1500	3	75	1	6	1	10	1	65.06	1.067
20	1500	3	75	1	8	2	6	2	18.49	1.088
21	1500	3	75	1	10	3	8	3	62.38	1.079
22	1500	3	110	2	6	1	6	2	23.62	1.088
23	1500	3	110	2	8	2	8	3	65.12	1.084
24	1500	3	110	2	10	3	10	1	80.75	1.067
25	1500	3	150	3	6	1	8	3	53.59	1.187
26	1500	3	150	3	8	2	10	1	73.18	1.032
27	1500	3	150	3	10	3	6	2	43.55	1.187
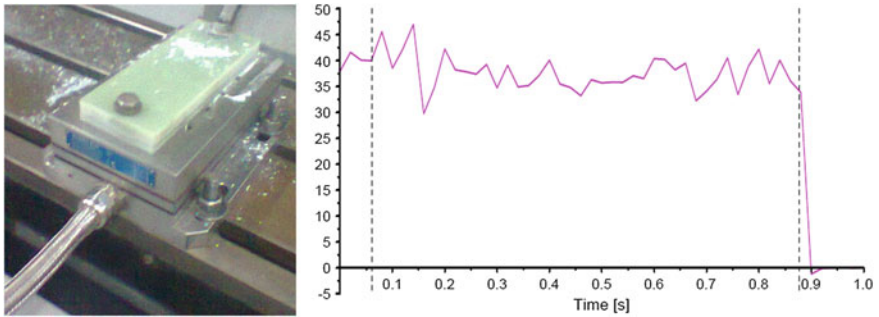
Fig. 3 Kistler piezoelectric dynamometer and typical thrust force profile over a drilling cycle for different combination of cutting conditions

Fig. 4 Schematic diagram of delamination analysis and 2D micrometre

3 Artificial Neural Network (ANN)

In the study, a feed-forward network with the back-propagation training algorithm was used to develop the thrust force and delamination factor predictive model, as it is extensively used by many researchers, and it was pointed out that this model gave the most accurate results [9, 10]. The basic structure of a feed-forward neural network consists of layers such as input, hidden, output and neurons also known as nodes. Input layer consists of four neurons that represent the four machining conditions, which are spindle speed, feed rate, thickness of plate and drill diameters. Two neurons for outer layer represent the predictive values of the thrust force and delamination. The number of hidden layers was selected by trial and error, and the proposed number of neurons in the hidden layer is $n/2$, $1n$, $2n$ and $2n + 1$, according to Zhang et al. [11]. However, the number of neuron in hidden layer equal to $2 \times$ number of input neurons $+ 1$ as suggested by Lippmann [12] was selected in the study. Therefore, this study used 4-9-2-2 as network architecture as shown in Fig. 5.
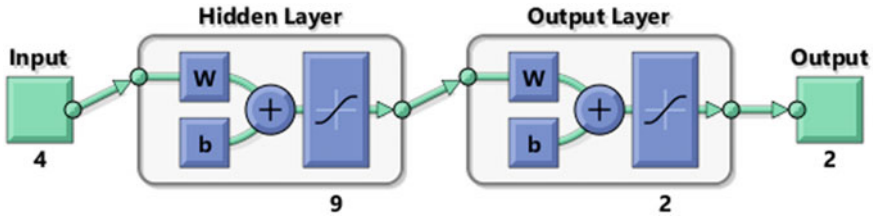
Fig. 5 Network architecture
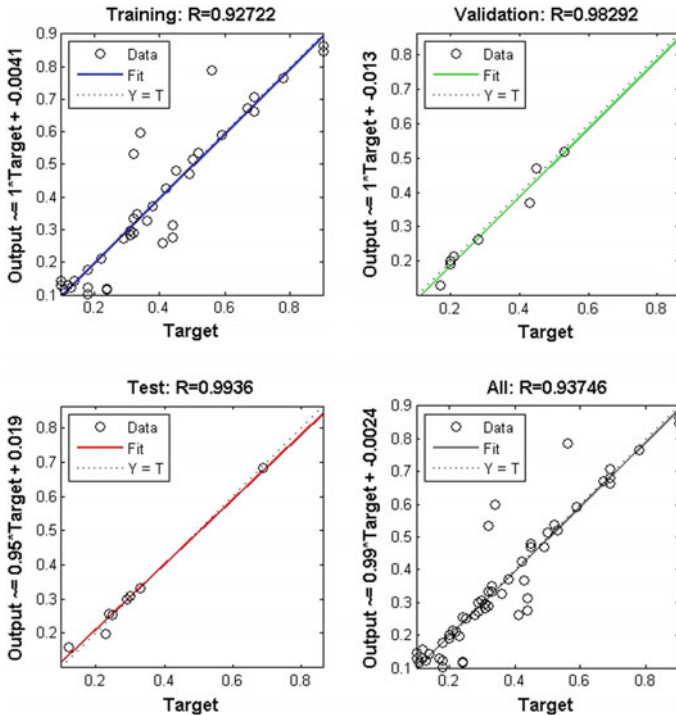
Fig. 6 Training, validation and testing regression fit

According to Zain et al. [10], network algorithm, transfer function, training function, learning function and performance function are the influencing factors, based on the ANN toolbox of MATLAB, while the effectiveness of the model was influenced by network structure, quantity of training data, quantity of validation data, quantity of testing data and normalisation of data inputs. Various functions like transfer function as transig, training function as trainlm, learning function as learngdm and performance function as MSE were selected in the study. A27 run experiment was designed using the Taguchi techniques, and out of the 27 runs given in Table 3, 19 readings were utilised for training the neural network
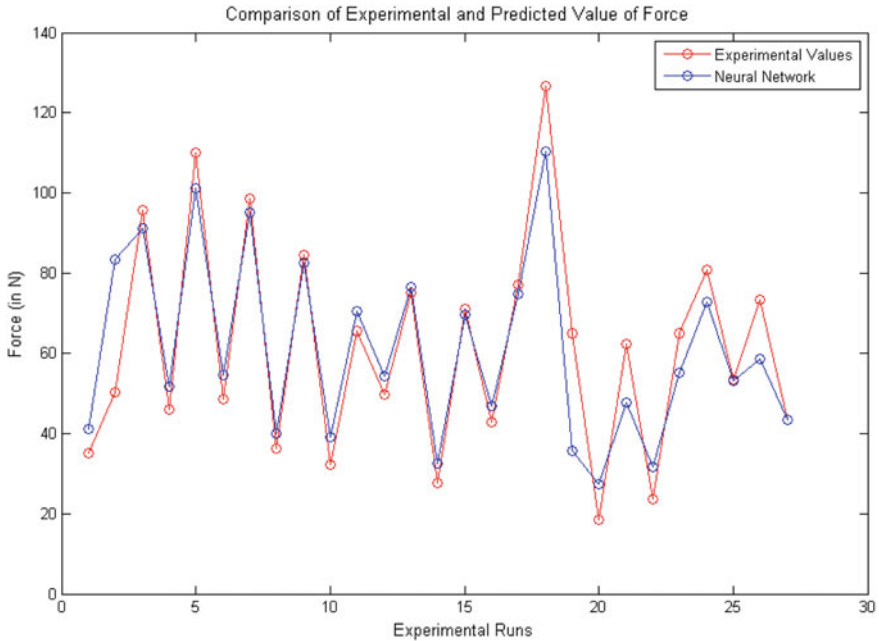
Fig. 7 Comparison graph of experiment and predicted value of cutting force

and 8 readings were reserved for testing and validation (70%:15%:15%) [10]. In order to facilitate the neural network training process, input and output variables were normalised in the range [0, 1].

4   Results and Analyses

The MSE for the ANN model was calculated for cutting force and delamination factor for each predicted response. The regression plots of training, testing validation and overall are illustrated in Fig. 6. The ANN regression fitting was found to be better (93.74%) with the actual predicted response as the experimental values of the delamination factor are closely aligned. The comparison between actual experimental values and ANN predicted data is shown in Figs. 7 and 8. The *x*-axis represents experimental runs, and the *y*-axis represents the ANN predicted values of responses, and it is indicated that ANN predicted values follow almost the same pattern as that of the experimental values for delamination factor (within ±5% of the experimental values of delamination factor). But in the case of cutting force, ANN predicted values showed a mixed tendency of overestimation and underestimation, because of nonlinearity and non-homogeneity of composite material.

Table 3 Normalisation of network input and ANN predicted values along with their percentage error w.r.t. experimental values

Run	Normalised values of cutting condition				Normalised values of experimental F and DF		Experimental values of F and DF		ANN predicted values of F and DF		% Relative error	
	A	B	C	D	F (N)	DF	F	DF	F (N)	DF	F (N)	DF
1	0.10	0.10	0.10	0.10	0.22	0.31	35.19	1.086	41.21	1.09	−17.1	−0.5
2	0.10	0.10	0.50	0.50	0.34	0.18	50.42	1.049	83.20	1.07	−65.0	−1.7
3	0.10	0.10	0.90	0.90	0.67	0.13	95.61	1.036	91.22	1.06	4.6	−1.9
4	0.10	0.47	0.10	0.50	0.30	0.24	46.11	1.066	51.77	1.08	−12.3	−1.6
5	0.10	0.47	0.50	0.90	0.78	0.12	110.11	1.035	101.25	1.06	8.0	−2.1
6	0.10	0.47	0.90	0.10	0.32	0.38	48.65	1.103	54.69	1.11	−12.4	−0.4
7	0.10	0.90	0.10	0.90	0.69	0.18	98.6	1.05	95.04	1.05	3.6	−0.4
8	0.10	0.90	0.50	0.10	0.23	0.12	36.25	1.035	39.99	1.06	−10.3	−2.7
9	0.10	0.90	0.90	0.50	0.59	0.90	84.35	1.242	82.55	1.21	2.1	2.4
10	0.50	0.10	0.10	0.50	0.20	0.43	32.23	1.118	39.19	1.09	−21.6	2.7
11	0.50	0.10	0.50	0.90	0.45	0.18	65.46	1.05	70.47	1.04	−7.7	0.5
12	0.50	0.10	0.90	0.10	0.33	0.25	49.77	1.07	54.40	1.07	−9.3	0.1
13	0.50	0.47	0.10	0.90	0.52	0.10	75.07	1.029	76.55	1.05	−2.0	−2.0
14	0.50	0.47	0.50	0.10	0.17	0.21	27.56	1.059	32.58	1.07	−18.2	−0.6
15	0.50	0.47	0.90	0.50	0.49	0.33	71.14	1.091	69.49	1.09	2.3	0.4
16	0.50	0.90	0.10	0.10	0.28	0.45	42.76	1.121	46.77	1.10	−9.4	1.4
17	0.50	0.90	0.50	0.50	0.53	0.20	76.93	1.056	74.68	1.06	2.9	−0.7

(continued)

Table 3 (continued)

Run	Normalised values of cutting condition				Normalised values of experimental F and DF		Experimental values of F and DF		ANN predicted values of F and DF		% Relative error	
	A	B	C	D	F (N)	DF	F	DF	F (N)	DF	F (N)	DF
18	0.50	0.90	0.90	0.90	0.90	0.41	126.77	1.112	110.34	1.07	13.0	3.6
19	0.90	0.10	0.10	0.90	0.44	0.24	65.06	1.067	35.69	1.05	45.1	1.6
20	0.90	0.10	0.50	0.10	0.10	0.32	18.49	1.088	27.47	1.08	−48.6	1.0
21	0.90	0.10	0.90	0.50	0.42	0.29	62.38	1.079	47.89	1.07	23.2	0.4
22	0.90	0.47	0.10	0.10	0.14	0.32	23.62	1.088	31.79	1.11	−34.6	−2.5
23	0.90	0.47	0.50	0.50	0.44	0.31	65.12	1.084	55.20	1.08	15.2	0.7
24	0.90	0.47	0.90	0.90	0.56	0.24	80.75	1.067	72.85	1.05	9.8	1.6
25	0.90	0.90	0.10	0.50	0.36	0.69	53.59	1.187	53.25	1.13	0.6	4.4
26	0.90	0.90	0.50	0.90	0.50	0.11	73.18	1.032	58.81	1.05	19.6	−1.8
27	0.90	0.90	0.90	0.10	0.29	0.69	43.55	1.187	43.55	1.19	0.0	0.0
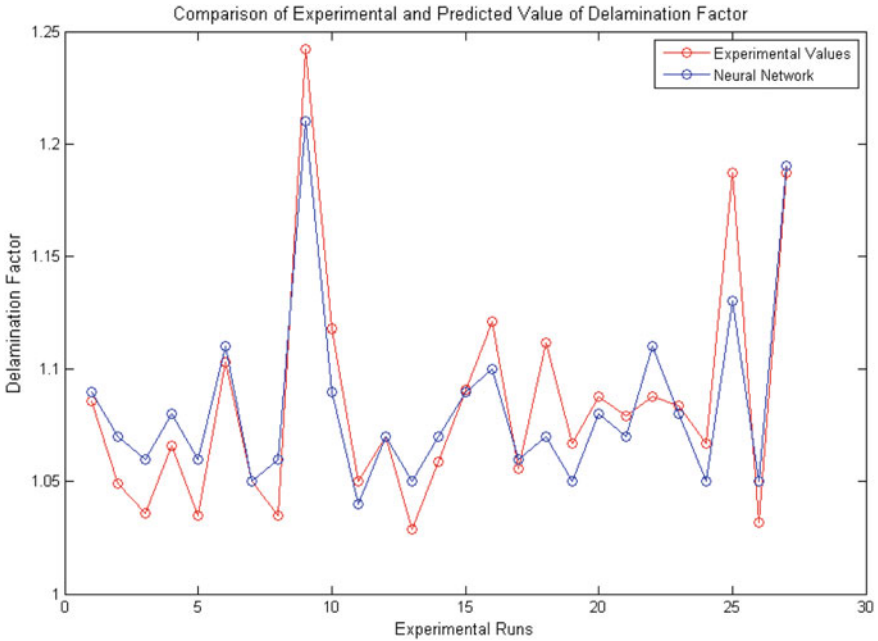
Fig. 8 Comparison graph of experiment and predicted value of delamination factor

5 Conclusion

A feed-forward back propagation with two hidden layers, having nine neurons with transfer function (trainlm), was used in the study as network architecture for developing the ANN model and for comparison between ANN model predicted results and experimental values. The average relative error between predicted results and experimental values was 0.070% for delamination factor and 4.387% for cutting force. The overall correlation coefficient between the ANN predicted result and experimental values was 0.937, which showed that the result between experimental values and predicted results was accurate. ANN model reflects that the material thickness and drill size are the most influencing machining parameters on cutting force in the drilling operation of GFRP epoxy-based composite materials, while spindle speed and feed rate do not have a notable effect on cutting force. ANN predicted model could also further improve the performance by increasing the number of training data.

References

1. Hari Vasudevan, Ramesh Rajguru, "A Review of Machining Processes and Machinability in the case of GFRP Composite Materials" in IPI Journal (The official publication of Indian Plastics Institute), August/September 2013, Vol. 18, issue 3.
2. Ramesh Rajguru, Hari Vasudevan and Naresh Deshpande "Analysis of a Multi-criteria optimization problem using Taguchi and Grey relational analysis: A case study in the machining of composite materials" in the International Conference on Advances in Mechanical Engineering organized by the department of Mechanical Engineering, College of Engineering Pune, Maharashtra, from 29th–31st May 2013.
3. Ramesh Rajguru, Hari Vasudevan and Naresh Deshpande "Multi-criteria optimization using Taguchi and Grey relational analysis in CNC drilling of GFRP/E composite material" in the International Conference on Advanced Manufacturing and Automation (INCAMA-2013, ISBN 978-93-80686-50-9) organised by the Department of Mechanical Engineering (DST-FIST Sponsored) Kalasalingam University, Madurai, Tamil Nadu from the 28th–30th March 2013.
4. A. Krishnamoorthy, S. Rajendra Boopathy and K. Palanikumar "Delamination prediction in drilling of CFRP composites using Artificial Neural Network" Journal of Engineering Science and Technology Vol. 6, No. 2 (2011) 191–203.
5. Suman Kant [] Application of Taguchi OA array and Artificial Neural Network for Optimizing and Modeling of Drilling Cutting Parameters International Journal of Theoretical and Applied Mechanics. ISSN 0973-6085 Volume 12, Number 1 (2017) pp. 1–12.
6. M.P. Jenarthanan A. Ajay Subramanian R. Jeyapaul, (2016), "Comparative analysis of surface roughness prediction using DOE and ANN techniques during endmilling of glass fibre reinforced polymer (GFRP) composites", Pigment & Resin Technology, Vol. 45 Iss 2 pp. 126–139.
7. Azlan Mohd Zain et al. (2010) "Prediction of surface roughness in the end milling machining using Artificial Neural Network" Expert Systems with Applications 37 (2010) 1755–1768.
8. Nilesh Pohokar et al. (2014) "Neural Networks Based Approach for Machining and Geometric Parameters optimization of a CNC End Milling" IJIRSET Vol. 3, Issue 2, February 2014.
9. Valluru Rao, Hayagriva Rao. C++, Neural Networks and Fuzzy Logic, BPB Publications, New Delhi, 1996.
10. Azlan Mohd Zain, Habibollah Haron, Safian Sharif, 'Prediction of surface roughness in the end milling machining using Artificial Neural Network', International Journal of Expert Systems with Applications, 37 (2): (2010), 1755–1768.
11. Zhang, G, Patuwo, B. E, Hu, M. Y., Forecasting with artificial neural networks: The state of the art. International Journal of Forecasting, 14 (1998) 35–62.
12. Lippmann R (1987) An introduction to computing with neural nets. IEEE ASSP Mag. 4(2):4–22.

Review of Application of Nitinol in the Manufacture of Bone Staples

Neel Sanghvi, Frank Crasta and Vijaya Kumar N. Kottur

Abstract Nickel titanium (commonly known as nitinol) is an alloy of nickel and titanium and is a nearly equiatomic alloy of nickel and titanium which exhibits two unique and closely related properties: *shape memory effect* and *pseudoelasticity* (also known as superelasticity). First discovered in 1959, these properties of nitinol have been exhaustively exploited in a multitude of applications in the robotics, aerospace, automotive, telecommunications and biomedical industries. Considering the fact that biocompatibility and biofunctionality are the primary attributes that a material must possess to qualify for use in the biomedical implant industry, nitinol is a premier choice. In this paper, in conjunction with the previously used orthopaedic implants, the design and advantages of the bone staple are discussed. A review of past and present materials used for manufacture of bone staples follows with a review of the methods available for manufacture of nitinol. This paper concludes that until a material possessing more biofunctionality and biocompatibility is discovered, nitinol is an ideal material for manufacture of bone staples.

Keywords Nitinol · Shape memory · Bone staple · Biocompatibility Orthopaedics

1 Introduction

The conventional bone staple used today aims at performing osteosynthesis like its functional predecessors: Lambotte spikes [1], Lane plates [2], Lambotte screws [3] and Hansman's plates [4] among many others. The use of these implants was abandoned due to corrosion, insufficient capacity and complications arising in the healing process [1]. The bone staple is a medical implant made of metal which is aimed at performing osteosynthesis. It is relatively simple in design and functioning.

N. Sanghvi (✉) · F. Crasta · V. K. N. Kottur
Mechanical Engineering Department, D. J. Sanghvi College of Engineering,
Vile Parle (West), Mumbai, India
e-mail: s.neel1998@gmail.com

Conventionally, a bone staple consists of a continuous body of single construction which can be easily fabricated [5]. Bone staples are preferred over external fixators like the Ilizarov apparatus and the Taylor spatial frame in some cases for these specific reasons as summarized here:

The fixators cannot be accommodated on the fracture site in certain cases, e.g. craniomaxillofacial fractures, Le Fort 1 fracture, comminuted fractures. Infection and hygiene considerations are practically eliminated in osteosynthesis when it is carried out with help of bone staples. In case of bone staples, the required compressive forces across the osteotomy surfaces will be achieved without the use of external mechanical structures, contrary to the use of external fixators [5].

The design process has to be adequately robust because the parts of a bone staple remain in a light to heavy stressed state after application. Sufficient attention must be paid to the fact that the compressive forces will be lost if the staple extrudes from the bone or if the leg to bridge angle changes. The current nitinol bone staple has a simple design and is made of a single piece of nitinol wire having a constant rectangular cross section [6]. Due to the recent advancements in manufacturing and machining technology, staple designers have employed these increased capabilities to manufacture staples having additional features like barbs [6]. The Barbed OSStaple manufactured by BioMedical Enterprises Inc has barbs on legs to prevent rotation of the fixture site and enhance staple security [7]. These barbs increase purchase and decrease the risk of pull-out/back-out and migration [8] (Fig. 1).

2 Material Selection for Manufacture of Bone Staples

The material used for the manufacture of a bone staple has always been a subject of constant examination and scrutiny due to the nature of application and the functional requirements of the bone staples. The material selection process for a bone staples is a major step in the design of a bone staple in the view of the fact that the primary goals of a bone staple are as summarized below:

The compressive stress distribution across the mating bone surfaces must be uniform. There must be a continuous and dynamic compression despite bone resorption. The material chosen must be analogous to human bone, in terms of mechanical properties, especially Young's modulus.

A review of scientific literature reveals that stainless steel (316L), titanium alloys (except nitinol) and nitinol have high biocompatibility among metals.

Considering SE508 ELI Nitinol, manufactured by Nitinol Devices and Components (NDC), Fremont, California, in a research partnership with American manufacturing company ATI Wah Chang [9, 10], ultra-high-purity and biocompatibility are obtained. As an outcome of 10 years of intense research, ELI (extra low interstitial) Nitinol is manufactured which is virtually free of carbon. This alloy is free of hard titanium carbide inclusions, and oxygen levels are lower than 60 parts per million (ppm), giving the enhanced purity. These purity levels are 10 times higher than mandated by ASTM-F2063-12, the standard which gives the exact physical, chemical, mechanical and metallurgical requirements and considerations for the manufacture and applications of biomedical nitinol. On further analysing composition data provided by NDC regarding the SE508 Nitinol [10], we realize that nitinol satisfies biocompatibility requirements for use in bone staples. As shown by Pal in 2014 [11], the mean Young's modulus of human bone is experimentally determined to be 18GPa. On comparing Young's modulus values of SE508 ELI Nitinol, 316L stainless steel, Ti-6Al-4V titanium alloy (summarized in Table 1), we observe that Young's modulus of SE508 ELI Nitinol (and hence nitinol in general) is most analogous to that of human bone. Considering Young's modulus to be an indicator of the stiffness of the material [12], we say that the stiffness of 316L stainless steel is more than 10 times that of human bone while that of nitinol is three times of that of human bone. This high stiffness of stainless steel may exert high forces at the fracture site, which may cause pressure necrosis and slow healing. It is also shown from [13] and [14] that nitinol has the ability to recover from strains ~ 35 times greater than stainless steels and titanium alloys. This property gives nitinol the property to store energy and release it slowly to exert dynamic compression forces at the fusion site.

Industrial manufacturing of nitinol uses vacuum arc remelting (VAR) or vacuum induction melting processes (VIM). VAR for nitinol uses a water-cooled copper crucible and a direct current electric arc in a 0.1–1 Pa vacuum [15]. VIM uses a high-density graphite crucible and electromagnetic induction to induce eddy currents which melt the metal [16]. VAR is a safer process compared to VIM in this case as carbon atoms from the graphite crucible can react with the titanium ions to form hard inclusions due to the high process temperatures [17]. This fact arises out of the

Table 1 Comparison of Young's modulus of nitinol, stainless steel, titanium alloy and human bone

Material	Young's Modulus (GPa)	ASTM Standard	References
SE 508 ELI Nitinol	41–75	ASTM-F2063-12	[10]
316L Stainless Steel	193	ASTM-F138-13a	[13]
Ti-6Al-4V Titanium	110–119	ASTM-F136-13	[14]
Cortical Human Bone	18	N/A	[11]

process environment, and more comparative studies are required to generate data about which process is more suitable for industrial manufacturing. Studies by Otubo et al. [16] show that electron beam melting (EBM) is an alternative to the VIM process giving NiTi alloy of a higher purity. But more analysis is needed to examine the feasibility of the EBM process for manufacture of nitinol at an industrial level. Other methods like induction skull melting, plasma arc melting and physical vapour deposition have been at experimental levels. But to determine whether these methods can be adopted for industrial manufacturing of nitinol, more studies will have to be performed in this area.

The unique properties possessed by nitinol—shape memory effect (SME) and superelasticity (SE)—are born out of the fact that nitinol shows strain recovery up to 8% and even up to 10% in certain cases [18]. When this recovery is obtained by temperature change, SME is observed and when it is obtained by deformation, PE is observed. Nitinol containing nominally 54.5–57.0% nickel is used to manufacture medical devices and implants. First discovered in 1959, these properties of nitinol have been exhaustively exploited in a multitude of applications in the robotics, aerospace, automotive, telecommunications and biomedical industries [19, 20].

3 Path of Action of a Bone Staple

In the following section, A_s and A_f refer to the austenite start and austenite finish temperatures, respectively. The austenite start temperature is the temperature at which the shape memory alloy begins to transition to an austenitic structure from a 100% martensitic state. The austenite finish temperature is the temperature at which the shape memory alloy achieves a 100% austenitic state [21].

Considering the use of bone staples in orthopaedic treatment procedures, broadly two kinds of nitinol bone staples are available [6]. The first kind of staples exert continuous compression by the shape memory effect while the second kind perform the same function by the superelasticity effect.

The primary aim of a bone staple is to apply a dynamic compression force across the two mating surfaces of the bone to establish suitable biomechanical conditions which will lead to osteosynthesis. The value of this force must be carefully regulated and is a design factor of paramount importance [22]. If too high, the force can cause

Fig. 2 Graph showing force generated versus angle of deflection behaviour for NiTi Euroflex wires for three different diameters [24]
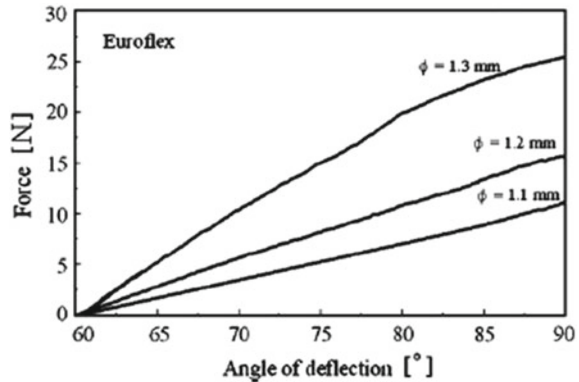
pressure necrosis, and if too low, the healing process may be very slow or the fracture may not heal at all [12, 23]. This compression force can be generated by the thermal shape memory effect or by superelasticity.

Four kinds of nitinol bone staples are commercially used and tabulated in Table 2:

1. Room temperature superelastic (RTSE): In this type of staple, the A_f temperature is an important design consideration because superelasticity is shown only at 0–40 °C above A_f. Hence, the A_f of the nitinol used should be near the body temperature (37 °C). The leg to bridge angle of such staples is kept ~60° in the manufactured product. After necessary considerations and calculations, holes of a suitable diameter are drilled at the exact location. The legs are mechanically opened by special tools such that the leg to bridge angle is 90°. The deformed staple is carefully handled and installed across the mating surface such that the legs fit into the holes without the possibility of the bone staple extruding from the site which requires osteosynthesis. The differences in the values of the initial and the final leg to bridge angles generate forces which are adequate for osteosynthesis. As experimentally determined by Z. Lekston et al. and shown in Figure X, NiTi Euroflex wires (Ti-50.8 at.% Ni) of 1.3 mm diameter give a compression force of ~25 N [24].
   (e.g. DYNAFIT system SE staples by Neosteo) [25] (Fig. 2).
2. Body temperature activated (BTA): The nitinol used for these kind of staples has A_f below body temperature and above room temperature. The temperature of the staple is maintained well below body temperature. The legs of the staple are inserted into the pre drilled holes, and the staple's temperature starts to increase. After the temperature crosses A_f, the staple achieves a complete austenitic structure and assumes the preset austenitic shape which is designed as to exert continuous compressive forces across the mating surfaces.
   (e.g. Insta-Fix fixation systems by OT Medical LLC) [26].
3. Heat activated (HA): The nitinol used for these kind of staples has A_s slightly above body temperature and A_f low enough for the staple to reach 100% austenitic structure without the application of excess amounts of heat. 60 °C is accepted

Staple	A_f range (°C)	Compression force
RTSE	0–25	High
BTA	25–35	Low
HA	45–55	Medium/high
CHA	45–55	Optimizable

as the general temperature at which tissue damage starts to occur, including thermal necrosis [27]. Hence, A_f is kept safely lower than this value, in this case at 45–55 °C. Heat is applied with an electrical cautery device.

(e.g. staples manufactured by InteliFUSE Inc.) [28].

4. Controlled heat activated (CHA): These have the same design and working principles as HA staples but the postinsertion heat treatment is done with the use of a specialized electrical heat energy source (e.g. warming system from the Memograph staple system) [29] to control the exact degree of shape recovery required.

(e.g. BME Barbed OSStaple^{TM}) [7].

4   Conclusion

This paper reviews the properties of stainless steel, titanium alloys and nitinol in conjunction with those of human bone and concludes that nitinol possesses the appropriate biofunctionality and biocompatibility to be used to manufacture bone staples until a more superior material is developed and is made feasible for such use.

The kind of bone staple, i.e. RTSE, BTA, HA or CHA which is to be used to cause internal osteosynthesis at a given fracture site, depends on factors as are summarized below:

– *Opinion of the Surgeon*: The surgeon may examine a given fracture site and may decide upon a number of factors: the amount of body heat available, the local temperature of the site, ease and safety of external heating, etc. As can be seen in the experimental work of Z. Lekston et al., superelastic staples are suggested for a zygomatic fracture and thermal shape memory staples are suggested for a mandibular condyle fracture.

– *Availability*: Emergency situations which demand that the staple be inserted soon after the injury is diagnosed require fast action. From the brochures of various companies manufacturing bone staples, it is observed that bone staples of various different designs are manufactured for different fracture sites. These staples will have different indications (e.g. metatarsal—phalange arthrodesis, Lisfranc arthrodesis, tibio—tarsal arthrodesis, phalange—metacarpal arthrodesis, chevron osteotomy). In these cases, the indication governs the kind of staple which is used, be it a superelastic staple or thermal shape memory staple.

This paper also concludes that more research is needed regarding the feasibility of the various methods used for experimental manufacture of nitinol, for the industrial manufacture of nitinol.

References

1. Delores Christina Schoen. *Adult Orthopaedic Nursing* Lippincott Williams & Wilkins.
2. Uhthoff HK, Poitras P, Backman DS. Internal plate fixation of fractures: short history and recent developments. *Journal of Orthopaedic Science*. 2006;11(2):118–126. https://doi.org/10.1007/s00776-005-0984-7.
3. Bonakdarpour A, Reinus W, Khurana J, *Diagnostic Imaging of Musculoskeletal Diseases: A Systematic Approach.* Springer Science & Business Media.
4. Material obtained from the Biomedical Engineering Department at the University of Iowa.
5. Smith T.F, DPM. *The Bone Staple: Tried and True Superhero of Bone Fixation.*
6. Russell S. Design Considerations for Nitinol Bone Staples, JMEPEG (2009) 18:831–835 https://doi.org/10.1007/s11665-009-9402-1.
7. Documentation obtained from BioMedical Enterprises Inc.
8. Documentation obtained from DePuySynthes Inc.
9. Documentation obtained from Confluent Medical Technologies.
10. Datasheet released by NDC.
11. Pal S. Chapter 2, *Design of Artificial Human Joints and Organs*, ISBN: 978-1-4614-6254-5.
12. Vegas M, Jose M.L, Stiffness, Compliance, Resilience, and Creep Deformation: Understanding Implant-Soft Tissue Dynamics in the Augmented Breast: Fundamentals Based on Materials Science, *Aesth Plast Surg* (2013) 37:922–930 https://doi.org/10.1007/s00266-013-0197-y.
13. Stainless Steel Grade Datasheets released by Atlas Steels, Australia.
14. Material obtained from AzoNetwork UK Ltd.
15. Ashish Patel and Daniel Fiore 2016 *IOP Conf. Ser.: Mater. Sci. Eng.* 143 012017 https://doi.org/10.1088/1757-899X/143/1/012017.
16. Otubo J. Low Carbon Content NiTi Shape Memory Alloy Produced by Electron Beam Melting, *Materials Research,* Vol.7 No.2 263–267, 2004.
17. ASM Handbook, Volume 15: Casting, Volume 15 Handbook Committee, p 1–8 https://doi.org/10.1361/asmhba0005200.
18. Kauffman, G.B. & Mayo, I. Chem. Educator (1997) 2: 1. https://doi.org/10.1007/s00897970111a.
19. D J Hartl *et al* 2010 *Smart Mater. Struct.* **19** 015020.
20. Wakjira, J.F. *The VT1 Shape Memory Alloy Heat Engine Design*. Thesis submitted to faculty of Virginia Polytechnic and State University.
21. Karamichailidou S. *The Unique Properties, Manufacturing Processes and Applications of Near Equiatomic Ni-Ti Alloys.* Laboratory of Materials, Department of Mechanical Engineering, University of Thessaly.
22. SPINI, Tatiana Sobottka, VALARELLI, Fabrício Pinelli, CANÇADO, Rodrigo Hermont, FREITAS, Karina Maria Salvatore de, & VILLARINHO, Denis Jardim. (2014). Transition temperature range of thermally activated nickel-titanium archwires. *Journal of Applied Oral Science*, *22*(2), 109–117. https://dx.doi.org/10.1590/1678-775720130133.
23. Parnell K, Hollis C, Hartdegen V. *Benefits of Nitinol for Bone fixation.*
24. Lekston Z, Preparation and Characterization of Nitinol Bone Staples for Cranio-Maxillofacial Surgery, JMEPEG (2012) 21:2650–2656 https://doi.org/10.1007/s11665-012-0372-3.
25. Documentation released by Neosteo, France.
26. Documentation obtained from OT Medical LLC.
27. Augustin G, Thermal Osteonecrosis and bone drilling parameters revisited, *Arch Orthop Trauma Surg.* 2008 Jan: 128(1):71–77.

28. Documentation obtained from InteliFUSE Inc.
29. FDA issued Premarket Notification for Memograph Warm system manufactured by InteliFUSE Inc.

A Review on Graphene

Farhan Sayed, Mitesh Parmar and Shashikant Auti

Abstract In today's time, when there is cutting edge competition, this kind of research will prove to help in many fields. A simple adhesive tape was used to achieve such a massive breakthrough in physics. Graphene is an allotrope of carbon having a two-dimensional structure. It exhibits excellent mechanical and electronic properties. Owing to its exceptional physical, it has received a tremendous attention and research interest. This material can be used to tackle the continuous device scaling and performance requirement. Having a honeycomb lattice structure and being densely packed, this one-atom-thick material has gained a lot of recognition over past few years. This article will mainly focus on the developing technologies by the use of graphene.

Keywords Graphene · Limitless energy · Transistor · Properties · CVD
Desalination

1 Introduction

New material is usually the emissary of new technologies and various developments in the existing technologies. One simple example of this is the transformation of Stone Age into the Bronze Age. This Bronze Age then was followed but the Iron Age and each age is labeled by the material that was bearing the new technology on or the new society at us as a whole and every new material was better than its

F. Sayed (✉) · M. Parmar
Department of Mechanical Engineering, D.J. Sanghvi College of Engineering,
Mumbai, India
e-mail: farhansayed696@gmail.com

M. Parmar
e-mail: parmarmike39@gmail.com

S. Auti
Department of Mechanical Engineering, Veermata Jijabai Technological Institute (VJTI),
Matunga, Mumbai, India

predecessor and it also made life simpler for people of that age. Still today, we always have new technologies that come with the introduction of new material [1]. This new development that has come only in the latest decades or so and that is the ability of using the basic sciences like chemistry, physics combined with material science, and we are now able to atom by atom by item design new materials having designer functionalities. This material of superlatives was founded by researchers at the University of Manchester, Prof. Andre Geim and Prof. Konstantin Novoselov in 2004 until when it was isolated [1].

2   Initial Development

They made use of a sticky tape repeatedly on a graphite to separate its fragment. By doing this, they obtained one-atom-thick layer of graphite known as graphene [2]. It is a platform material which will enable a 100 of new application. This one-atom-thick material can be as large as a piece of paper or a roll of newspaper. It is made up of little hexagon of carbon all join together to make a sheet. It is made completely of carbon and looks like an atomic-scale chicken wire because of its unique property, it can replace existing material and make those end applications better [1]. Graphene is one of the brand-new materials that the world is focusing on, and it is only one of the pieces in the puzzle of nanotechnologies which will further help in unlocking various new horizons [2]. Here, what happens is three of them will fall in a plain and will form a SP2 hybridization, and the neighboring carbon atom wants to share the electron with each other, and they do this very well as it forms a covalent bond, and this bond is extremely strong which makes graphene the strongest and also the most flexible material. Graphene is actually the stable form of carbon which makes it stronger than diamond. If the excitation of diamond is done beyond threshold, then it falls to graphene as it is unstable. Graphene has a width and length, but it has no thickness so you can address it all over as a big sheet. Moreover, it has a quality of being impermeable to other elements and substances [2]. As we are aware that carbon is capable of making a lot of different compounds and the four electrons which are present in the outer shell are responsible of it forming a chicken wire structure and has these blobs as shown in Fig. 1.

Graphene usually has a honeycomb-like structure. It is made up of a hexagonal lattice. It is only one-atom thick. It absorbs about 2.3% of light so it can be seen with naked eyes. It can be obtained either in the form of corrugated sheets or chunks weighing in milligrams [3]. It is ultra-thin yet immensely tough. It is 200 times stronger than steel but incredibly flexible.

Fig. 1 Upper figure shows the internal arrangement in the carbon atom in graphene. From second figure, honeycomb structure of graphene and the bond between carbon atoms can be visualized. (Image: www. understandingnano.com and Nanotechnology for Dummies (2nd edition), from Wiley Publishing)
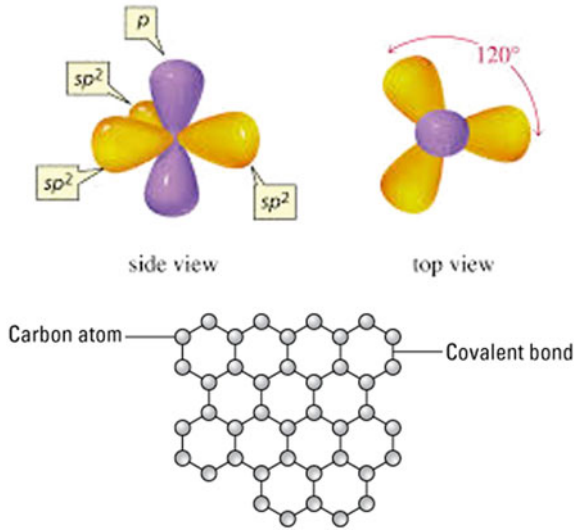
3 Techniques of Graphene Production

3.1 Mechanical Exfoliation

R. Ruoff and group introduced this technique first. This method is either called a drawing method or scotch tape method. In this, the adhesive tape is used to separate the layer of graphene from the graphite fragment [4]. For obtaining layer, multiple exfoliating steps are required. Dry deposition technique is used to deposit this exfoliated layer on a silicon wafer. Back in 2014, this method was used for obtaining graphene with the highest electron mobility and list amount of defects [5].

3.2 Chemically Derived Graphene

In 2006, R. Ruoff and group were the first to use this process for producing graphene by using this method [2, 6]. One of the major plus in using this method was the quantity of graphene produced and also the low cost. In this method, firstly, graphene oxide is obtained from graphite, and then, graphite oxide is reduced to graphene. In these, hummers' method is used to modify graphene into a water dispersal intermediary graphite oxide. This graphite oxide is then subjected to exfoliation because of the mechanical force when these graphite oxide sheets are stacked [6].

3.3   Chemical Vapor Deposition

The most popular technique of graphene production is chemical vapor deposition. It can be used for producing graphene on large scale and also having high quality. The gaseous substances are put on a substrate by the use of a CVD [4]. In this, a reaction chamber is used which is set at an ambient temperature in which the combination of various gas molecules takes place. The substrate surface gets covered with a thin film of material as the gases in the reaction chamber come in contact with the substrate [1]. The temperature in the reaction chamber plays a vital role in this process. The waste gases after the process are pumped out of the reaction chamber. This process takes place at a very slow speed often described in microns of thickness per hour, and the substrate is usually quoted within a very small amount. The quality of the material produced is quite high and has high purity, and its hardness is also increased [3].

4   Properties

4.1   Mechanical

One of the main reasons why graphene stands out from the other materials either on individual basis or as an agent for reinforcing composites of its impeccable mechanical properties [7]. Major contribution in the stability graphene comes from the SP2 hybridization bond which forms a hexagonal lattice [8]. When the effective thickness of the graphene sheet was 0.335 nm, its young modules was about $1.0 + 0.1$ TPa. A monolayer of graphene which is defect-free is considered to be the strongest material ever tested which has an intrinsic strength of 130 GPa for suppose wrinkled graphene whose aspect ratio is adjusted to 0.17 in Figs. 2 and 3 for strength and shear modules are 610 and 1100 MPa, respectively [9]. Mechanical properties of an isotropic member are mainly described by focusing on four parameters. These four parameters are as follows—Young's modulus, Poisson's ratio, breaking stress/strain, and bending rigidity [10]. The weight of strength ratio of graphene is commendable which makes it so unique for all the other materials present out there. For a piece of 1 s m, the weight is approximately 0.77 mg, which is roughly 1000 times lighter than the paper of the same size [11].

4.2   Electronics

The main feature of graphene is that in this, both the holes and the electrons act as a charge carrier. As graphene is an allotrope of carbon so it has six electrons. Out of these six electrons, two are in the inner shell and four in the outer shell. Now, if we

consider an individual carbon atom, then these four electrons in the outer shell are available for further chemical bonding [12]. But in graphene, one electron is freely available for electronic conduction, whereas each atom is connected to other carbon atoms. The carbon-to-carbon bonds are enhanced by the pi electrons located above and below the graphene sheet [13]. The pi orbital electron bonding and antibonding are responsible for the major fundamental electronic properties of graphene. This electronic mobility of graphene is quite high [14]. This is usually limited by the photon scattering. The limiting factor for this is the quality of graphene and the substrate which is used. The mobility of electron is usually not dependent on the temperature [7].

4.3 Optical

The direct interband electron transmissions are responsible for all the optical properties in graphene. The optical properties like transmission refraction can be manip-
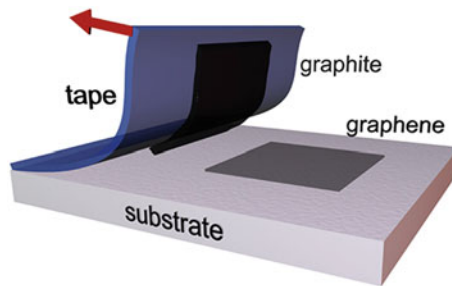
Fig. 2 Process of mechanical exfoliation of graphene with the help of tape (www.graphene.ac.rs)
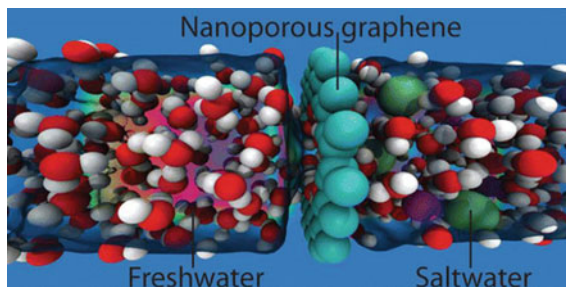
Fig. 3 Desalination of saltwater using nanoporous graphene membrane. When water molecules (red and white), and sodium and chlorine ions (green and purple) in saltwater, on the right, encounter a sheet of graphene (pale blue, center) perforated by holes of the right size, the water passes through (left side), but the sodium and chlorine of the salt are blocked. Graphic: David Cohen-Tanugi (www.wordlesstech.com)

ulated easily by varying the intensity of light traveling through graphene [15]. The reflectant from multilayer graphene has a sharp downfall when the temperature is low and the carrier density is low. It can absorb 2.3% of light even when it is one-atom thick [16]. More the layers of graphene, more will be the absorption of white light. The presence of oxygen functionalities may affect the optical parameters [17]. As the carrier density increases with the temperature so does the reflectance. Graphene's transmittance is a function of carrier density frequency and temperature. At low temperature, the conductivity of graphene goes a minimum value [18]. These strong interactions of direct fermions with electromagnetic radiation, linear structure are the factors with separate graphene from other materials and impart the required optical properties [19].

5   Applications

5.1   Limitless Energy

This project was proposed by Mr. Manoj Bhargava. In this, the main aim was to bring the heat which is present in the earth's crust to the surface by some means so that this heat could be used for producing energy. So, for this purpose, strings made up of graphene were used. The numbers of strings were arranged in such a fashion that they sort of form a cable of graphene. This rope would then be travelled to the earth's crust from where the heat would be brought up. This heat which is brought up would then be used for producing electricity, and this electricity produced would be free of harmful emissions. Moreover, the source from which it is produced is limitless.

5.2   Detecting System

It can be used to make a good artificial system to smell the chemicals in the air detecting a bomb or drugs can be done by an electronic system when the detection properties of graphene are combined with the protein molecules of that of our nose or a dogs' nose this electronic system will have some ability to smell as a person does or as a dog does [20, 21].

5.3   Diagnostic Tool

It can be used to make a diagnostic tool that will be capable of testing various diseases with single drop of blood, and the physician will give the results within a couple of minutes [21].

5.4 Graphene Transistors

If suppose a person's eye gets destroyed but the visual code is intact, then we could connect it with some biocompatible material and give it impulses, then the site may be regained as graphene is biocompatible material, and if graphene is allowed to interact with a nerve cell, it will be ready to take electrical stimulus that we feed it [22]. That could be done by placing a camera which would give impulses to the graphene membrane and that it would trigger impulse for this [23].

5.5 Desalination of Sea Water

Almost 97.2% of water on earth is held by the ocean that means it is salty water. This water could be converted into drinkable by using a graphene divider which has nanoholes in it, these holes are decorated by hydroxyl molecules, and then the pressure gradient is applied. This process is a kind of reverse osmosis [24]. This results in salt getting extracted from the water, and the water only passes through the graphene divider, and this process is much more efficient. The energy required for reverse osmosis is quite high if we make use of any other membrane, but if we use a graphene oxide membrane, this energy could be reduced anywhere between 15 and 46% [25].

Desalination when done by reverse osmosis requires an osmotic membrane. This membrane allows the water to pass through it at a much higher rate as compared to the salts [26]. This osmotic membrane occurs naturally in living beings all over everywhere. It may also be referred as semipermeable membrane because of its ability which allows it to pass some constituents while holding back the others. In reverse osmosis, a pressure gradient is applied to the sea water and this gradient is much higher than that of the osmotic pressure applied [27]. This gradient will cause the water to pass through the semipermeable membrane leaving behind the salts. The freshwater is then obtained from the other side of the membrane. The greater the pressure gradient, the higher will be the rate of freshwater transported across the membrane. Shells of water molecules are formed because of the salts which are present in the water [28]. These tiny capillaries of graphene oxide membrane block the salt from flowing along with the water. Water molecules are able to pass through the graphene membrane, whereas the salts are not able to flow. There should be precise control on the size of the hole in the graphene oxide membrane. If too large hole is created, then salts will also flow along the water, whereas if the hole is too small, it will not let the water pass. Ideally, the hole should be 1 nanometer or 1 billionth of meter [29]. For creating such small holes various processes such as helium ion bombarding, chemical etching, oxygen plasma treatment, gallium ion bombarding with chemical oxidation.

6   Conclusion

Graphene shows favorable growth in technology and applications. However, a few key challenges must be addressed and resolved to realize the potential of graphene-based nanocomposites regarding synthesis methods, costs, and applications. The future of gadgets can be completely based on graphene due to its extraordinary properties. Due to the high diversity, properties, and advantages of graphene, a multitude of nanocomposite-based applications has been envisioned to be practical. These multifunctional graphene composites coupled with affordable cost will soon be seen in the global market.

References

1. A. H. Castro Neto, F. G. (2009). The electronic properties of graphene. Rev. Mod. Phys. 81, 109–110.
2. Arash Aghigh, V. A. (2015). Recent advances in utilization of graphene for filtration and desalination of water: A review.
3. Caterina soldano, A. M. (2010). Production, properties and potential of graphene. Carbon Volume 48, Issue 8.
4. Changgu Lee, X. W. (2008). Measurement of the Elastic Properties and Intrinsic Strength of Monolayer Graphene. 385–388.
5. Claire Berger, Z. S. (2006). Electronic Confinement and Coherence in Patterned Epitaxial Graphene. Vol. 312, Issue 5777, 1191–1196.
6. Deepthi Konatham, J. Y. (2013). Simulation Insights for Graphene-Based Water Desalination Membranes. Langmuir 29 (38), 11884–11897.
7. Falkovsky, L. A. (2008). Optical properties of graphene. Journal of Physics, Volume 129, 1.
8. Falkovsky, L. A. (2008). Optical properties of graphene and IV–VI semiconductors. Physics-Uspekhi, Volume 51, 9.
9. Fengnian Xia, D. B.-m. (2010). Graphene Field-Effect Transistors with High On/Off Current Ratio and Large Transport Band Gap at Room Temperature. Nano Letter, 10 (2), 715–718.
10. Grossman, D. C.-T. (2012). Water Desalination across Nanoporous Graphene. Nano Lett., 12 (7), 3602–3608.
11. He Shen, L. Z. (2012). Biomedical Applications of Graphene. Theranostice, 283–294.
12. K. S. Novoselov, S. V. (2007). Electronic properties of graphene.
13. K. S. Novoselov, V. I. (2012). A roadmap for graphene. Nature volume 490, 192–200.
14. Kumar Mishra S. Ramaprabhu, A. (2011). Functionalized graphene sheets for arsenic removal and desalination of sea water. Desalination vol 282, 39–45.
15. Matthew J. Allen, V. C. (2009). Honeycomb Carbon: A Review of Graphene. Materials for Electronics.
16. Mi, M. H. (2013). Enabling Graphene Oxide Nanosheets as Water Separation Membranes. Environ. Sci. Technol., 3715–3723.
17. Mohammad A. Rafiee, J. R.-Z. (2009). Enhanced Mechanical Properties of Nanocomposites at Low Graphene Content. ACS Nano.
18. Ovid, I. (2013). Mechanical properties of Graphene. Rev. Adv. Master Science, 34, 2013.
19. Ruoff, S. P. (2009). Chemical methods for the production of graphene. Nature Nanotechnology volume 4, 217–224.
20. Ruoff, Y. Z. (2010). Graphene and Graphene Oxide: Synthesis, Properties, and Applications.
21. Schwierz, F. (2010). Graphene transistors. Nature Nanotechnology volume 5, 487–496.

22. Sumedh P. Surwade, S. N. (2015). Water desalination using Nanoporous single-layer graphene. Nature Nanotechnology volume 10, 459–464.
23. Tanenbauma, I. W. (2007). Mechanical properties of suspended graphene sheets. Journal of Vacuum Science and Technology B 25, 2558.
24. Thomas G. Pedersen, C. F.-P. (2008). Optical properties of graphene antidot lattices. Phys. Rev. B 77.
25. V.G. Bayev, J. (2018). CVD graphene sheets electrochemically decorated with core-shell.
26. Y C Huang, C. P. (2007). Magnetic and quantum confinement effects on electronic and optical properties of graphene ribbons. Nanotechnology, Volume 18, 49.
27. Yanfei Xu, Z. L. (2009). A Graphene Hybrid Material Covalently Functionalized with Porphyrin: Synthesis and Optical Limiting Property.
28. Ying Wang, Y. L. (2009). Application of graphene-modified electrode for selective detection of dopamine.
29. Yu Wang, Y. Z. (2011). Electrochemical Delamination of CVD-Grown Graphene Film.

Comparative Wear Analysis of (3 × 3) PTFE Composite Materials

A. D. Diwate and S. B. Thakre

Abstract This paper investigated experimentally the wear analysis of PTFE and its fillers of different weight percentage by using Pin-on-disc test rig. In this experiment, the parameter used is sliding distance, sliding speed, load, time, etc. The load is the most influencing factor on wear. It is analysed by using mini tab R14 software. From the experimental investigation, it is revealed that PTFE containing 35% Carbon is the low wear rate than the other PTFE-filled materials.

Keywords PTFE-filled materials · Pin-on-disc test rig · Mini tab R14 software

1 Introduction

Though PTFE material is conceptually simple for bearing materials, there are many problems associated to the friction and wear. After a decade of research, PTFE materials are extensively used for simple application such as bearing materials [1], in petrochemical- and chemical-processing material of select for gaskets and vessel linings and in electrical applications as an insulator also in food, beverage and pharmaceutical industries [1, 2]. At low temperatures, PTFE is having high flexural strength; it is water resistance, electrical resistance and high dielectric strength; moreover, coefficient of friction is low [3]. PTFE density is very high up to 2200 kg/m^3. This paper studied the tribological characteristics of PTFE-filled filler materials such as: (1) 25% Carbon, 25% Bronze, 25% Glass; (2) 30% Carbon, 30% Bronze, 30% Glass; (3) 35% Carbon, 35% Bronze, 35% Glass.

B. M. Rudresh et al. [4] studied the tribological behaviour of Polyamide 66 and Polytetrafluoroethylene composites with PTFE wt. 5, 10, 15, 20, 25 and 30% by

A. D. Diwate (✉)
TSSM'S BSCOER Narhe, Pune, Maharashtra, India
e-mail: addiwate@gmail.com

S. B. Thakre
Mechanical Department, PRMITR, Badnera, Amravati, India
e-mail: sbthakre2007@gmail.com

using abrasion tester with rubber wheel. The outcome shows that the volume of wear and the specific wear rate are the functions of sliding distance, load and the material composition. J. B. Singh et al. [5] have explained the dry sliding wear of Cu–15Ni–8Sn (in wt%) Bronze against a stainless steel 440C is investigated using a Pin-on-disc tribometer. The debris microstructure of the worn surface of the pin have been characterized using X-ray diffraction, scanning electron microscopy (SEM), transmission electron microscopy (TEM), energy-dispersive spectroscopy (EDS) and X-ray photoelectron spectroscopy. The debris consists of particles of Fe_2O_3 and CuO, in addition to Bronze particles. EDS analysis discovered that Fe and Cr elements are picked up by the Bronze from the stainless steel while the Cu, Ni and Sn are picked up by Fe_2O_3 from the pin, during the test. Cross-section SEM of the worn pin resulted in highly deformed subsurface layer, capped by a thin layer separating the outer surface and the deformed layer. M. Conte [6] has explained the analysis of PTFE composites showing characteristic can be improved by low friction is lost due to the presence of hard particles. Self-lubricating and the load-carrying properties were improved by improving the wear properties of the PTFE in both soft and hard phases in a composite [7].

2   Objectives

The objective of this research work is to generate the sustainable bearing materials for that we need to analyse the effect of following composite materials on wear rate.

1. To study the effect of PTFE with 25% Carbon, 25% Glass, 25% Bronze on rate of wear.
2. To study the effect of PTFE+30% Carbon, PTFE+30% Glass, PTFE+30% Bronze on rate of wear.
3. To study the effect of PTFE+35% Carbon, PTFE+35% Glass, PTFE+35% Bronze on rate of wear.
4. To study the effective parameters like load, velocity of sliding, sliding distance on wear rate.
5. To develop mathematical model for wear which includes load, velocity of sliding, sliding distance.

The above objectives have been achieved by Pin-on-disc tribometer in sliding at dry environment.

3   Material Preparations

PTFE and its composite in the form of rod are available in the marketplace. Necessary turning and facing operations have been performing on the respective rods (Fig. 1).

Fig. 1 Test specimen

The specimen of pins is fitted into the pin holder, and observations are noted in the following section.

4 Experimental Approach

The PTFE-filled various composites such as 25% Carbon, 25% Bronze, 25% Glass and 30% Carbon, 30% Bronze, 30% Glass and 35% Carbon, 35% Bronze, 35% Glass investigated the wear behaviour by using Pin-on-disc test rig (Figs. 2 and 3) under normal room temperature in dry sliding condition. The specimen diameter size 10–30 mm and length 30–50 mm have been held in the specimen holder. The specimen is in contact with the disc. The disc material is EN-31 with hardness 60 HRC and Ra 0.3 [8]. The factors used are load, velocity of sliding, sliding distance and time. The time is the constant factor, and others are variables. Each factor having three different levels is shown in Tables 1 and 2.

5 Results and Discussion

As per the standard orthogonal arrangement, the experiments were conducted. The degrees of freedom for the orthogonal array should be greater than or equal to sum of those wear parameters on this condition the selection of the orthogonal array was based. In this research, orthogonal array was chosen L9, which has 9 rows and 4 columns. The tribological parameters selected for the experiments were speed (S), load (L), sliding distance (SD), velocity (V).

Following graphs shows the effect of addition of filler materials in PTFE on wear rate. Graph 1 shows the PTFE containing 35% Carbon having 1 µm wear at constant
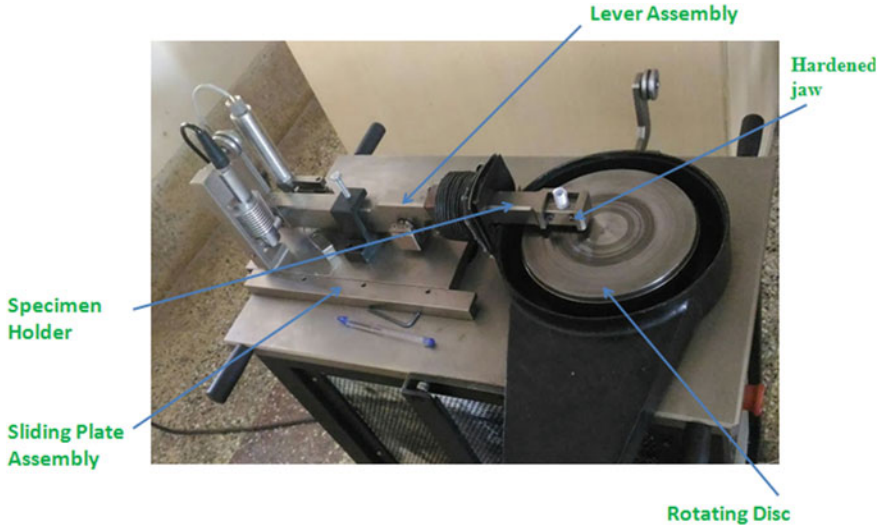
Fig. 2 Experimental set-up of friction and wear test rig

Fig. 3 Experimental set-up of friction and wear test rig

room temperature and load at 4 kg at 900 rpm speed. Similarly, Graph 2 shows the PTFE containing 30% Carbon having 4 μm wear. Graph 3 shows the PTFE containing 25% Carbon having 6 μm. Graph 4 shows the PTFE containing 35% Bronze having 13 μm. Graph 5 shows the PTFE containing 30% Bronze having 14 μm. Graph 6 shows the PTFE containing 25% Bronze having 15 μm. Graph 7 shows the PTFE containing 25% Glass having 30 μm. Graph 8 shows the PTFE containing 30% Glass

Table 1 Assigning of levels to the variable as applicable to Pin-on-disc machine

Sr. No	Factors	Levels		
		1	2	3
1	Load (kg)	2	3	4
2	Sliding distance	1500	3000	4500
3	Sliding speed	300	600	900
4	Material	Material 1-PTFE+25% Carbon	Material 2-PTFE+25% Bronze	Material 3-PTFE+25% Glass
		Material 1-PTFE+30% Carbon	Material 2-PTFE+30% Bronze	Material 3-PTFE+30% Glass
		Material 1-PTFE+35% Carbon	Material 2-PTFE+35% Bronze	Material 3-PTFE+35% Glass

Table 2 Designation for PTFE materials

Material	Composition in weight %
I	PTFE+Carbon 25%
II	PTFE+Bronze 25%
III	PTFE+Glass 25%
IV	PTFE+30% Carbon
V	PTFE+30% Bronze
VI	PTFE+30% Glass
VII	PTFE+35% Carbon
VIII	PTFE+35% Bronze
IX	PTFE+35% Glass

having 34 µm. Graph 9 shows the PTFE containing 35% Glass having 38 µm. All these results are showed at constant room temperature, load 4 kg and speed 900 rpm. From the figure, it is revealed that PTFE containing 35% Carbon has low wear rate than the PTFE-filled other Carbon percentage by wt. Moreover, PTFE containing 35% Bronze has low wear rate than the PTFE-filled other Bronze percentage by wt. And PTFE containing 35% Glass has more wear rate than the PTFE-filled other Glass percentage by wt.

6 Conclusions

Addition of Carbon, Bronze and Glass filler material to PTFE resulted an increase in hardness and wear resistance. 35% Carbon-filled PTFE in properties is much better than other filled PTFE for their wear performance. Wear resistance significantly
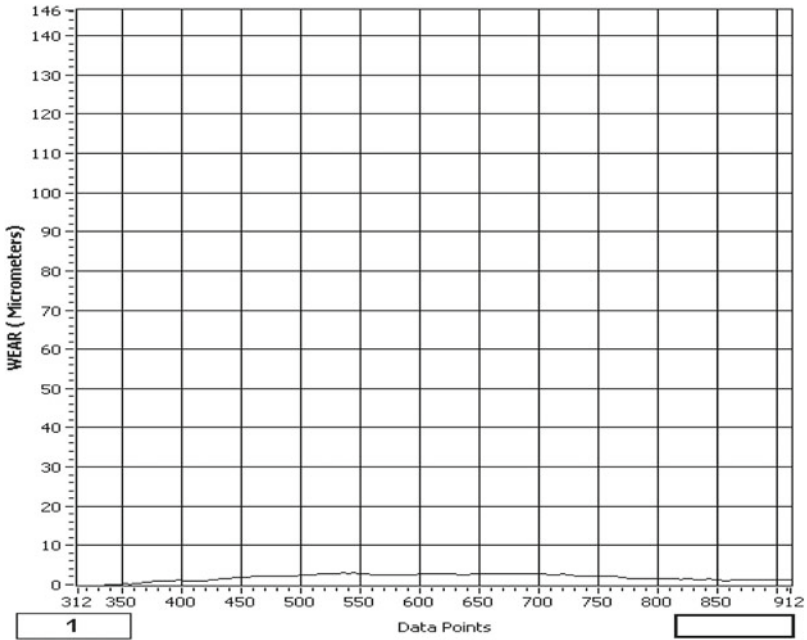
Graph 1   Wear versus Time PTFE containing 35% Carbon

improves by the addition of Carbon filler to virgin PTFE as compared to Bronze and Glass filler.

7   Scope for Future Work

The same experimental work can be performing under different working conditions. The experimentation can be performed at different conditions of load, sliding speed and distance of sliding. The testing can be carried out for different combination of fillers.
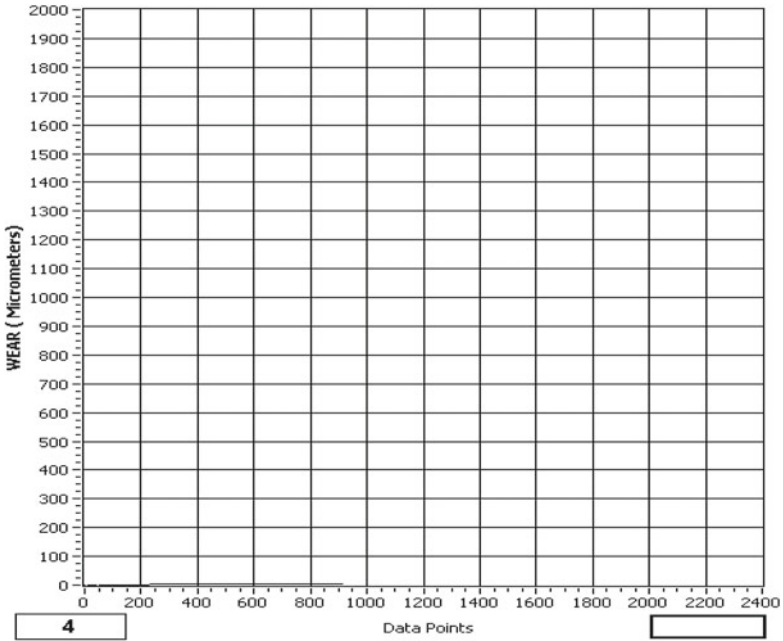
Graph 2 Wear versus Time PTFE containing 30% Carbon
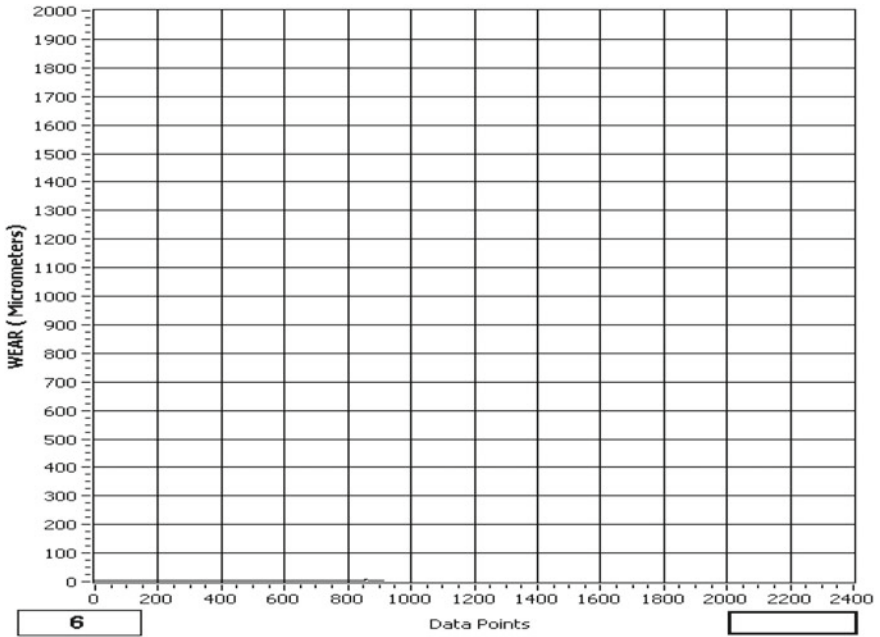
Graph 3 Wear versus Time PTFE containing 25% Carbon
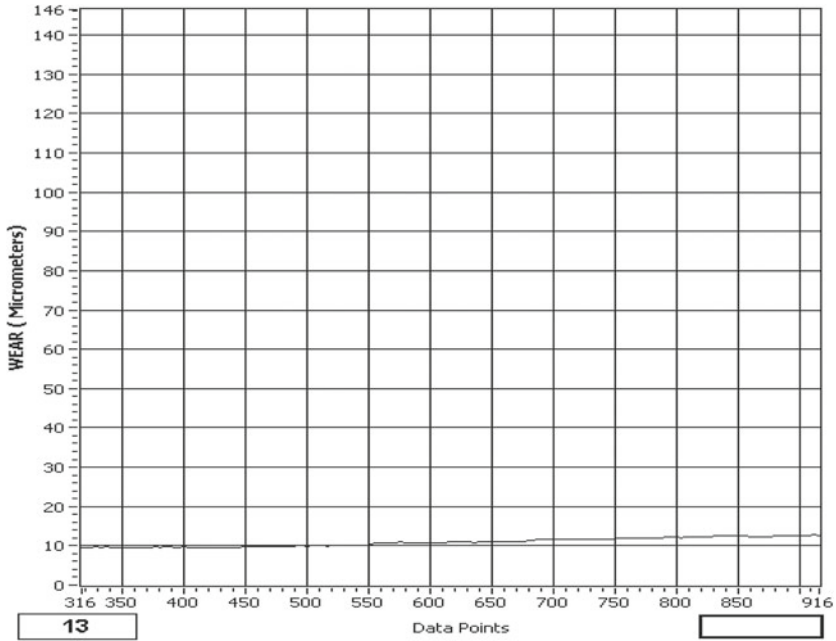
Graph 4 Wear versus Time PTFE containing 35% Bronze
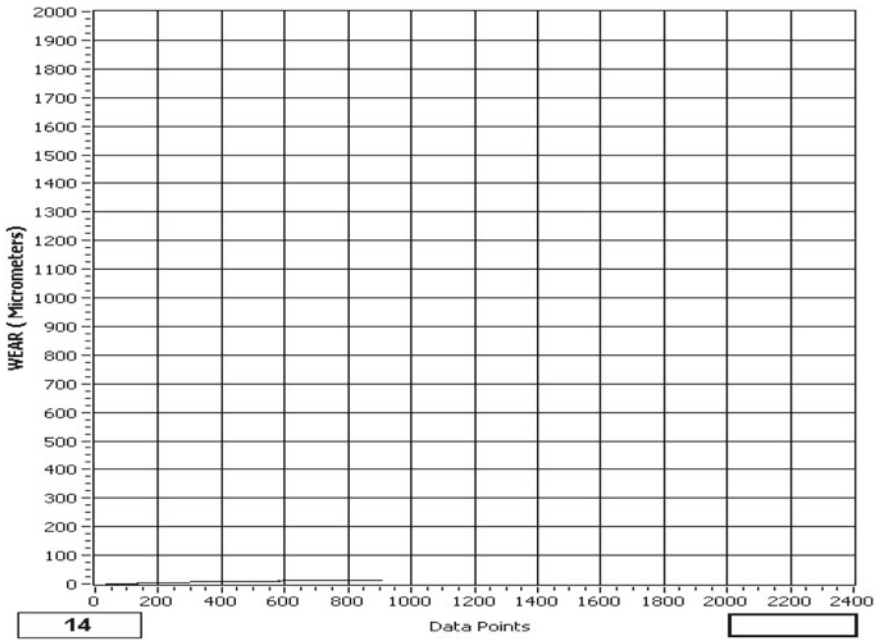
Graph 5 Wear versus Time PTFE containing 30% Bronze
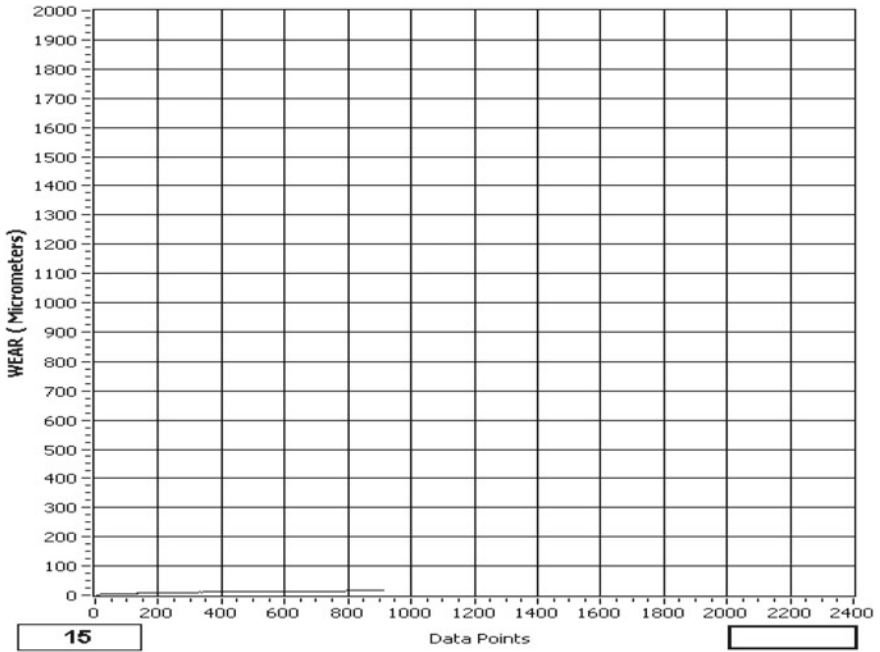
Graph 6   Wear versus Time PTFE containing 25% Bronze
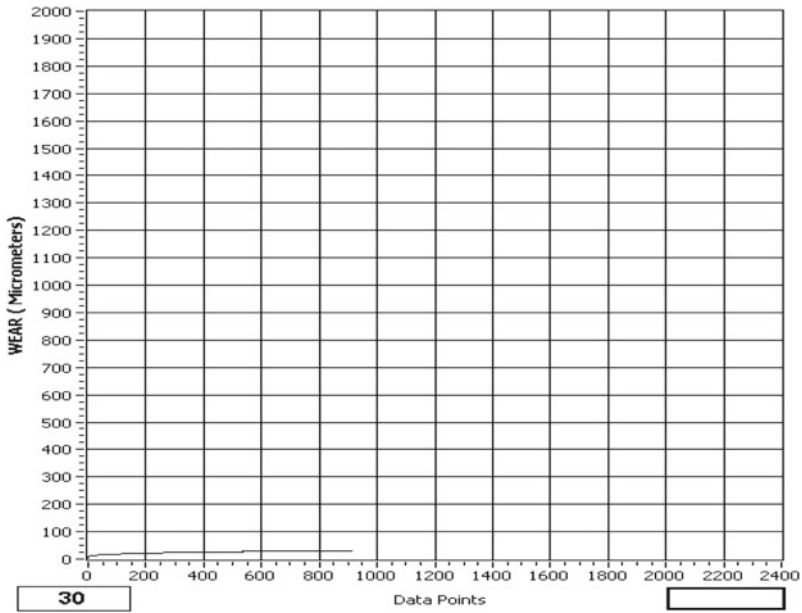
Graph 7   Wear versus Time PTFE containing 25% Glass
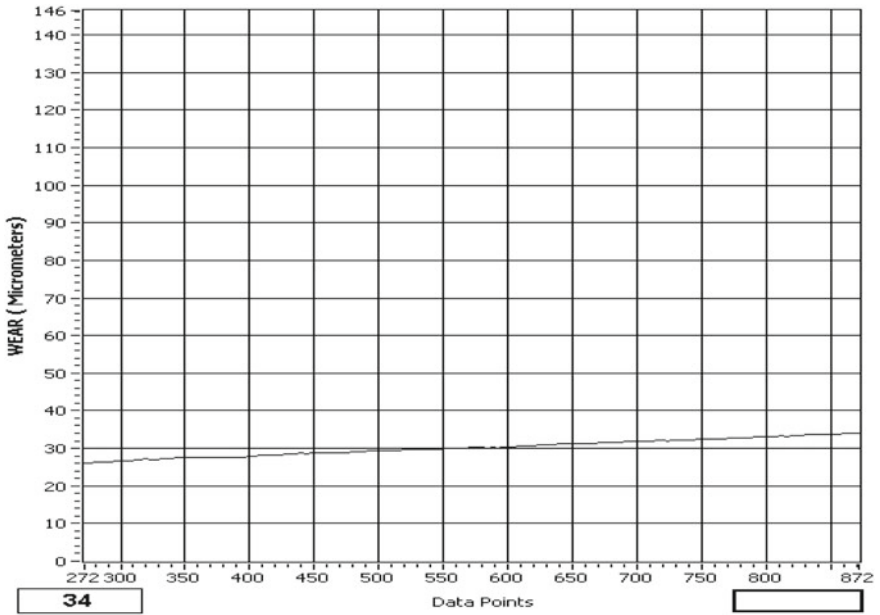
Graph 8   Wear versus Time PTFE containing 30% Glass
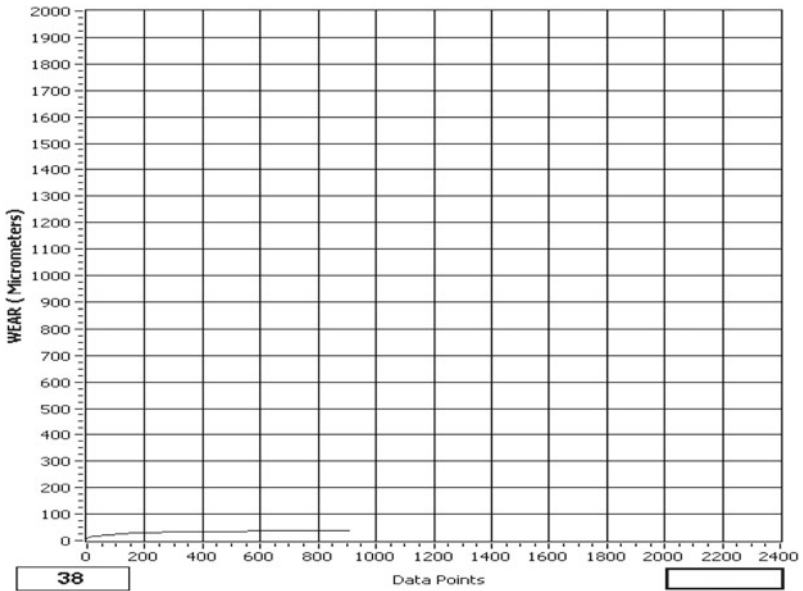
Graph 9   Wear versus Time PTFE containing 35% Glass

References

1. W. Gregory Sawyer, Kevin D. Freudenberg, Praveen Bhimaraj, Linda S. Schadler, (2003) A study on the friction and wear behavior of PTFE filled with alumina nanoparticles. Wear 254 (5–6):573–580
2. Talat Tevruz, : Tribological behaviors of carbon filled Polytetrafluroethylene (PTFE) dry journal bearings, Wear 221, 61–68 (1998)
3. J. Li, "Friction and wear properties of PTFE composites filled with PA6", Polymer composites, Volume 31, Issue 1 January 2010, Pages 38–42
4. B. M. Rudresh, B. N. Ravikumar, D. Madhu, "Hybrid Effect of Micro Fillers on the Mechanical Behavior of Polyamide66/Polytetrafluoroethylene Blend", IJACS 4(1) (2016) 77–84
5. J. B. Singh W. Cai, P. Bellon, Dry sliding of Cu–15 wt% Ni–8 wt% Sn bronze: Wear behaviour and microstructures, Wear 263 (2007) 830–841
6. M. Conte, A. Igartua, (2012) Study of PTFE composites tribological behavior. Wear 296 (1–2):568–574
7. B. Suresha, Kunigal Shiva Kumar, S. Seetharamu, P. Sampath Kumaran, "Friction and dry sliding wear behavior of carbon and glass fabric reinforced vinyl ester composites" Tribology International Volume 43, Issue 3, March 2010, Pages 602–609
8. Jaydeep Khedkar, Ioan Negulescu, Efstathios I Meletis, (2002) Sliding wear behavior of PTFE composites. Wear 252 (5-6):361-369

Synthesis of Polyaniline-Vanadium Pentoxide Nanocomposites: A High-Performance Conducting Material for Energy Storage

Sugam Shivhare, Praveen Kumar Loharkar, Supriya Vyas, Vivekanand Bagal and Malvika Sharma

Abstract Polyaniline-vanadium pentoxide (PANI-V_2O_5) nanocomposites have been synthesized via hydrothermal autoclave polymerization approach in acidic environment. The synthesis has not only stabilized the bulk morphology but has also improved the electronic conductivity due to the presence of doped polyaniline (PANI). This property is an important criterion for any material to be used as an electrode. The synthesized material is characterized by using FTIR, XRD and four-probe method, and the particle size is revealed by optical microscopy. It has been observed that the band gap value of nanocomposites has increased. This is attributed to increase in the concentration of metal oxides in nanocomposites. The results acquired are encouraging and presents themselves as a base for future advancements in energy storage applications.

Keywords Doping · Electrical conductivity · PANI-vanadium pentoxide
Metal oxide

1 Introduction

Nanocomposites (NCPs) offer extensive possibilities as hybrid conducting materials. These are formed by combining both the organic and inorganic entities and have exhibited improved characteristics in comparison with that shown by the conven-

S. Shivhare (✉) · V. Bagal · M. Sharma
Department of Applied Science, SVKM's NMIMS MPSTME, Shirpur Campus, Dhule 425405, Maharashtra, India
e-mail: Shivhare77@gmail.com

P. K. Loharkar
Department of Mechanical Engineering, SVKM's NMIMS MPSTME, Shirpur Campus, Dhule 425405, Maharashtra, India

S. Vyas
Department of Applied Science, SVVV, Indore 452001, Madhya Pradesh, India

tional materials used in solitude [1–4]. An important development in synthesis of nanocomposites has been advent of conducting polymers. These have been comprehensively examined by several researchers. Polyaniline (PANI) has presented itself as one such compound with several characteristics suitable for wide range of applications such as electronics, biosciences and pharmaceutics [5].

The primary reason behind extensive amount of research carried out on polyaniline is its molecular structure and more specifically, its conducting ability. PANI has intrinsic redox states which is key to its unique properties. For evaluating NCPs as electrode materials, the properties that are needed to be evaluated are, "Specific capacity (m Ah g^{-1})," "Charge/discharge cycle" and "Degree of capacity change upon cycling at different demands" [6–8].

The aim of this research is to synthesize polyaniline-vanadium pentoxide nanocomposites and to explore their morphology and characteristics. PANI-vanadium pentoxide NCPs have been prepared using hydrothermal autoclave polymerization approach in acidic environment.

2   Material and Experimental Method

The chemicals used for synthesis of nanocomposites (NCPs) were procured from "Sigma Aldrich" and used directly in as received form. These chemicals are "AR"-graded. It means that these are analytical reagents with high degree of purity.

2.1   Synthesis of V_2O_5 Particles

As per reported stoichiometry, a mixture of $Fe_3O_4 \cdot 9H_2O$ and V_2O_5 were added to base solution of NaOH and mechanically stirred for half an hour at 500 rpm [9]. The mix is then transferred into the autoclave for hydrothermal synthesis of the powder. The sample was heated for 8 h by ensuring temperature of 180 °C. The resultant product was taken together and cleaned up with distilled water. Drying was carried out using IR lamp with the temperature around 60 °C.

2.2   Synthesis of Polyaniline-Vanadium Pentoxide Nanocomposites (NCPs)

The synthesis was carried out by vigorous stirring along with addition of appropriate amount of V_2O_5 particles and aniline (1.25M) for 20 min. Then, ammonium peroxydisulfate was added to the mix and kept undisturbed for half an hour until dark green color was obtained in the presence of HCl (1M). The polymerization process
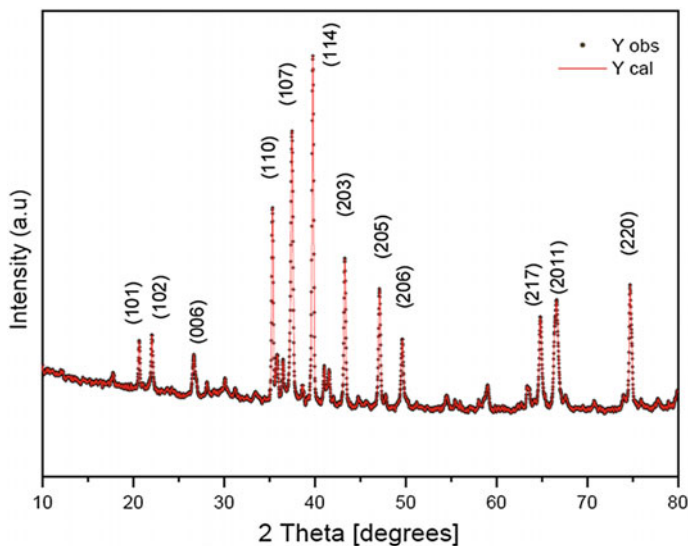
Fig. 1 XRD spectrum of $V_2Fe_3O_9$

took place for 24 h. The temperature of synthesis was 30 °C. The shady olive color products were filtered and washed by ethanol several times and dried at 60 °C by IR lamp. Pure PANI with a doping of HCl has also been synthesized by following the same procedure.

3   Results and Discussion

In order to verify the applicability of the synthesized nanocomposites, characterization of the powdered samples has been carried out using X-ray diffraction (XRD) done through Bruker D8 Advance XRD. Particle size is determined by optical microscope. For the identification of functional groups in the nanocomposites, Fourier transform infrared (FTIR) images were obtained using Burker Germany model vertex 70 FTIR Spectrometer. The most important characteristics for any material to be used as an electrode, i.e., electrical conductivity has been determined using a standard four-probe apparatus.

XRD spectra (See Figs. 1 and 2) of the synthesized NCPs observed sharp Bragg peaks signifying excellent morphology of vanadium ferrites. The results endorse hexagonal structure. The crystalline morphology of magnetic particles seems to be well-preserved during synthesis. This fact supports that there is no variation in peak position between $V_2Fe_3O_9$ and the NCPs observed. Moreover, wide peak in the range of $2\theta = 20–35°$ verifies the presence of PANI polymer [9, 10]. It has been observed that the peak falls with aggregation of hexaferrite in the polymer.
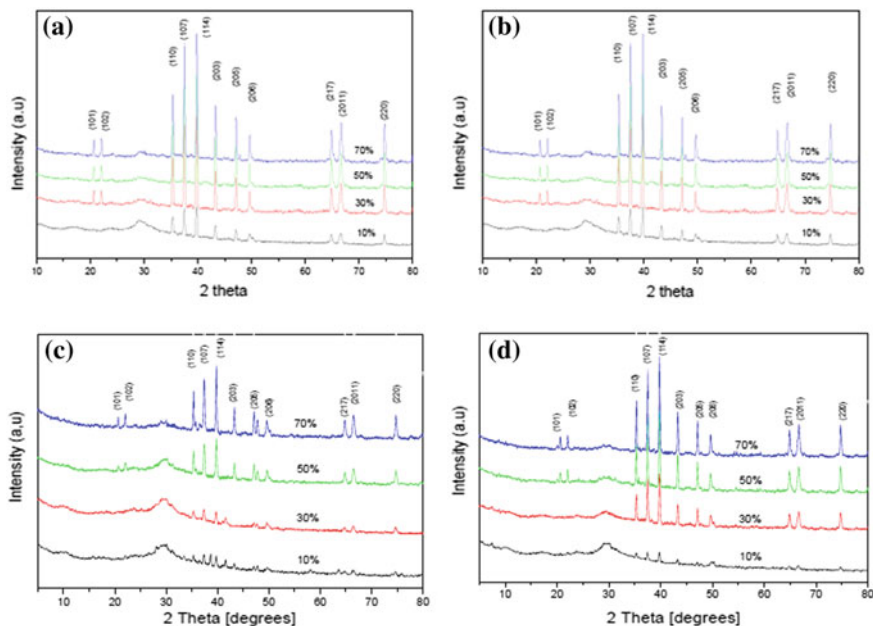
Fig. 2 XRD spectra of polyaniline-V$_2$Fe$_3$O$_9$ composites

FTIR spectrum (See Fig. 3) image of the sample has been generated in the frequency band of 400–4000 cm^{-1} to reveal the nature of chemical bonds along with the functional groups in the NCPs. The absorption peaks around 1485.19 cm^{-1} is due to the presence of benzene ring. The sudden peaks and valleys around the band at 1535 cm^{-1} is due to symmetric–nonsymmetric stretching in C–C bond. FTIR images of V$_2$O$_5$ nanosized particles have shown three characteristic vibration modes: V=O vibrations at 960.55 cm^{-1}, the symmetric stretch of V–O–V around 516 cm^{-1} and the asymmetric stretch of V–O–V at 802 cm^{-1}. As clearly seen, the bands appearing between 914 and 1095 cm^{-1} are attributed to vanadium-oxide stretching modes. Bands between 800 and 914 cm^{-1} represents the bridged V–O–V stretching [11, 12].

Electrical conductivity (at room temperature) of the NCPs has been measured by the four-probe method. The process involved compression of composite powders in the form of pellets having thickness of 0.71 mm diameter of 8.0 mm under constant pressure. Values of electrical conductivity (σ_{dc}) reduce with the accumulation of vanadium particles in the NCPs [13, 14]. Their extreme σ_{dc} value is found to be 1.4×10^{-3} S cm^{-1} which supports the excellent conductivity characteristics of the synthesized NCPs.

During synthesis, acidic environment is maintained throughout. Mechanical stirring helped in reducing the acid attack of the iron-oxide coat on NCPs, thereby preventing it from getting suspended.
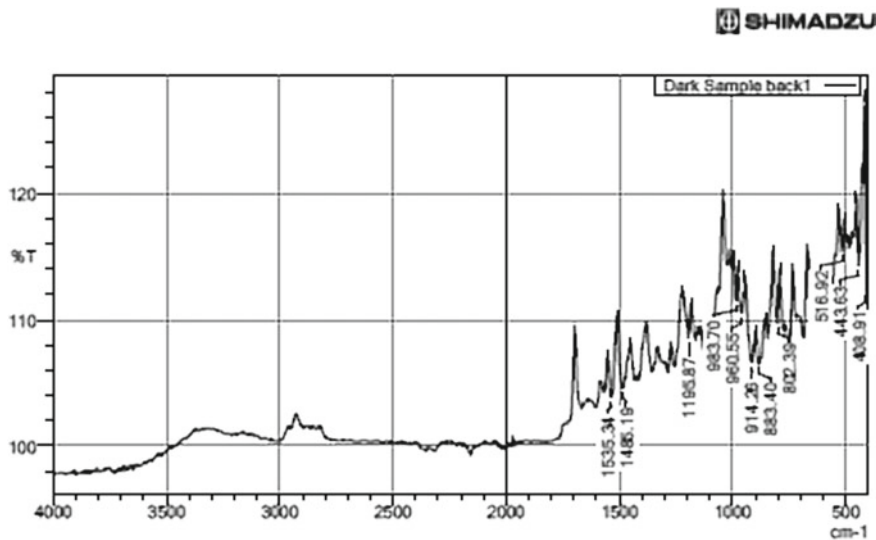
Fig. 3 Polyaniline-$V_2Fe_3O_9$ composites-FTIR spectra
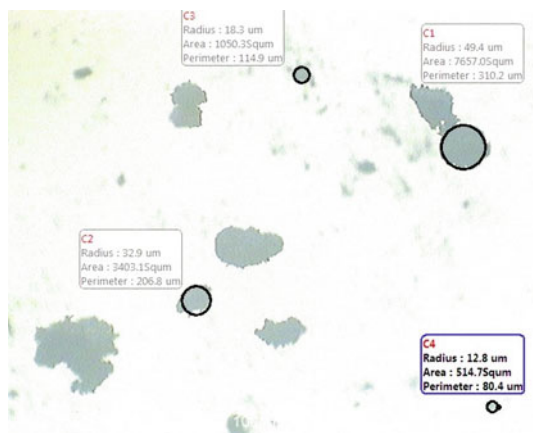
Fig. 4 Polyaniline-$V_2Fe_3O_9$ composites (10X magnification)

The size of the particle was analyzed by optical microscopy. The image was captured at $10\times$ magnification. The clusters of the particles have radius size in microns which reveals that the individual particles are of nanosize. For instance, in Fig. 4, the greenish part has nine particles and covers only $1.24 \times 10^{-3}\%$ of the total area of the image, and thus it is evident that the particles synthesized are of nanodimensions.

4   Conclusion

Polyaniline-vanadium pentoxide NCPs have been successfully synthesized by hydrothermal approach. The synthesized material exhibits desired morphology and material characteristics required for conducting materials. The electric conductivity of NCPs obtained is admirable and enhances as the content of vanadium-hexaferrite increases in NCPs. Peaks obtained by FTIR reveals that synthesized NCPs possess excellent conductivity due to elevated oxidation intensity and doping degree.

Thus, the hydrothermal approach of polymerization is a reliable process, and at the same time, it is found to be convenient for processing, eco-friendly and appropriate with reference to desired outcome for bulk fabrication of NCPs.

References

1. G.R. Pedro, Hybrid organic-inorganic materials-in search of synergic activity, Adv. Mater. (2001) 163–174.
2. P.T. Nguyen, U. Rammelt & W. Plieth, Electrochemical impedance spectroscopy for characterization of coatings with intrinsically conducting polymers, Macromol. Symp. 187 (2002) 929–938.
3. G.A. Lamzoudi, F. Pillier, H. Nguyen, Thi Le & C. Deslouis, Oxide/Polypyrrole composite films for corrosion protection of iron, J. Electrochem. Soc. 149 (2002) 560–566.
4. P.H.C. Camargo , K.G. Satyanarayana & F. Wypych, Nanocomposites: synthesis, structure, properties and new application opportunities. *Materials Research*, *12*(1) (2009) 1–39.
5. H. Ahmad, Magnetic polyaniline composites: recent developments in preparation, properties and applications, J. Colloid Sci. Biotechnol. 2 (2013) 155–170.
6. Y. Wang, Microwave absorbing materials based on polyaniline composites: a review, Int. J. Mater. Res. 105 (2014) 3–12.
7. M.X. Wan & J.H. Fan, Synthesis and ferromagnetic properties of composites of a water-soluble polyaniline copolymer containing iron oxide, J. Polym. Sci. Part A: Polym. Chem. 36 (1998) 2749–2755.
8. J. Zhao, Y. Xie, C. Yu, Z. Le, R. Zhong, Y. Qin, J. Pan & F. Liu, Preparation and characterization of the graphene-carbon nanotube/CoFe2O4/polyaniline composite with reticular branch structures, Mater. Chem. Phys. 123 (2013) 395–402.
9. M. Drofenika, I. Bana, D. Makovec, A. Znidarsicc, Z. Jaglicic, D. Hanzel & D. Lisjak, The hydrothermal synthesis of super-paramagnetic barium hexaferrite particles, Mater. Chem. Phys. 127 (2011) 415–419.
10. S. Ejiri, T. Sasaki & Y. Hirose, Residual Stress Analysis of Textured Materials by X-Ray Diffraction Method, Materials Science Forum. 706–709 (2012) 1673–1678.
11. M. Qiu, Y. Zhang, & B.J. Wen, Facile synthesis of polyaniline nanostructures with effective electromagnetic interference shielding performance, Journal of Materials Science: Materials in Electronics 29.12 (2018),10437–10444.
12. D. Mishraa, S. Ananda, R.K. Pandab, R.P. Dasa, Studies on characterization, microstructures and magnetic properties of nano-size barium hexa-ferrite prepared through a hydrothermal precipitation—calcination route, Mater. Chem. Phys. 86 (2004)132–136.

13. S.H. Deng, Y. Wang & X.Yang, The study of electrochemical synthesis, properties and composite mechanism of PANI/PVA and PANI/PVA/Ag composite films. Pigment and Resin Technology. 47 (2018) 133–14.
14. N. Odzak, D. Kistler, R.Behra & L. Sigg, Dissolution of metal and metal oxide nanoparticles in aqueous media, Environmental pollution, 191C (2014) 132–138.

Effect of Benzoxazine on Epoxy Based Carbon Fabric Reinforced Composites for High Strength Applications

C. Venkateshwar Reddy, Ch. Joseph S. Raju, P. Ramesh Babu
and R. Ramnarayanan

Abstract Benzoxazine (BZ) is novel class of thermoset polymers exhibiting tailor-made properties in a wide range of structural applications especially in aerospace industries. When BZ is used as hybrid resin in composite preparation, it offers attractive mechanical properties. An attempt was made with combination of DGEBA epoxy resin and an aromatic diamine hardener with different weight proportions of BZ 2, 4, 6, 8 and 10% reinforced with PAN-based carbon fabric, in order to study the mechanical characteristics. The weight proportions of BZ enhanced the properties of tensile strength, Flexural strength and inter-laminar shear strength (ILSS) due to strong interfacial adhesion between fabric and hybrid resin system. The studies reveal that 4% of BZ-reinforced composites possess better properties than those of the reference neat epoxy–amine matrix and other weight percentages of composites. In this study, the mechanical, thermal properties of the hybrid were compared with reference epoxy–amine matrix composite. Optical microscope images ascertain the existence of homogeneous distribution of benzoxazine in the composites. The Glass transition temperature (T_g) was determined by Dynamic Mechanical Analyzer (DMA) technique reveals lowering of T_g in hybrid due to off-stoichiometry by the incorporation of BZ. However, post-curing of the composite enhanced both mechanical and thermal properties.

Keywords Benzoxazine (BZ) · Hybrid resin · Weight proportions · DMA
Mechanical properties · Off-stoichiometry · Post-curing

C. V. Reddy (✉)
Matrusri Engineering College, Hyderabad 500059, India
e-mail: cvreddy36@gmail.com

Ch. J. S. Raju · R. Ramnarayanan
Advanced Systems Laboratory, Hyderabad 500069, India

P. R. Babu
University College of Engineering, Osmania University, Hyderabad, India

1 Introduction

An advanced composite material based on carbon fabric-reinforced thermoset polymers (CFRTP) plays a vital role in aerospace structural applications, as well as high-performance sports goods and windmill structures. However, there are still challenges for CFRTP to achieve the desired mechanical properties [1–3].

Many processing techniques are available to fabricate the laminates to meet the requirements of different applications. The selection of manufacturing process technique depends on size and quality of composites. There are two manufacturing process techniques: autoclave process and out-of-autoclave process. The autoclave process is the only means to fabricate carbon fabric structures with good quality for aerospace applications, whereas the out-of-autoclave processes such as liquid composite moulding (LCM), liquid resin infusion (LRI) and automated tape placement (ATP) are predominant processes having its less-expensive equipment to fabricate composite components. Fabrication of CFRTP is made with autoclave process with pressure bag moulding, by providing heat and pressure to the composite product [4, 5].

Benzoxazine (BZ) is a novel class of thermosetting polymeric material which has various outstanding properties such as zero shrinkage, low-moisture absorption, good thermal and mechanical properties [6]. It possesses an important property, that is their ability to blend with various other resins such as epoxy and polyurethane; therefore, this leads to their easy processability and improved mechanical properties in addition to some unique physical, mechanical properties and application. BZ co-cures with epoxy resin; therefore, in recent years, BZ blends have attracted considerable attention by researchers, engineers and polymer industries. The blending of BZ with epoxy resins was reported [7–10]. The addition of epoxy resin with the BZ forms hybrid resin network which greatly increases the crosslink density of the thermosetting matrix and strongly influences on its mechanical properties. In this work, benzoxazine polymer was blended with epoxy–amine resin in different proportions and the composite laminates prepared by autoclave technique were studied for their physical, mechanical and thermal properties.

2 Experimentation

2.1 Materials

Bisphenol F-based benzoxazine (BZ) is mixed with Bisphenol A-based epoxy resin (DGEBA) and a low-viscosity liquid aromatic hardener Diethyl toluene diamine (DETDA) to form a hybrid resin system. PAN-based high-strength carbon fabric-3 K grade with 8-harness style was used as a reinforcement for making composite laminates. The chemical structures of the polymers used were depicted in the Fig. 1.
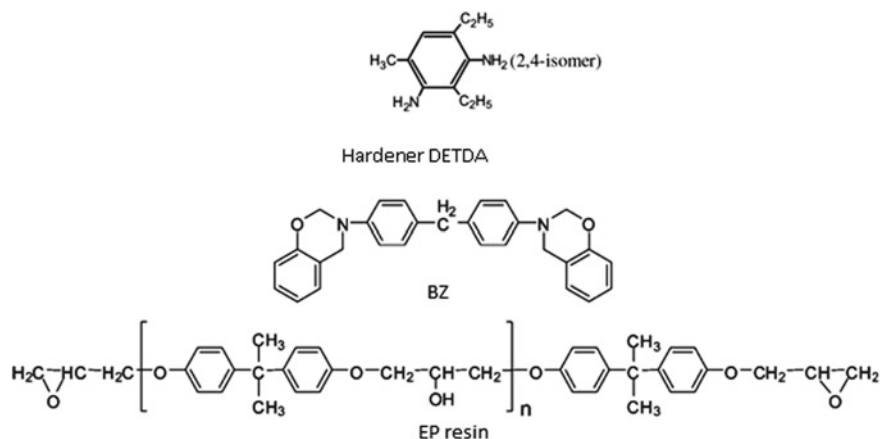
Fig. 1 Chemical structures of the polymer materials

Table 1 Hybrid resin

Laminates	Resin		
	Epoxy DGEBA	Hardener DETDA	Benzoxazine BZ (%)
L0	100	24	0
L1	98	24	2
L2	96	24	4
L3	94	24	6
L4	92	24	8
L5	90	24	10

2.2 Preparation of Benzoxazine/Epoxy Resin Carbon Fabric-Reinforced Composites

Benzoxazine resin provides relatively mild condition for polymerization, very low-melt viscosity, broad processing window, high reactivity and good overall properties. Before preparation of carbon fabric with BZ/epoxy prepreg, the BZ which is in solid powder form that cannot be used directly with epoxy resin was dissolved in acetone solvent in the proportion of 1:2 ratio by weight, which makes BZ to become liquid form. The liquid BZ of different proportions of 2, 4, 6, 8, 10% was mixed with epoxy resin DGEBA-DETDA in parts by weight (pbw) in a vessel and mixed thoroughly with the help of stirrer at room temperature for 10 min to obtain a clear solution of hybrid BZ/epoxy resin. The prepared hybrid resin solution was uniformly spread on the carbon fabric with brush and made to allow for drying at room temperature around 24 h to get tackiness in prepreg. The mechanical properties of carbon fabric with resin DGEBA- and hardener DETDA (100:24)-prepared samples were taken as reference. The following table shows the details of hybrid resin (Table 1).

The prepared prepregs were cut into 15 no. of plies of 300×300 mm size, and all plies were placed on a release agent (wax)-coated metallic mould. Autoclave was used to provide heat and pressure to the composite during curing. In this method, prepregs were stacked in a mould in a definite sequence to avoid any relative movement in between the prepreg sheets. After stacking the prepregs, the whole assembly was vacuum bagged to remove any air entrapped in between the layers. After a definite period of time when it was ensured that all air was removed, the entire assembly was transferred to autoclave. Here, heat and pressure were applied for a definite interval of time. In this process, matrix is uniformly distributed and intimate contact was achieved through proper bonding between fibres and matrix. After the processing, the assembly was cooled at a definite rate and then vacuum bag was removed. The composite part was taken out from the mould. Initially, a release gel was applied onto the mould surface to avoid sticking of polymer to the mould surface. This process is mainly used in applications requiring high strength-to-weight ratio components such as aircraft parts, marine, military, spacecraft and missiles. The schematic autoclave-moulding process is shown in Figs. 2 and 3.

Fig. 2 Hybrid resin impregnated on carbon fabric

Fig. 3 Prepreg cut into 300×300 mm size

The main advantages of this composite processing method allow high-volume fraction of reinforcement in the composite part, high degree of uniformity in part consolidation, better adhesion characteristics between layers and good control over resin and carbon fabric was achieved. No void content in the finished part due to removing entrapped air through vacuum and complete wetting of fibres was achieved.

2.3 Composite Curing

Autoclave was used for curing the composite as shown in Fig. 4. The oven air temperature was controlled with digital temperature indicator cum controller. The following cure cycle was applied and curing under vacuum and pressure as shown in Fig. 5. The main advantages of this composite processing method allow high-volume fraction of reinforcement in the composite part, high degree of uniformity in part consolidation, better adhesion characteristics achieved between layers and good control over resin and carbon fabric. Due to removing entrapped air through vacuum, no void content found in the finished component and complete wetting of fibres was achieved.

Fig. 4 Curing process using autoclave

Fig. 5 Curing under
vacuum and pressure

2.4 Cure Cycle

- Autoclave curing has been carried out under vacuum with the following cure cycle.
- Temperature of the oven increased from room temperature to 80 °C in 30 min. Held the temperature for 4 h. After 4 h applied pressure of 5 bars.
- Increased the temperature after 4 h 80–120 °C in 20 min. Held the temperature for 2 h.
- Further increased the temperature from 120 to 180 °C in 20 min. Held the temperature for 4 h.
- After completion of cure time 4 h switched off the oven and allowed the laminate, cool to room temperature within 4–5 h.
- Extracted the laminates from the mould.

3 Testing, Results and Discussion

3.1 Physical Properties

The strength of any composite material depends on physical properties like fibre volume fraction and density. Estimated the fibre volume fraction and density of the laminates.

3.2 Tensile Strength

The tensile behaviour of prepared samples was determined at room temperature by using universal testing machine (UTM) according to ASTM D3039 standard. Tensile test set-up and specimen tensile failure modes are shown in Figs. 6 and 7, respectively. Six test specimens having dimensions of width 15 mm and thickness 2.0 mm were loaded between two adjustable grips of a 100 KN computerized universal testing machine with data acquisition system. Failure modes observed during the testing were identified. Tensile strength and modulus of specimens shown in Figs. 8 and 9, respectively.

The weight per cent of benzoxazine resin up to 4% (L2 laminate) improved tensile strength and modulus due to strong interfacial adhesion between composite layers and also due to the increased crosslink density. The improvement was compared with the reference epoxy composite. Failure mode of specimens at higher strength is a clean-cut mode in the gauge length, whereas at higher percentage addition of BZ the specimens broken in in-plane mode resulted in lower strength and modulus.

3.3 Flexural Strength

The Flexural strength is determined by three-point bend test in accordance with ASTM D790 (Fig. 10). The size of the test specimens is 10 mm width and 3 mm thickness. Three-point bend test was performed in a servo-controlled UTM machine having load cell capacity of 5 KN. The cross head speed 2 mm/min and span length to specimen depth ratio $s/t = 16$ were selected. Six specimens were tested and average value is considered (Fig. 11).

Fig. 6 Tensile test set-up
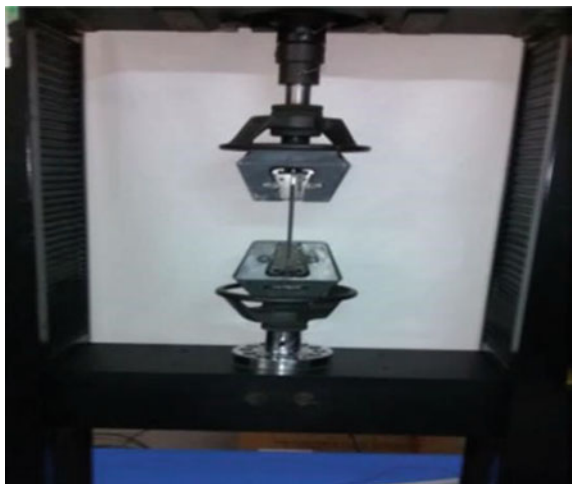
Fig. 7 Tensile failure modes

Fig. 8 Tensile strength (MPa)
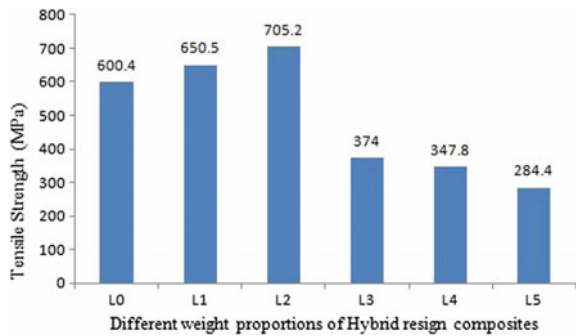
Flexural strength and modulus for tested specimens were shown in Figs. 12 and 13. Flexural strength and modulus increased up to 4% by parts addition of BZ on reference epoxy–amine due to flexing of composite at higher loads due to strong inter-laminar strength.

3.4 Inter-laminar Shear Strength

The inter-laminar shear strength was calculated by using short-beam shear test as per ASTMD2344. Six samples were tested in electro-mechanical testing machine INSTRON 4505 with the crosshead speed of 1 mm/min, and span length to specimen ratio $s/t = 4$ was maintained. Test set-up and specimen failure modes were shown in Figs. 14 and 15, respectively.
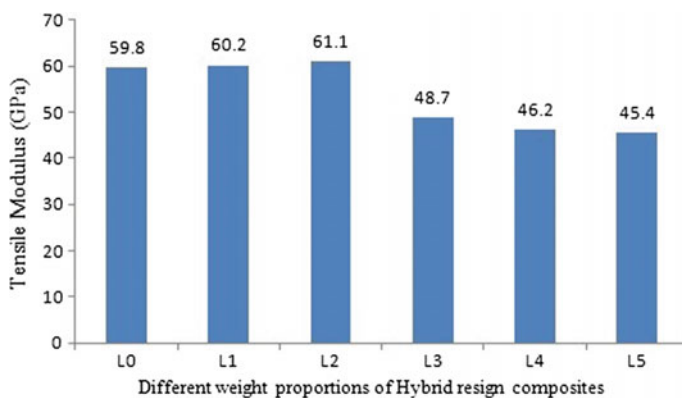
Fig. 9 Tensile modulus (GPa)

Fig. 10 Flexural test set-up

Tested specimens values were shown in Fig. 16. Highest value of ILSS achieved at 4% addition of BZ due to strong interfacial shear property.

3.5 *Optical Microscope Images*

The following optical images in Figs. 17 and 18 reveal comparative topography of reference epoxy–amine to BZ/epoxy–amine. Homogenous distribution of reinforcement to matrix adhesion of BZ is quite evident.
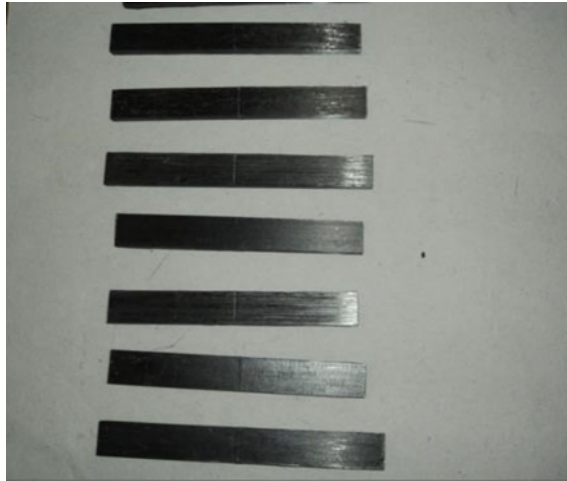
Fig. 11 Failure modes in flexural specimens
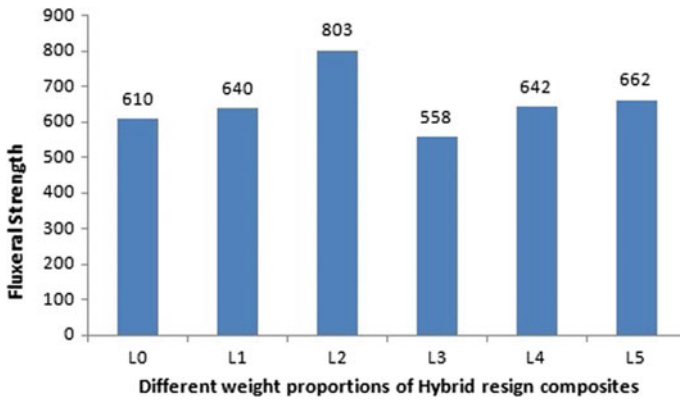
Fig. 12 Flexural strength (MPa)

The amine-hardened EP formed a co-network with the BZ. This contained nanoscaled inclusions of the homopolymerized BZ. Figure 18 reveals the finest dispersion characteristics of the BZ traced to the phase segregation and crosslinking with EP.
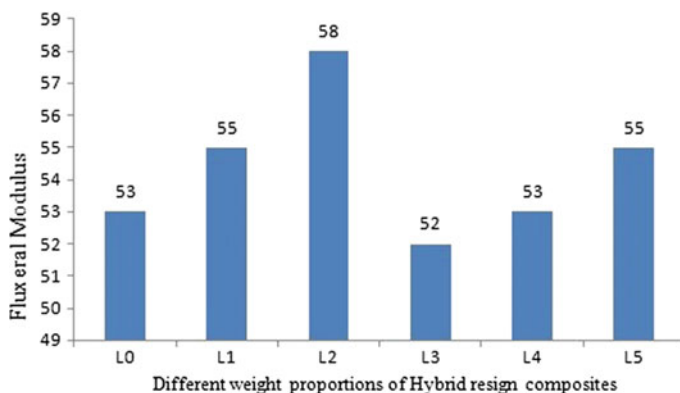
Fig. 13 Flexural modulus (GPa)

Fig. 14 Three-point bend test set-up

3.6 Thermal Properties

3.6.1 Differential Scanning Calorimeter (DSC) Scan

DSC thermograms were registered in the temperature range from $T = 0$ to 300 °C at a heating rate of 10 °C/min under N2 flushing (30 ml/min). The sample weight of around 10 mg was taken for both BZ and EP individually. Exothermic peak for BZ at 250 °C and exothermic peak for EP at 180 °C were observed. DSC curves were shown in Fig. 19.
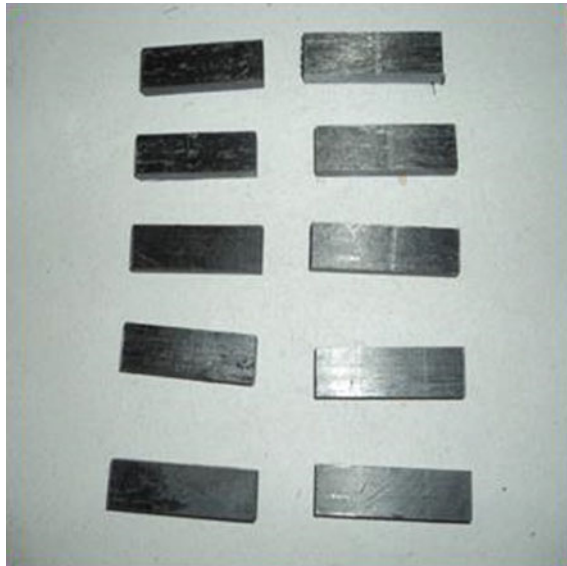
Fig. 15 Failure modes in ILSS specimens
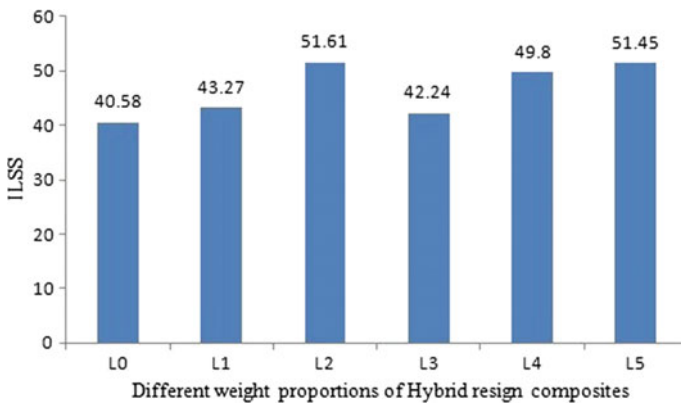
Fig. 16 Inter-laminar shear strength (ILSS)

The individual exothermic peak T_{peak} at 180 °C relates to the complete crosslinking of EP-Amine reaction and which is in line with the Glass transition temperature (T_g) for laminate L_0 composite. T_{peak} at 250 °C relates to homopolymerization of BZ itself. The incorporation of BZ to EP-Amine reduced the T_g in hybrid composites due to off-stoichiometry and increase observed upon post-curing due to homopolymerization and crosslinking with EP-Amine.

Fig. 17 Image of EP-Amine

Fig. 18 Image of
BZ/EP-Amine
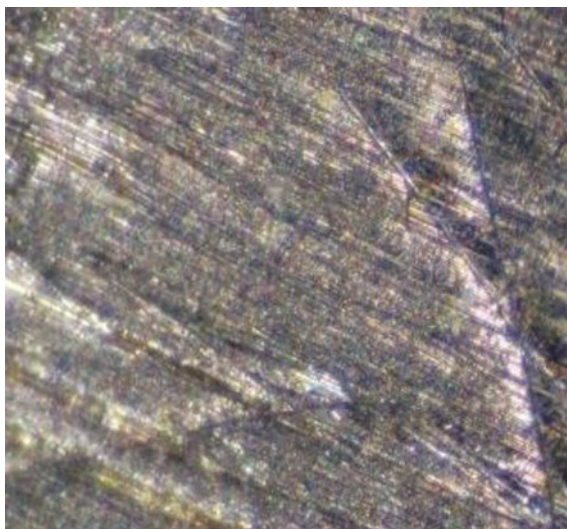
3.6.2 Dynamic Mechanical Analysis (DMA) Scan

T_g is determined by DMA technique for the specimens having dimensions of
35 mm × 10 mm with 3 mm thickness. DMA curves for the laminates L_0 to L_5 were
shown in Fig. 20. T_g was reduced by the incorporation of BZ due to off-stoichiometry
caused by BZ and epoxy–amine reaction (which is in line with the DSC results). How-
ever, upon post-curing, enhancement in T_g was observed (as shown in Table 2) due
to further reaction of BZ with epoxy–amine resulting in higher crosslink density.
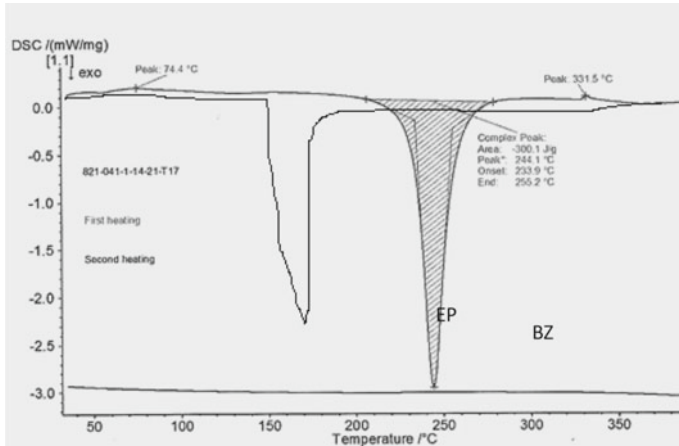
Fig. 19 DSC curves for BZ and EP
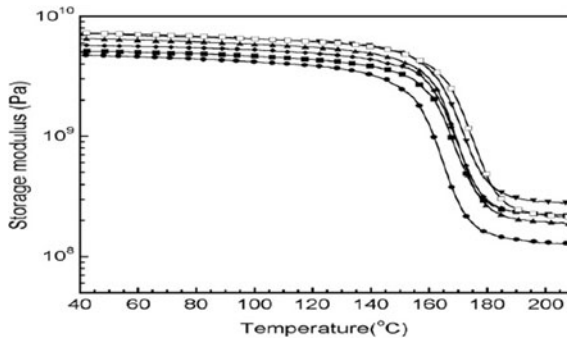
Fig. 20 DMA curves for laminates

Table 2 Glass transition temperatures

Laminate	BZ (%)	T_g	T_g (After post-cure)
L0	0	180	180
L1	2	175	185
L2	4	170	180
L3	6	165	175
L4	8	155	165
L5	10	145	160

4 Conclusion

It was studied the effect of aromatic amine hardener on epoxy modified with ben-zoxazine at different ratios and the thermal and mechanical properties of the cor-

responding hybrid was determined. It was observed from the results that aromatic amine-hardened epoxy formed a co-network with the benzoxazine resin. The weight per cent of benzoxazine resin up to 4% improved mechanical properties due to strong interfacial adhesion between composite layers and also due to the crosslink density. The improvement was compared with the reference epoxy composite. Thermal properties—the T_g of the hybrid was lower than the reference EP that was traced to off-stoichiometry caused by the amine/oxazine reaction. However, T_g increased upon post-curing due to nanoscaled homopolymerized BZ was well connected to the EP network.

References

1. Hossein Rahmani, S. Heydar Mahmoudi Najafi and Alireza Ashori: Mechanical performance of epoxy/carbon fibre laminated composites, Journal of Reinforced Plastics and Composites, 33(8) (2014) 733–740.
2. Hong-wei He, Feng Gao: Effect of Fibre Volume Fraction on the Flexural Properties of Unidirectional Carbon Fibre/Epoxy Composites, International Journal of Polymer Analysis and Characterization, 20 (2015) 180–189.
3. Umar Farooq, Peter Myler: Preparation of Aerospace Grade Carbon Fibrous Laminated Composite Panels with Improved Performance and Reduced Fabrication Process Defects and Flaws, ARPN Journal of Engineering and Applied Sciences, 12(4) (2017) 1128–1143.
4. D. Purslow, R. Childs: Autoclave moulding of carbon fibre-reinforced epoxies, Composites, 17(2) (1986) 127–136.
5. Timotei Centea, Lessa K. Grunenfelder, Steven R. Nutt: A Review of Out-of-Autoclave Prepregs-Material properties, Process phenomena and Manufacturing considerations, Composite part A, Applied science mfg. 70 (2014) 132–154.
6. S. Rajeshkumar, J. Dhanasekaran, S. Krishna Mohan: Epoxy benzoxazine based ternary systems of improved Thermo-mechanical behaviour for structural composite applications, RSC Advances, (2014), 1–15.
7. Mingzhen Xu, Xulin Yang, Rui Zhao, Xiaobo Liu: Copolymerizing Behaviour and Processability of Benzoxazine/Epoxy Systems and their Applications for Glass Fibre Composite Laminates, Journal of Applied Polymer Science, (2013) 1176–1184.
8. S. Grishchuk, Z. Mbhele, S. Schmitt, J. Karger-Kocsis: Structure, Thermal and Fracture Mechanical Properties of Benzoxazine-Modified Amine-cured DGEBA Epoxy Resins, eXPRESS Polymer Letters, 5(3) (2011), 273–282.
9. K.S. Santhosh Kumar, C.P. Raghunathan Nair, R. Sadhana, K.N. Ninan.: Benzoxazine-bismaleimide blends: Curing and thermal properties, European Polymer Journal, 43(12) (2007) 5084–5096.
10. V. Garcia-Martinez, M.R. Gude, A. Urena: Understanding the Curing Kinetics and Rheological Behaviour of a New Benzoxazine Resin for Carbon Fibre Composites, Reactive and Functional Polymers, Elsevier, February (2017).

Microwave Assisted Synthesis of Palladium Doped Zinc Oxide Nanostructures and Their Gas Sensing Applications

Yogita S. Patil, Sushil Charpe, F. C. Raghuvanshi and Ramzan Muhammad

Abstract Palladium-doped zinc oxide nanostructures were synthesized by a microwave-assisted chemical method. The structural and morphological characteristics were studied from X-ray diffractogram and field emission scanning electron microscopy. The Pd–ZnO nanostructure film sensor was prepared by screen-printing technique. The sensors were tested for gas-sensing properties for NH_3, H_2S, CO_2, LPG and ethanol and compared with undoped sample. The Pd-doped zinc oxide showed highest response to LPG.

Keywords Palladium · Gas sensor · Thick film · Zinc oxide
Microwave synthesis · LPG

1 Introduction

Semiconductor zinc oxide nanocrystals play an important role in optoelectronics and electronic device applications, particularly for sensing of hydrogen gas [1–6]. The gas-sensing characteristics and optical properties of zinc oxide nanostructures are different from those of the bulk. The sensitivity and selectivity in case of zinc oxide bulk material are not suitably high. Zinc oxide nanocrystals have larger bulk atom or surface atom ratio [7]. Due to this, zinc oxide nanostructures are potentially the most excellent gas sensors and compatible with other nano devices having higher sensitivity and thermal stability [8]. Oxides cannot easily differentiate between different types of gases but by adding/doping some noble metals can support the performance of gas sensors [9–11]. The electronic and optical properties of zinc oxide can be

Y. S. Patil
Government College of Engineering, Jalgaon, Maharashtra, India

S. Charpe · F. C. Raghuvanshi
Department of Physics, Vidyabharati Mahavidyala, Amravati, Maharashtra, India

R. Muhammad (✉)
MMANTC College of Engineering, Malegaon, Nashik, Maharashtra, India
e-mail: ramzan145@gmail.com

changed by doping the noble metals to improve the sensing performance [12–14]. Palladium, a 4d metal, is used as an impurity in zinc oxide to improve the sensitivity and specificity [15–17]. In the recent years, since hydrogen gas sensor applications, palladium-doped zinc oxide nimrods have received wide interest [18]. Gas sensors are significant in aerospace applications such as solid fuel cells and proton exchange membrane for sensing the hydrogen [19]. By using the minimum power and weight, the sensor should detect hydrogen at room temperature [20]. Zinc oxide nano rods are having large exciton energy, wide band gap and large surface area [21]. They are lighter in weight and oppose the rust formation and also biocompatible [22]. Thus, zinc oxide nanowires and nanorods show potential for detecting chemical-sensing devices, gas and humidity [23, 24]. Molecular hydrogen gets segregated into atomic hydrogen at room temperature due to doping of Pd on zinc oxide nanorods and nanowires [25]. Chemical vapor deposition (CVD) and molecular beam epitaxy (MBE) are two major techniques known to prepare the zinc oxide nanorods for this particular application [26]. For the preparation of zinc oxide nanowires and nanorods, gold (Au) and metal coatings are required [25] in CVD and MBE methods. Besides this, RF sputtering with an expensive laboratory setup is essential for doping of Pd onto the prepared zinc oxide [26].

In this work, we describe the microwave-assisted synthesis of undoped and palladium-doped zinc oxide nanorods with better crystalline. The special effects of doping concentrations on structural properties were studied from X-ray diffraction, and morphological properties were studied using SEM. This nanocrystalline zinc oxide powders were used to produce the sensor elements in the form of thick films with a screen-printing method and tested for different conventional gases. A comparative study of undoped and doped zinc oxide with different palladium concentration has been studied.

2 Experimental

In the preparation of undoped and palladium-doped ZnO nanoparticles, zinc acetate $((CH_3 \cdot COO)_2 \cdot Zn \cdot 2H_2O)$ and palladium chloride (0 wt%, 1 wt%, 3 wt%, and 6 wt%) were dissolved in 100 mL of deionized water and magnetically stirred for 30 min. Then 2 M sodium hydroxide (NaOH) solution was prepared and introduced into the zinc acetate solution with continues stirring. The solution was ultrasonicated for 15 min. The beaker was kept in microwave for 15 min. The solution was allowed to cool down at room temperature naturally, filtered, and washed with deionized water and absolute ethanol many times to eliminate the extra and impure salts. The obtained powder of pure ZnO was dried at 70 °C in air oven. The same process was repeated for Pd-doped (1 wt%, 3 wt%, and 6 wt%) zinc oxide.

Fig. 1 XRD of pure ZnO, 1 wt% Pd, 3 wt% Pd, and 6 wt% Pd in ZnO
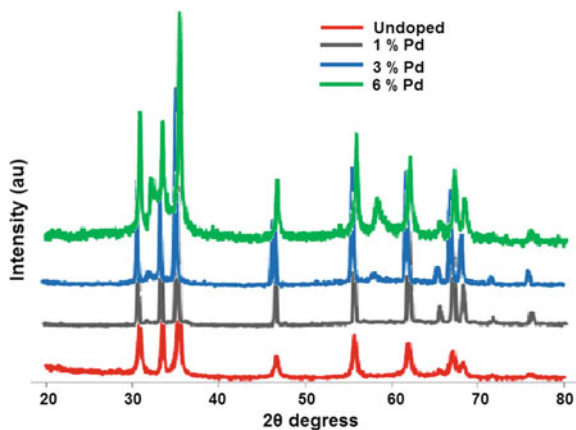
3 Result and Discussion

3.1 Material Characterization

3.1.1 Structural Properties (X-Ray Diffraction Analysis)

X-ray diffractometry of undoped and Pd-doped ZnO powders was carried out using BRUKER AXSD8 (Germany) advance model X-ray diffraction with CuKα_1 (λ = 1.54056 Å) radiation in the 2θ range 20°–80°. The scanning speed of the sample was kept 0.5°/min.

Figure 1 shows XRD spectra of undoped and Pd-doped ZnO nanostructures. The highest peaks of ZnO are obtained at (101), (002), and (110) planes. It is observed that two additional peaks are obtained at 30.61° and 57.43° for Pd-doped ZnO, and these peaks can be associated with PdO [27]. The intensities of the peaks obtained at 30.61° and 57.43° increase with increase in percentage of Pd doping in ZnO. From the XRD results, it is observed that 1 wt% Pd, 3 wt% Pd, and 6 wt% Pd in ZnO are more crystalline as compared to pure ZnO.

No diffraction peaks of other compounds were observed in ZnO which indicates that the ZnO nanostructures have high purity. The crystallite size for pure, 1 wt% Pd, 3 wt% Pd, and 6 wt% Pd is found to be 3.38, 3.38, 4.2, and 4.9 nm, respectively. Thus, it is observed that the increase in the percentage of Pd doping increases the crystallite size.

3.1.2 Microstructural Analysis

Field Emission Scanning Electron Microscopy (FESEM)
FESEM images in Fig. 2a–e show bulk quantity of flower-like structure of pure ZnO
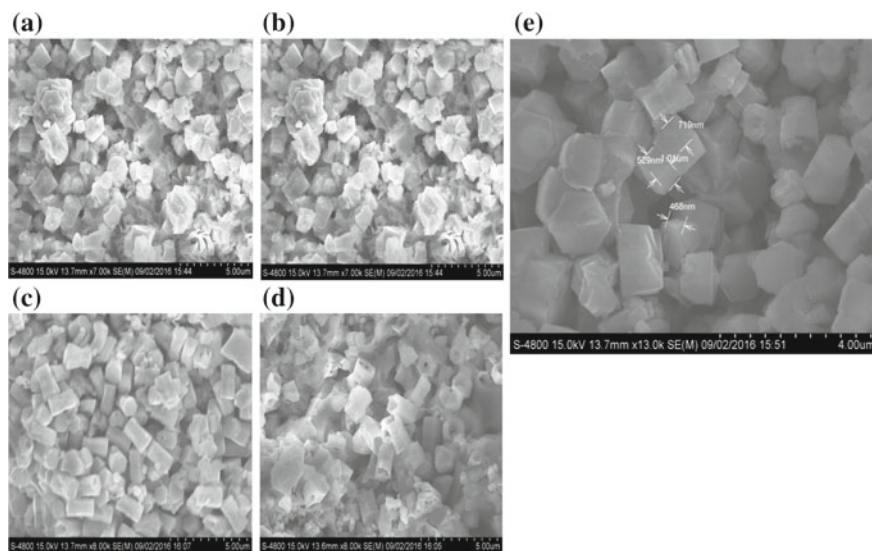
Fig. 2 **a** Undoped ZnO, **b** 1 wt% Pd, **c** 3 wt% Pd, **d** 6 wt% Pd, **e** size of 3 wt% Pd–ZnO

and 1 wt% Pd-doped ZnO. Figure 2c, d shows FESEM images for 3 wt% of Pd-doped ZnO and 6 wt% Pd-doped ZnO, and it is observed that the powder samples for both consist of hexagonal prism-like structure of ZnO crystalline phase. Figure 2d shows FESEM image of 3 wt% Pd-doped ZnO at higher resolution, and it is observed from the figure that the height and width of the prism ranges from 400 nm to 1 μm.

3.2 Preparation of ZnO Thick Films

A temporary binder solution (ethyl cellulose) was mixed with the synthesized nanostructured powders of undoped and Pd-doped ZnO, along with organic solvent mixture of butyl carbitol acetate and turpineol in the ratio 3:1 to prepare the thixotropic pastes. The paste was then formed in desired patterns on glass substrates through screen-printing technique. The films obtained were tempered at 500 °C for 30 min in air to eliminate the binder.

Fig. 3 *I–V* characteristics of pure and Pd-doped ZnO thick films
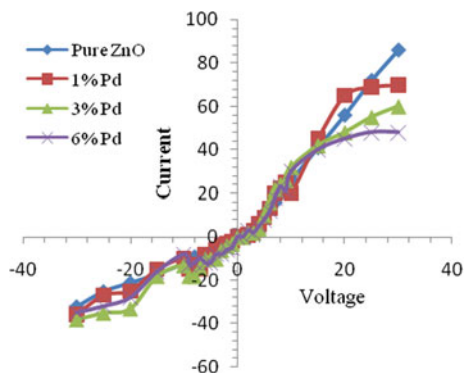
3.3 Electrical Measurements

3.3.1 I-V Characteristics

Figure 3 represents the *I–V* characteristics of pure and Pd-doped ZnO thick films at 100 °C. Keithley 6487 pico-ammeter cum voltage source was used for this measurement. Current was measured with forward bias voltage from 0 to 25 V with the step of 5 V. The measurement was repeated with negative voltage. The similar nature of the *I–V* characteristics for pure and Pd-doped ZnO shows that the contacts are ohmic in nature [28].

3.3.2 Electrical Conductivity

Figure 4 depicts the variation of log (conductivity) with operating temperature of all undoped and Pd-doped ZnO thick film samples. All the fabricated films show the semiconducting nature from the measurement of conductivity with temperature. The conductivity of all samples was higher at ambient temperature as compared to elevated temperature, which is a consequence of humid atmosphere at ambient temperature. However, above 100 °C, improvement in conductivity is due to semiconducting attribute of ZnO and its negative temperature coefficient.

3.4 Gas-Sensing Properties

The gas-sensing properties of pure and 1 wt%, 3 wt%, and 6 wt% Pd-doped ZnO have been studied. Operating temperature optimization is main objective of gas film sensors. At ambient temperature condition and 1000 ppm fixed gas concentration, the sensitivity, selectivity, and response time are calculated. At optimized operating

temperature, the response of the sensors is also determined at different gas concentrations.

3.4.1 Effect of Operating Temperature

Optimization of operating temperature and Sensitivity of gas sensor
The performance of undoped and Pd-doped ZnO gas sensors was determined through static gas-measuring arrangement, by varying the temperature at 50 °C steps. Half bridge technique was applied, to measure the DC resistance, as a function of temperature, of formulated gas sensor films. The efficiency of the thick film gas sensors was evaluated in different environments such as air, NH_3, H_2S, CO_2, LPG, and ethanol.

From Fig. 5a–e, it is observed that the Pd-doped ZnO thick films are more sensitive to LPG gas than other tested gases (NH_3, H_2S, CO_2, and Ethanol vapors). The 3 wt% Pd-doped ZnO thick films show higher sensitivity to LPG than other doping concentrations. These films have shown 84% sensitivity to LPG at 573 K operating temperature.

3.4.2 Selectivity of Other Gases Against LPG

Selectivity of a sensor may be defined as the ability to react for a specific gas in the presence of other gases. The ratio of peak response of any gas to that of the target gas at optimum temperature is known as percent selectivity [29, 30]. Figure 6 shows selectivity of 3 wt% Pd-doped ZnO thick films for different gases, and it is found that 3 wt% Pd-doped ZnO thick films show maximum selectivity for LPG over other gases.
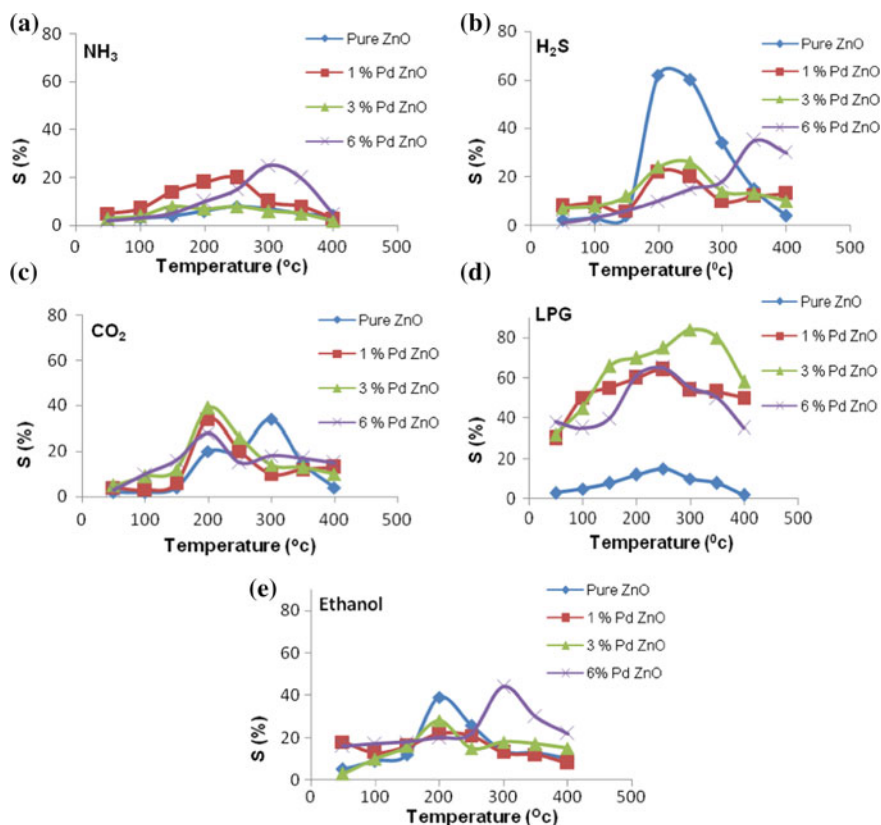
Fig. 5 (**a–e**) Sensitivity versus operating temperature of pure and Pd-doped ZnO thick films with different doping concentrations for different gases
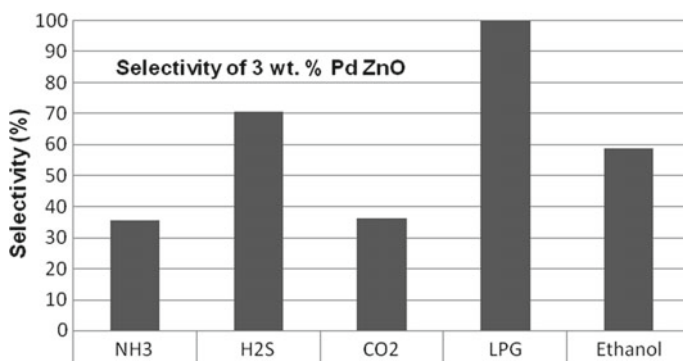
Fig. 6 Selectivity of 3 wt% Pd-doped ZnO thick films for different gases
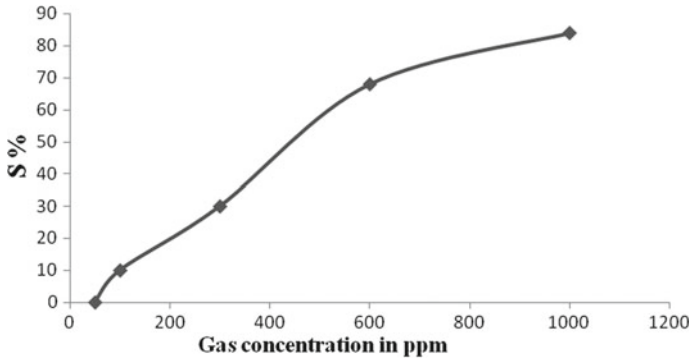
Fig. 7 Change in sensitivity with gas concentration at 300 °C

3.4.3 Variation of Sensitivity with Gas Concentration (Ppm)

The variation of sensitivity with LPG concentration for 3 wt% Pd-doped ZnO sample at optimum operating temperature of 300 °C is shown in Fig. 7. It was predicted that the sensitivity is a function of gas concentration and increases up to 1000 ppm. However, the increase in sensitivity is much faster up to 600 ppm concentration, slower between 600 and 1000 ppm, and remains constant above 1000 ppm. The slower response at higher concentration is a consequence of formation of multilayer gas molecules which results in saturation and hence decreasing the response [31].

4 Conclusion

Pure and Pd-doped ZnO nanostructures were synthesized by microwave-assisted precipitation method. XRD analysis confirmed that the synthesized powders correspond to hexagonal wurtzite structure of ZnO. The FESEM images showed the hexagonal prism-like structure of ZnO. The thick films of ZnO powders were prepared by screen-printing method. The gas response of Pd-doped ZnO was observed highest for LPG with 3 wt% Pd.

References

1. Mitra, P., Ap P. Chatterjee, and Himadri Sekhar Maiti. "ZnO thin film sensor." Materials Letters 35.1–2 (1998): 33–38.
2. Chatterjee, A. P., P. Mitra, and Anoop Kumar Mukhopadhyay. "Chemically deposited zinc oxide thin film gas sensor." Journal of materials science 34.17 (1999): 4225–4231.
3. Wang, Hung-Ta, et al. "Hydrogen-selective sensing at room temperature with ZnO nanorods." Applied Physics Letters 86.24 (2005): 243503.

4. Tien, L. C., et al. "Hydrogen sensing at room temperature with Pt-coated ZnO thin films and nanorods." Applied Physics Letters 87.22 (2005): 222106.
5. Verhelst, Sebastian, and Roger Sierens. "Hydrogen engine-specific properties." International Journal of Hydrogen Energy 26.9 (2001): 987–990.
6. Bevenot, X., et al. "Hydrogen leak detection using an optical fibre sensor for aerospace applications." Sensors and Actuators B: Chemical 67.1–2 (2000): 57–67.
7. Wan, Qing, et al. "Fabrication and ethanol sensing characteristics of ZnO nanowire gas sensors." Applied Physics Letters 84.18 (2004): 3654–3656.
8. Do, Anh-Thu Thi, et al. "Effects of palladium on the optical and hydrogen sensing characteristics of Pd-doped ZnO nanoparticles." Beilstein journal of nanotechnology 5 (2014): 1261.
9. Liu, Zhifeng, et al. "Mechanism and characteristics of porous ZnO films by sol–gel method with PEG template." Materials Letters 62.8–9 (2008): 1190–1193.
10. Pawinrat, Pongsapak, Okorn Mekasuwandumrong, and Joongjai Panpranot. "Synthesis of Au–ZnO and Pt–ZnO nanocomposites by one-step flame spray pyrolysis and its application for photocatalytic degradation of dyes." Catalysis Communications 10.10 (2009): 1380–1385.
11. Zeng, Haibo, et al. "ZnO-based hollow nanoparticles by selective etching: elimination and reconstruction of metal—semiconductor interface, improvement of blue emission and photocatalysis." ACS nano 2.8 (2008): 1661–1670.
12. Georgekutty, Reenamole, Michael K. Seery, and Suresh C. Pillai. "A highly efficient Ag-ZnO photocatalyst: synthesis, properties, and mechanism." The Journal of Physical Chemistry C 112.35 (2008): 13563–13570.
13. Hayakawa, I., et al. "Gas sensing properties of platinum dispersed-TiO2 thin film derived from precursor." Sensors and Actuators B: Chemical 62.1 (2000): 55–60.
14. Hayakawa, I., et al. "Gas sensing properties of platinum dispersed-TiO2 thin film derived from precursor." Sensors and Actuators B: Chemical 62.1 (2000): 55–60.
15. Garcia-Serrano, O., et al. "Pd-decorated ZnO and WO 3 nanowires for sensing applications." Sensors, 2011 IEEE. IEEE, 2011.
16. Srinivasan, Supramaniam. Fuel cells: from fundamentals to applications. Springer Science & Business media, 2006.
17. Fardindoost, Somayeh, Fereshteh Rahimi, and Roghayeh Ghasempour. "Pd doped WO3 films prepared by sol–gel process for hydrogen sensing." International Journal of Hydrogen Energy 35.2 (2010): 854–860.
18. Fardindoost, Somayeh, Fereshteh Rahimi, and Roghayeh Ghasempour. "Pd doped WO3 films prepared by sol–gel process for hydrogen sensing." International Journal of Hydrogen Energy 35.2 (2010): 854–860.
19. Kashif, M., et al. "Morphological, optical, and Raman characteristics of ZnO nanoflakes prepared via a sol–gel method." physica status solidi (a) 209.1 (2012): 143–147.
20. Ali, Syed M. Usman, et al. "Selective potentiometric determination of uric acid with uricase immobilized on ZnO nanowires." Sensors and Actuators B: Chemical 152.2 (2011): 241–247.
21. Arafat, M. M., et al. "Gas sensors based on one dimensional nanostructured metal-oxides: a review." Sensors 12.6 (2012): 7207–7258.
22. Wang, H. T., et al. "Detection of hydrogen at room temperature with catalyst-coated multiple ZnO nanorods." Applied Physics A 81.6 (2005): 1117–1119.
23. Wang, Hung-Ta, et al. "Hydrogen-selective sensing at room temperature with ZnO nanorods." Applied Physics Letters 86.24 (2005): 243503.
24. Ren, Shoutian, et al. "Enhanced H2 sensitivity at room temperature of ZnO nanowires functionalized by Pd nanoparticles." Journal of Applied Physics 110.8 (2011): 084312.
25. Pluym, T. C., et al. "Palladium metal and palladium oxide particle production by spray pyrolysis." Materials research bulletin 28.4 (1993): 369–376.
26. Keyes, Frederick G. "Temperature—Its Measurement and Control in Science and Industry." Journal of the American Chemical Society 78.21 (1956): 5707–5708.
27. Liu, Zhifeng, et al. "Mechanism and characteristics of porous ZnO films by sol–gel method with PEG template." Materials Letters 62.8–9 (2008): 1190-1193.

28. Patil, D. R., and L. A. Patil. "Room temperature chlorine gas sensing using surface modified ZnO thick film resistors." Sensors and Actuators B: Chemical 123.1 (2007): 546–553.
29. Georgekutty, Reenamole, Michael K. Seery, and Suresh C. Pillai. "A highly efficient Ag-ZnO photocatalyst: synthesis, properties, and mechanism." The Journal of Physical Chemistry C 112.35 (2008): 13563–13570.
30. Hayakawa, I., et al. "Gas sensing properties of platinum dispersed-TiO2 thin film derived from precursor." Sensors and Actuators B: Chemical 62.1 (2000): 55–60.
31. Arbiol, J., et al. "Effects of Nb doping on the TiO2 anatase-to-rutile phase transition." Journal of Applied Physics 92.2 (2002): 853–861.

Investigation of Moisture Absorption in Jute Fiber Polymer Matrix Composites

Manohar Reddy Kunuthur and B. Chandramohan Reddy

Abstract Nowaday's Natural Fiber Composites owing importance because of biodegradability, lightweight and strength, etc. This investigation proposed to identify the moisture absorption of natural jute fiber composites. The samples were prepared with epoxy and hardener taken constant in 10:1 ratio; fiber content increased to 5, 10, 15, and 20 g, respectively. The absorption test was initially conducted in distilled water, and then, different chemical compositions prepared with pellets of Hcl, NaCl, and NaOH in 100 ml were investigated.

Keywords Jute fiber · Unidirectional · Saline water · Moisture absorption

Nomenclature

UD   Unidirectional
RJF   Jute fiber
PMC   Polymer matrix composite
NFRP   Natural fiber reinforced composites

1   Introduction

In recent technologies, use of NFRC materials gained substantial interest where are fibers in Materials Sciences, [1, 2] where these fibers may be combined with thermoplastic polymers and to create the natural fiber composites especially identified for the substantial attributes the applications [3, 4]. The PMCs [5] have some prop-

M. R. Kunuthur (✉)
JNTUA, Ananthapuramu 515002, India
e-mail: btech.manohar@gmail.com

B. C. Reddy
Department of Mechanical Engineering, JNTUA, Ananthapuramu 515002, India

erties including renewable biodegradable, short growing (crop time), observing CO_2 returning O_2 to the environment, mold ability, handling, and Working [2].

The fiber and matrix materials mechanical properties are in form of new jute fibers, but here by using jute fibers which are extracted from the of jute and having the similarity of jute fiber, the availability of jute fiber is rare except in Bengal states. Here, the jute fiber is extracted from the jute mate. Actually, the mate is bidirectional in orientation, so it is extracted linearly from the mate [6].

The jute as UD under dry condition is difficult to obtain [6, 7], and hackling under wet/dry condition causes more defects on the performance of fiber. By the results, preparation of UD jute roving becomes a valuable step and that nowadays it is getting more importance [4]. The following table shows the properties of fiber which was from mate without any chemical treatment.

2 Paper Preparation

2.1 Materials and Method

2.1.1 Materials

Matrix Materials

In the present work, the epoxy resin [8] (LY556) is obtained from authorized dealer for Araldite (HY951) Huntsman [9], Ciba- Geigy India Ltd Company, Hyderabad (Invoice number 10,121). The following Table 1 shows the properties of matrix material.

Fiber Material

The jute FRC possesses moderately more specific strength and stiffness [10, 11]. Therefore, it is suitable as reinforcement in a polymeric resin matrix [12, 13]. The chemical composition of jute fiber is shown in Table 2.

The fiber properties depends on the characteristics and process used for extraction of the fiber [6]. The table shows mechanical properties of jute fiber showed in Table 3.

Table 1 The ingredients of matrix system

Ingredients	Molar mass (g/mol)	Supplier
Hydrochloric acid (Hcl)	36.46	Hindustan Ciba Gieg Ltd
Sodium hydroxide (NaOH)	39.997	Hindustan Ciba Gieg Ltd
Sodium chloride (NaCl)	58.4	Hindustan Ciba Gieg Ltd

Table 2 Chemical composition of jute [13]

Constituents	Percentage (%)
Cellulose	60–62
Hemi cellulose	22–24
Lignin	12–14
Others	1–2

Table 3 Mechanical properties of jute fiber [13]

Fiber	Density (g/cm^3)	Young's modulus (GPa)	Tensile strength (MPa)	Elongation at break (%)
Jute	1.3	26.5	393–773	1.5–1.8

Table 4 List of raw materials used in the present work

Description	Raw materials
Matrix	Epoxy resin (LY556)
Hardener	Hardener (HV951)
Reinforcing agent	Jute fiber
Mold releasing agent	OHP sheet and wax
Casting	Wooden molds

2.1.2 Method

The following figure shows the process of jute fiber composite.

Fiber Orientation

The fiber orientation is unidirectional, and it is stretched under certain load for uniform arrangement of jute fiber.

Mold Preparation

The matrix (epoxy and hardener) is weighed with the jewelry weighing machine (make: BOLT MH Series 200 g/0.01 g). The 50 g of epoxy and 5 g of hardener were mixed in ultrasonicator. The mold prepared [14] with A4 wooden sheet of 8 mm in thick is used. A polythene OHP sheet (for easy removal) is placed on the surface [15] of the wooden sheet and nails used to fit the boarders which are having thickness of 3 mm (Table 4).
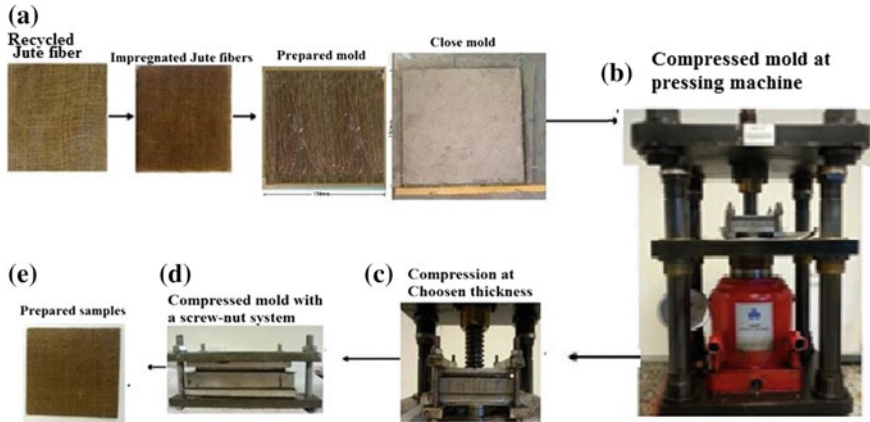
Fig. 1 **a** Processing jute fiber and molding. **b** Compressed mold at pressing machine. **c** Compression at chosen thickness. **d** Compressed mold with screw-nut system. **e** Prepared samples

2.1.3 Compressing the Specimen and Finishing

The compression mold, it is applied where the specimens were not in required thickness [16]. Figure 1a, b shows mold has been closed with the polythene sheet and top surface of mold closed with wooden sheet to avoid matrix contact with machine jaws. Figure 1c shows the compressing of the mold to a required thickness of specimen [17]. Then, Fig. 1d shows the after obtaining the required thickness of the specimen then compression machine stopped, immediately the mold has been tightened with the screw-nut system (inbuilt feature of compression machine). After all impregnated steps, the samples were prepared and displayed in Fig. 1e.

2.1.4 Water Absorption

Specimen dimensions for water uptake experiments were $10 \times 10 \times 3$ mm length x width x thickness, respectively [16]. The samples were removed at specific intervals and blotted to remove the excess water on the surface. After weighing on a four-digit analytical balance, the weight percentage increase was calculated as follows:

$$\text{Water absorption } (\%) = \frac{M2 - M1}{M1} 100$$

where $M2$ and $M1$ are the weights of the sample after t min exposure to water and before exposure to water, respectively. The water uptake data were reported after subtracting the water uptake of the matrix each time.
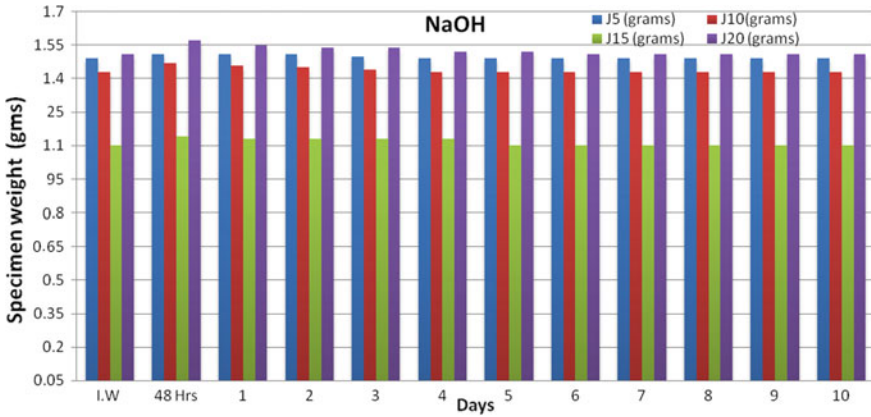
Graph 1 *NaOH chemical treatment*, percentage with exposure time (days)

3 Results and Conclusion

3.1 NaOH

The specimens of NaOH J5 and J10 has a minimum variations in between initial and final days of absorption Results, a couple of days (48 h) later specimen weights are slightly higher than initial weight, but when goes on increasing fiber content in J15 to J20 FRC the gaining of NaOH absorption it could leads to decrease in fiber strength [18, 19]. The results were followed for up to 10 days, and the chemical reaction after 48 h has shown a high variant reaction on the samples. The samples' weight gradually increases and becomes constant 7 days later.

The following Graph 1 NaOH plotted as per the Table 5 the analytical Numerics on the *X* axis taken days and on *Y* axis Specimen weight in grams respectively. The graph shows the sample weights increase or decrease in absorption.

3.2 NaCl

The all samples' weight increases when taken out from the immersed water. The NaCl absorption results are initial 8 days of specimens J5, J10, and J15 got the higher values comparing to initial and last days of sample weights [20]. The specimen J20 absorption is more when comparing with other specimens [21, 22]. And for sample J20 noticed that the slightly increase in weight Initial days to 8th day and then J20 also got its initial weight. The last 3 days observed that constant values which means no chemical reaction on samples at 8 days later. The following Table 6 shows the NaCl absorptions for 10 days.

The following Graph 2 of Nacl plotted as per the Table 5 the analytical results on the *X* axis Days and *Y* axis Specimen weight in grams respectively, when comparing the 48 h immersed samples to the Initial weights it is observed that absorption happened in between 0.266% and 2.07%. The J5 sample became initial weight after 5 days. But the sample with exposure time (Days).

Table 5 *NaOH testing* composite samples specimens data

Specimen name	J5 (g)	J10 (g)	J15 (g)	J20 (g)	J5%	J10%	J15%	J20%
I.W	1.49	1.43	1.1	1.51	–	–	–	–
48 h	1.51	1.47	1.14	1.57	1.34228	2.797203	3.636	3.973
1	1.51	1.46	1.13	1.55	1.34228	2.097902	2.7272	2.6490
2	1.51	1.45	1.13	1.54	1.34228	1.398601	2.7272	1.9867
3	1.5	1.44	1.13	1.54	0.67114	0.699301	2.7272	1.9867
4	1.49	1.43	1.13	1.52	0	0	2.7272	0.6622
5	1.49	1.43	1.1	1.52	0	0	0	0.6622
6	1.49	1.43	1.1	1.51	0	0	0	0
7	1.49	1.43	1.1	1.51	0	0	0	0
8	1.49	1.43	1.1	1.51	0	0	0	0
9	1.49	1.43	1.1	1.51	0	0	0	0
10	1.49	1.43	1.1	1.51	0	0	0	0

Table 6 *NaCl testing* composite samples specimens data

Specimen name	J5 (g)	J10 (g)	J15 (g)	J20 (g)	J5	J10	J15	J20
I.W	2.7	3.38	3.75	4.5				
48 h	2.74	3.45	3.76	4.55	1.481481	2.071006	0.266667	1.111111
1	2.74	3.45	3.76	4.55	1.481481	2.071006	0.266667	1.111111
2	2.73	3.38	3.75	4.54	1.111111	0	0	0.888889
3	2.73	3.38	3.75	4.54	1.111111	0	0	0.888889
4	2.72	3.38	3.75	4.54	0.740741	0	0	0.888889
5	2.71	3.38	3.75	4.54	0.37037	0	0	0.888889
6	2.7	3.38	3.75	4.54	0	0	0	0.888889
7	2.7	3.38	3.75	4.5	0	0	0	0
8	2.7	3.38	3.75	4.5	0	0	0	0
9	2.7	3.38	3.75	4.5	0	0	0	0
10	2.7	3.38	3.75	4.5	0	0	0	0
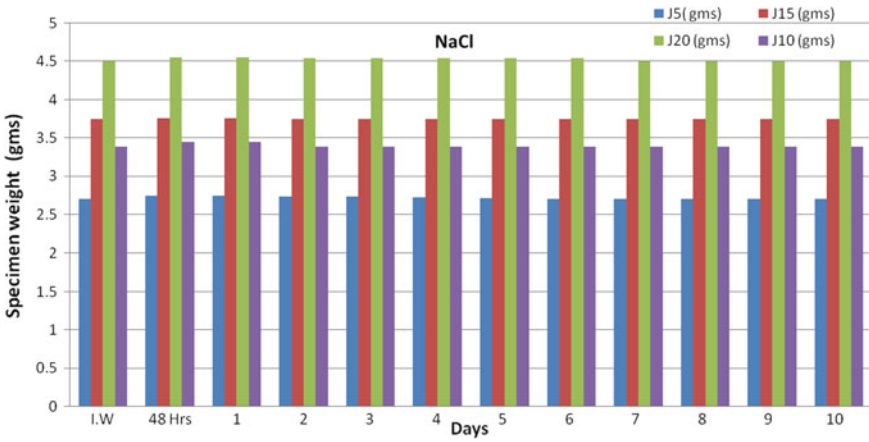
Graph 2 *NaCl*
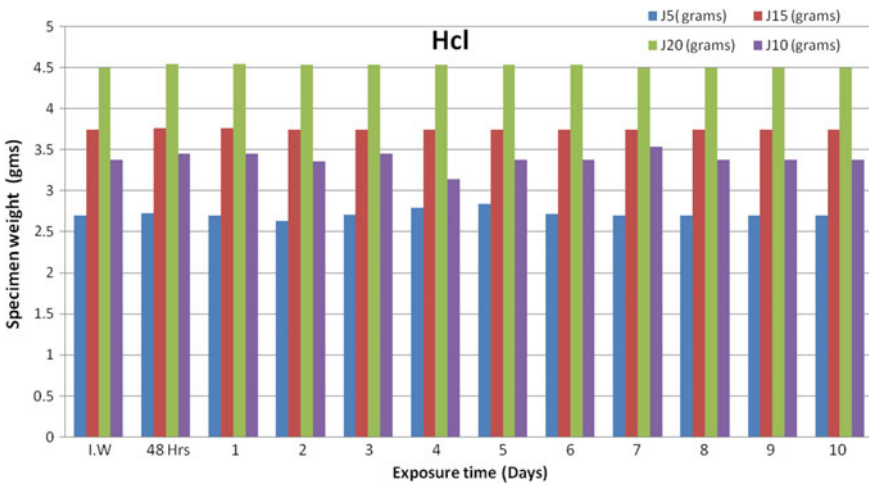
Graph 3 *Hcl*

3.3 Hcl

The Hcl results followed for up to 10 days the chemical reaction on the samples at 48 h later the samples water absorption is observed in J5 specimen is higher comparing to overall water absorption test were taken out from immersed water the absorption is for sample J15 and J20 shown no chemical reaction. Initial following to 4 days later all samples got their initial weight and didn't lose the initial weight up to 10 days. The following Table 7 shows the detailed day-to-day chemical reaction and samples.

Table 7 Hcl testing composite samples specimens data

Specimen name	J5 (g)	J10 (g)	J15 (g)	J20 (g)	J5 (g)	J10 (g)	J15 (g)	J20 (g)
B.W	1.56	1.68	1.73	1.76				
48 h	1.59	1.7	1.75	1.77	1.923	1.190	1.156	0.568
1	1.57	1.7	1.73	1.76	0.641	1.190	0	0
2	1.57	1.68	1.73	1.76	0.641	0	0	0
3	1.56	1.68	1.73	1.76	0	0	0	0
4	1.56	1.68	1.73	1.76	0	0	0	0
5	1.56	1.68	1.73	1.76	0	0	0	0
6	1.56	1.68	1.73	1.76	0	0	0	0
7	1.56	1.68	1.73	1.76	0	0	0	0
8	1.56	1.68	1.73	1.76	0	0	0	0
9	1.56	1.68	1.73	1.76	0	0	0	0
10	1.56	1.68	1.73	1.76	0	0	0	0

The following graph shows the chemical absorption of the samples and on the graph taken on the X axis Days and Y axis Specimen weight in grams respectively.

The graph shows the sample weights are the analytical results on the X and Y axes taken days and specimen weight in grams, respectively. Graph 3 shows the sample weights increase or decrease in absorption percentage.

4 Conclusions

4.1 NaOH

The NaOH results concluded that increase in fiber content can lead to absorb more moisture. The samples got initial weights after 7 days later, which means last days it is noticed that no chemical reaction on the samples.

4.2 NaCl

The NaCl results shown as the chemical effect on samples became constant weights after 8 days. This means beyond 8 days there is no moisture gain in the content.

4.3 HCl

The Hcl results shown as the chemical effect on samples became constant weights after 7 days. This means beyond 4 days there is no moisture gain in the content.

References

1. K. Pickering, Aruan efendy, m.g., le, t.m., A review of recent developments in natural fibre composites and their mechanical performance, composites: Part A http://sci-hub.tw/10.1016/j.compositesa.2015.08.038
2. Hoi-yan Cheung, Mei-po Ho, Kin-tak Lau, Francisco Cardona, David Hui, Natural fibre-reinforced composites for bioengineering and environmental engineering applications, Composites Part B: Engineering, Volume 40, Issue 7, 2009, Pages 655–663, ISSN 1359-8368. http://sci-hub.tw/10.1016/j.compositesb.2009.04.014
3. S. J. S. DA, Book: . Chap.1, On the recyclability of a cyclic thermoplastic composite (2005) 1–10
4. S. A. R. L. F. M. R. L. A. D. Alves C, Ferrao P. M. C, Ecodesign of automotive components making use of natural jute fiber composites, L. B, Alves, Rodrigues. http://sci-hub.tw/10.1016/j.jclepro.2009.10.022
5. Polymer matrix composites and technology Ru-Min Wang, Shui-Rong Zheng and Ya-Ping Zheng Woodhead Publishing ISBN 978-0-85709-221-2 (print)
6. S. M. Sapuan, K. F. Tamrin, Y. Nukman, Y. A. El-Shekeil, M. S. A. Hussin and S. N. A. Aziz, 1.8 Natural Fiber-Reinforced Composites: Types, Development, Manufacturing Process, and Measurement, In Comprehensive Materials Finishing, edited by MSJ Hashmi, Elsevier, Oxford, 2017, Pages 203–230, ISBN 9780128032497, http://sci-hub.tw/10.1016/B978-0-12-803581-8.09183-9
7. Ming Cai, Hitoshi Takagi, Antonio N. Nakagaito, Yan Li, Geoffrey I. N. Waterhouse, Effect of alkali treatment on interfacial bonding in abaca fiber-reinforced composites, Composites Part A: Applied Science and Manufacturing, Volume 90, 2016, Pages 589–597, ISSN 1359-835X, http://sci-hub.tw/10.1016/j.compositesa.2016.08.025
8. Araldite DBF/HY 951 Page. 3, Mix Ratio, February 2005 2/6
9. R. A. Braga, P. A. A. Magalhaes, Analysis of the mechanical and thermal properties of jute and glass fiber as reinforcement epoxy hybrid composites, Vol. 2015. http://sci-hub.tw/10.1016/j.msec.2015.06.031
10. Characterization on the Properties of Jute Fiber at Different Portions, International Journal of Polymer Science Volume 2015 (2015), http://dx.doi.org/10.1155/2015/262348 Sweety Shahinur, 1, 2 Mahbub Hasan, 2 Qumrul Ahsan, 3 Dilip Kumar Saha, 4 and Md. Saiful Islam 5
11. Processing and Characterization of Jute Fiber Reinforced Thermoplastic Polymers A. C. Karmaker & G. Hinrichsen Pages 609–629| Published online: 22 Sep 2006 Download citation http://sci-hub.tw/10.1080/03602559108019223
12. International Journal of Textile Science 2012, 1(6): 84–93 DOI:http//doi.org/http://sci-hub.tw/10.5923/j.textile.20120106.05 Jute Composites asWood Substitute Debiprasad Gon1,*, Kousik Das2, Palash Paul2, SubhankarMaity2 1Indian Jute Industries' ResearchAssociation, 17, Taratala Road, Kolkata-88 2Panipat Institute of Engineering, Technology, Samalkha, Panipat, Haryana

13. Ming Cai, Hitoshi Takagi, Antonio N. Nakagaito, Yan Li, Geoffrey I. N. Waterhouse, Effect of alkali treatment on interfacial bonding in abaca fiber-reinforced composites, Composites Part A: Applied Science and Manufacturing, Volume 90, 2016, Pages 589–597, ISSN 1359-835X, http://sci-hub.tw/10.1016/j.compositesa.2016.08.025

14. Josh Kelly, Mohsen Mohammadi, Uniaxial tensile behavior of sheet molded composite car hoods with different fibre contents under quasi-static strain rates, Mechanics Research Communications, Volume 87, 2018, Pages 42–52, ISSN 0093-6413. http://sci-hub.tw/10.1016/j.mechrescom.2017.12.007

15. R. Sothornvit, C. W. Olsen, T. H. McHugh, J. M. Krochta, Tensile properties of compression-molded whey protein sheets: Determination of molding condition and glycerol-content effects and comparison with solution-cast films, Journal of Food Engineering, Volume 78, Issue 3, 2007, Pages 855–860, ISSN 0260-8774. http://sci-hub.tw/10.1016/j.jfoodeng.2005.12.002

16. Satish Pujari, A. Ramakrishna, K. T. Balaram Padal, Comparison of ANN and Regression Analysis for Predicting the Water Absorption Behaviour of Jute and Banana Fiber ReinforcedEpoxy composites, Materials Today: Proceedings, Volume 4, Issue 2, Part A, 2017, Pages 1626–1633, ISSN 2214-7853. http://sci-hub.tw/10.1016/j.matpr.2017.02.001

17. Ram Krishna Adhikari, B. S. Keerthi Gowda, Exploration of mechanical properties of banana/jute hybrid polyester composite, Materials Today: Proceedings, Volume 4, Issue 8,2017, Pages 7171–7176, ISSN 2214-7853. http://sci-hub.tw/10.1016/j.matpr.2017.07.043

18. Radhika Londhe, Ashok Mache, Aparna Kulkarni, An experimental study on moisture absorption for jute-epoxy composite with coatings exposed to different pH media, Perspectives in Science, Volume 8, 2016, Pages 580–582, ISSN 2213-0209. http://sci-hub.tw/10.1016/j.pisc.2016.06.026

19. T. Alomayri, I. M. Low, Synthesis and characterization of mechanical properties in cotton fiber-reinforced geopolymer composites, Journal of Asian Ceramic Societies, Volume 1, Issue 1, 2013, Pages 30–34, ISSN 2187-0764. http://sci-hub.tw/10.1016/j.jascer.2013.01.002

20. Pruttipong Pantamanatsopa, Warunee Ariyawiriyanan, Tawatchai Meekeaw, Rattiyakorn Suthamyong, Ketsara Arrub, Hiroyuki Hamada, Effect of Modified Jute Fiber on Mechanical Properties of Green Rubber Composite, Energy Procedia, Volume 56, 2014, Pages 641–647, ISSN 1876-6102. http://sci-hub.tw/10.1016/j.egypro.2014.07.203

21. P. Deepak, R. Vignesh Kumar, S. Badrinarayanan, H. Sivaraman, R. Vimal, Effects of Polyamide and/or Phenalkamine Curing Agents on the Jute Fibre Reinforcement with Epoxy Resin Matrix, Materials Today: Proceedings, Volume 4, Issue 2, Part A, 2017, Pages 2841–2850, ISSN 2214-7853. http://sci-hub.tw/10.1016/j.matpr.2017.02.164

22. A.B. Maslinda, M.S. Abdul Majid, M.J.M. Ridzuan, M. Afendi, A.G. Gibson, Effect of water absorption on the mechanical properties of hybrid interwoven cellulosic-cellulosic fibre reinforced epoxy composites, Composite Structures, Volume 167, 2017, Pages 227–237, ISSN 0263-8223. http://sci-hub.tw/10.1016/j.compstruct.2017.02.023

Experimental Performance and Analysis of Domestic Refrigeration System Using Nano-Refrigerants

Deepak Bondre, Apurav Joshi, Tejas Shinde, Apurv Deshmukh and Kavita Dhanawade

Abstract Advancement of nanotechnology played a crucial role in improving efficiency in many sectors of engineering and refrigeration is not an exception. Metal oxide such as Al_2O_3 is a most commonly used nanoparticle. Present study scrutinizes domestic refrigerator's performance using nanofluids. Different methods to prepare nanofluid were investigated, which indicated ultrasonic probe method was most effective and faster. Four distinct configurations of heat transfer fluid were tested, which includes three nanoparticle concentrations in POE oil and one with pure POE oil. Concentrations investigated were as follows, 0.05, 0.1, 0.2% of Al_2O_3 nanoparticle; however, 0.1% Al_2O_3 nanoparticle concentration was found to give superior performance in all. COP of system was improved by 17.27% and energy consumption was reduced by 32.48%. The whole study was carried out without any additional component to domestic refrigerator test rig. COP improvement and energy consumption reduction conveys future scope of more compact and energy efficient refrigeration system.

Keywords Nano-refrigeration system · Nanofluids · Al_2O_3 · Nanoparticle · COP R134a · Sonication method · Compact systems

D. Bondre (✉) · A. Joshi · T. Shinde · A. Deshmukh · K. Dhanawade
Department of Mechanical Engineering, Lokmanya Tilak College of Engineering,
Sector 4, Vikas Nagar, 400709 Koparkhairane, Navi Mumbai, Maharashtra, India
e-mail: dmbondre1@gmail.com

A. Joshi
e-mail: apurav.joshi95@gmail.com

T. Shinde
e-mail: shindetejas96@gmail.com

A. Deshmukh
e-mail: apurvdeshmukh878@gmail.com

K. Dhanawade
e-mail: kavitadhanawade2@gmail.com

Nomenclature

C_p	specific heat of water $= 4.186$ kJ/Kg K
EMC	energy meter constant (imp/KWh)
FT	final temperature of water (°C)
IT	initial temperature of water (°C)
M	$\rho V =$ mass of POE oil (gm)
$P_{1,2,3,4}$	refrigerant pressure at specific point
t	time required to reach a final temperature of water (sec)
t_b	time for 10 blinks of energy meter (sec)
$T_{1,2,3,4,5}$	refrigerant temperature at specific point
V	=volume of POE oil (mL)
w	weight of water in evaporator coil (Kg)
X	mass of Al_2O_3 nanoparticle (gm)
ρ	density of POE oil (gm/mL)

1   Introduction

In the running era of innovations and technology, the development in the field of the refrigeration and air-conditioning culminated. The refrigerator market in last decade increased significantly. Due to the highest use of the refrigerants, consequences are global warming, melting polar ice, and rising sea level. Already hydrofluorocarbon refrigerants seized the place of chlorofluorocarbons. Since R134a have zero ozone depletion potential (ODP), most of the domestic refrigerators run on the R134a refrigerants. But the global warming potential (GWP) of R134a is 1300. Basically, refrigeration is the process of heat removal from the lower temperature body. Refrigeration has many applications such as a home appliance, food industry, chemical industry, laboratories, hospitals, and hotels [1]. These refrigeration systems consume a huge amount of electricity and to reduce the electric consumption of the system we have to improve the performance of the system either by replacing the old components periodically or by introducing the newer technology. To improve the performance of the system, heat transfer rate of the system must be increased. Nanoparticle holds better thermal conductivity than conventional refrigerants. Thus, we can introduce nanoparticles by forming a stable nanofluid solution. The power consumption can be reduced by 20–30% after inserting nanofluid into the system. As well as the coefficient of performance (COP), heat transfer rate, and cooling capacity can be enlarged. Therefore, nanofluids can be the future of refrigeration.

Nanofluid is an advanced form of fluid which can be formed by adding nanoparticle into the fluid like water, oil, and glycol. The size of this nanoparticle ranges from 1 to 100 nm. Nanoparticles behave differently from their parent in properties like molecular bond and nature of response for mass and energy application. Nanoparticle augments the thermo-physical properties like thermal conductivity, convective

heat transfer, viscosity, and thermal diffusivity as associated with base fluids oil or water. This enhancement in the properties validates the countless future in many fields of engineering application such as refrigerator, an air-conditioning system, heat exchanger, nuclear plants, and coolant in machining. Nanoparticles basically exist in colloidal form of metals like copper, nickel, and aluminum or metal oxide like silicon oxide, copper oxide, aluminum oxide, and titanium oxides. Nanofluid comprises high specific surface area, and hence, additional heat transfer between suspended particle and fluids, more thermal conductivity, lessens power consumption to achieve system size minimization.

2 Literature Review

The invention of the nanotechnology is one of the major inventions ever done in the history. Many returns of nanotechnology rest on the fact that it is possible to modify the structures of materials at extremely small scales to achieve specific properties, thus have greater scope. In early days (1995), Choi et al. [2] proposed the new level of heat transfer fluid using nanoparticle in the base fluid. The result of the theoretical studies showed that the heat transfer is drastically improved when nanoparticles are used. Hays et al. [3] observed the preparation method of the nanofluid can have large effect on the resultant thermal conductivity. Jiang et al. [4] performed the experimental analysis on the nano-refrigerant thermal conductivity and model on nanofluid thermal conductivity. They observed that thermal conductivity significantly increases with increase in the nanoparticle concentration. Mahbubul et al. [5] studied the theoretical investigation of performance system using Al_2O_3 with R-134a refrigerant under different conditions. After analyzing the equations, they concluded that the thermal conductivity, viscosity of nano-refrigerant and pumping power system increases, and thermal conductivity varies with the concentration of nanoparticle. Coumaressin et al. [6] studied major disadvantages of the R134a. Due to its high global warming potential author believed, the use of nanoparticle would increase the performance of the system which indirectly reduces the environmental issues. CFD analysis is done using FLUENT software using CuO_2-R134a combination. It is observed that system works efficiently and evaporative heat transfer is enhanced. Whereas, Jwo et al. [7] performed an experiment using Al_2O_3 nanoparticle in three different concentrations, 0.5, 0.1, and 0.2%. Forthe preparation of nanofluids researcher used ultrasonic vibration for 50 min. For each sample, the performance of the system found to be best at 0.1% Al_2O_3 + R134a combination. Rejikumar et al. [8] analyzed improvement in heat transfer of domestic refrigeration system using refrigerant R134a with mineral oil with Al_2O_3 Nanoparticle. It was observed that the freezing capacity of the system with Al_2O_3 + mineral oil was maximum as compared to a convention system. Sendil Kumar et al. [9] carried out an experiment on the domestic refrigerator using Al_2O_3 as nanoparticle and PAG oil as a base lubricant. The proportion of the nanoparticle was 0.2%. The result indicates using nano-refrigerant reduces the length of the capillary tube. Subramanian et al. [10]

Fig. 1 Different concentration of nanofluids

performed an experiment on the VCRS using nanofluid as a mixture of Al_2O_3 with POE/Mineral oil. The refrigerant used was R134a. To form a stable solution of the nanofluid, he used ultrasonic vibration method and kept it for 72 h under observation for sedimentation test. It is observed that freezing capacity is higher and power consumption is reduced by 25%. The coefficient of performance is increased by 33%.

From literature survey, it was clear that nanoparticles in refrigeration have a huge scope of improvement and some more research needs to be carried out. Very few researchers did detail observation of different compositions of the same nanofluid and whoever did the data available was not so trustable. There was lack of information available about testing these samples on domestic refrigeration system without any special component added extra. Only a few experiments were done with R-134a and even though it's most widely used in domestic places. Very few researchers explained about nanofluid preparation methods. Information on processes used for nanoparticles dispersion is lacking. In this research, most common refrigerant R-134 is tested with three different compositions of nanofluids. Al_2O_3 was the selected metal oxide. The objective of this research is to study nanofluid preparation methods and R-134a and Al_2O_3 nanofluid combination in a much detailed way.

3 Experimental Setup and Instrumentation

3.1 Nanofluid Preparation and Optimization

The key stage of the experiment is the preparation of nanofluids solution. The test samples were prepared by two different methods of sonication. For the process of mixing, nanoparticle in 3 different concentrations is selected, 0.05, 0.1, and 0.2% (by mass fraction) (Fig. 1). These concentrations were mixed with POE oil. Ultrasonic treatment is a most effective method for nanoparticles dispersion. Primarily, ultrasonic bath method was used with vortex mixer as the first step. Nanoparticles and POE oil were kept in a sonication bath for 4 h. This test sample failed in sed-

Fig. 2 Agglomeration of
nanoparticles
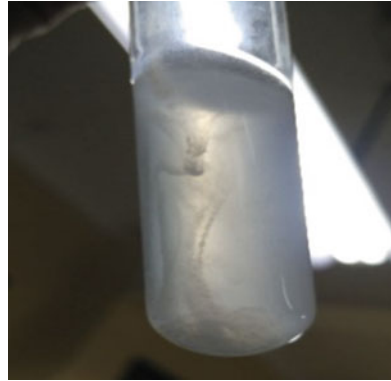
imentation test (Fig. 2), as particles sedimented within 24 h of span. For the next try, probe sonicator was used with a magnetic stirrer in it. The probe sonicator of 750 W was running on 35% power with a frequency of 20 kilohertz. Sample kept for 4 h sonication. Afterward sample kept for stability test and sedimentation was not observed even after 11 days.

3.2 Evacuation System and Test Procedure

Optimization of nanofluid and refrigerant proportion was done. Refrigerant was charged till system pressure raised to 60 psi. Nanofluid volume for every concentration was 220 ml.

1. At 32 °C ± 1 °C ambient temperature, vacuum has been created in an experimental setup with the help of vacuum pump to withdraw air and moisture from the refrigeration system.
2. After system evacuation, pure refrigerant R134a has been charged into the system. Performance parameters are measured for first set of reading.
3. After collecting data for pure R134a, the refrigerant is discharged from the system. The compressor is disassembled from circuit, and nitrogen flushing of the system is done at high pressure.
4. Nanofluid is inserted in the compressor and the whole system is assembled again nitrogen leak test is carried out. After confirming no leak from the system, the system is further evacuated using a vacuum pump.
5. The Refrigerant is injected into the system and reading has noted down.

And the whole process is repeated again for other two sets of reading.
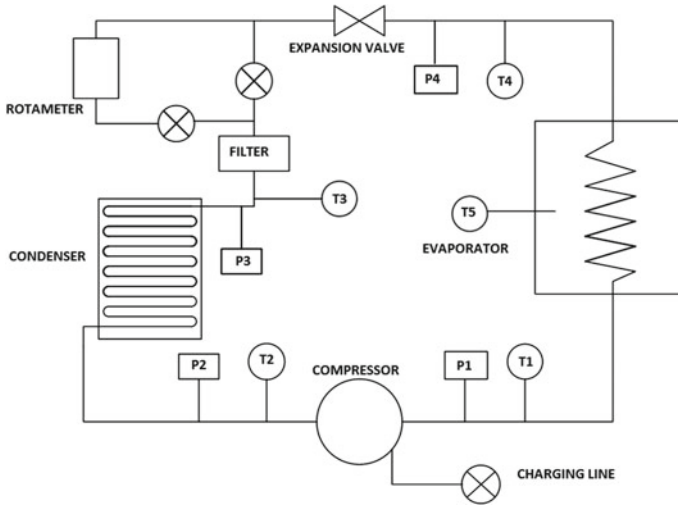
Fig. 3 Schematic diagram of experimental setup

3.3 Experimental Setup

An experimental setup of the vapor compression refrigeration system has been fabricated to carry out the experiments. The system is very much similar to the domestic refrigerator. It consists of hermetically sealed LG refrigeration compressor of capacity 548 Btu/hr, EER is 421 Btu/hr. Air cooled condenser (natural convection) of material copper is selected and diameter of pipe is 4.87 mm and length of pipe is 13.7 m. Capillary tube, as an expansion device, is of material copper having a 0.044-in. diameter and a coil type evaporator contains water that to be cooled. Total 4 pressure gauges and 5 temperature gauges installed at the required position. A rotameter (0–20 LPH) is a device that measures the flow rate of liquid or gas in a closed tube, which is located between condenser and expansion valve. The schematic diagram is shown (Fig. 3).

4 Data Analysis

Various samples of nanofluids are tested on an experimental test setup. System performance has been studied by evaluating COP. Temperature in evaporator is noted down after particular period of time. Refrigeration effect is calculated using different samples of Nanofluid.

Calculation of Weight of Nanoparticle by % Mass Fraction

$$\% \text{ Mass fraction} = \frac{\text{Mass of Al}_2\text{O}_3 \text{ Nano particle}}{\text{Mass of Al}_2\text{O}_3 \text{ Nano particle} + \text{Mass of POE oil}} \times 100.$$

Calculation of Actual COP of the System

The coefficient of performance is defined as the ratio of net refrigeration effect produced to the work input to the system.

$$\text{COP} = \frac{\text{Net refrigeration effect produce}}{\text{work input to the system}} = \frac{Q_a}{W}.$$

Work input to the system can be found out by energy meter reading which is given by,

$$W = \frac{10 \times 3600}{t_b \times \text{EMC}}.$$

Net refrigeration effect can be found out by basic heat transfer equation,

$$Q_a = \frac{w \times C_p \times (\text{IT} - \text{FT})}{t}.$$

5 Results and Discussions

5.1 COP

COP is influenced by operating conditions, especially ambient temperature and relative temperatures between sink and source, hence all experiments are carried out at approximately same ambient temperature. Here in this experimental study, actual COP of the refrigeration system has been investigated. Initially, the experiment is performed with pure R134a. As Fig. 4 shows, the COP of the system with pure R134a is found to be 2.47 whereas with R134a + 0.05% Al$_2$O$_3$, 0.1% Al$_2$O$_3$, and 0.2% Al$_2$O$_3$ found to be 2.653, 2.895, and 2.698, respectively. So, for R134a + 0.5% Al$_2$O$_3$ nano-refrigerant sample COP is improved by 7.40%, for R134a + 0.1% Al$_2$O$_3$ COP is increased by 17.2% and for 0.2% Al$_2$O$_3$ COP is increased by 9.23%. The maximum percentage change is observed in 0.1% of nanofluid concentration (Fig. 5).

Fig. 4 COP versus concentration of nanoparticle in R134a
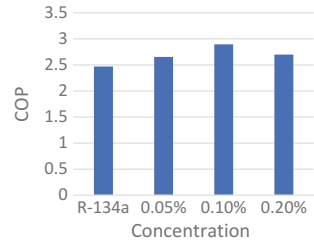
Fig. 5 Percentage change in COP versus concentration of nanoparticle in R134a
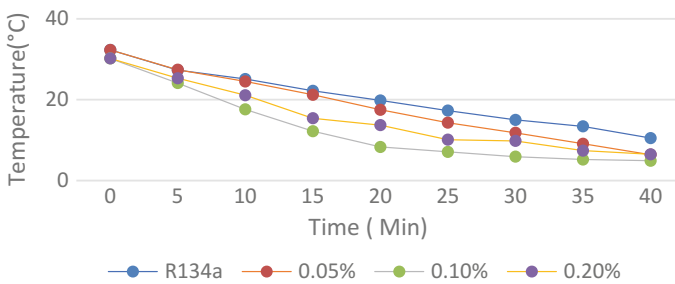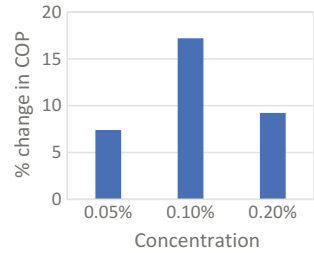
Fig. 6 Temperature (°C) versus time (minutes) plot for pure R134a and nano-refrigerants

5.2 Evaporator Temperature

With 40 min of span all the final temperatures of the systems noted down and the time-based graph is plotted. As Fig. 6 shows, the cooling capacity of the system is increased when Nanofluid is used in the system. As observed from the graph, the minimum temperature was attained most quickly by the 0.1% concentration of the nanofluid for the same set of periods.

Fig. 7 Refrigeration effect (kW) versus time plot for pure R134a and nano-refrigerants
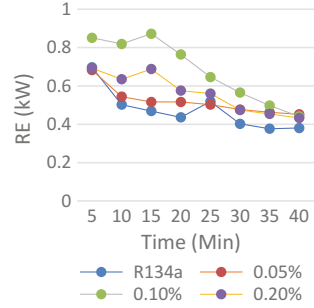
Fig. 8 Power consumption (kWh) versus concentration of nanoparticle in R134a
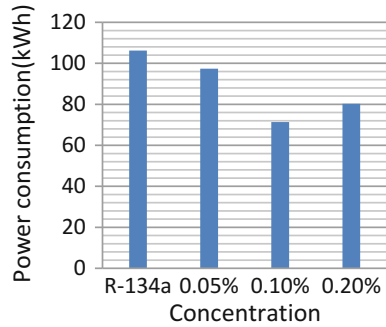
5.3 Refrigeration Effect

Refrigeration effect for the different samples has been calculated, and it is seen that the refrigeration effect in case of a system using nanofluid with concentration of 0.1% mass fraction is maximum (Fig. 7). In case of 0.05% mass fraction, a percentage increase of refrigeration effect is found to be 20.06% and for 0.2% mass fraction it was 37.97%.

5.4 Power Consumption

Power input to any refrigeration system is an important parameter to evaluate its performance and COP of refrigeration system depends on it. In this section, the power requirement to run the system to achieve the desired temperature has been examined. As Fig. 8 shows, the power consumption of a system using nano-refrigerant is reduced. Power consumption is reduced by 8.3% with 0.05% Al_2O_3, 34.48% with 0.1% Al_2O_3, and 22.41% with 0.2% Al_2O_3.

6 Future Scope

The research shows that there is significant increase in the heat transfer characteristics of refrigeration system with help of nanofluid. There are few challenges that need to be counterfeit. New techniques should be introduced for synthesis of nanoparticle and effective nanofluid preparation which will reduce the agglomeration difficulties. Different concentration of nanofluid and multiple combinations of nanoparticle in same fluid should be explored. As it is observed that compressor works properly for the system, but there is need of utmost study of compressor characteristic when the nanofluid is inserted inside the compressor as well as effect on life of compressor. Long-term effects of nanoparticle circulation and its effects on crucial components like expansion valve/capillary tube, filter, inside surface of copper tubes are to be studied. More investigation should be done on the influencing factors like nanoparticle material, size, shape, and refrigerant boiling performance. More exploration should be carried out for density, specific heat, flow characteristic, and viscosity of nanofluid.

7 Conclusion

In this study, the performance of domestic refrigerator-based experimental test setup has been investigated by using pure refrigerant R134 and with nanofluid (R134a + Al_2O_3). Results show that the use of nano-refrigerant (R134a + Al_2O_3) instead of pure refrigerant R134a is beneficial. It has been observed that there is a substantial improvement in the performance of the system when nanoparticles are used along with conventional refrigerant (R134a) within a certain limit. Following conclusions are derived from this experimental study.

- The coefficient of performance (COP) of vapor compression system is found to be improved by maximum 17.2% using R134a + Al_2O_3 (0.1% mass Fraction).
- The time required for cooling is found to be reduced using nanofluid.
- Energy consumed by compressor was reduced by 32.48% in case of 0.1% Al_2O_3, 8.4% in case of 0.05% Al_2O_3, 22.41% in case of 0.2% Al_2O_3.
- 0.1% Al_2O_3 was found to be a better option among all.

References

1. P.N. Ananthanarayanan: Basic refrigeration and air conditioning. Tata McGraw-Hill Education Pvt. Ltd. (2013).
2. Choi, S.U.S., Eastman, J.A.: Enhancing thermal conductivity of fluids with nanoparticles. ASME FED, 231, p. 99–103 (1995).
3. Alexander Hays, Charles P. Marsh, Jorge Alvarado, Ryan Franks.: The effect of nanoparticle agglomeration on enhanced nanofluidic thermal conductivity. International Refrigeration and Air Conditioning Conference, Purdue University, paper R132. (2006).
4. Weiting Jiang, Guoliang Ding, Hao Peng, Yifeng Gao, Kaijian Wang.: Experimental and Model Research on Nano refrigerant Thermal Conductivity. American Society of Heating, Refrigerating and Air-Conditioning Engineers, Inc. (www.ashrae.org). Published in HVAC&R Research, Vol 15, No. 3, (May 2009).
5. I.M. Mahbubul, S.A. Fadhilah, R. Saidur, K.Y. Leong, M.A. Amalina.: Thermophysical properties and heat transfer performance of Al_2O_3/R134a nanorefrigerants. International Journal of Heat & Mass Transfer, 57, pp. 100–108. (2013).
6. T. Coumaressin and K. Palaniradja: Performance Analysis of a Refrigeration System Using Nano Fluid. International Journal of Advanced Mechanical Engineering, ISSN 2250-3234 Volume 4, Number 4 pp. 459–470 (2014).
7. Jwo, C.S., Jeng, L.Y., Teng, H.: Effect of Nano lubricant on the performance of Hydrocarbon refrigerant system, J. Vac. Sci. Techno., Vol.27, Issue 3, pp. 1473–1477. (2009).
8. Rejikumar R and Sridhar K.: Heat transfer enhancement in domestic refrigerator using Nano refrigerant as working fluid. Int. J. Comp. Eng. Res, 3(4). (April 2013).
9. D. Sendil Kumar and Dr. R. Elansezhian: Experimental study on Al_2O_3-R134a Nano refrigerant in refrigeration system. International journal of Modern Engineering Research, Vol. 2, Issue 5, pp. 3927—3929. (October 2012).
10. N. Subramani and M. J. Prakash.: Experimental studies on a vapour compression system using Nano refrigerants. International Journal of Engineering, Science and Technology Vol. 3, pp. 95–102. (2011).

Experimental Investigation and Optimization of End-Milling Parameters in the Machining of Inconel 825 Using Carbide-Coated Tool

Hari Vasudevan, Ramesh Rajguru, Geet Dave, Arun Alva, Vinil Punjani and Devdatt Bhurke

Abstract In order to achieve reduction in machining cost and increase in productivity in machining processes, optimization of cutting conditions involving cutting speed, feed per tooth and radial depth of cut is very critical. In this study, optimization of cutting parameters with various performance characters that rely on the grey relational analysis with Taguchi method is performed in order to obtain minimum surface roughness and maximum material removal rate during dry end-milling process. The experiments were conducted on Inconel 825 material using carbide inserts, with physical vapour deposition and TiAlN coating. Sixteen experiments were conducted, based on the design of experiments with three factors constituting four levels each. The surface measurement was done using Talysurf. The optimal parameters achieved are cutting speed of 55 m/min, feed per tooth of 0.09 mm/tooth and the radial depth of cut, 1.2 mm. The analysis of grey relational grade indicated that the radial depth of cut is the more influential parameter, followed by the feed rate.

Keywords Inconel 825 · End milling · Dry machining · Taguchi
Grey relational analysis · Talysurf · PVD · Coated insert

H. Vasudevan
D. J. Sanghvi College of Engineering, Mumbai, India
e-mail: harivasudevan@iitb.ac.in

R. Rajguru (✉) · G. Dave · A. Alva · V. Punjani · D. Bhurke
Department of Mechanical Engineering, D. J. Sanghvi College of Engineering,
Mumbai, India
e-mail: ramesh.rajguru9@gmail.com

1 Introduction

Conventionally, super alloys are materials that are heat resistant; i.e., it can be machined at temperatures over 540 °C. Nickel-based super alloys find widespread use in the aerospace, oil and gas well piping, chemical and nuclear fuel processing and pollution control equipment, etc., due to its unique characteristics, such as high-temperature corrosion resistance, oxidation resistance and creep resistance. In the chemical processing industries, it is used for sulphuric acid piping and vessels, pickling tank heaters, pickling tanks and equipment, phosphoric acid evaporators, ammonium sulphate vessels, etc. It also finds use in power station hoppers, marine exhaust systems, expanding bellows, calorifiers and electrostatic precipitator electrodes [1].

Nickel-based super alloys often contain other alloying metals in it, and the presence of chromium, cobalt, aluminium, titanium, rhenium, ruthenium, etc. may be found among other metals. The nickel content helps with the resistance to stress corrosion cracking, and molybdenum and copper give resistance to chemically reducing environment like containing sulphuric and phosphoric acids. Molybdenum also resists pitting and crevice corrosion, and chromium helps to counter oxidizing substances. Titanium with suitable heat treatment helps in preventing inter-granular corrosion.

These alloys have many advantages like high corrosion resistance and high heat strength, but it also possesses some disadvantages or rather certain difficulties. The low thermal conductivity causes the heat to be concentrated at the cutting edge, instead of transferring to the chips or work piece. These temperatures can cause cutting edge deformation and crater wear, which in turn could cause a catastrophic failure. The reactivity of these materials aids the formation of built-up edge (BUE) and coating delamination, which leads to a very poor tool life. The chips formed during the machining are very hard and continuous, and hence, there is a requirement for chip-breaking geometry [2].

Thakur et al. [3] conducted an experiment to evaluate the machinability of Inconel 825 alloy under dry conditions. Experimentation conducted was at a constant feed rate (0.198 mm/rev) and depth of cut (1 mm) with three different levels of cutting speed (51, 84 & 124 m/min) using coated and non-coated cemented carbide (ISO P30) tools. The study showed that the surface integrity produced by the coated tool is superior to that of the machining in case of Inconel 825, with the uncoated tool. Thakur et al. [4] also studied different facets of surface integrity, example surface roughness, crystal structure & microstructure of the sub-surface & over surface region, white layer thickness and tendency for work hardening using constant feed rate, depth of cut and CVD multilayer tool coating (TiN/TiCN/Al$_2$O$_3$/ZrCN) during dry machining of Inconel 825. The study pointed out that the coated tool gave better surface finish in comparison with that with non-coated tool only at high cutting speed.

Maiyar et al. [5] experimented with the optimal cutting parameters during the machining process. They concluded that the cutting velocity was the highest significant machining parameter, followed by feed rate with 56.88 and 34.64% influence,

respectively. Jindal et al. [6] concluded that TiAlN- and TiCN-coated carbide tool performed better at higher cutting speeds, having higher metal cutting performance than TiN. For this verification, ion-plated PVD TiN, TiCN and high-ionization sputtered PVD TiAlN coatings were deposited on WC±6 wt%Co hard metal inserts. They were evaluated in the turning of Inconel 718, medium carbon SAE 1045 steel and ductile cast iron. For Inconel 718, two cutting speeds were selected, 46 and 76 m/min with the feed rate of 0.15 mm/rev and depth of cut 0.75 mm. For both, the speeds of TiAlN- and TiCN-coated tools performed significantly better than TiN coating.

Narasimha et al. [7] noticed that the coated tools had higher wear resistance as compared to uncoated tools. This was verified by the fact that flank wear on coated tools was much less as compared to uncoated tools. Sahu [8] concluded that the feed rate had a significant effect on Ra. For both the uncoated and coated tools, the Ra value decreased with increase in cutting speed. Veldhuis et al. [9] concluded that the PVD coating is tougher and has less chance of thermal cracking. Cutting forces do not change in PVD+CVD and give higher production rate economically. Yildiz et al. [10] observed that the CVD-coated samples have higher Ra values as compared to PVD coated with respect to feed rate. Moreover, the resultant force and surface roughness decreased with increase in nose radius. The experimental investigation conducted was on machinability of Ti6Al4 V titanium alloy by turning method. The cutting parameters used were cutting speed (75, 100 m/min), feed rate (0.15, 0.2, 0.25 mm/rev), and nose radius (0.8, 1.2, 1.6 mm). The tool used was PVD- and CVD-coated cemented carbide. It was concluded that the feed rate and tool nose radius are important parameters, which influenced the surface properties.

The current study is an attempt to delve into the research of the machining of material Inconel 825, which even after having an exhaustive list of applications and value-adding qualities to its merit remains by and large unexplored. The objective of the study basically was to ascertain the optimal feed per tooth, radial depth of cut and cutting speed in the end-milling operation under dry machining conditions to achieve comparatively better surface roughness and maximum material removal rate.

2 Methodology

The methodology used in the experimental study is depicted in the flow chart as shown in Fig. 1.

Fig. 1 Methodology of
experimentation
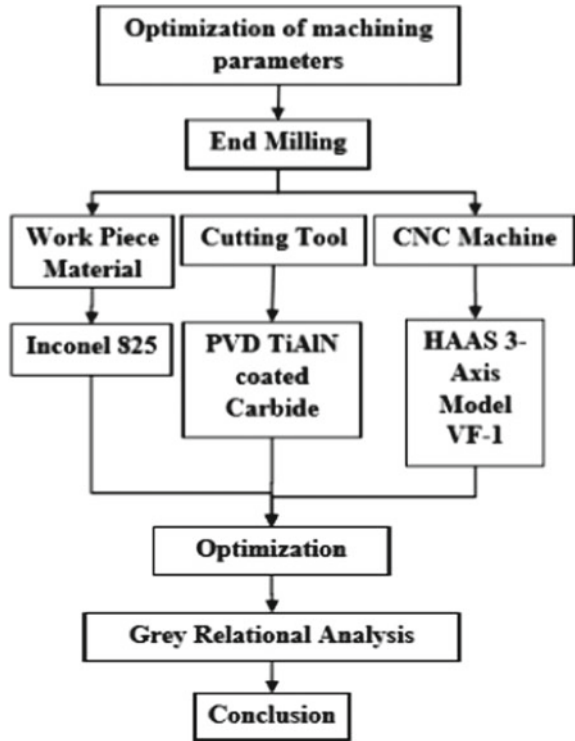
Fig. 2 Specimen work piece

3 Experimental Details

3.1 Work Material

The material used for the purpose of the experimentation was Inconel 825. The
chemical composition and properties of Inconel 825 are shown in Tables 1 and 2,
respectively. For the experimental purpose, it was decided to make use of 4 plates
with a dimension of 150 mm length to 50 mm breadth and the thickness of each piece
was 6 mm. The kind of specimen used is shown in Fig. 2.

Table 1 Chemical composition of Inconel 825

Element	Content %
Nickel	38.0–46.0
Iron	22.0 min (~33%)
Chromium	19.5–23.5
Molybdenum	2.5–3.5
Copper	1.5–3.0
Titanium	0.6–1.2
Manganese	1.0 max
Silicon	0.5 max
Aluminium	0.2 max
Carbon	0.05 max
Sulphur	0.03 max

Table 2 Properties of Inconel 825

Property	Value
Density	8.14 mg/m^3
Melting range	1370–1400 °C
Specific heat	440 J/kg°C
Curie temperature	<-196 °C
Permeability	1.005

3.2 Cutting Tool

Tool inserts utilized were 5745715 Grade: 1030, which are TiAlN coated by the physical vapour deposition method as shown in Table 3. The inserts belonged to Sandvik and were used two at a time, i.e. two fluted holders were used. The holder material was tungsten carbide of 16 mm diameter. A representation for the inserts used is given in Fig. 3.

3.3 Process Parameters

Variable parameters set for the experiment were feed per tooth, radial depth and cutting speed. These parameters were considered as the output parameters: material removal rate and surface roughness. Certain parameters were kept to be a constant for all the readings, work material, tool material, tool holder and dry cutting environment. The variables and their respective designations are represented in Table 4.

Table 3 Specification of tool inserts

Insert data	
Operation type (CTPT)	Medium
Insert size and shape	CoroMill 390-11T3
Insert width (W1)	0.268 in.
Cutting edge effective length (LE)	10 mm
Wiper edge length (BS)	1.2 mm
Corner radius (RE)	0.8 mm
Major cutting edge angle (KRINS)	90°
Coating (Coating)	PVD (Ti, Al) N
Insert thickness (S)	3.59 mm
Weight of item (WT)	0.003 kg
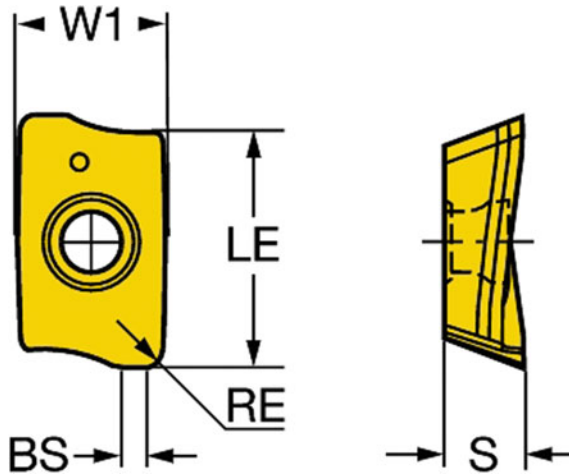
Fig. 3 Tool insert

3.4 Experimental Details

The process of end milling was done on a HASS 3-axis vertical milling machine, Model VF-1. It has a traversing distance of 508 mm on the X-axis, 406 mm on the Y-axis and 508 mm on the Z-axis. The table dimensions were 660 mm by 356 mm, enough for the specimen size. The machine output in terms of spindle speed is 8100 rpm, and the power is a constant 30 hp. The end-milling experimental set-up used is represented by means of a labelled depiction as shown in Fig. 4.

MRR (cm^3/min) in end-milling process was calculated as follows:

$$MRR = \frac{fz \times N \times Z \times ap \times ae}{1000} \tag{1}$$

Table 4 Input factors and their levels

Designation	Process parameters	Units	Factor levels			
			1	2	3	4
A	Cutting speed	m/min	45	55	65	75
B	Feed/tooth	mm/tooth	0.03	0.06	0.09	0.12
C	The radial depth of cut	mm	0.4	0.8	1.2	1.6
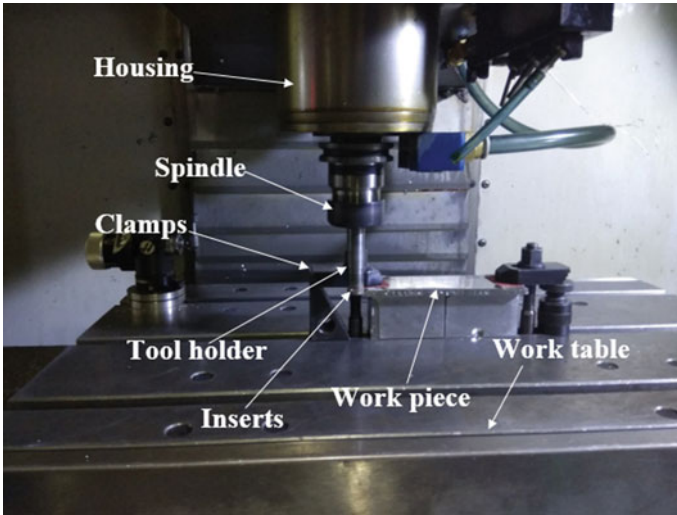
Fig. 4 Experimental set-up

where,

f_z (feed per tooth, mm/tooth),
N (spindle speed, RPM),
Z (number of effective teeth of the tool).

The Measurement for roughness was done on a Taylor Hobson Talysurf-4 set-up with data acquisition by a diamond tip stylus profiler using Se-surf software. The set-up is clearly shown in Fig. 5. An example for the Talysurf output is shown in Fig. 6. The final roughness and MRR values were recorded and are given in Table 5.
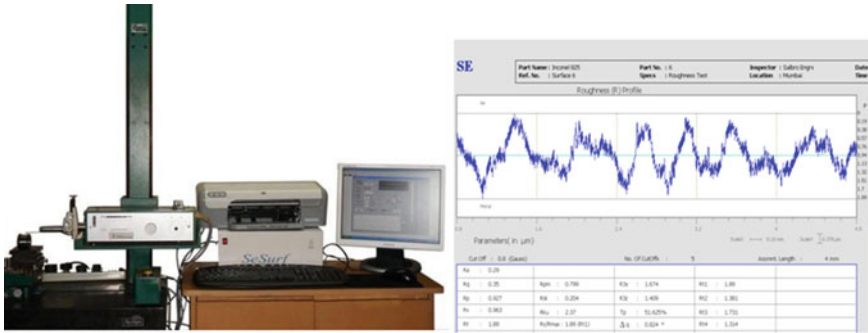
Fig. 5 Talysurf set-up and output graph
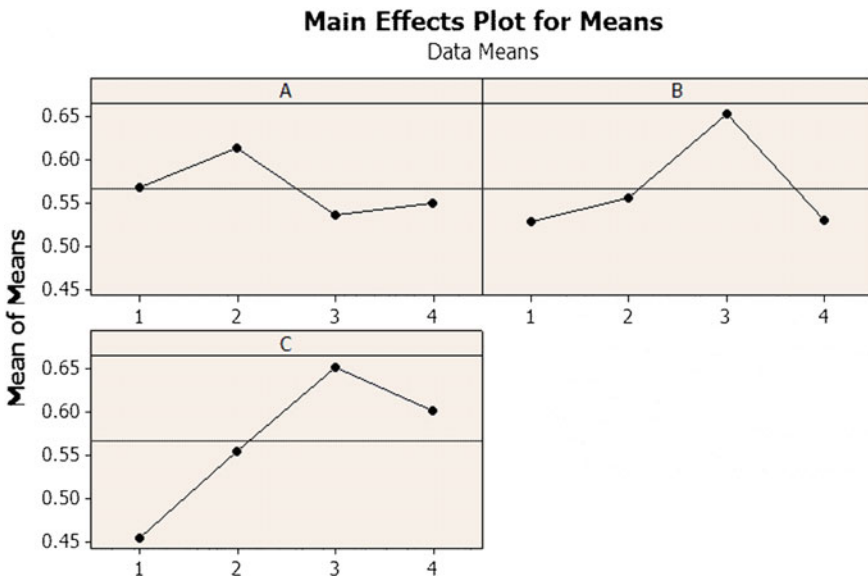
Fig. 6 Main effects plot of GRG

4 Grey Relational Analysis

The grey system theory was proposed by Deng in 1982. This theory is suitable for handling various problems with meagre, inadequate and ambiguous information. The grey relational analysis (GRA) based on this theory can be productively adopted for solving multi-objective optimization problems. Three different equations are used for this normalization procedure, depending upon the type of quality characteristics. If the true data sequence has a characteristic of quality as 'greater-the-better', then it is pre-processed by using the following equation.

Table 5 Experimental plan L$_{16}$ OA and values of Ra and MRR

Experiment	Coded parameters			Actual parameters			Ra	MRR
	A	B	C	A	B	C		
1	1	1	1	45	0.03	0.4	1.14	0.0322
2	1	2	2	45	0.06	0.8	0.481	0.1289
3	1	3	3	45	0.09	1.2	0.253	0.2900
4	1	4	4	45	0.12	1.6	1.146	0.5157
5	2	1	2	55	0.03	0.8	0.421	0.0645
6	2	2	1	55	0.06	0.4	0.29	0.0645
7	2	3	4	55	0.09	1.6	0.387	0.3867
8	2	4	3	55	0.12	1.2	0.66	0.3867
9	3	1	3	65	0.03	1.2	0.243	0.0967
10	3	2	4	65	0.06	1.6	0.736	0.2578
11	3	3	1	65	0.09	0.4	0.54	0.0967
12	3	4	2	65	0.12	0.8	0.69	0.2578
13	4	1	4	75	0.03	1.6	0.406	0.1288
14	4	2	3	75	0.06	1.2	0.389	0.1933
15	4	3	2	75	0.09	0.8	0.284	0.1933
16	4	4	1	75	0.12	0.4	1.046	0.1290

$$x_i^*(k) = \frac{x_i^o(k) - \min x_i^o(k)}{\max x_i^o(k) - \min x_i^o(k)} \tag{2}$$

If the true data have the characteristic of quality as 'lesser the better', then following equation is used.

$$x_i^*(k) = \frac{\max x_i^o(k) - x_i^o(k)}{\max x_i^o(k) - \min x_i^o(k)} \tag{3}$$

The grey relational coefficient is calculated from the deviation sequence using the following relation (it is shown in Table 6) [11].

$$\gamma\left(x_o^*(k), x_i^*(k)\right) = \frac{\Delta \min + \xi \Delta \max}{\Delta_{ik} + \xi \Delta \max} \tag{4}$$

5 Results and Analyses

Determination of optimum parameters: The weighted grey relational grade calculated for each sequence was taken as a response for further analyses. The larger-the-better quality characteristic is used for analysing the grey relational grade (GRG), since

Table 6 Calculated grey relational coefficient and grey relational grade

Actual		Normalization		Deviation		GRC		GRG
Ra	MRR	Ra	MRR	Ra	MRR	Ra	MRR	
1.1400	0.0322	0.0066	0.0000	0.9934	1.0000	0.3348	0.3330	0.3341
0.4810	0.1289	0.7364	0.2000	0.2636	0.8000	0.6548	0.3850	0.5197
0.2530	0.2900	0.9889	0.5330	0.0111	0.4670	0.9783	0.5170	0.7478
1.1460	0.5157	0.0000	1.0000	1.0000	0.0000	0.3333	1.0000	0.6668
0.4210	0.0645	0.8029	0.0670	0.1971	0.9330	0.7172	0.3490	0.5330
0.2900	0.0645	0.9480	0.0670	0.0520	0.9330	0.9057	0.3490	0.6273
0.3870	0.3867	0.8405	0.7330	0.1595	0.2670	0.7582	0.6520	0.7052
0.6600	0.3867	0.5382	0.7330	0.4618	0.2670	0.5199	0.6520	0.5860
0.2430	0.0967	1.0000	0.1330	0.0000	0.8670	1.0000	0.3660	0.6829
0.7360	0.2578	0.4540	0.4670	0.5460	0.5330	0.4780	0.4840	0.4810
0.5400	0.0967	0.6711	0.1330	0.3289	0.8670	0.6032	0.3660	0.4845
0.6900	0.2578	0.5050	0.4670	0.4950	0.5330	0.5025	0.4840	0.4932
0.4060	0.1288	0.8195	0.2000	0.1805	0.8000	0.7347	0.3850	0.5597
0.3890	0.1933	0.8383	0.3330	0.1617	0.6670	0.7556	0.4290	0.5921
0.2840	0.1933	0.9546	0.3330	0.0454	0.6670	0.9168	0.4290	0.6726
1.0460	0.1290	0.1107	0.2000	0.8893	0.8000	0.3599	0.3850	0.3723

Table 7 Response table for grey relational grade

	Level 1	Level 2	Level 3	Level 4	Max–Min	Rank
A	0.5671	0.6129	0.5354	0.5492	0.0775	3
B	0.5274	0.555	0.6525	0.5296	0.1251	2
C	0.4545	0.5547	0.6522	0.6032	0.1977	1

a larger value indicates the better performance of the process. The grey relational grade is further analysed by using Taguchi method.

From response table (Table 7), it was observed that the deviation between the maximum and minimum value of the GRG for end-milling parameters is: 0.0775 for cutting speed, 0.1251 for feed per tooth and 0.1977 for radial depth of cut.

By the comparison of values given in the above table, the most compelling factor affecting multiple performance characteristics was found out. This comparison leads to identify the level of importance of the controllable factors over the multiple performance characteristics. Maximum of these values was the most significant controllable factor. Here, the maximum value is 0.1977. This shows that the radial depth of cut has substantial effect on the various performance characters among other milling parameters. In the table for response parameter setting, A2B3C3 showed the greatest value of GRG. Therefore, A2B3C3 is the optimal parameter combination for the end-milling process. The results clearly indicate that the optimum values are A2B3C3 as shown in Fig. 6.

6 Conclusion

This study has proposed a grey relational analysis approach to multi-objective optimization of cutting parameters. For performing the end-milling operation of Inconel 825, the most optimal conditions were found, when the speed of cutting was 55 m/min, and feed per tooth is 0.09 mm/tooth and the radial depth of cut of 1.2 mm. It can be concluded that these parameters lead to better surface roughness and maximum MRR in the machining process. However, it was observed through response table of grey relational grade that the radial depth of cut had a substantial effect on the different performance characteristics among other parameters for milling, when minimization of surface roughness and maximization of MRR are simultaneously considered.

References

1. I.A. Choudhury, M.A. El-Baradie, "Machinability of nickel-base super alloys: a general review", Journal of Materials Processing Technology vol. 77, pp. 278–284, 1998, https://doi.org/10.1016/s0924-0136(97)00429-9
2. A. Thakur, S. Gangopadhyay "State-of-the-art in surface integrity in machining of nickel-based super alloys" International Journal of Machine Tools and Manufacture Vol. 100 (January 2016) pp 25–54, https://doi.org/10.1016/j.ijmachtools.2015.10.001
3. A. Thakur, A. Mohanty, S. Gangopadhyay "Comparative study of surface integrity aspects of Incoloy 825 during machining with uncoated and CVD multilayer coated inserts" Applied Surface Science 320 (2014) 829–837, DOI: 10.1016/j. apsusc.2014.09.129
4. A. Thakur, S. Gangopadhyay, A. Mohanty "Investigation on Machinability Aspects during Dry Turning of Ni-Based Super Alloys" Materials and Manufacturing Processes (2014). https://doi.org/10.1080/10426914.2014.984216. 1.12
5. Lohithaksha M Maiyar, Dr. R. Ramanujam, K. Venkatesan, Dr. J. Jerald, Optimization of Machining Parameters for End Milling of Inconel 718 Super Alloy Using Taguchi Based Grey Relational Analysis, 2013, https://doi.org/10.1016/j.proeng. 2013.09.208
6. P.C. Jindal, A.T. Santhanam, U. Schleinkofer, A.F. Shuster, "Performance of PVD TiN, TiCN, and TiAlN coated cemented carbide tools in turning", International Journal of Refractory Metals & Hard Materials, vol. 17, pp. 163–170, 1999 https://doi.org/10.1016/s0263-4368(99)00008-6
7. M. Narasimha, R. Reiji Kumar, Achamyelehaemro Kassie, "Performance of Coated Carbide Tools", The International Journal of Engineering and Science (IJES), vol. 2 (6), pp. 47–54, 2013
8. Supriya Sahu, "Performance evaluation of uncoated and multilayer tin coated carbide tool in hard turning", Thesis, NIT Rourkela, 2012
9. M.A. Zeb, S.C. Veldhuis, M.A. Irfan, Hamid Ullah, "Comparison between PVD and CVD+ PVD coated inserts for cutting forces and tool wear during turning of ramax-2.", Journal of Engineering and Applied Sciences, Vol. 28, No.2, pp. 31–38, 2009, https://doi.org/10.1111/j.1747-1567.2007.00269.x

10. Tugce Yildiz, Alaeddin Burak Irez, Gokhan Sur, "Effect of Cementite Carbide Tool Coating Type and Tool Radius on Cutting Performance", 7th International Conference on Mechanical and Aerospace Engineering, 2016, https://doi.org/10.1109/icmae.2016.7549512
11. Deng, J.L. (1989). Introduction to Grey system. Journal of Grey System, 1: 1–24

Optimization of Machining Parameters in the Turning Operation of Inconel 825 Using Grey Relation Analysis

Hari Vasudevan, Ramesh Rajguru, Shreyans Jain, Milan Kaklotar, Jaineel Desai and Sanidhya Mathur

Abstract This study has attempted to optimize the machining parameters, when conducting the dry-turning operation of Inconel 825 work piece by utilizing two types of coated carbide inserts, such as physical vapour deposition (PVD) and chemical vapour deposition (CVD). The cutting parameters were 4 in number, namely speed of cut, rate of feed, depth of cut and coating of the tool, and the response parameters included roughness of the machined surface and the rate of material removal. Grey relation analysis coupled with Taguchi was used for optimization. The optimum cutting parameters, which resulted in the maximization of rate of material removal and efficacious finish of the surface, were cutting speed = 140 m/min, feed rate = 0.075 mm/rev and depth of cut = 0.3 mm, using CVD-coated carbide insert. However, a direct proportionality is observed between the roughness of the surface and the feed in the range of 0.075–0.15 mm/rev and has an inflated value, when using PVD-coated insert as compared to CVD-coated insert. Further, it can be noted that the material removal rate obtained is more with the CVD-coated insert as compared to PVD-coated insert.

Keywords Inconel 825 · Dry turning · Taguchi · Grey relational analysis
Surface roughness · CVD · Coated insert

1 Introduction

Machining as a part of the manufacturing processes is one of the most critical and complex amongst the operations used for the production of high-quality products. In

H. Vasudevan
D. J. Sanghvi College of Engineering, Mumbai, India
e-mail: harivasudevan@iitb.ac.in

R. Rajguru (✉) · S. Jain · M. Kaklotar · J. Desai · S. Mathur
Department of Mechanical Engineering, D. J. Sanghvi College of Engineering,
Mumbai, India
e-mail: ramesh.rajguru9@gmail.com

413

recent years, nickel-based super-alloys are being extensively used in the aerospace industries due to their resilience towards high temperature, superior ultimate tensile strength, comparatively higher yield strength, endurance towards fatigue loading due to hot hardness and superlative resistance to oxidation reactions and other damage-causing chemical attacks. Due to these properties, these materials are being extensively used in various other industries as well, such as power plants, aviation, nuclear, medical, marine engineering, pollution control system, oil and gas well piping, acid production and more [1]. However, these materials are difficult to machine and have poor machinability and cannot be machined using ordinary tools. These materials also have certain disadvantages like low thermal conductivity, which causes the heat to get concentrated at the cutting edge rather than being carried away by the chips during machining, leading to cutting-edge deformation, crater wear, tool-coating delamination and also the formation of built-up edge (BUE), which truncates the life of the tool used. In the aerospace industry, Inconel 825 is machined using various conventional machining processes, such as turning, milling and drilling to produce the required components [2]. Due to the wide-spread application of the Ni-based super-alloys and the challenges faced during its machining, machinability of these alloys has become an active topic for research. Moreover, optimization of process parameters in machining is also very important and crucial in determining the economic feasibility of manufacturing that product.

Thakur et al. [3] estimated the machinable property of Inconel 825 by performing numerous experiments under dry conditions. The experiment was performed at invariable rate of feed (0.198 mm/rev) along with the depth of cut (1 mm) with three discrete levels of cutting speed (51; 84 & 124 m/min) utilizing a coated as well as an uncoated cemented carbide(ISO P30) tool. The data extrapolated from the study implied that the surface integrity produced by the coated tool is of better quality as compared to that of the uncoated tool. The study also asserted that phenomenon such as abrasion, diffusion and adhesion was one of the major factors which contributed to the wear of the tools used while machining of Inconel 825.

Thakur et al. [4] probed several characteristics of surface integrity, during high-speed machining of Inconel 825 under dry conditions. Their study pointed out that a higher surface finish was obtained using a coated tool in comparison with that obtained with uncoated tool. In addition, the tool which was coated acted as a repelling agent for the white layer formation and served as a catalyst to reduce the work hardening of Inconel 825. Shenoy et al. [5] formulated an elaborated multi-scale model and a mathematical procedural with an aim to acquire a crystal plasticity model emanated from the microstructure of IN-100 alloy. The specimen was subjected to fatigue loading at 650 °C. Jindal et al. [6] analysed the comparative advantages of PVD TiN, TiCN and TiAlN coatings on cemented carbide substrate (WC-6 wt% Co alloy) in the turning of Inconel 718.

The grey relational analysis (GRA) being an analytical method is successfully applied already in the case of many machining processes. Chiang et al. [7] utilized the grey relational analysis method for optimization of the wire electric discharge machining process of particle-reinforced material with several performance peculiarities. Chorng-Jyh et al. [8] employed the Taguchi method with GRA to optimize sev-

Fig. 1 Methodology
followed in experimentation
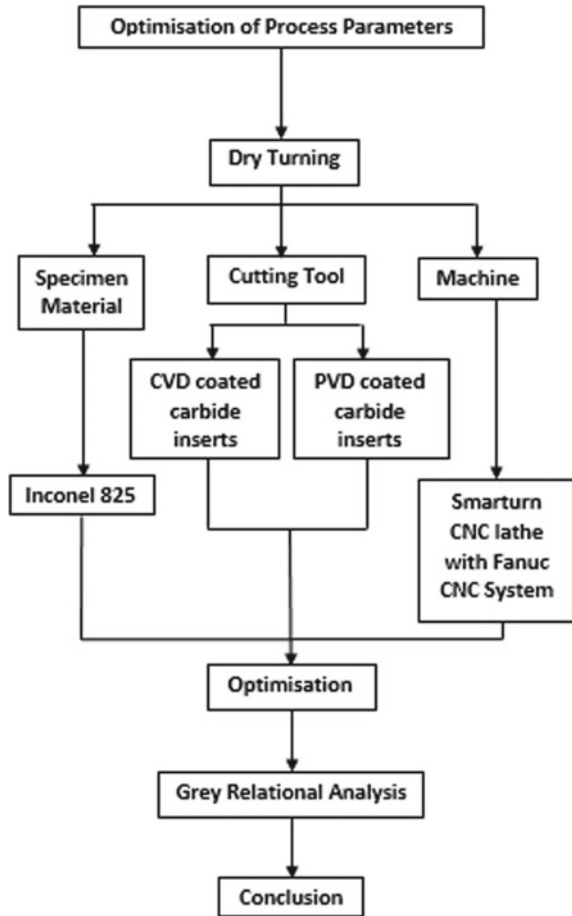
eral performance parameters during the turning operation. Hari Vasudevan et al. [9] employed the Taguchi method with GRA to optimize multiple performance parameters during the turning operation. Based on the information extrapolated from these observations, it was established that the grey relational analysis is an optimizing technique having a relatively higher degree of primacy.

2   Methodology

The methodology used in following the experiment is as depicted in the flow chart given in Fig. 1.

Table 1 Chemical composition of Inconel 825

Element	Content %
Nickel	39.95
Chromium	21.62
Molybdenum	3.16
Copper	1.68
Titanium	0.79

Table 2 Properties of Inconel 825

Property	Value
Density	8.14 mg/m^3
Melting range	1370–1400 °C
Specific heat	440 J/kg°C
Curie temperature	<-196 °C
Permeability	1.005

3 Experimental Procedure

3.1 Work Specimen

The specimen used in conducting this experiment was Inconel 825, a nickel-based super-alloy, which comprises of nickel, chromium, molybdenum, copper and titanium. Inconel 825 material specimen used for experimentation was in cylindrical bar form. The chemical composition and attributes of Inconel 825 are shown in Tables 1 and 2, respectively. For the experimental purpose, it was decided to make use of 6 cylindrical bars with the dimensions of 30 mm diameter and 70 mm length, as shown in Fig. 2.

3.2 Cutting Tool

Two types of tool inserts were utilized. The 1st insert (ISO: CNMG 12 04 08-PM 4235), which had Ti(C, N) + Al$_2$0$_3$ + TiN coating done by chemical vapour deposition (CVD) method and was Sandvik make. The 2nd insert (ISO: CNMG 12 04 08-AH 8015), which had (Al, Ti)N coating done by physical vapour deposition (PVD) method and was Tungaloy make. The tool holder material was steel (Tungaloy make) with model no. ACLNR2525M12-A and nose radius 0.0762 cm. The tool holder and carbide inserts used in the experiment are shown in Fig. 3.

Fig. 2 Specimen material
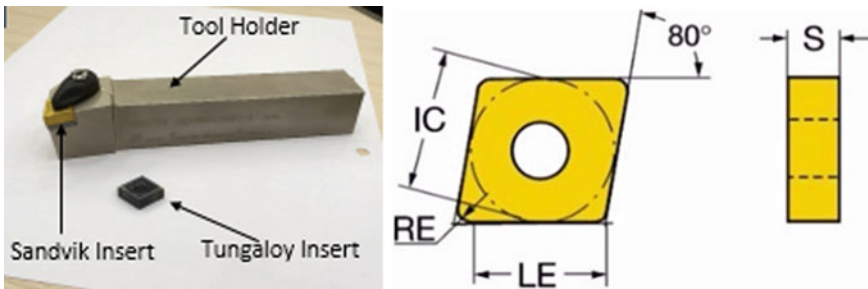
(RE = 0.7874 mm, LE = 12.09 mm, IC = 26.2 mm, S = 4.7498 mm)

Fig. 3 Tool holder and carbide insert

3.3 Research Design Variables

The input variable parameters for the experiment chosen were feed rate (mm/rev), depth of cut (mm) and cutting speed (m/min). These parameters were taken into consideration for the determination of material removal rate and surface roughness. These parameters were selected as recommended by the insert manufacturer and the extant literature surveyed during the commencement of our study. Parameters along with their respective levels are shown in Table 3.

Table 3 Input parameters

Process parameters	Levels		
	1	2	3
Cutting tool insert	PVD	CVD	–
Cutting speed (N) (m/min)	100	120	140
Feed rate (f) (mm/rev)	0.075	0.15	0.225
Depth of cut (mm)	0.3	0.6	0.9

Fig. 4 Experimental set-up

3.4 Experimental Details

The process of dry turning was done on a Smartun CNC lathe with Fanuc CNC control system. The maximum bar capacity was 42 mm. The machine spindle had a maximum speed of 4500 rpm and motor power of 5.5 kW. Two pilot readings were conducted, where the input parameters of feed rate were 0.4, 0.8, 1.2 and 0.15, 0.3, 0.45, respectively and experimental setup as shown in Fig. 4.

Since the surface roughness obtained was very poor in the two pilot readings, the parameters as arrayed in Table 3 were selected.

The surface roughness measurement of the specimens was done on a Taylor Hobson Talysurf-4 machine set-up with data acquisition by a diamond tip stylus profiler using Se-surf software. The machine along with the output graph of a specimen is shown in Fig. 5. The experimental plan and measured values of surface roughness along with the material removal rate are shown in Table 4.

Table 4 Experimental plan L_{18} OA and values of Ra and MRR

Experiment	Coded parameters				Actual parameters				Ra	MRR
	A	B	C	D	A	B	C	D		
1	1	1	1	1	PVD	100	0.075	0.3	1.0270	0.2222
2	1	1	2	2	PVD	100	0.15	0.6	1.3000	1.1667
3	1	1	3	3	PVD	100	0.225	0.9	2.1050	1.6000
4	1	2	1	1	PVD	120	0.075	0.3	0.4020	0.3333
5	1	2	2	2	PVD	120	0.15	0.6	1.0370	1.2000
6	1	2	3	3	PVD	120	0.225	0.9	2.5200	1.6000
7	1	3	1	2	PVD	140	0.075	0.3	0.3640	0.4167
8	1	3	2	3	PVD	140	0.15	0.6	1.0020	1.2000
9	1	3	3	1	PVD	140	0.225	0.9	2.4460	1.6000
10	2	1	1	3	CVD	100	0.075	0.3	1.9050	0.2353
11	2	1	2	1	CVD	100	0.15	0.6	0.9690	1.1667
12	2	1	3	2	CVD	100	0.225	0.9	1.7800	1.4000
13	2	2	1	2	CVD	120	0.075	0.3	0.5150	0.2667
14	2	2	2	3	CVD	120	0.15	0.6	0.8690	1.0000
15	2	2	3	1	CVD	120	0.225	0.9	1.2640	1.6000
16	2	3	1	3	CVD	140	0.075	0.3	0.5560	0.2222
17	2	3	2	1	CVD	140	0.15	0.6	0.6000	1.0000
18	2	3	3	2	CVD	140	0.225	0.9	0.8430	2.0000
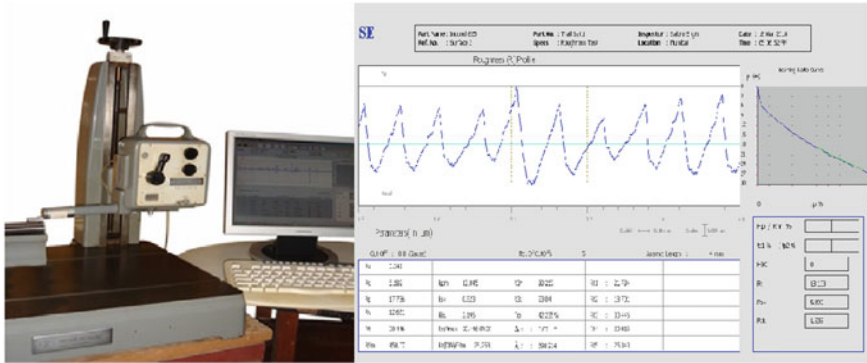
Fig. 5 Talysurf and surface roughness graph of specimen

4 Grey Relational Analysis

The grey relational analysis theory aims to handle the problems, which have poor, uncertain and insufficient information. This theory was proposed by Deng in the year 1982. Therefore, the grey relational analysis (GRA) could be effectively adopted for solving multi-objective optimization problems [10]. Three different equations are used for this normalization procedure, depending upon the type of quality characteristics. If the original sequence data have a quality characteristic as 'larger-the-better', then it is pre-processed by using the following equation.

$$x_i^*(k) = \frac{x_i^o(k) - \min x_i^o(k)}{\max x_i^o(k) - \min x_i^o(k)} \tag{1}$$

If the original data have the quality characteristic as 'smaller the better', then following equation is used.

$$x_i^*(k) = \frac{\max x_i^o(k) - x_i^o(k)}{\max x_i^o(k) - \min x_i^o(k)} \tag{2}$$

The grey relational coefficient is computed from the deviation sequence using the following relation:

$$\gamma\left(x_o^*(k), x_i^*(k)\right) = \frac{\Delta \min + \xi \Delta \max}{\Delta_{ik} + \xi \Delta \max} \tag{3}$$

$$0 < \gamma\left(x_o^*(k), x_i^*(k)\right) \leq 1 \tag{4}$$

$$\Gamma\left(x_o^*, x_i^*\right) = \sum_{k=1}^{n} W_k \gamma\left(x_o^*(k), x_i^*(k)\right); \tag{5}$$

Table 5 Grey relational coefficient and grey relational grade

Actual		Normalization		Deviation		GRC		GRG
Ra	MRR	Ra	MRR	Ra	MRR	Ra	MRR	
1.0270	0.2222	0.6924	0.0000	0.3075	1.0000	0.3274	0.6923	0.5099
1.3000	1.1667	0.5658	0.5312	0.4341	0.4687	0.2777	0.3000	0.2889
2.1050	1.6000	0.1924	0.7750	0.8075	0.2250	0.1919	0.2381	0.2150
0.4020	0.3333	0.9823	0.0624	0.0176	0.9375	0.5543	0.6000	0.5772
1.0370	1.2000	0.6878	0.5500	0.3121	0.4500	0.3253	0.2941	0.3097
2.520	1.6000	0.0000	0.7750	1.0000	0.2250	0.1655	0.2381	0.2018
0.3640	0.4167	1.0000	0.1094	0.0000	0.8906	0.5787	0.5454	0.5621
1.0020	1.2000	0.7041	0.5500	0.2959	0.4500	0.3328	0.2941	0.3135
2.4460	1.6000	0.0343	0.7750	0.9657	0.2250	0.1697	0.2381	0.2039
1.9050	0.2353	0.2852	0.0074	0.7147	0.9926	0.2079	0.6800	0.4439
0.9690	1.1667	0.7194	0.5313	0.2806	0.4687	0.3403	0.3000	0.3202
1.780	1.4000	0.3432	0.6625	0.6567	0.3375	0.2193	0.2632	0.2412
0.5150	0.2667	0.9299	0.0250	0.0700	0.9750	0.4926	0.6521	0.5724
0.8690	1.0000	0.7657	0.4375	0.2342	0.5625	0.3652	0.3333	0.3493
1.2640	1.6000	0.5825	0.7750	0.4174	0.2250	0.2834	0.2381	0.2608
0.5560	0.2222	0.9109	0.0000	0.0890	1.0000	0.4734	0.6923	0.5829
0.6000	1.0000	0.8905	0.4375	0.1094	0.5625	0.4545	0.3333	0.3939
0.8430	2.0000	0.7778	1.0000	0.2221	0.0000	0.3723	0.2000	0.2862
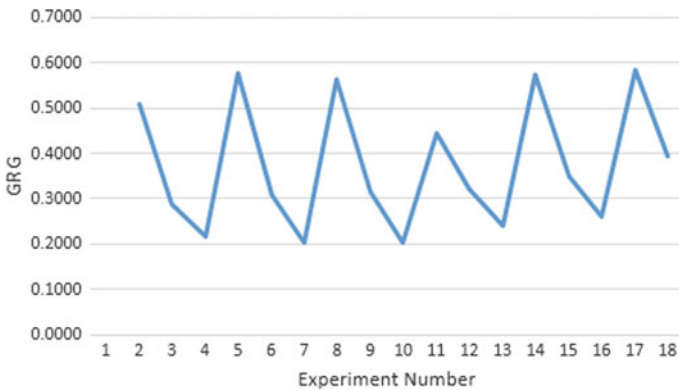
Fig. 6 Variation of GRG for the 18 experiments

Equation 1 is used for normalization of MRR, whereas Eq. 2 is used for normalization of surface roughness. Equations 3 to 5 are used to calculate grey relation coefficient and grey relation grade [10] and are recorded in Table 5. Also, variation of GRG for the 18 experiments is shown in Fig. 6.

Table 6 Response table for grey relational grade

	Level 1	Level 2	Level 3	Max–Min	Rank
A	0.3536	0.3834	–	0.0299	3
B	0.3365	0.3785	0.3904	0.0539	2
C	0.5414	0.3269	0.2348	0.3061	1
D	0.3776	0.3767	0.3511	0.0266	4

5 Results and Analyses

Calculation of optimum parameters: the grey relational grade determined for each of the sequence was considered as the response for further analysis. The larger-the-better quality characteristic was utilized for analysing the GRG, since a greater value indicated more efficient performance of the process. The grey relational grade as obtained using Eq. (5) was further analysed by using Taguchi method. As observed from the response data collected as given in Table 6, the difference between the extremities of the GRG value for dry-turning parameters was as follows: 0.0299 for the insert of the cutting tool, 0.0539 for cutting speed, 0.3061 for rate of feed and 0.0266 for depth of cut.

With the help of a comparative analysis on the data extrapolated, most significant factor influencing several performance attributes was determined. This collation would denote the level of significance of the controllable factors over several performance characteristics. The most significant controllable factor was the maximum of these values. Herein, the highest value was 0.3061, which relates to the rate of feed. This implies that the rate of feed has the most influence on several performance characteristics out of the other parameters involved in dry turning. As observed from the response (Table 6), parameter-setting A2B3C1D1 indicates the highest value of GRG. Therefore, A2B3C1D1 is the condition for the optimal parameter combination of the dry-turning process. The results clearly indicate that the optimum values are A2B3C1D1, as shown in Fig. 7.

From the variance in the roughness of the surface and MRR with respect to the rate of feed as shown in Fig. 8, it can be seen that the surface roughness is directly proportional to the feed in the range of 0.075–0.15 mm/rev and has a higher value, when using PVD-coated insert as compared to CVD-coated insert. Further, it can be noted that the MRR obtained is more with the CVD-coated insert as compared to the PVD-coated insert.

6 Conclusion

A grey relational analysis approach to multi-objective optimization of machining parameters was proposed and experimented as part of the study. For performing the dry turning of Inconel 825, the most optimal conditions were found, when a

Main Effects Plot for Means
Data Means
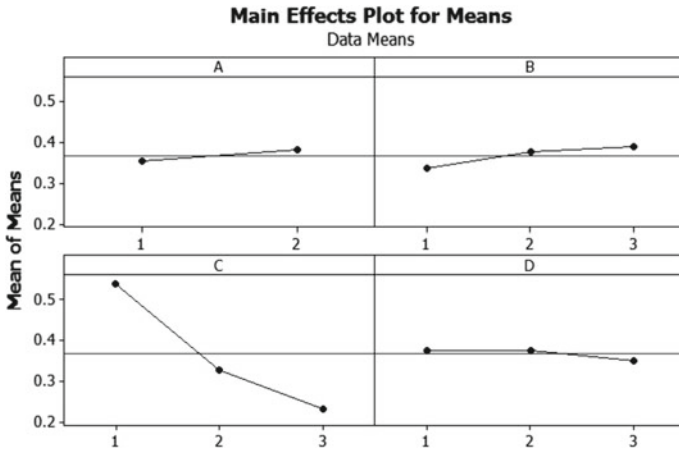
Fig. 7 Main effects plot of GRG
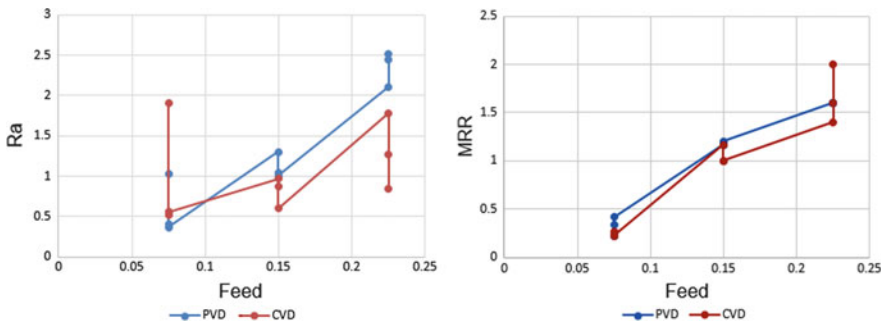
Fig. 8 Variation of Ra and MRR with respect to feed rate

cutting speed of 140 m/min, a feed rate of 0.075 mm/rev and depth of cut of 0.3 mm were set and when using the CVD-coated carbide insert. Also, the CVD-coated insert provided better surface finish and metal removal rate as compared to the PVD-coated carbide inserts. However, the observations of the response table of grey relational grade suggest that the rate of feed is the most prominent factor which affects the multiple performance characteristics.

References

1. S. K. Tamang, M. Chandrasekaran, "Integrated optimization methodology for intelligent machining of Inconel 825 and its shopfloor application" J Braz. Soc. Mech. Sci. Eng.
2. Thakur, S. Gangopadhyay "State-of-the-art in surface integrity in machining of nickel-based super alloys" International Journal of Machine Tools and Manufacture Vol. 100 pp 25–54.
3. A. Thakur, S. Gangopadhyay, A. Mohanty "Investigation on Machinability Aspects during Dry Turning of Ni-Based Super Alloys" Materials and Manufacturing Processes. https://doi.org/10.1080/10426914.2014.984216.1.
4. A Thakur, S Gangopadhyay, K.P. Maity "Effect of Cutting Speed and Tool Coating on Machined Surface Integrity of Ni-based Super Alloy" Procedia CIRP 2014.
5. Mahesh Shenoy, Yustianto Tjiptowidjojo, David McDowell "Microstructure-sensitive modeling of polycrystalline IN 100" International Journal of Plasticity 2008.
6. P.C Jindal, T Santhanam, U Schleinkofer, A.F Shuster "Performance of PVD TiN, TiCN, and TiAlN coated cemented carbide tools in turning" International Journal of Refractory Metals and Hard Materials.
7. Chiang, K.T. and Chang, F.P. "Optimization of WEDM Process of Particle Reinforced Material with Multiply Performance Characteristics using Grey Relational Analysis" Journal of Materials Processing Technology, 180: 96–101.
8. Chorng-Jyh, T., Yu-Hsin, L., Yung-Kuang, Y. and Ming-Chang, J. "Optimization of Turning Operations with Multiple Performance Characteristics using the Taguchi Method and Grey Relational Analysis" Journal of Materials Processing Technology, 209: 2753–2759.
9. Hari Vasudevan, Ramesh Rajguru, Naresh Deshpande, Sandip Mane, "Experimental investigation and Optimization of milling parameters in the machining of NEMA G11 GFRP Composite Material using PCD Tool" All India Manufacturing Technology, Design and Research Conference (AIMTDR) IIT Guwahati.
10. Deng, J.L. (1989). Introduction to Grey system. Journal of Grey System, 1: 1–24.

A Review and Analysis of the Machining Process Involving Nickel-Based Super Alloy

Ramesh Rajguru and Hari Vasudevan

Abstract This article involves a review and analysis of the current study and progress work in the machining of the nickel-based super alloy. The review focuses on producing a perception into the machining of nickel-based super alloy and points out higher capability for further explorations and alterations in the field of nickel-based super alloy. Machining is one of the most crucial and vastly used manufacturing processes. Of late, due to entanglement and unreliability of the machining processes, soft computing techniques are being deployed to create physics-based models for forecasting the performance of the machining processes and optimizing them. The proposed hypothesized work is aimed at the investigation of the relationship between input cutting parameters and tool geometry parameters like feed per tooth, cutting speed, radial depth of cut, and various key aspects of surface integrity, such as residual stress, micro-hardness, and surface roughness, while end milling of Inconel 625, nickel-based super alloy.

Keywords Inconel 625 · Difficult to cut material · End milling · Surface integrity
Residual stresses and micro-hardness

1 Introduction

Ni-based super alloy is an uncommon class of metallic materials with an excellent blend of greater thermal strength, toughness, and resistance to deterioration in an acidic environment. Applications and use of many such uncommon materials lead us to critical areas in manufacturing operations such as machining. With the progress in

R. Rajguru (✉)
Department of Mechanical Engineering, D. J. Sanghvi College of Engineering,
Mumbai, India
e-mail: ramesh.rajguru@djsce.ac.in

H. Vasudevan
D. J. Sanghvi College of Engineering, Mumbai, India
e-mail: harivasudevan@iitb.ac.in

the technology of aero engines, many difficult to machine materials such as Inconel 625 are being used broadly in the manufacturing of new engines, besides its enormous uses in aerospace, aircraft, marine, chemical and oil and petrochemical industries [1, 2]. In the context of its wide range of applications, there is a need for efficiently processing better methods in the manufacturing of such difficult to cut materials [1]. Therefore, this study is an attempt to review and accordingly analyze various key aspects of the machining process, involving nickel-based super alloys. The study consisting of review of extant literature and analyses also proposes few hypotheses that are set to be tested in the future.

2   Literature Survey and Problem Identification

This study reviews the machinability aspects of Ni-based super alloy during various machining processes, such as milling and turning. It throws light on the progress achieved so far, in the area of machining of the alloy and in this section the issues that are required to be addressed are discussed. Cai et al. [3] investigated the surface integrity behaviors of Inconel 718 with cutting parameters. The tool used for performing the desired operation was solid-coated carbide end mill cutters. They found that, at a higher cutting speed high residual tensile stresses come out in both directions and further as the cutting speed increases residual stresses also increases speedily.

Thakur et al. [4] reviewed the state of the art in machining on the surface integrity of machining of difficult to machine material such as Inconel 718. They reviewed and identified different surface defects, surface hardness, microstructure alteration, formation of the white layer, residual stresses, and work hardening layers as being key surface integrity problems to get better surface qualities of the finish products. Nath et al. [5] investigated on the machinability of 3 hard and advanced alloys, such as stainless steel 403 cb+, Inconel 718, and Inconel 625. Their study covered in terms of cutting forces, force coefficients, material removal rate, and tool life during face milling with indexable round milling inserts to optimize cutting variables for minimum machining cost, considering trade-off between MRR and tool life for each alloy. Experiments were performed on full factorial design, considering different combination of feed rate and cutting speed. The results revealed that, among 3 alloys, machinability of Inconel 625 was the poorest followed by Inconel 718.

Waseem et al. [6] conducted an experiment in the case of super alloy GH4169/Inconel 718 material, using two coated inserts. Surface roughness, microhardness, and residual stresses were the three important aspects of surface integrity that were considered as response parameters. The results revealed that all the three machining parameters were found to have significant effect on the surface integrity of machined components. Further, as compared to ceramic inserts, carbide inserts produced superior surface integrity of the machined components. Cai et al. [7] experimentally investigated surface integrity of nickel-based super alloy Inconel 718 by end milling process using cutting speed and feed as input parameters. They con-

cluded that the feed rate and cutting speed significantly affect the surface roughness and surface topography. Therefore, it is hypothesized that:

H1: *It is possible to achieve desirable residual stress and a significant positive effect on micro-hardness of top surface layer by selecting proper process parameters during milling of nickel-based super alloy.*

Sonawane et al. [8] investigated the surface integrity aspects using cutting parameters during ball end milling on nickel-based super alloy Inconel 718. The study pointed out that the poorest surface finish of 3 μm was obtained and best surface finish of 0.2 μm was reported in the stable cutting zone. Patel Jaymin et al. [9] investigated the effect of process parameters, such as cutting speed, feed rate, and constant depth of cut at 0.5 mm with cutting conditions (dry and MQL) on cutting force, surface roughness, and tool wear. Cutting tool was carbide insert with TiAlN coating. They reported that the most optimal condition for performing the milling operation was having a cutting speed of 45 m/min, feed rate of 0.05 mm per tooth, and cutting condition of 20 ml/hr.

Wang et al. [10] performed an end milling experiment on Inconel 718 to study the influence of machining conditions on surface finish using a solid carbide end mill cutter and the best possible blend of the cutting parameters for the preferred surface finish. The optimization technique used was Taguchi Design of Experiments. Feed rate, cutting speed, axial depth of cut, and radial depth of cut were the input parameters. According to the reported S/N ratios, the best possible blend of cutting parameters for the best surface roughness was A4 B1 C1 D1(cutting speed 50 m/min, feed per tooth 0.05 mm/tooth, axial depth of cut 0.8 mm, and radial depth of cut 0.6 mm). Finally, the verification tests indicated that there is a good harmony between the predictive results and the experimental measurements. In view of this, it is hypothesized as:

H2: *It is possible to achieve desirable surface finish by selection of proper process parameters in the machining of Nickel-Based Super Alloy.*

Kasim et al. [11] investigated as to how the HSM (high-speed milling) of nickel-based super alloy Inconel 718 with ball nose end mill could enhance the yield and superiority of the finish parts. The tool used was tungsten carbide with TiAlN PVD coating and cutting speed, depth of cut, feed rate, and width of the cut were the input parameters. They employed the response surface methodology (RSM) as an optimization technique to gain maximum productivity and 60 min of tool life, along with least amount of cutting force and superior surface finish. Pawade et al. [12] conducted turning experiment on Inconel 718, using polycrystalline cubic boron nitride (PCBN) cutting tools to optimize the cutting force and surface roughness, considering cutting parameters along with tool cutting edge geometry. They concluded that the effect of depth of cut and feed rate in a variation of cutting force were affected more as compared to the cutting speed.

Kushwala et al. [13] investigated on the effect of machining conditions and turning process parameters, such as dry and wet machining during CNC turning operations

on Inconel 625, using PVD-coated carbide tool (TiAlN/TiN). Independent variables were cutting speed, feed rate, and depth of cut, and the performance of the operation was measured in the case of both the surface roughness and material removal rate (MRR). They found that the wet turning produced superior surface roughness as compared to dry machining. Jawaid et al. [14] studied the wear behavior of PVD- and CVD-coated carbide tools, during milling operation Inconel 718, using cutting speed and feed rate as the variable input parameters, whereas the depth of cut was the constant input parameter. They concluded that the CVD-coated tool outperformed the PVD-coated tool.

Zhuan et al. [15] experimentally investigated on the wear mechanism of alumina-based ceramic cutting tools during dry turning of Inconel 718 with cutting depth as the varying parameter, whereas feed rate and cutting speed were the constant parameters. Alauddinet et al. [16] studied the tool deterioration in the end milling of Inconel 718 using uncoated tungsten carbide inserts under dry conditions using cutting time, cutting speed, and feed as constant parameters and performing up-milling and down-milling either with a full immersion or half immersion. They found that full immersion end milling increased the tool life, as compared to half immersion end milling and better tool life in down-milling as compared to up-milling.

Schorník et al. [17] examined the influence of the work conditions and machining environment on tool wear in the machining of nickel-based super alloys, using cutting speed as the variable input parameter, whereas the constant input parameters were coolant pressure of 40 bar and time of cut of 12.8 min. The result concluded that, the lowest tool wear is achieved at 0.21 mm/min and 30 m/min feed rate and cutting speed, respectively. But for higher productivity, best cutting conditions were feed rate and cutting speed at 0.4 mm/min & 30 m/min, respectively.

Alauddinet et al. [18] developed a numerical model for cutting force under dry cutting conditions during end milling operations on Inconel 718, using uncoated carbide inserts. Feed rate, cutting speed, and axial depth of cut were the input parameters, and optimization technique used was RSM.

Suresh Kumar Reddy et al. [19] developed a genetic algorithm (GA) optimization approach for optimization of the surface roughness prediction model in dry milling, using speed, feed, radial rake angle, and nose radius (all with 3 levels: low, medium, and high] as the variable input parameters. The optimization techniques used were RSM for building the mathematical model and genetic algorithm optimization technique. They concluded that the dry machining is possible by proper selection of cutting tools and tool geometry, hence making the machining environmentally friendly. Hence, it is hypothesized as:

H3: *Response Surface Methodology approach successfully models the process for prediction residual stress and surface roughness.*

Kondayya et al. [20] developed modeling and optimization of the CNC end milling process using spindle speed, feed, and axial depth of cut as the variable input parameters. The optimization techniques used were genetic programming (GP) and GA. They concluded that the MRR and tool wear are important machining performance

measures, which directly influence the productivity and accuracy of the process. Marimuthu et al. [21] developed a mathematical model to optimize the cutting parameters for achieving high quality and high production rate in the turning operation of lnconel 625, using TiAlN-coated cutting tool under dry conditions. The optimization technique used was Taguchi Design of Experiments. Feed rate, cutting speed, and axial depth of cut were the input parameters. It was observed that the feed and the cutting speed were important cutting parameters for affecting the surface roughness and the feed and depth of cut were the significant cutting parameters for affecting the material removal rate.

Guo et al. [22] reviewed surface integrity characterization and prediction in the machining of hardened steels, titanium and nickel-based super alloys. They presented multi-scale simulation models for predicting residual stresses in the machining of the super alloy. Kanta et al. [23] developed a predictive and optimization model of an artificial neural network (ANN) technique coupled with genetic algorithm in predicting the optimal value of machining parameters, leading to minimum surface roughness. They found and reported excellent harmony between the predicted values and experimental values.

Zain et al. [24] developed an ANN predictive model for surface roughness during dry end milling operation, using cutting parameters, such as cutting speed, feed rate (mm/tooth), and radial rake angle as tool geometry parameters. They found that ANN structure 3-1-1 predict the best performance for surface roughness. Pohokar et al. [25] employed an ANN model for optimization of geometric and cutting parameters in the tool life analysis. The experiments were conducted on AISI 1040 material with cutting speed, depth of cut, feed rate, and rake angle as cutting parameters. ANN shows an excellent performance for tool life analysis. Jenarthanan et al. [26] conducted end milling operations on GFRP and developed RSM and ANN models for the prediction of surface roughness. The experiments were conducted with four independent variables, namely cutting speed, fiber orientation angle, depth of cut, and feed rate. They found that the ANN model is much more robust and accurate than RSM for predicting the surface roughness response value.

Ayket et al. [27] created an ANN model for the prediction of surface roughness of Al 2024, Al7075, AISI 1040, and AISI 4140 workpiece materials during turning operation. They selected five input parameters for the model, such as the cutting depth, tool overhand length, the number of revolutions, workpiece diameter, and side cutting angle and the conducted experiments were based on Taguchi orthogonal array. ANN results were used to predict the surface roughness in machining operations effectively. Razfar et al. [28] carried out experimental investigations on the face milling process of X20Cr13 stainless steel. Apart from the depth of cut, feed per tooth, and cutting speed, they included the percentage of cutter meeting as independent variables. They developed an ANN model to provide reliably, successfully, and accurately the surface roughness of stainless steel. It can be concluded that the artificial neural network has been widely used in the predictive modeling of manufacturing processes. Therefore, it is hypothesized as:

H4: *It is possible to model the milling process parameters for prediction of residual stress, surface roughness and micro-hardness using an Artificial Neural Network modeling approach.*

3 Importance of the Study

1. Although considerable work on machining of nickel-based alloy Inconel 718 has been investigated, similar work on different other grades is relatively limited and is not reported in the literature. It is known that the machining characteristics of a particular workpiece material depend primarily on its composition, microstructure, and thermo-mechanical properties. Therefore, it is also important to evaluate the machinability characteristics of other grades with prominent engineering applications. Machinability aspects of Inconel 625 with a sizable distinction in chemical and mechanical properties from other grades are so far unidentified.
2. Numerous studies had been carried out on nickel-based super alloy for exploring various aspects of machinability, but so far, very few studies have been carried out on Inconel 625.
3. No effort has so far been made to predict surface roughness, micro-hardness, and residual stress during milling of nickel-based super alloy Inconel 625 by researchers.
4. Predictive modeling is helpful in the selection of various process parameters to achieve the desired values for surface roughness and residual stress.
5. The relationship between input variable such as cutting speed, radial depth of cut, and axial feed and surface integrity parameters like residual stress, micro-hardness, and microstructure is not well established and there is a lot of scope for developing reliable models to establish their relationships.

4 Proposed Work and Scope of the Study

The proposed work consists of:

1. Investigation of the effect of cutting parameters on surface integrity during milling of Inconel 625.
2. Development of process models for surface integrity aspects, like residual stress and surface roughness.
3. Multi-objective optimization for getting the optimum setting of the process parameters, so as to attain minimum tensile residual stress and surface roughness.
4. The scope of the proposed work is limited to experimental investigation and modeling for surface integrity aspects like residual stress, surface roughness, and micro-hardness, while milling of nickel-based super alloy Inconel 625.

5   Conclusion

Nickel-based super alloys among the high-temperature alloys are extensively used in aircraft engine components and in industrial gas turbine components for power generation. One of the major concerns related to the machining of nickel-based super alloy is surface integrity, since it directly affects the performance of the machined component during its intended application. Numerous studies have been carried out on nickel-based super alloy Inconel 718 for various aspects of machinability, but so far no effort has been made to predict the residual stress, surface roughness, and micro-hardness during milling of nickel-based super alloy Inconel 625 by the researchers. Hence, the proposed hypothesized work is aimed at the investigation of the relationship between input cutting parameters and surface integrity aspects, while milling of nickel-based super alloy Inconel 625.

References

1. T.M. Pollock, S. Tin, "Nickel based superalloys for advanced turbine engines: chemistry microstructures and properties" Journal of Propulsion & power 22(2) (2006) 361–374.
2. Ravindra I. Badiger S. Narendranatha, M.S. Srinath "Joining of Inconel-625 alloy through microwave hybrid heating and its characterization" Journal of Manufacturing Processes 18 (2015) 117–123.
3. Xiaojiang Cai, Sheng Qin, Junli Li, Qinglong An & Ming Chen, "Experimental investigation on surface integrity of end milling nickel-based alloy - Inconel 718" Machining Science and Technology: An international Journal https://doi.org/10.1080/10910344.2014.863627.
4. A. Thakur, S. Gangopadhyay "State-of-the-art in surface integrity in machining of nickel-based super alloys" International Journal of Machine Tools and Manufacture Vol. 100 (January 2016) pp 25–54.
5. Chandra Nath, Zachary Brooks and Thomas R. Kurfess " On Machinability Study and Process Optimization in Face Milling of stone Alloys with Indexable Copy Face Mill Insrts" Procedia Manufacturing Volume 1, 2015, Pages 487–500.
6. Waseem Akhtar, Jianfei Sun & Wuyi Chen (2014): "Effect of Machining Parameters on Surface Integrity in High-Speed Milling of Super Alloy GH4169/Inconel 718", Materials and Manufacturing Processes, https://doi.org/10.1080/10426914.2014.994769.
7. Xiaojiang Cai, Sheng Qin, Qinglong An, and Ming Chen, "Experimental investigation on surface integrity of end milling nickel-based alloy-Inconel 718" Advanced Materials Research Vol. 500 (2012) pp 51–57.
8. Harshad A. Sonawane, Suhas S. Joshi "Analysis of machined surface quality in a single-pass of ball-end milling on Inconel 718" Journal of Manufacturing Processes 14 (2012) 257–268.
9. Patel Jaymin K., Geet V. Raval & Kuppan P. " Study of cutting forces, surface roughness and tool wear on end milling of inconel 625 in DRY and MQL conditions" Proceeding of 6th international and 27th all India Manufacturing Technology, Design and Research Conference (AIMTDR-2016).
10. Yuanwei Wang, Song Zhang, Jianfeng Li and Tongchao Ding, "Optimal cutting parameters for desired surface roughness in end milling Inconel 718" Advanced Materials Research Vols 126–128 (2010) pp 911-916.
11. M. S. Kasim, C. H. CheHaron, J. A. Ghani, E. Mohamad, R. Izamshah, M. A. Md. Ali, J. B. Saedon, "Multi-objective Optimization using Box-Behken of Response Surface Methodology

for High-Speed Machining of Inconel 718" Applied Mechanics and Materials Vol. 629 (2014) pp 487–492.

12. R.S. Pawade, Harshad A. Sonawane, Suhas S. Joshi "An analytical model to predict specific shear energy in high-speed turning of Inconel 718" International Journal of Machine Tools & Manufacture 49 (2009) 979–990.

13. Abhishek Kushwaha, Ramandeep Singh, "Optimization of CNC process parameters on Inconel 625 using response surface methodology" International Journal of Mechanical Engineering and Technology (IJMET) Volume 8, Issue 7, July 2017, pp. 1830–1836, Article ID: IJMET_08_07_203.

14. A. Jawaid, S. Koksal& S. Sharif, "Wear Behavior of PVD and CVD Coated Carbide Toolswhen Face Milling Inconel 718" Tribology Transactions https://doi.org/10.1080/10402000008982347.

15. Kejia Zhuang, Dahu Zhu, Xiaoming Zhang, Han Ding, "Notch wear prediction model in turning of Inconel 718 with ceramic tools considering the influence of work hardened layer" Wear 313 (2014) 63–74.

16. M. Alauddin, M.A. El Baradie, M.S.J. Hashmi, "Tool-life testing in the end milling of Inconel 718" Journal of Materials Processing Technology 55 (1995) 321–330.

17. VáclavSchorník, MiroslavZetek, Milan Daňa, "The Influence of Working Environment and Cutting Conditions on Milling Nickel – Based Super Alloys with Carbide Tools" Procedia Engineering 100 (2015) 1262–1269.

18. M. Alauddin, M.A. El Baradie and M.S.J. Hashmi, "Modelling of cutting force in end milling Inconel 718" Journal of Materials Processing Technology 58 (1996) 100–108.

19. N. Suresh Kumar Reddy & P. Venkateswara Rao, "A genetic algorithmic approach for optimization of surface roughness prediction model in dry milling" Machining Science and Technology: An International Journal https://doi.org/10.1081/mst-200051263.

20. D. Kondayya& A. Gopala Krishna, "An integrated evolutionary approach for modeling and optimization of CNC end milling process" International Journal of Computer Integrated Manufacturing https://doi.org/10.1080/0951192x.2012.684718.

21. P. Marimuthu and R. Baskaran, "Optimal setting of machining parameters for turning Inconel 625 using coated tool, Optimization of cutting parameter for the achievement of high quality and high rate of production" Applied Mechanics and Materials Vol. 573 (2014) pp 632–637.

22. Y. B. Guo, W. Li, and I. S. Jawahir "surface integrity characterization and prediction in machining of hardened and difficult-to-machine alloys: a state-of-art research review and analysis" Machining Science and Technology, 13:437–470 https://doi.org/10.1080/10910340903454922.

23. Girish Kanta, Kuldip Singh Sangwan "Predictive Modelling and Optimization of Machining Parameters to Minimize Surface Roughness using Artificial Neural Network Coupled with Genetic Algorithm" Procedia CIRP 31 (2015) 453 – 458.

24. Azlan Mohd Zain, Habibollah Haron, Safian Sharif "Prediction of surface roughness in the end milling machining using Artificial Neural Network" Expert Systems with Applications 37 (2010) 1755–1768.

25. Nilesh Pohokar, Lalit Bhuyar et al. "Neural Networks Based Approach for Machining and Geometric Parameters optimization of a CNC End Milling" IJIRSETVol. 3, Issue 2, February 2014.

26. M.P. Jenarthanan A. Ajay Subramanian R. Jeyapaul, "Comparative analysis of surface roughness prediction using DOE and ANN techniques during end milling of glass fibre reinforced polymer (GFRP) composites", Pigment & Resin Technology, Vol. 45 Iss 2 pp. 126–139.

27. R. Aykut Arapoglu, Mehmet Alper Sofuoglu, Sezan Orak "An ANN-Based Method to Predict Surface Roughness in Turning Operations" Arab J Sci Eng https://doi.org/10.1007/s13369-016-2385-y.

28. Mohammad Reza Razfar, Reza Farshbaf Zinati, Mahdiar Haghshenas et al. (2011) "Optimum surface roughness prediction in face milling by using neural network and harmony search algorithm" Int J Adv Manuf Technol (2011) 52:487–495 https://doi.org/10.1007/s00170-010-2757-5.

Part III
Manufacturing

Minimization of Shrinkage Porosity in HPDC Process with Local Squeeze Pin Using Flow Simulation

Shivkumar Biradar and Prashant T. Borlepwar

Abstract In high-pressure die-casting process, molten metal is forced under high pressure into a mold cavity; the most commonly used metals are alloys of aluminum, zinc, magnesium, and copper–brass. Nowadays, squeeze pin application is one of the popular ways of reducing the shrinkage porosity in high-pressure die-casting components. Squeeze pins can be used to compensate for shrinkage defects in these components. The main reason for the formation of shrinkage porosity at the critical location of given component is large and poorly fed hot spot. In this paper shrinkage porosity of casting reduced from level III to level I by determining optimum values squeeze pin parameters by DOE and flow simulation, obtained results are implemented in order to test and verify effectiveness of the method. An excellent agreement is indicated for the simulation result and the experimental results.

Keywords Local squeeze pin · Flow simulation · HPDC process Shrinkage porosity

1 Introduction

High-pressure die-casting (HPDC) process has been widely used to manufacture a large variety of products with high dimensional accuracy and productivity; also, it is an economical and efficient method for producing components with low surface roughness. The control over solidification process is very essential to get reproducible and isotropic properties of casting components in modern casting technology. Nevertheless, the prediction of the characteristics of the structure is difficult, because these are determined by intricate solidification processes. Aluminum alloy castings usually form a mashy zone during solidification; therefore, it is probable that shrink-

S. Biradar (✉) · P. T. Borlepwar
Department of Mechanical Engineering, Maharashtra Institute of Technology, Aurangabad, Maharashtra, India
e-mail: biradarscb@gmail.com

age porosity is developed in the casting which affects the fatigue strength [1] and fatigue behavior [2] of casting.

Anglada et al. [3] developed a pseudo-2D model to reproduce the thermal behavior of the mold and of the cast part appropriately, by reducing the calculation time over detailed 3D simulation model. Hu et al. [4] proposed a cellular automata (CA) technique utilizing back-propagation neural network (BPNN) to establish the relations between porosity and solidification parameters. Singh et al. [5] detected mathematical model, which applies a joint structure such as neural synapses for information processing. Ghosh et al. [6] observed that the BPNN model has nearly precise predictive potential to characterize porosity defect.

Ashiri et al. [7] observed thin grain morphology having 3 small dendrite arm spacing for high injection pressure in HPDC process. Adamane et al. [8] reviewed the effect of injection parameters in HPDC process, specially the injection pressure and gate velocity on the porosity and tensile properties of Al–Si alloys. Bodhayana et al. [9] investigated on the importance of integration of design and analysis which yields to better results. Swamy et al. [10] observed that shrinkage and gas porosities found in front axle are because of flawed gating system. Ling et al. [11] derived the boundary criterion by using the principle of minimum potential energy. This model is useful for casting solidification simulation and shrinkage defects prediction.

Yue et al. [12] developed a primary expert system which reduces time for die design and manufacture and results in the production of high-quality die castings in a shorter time. Kwon et al. [13] performed a CAE simulation on (AnyCasting) which is CFD software to optimize the gate and runner design of an HPDC component. By using solidification analysis, internal porosities caused by the solidification shrinkage were also predicted. Apparao et al. [14] conceptualized Taguchi approach to obtain optimal settings of the die-casting parameters. Hu et al. [15] used a numerical simulation technique for optimization of the runner and gating systems for the hot chamber die casting of a component which has thin-wall thickness. Two types of runner and gating systems were numerically analyzed. Vispute et al. [16] designed casting dies using process parameter inputs from the flow simulation. This analysis highlights the critical areas in the component geometry and the locations where the process defect is likely to occur.

However in many of these works, the geometry of the part is simple and there are few researches on very complex part in industry also most of them propose model to predict shrinkage porosity in casting process. The aim of this work is to propose solution to shrinkage porosity in complex die-casting component by finding optimum value of process parameters of squeeze pin by using flow simulation.

2   Problem Definition

The HPDC component oil pump casing as shown in Fig. 1 has complex shape; it includes irregular outer profile with varied height. The inside area of casing is filled with oil at high pressure. The quality requirement in the highlighted area of
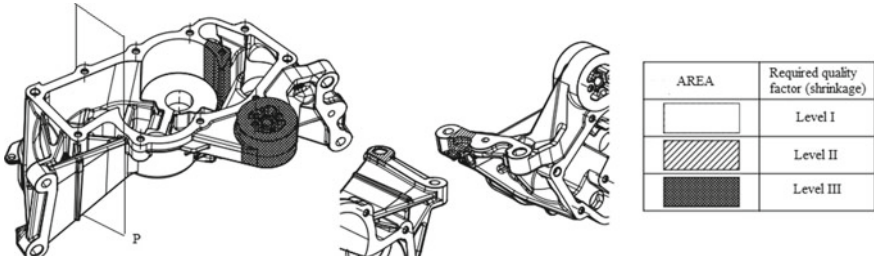
Fig. 1 Component area and quality requirement for shrinkage as per ASTM-E505

Fig. 2 Component section at plane-P with maximum wall thickness in thick mass zone
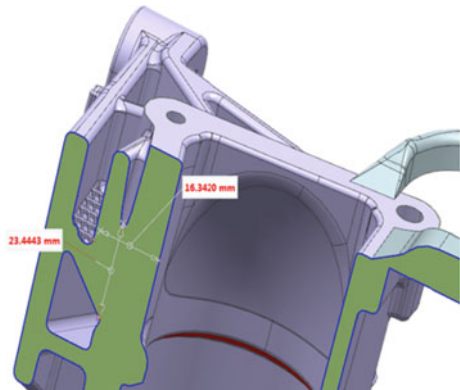
component is shown in Fig. 1, except some area component which requires level I in shrinkage porosity.

The 3D model of component is created, and then, the 3D model of the fix and moving insert is created with considering machining allowance, shrinkage and draft by using the NX11 CAD software. Figure 2 shows maximum wall thickness 23.44 and 16.34 mm observed at plane-P; this generates hottest spot in the casting which solidifies at last point and generates shrinkage porosity due to volumetric contraction.

3 Methodology

To minimize shrinkage porosity at thick mass zone, local squeeze pin is added on the wall of machining face near thick mass zone, which remains at bottom position during start of cycle, and at this position, molten metal moves from die to sleeve and after actuation of hydraulic cylinder which is connected to squeeze pin locally pressurizes the molten metal into a cavity of a metal mold to compensate for shrinkage defects in casting. Figure 3 shows working of local squeeze pin.
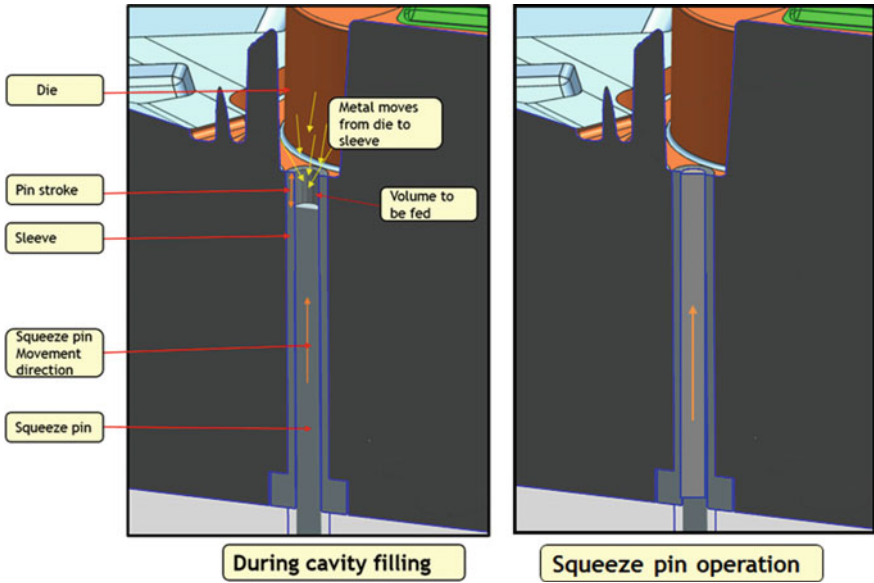
Fig. 3 Working of local squeeze pin during cavity filling and during operation

Table 1 Material property and initial and boundary conditions

Initial boundary condition	Value	Material property	Value
Ram velocity	2–4 m/s	Solidus temperature	595 °C
Die temperature	200 °C	Liquidus temperature	521 °C
Melt temperature	680 °C	Specific heat	1.13044 kJ/kg/K
Heat transfer coefficient	9000 w/m^2 K	density	2480 kg/m^3
Number of mesh elements	572,362 (obtained during meshing)	conductivity	100.4832 kJ/kg/K
		Latent heat	218.644 kJ/kg

3.1 Determination of Fixed Parameters

A 3-dimensional model of the component with runner and gate is an important input for analysis functions in ProCAST and imported in Parasolid format. The material properties and initial boundary conditions input parameters to ProCAST based on PQ2 calculations are shown in Table 1.

Table 2 Variable parameters

Variable parameters	Range due to design constrains
Squeeze pin diameter	5–9 mm (product geometry)
Squeeze pin stroke	10–20 mm (die design constrain)
Pressure to be applied	25–30–35 bar (compact cylinder capacity)
Time of squeeze pin actuation	Time between gate solidification and before component solidification App (2.46–3.22 s)

Table 3 Experiment 1

S. No.	Squeeze pin diameter (mm)	Squeeze pin stroke (mm)	Pressure to be applied (bar)	Time of squeeze pin actuation (sec)
1	5	15	30	3
2	6	15	30	3
3	7	15	30	3
4	8	15	30	3
5	9	15	30	3

Table Table 4 Experiment 2

S. No.	Squeeze pin diameter (mm)	Squeeze pin stroke (mm)	Pressure to be applied (bar)	Time of squeeze pin actuation (sec)
1	7	10	30	3
2	7	12.5	30	3
3	7	15	30	3
4	7	17.5	30	3
5	7	20	30	3

3.2 Determination of Variable Parameters

To determining optimum values, squeeze pin parameters by DOE and flow simulation range of variable parameter are fixed as per die design constrains. Table 2 shows variable parameters.

3.3 Design of Experiments

Following experiments designed to determine optimum value of squeeze pin diameter, squeeze pin stroke, pressure to be applied, and time of squeeze pin actuation; for this, each parameter is varied in equal interval in each experiment. Tables 3, 4, 5, and 6 show experiment 1 to experiment 4.

Table 5 Experiment 3

S. No.	Squeeze pin diameter (mm)	Squeeze pin stroke (mm)	Pressure to be applied (bar)	Time of squeeze pin actuation (sec)
1	7	15	25	3
2	7	15	30	3
3	7	15	35	3

Table Table 6 Experiment 4

S. No.	Squeeze pin diameter (mm)	Squeeze pin stroke (mm)	Pressure to be applied (bar)	Time of squeeze pin actuation (sec)
1	7	15	30	2.46
2	7	15	30	2.65
3	7	15	30	2.84
4	7	15	30	3.03
5	7	15	30	3.22
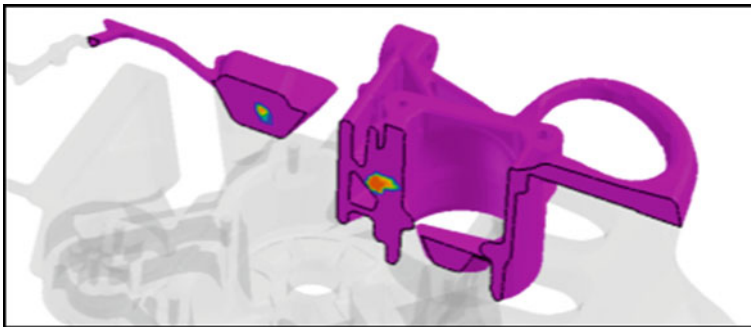
Fig. 4 Section of solid fraction result at plane-P red color shows shrinkage porosity

3.4 Flow Simulation

The simulations were conducted as per DOE on the software ProCAST. To determine shrinkage porosity, this software solves the conservation equations using the finite element method. The component geometry is meshed by dividing into fine tetrahedral volume elements. The conservation equations are solved at each volume element level. Fraction solid results are analyzed to determine the volume of shrinkage porosity. Fraction solid is the percentage of solid phases formed at any point in time during the solidification. ProCAST simulation model uses fraction solid curve to predict shrinkage porosity formation in examined aluminum alloy. Figure 4 shows fraction solid result in which red color shows shrinkage porosity.
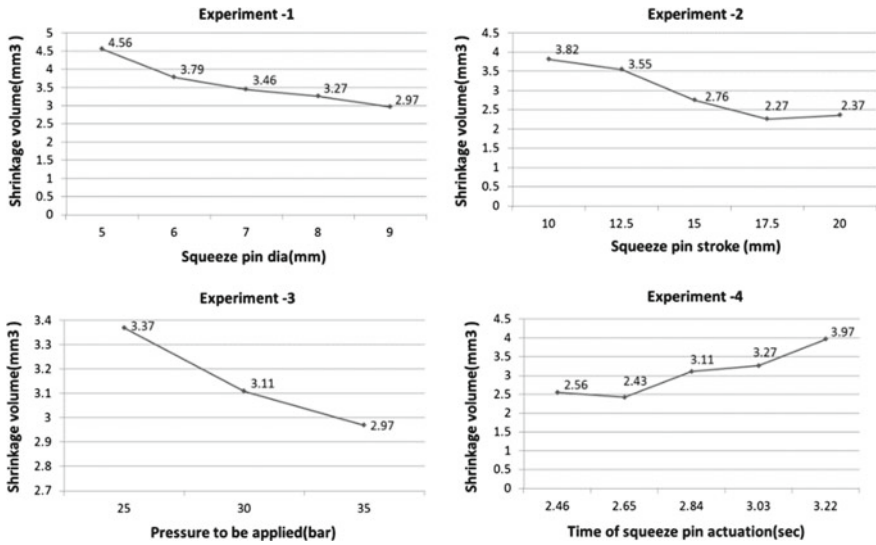
Fig. 5 Results of experiment 1 to experiment 4

4 Simulation Results and Discussion

The volume obtained during flow simulation is plotted on Y-axis, and the variable parameters are plotted on X-axis as shown in Fig. 5.

From the experiment 1 to experiment 4, results of optimum values obtained are given below-optimum squeeze pin diameter 9 mm, optimum squeeze pin stroke 17.5 mm, optimum pressure to be applied 35 bar, and optimum time of squeeze pin actuation 2.65 s.

Validation of optimized simulation result is done by conducting die trials on HPDC machines in manufacturing shop with squeeze pin actuation using obtained parameters and without squeeze pin actuation. Figure 6 shows radiography X-ray inspection report which shows shrinkage porosity of casting reduced from level III to level I

5 Conclusions

- The experimentally obtained locations of shrinkage porosity are same as predicted by simulation.
- Local squeeze pin can be used as tool to minimize shrinkage porosity under acceptable level.
- The method used to optimize squeeze pin parameters reduces trials in foundry, hence very useful to reduce lead time for component development.

X-ray of component without squeeze pin   X-ray of component with squeeze pin

Fig. 6 Radiography X-ray inspection report with and without squeeze pin actuation

- The product thus formed is defect proof from first trial; therefore, productivity of foundry increases.

References

1. Pierre Osmond, Viet-Duc LE, Franck Morel, Daniel Bellett, Nicolas Saintier: Effect of porosity on the fatigue strength of cast aluminium alloys: from the specimen to the structure. In: Procedia Engineering 213, pp. 630–643 (2018)
2. L. Lattanzi, A. Fabrizi, A. Fortini, M. Merlin, G. Timelli: Effects of microstructure and casting defects on the fatigue behavior of the high-pressure die-cast AlSi9Cu3(Fe) alloy. In: Procedia Structural Integrity 7, pp. 505–512 (2017)
3. E. Anglada, A. Meléndez, I. Vicario, E. Arratibel G. Cangas: Simplified models for high pressure die casting simulation. In: Procedia Engineering 132, pp. 974–981 (2015)
4. Yuanyuan Hu, Jiang Xie, Zhixiang Liu, Qinggong Ding, Wenhao Zhu, Jieyu Zhang, Wu Zhang: CA method with machine learning for simulating the grain and pore growth of aluminum alloys. In: Computational Materials Science 142, pp. 244–254 (2018)

5. S. Singh, A.I. Kanli, S. Sevgen: A general approach for porosity estimation using artificial neural network method: a case study from Kansas gas field. In: Stud. Geophys. Geod. 60 (1). pp. 1–11(2016)
6. I. Ghosh, S.K. Das, N. Chakraborty: An artificial neural network model to characterize porosity defects during solidification of a356 aluminum alloy. In: Neural Comput. Appl. 25 (3) pp. 653–662 (2014)
7. Ashiri, R. Karimzadeh, F. Niroumand, B.; On effect of squeezing pressure on microstructural characteristics, heat treatment response and electrical conductivity of an Al Si Mg Ni Cu alloy, In: Materials Science and Technology 30, pp. 1162–1169 (2014)
8. Adamane A.R., Arnberg L., Fiorese E.E., Timelli G., Bonollo F.; Influence of injection parameters on the porosity and tensile properties of high pressure die cast Al Si alloys: a review, In: American Foundry Society 9, pp. 43–53 (2015)
9. M.R. Bodhayana, N. Ramesha.: Tool design for pressure dies casting of Housing Component. In: International Journal of Theory and Applied Research in Mechanical Engg 3, pp. 30–33 (2014)
10. H. M. ManjunathSwamy, J. R. Nataraj, C. S. Prasad.: Design Optimization of Gating System by Fluid Flow and Solidification Simulation for Front Axle Housing. In: International Journal in Engineering Research and Development 4, pp. 83–88 (2012)
11. Yun Ling, Jianxin Zhou, Hai Nan, Yajun Yin, Xu Shen: A shrinkage cavity prediction model for gravity castings based on pressure distribution: A casting steel case. In: Journal of Manufacturing Processes 26, pp. 433–445 (2017)
12. Shuhua Yue, Guoxiang Wang, Fei Yin, Yixin Wang, Jiangbo Yang: Application of an integrated CAD/CAE/CAM system for die casting dies. In: Journal of Materials Processing Technology 139, pp. 465–468 (2003)
13. Hyuk-Jae Kwon., Hong-Kyu Kwon: Computer aided engineering (CAE) simulation for the design optimization of gate system on high pressure die casting (HPDC) process In: Robotics and Computer–Integrated Manufacturing 000, pp. 1–7 (2018)
14. K.Ch. Apparao, Anil Kumar Birru: Optimization of Die casting process based on Taguchi approach. In: Materials Today: Proceedings 4, pp. 1852–1859 (2017)
15. B.H. Hu, K.K. Tong, X.P. Niu, I. Pinwill: Design and optimisation of runner and gating systems for the die casting of thin-walled magnesium telecommunication parts through numerical simulation. In: Journal of Materials Processing Technology 105, pp. 128–133 (2000)
16. Priyanka Vispute, Digambar Chaudhari: Utilizing Flow Simulation in the Design Phase of a Casting Die to Optimize Design Parameters and Defect Analysis. In: Materials Today: Proceedings 4, pp. 9256–9263 (2017)

Optimization of Injection Moulding Process Parameters Using Response Surface Methodology

Khavekar Rajendra, Hari Vasudevan and Gosar Vimal

Abstract Manufacturing process can be optimized to obtain better quality of the products manufactured by particularly reducing the defects. In this study, application of a design of experiments (DOE) tool i.e., response surface methodology (RSM) was carried out on parameters of injection moulding of polybutylene terephthalate (PBT) material. The influences of process parameters are injection pressure, suck back pressure, injection time, cooling time, zone 1 temperature and zone 2 temperature (barrel temperatures) on dark-spots and short-shots (defects) considered under the investigation. Orthogonal array L16 of Taguchi method was used to screen six factors at two levels each with the response being % defectives. It was found that the injection pressure, injection time and zone 1 temperature had a major effect on the response. Central composite design of RSM was then applied to investigate further tuning of the parameters: injection pressure, injection time and zone 1 temperature. It was found that the reduction in % defectives had been reduced to 3.00% from 9.22%.

Keywords Response surface methodology · Taguchi method · DOE
Injection moulding · Optimization

1 Introduction

Plastics have attracted much interest in electrical applications during the past few years. Plastics, such as polybutylene terephthalate (PBT), are used in the manufacturing of electrical components for its heat resistance, electrical resistance, dimensional stability and toughness. Some of the typical electrical applications include electrical

K. Rajendra (✉) · H. Vasudevan · G. Vimal
D. J. Sanghvi College of Engineering, Mumbai 56, India
e-mail: khrajendra@rediffmail.com

H. Vasudevan
e-mail: principal@djsce.ac.in

G. Vimal
e-mail: gosarvimal@gmail.com

connectors, switches and electrical appliance components. Optimization of the process parameters of manufacturing has invariably become the prime focus on these applications to minimize the defects and thus improve the quality along with the productivity. Design of experiments (DOE) is a set of tools that help in optimizing the processes, using methods like Taguchi method and response surface methodology. Manufacturing of electronics appliance components involves processes such as plastic injection moulding, which is mainly used to manufacture moulded plastic products.

In this study, optimization of a plastic injection moulding process is carried out using response surface methodology (RSM). In a related study, previously done by the authors, Taguchi method was applied to optimize the process of plastic injection moulding for manufacturing bulb holders. Plastic injection moulding, which is a manufacturing process for processing polymers, is a very popular process due to its high production rate. In this process, the part is produced by injecting the molten material into the mould. The raw material in granular form is fed into the machine by means of a hopper which pre-heats the material. The material is then heated into the barrel and maintained at required temperatures at different zones of the barrel. The molten polymer is then injected into the mould at required pressure from the nozzle, where it is held for a given time to cool down, and then with the help of an ejector pin, the part is ejected when the mould opens. The mould is generally made up of steel or aluminium depending upon the type of application. In injection moulding process, defects are generated when the process is not stable and there is non-conformance with the dimensions of the product. These defects are developed due to the improper setting of the machine parameters. A number of defects like dark-spots, short-shots, shrinkage and warpage could be observed, if the machine parameters are not set properly. Even with the proper setting of machine parameters, sometimes due to noise factors, the settings may change a little; due to which, again the defects may occur. Therefore, optimization of the process is very important to be followed up.

The next section i.e., Sect. 2 in the paper brings out a detailed literature review, and Sect. 3 covers the experimental planning methods adopted in the study. Section 4 contains the experimental details and analyses. Results and discussion are covered in Sect. 5, and the conclusion is presented in Sect. 6.

2   Literature Review

Guo et al. [5] predicted warpage in injection plastic moulding, based on RSM of design of experiments. Central composite design (CCD) was used to find the mathematical model of the parameters such as coolant temperature, injection time, V/P switch over and mould temperature. It was found that the deviations were in between -0.5 and 0.8%, indicating the reliability of CCD on RSM. Akbarzadeh and Sadeghi [1] applied analysis of variance (ANOVA) method and IWO algorithm for parameter study in plastic injection moulding process, where the effect of injection moulding

parameters: melting temperature, injection pressure, packing pressure and packing time on shrinkage in polypropylene (PP) and polystyrene (PS) were considered. It was found that the models and algorithms for optimizing the process were effective in solving the problem of shrinkage with an improvement of 35.7% in PP and 25.7% in PS. Mohammad [3] implemented a hybrid response surface methodology and simulated annealing algorithm to optimize the process parameters of plastic injection moulding. Process parameters, such as mould temperature, melt temperature and injection pressure, were considered for the optimization. Two mathematical models were developed for shrinkage and warpage, and the predictions were fairly fitting with the actual values of the response with the error ranging from −0.96 to 0.04. Humbe and Kadam [2] optimized the process parameters, such as melt temperature, injection pressure, holding pressure and cooling time of plastic injection moulding for polypropylene, to enhance productivity and reduce time for development. The RSM's D-optimal method was used to analyse the effect of each parameters on tensile strength and cycle time. Two mathematical models were obtained for tensile strength and cycle time using RSM. Optimal settings were obtained for both the responses. Hence, in order to get the optimized value of input parameters for reduction of defects in injection moulding, RSM is the most appropriate method, as applicable and pertinent to the injection moulding process, being studied.

3 Experimental Planning Methods

3.1 Response Surface Methodology

The steps followed in the response surface methodology are shown in Fig. 1.

4 Experimental Details

4.1 Defining the Objective

The experimental objective was to minimize the defectives and hence reduce the rejection rate of the product manufactured, the defects being dark-spots, short-shots, silver-spots and shrinkage. The principal defects were found out to be dark-spots and short-shots from the manufacturing history. Approximately, 11% was observed to be the rejection rate in the manufacturing of this product and is as shown in Fig. 2.

Fig. 1 Response surface
methodology *Source* Myers
et al. [4]

Step 1	• Defining the Objective
Step 2	• Identifying Factors & Levels
Step 3	• Screening the Factors
Step 4	• Selecting RSM Design & Conducting Runs
Step 5	• Analyzing Results
Step 6	• Predicting the Response for Optimum Setting
Step 7	• Confirmation Run
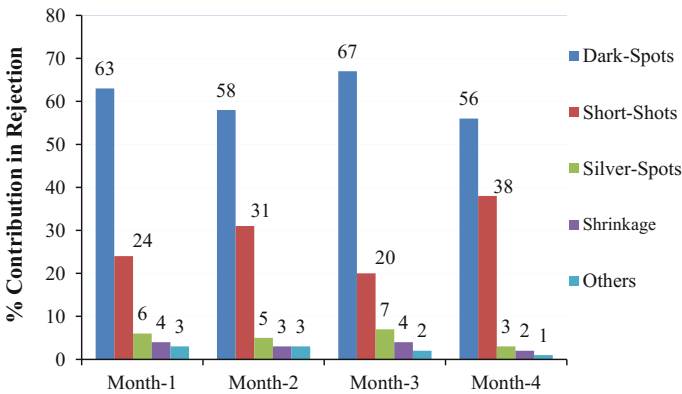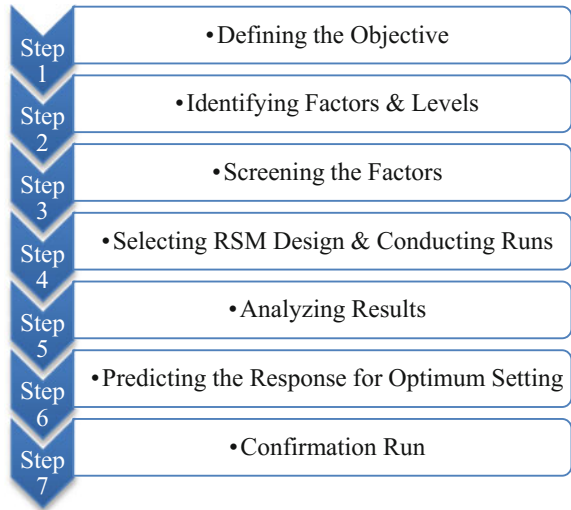
Fig. 2 % contribution of rejection

4.2 Identifying the Factors and Levels

There are three factors which play a major role in the injection moulding process:
temperature, pressure and time. Injection moulding process starts with sucking and
heating of the material at 'suck back pressure'. The material then flows through the
barrel at different 'zone 1 temperature' and 'zone 2 temperature' in barrel zones and
enters into the mould through the nozzle at a particular flow rate, which depends upon
the 'injection time' at a given 'injection pressure'. The mould is then locked and held
at a particular pressure for the melt to cool and solidify for a particular 'cooling time'.
In total, there were six factors identified at two different working levels as given in

Table 1 Injection moulding parameters

A. Temperature (°C)	1. Zone 1 temperature
	2. Zone 2 temperature
B. Pressure (MPa)	3. Injection pressure
	4. Suck back pressure
C. Time (sec)	5. Injection time
	6. Cooling time
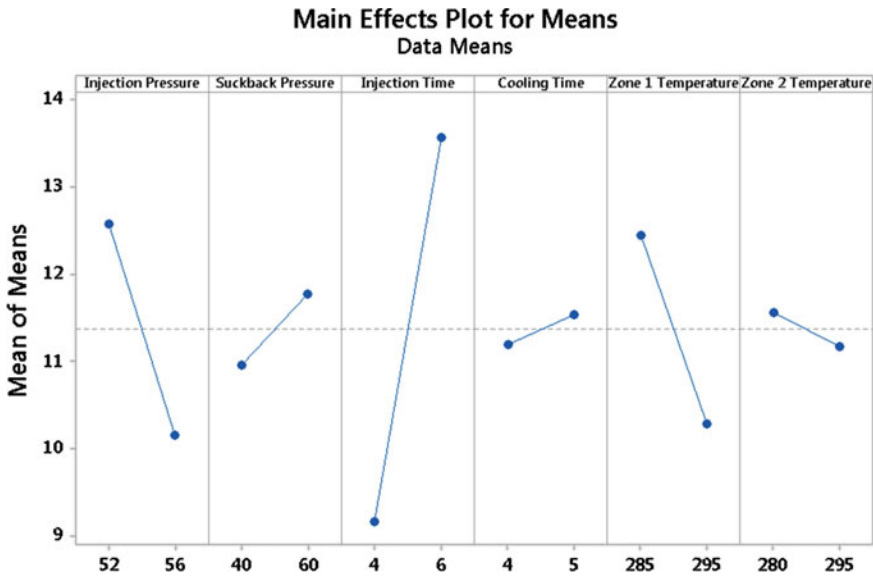
Fig. 3 Main effect plot

Table 1. These levels were selected as per the opinion of the machine and process experts in the firm.

4.3 Screening of Factors

Screening of these six factors was done using orthogonal arrays of Taguchi method. L16 design was used, and it was found from the main effect plot, which is shown in Fig. 3 that out of the six factors only three had dominant effect on the process. With the optimum settings, a trial run was carried out to set the baseline of the response, which was found to be 9.22%.

The factors and their levels selected are shown in Table 2.

Table 2 Factors and levels

1. Zone 1 temperature (°C)	High	295
	Low	285
2. Injection pressure (kPa)	High	56
	Low	52
3. Injection time (s)	High	6
	Low	4

Table 3 RSM design CCD

Run no.	Injection pressure (kPa)	Injection time (s)	Zone 1 temperature (°C)
1	50.637	5.000	290.00
2	54.00	5.000	290.00
3	56.00	4.000	285.00
4	54.00	5.000	290.00
5	54.00	5.000	290.00
6	54.00	5.000	298.41
7	52.00	6.000	295.00
8	56.00	4.000	295.00
9	54.00	3.318	290.00
10	56.00	6.000	295.00
11	52.00	4.000	285.00
12	54.00	5.000	290.00
13	54.00	5.000	290.00
14	56.00	6.000	285.00
15	52.00	4.000	295.00
16	54.00	6.682	290.00
17	57.364	5.000	290.00
18	52.00	6.000	285.00
19	54.00	5.000	281.59
20	54.00	5.000	290.00

4.4 Selecting RSM Designs

Minitab 17 statistical software package was used for designing the experiments for six factors at two levels. The orthogonal array was selected from *Stat > DOE > RSM > Create RSM Design* in the software. Rotatable Central compsite design for three factors at two levels with one centre point and two start points was selected. There were in total 20 runs and is as shown in Table 3.

Table 4 Responses actual and predicted

Run no.	Injection pressure (kPa)	Injection time (s)	Zone 1 temp (°C)	Response		
				Actual	Predicted	Residual error
1	50.637	5.000	290.00	14.07	14.59	0.52
2	54.00	5.000	290.00	8.89	7.71	−1.18
3	56.00	4.000	285.00	9.63	8.40	−1.23
4	54.00	5.000	290.00	8.89	7.71	−1.18
5	54.00	5.000	290.00	6.67	7.71	1.04
6	54.00	5.000	298.41	5.93	6.68	0.75
7	52.00	6.000	295.00	13.33	12.75	−0.58
8	56.00	4.000	295.00	5.19	5.34	0.15
9	54.00	3.318	290.00	6.67	6.32	−0.35
10	56.00	6.000	295.00	12.59	10.44	−2.15
11	52.00	4.000	285.00	11.85	12.19	0.34
12	54.00	5.000	290.00	6.67	7.71	1.04
13	54.00	5.000	290.00	7.41	7.71	0.3
14	56.00	6.000	285.00	11.11	9.44	−1.67
15	52.00	4.000	295.00	7.41	7.27	−0.14
16	54.00	6.688	290.00	8.89	11.80	2.91
17	57.364	5.000	290.00	7.41	9.46	2.05
18	52.00	6.000	285.00	15.56	13.60	−1.96
19	54.00	5.000	281.59	8.15	9.97	1.82
20	54.00	5.000	290.00	8.15	7.71	−0.44

The experimentation carried out was completely randomized and replicated. Therefore for every settingRegression equation in uncoded units:. These two values were taken as one average value. The details are as shown in Table 4.

Regression equation in uncoded units:

%Defective $= 2960 - 55.2$ Injection Pressure $- 59.6$ Injection Time $- 8.8$ Zone 1 Temperature $+ 0.381$ Injection Pressure * Injection Pressure $+ 0.479$ Injection Time * Injection Time $+ 0.0087$ Zone 1 Temperature * Zone 1 Temperature $- 0.047$ Injection Pressure*Injection Time $+ 0.0464$ Injection Pressure * Zone 1 Temperature $+ 0.203$ Injection Time * Zone 1 Temperature

4.5 Analysis of Results

From the obtained results, it can be observed that the predicted values obtained are very close to the actual value as shown in Fig. 4, thus making this mathematical model

Fig. 4 Actual response
versus predicted response
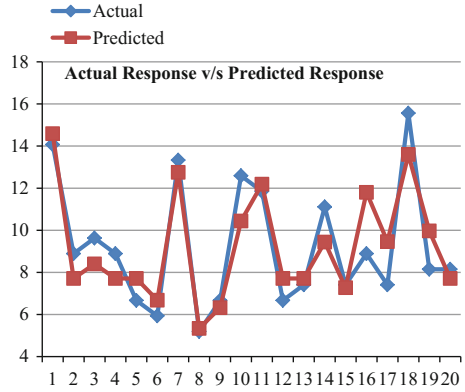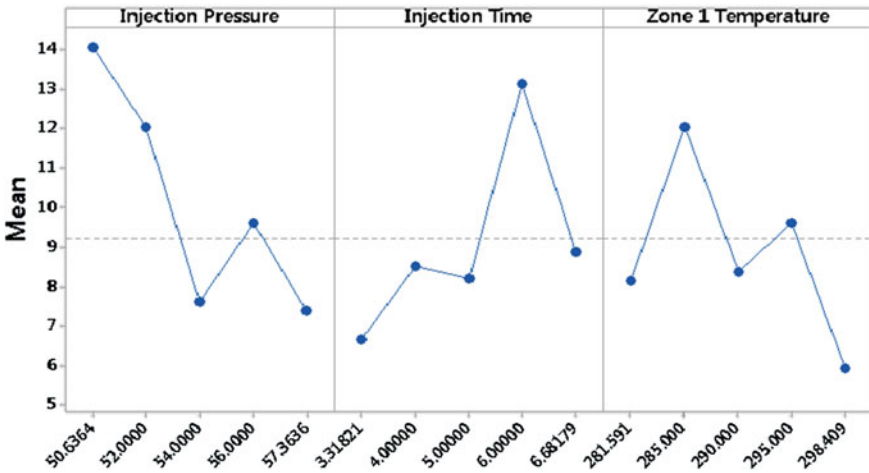
Fig. 5 Main effect plot for response

reliable. Response optimizer was then used to predict the behaviour of response at different settings of the factors. As the problem contains Minimum-the-Better case, response optimizer was set to give the optimum setting so as to obtain the minimum % defectives.

From the main effect plot for response it is clear that to obtain minimum % defectives, the factors have to be tuned as suggested in the plot as shown in Fig. 5.

Table 5 Response optimizer setting and predicted response value

Variable	Setting	Predicted response value
Injection pressure	54	2.72%
Injection time	3.4	
Zone 1 temperature	298	
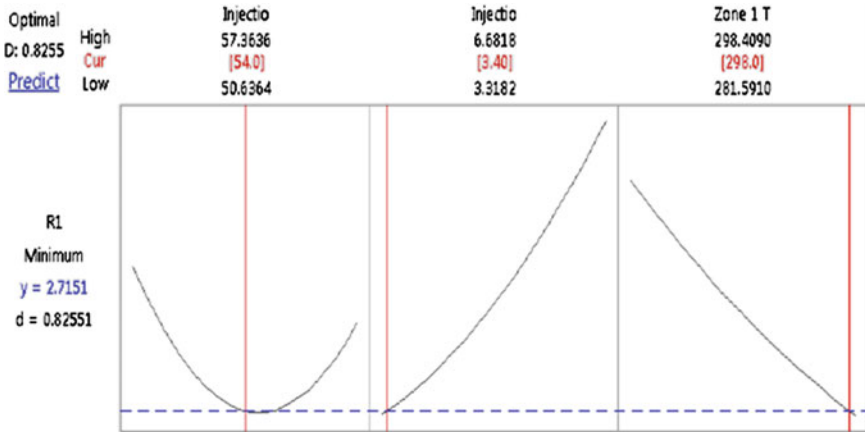
Fig. 6 Response optimizer

Table 6 Confirmation details

Set no.	No. of pieces	No. of defectives observed	Actual % defectives	Predicted % defectives	% difference
1	$45 \times 3 = 135$	4	2.963	2.72	0.243
2	$55 \times 3 = 165$	5	3.030	2.72	0.310
Total	300	9	2.993	2.72	0.2765

4.6 Predicting Response for Optimum Setting

Minitab 17 statistical software was used to obtain the prediction of response value for optimum setting using response optimizer. With Smaller-the-Better case of this study, response optimizer produced the setting as shown in Table 5 and Fig. 6.

4.7 Confirmation Run

With the following setting, two sets of observations were taken with 45 shots as well as 55 shots, and the observations are given in Table 6.

$$\text{Reduction in \% Defects} = \frac{9.22 - 2.99}{9.22} = 67.46\%$$

5 Results and Discussion

It is clear from the confirmation run that % defectives have been reduced by 67.46% and that the actual response value is falling near the predicted response value; the difference being marginal at 0.273%, and thus making RSM as a reliable tool for predicting and optimizing the plastic injection moulding process. The difference obtained in the predicted and actual response value may be due to the noise factors and the limitations of the machine of deviating value in a given setting. Further, with the machine limitation of resolution, the values of dominant factors play a major role with even a small change in input parameters.

6 Conclusion

Response surface methodology (RSM) was successfully implemented in the study to optimize the plastic injection moulding process. Confirmation runs tested the accuracy of the developed mathematical model; the deviation being 0.273%. Expected savings from this case study is approximately Rs. 3 lakhs/annum for the company. This method gives the global optimum value of the parameters. Semi-skilled workers are not in a position to handle this methodology very easily, as it requires more data and software tool to conduct the experiments. It also provides breakthrough improvements in quality of the process under investigation.

References

1. Alireza Akbarzadeh & Mohammad Sadeghi: Parameter Study in Plastic Injection Moulding Process using Statistical.
2. A Humbe & M Kadam: Optimization of process parameters of plastic injection moulding for polypropylene to enhance productivity and reduce cycle time, International Journal of Mechanical Engineering and Technology, 5,5,150–162 (2014).
3. Molani Aghdam Mohhammad: A hybrid response surface methodology and simulated annealing algorithm, International Conference on Computer Communication and Management, 5,570–576 (2011).
4. Myers, Montgomery, Anderson-Cook: Response Surface Methodology, Wiley & Sons Inc., Third Edition (2016).
5. Wei Guo, Lin Hua, Huajie Mao, Z Meng: Prediction of warpage in plastic injection molding based on design of experiments, Journal of Mechanical Science and Technology, 26 (4), 1133–1139 (2012).

Optimization of Cutting Parameters in Dry Turning of AISI 4140 Hardened Alloy Steel with Coated Carbide Tool

Sandip Mane and Sanjay Kumar

Abstract This article focuses on optimization of cutting parameters during the turning of hardened AISI 4140 alloy steel using with TiAlN–TiN, PVD-coated, tungsten carbide insert. The Analysis of Variance and Taguchi's technique are used for analysis. The three levels of feed, speed, and depth of cut are selected. A L9 orthogonal array is selected based on Taguchi's design of experiments (DoE), and the experimental investigation is carried out. The performance measures, cutting forces, and tool-chip interface temperature are analyzed by signal-to-noise (S/N) ratio. Analysis of variance is used to determine the most contributing factor, which shows that cutting speed is the most prominent parameter contributing by 62.71%, cutting speed by 7.04%, and depth of cut by 19.78%.

Keywords Analysis of variance · Taguchi · Signal-to-noise (S/N) ratio

1 Introduction

Metal machining is a coupled thermo-mechanical process. The heat generation occurs as a result of plastic deformation and friction along the tool-chip and tool-workpiece interface, which in turn raises the temperature in the cutting zone. This factor is of a major importance to the performance of the cutting tool and quality of the workpiece. The heat generation and temperature at the cutting zone due to the friction at tool-chip interface and tool-workpiece interface are significant parameters which influence chip formation mechanism, tool wear, tool life, surface integrity, and hence machining quality. The investigation of the temperature at the cutting region is imperative because of its impact on machining responses. It has been shown that lessening

S. Mane
D J Sanghvi Engineering College, Mumbai, Maharashtra, India

S. Kumar (✉)
Thakur College of Engineering and Technology, Mumbai, Maharashtra, India
e-mail: sanjay_mast@yahoo.co.in

the temperature at the critical area during the machining process enhances the tool life and surface integrity of the workpiece.

Mohammad et al. [1] have performed numerical simulations to investigate the effects of cutting parameters on cutting force in turning of hardened alloy steel AISI 52100, 4340, and D2. The results revealed that turning AISI 52100 has the maximal feed force, turning AISI 4340 attains the maximal cutting force, and turning AISI D2 has the least cutting and feed force. The cutting force turns out to be a smaller force component and feed force as a major force component in turning hardened alloy steel. Cutting force components raises with increasing feed, negative rake angle, and nose radius. Ozel et al. [2] investigated the effect of cutting speed, feed cutting edge geometry, and workpiece hardness on cutting force in the hard turning of AISI H13 steel. In this research, it has been observed that the cutting tool geometry, cutting speed, and hardness of workpiece are found to be influencing force components. Aspinwall et al. [3] have explored the effects of cutting speed and workpiece hardness on cutting forces. Aouici et al. [4] have studied the effects of cutting speed, feed, depth of cut, and workpiece hardness on the cutting force in turning AISI H11 hardened steel. Fnides et al. [5] interpreted the effects of the cutting parameters on cutting force components in hard turning of AISI H11 tool steel. More et al. [6] have used ANOVA technique and interpreted the effect of cutting speed and feed on forces. Umbrello and Jawahir [7] have developed a finite element model which was applied to envisage the white layer formation during turning of AISI 52100 hardened steel. Chu and Wallbank [8] in 1998 stated a relationship between the cutting parameters and cutting temperature for specific range of cutting speed and feed rate. Abdil and Yashya [8] has concluded that during turning of hardened steel, the cutting speed is observed as the most influencing parameter on the tool-chip interface temperature whereas feed rate is less significant. A FEM-experimental methods for obtaining the cutting tool's temperature fields developed and compared with physical conditions [9]. Shihab [10] presented the RSM model-based study using ANOVA for turning of AISI hard alloy steel.

Thus, there is a need for a process optimization to determine optimal values of cutting parameters, such as cutting speed, feed rate, and depth of cut to fully explore the performance turning of hardened alloy steel. The present paper aims to examine the role of cutting parameters in turning hardened AISI 4140 steel (55 HRC).

1.1 Taguchi Techniques

Taguchi design is powerful tool and efficient method for designing processes that operate persistently and optimally over a variety of conditions. To determine, the finest design needs the use of a strategically designed experiment which reveals the process to discrete levels of design parameters. Taguchi's approach to design of experiments is easy to use and implement, and therefore it has attained immense acceptance in the field of Science and Technology [11]. There has been a great deal of ongoing applications of Taguchi method for process optimization [12]. Taguchi

Table 1 Chemical configuration of AISI 4140 steel

C	Si	Ni	Mn	Cr	Mo	P	S
0.4	0.25	0.20	0.9	1.0	0.2	0.035	0.040

design is suggested for analyzing machining process problems for finding the optimum parameters.

The objective of this study is to investigate the influence of the cutting speed, feed, and depth of cut on tool-chip interface temperature and cutting force in dry turning of AISI 4140 hardened alloy steel by applying Taguchi's technique and analysis of variance (ANOVA).

2 Experimental Procedure

2.1 Equipment and Materials

The main objective of this work was to investigate the response of cutting parameters on tool-chip interface temperature and cutting force. The cutting parameters were selected as process parameters, and AISI 4140 hardened alloy steel (55 HRC) having 50 mm dia. and 300 mm length was selected as a workpiece material for this study. The chemical configuration of the AISI 4140 hardened alloy steel is listed in Table 1. AISI 4140 is commonly used for a variety of applications in the oil and gas sector. The typical applications include components such as connection rods, collets, conveyor pins, gears, stem assemblies, pump shafts, and tool holders, etc. The turning tests were conducted in dry conditions on NH-18 lathe (HMT Make) having a maximum spindle speed of 1800 rpm and a maximum power of 7.5 kW. The cutting tool used was coated carbide cutting tool insert with 6° rake angle, 6° clearance angle, and 0.02 mm nose radius. The Al_2O_3 and TiC were the two-tool coating material having thickness of 5 micron and 3 microns, respectively. IEICOS lathe tool dynamometer (model 652) with digital multicomponent force indicator with 3 independent digital panel meter is used to measure *XYZ* force. Also, IEICOS hand-held digital infrared thermometer (Range: 50–1850 °C) and K-type thermocouple are used for temperature measurement.

2.2 Design of Experiments

The Taguchi method is an effective technique of optimization and employs the distinctive design of orthogonal array (OA) to investigate the quality aspect through a least possible number of experiments. Based on the orthogonal array, the results obtained are then transformed into S/N ratio to appraise the performance. Design of

Table 2 Factors and their levels

AISI 4140-55 HRC				
	Symbol	Level 1	Level 2	Level 3
Cutting speed (m/min)	A	86.39	109.96	133.52
Feed (mm/rev)	B	0.08	0.10	0.12
Depth of cut (mm)	C	0.10	0.20	0.30

Table 3 Orthogonal array L9 of Taguchi (coded form)

L9 combinations (coded)			
Test no "L"	Cutting speed (m/min)	Feed (mm/rev)	Depth of cut (mm)
L1	1	1	1
L2	1	2	2
L3	1	3	3
L4	2	1	2
L5	2	2	3
L6	2	3	1
L7	3	1	3
L8	3	2	1
L9	3	3	2

experiments method is applied to plan the orthogonal array for 3 parameters such as cutting speed, feed, depth of cut, and for each parameter, 3 different values are selected within the intervals recommended by the cutting tool manufacturer (Table 2).

The least number of experiments that need to be performed for the parametric optimization is determined as,

$$\text{No. of experiments} = [(L - 1) \times P] + 1 = [(3 - 1) \times 3] + 1 = 7 \approx \text{L9}$$

Based on the designed L9 orthogonal array, experiments are carried out and the response parameters such as resultant cutting force and tool-chip interface temperature are determined. The numerical measure of performance characteristic like signal-to-noise ratio is used to analyze the effect of process parameters on the output parameters. For investigation, there are three types of quality characteristics, (i.e.) smaller-the-better, larger-the-better, and nominal-the-better (Tables 3, 4 and 5).

$$\text{Smaller-the-better (minimize): S/N} = -10 * \log\left(\sum \left(Y^2\right)/n\right)$$

$$\text{Larger-the-better (maximize): S/N} = -10 * \log\left(\sum \left(1/Y^2\right)/n\right)$$

$$\text{Nominal-the-best: S/N} = -10 * \log\left(s^2\right)$$

Table 4 Orthogonal array L9 of Taguchi (uncoded form)

L9 combinations (uncoded)			
Test no "L"	Cutting speed (m/min)	Feed (mm/rev)	Depth of cut (mm)
L1	86.39	0.08	0.10
L2	86.39	0.10	0.20
L3	86.39	0.12	0.30
L4	109.96	0.08	0.20
L5	109.96	0.10	0.30
L6	109.96	0.12	0.10
L7	133.52	0.08	0.30
L8	133.52	0.10	0.10
L9	133.52	0.12	0.20

Table 5 Experimental results for force and interface temperature

Test no "L"	Cutting speed (m/min)	Feed (mm/rev)	Depth of cut (mm)	Force in X (N)	Force in Y (N)	Temp. (°C)
L1	86.39	0.08	0.10	110.48	67.12	667.50
L2	86.39	0.10	0.20	44.60	24.08	787.75
L3	86.39	0.12	0.30	183.90	95.55	907.93
L4	109.96	0.08	0.20	92.93	50.76	684.25
L5	109.96	0.10	0.30	153.97	86.16	707.64
L6	109.96	0.12	0.10	63.24	30.98	716.84
L7	133.52	0.08	0.30	128.34	74.28	649.65
L8	133.52	0.10	0.10	153.38	84.16	674.54
L9	133.52	0.12	0.20	117.52	56.70	827.91

3   Results and Discussion

The analysis is carried out using Minitab-17 statistical software. By employing the smaller-the-better technique of signal-to-noise ratio, the combined S/N ratio is computed, which is shown in Table 6. Based on the determined combined S/N ratio, the response table for cutting speed, feed rate, and depth of cut are determined by averaging the combined S/N ratio for each level of input parameters, as shown in Table 7. From the response table, the main effects plot of S/N ratio is plotted for cutting speed, feed rate, and depth of cut which are shown in Fig. 1. From the response table and main effects plot of combined S/N ratio, the finest level of parameters are identified as cutting speed of 86.39 m/min, feed rate of 0.10 mm/rev, and depth of cut of 0.1 mm, (A1B2C2). Analysis of variance (ANOVA) is a valuable method for analyzing the effect of categorical factors on a response. It is performed to determine the factors that contribute to the quality characteristics. Minitab-17 statistical software is used to perform the analysis. Table 9 shows the ANOVA table for the combined S/N ratio.

Table 6 Combined S/N ratio of the response parameters

Test no "L"	Cutting speed (m/min)	Feed (mm/rev)	Depth of cut (mm)	Resultant force (N)	Temp. (°C)	S/N ratio
L1	86.39	0.08	0.10	129.27	667.50	−53.639
L2	86.39	0.08	0.10	50.69	787.75	−54.935
L3	86.39	0.08	0.10	207.24	907.93	−56.371
L4	86.39	0.10	0.20	105.89	684.25	−53.797
L5	86.39	0.10	0.20	176.44	707.64	−54.248
L6	86.39	0.10	0.20	70.42	716.84	−54.140
L7	86.39	0.12	0.30	148.28	649.65	−53.464
L8	86.39	0.12	0.30	174.95	674.54	−53.853
L9	86.39	0.12	0.30	130.48	827.91	−55.456

Table 7 Response table for signal to noise ratios (smaller is better)

Level	CS	Feed	DOC
1	458.4	397.5	405.6
2	410.2	428.7	431.2
3	434.3	476.8	466.2
Delta	48.1	79.3	60.6
Rank	3	1	2

Table 8 Optimal conditions of cutting parameters

Optimum conditions		
Cutting speed (m/min)	Feed (mm/rev)	Depth of cut (mm)
86.39	0.10	0.20
A1	B2	C2

Table 9 ANOVA table

	Analysis of variance						
Source	DF	Seq SS	C (%)	Adj SS	Adj MS	F-value	P-value
Cutting speed	2	8,156,647	62.71	8,156,647	4,078,324	5.99	0.143
Feed	2	915,616	7.04	915,616	457,808	0.67	0.598
Depth of cut	2	2,573,348	19.78	2,573,348	1,286,674	1.89	0.346
Error	2	1,361,362	10.47	1,361,362	680,681		
Total	8	13,006,973	100.00				

From the ANOVA table, it is observed that the cutting speed is the most significant factor contributing by 62.71%, followed by cutting speed by 7.04%, depth of cut by 19.78% (Tables 8, 9, 10 and 11).

Main Effects Plot for SN ratios
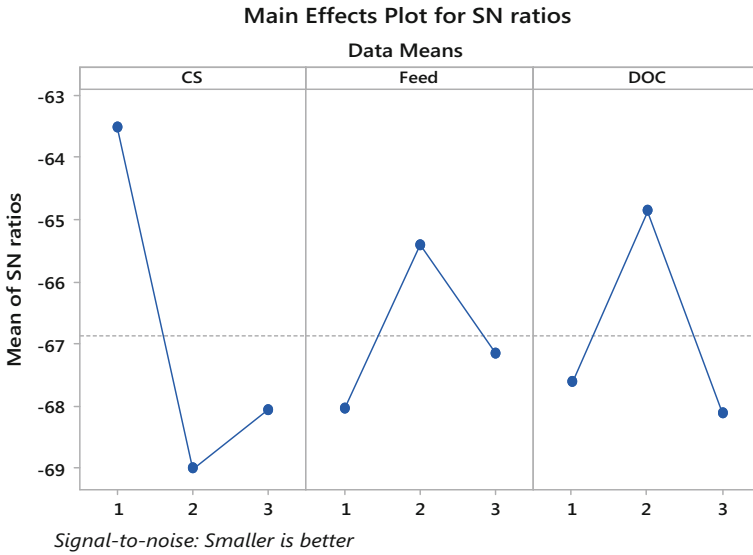
Fig. 1 Mean effects plot for SN ratios

Table 10 Model summary

S	R-sq	R-sq (adj)	Press	R-sq (pred)
825.034	89.53%	58.13%	27,567,578	0.00%

Table 11 Output quality characteristics of optimal condition

Tool-chip temperature (°C)	Cutting force (N)		
	F_X	F_Y	Resultant
573.94	76.29	41.57	86.88

4 Conclusion

The results showed that the Taguchi technique is an impressive method of deciding the optimal cutting parameters for attaining the minimal value of cutting temperature and cutting force. Also, it has been proved that the appropriate selection of process parameters and their levels enhances the quality characteristics in turning of hard to cut material.

References

1. Mohammad R H (2007) Effect on cutting force in turning hardened tool steels with cubic boron nitride international. J Mater Process Technol 191(1/3):274–278.
2. Ozel T, Hsu T K, Zeren E (2005) Effects of cutting edge geometry, workpiece hardness, feed rate and cutting speed on surface roughness and forces in finish turning of hardened AISI H13 steel. Int J Adv Manuf Technol 25(3/4):262–926.
3. Aspinwall DK (2002) The effect of workpiece hardness and cutting speed on the machinability of AISI H13 Hot work die steel when using PCBN tooling. ASME JManuf Sci Engg 124(3):588–594.
4. Aouici H, Yallese MA, Chaoui K, Mabrouki T, Rigal JF (2002) Analysis of surface roughness and cutting force components in hard turning with CBN tool: prediction model and cutting conditions optimization. Measurement 45(3):344–353.
5. Fnides B, Yallese MA, Mabrouki T, Figal J (2011) Application of response surface methodology for determining cutting force model in turning hardened AISI H11 hot work tool steel. Sadhana 36(1):109–123.
6. More A S, Jiang W, Brown W D, Malshe AP (2006) Tool wear and machining performance of CBN-TiN coated carbide inserts and PCBN compact inserts in turning AISI4340 hardened steel. J Mater Process Tech 180(1–3):253–262.
7. Umbrello D, Jawahir I (2009) Numerical modeling of the influence of process parameters and work-piece hardness on white layer formation in AISI 52100 steel. Int J Adv Manuf Technol 44(9/10): 955–968.
8. Kus A, Isik Y, Cakir C, Coskun S, Ozdemir K. Thermocouple and Infrared Sensor-Based Measurement of Temperature Distribution inMetal Cutting. Sensors 2015:15:1274–1291.
9. Kryzhanivskyy V, Bushlya V, Gutnichenko O, Petrusha IA, Stahl JE. Modelling and Experimental Investigation of Cutting Temperature when Rough Turning Hardened Tool Steel with PCBN Tools. Procedia CIRP 2015:31:489–495.
10. Suha, Zahid, Aas, Arshad. RSM based study of cutting temperature during Hard turning with Multilayer Coated Carbide insert. Procedia Materials Science 2014:6:1233–1242.
11. Yang WH, Tarng YS. Design optimization of cutting parameters for turning operations based on the Taguchi method. J Mater Process Technol 1998; 84:122–9.
12. Ghani JA, Choudhury IA, Hassan HH. Application of Taguchi method in the optimization of end milling operations. J Mater Process Technol 2004; 145:84–92.

A Perspective of Integrated Machine Vision Based-Multivariate Statistical Process Control

Ketaki N. Joshi and Bhushan T. Patil

Abstract Machine vision systems have proven their potential of effectively inspecting objects under consideration for surface and dimensional defects using various texture analysis techniques. However, current use of machine vision systems in industry is broadly limited to acceptance or rejection of product based on its quality. Their potential of providing complete solution to quality is not completely explored and utilized. Hence their exist opportunities for utilizing machine vision systems not only for inspection, but going one step ahead and using it for quality control. The information extracted by machine vision systems, over the period, can be analysed for monitoring production processes and detecting out-of-control signals. This paper provides a review of the attempts made by various researchers in the direction of integrating machine vision techniques with statistical quality control methods for providing vision based solution for quality control.

Keywords Machine vision · Multivariate techniques · Statistical process control

1 Introduction

Automatic inspection systems using computer vision and image processing techniques are capable of accurate inspection and effective process monitoring. There has been a significant development in the field of machine vision systems (MVS) and have proven their potential to replace the traditional measurement systems. There exists an opportunity to extend their current usage for inspection to monitoring of

K. N. Joshi (✉)
Mechanical Engineering, Fr. Conceicao Rodrigues College of Engineering,
Affiliated to University of Mumbai, Bandra, Mumbai, Maharashtra, India
e-mail: ketaki.joshi@fragnel.edu.in

B. T. Patil
Fr. Conceicao Rodrigues College of Engineering, Affiliated to University of Mumbai,
Bandra, Mumbai, Maharashtra, India
e-mail: bhushan.patil@fragnel.edu.in

production processes and utilizing this data in order to control the system before non-conformities occur.

Woodall and Montgomery [1] have stated that use of images for process monitoring is one of the latest trends in the area of quality control. The images of the products are often used in the industry for inspection, i.e. to separate non-conforming items from conforming items. However, they clearly stated the opportunity of developing solutions for detection of quality changes before non-conforming items are actually produced in the system by encouraging investigations and research in the area of control charting using image data.

Vining et al. [2] have also stated that currently the image data is being primarily used for quality inspection purpose; however, the future scope for research in the field of machine vision lies in exploring the opportunity of using this information to improve quality of the processes. Hence they enforce on development of statistical monitoring methodologies for image data to be the next logical step in the near future.

In the present paper, authors attempt to survey the current state of research progress achieved in the field of machine vision-based multivariate statistical control. The paper presents a review of developments in multivariate statistical quality control techniques, integration of MVS with control charting techniques and its implementation in various product and process industries carried out by various researchers.

1.1 Integration of Machine Vision Systems and Statistical Process Control

Applications of modern industrial machine vision systems can be broadly categorized in four types of inspections: dimensional quality, surface quality, structural quality and operational quality [3].

Dimensional quality characteristics can be extracted by processing images of the product under inspection using various image processing techniques and feature extraction techniques. Inspection for surface quality using MVS is based on the principle that, an image is a two dimensional image intensity function characterized by the amount of light incident on the object under observation (illumination) which is dependent on the light source and the amount of light reflected from the object (reflectance) which is dependent on the characteristic of the surface of object [4]. Structural quality refers to correct assembling, which can be extracted from images of the assemblies using statistical techniques based on greyscale levels, template matching or various stochastic model-based algorithms. Operational quality deals with accuracy with which a particular operation is carried out.

Effective management of quality involves three activities namely quality planning, quality assurance and quality control and improvement [5]. Quality control and improvement is one of the philosophical pillars of quality and can be achieved primarily by using statistical process control (SPC).

Traditional process monitoring and quality control from univariate perspective is based on the assumption that only one process output is of prime concern. However in practice, a product's utility value depends on a number of quality characteristics all of which need to be controlled in the production process in order to avoid rejection of components based on non-conformance to quality. Univariate approach also affects the joint probability of sample means lying within the control limits when the process is actually in control, calculated as $(1 - \alpha)^p$, with α being the individual probability of sample means lying in the control limits and p being number of variables. This increases the probability of type I errors. Also, the above formula is applicable only if all the characteristics are truly independent in nature, which is rarely the case in actual practice.

In these scenarios, multivariate quality control provides a more effective way to monitor process quality by simultaneously monitoring all the variables under consideration. Multivariate techniques not only extract the information on individual characteristics but also extract and monitor correlations among data [5]. The method is suitable for processes with quality characteristics up to ten in number. However, it can also be used with more variables after reducing the dimensionality using principal component analysis [6].

The multivariate process control techniques can be effectively used to monitor a process involving multiple output characteristics. If this technique is integrated with machine vision system, can provide a very effective automated system for process monitoring and control. Researchers have made an attempt to use machine vision system with multivariate statistical techniques for process control. Most of the researchers have used this technique for surface quality control whereas very few have used it for dimensional aspects of quality. It can be concluded that integration of machine vision systems and statistical process control techniques can provide a very effective, economic and reliable tool for facilitating quality control in the industries.

1.2 Methodology for Developing MVS Based-Process Monitoring and Control

Methodology developed by Rogalewicz and Poznańska [7] can be adopted for developing machine vision-based multivariate quality control system.

It consists of three phases: planning phase, process capability study phase and process monitoring phase. In planning phase, process to be controlled is studied and the variable critical to its quality are selected with their tolerance limits and targets. Then the data acquisition system is to be built, which for machine vision-based approach, will include system for acquisition of images using camera and transferring them to computer systems for further analyses. Then the measurement system is to be developed, which for machine vision-based approach, will include the use of image processing techniques for measurement of quality parameters. Then in the process capability study phase, sample data with suitable sample size and

sampling frequency is to be collected, analysed, then plotted using proper control chart and further analysed for examining the process stability and capability. The last phase is process monitoring phase, where control limits are to be calculated followed by process monitoring and diagnosis of out of control scenarios.

2 Multivariate Control Charts

Most widely used multivariate quality control charts are Hotelling T^2 charts. These charts use information from current sample and hence are insensitive to small and moderate shifts in process mean. Multivariate exponentially weighed moving average (MEWMA) charts overcome this limitation [8].

2.1 Hotelling T^2 Chart

Hotelling T^2 control chart developed by Hotelling [9] is the most widely used method for multivariate quality control. This method is a direct analogue of univariate Shewart chart. Hotelling T^2 charts for subgroup data can be represented using control region or chi-square chart with an upper control limit. First method suffers from loss of time sequence of data and complexity for more number of variables. Second method overcomes these limitations by plotting the statistics value for all samples. These charts can be extended for estimating population mean and standard deviation, charts in which case are called Hotelling T^2 charts.

$$T^2 = n(\bar{x} - \bar{\bar{x}})' S^{-1} (\bar{x} - \bar{\bar{x}})$$

Two distinct phases in the use of control charts have different control limits based on the usage as proposed by Alt. Phase-I has the objective to obtain in control observations in order to establish control limits for phase-II. Whereas phase-II is for monitoring the production. Accordingly, the control limits set for two phases are as follows:

Control limits for phase-I:	Control limits for phase-II:
UCL $= \frac{p(m-1)(n-1)}{mn-m-p+1} F_{\alpha, p, mn-m-p+1}$	UCL $= \frac{p(m+1)(n-1)}{mn-m-p+1} F_{\alpha, p, mn-m-p+1}$
LCL $= 0$	LCL $= 0$

Interpretation of out of control signals is the most critical step in the use of Hotelling T^2 charts as it differs from univariate approach. Runger et al. [10] suggested the use of decomposition method where $T_{(i)}^2$ indicates the T^2 statistics for all process variables except the ith one. Then d_i calculated as $T^2 - T_{(i)}^2$ indicates the relative contribution of each parameter to the overall statistics.

Other methods include use of principal component analysis (PCA), partial least squares (PLS) for dimensionality reduction or discriminant analysis for classification of observations into groups [8, 11, 12]. PCA and projection of latent structure allow systematic examination and interpretation of highly correlated high-dimensional data [13]. Bersimis et al. [14] have discussed all the types of multivariate control charts, autocorrelation, dimensionality reduction using PCA and PLS and interpretation of out of control signals in detail.

2.2 *Multivariate Exponentially Weighted Moving Average (MEWMA) Chart*

Multivariate exponentially weighted moving average (MEWMA) chart developed by Lowry et al. [15] can sense the small or moderate shift in the mean vector over period as compared to Hotelling T^2 chart. MEWMA statistics is given as follows:

$$Z_i = \lambda x_i + (1 - \lambda)Z_{i-1}$$

where λ lies between 0 and 1 and $Z_0 = 0$

Quality term plotted on the chart is given as follows:

$$T_i^2 = Z_i' \sum_{zi^{-1}} Z_i$$

where covariance matrix

$$\sum_{zi} = \frac{\lambda}{2 - \lambda}\big[1 - (1 - \lambda)^{2i}\big] \sum$$

3 Literature Review

Horst and Negin [16] used two charge-coupled devices and computer server for inspecting thickness of textile and plotting control charts for mean and standard deviation in real time.

Nembhard et al. [17] implemented integrated model for statistical and vision monitoring in order to monitor the colour transition of the extruded polymer at different levels as it cools down in order to identify quality improvement opportunities. The colour transition data was captured by processing images of the polymer taken at predetermined intervals and then plotted using EWMA control chart in order to detect process shift.

Jiang et al. [18] proposed machine vision-based inspection of TFT-LCD panels for mura defects using colour/greyscale values in different regions of the panel using

EWMA chart. The positions of mura defects were easily located using EWMA chart which were further analysed for classification. Lin and Chiu [19] proposed use of Hotelling T^2 chart to determine the regions of small colour variation representing the mura defects. According to the survey on use of automated visual inspection in the field of semiconductors by Huang and Pan [20], semiconductor products including wafers, TFT-LCDs and LEDs are inspected for defects using many multivariate techniques one of which is the use of Hotelling statistics for texture analysis.

Tong et al. [21] used machine vision approach integrated with Hotelling T^2 chart to monitor wafer (IC) production process. The quality characteristics selected for charting included number of defects and clustering indices to be monitored for inspection purpose.

Liu et al. [22] developed an MVS system for capturing patterns such as stripes, swirls and ripples with different dimensions. They used wavelet transformation and principal component analysis for texture analysis and Hotelling T^2 and SPE charts for detection of off-specification countertops.

Lin [23, 24] used wavelet characteristics for describing texture properties and Hotelling T^2 control charts of different texture parameters to detect existence of ripple defects in SBL chips of ceramic capacitor. Lin et al. [25] compared the capabilities of a wavelet-Hotelling T^2 control chart approach with that of wavelet-PCA-based approach in detecting surface defects in light-emitting diode (LED) chips and found wavelet-PCA-based approach to be more effective.

Tunak and Linka [26] extracted GLCM features energy, correlation, homogeneity, cluster shade and cluster prominence and plotted using multivariate T^2 charts for detecting the occurrence and location of woven defects.

Tunak et al. [27] used 2D discrete Fourier transform (DFT) and its inverse processed further for getting the images containing only warp and weft. The restored images were then used for assessing weaving density with the help of X-bar control chart in order to locate the sites of potential defects.

Lyu and Chen [28] integrated image processing technologies and multivariate statistical control chart for a component type having two concentric circles. The diameters of the two circles were obtained using image processing techniques and results of 35 samples were plotted in T^2, X^2 and MEWMA chart. Out of control signals were interpreted using Fuchs and Benjamin's MSSD (mean square successive difference) method [29] and Doganaksoy method [30]. They stated that the future scope for this research to use various inspection techniques, different shaped components and develop testing rules for analysing the process using control charts.

Megahed et al. [31] reviewed the work on image monitoring as a special case of spatiotemporal surveillance and use of control charts for process monitoring. Megahed et al. [32] applied spatiotemporal methods for analysis of the image data.

Grieco et al. [33] used integrated machine vision-based control charting approach for monitoring leather cutting process wherein the shape of the monitored profile was compared with baseline model using image data and deviation area was used as the quality characteristic for monitoring. Univariate and multivariate control charting approaches were simulated by using deviation area of the entire profile in first case

Table 1 Summary of research work in MVS-based process monitoring, control

Charting technique	Researcher	Product/process under monitoring
Hotelling T^2	Horst and Negin [16]	Thickness of textile
	Lin and Chiu [19]	Mura defects in TFT-LCD panels
	Tong et al. [21]	Wafer (IC) production process
	Liu et al. [22]	Patterns-stripes, swirls and ripples
	Lin [24]	Ripple defects in SBL chips of ceramic capacitor
	Lin et al. [25]	Surface defects in LED chips
	Tunák and Linka [26]	Woven defects
	Tunák et al. [27]	Weaving density
	Lyu and Chen [28]	Component with 2 concentric circles
EWMA	Nembhard et al. [17]	Colour transition of extruded polymer
	Jing et al. [18]	Mura defects in TFT-LCD panels
MEWMA	Lyu and Chen [28]	Component with 2 concentric circles
Shewhart	Grieco et al. [33]	Leather cutting process

and deviation area vector for different segments of profile in the multivariate case. They concluded that multivariate approach provides better results.

The summary of previous research work in the field is tabulated in Table 1.

4 Conclusion and Future Scope

An integrated approach of machine vision-based control charting can effectively facilitate process control. Multivariate approach will be beneficial over univariate in industrial practices due number of variables determining final quality and utility value of the product. Machine vision systems have been successfully used for inspection and can be implemented further for real time monitoring of production processes to detect out of control signals and shifts in process means to predict the probability of occurrence of non-conformities and control the processes before non-conformities occur.

From the literature reviewed, it is clear that MVS-based process monitoring and control is explored by very few researchers and their results indicate that the approach is feasible. It needs to be explored further for providing a mature vision-based mul-

tivariate statistical control solution to the industry [1, 2]. Most of the attempts have been made to implement this technique for quality control in electronic products and process industries. Their application in mechanical industries is still not explored to the extent required for acceptance of this technique by the industry. The research gaps identified from the literature review include application of MVS-based multivariate control charting technique to various mechanical components and assemblies for identifying dimensional errors and assembly errors, respectively. Further research in this direction would provide a new dimension to industrial quality control systems.

References

1. Woodall, W. and Montgomery, D.: Some Current Directions in the Theory and Application of Statistical Process Monitoring. Journal of Quality Technology, 46(1), (2014) 78–94.
2. Vining, G., Kulahci, M. and Pedersen, S.: Recent Advances and Future Directions for Quality Engineering. Quality and Reliability Engineering International, 32(3), (2015). pp. 863–875.
3. Malamas, E. N., Petrakis, E. G., Zervakis, M., Petit, L., & Legat, J. D.: A survey on industrial vision systems, applications and tools. Image and vision computing, 21(2), (2003) 171–188.
4. Palani, S., & Natarajan, U.: Prediction of surface roughness in CNC end milling by machine vision system using artificial neural network based on 2D Fourier transform. The International Journal of Advanced Manufacturing Technology, 54(9–12), (2011) 1033–1042.
5. Chen, K. H., Boning, D. S., & Welsch, R. E.: Multivariate statistical process control and signature analysis using eigenfactor detection methods. In The 33rd Symposium on the Interface of Computer Science and Statistics, Costa Mesa Ca (2001).
6. Montgomery, D. C.: Introduction to statistical quality control. John Wiley & Sons. (2007).
7. Rogalewicz, M., & Poznańska, P.: The Methodology of Controlling Manufacturing Processes with the Use of Multivariate Statistical Process Control Tools. Journal of Trends in the Development of Machinery and Associated Technology, 17(1), (2013) 89–93.
8. Bersimis, S., Panaretos, J., & Psarakis, S.: Multivariate statistical process control charts and the problem of interpretation: a short overview and some applications in industry. arXiv preprint arXiv:0901.2880. (2009).
9. Hotelling, H.: Multivariate quality control. Techniques of statistical analysis (1947).
10. Runger, G. C., Alt, F. B., & Montgomery, D. C.: Contributors to a multivariate statistical process control chart signal. Communications in Statistics–Theory and Methods, 25(10), (1996) 2203–2213.
11. Jackson, J. E.: Principal components and factor analysis: part I-principal components. Journal of Quality Technology, 12(4), (1980) 201–213.
12. Chua, M. K., & Montgomery, D. C.: Investigation and characterization of a control scheme for multivariate quality control. Quality and Reliability Engineering International, 8(1), (1992) 37–44.
13. Dudzic, M. and Zhang, Y.: On-Line Industrial Implementation of Process Monitoring/Control Applications Using Multivariate Statistical Technologies: Challenges and Opportunities. IFAC Proceedings Volumes, 37(9), (2004) 269–279.
14. Bersimis, S., Psarakis, S. and Panaretos, J.: Multivariate statistical process control charts: an overview. Quality and Reliability Engineering International, 23(5), (2007) 517–543.
15. Lowry, C. A., Woodall, W. H., Champ, C. W., & Rigdon, S. E.: A multivariate exponentially weighted moving average control chart. Technometrics, 34(1), (1992) 46–53.
16. Horst, R. L., & Negin, M.: Vision system for high-resolution dimensional measurements and on-line SPC: Web process application. IEEE Transactions on Industry Applications, 28, (1992) 993–997.

17. Nembhard, H. B., Ferrier, N. J., Osswald, T. A., & Sanz-Uribe, J. R.: An integrated model for statistical and vision monitoring in manufacturing transitions. Quality and Reliability Engineering International, 19(6), (2003) 461–476.
18. Jiang, B. C., Wang, C. C., Tsai, D. M., & Lu, C. J.: LCD surface defect inspection using machine vision. In Proceedings of the fifth Asia pacific industrial engineering and management systems conference. (2004).
19. Lin, H. D., & Chiu, S. W.: Computer-aided vision system for MURA-type defect inspection in liquid crystal displays. In Pacific-Rim Symposium on Image and Video Technology (pp. 442–452). Springer, Berlin, Heidelberg (2006).
20. Huang, S. H., & Pan, Y. C.: Automated visual inspection in the semiconductor industry: A survey. Computers in industry, 66, (2015) 1–10.
21. Tong, L. I., Wang, C. H., & Huang, C. L.: Monitoring defects in IC fabrication using a Hotelling T/sup 2/control chart. IEEE transactions on semiconductor manufacturing, 18(1), (2005) 140–147.
22. Liu, J. J., MacGregor, J. F., Duchesne, C., & Bartolacci, G.: Flotation froth monitoring using multiresolutional multivariate image analysis. Minerals Engineering, 18(1), (2005) 65–76.
23. Lin, H. D.: Automated visual inspection of ripple defects using wavelet characteristic based multivariate statistical approach. Image and Vision Computing, 25(11), (2007) 1785–1801.
24. Lin, H. D.: Computer-aided visual inspection of surface defects in ceramic capacitor chips. Journal of Materials Processing Technology, 189(1), (2007) 19–25.
25. Lin, H. D., Chung, C. Y., & Lin, W. T.: Principal component analysis based on wavelet characteristics applied to automated surface defect inspection. WSEAS Transactions on Computer Research, 3(4), (2008) 193–202.
26. Tunák, M., & Linka, A.: Directional defects in fabrics. Research Journal of Textile and Apparel, 12(2), (2008) 13–22.
27. Tunák, M., Linka, A., & Volf, P.: Automatic assessing and monitoring of weaving density. Fibers and Polymers, 10(6), (2009) 830–836.
28. Lyu, J., & Chen, M.: Automated visual inspection expert system for multivariate statistical process control chart. Expert Systems with Applications, 36(3), (2009) 5113–5118.
29. Fuchs, C., & Benjamini, Y.: Multivariate profile charts for statistical process control. Technometrics, 36, (1994) 182–195.
30. Doganaksoy, N., Faltin, F. W., & Tucker, W. T.: Identification of out-of-control quality characteristics in a multivariate manufacturing environment. Communications in Statistics – Theory and Methods, 20, (1991) 2775–2790.
31. Megahed, F.M.; Woodall, W.H.; and Camelio, J. A.: A Review and Perspective on Control Charting with Image Data. J. Qual. Technol., 43(2), (2011) 83–98.
32. Megahed, F. M., Wells, L. J., Camelio, J. A., & Woodall, W. H.: A spatiotemporal method for the monitoring of image data. Quality and Reliability Engineering International, 28(8), (2012) 967–980.
33. Grieco, A., Pacella, M., & Blaco, M.: Image based quality control of free-form profiles in automatic cutting processes. Procedia CIRP, 62, (2017) 405–410.

Development of Facility Layout for Medium-Scale Industry Using Systematic Layout Planning

Onkar V. Potadar and Ganesh S. Kadam

Abstract In the global competition, it is vital for any organization to minimize the cost of manufacturing or services and at the same time maintain the quality of process. Facility layout problem (FLP) is an important consideration to reduce the material-handling cost and thus improve the productivity. Optimal design and arrangement of facilities have a significant effect on the overall production cost and manufacturing lead time. In this work, the existing process type layout is studied and its transportation cost is determined. The tool SLP (systematic layout planning) is used to propose a new improved layout. As a part of research work, the existing facility layout of IWAI electronics, which is a speaker manufacturing industry, has been studied. The important parameter considered to improve the layout is the relationship between the departments. Computerized Relationship Layout Planning (CORELAP) was used analytically to investigate the total closeness rating (TCR) for the existing layout. The TCR helps to reposition the departments according to their relationship and closeness ranking. A new layout is then proposed which reduced the material-handling cost by 11.63%.

Keywords Process type layout · Facility layout problem (FLP)
Relationship chart (REL) · Systematic layout planning (SLP) · CORELAP

1 Introduction

Plant layout is a plan of optimum arrangement of facilities including personnel, operating equipment, storage space, material-handling equipment, and all other supporting services along with design of best structure to contain all these facilities.

O. V. Potadar (✉) · G. S. Kadam
Department of Mechanical Engineering, SIES Graduate School of Technology, Nerul, Navi
Mumbai 400706, Maharashtra, India
e-mail: onkarhubli@gmail.com

G. S. Kadam
e-mail: gskadam@ymail.com

The aim of a production facility is to manufacture products with minimum cost and maximize the profit. Plant layout of a production facility is a crucial factor in deciding the profitability, cost of product, time required for production, and the total cost incurred. A good layout avoids disruption in material flow, unwanted traveling of material or manpower and thus reduces the cost of transportation. Different authors have worked on various algorithms to come out with best possible layout. But the question is, for small industries why it is important to optimize the layout? What is the overall benefit in terms of cost reduction if one modifies the existing layout? In this work, systematic preparation of a process type layout for small industry is proposed by using SLP method. The study focuses on developing new layout for a leading manufacturer of subwoofers, woofers, full-range speakers, etc., in concern to increase the productivity.

The entire paper is divided into five sections. First section gives an introduction to the current research carried out. Second section summarizes literature review. Third section explains the methodology used in current research to optimize the layout. Results and conclusion parts make the fourth and fifth sections, respectively, which present the outcome of research.

2   Literature Review

Planning a layout in a well-organized manner before any construction is made is highly crucial as it may help in reducing the cost to an appreciable extent. There are many research papers on development of improvement of layouts using various algorithms. Systematic layout planning (SLP) was suggested by Muther [1]. Extending the SLP technique, a study was proposed on concepts and algorithms such as grouping, compounding, and hypothetical distance to modify procedures and improve flexibility in SLP [2]. This study also helped to make the layouts in different shapes. In another work, plant layout of canned fish in terms of material flow, activity relationship, optimum process areas and locations has been designed by SLP [3]. Factors studied in canned fish factory consisted of numbers of machines, space requirements, and process area. The problem in terms of material flow of each operation department was identified. With the SLP method, the new plant layout significantly decreased the distance of material flow. For a jute industry production layout was studied and a new layout was developed based on the systematic layout planning method to reduce production cost and increase productivity [4]. The number of equipments and the traveling area of materials in yarn production were analyzed. The detailed study of the plant layout such as operation process chart, activity relationship chart, and relationship between equipment and area was investigated. The new plant layout showed that the distance and overall cost of material flow from stores to dispatch area were greatly decreased. For a chemical process plant, the plant layout was optimized in reducing the costs of piping, supports, and pumping, while keeping in mind the requirements of distance for safety, operation, and maintenance [5]. The issue was formulated as a quadratic assignment problem,

comprising all costs such as piping, pumping, installation, and supports. In another work [6], Graph-based theory (GBT) was suggested with two phases: adjacency phase and design phase. With these two separate phases, the GBT becomes more powerful and facilitates to design the layout. Pairwise exchange method (PEM) was also found appropriate for reformatting the existing layout [7]. PEM can be used for both equal and unequal sections. Adjacency-based and distance-based problems can be solved by this method. A review article suggested that the particle swarm optimization technique, genetic algorithm, ant colony optimization, and simulated annealing can be effectively used for optimization of multi-objective layout problem [8]. It was also suggested that particle swarm optimization (PSO) can be a proficient algorithm for solving FLP [9]. In another study, a mixed integer optimization was used for efficient solution of large-scale single-floor chemical process plant layout [10]. The final coordinates and dimensions for each of the equipment were obtained from initial feasible solution followed by an iterative improvement procedure.

From the literature review, it is found that many algorithms have been developed for construction and improvement of layouts. For medium-scale industry where the number of facilities or equipment is less it is more feasible and easy to use SLP method and concept of CORELAP algorithm to manually design the layout.

3   Methodology

The work presented here is to develop a new layout for speakers manufacturing industry using SLP. It is a systematic procedure to plan and design the layout. It uses many charts like travel chart, graphs, load–distance chart, REL chart. To modify and propose a new layout using SLP, travel chart, REL chart, and space relationship diagram (SRD) have been used. Travel chart gives the distance between the departments. With the number of pallet loads between the departments and product sequence, one can find out the total cost of transportation incurred using travel chart. REL chart helps to know the closeness between the departments. The detailed work using these techniques has been presented here for the selected industry.

3.1   Travel Chart for Current Layout (From-To-Chart)

This tool helps in obtaining the data of how much entities are being transported from one department to the other. This data is crucial for the analysis of the transportation cost in SLP. Flow matrix along with the distance matrix gives a cumulative result of the cost matrix which is to be optimized (Table 1).

Product sequences listed in Table 2 are helpful in determining the number of parts which move from one section to the other in a given period. The total transportation cost is calculated on the basis of the product sequence. The flow of parts within various departments is counted over a period of one month and assuming that the

Table 1 Information regarding area allotted for various departments

Sr. no.	Departments	Area
1	Woodwork section	60' × 30'
2	Administration section	65' × 30'
3	Component winding	20' × 20'
4	Power room	28' × 30'
5	Assembly line	60' × 60'
6	Quality assurance	15' × 24'
7	Spray painting	30' × 30'
8	Powder painting	30' × 10'
9	Tool room	40' × 20'
10	Packing	15' × 15'

Table 2 Processing sequence for products

Sr. no.	Departments	Area
1	Tweeter speaker	3-5-7-9-6-10
2	Subwoofer speaker	3-5-8-6-10
3	Cabinet speaker	1-9-3-2-8-6-10
4	Full-range speaker	3-5-7-9-8-10
5	Dome tweeter speaker	1-5-3-8-6-10
6	Woofer speaker	3-5-7-6-9-10

transportation cost for any type of product over fixed distance is same. With this assumption and by using travel chart, one can easily find out the total cost incurred for material handling.

Center-to-center distance is taken as distance between the departments. Table 3 shows number of parts transported between each department in one month. This data is found from the number of pallet loads and demand for each part. Cost matrix is found by multiplying the distance traveled and cost for transporting per unit distance. Unit cost per distance can be assumed to find the total cost of transportation between the departments and hence the total cost of transportation for all products in one month (Tables 4 and 5).

It is observed that the exact resultant cost comes out to be Rs. 177,372.7 per month. Thus, the facility has to devote nearly two lakhs to overcome the cost of transport. This total cost is to be minimized.

Table 3 Number of parts transported between each department in one month

Departments→ ↓	1	2	3	4	5	6	7	8	9	10
1	0	0	0	0	525	0	0	0	350	0
2	0	0	0	0	0	0	0	350	0	0
3	0	350	0	0	795	0	0	525	0	0
4	0	0	0	0	0	300	0	0	0	0
5	0	0	525	0	0	0	715	80	0	0
6	0	0	0	0	0	0	0	0	155	1065
7	0	0	0	0	0	155	0	0	560	0
8	0	0	0	0	0	605	0	0	0	450
9	0	0	350	0	0	110	0	0	0	155
10	0	0	0	0	0	0	0	0	0	0

Table 4 Distance matrix for current layout

Departments→	1	2	3	4	5	6	7	8	9	10
1	0	7.6	6.7	1.21	7.62	10.6	37.4	32.9	25.9	39.3
2	7.6	0	2.1	6.4	6.09	12	42	34.4	27.4	45.4
3	6.7	2.1	0	5.4	3.9	10	40	32.3	28.3	41.7
4	1.2	6.4	5.4	0	6.4	8.8	38.7	31.6	33.8	40.5
5	7.6	6	3.9	6.4	0	6	35.9	28.3	27.4	37.7
6	10.6	12.1	10	8.8	6	0	29.8	31.3	33.5	31.6
7	37.4	42	40	38	35.9	29.8	0	7.62	20.7	4.26
8	32.9	34.4	32	32	28	31.3	7.6	0	13.1	11.8
9	25.9	27.4	28	34	27	33.5	20.7	13.1	0	22.5
10	39.3	43.8	42	40	37	31.6	4.2	11.8	22.5	0

Table 5 Resultant cost matrix (×100 Scale) in Rs.

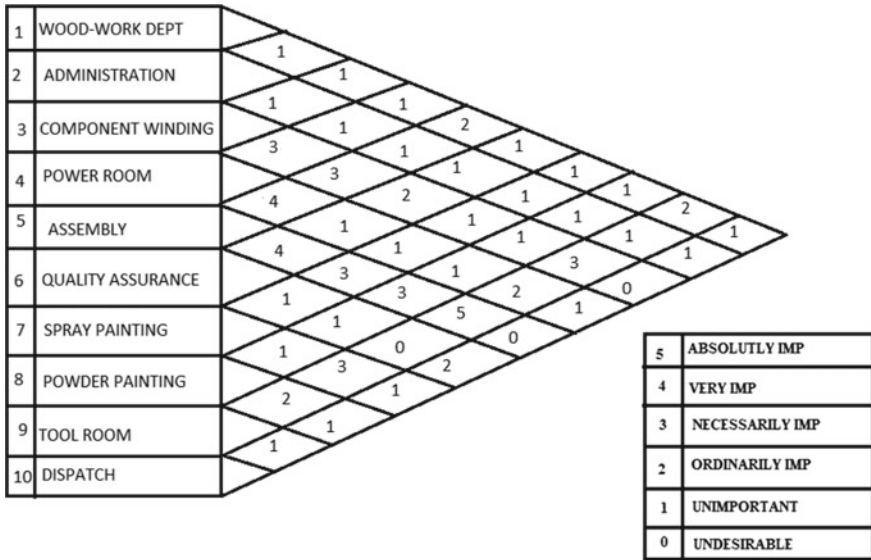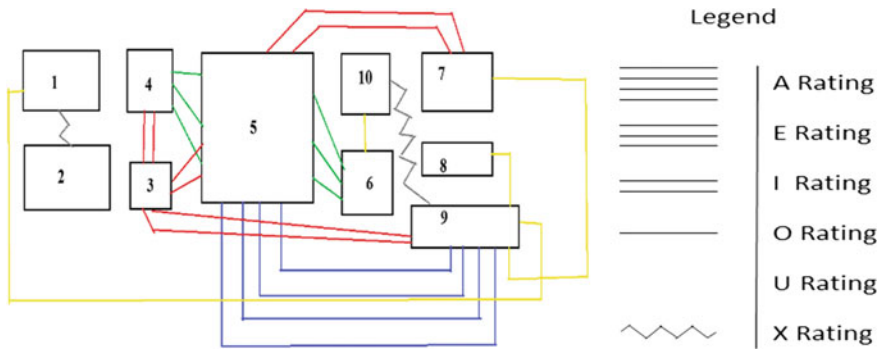| Departments→	1	2	3	4	5	6	7	8	9	10
1	0	0	0	0	40	0	0	0	90	0
2	0	0	0	0	0	0	0	120	0	0
3	0	54	0	0	31	0	0	169	0	0
4	0	0	0	0	0	0	0	0	0	0
5	0	0	2	0	0	0	25	22	0	0
6	0	0	0	0	0	0	0	0	51	337
7	0	0	0	0	0	46	0	0	116	0
8	0	0	0	0	0	189	0	0	0	53
9	0	0	99	0	0	36	0	0	0	34
10	0	0	0	0	0	0	0	0	0	0

Fig. 1 REL chart for various sections

Fig. 2 Space relationship diagram

3.2 Relationship (REL) Chart

The stage of activity relationships performs qualitative analysis toward the closeness relationship decision between activities and resources. The outcomes will be displayed into an activity relationship chart. From the available information, activity relationship diagram was generated, where closeness and relationship between the departments are visually evident. The relationship is defined by a closeness rating system (Figs. 1 and 2; Table 6).

Table 6 Values for closeness or adjacency of departments

Sr. no.	Departments	Area
5	Absolutely necessary	A
4	Especially necessary	E
3	Important the activities be close to each other	I
2	Ordinary closeness to be maintained	O
1	Unimportant	U
0	Not to be close to each other	X

Table 7 TCR for each department

Departments→ ↓	5's	4's	3's	2's	1's	0's	TCR
1	–	–	–	2	7	–	11
2	–	–	–	–	9	–	9
3	–	–	3	2	2	2	15
4	–	1	1	1	6	–	15
5	1	3	4	1	–	–	31
6	–	1	1	4	3	–	18
7	–	–	1	1	7	–	12
8	–	–	1	1	7	–	12
9	1	–	1	5	1	1	19
10	–	–	1	2	4	2	11

3.3 Improving the Layout Based on Total Closeness Rating (TCR)

Closeness rating is the sum of absolute values of relationship between the departments. Based on the TCR, the departments are ranked with highest TCR as the first ranked department. The department with highest TCR or first rank is selected first to start the layout placement (Table 7).

The placement sequence obtained based on the TCR score is as below.

Department sequence → 5-9-6-4-3-10-7-8-1-2

With the sequence of placement obtained, the first department is placed at the middle. The other departments are positioned based upon the weighted placement value which is the sum of the numerical values for all pairs of adjacent departments. Based on the weighted placement rating (WPR), following the CORELAP algorithm technique, the departments are positioned staring from western edge, in counterclockwise direction as shown in Fig. 3. WPR of a department is the sum of closeness ratings with respect to already entered departments in new layout.

Fig. 3 Alternate layout from CORELAP algorithm

$$\text{WPR} = \sum_{k=0}^{i} W \tag{1}$$

where $k = \{\text{departments already placed}\}$.

According to the WPR obtained at various procedures during the CORELAP algorithm, the below layout is formulated.

4 Results

As discussed earlier using the travel charts, the distance matrix and the total cost matrix for new layout are prepared. From the cost matrix, it was found that the total cost comes out to be Rs. 156,739.3 per month which is clearly less than the current estimated cost of the layout.

The speaker manufacturing plant layout was studied for the scope of improvement for reduction in the transportation cost. The on-paper research methodology which included studying the relations between the departments and 'systematic layout planning' gave us a fair reduction in the prime transportation cost. The total saving in transportation cost is Rs. 20,633.4, approximately 11.63%.

5 Conclusion

The objective of our project to reduce the transportation cost incurred within the plant for material movement and develop an alternative layout having least cost for a speaker manufacturing company in order to increase profit margin was achieved. A lot of research have been carried out as it is discussed in the literature review on improving the layouts. The method used in this work is the systematic approach one has to work on before building the layout or installing any facility. The SLP gives the best initial feasible solution for the layout and one can further use advanced techniques to optimize and reduce cost of parts movements within the facility. The important parameter in the work is the relationship between the departments. Many

small and medium scale industries often neglect the importance of adjacency or relationship between the departments and assume that it may not cost the industry much. Since from the results, the decrease in cost by 11.63% is very significant in present global competition. The industry which has been selected for the research work is a medium-scale industry where the total facility area is not too large. Hence, the number of machines or other facilities is less. Though from the literature review, it is found that lot of computer-based techniques are available to improve the layouts, for the current industry it is feasible to use manual method to modify the layout. This also saves confusion over the different methods of optimization. Hence, the method suggested in the work is a manual CORELAP technique which gave better results in terms of cost reduction.

References

1. Muther R.: Systematic Layout Planning, 2nd Edition, CBI Publishing Co Inc., U.S. (1973).
2. Te-King Chien: An empirical study of facility layout using a modified SLP procedure, Journal of Manufacturing Technology Management, vol. 15, pp. 455–465 (2004).
3. W. Wiyaratn, A. Watanapa, P. Kajondecha: Improvement Plant Layout Based on Systematic Layout Planning, IACSIT International Journal of Engineering and Technology, vol 5/1, pp. 76–79 (2013).
4. Md. RiyadHossain, Md. Kamruzzaman Rasel, Subrata Talapatra: Increasing Productivity through Facility Layout Improvement using Systematic Layout Planning Pattern Theory, Global Journal of Researches in Engineering. J General Engineering, vol. 14/7, pp. 71–75 (2014).
5. Sergio N. Franceira, Sheila S.de Almeida, Reginaldo Guirardello: Optimization of Process Plant Layout Using a Quadratic Assignment Problem Model, UNICAMP, School of Chemical Engineering (2005).
6. L.R. Foulds, P.B. Gibbons, J.W. Giffin: Facilities Layout Adjacency Determination - An Experimental Comparison of Three Graph Theoretic Heuristics, Institute for Operations Research and the Management Sciences, Operations Research, vol. 33/5, pp. 1091–1106 (1985).
7. James A. Tompkins, John A. White, Yavuz A. Bozer, J.M.A. Tanchoco: Facilities Planning, 4th Edition, Wiley, US (2010).
8. Parveen Sharma, Ravi Pratap Singh, Dr. Sandeep Singhal: A Review of Meta-heuristic Approaches to Solve Facility Layout Problem, International Journal of Emerging Research in Management & Technology, vol. 2/10, pp. 29–33 (2013).
9. Sujit Kumar Jha, Shiv Ranjan Kumar: Optimal Design of the Facility Layout using Improved Particle Swarm Optimization, International Journal of Research in Mechanical Engineering and Technology, vol. 6/2, pp. 129–134 (2016).
10. Gang Xu, Lazaros G. Papageorgiou: Process plant layout using an improvement-type algorithm, Chemical Engineering Research and Design, vol. 87/6, pp. 780–788 (2009).

Intelligent Unmanned Aerial Vehicles

Parth Thakkar, Anand Balaji and Vaibhav S. Narwane

Abstract Applications of unmanned aerial vehicles technology have shown a very big rise in the recent times. One of the main reasons is less cost, tropical deforestation and advancement in remote sensing technology. Artificial intelligence will become an integral part of unmanned aerial vehicles and can be used for various applications. Incorporation of such intelligence in a practical system is the need of hour. The aim of this paper is to embed artificial intelligence in drones using image processing. Intelligent drones are now the requirement of many fields right from courier delivery to defence, surveillance and rescue. Face-recognition system is proposed which is based on dataset creation, training and recognizer. Implementation of face-recognition system shows acceptable results. We have created an artificial intelligence which is capable of doing face recognition and incorporated it with an UAV.

Keywords Artificial intelligence (AI) · Image processing (IP) · Face recognition
Unmanned aerial vehicles (UAV) · Enhanced vision
Applications of artificial intelligence

Nomenclature

UAV   Unmanned aerial vehicle

P. Thakkar (✉) · A. Balaji
Department of Mechanical Engineering, K. J. Somaiya College of Engineering,
Mumbai, Maharashtra, India
e-mail: parth.st@somaiya.edu

A. Balaji
e-mail: anand.balaji@somaiya.edu

V. S. Narwane
Faculty, Department of Mechanical Engineering, K. J. Somaiya College of Engineering,
Mumbai, Maharashtra, India
e-mail: vsnarwane@somaiya.edu

AI   Artificial intelligence
IP   Image processing
PC   Personal computer
SQL   Structured query language

1 Introduction

Unmanned aerial vehicles (UAVs) also popularly known as drones can be defined as a flying object without any human pilot on board. The first drone came in this world in the year 1849, and since then the technology for drones has developed to a great extent. Initially, drones were used in military applications. But, seeing the cost at which these drones function, attempts were then made to make them more humane [1]. Since the early 1990s, UAV were being used for various applications. Also they were now serving as a platform for robotic studies [2]. With applications in fields such as aerial cinematography, journalism, surveillance and delivery systems, drone technology is one of the highest worth technology [3].

Artificial intelligence (AI) and robotics are becoming one of the next industry buzzwords and are now being used in almost every field. In 1956, John McCarthy held the first academic conference on AI. AI is nothing but an intelligent behaviour of machines rather than the normal behaviour. In subsequent years, it has experienced several waves of optimism. In today's world, AI is considered as a fast growing and an advanced field of science. AI can be achieved in many ways. Various scientists have framed various pathways for achieving AI. But as such, there is no general procedure or method for AI research.

Devices or machines with AI prove to be more efficient and user-friendly than traditional machines. Thus, enormous researchers are working on imparting AI in industrial as well as domestic applications.

The main objective of our paper is to develop an AI which can perform face recognition and incorporating such a system in various platforms such as drones, surveillance cameras and mobile phones. The flow of the paper will be as follows: Sect. 2 briefs about literature review carried out. Adopted methodology is discussed in Sect. 3 followed by conclusion and future scope in Sect. 4.

2 Literature Review

In this section, we produce the literature survey regarding AI, image processing (IP) and drone technology. Various researchers have worked in these fields. For better understanding, this section is divided into two subsections: (i) UAV and its applications and (ii) UAV with AI.

2.1 UAV and Its Applications

When introduced for the first time, UAVs were used as a weapon for war. This raised many questions about how they can be used fruitfully. Its capability to be used as a tool of vision was neglected. This started the research work in using this ability of drones [4]. Construction companies started using these drones to monitor surrounding areas for safety and inspection [5]. It was this time that UAVs found its place in journalism [6]. UAVs equipped with camera have recorded major events such as natural calamities [7] and terrorist activities [8], thus providing a inexpensive but effcient way to collect data from parts where it is not feasible for people to reach [9]. Not only journalism, but also these UAVs found its application in cloud computing as carriers of wireless base stations [10]. Attempts are also going on to use UAVs as a tool for conserving environment. They are used to collect data about forest areas or areas near rivers to analyse and conserve them [11–13].

2.2 UAV with AI

While few researchers were studying about UAV, advancements were made simultaneously in existing UAV by other researchers, which involved using various other concepts like AI or IP along with UAV. AI in UAV can enhance its functioning many folds. Even they can be made to fly autonomously using different techniques like localization and mapping [14]. Various sensors can be used to localize and automate an UAV [15]. After localization, it is important to make the UAV follow desired path. Various controllers such as PID and IMC controllers can be used for this purpose [16]. And in order to fly it continuously, it is necessary to develop a system to replace batteries automatically [17].

Such intelligent UAVs can be used for various applications such as: using radar drone for accident control [18], detecting different types of sinkholes (natural or man-made) using thermal cameras [19], detecting source for gas leaks using particle-filter-based algorithm [20], following a person by position estimation, person detection and trajectory planning [21], path planning using image processing [22], improve somatic sensation [23], botmaster to steal data using Wi-Fi network [24], automation using built-in sensors [25], detecting empty parking slots using car detection via image processing [26], trajectory planning using fuzzy logic controllers [27], object tracking using neural networks and image processing [28].

From above literature review, it is clear that the research work in UAVs and their enhancement is at a different level than it was few years back. But, there can be more advancement in current working of drones. These drones can be used as a tool for searching and surveillance using the camera attached to it. This can be done by modifying the main microcontroller of the drone, or by simply controlling the motion using the feed obtained by the UAV camera. Such UAVs are known as UAV with FPV (first-person view). In this

research paper, we have discussed the use of feed from the camera in order to do face recognition in an external device and control the UAV accordingly.

3 Methodology

The drone which we used is as shown in Fig. 1.

The main step of this paper is incorporation of AI in a camera drone. In this research we have created an AI which can do face recognition. For facial recognition, it is necessary to send the live video feed from the camera drone to a device where actual IP is done. This can be achieved by using the signals from the drone camera using a Wi-Fi module. The device in which actual IP is done is connected with the drone using Wi-Fi. The camera feed from the drone is sent to the external device like PC or laptop. This feed is used for IP and facial recognition to obtain the final output.

Fig. 2 shows the procedure of proposed scheme.

3.1 Face Recognition

A facial recognition system identifies a person from a digital image or a video frame from a video source. It can be done by comparing selected facial features from the image and a face database. Security systems with this capability are preferred
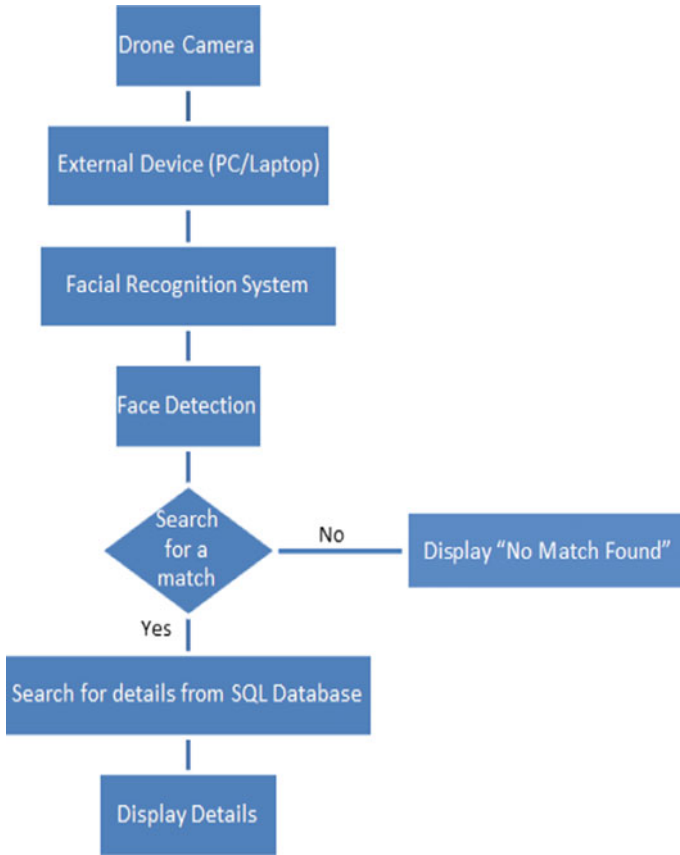
Fig. 1 Pluto drone
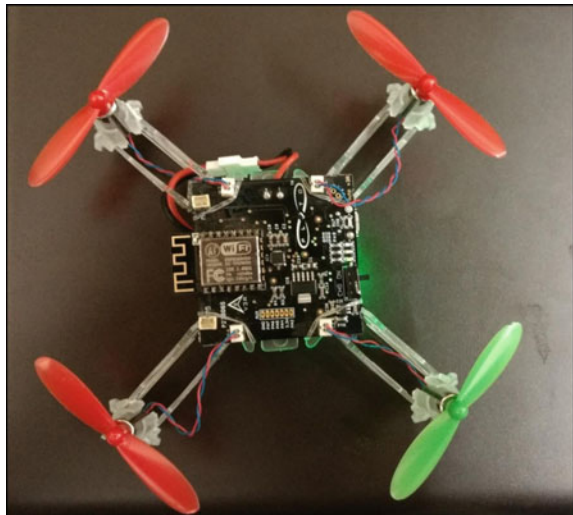
Fig. 2 Flow chart of proposed scheme

over biometrics such as fingerprint or eye iris recognition systems. Recently, it has also become popular as a commercial identification and marketing tool. A face-recognition system can be made using Python, SQL and OpenCV library.

The major components of a face recognition system are elaborated in Sects. 3.1.1–3.1.5.

3.1.1 Face Detection

Face detection can be done using Python and OpenCV library. We are using a cascade classifier in this programme, which can be loaded with a pre-trained xml file. OpenCV already have these pre-trained classifiers ready for face detection. Algorithm of face detection is as follows:
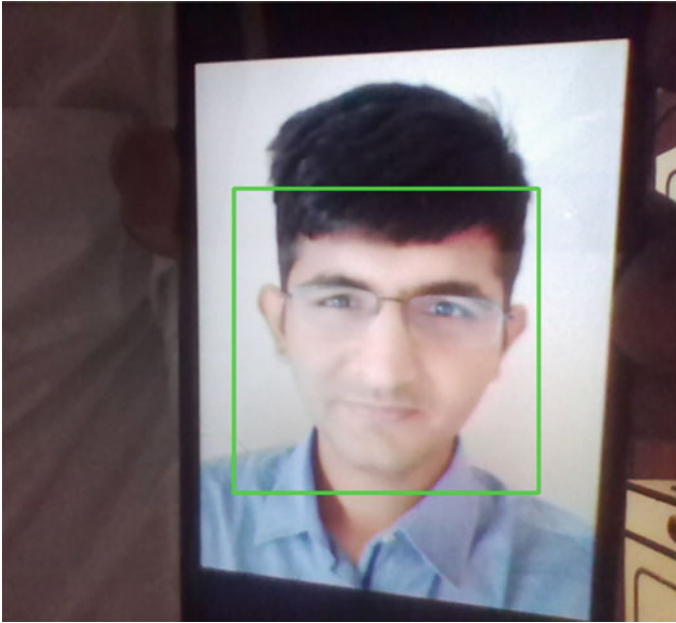
Fig. 3 Result of face detection

Step (1)   Define the device used to capture the images.
Step (2)   Convert the images captured into greyscale images.
Step (3)   Use the face detection classifier to detect the faces.
Step (4)   Display the output on the laptop/computer screen.

Fig. 3 shows the output of face detection with camera. The face is surrounded by a green box.

3.1.2   DataSet Creation

The dataset generator captures few sample faces of one person from a real-time live video frame and assigns a unique ID to it, and it will save those samples images in a folder for future references. All the images that are saved in the dataset are converted into greyscale images. Algorithm of dataset creation is as follows:

Step (1)   Using face detection, detect the faces from the input device.
Step (2)   Creating a dataset folder.
Step (3)   Take id and name from the user.
Step (4)   Take 100 pictures and saving them inside the dataset folder.

Fig. 4 shows the contents of dataset folder.

Fig. 4 Dataset folder

3.1.3   Trainer

To perform face recognition, a face recognizer must be trained first using a pre-labelled dataset. In my previous step, we created a labelled-dataset for our face-recognition system; now, it's time to use that dataset to train a face recognizer using OpenCV and Python. We are using a local binary pattern histogram (LBPH) to train the face images. Algorithm of trainer is as follows:

Step (1)   Access the images from the dataset folder.
Step (2)   Extract the features of the images using local binary pattern histogram (LBPH).

3.1.4   Recognizer

The recognizer is used to recognize faces in real time. If a particular face matches with the database that is created, it would display all the information related to that particular individual. Algorithm of recognizer is as follows:

Step (1)   Define the device used to capture the images.
Step (2)   Use face detection, to detect the face from the input feed.
Step (3)   Access the trained dataset.
Step (4)   Check if information related to the detected image in the database.
Step (5)   If yes, then display the information related to that person on the screen.
Step (6)   If no, then display no match found.

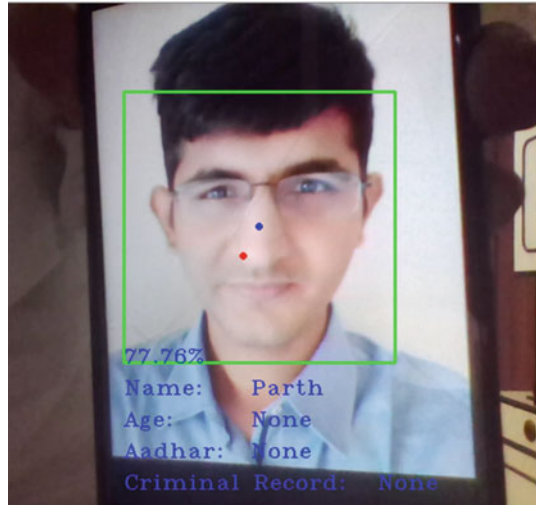**Fig. 5** Result of face
recognition

Fig. 5 shows the result of face recognition, and it displays the information related
to a particular person from the SQL database.

3.1.5   SQL Database

A SQL database is created which is linked with our face-recognition software. When
the detector recognizes a particular face and its unique identity, it would display all
the information linked with that unique identity on the screen. The SQL database
that is created is shown in Fig. 6.

4   Conclusion and Future Scope

AI is considered to be the most advanced and important field in current
world. A lot of researchers are currently working on AI. This proves the
presence of AI in almost all the devices developed in this decade, such
as mobile phones and surveillance cameras. Also, AI-based UAV are nowa-
days seeing an uptrend in domestic applications such as photography. But a
further advancement in the technology would result in high-end applications
too.

Developing UAV with IP would result in a great impact in defence-related appli-
cations. Not only that, but also such UAV would prove helpful in rescue operations.
Implementing advanced AI in such systems could result in complete automation of
UAV.

Implementing systems like the one discussed above can prove effective in appli-
cations like surveillance. It can also be used to track down criminals using facial
recognition techniques. Law enforcements can use such systems to track underage
citizens going off-track. In a domestic basis, schools and colleges can use this method
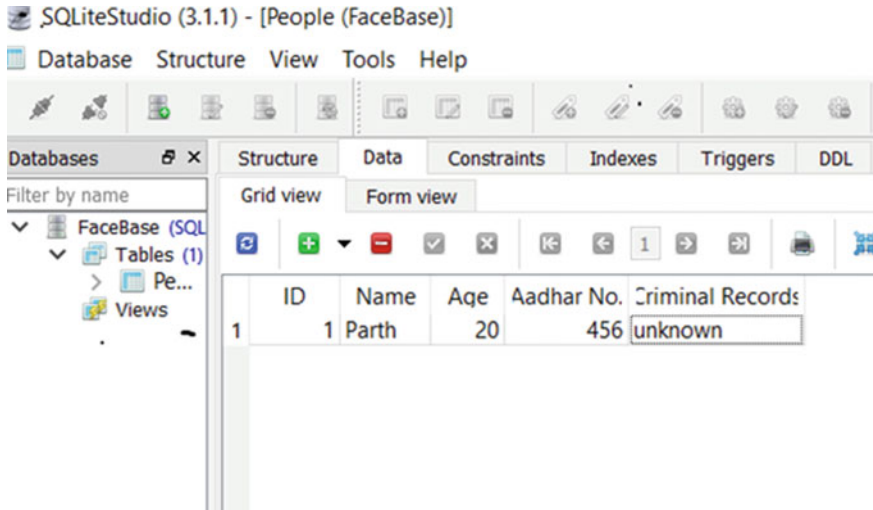
Fig. 6 shows the SQL database which is created and contains the details related a particular person

for the sake of attendance. UAVs are still a growing field of technology with many applications still untouched. A number of applications particularly in big data analytics have not even been thought of as yet.

The AI developed by us right now can only perform face recognition, although in future, it can be improved. We can also create an AI which can perform object recognition, pattern recognition to further enhance its real-life applications. Also, the AI developed can be incorporated with different types of devices such as mobile phones, laptops, robots and surveillance cameras.

References

1. Sandvik, K.B., Lohne, K: The rise of the humanitarian drone: giving content to an emerging concept. Millennium, 43(1), pp. 145–164. (2014)
2. Krajník, T., Vonásek, V., Fišer, D. and Faigl, J, June: AR-drone as a platform for robotic research and education. In International conference on research and education in robotics (pp. 172–186). Springer, Berlin, Heidelberg. (2011)
3. Hall, A.R. and Coyne, C.J.: The political economy of drones. Defence and Peace Economics, 25(5), pp. 445–460. (2014)
4. Stahl, R.: What the drone saw: the cultural optics of the unmanned war. Australian Journal of International Affairs, 67(5), pp. 659–674. (2013)
5. Irizarry, J., Gheisari, M. and Walker, B.N. Usability assessment of drone technology as safety inspection tools. Journal of Information Technology in Construction (ITcon), 17(12), pp. 194–212. (2012)
6. Holton, A.E., Lawson, S. and Love, C. Unmanned Aerial Vehicles: Opportunities, barriers, and the future of "drone journalism". Journalism Practice, 9(5), pp. 634–650. (2015)
7. Gynnild, A. The Robot Eye Witness: Extending visual journalism through drone surveillance. Digital journalism, 2(3), pp. 334–343. (2014)
8. Tremayne, M. and Clark, A. New perspectives from the sky: Unmanned aerial vehicles and journalism. Digital journalism, 2(2), pp. 232–246. (2014)

9. Culver, K.B. From battlefield to newsroom: Ethical implications of drone technology in journalism. Journal of mass media ethics, 29(1), pp. 52–64. (2014)

10. Mozaffari, M., Saad, W., Bennis, M. and Debbah, M. Drone small cells in the clouds: Design, deployment and performance analysis. In Global Communications Conference (GLOBECOM), 2015 IEEE (pp. 1–6). IEEE. (2015)

11. Koh, L.P. and Wich, S.A. Dawn of drone ecology: low-cost autonomous aerial vehicles for conservation. Tropical Conservation Science, 5(2), pp. 121–132. (2012)

12. Tang, L. and Shao, G. Drone remote sensing for forestry research and practices. Journal of Forestry Research, 26(4), pp. 791–797. (2015)

13. Taufik, A., Okamoto, S. and Lee, J.H. 3D Mapping of an Environment around a River Using Image Processing of Photo Images Captured by a Multi-Rotor Drone and 3D Map Modeling Using a 3D Printer. (2016)

14. Dijkshoorn, N. Simultaneous localization and mapping with the ar. drone. PhD diss., Masters thesis, Universiteit van Amsterdam. (2012)

15. Dijkshoorn, N. and Visser, A. Integrating sensor and motion models to localize an autonomous ar. drone. International Journal of Micro Air Vehicles, 3(4), pp. 183–200. (2011)

16. Hernandez, A., Copot, C., De Keyser, R., Vlas, T. and Nascu, I. Identification and path following control of an AR. Drone quadrotor. In System Theory, Control and Computing (ICSTCC), 2013 17th International Conference (pp. 583–588). IEEE. (2013)

17. Fujii, K., Higuchi, K. and Rekimoto, J. Endless flyer: a continuous flying drone with automatic battery replacement. In Ubiquitous Intelligence and Computing, 2013 IEEE 10th International Conference on and 10th International Conference on Autonomic and Trusted Computing (UIC/ATC) (pp. 216–223). IEEE. (2013)

18. Freedman, M., Teed, N. and Migletz, J. Effect of radar drone operation on speeds at high crash risk locations. Transportation Research Record, 1464, p. 69. (1994)

19. Lee, E.J., Shin, S.Y., Ko, B.C. and Chang, C. Early sinkhole detection using a drone-based thermal camera and image processing. Infrared Physics & Technology, 78, pp. 223–232. (2016)

20. Bartholmai, M. and Neumann, P. Micro-drone for gas measurement in hazardous scenarios via remote sensing. In Proceedings of. (2010)

21. Lugo, J.J. and Zell, A. Framework for autonomous on-board navigation with the AR. Drone. Journal of Intelligent & Robotic Systems, 73(1-4), pp. 401–412. (2014)

22. Taufik, A., Okamoto, S. and Lee, J.H. Multi-Rotor Drone to Fly Autonomously along a River Using a Single-Lens Camera and Image Processing. International Journal of Mechanical Engineering, 4(6), pp. 39–49. (2015)

23. Ikeuchi, K., Otsuka, T., Yoshii, A., Sakamoto, M. and Nakajima, T. KinecDrone: enhancing somatic sensation to fly in the sky with Kinect and AR. Drone. In Proceedings of the 5th Augmented Human International Conference (p. 53). ACM. (2014)

24. Reed, T., Geis, J. and Dietrich, S. SkyNET: A 3G-Enabled Mobile Attack Drone and Stealth Botmaster. In WOOT (pp. 28–36). (2011)

25. Sun, Y. Modeling, identification and control of a quad-rotor drone using low-resolution sensing. (2012)

26. Maria, G., Baccaglini, E., Brevi, D., Gavelli, M. and Scopigno, R. A drone-based image processing system for car detection in a smart transport infrastructure. In Electrotechnical Conference (MELECON), 2016 18th Mediterranean (pp. 1–5). IEEE. (2016)

27. Prayitno, A., Indrawati, V. and Utomo, G. Trajectory tracking of AR. Drone quadrotor using fuzzy logic controller. TELKOMNIKA (Telecommunication Computing Electronics and Control), 12(4), pp. 819–828. (2014)

28. Kurniawan, M.N. and Widiyanto, D. Implementation of Image Processing Algorithms and Glvq to Track an Object Using Ar. drone Camera. Jurnal Ilmu Komputer dan Informasi, 7(2), pp. 108–115. (2014)

Study on Power Consumption of Split Air Conditioner Depending on Distance Between Condenser and Evaporator Units

Bysani Malakondaiah

Abstract Small- and medium-scale industries, residential buildings and offices are usually using split air conditioners for comfort of people and sometimes for storing of hygroscopic materials. Air-conditioning units are desired to have more energy efficiency, low cost and reliable operation. The installer would be using a length of pipe which is convenient to him between indoor and outdoor units. However, 50% of installations are too far away from the manufacturers stipulated length. As per industry sales trends, more and more people are going for split AC than window AC. Even some reputed builders in metropolitan cities are providing concealed copper pipes for fitting split AC, and no provision for window AC fitting. This theoretical analysis is trying to assess the power consumption of split air conditioner depending on the distance between condenser and evaporator units. The installation aspects of the air-conditioning system must be considered to improve the efficiency. The length of the pipe connecting indoor and outdoor units affects the power consumption to a large extent. The results showed that there is almost 40% increase in power consumption for a pipe length of 30.48 m (100 ft).

Keywords Equivalent length · Split AC · Power consumption · Pipe length

1 Introduction

Saving of energy means effective utilization of the available energy. Residential houses, small-scale industries and offices mostly use split air-conditioning system due to small working load. With rapid change in global environment, the quantity of power consumed by household appliances like air conditioners, fridges and water heaters is increasing tremendously. The current consumption by AC systems alone

B. Malakondaiah (✉)
Basic Science and Humanities Department, SFIT, Borivali (W),
Mumbai, India
e-mail: mbysani@gmail.com

is around 20% of the entire consumption and is steadily increasing every year, so it is worth in concentrating on reduction of this power consumption.

Split air conditioners are preferred by only industries and affluent homes is no more a fact. The less price difference between window air conditioners and split air conditioners is also supporting this transition. The better aesthetic appearance and silent operation of the split air conditioners are also a desirable feature supporting the migration from window air conditioners to split air conditioners [1]. One of the AC manufacturers Samsung India announced that they are discontinuing the production of window AC systems from 2012, because of decrease in the sales of window AC. There are around 3.2 million air conditioners in India. The split air conditioners account over 75%. According to Samsung India Vice President Mr. Mahesh Krishnan, use of window ACs in India will come down drastically to nil in the near future. In 2011, 85% of ACs sold were split ACs. However, as per L.G., there is market for L.G. window ACs. At present, L.G. split AC share is 70%. Air conditioners usage in India is very low around 3%. If more and more people start using AC, there is lot of growth for air conditioners in India, as well as power requirement (Tables 1 and 2).

Nowadays all the reputed builders in metropolitan cities, in their new construction installing, concealed copper pipes for installation of split AC only and no provision for window AC fitting. All the outdoor units are rooted to duct area, leading to more equivalent pipe length for some flats. One of the reputed manufacturers of split AC company after service engineer inspects the system only allows the system to start. If the equivalent length of pipe between indoor and outdoor units exceeds the specified length, they don't give warranty for the compressor. The maximum distance suggested by different manufacturers for 0.8, 1 and 1.5 ton is 35 ft and for 2.0, 3.0 ton it is 50 ft. Survey of literature shows that there is no study has been carried out on this aspect.

Table 1 Household population of air conditioners in India (millions) [2]

Year	2006	2011	2016	2021	2026	2031
Urban	1.7	4.0	8.9	17.5	28.5	40.0
Rural	0.3	0.6	1.3	2.6	4.8	8.0
Total	2.0	4.7	10.2	20.1	33.3	48.0

Table 2 Total power consumed by household air conditioners in India

Year	2006	2011	2016	2021	2026	2031
Air-conditioning operating $10^6 \times$ kWh/Yr	2298	5084	10,783	20,966	34,675	49,913

2 Theoretical Analysis

As the pipe length increases between indoor and outdoor units, there is a pressure drop. The pressure drop is tabulated by Lennox Refrigerant Piping Design and Fabrication Guide as shown in Table 3.

Table 3 simplifies vapour/suction line selection by incorporating all of the calculations involving vapour line sizing, pressure drop, velocity range and tonnage. Assumptions: 3 elbows every 15.24 m (50 ft).

2.1 Effects of Pressure Drop [3]

The design of refrigerant piping involves complex circulation of the refrigerant and oil. The nature of flow is the synergy of many factors, including viscosity, density,

Table 3 R–22 vapour line pressure drop [3]

Unit capacity tons	Suction/vapour line size	R–22 pressure drop Psi/100 ft
1	1/2″	13.0
	5/8″	3.1
1.5	5/8″	6.5
	3/4″	2.4
2	5/8″	12.0
	3/4″	4.2
2.5	3/4″	6.0
	7/8″	3.1
3	3/4″	8.5
	7/8″	4.6
3.5	7/8″	5.9
	1–1/8″	1.4
4	7/8″	7.8
	1–1/8″	1.9
5	7/8″	12.0
	1–1/8″	2.8
6	1–1/8″	4.0
	1–3/8″	1.4
7.5	1–3/8″	2.0
	1–5/8″	0.9
10	1–3/8″	2.4
	1–5/8″	1.4

pressure, velocity, friction and the work involved in forcing the flow. There is a certain pressure drop during the flow of any fluid through the pipe due to friction losses. The pressure drop is a major factor deciding the performance of air-conditioning system. Pressure drop in suction line affects adversely on the cooling capacity and power consumption. Approximately, one per cent reduction in capacity is noted for pressure drop of one pound in the suction line. For R–22 system, a pressure drop of up to 3 psi is generally acceptable in suction line. Pressure drop in suction line increases the volume of refrigerant gas that must be handled by the compressor for a given tonnage. Since the compressor is a constant volume machine, pressure drop means reduced capacity. At a fixed condensing temperature, the compression ratio increases, as the suction pressure drops. As the compression ratio increases, the volumetric efficiency drops, which results in drop in compressor capacity.

The power required to drive the compressor also increases as the compression ratio increases. If 100% liquid with adequate pressure to maintain the required flow is delivered to the expansion valve, pressure drop in line does not cause any capacity loss. There will be a pressure drop due to lift which needs to be considered in calculation of whole pressure drop. At standard liquid temperatures, R–22 pressure descends 0.5 lb per foot of upright liquid lift. The liquid pressure before expansion device must be high enough to maintain the flow through expansion device. For R-22, to have full refrigerant flow at rated capacity, a pressure drop of 100 psi across the expansion valve and distributor is necessary. So, the refrigerant has to be delivered to expansion valve at a pressure more than 11.90 kg/cm^2 (175 psi) for R–22.

Along with above considerations, in commercial split air conditioners and residential installations more than 50 ft pipe length, special design considerations has to be followed to have satisfactory system performance. An improper design of system may result in a considerable loss of cooling capacity or even the compressor damage.

3 P–H Diagram and Power Calculations

R-22 system works properly at a suction pressure of around 4.08 kg/cm^2 (60 psi), so the general range of working pressures of R-22 system is 4.08–4.42 kg/cm^2 (60–65 psi) suction pressure and 13.60–17.00 kg/cm^2 (200–250 psi) condensing (discharge) pressure. It was assumed that a system working in between 4.08 kg/cm^2 (60 psi) suction and 13.60 kg/cm^2 (200 psi) condenses pressure, at 34 °C. Then by considering the pressure drop for 100 ft pipe, the theoretical calculations were carried out.

From Tables 3 and 4 ton AC with 5/8″ suction pipeline the pressure drop for every 100 feet increase in length is 12 psi. Plotted both cycles, i.e., the cycles working between 4.08 kg/cm^2 (60 psi) suction and 13.60 kg/cm^2 (200 psi) discharge or condensing pressure at 34 °C, and another cycle working between 3.26 kg/cm^2 (48 psi) suction (60−12 psi pressure drop =

Table 4 Power consumption at different lengths

S. No.	Power consumption at 5.8 m (19 ft) el (kW)	Power consumption at different EL (kW)	% change in power consumption wrt to 19 ft
1	1.188	At 9.14 m (30 ft) EL = 1.248	5.05
2	1.188	At 12.2 m (40 ft) EL = 1.308	10.1
3	1.188	At 15.24 m (50 ft) EL = 1.368	15.15
4	1.188	At 18.3 m (60 ft) EL = 1.428	20.20
5	1.188	At 21.34 m (70 ft) EL = 1.488	25.25
6	1.188	At 24.38 m (80 ft) EL = 1.548	30.30
7	1.188	At 27.43 m (90 ft) EL = 1.608	35.35
8	1.188	At 30.48 m (100 ft) EL = 1.667	40.40

48 psi) and 13.60 kg/cm^2 (200 psi) discharge on P–h Chart for R-22.
For expansion from 200 to 60 psi the refrigerating effect = 393−233 = 160 kJ/kg

$$\text{Isentropic compression work done} = 420-393 = 27 \text{ kJ/kg}$$

For expansion from 200 to 48 psi the refrigerating effect = 389−233 = 156 kJ/kg

$$\text{Isentropic compression work done} = 425-389 = 36 \text{ kJ/kg}$$

Anas Farraj et al. have studied the replacement of R-22 with Drop—In Hydro Carbon Mixture. The R-22 flow rate for the 1 ton split AC is 0.022 kg/s. (refer Fig. 1) [4].

Therefore, for 2 Ton split ac the mass flow rate = 0.044 kg/s.

For expansion from 200 to 60 psi the refrigerating effect
$$= 160 \text{ kJ/kg} \times 0.044 \text{ kg/s}$$
$$= 7.04 \text{ kJ/s}$$

Isentropic compression work done $= 27 \text{ kJ/kg} \times 0.044 \text{ kg/s}$
$$= 1.188 \text{ kJ/s}$$
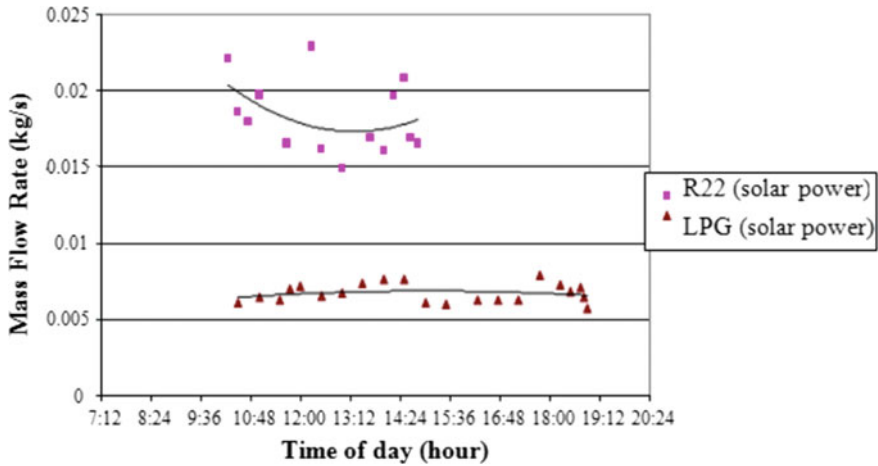
For expansion from 200 to 48 psi the refrigerating effect

Fig. 1 Mass flow rate using R–22 and LPGM

$$= 156\,\text{kJ/kg} \times 0.044\,\text{kg/s}$$
$$= 6.864\,\text{kJ/s}$$

$$\text{Isentropic compression work done} = 36\,\text{kJ/kg} \times 0.044\,\text{kg/s}$$
$$= 1.584\,\text{kJ/s}.$$

As the compression ratio increases, the volumetric efficiency drops, which results in drop in compressor capacity. If the volumetric efficiency is assumed to be 5% less in the case of 48 psi cycle, then the work done $= 1.584/0.95 = 1.667$ kJ/s.

$$\text{Therefore the \% change in power consumption or work done}$$
$$= (1.667-1.188)/1.188 \times 100$$
$$= 40.35\%$$

The pressure drop given by Darcy–Weisbach equation is linear for constant velocity.

$$h_\text{f} = f_\text{D} \cdot \frac{L}{D} \cdot \frac{V^2}{2g}$$

So the pressure drop for every 5.8 m (10 ft) length is 1.2 psi. Therefore, the power consumption at different lengths recorded in Table 2. DBT and RH assumed to be constant at all lengths and at all the time (Fig. 2).
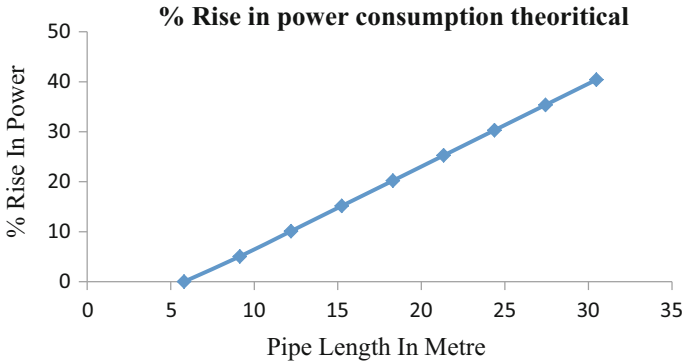
% Rise in power consumption theoritical

Fig. 2 Theoretical analysis of power consumption at different lengths

4 Conclusions

- The installation aspects of the air-conditioning system must be considered to improve the efficiency.
- The length of the pipe connecting indoor and outdoor units affects the power consumption to a large extent.
- The results showed that there is almost 40% increase in power consumption for a pipe length of 30.48 m (100 ft).

References

1. The Hindu Business line article: Air Conditioner sales in India: February 15, 2012
2. The World Bank, Draft: Residential consumption of Electricity in India: July 2008, pp 18 & 59
3. Lennox Refrigerant Piping Design and Fabrication guide: Lennox Industries Inc. (2006)
4. Farraj A., Mallouhb M.A., Kalendarc A., Al-Shqirated A. and Hammada M.: Experimental Study of Solar Powered Air Conditioning Unit Using Drop – In Hydro Carbon Mixture to Replace R-22. Jordan Journal of Mechanical and Industrial Engineering. Volume 6, Number 1, 63–70 (2012)

Monte Carlo Simulation of Arrival of Materials on Assembly Line

Jimit Shelat

Abstract With the increase in market demand and to meet the requirements of customer, it is very difficult for any factory to achieve its target with full efficiency to make a product with a number of small assemblies we need material planning and we need to ensure that the flow of material on production line is uninterrupted. In this paper, I have simulated material arrival using Monte Carlo simulation, which can predict future arrival of material. By using predicted data, we can manage future irregularities in arrival of material.

Keywords Chi-square test · Random numbers · Cumulative probability

1 Introduction

Simulation is a representative model for real-time situations according to **DONALD G MALCOLN** a simulated model may be defined as one which depicts working of a large-scale system of men, machines, materials, and information operating over a period in a simulated environment of the actual real-world condition Monte Carlo simulation is a type of simulation that relies on repeated random sampling and statistical analysis to compute the results. Mathematical model is defined as shown in Fig. 1. This method of simulation is the result of random experiments, experiments for which the specific result is not known in advance [1]. This technique is used only for application involving random numbers to solve deterministic problem. Deterministic models are those models in which input and output variables are not permitted to be a random variable. This method can be applied where there is randomness in the system, e.g., randomness in arrival of material.

The remaining part of the paper is as follows: In next section, we will discuss a few terminologies about the simulation. Then we will discuss methodology (steps) to do Monte Carlo simulation, and then real-life problem of factory material arrival to
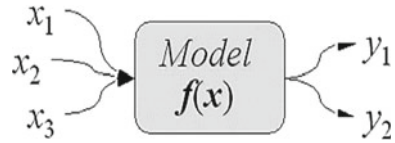
J. Shelat (✉)
Fr. Conceicao Rodrigues College of Engineering, Bandra, Mumbai 400050, India
e-mail: jimitshelat@gmail.com

Fig. 1 Mathematical model

illustrate the simulation method. And at the end chi-square test to see that distribution is uniform or not.

2 Terminologies

Statistical distributions. *probability distributions* are defined as the outcome which comes by changing the random variable, and the probability of occurrence of those outcomes. When the random variable takes the value, which is discrete in nature, the corresponding probability distributions are called discrete probability distributions. Examples of this kind are the binomial distribution, Poisson distribution, hypergeometric distribution, when the random variable takes values which are continuous in nature, the corresponding probability distributions are called continuous probability distributions. E.g., normal, exponential, and gamma distributions.

Random sampling. In statistics, selection of representative unit from population is called a *sample*. In random sampling, the samples are drawn at random from the population, which implies that each unit of population has an equal chance of being included in the sample, e.g., from 1000 material for testing we choose 50 of them then there is an equal probability for each material being chosen.

Random number generator. Monte Carlo simulation needs the generation of a sequence of random number which constitutes an integral part of the simulation model and also helps to determine probability distribution. Generally, roulette wheel, dice rolling, mid-square method, by computer, computer codes, etc., are used for random number generation.

2.1 Steps for Monte Carlo Simulation

The following steps are mainly performed for the Monte Carlo simulation.

Model Generation. Every Monte Carlo simulation of a problem starts with defining the objective of problem and the factors which can affect the objective of problem.

Construction of model. When we are satisfied with the objective of the model, we specify the parameters for model. We also decide which distribution will be used, for how many number of times we want to simulate, defining the relationship between variables.

Random Variable Generation. After we have identified the nature of distributions for the input variables, we generate a set of random numbers (also called random samples) from these distributions. This random number can be generated by any one above-mentioned method.

Final Analysis and Decision Making. After this, we perform simulation for 'n' number of times and we get the results, then we will evaluate the results and formulate the report for advice to management on the actions to be taken.

2.2 *Nonlinear Optimization [2]*

We can also use nonlinear optimization for estimating the unknown parameters of a distribution.e.g., curve of distribution i.e. normal distribution, uniformity of distribution etc.. Different methods can be used for this purpose, such as: goodness-of-fit statistics, sum-squared difference from sample moments (mean, variance, skewness, kurtosis), or sum-squared difference from the sample percentiles (or quartiles or deciles). E.g., chi-square test

3 Material Arrival Data on Assembly Line for 10 Days

See Table 1.

3.1 *Assigning Random Numbers*

1. To generate an event in simulation in an unbiased manner, we assign random numbers to events in the same proportion as their probability of occurrence.
2. Suppose we have 100 random numbers from 0 to 99 then 12% of them will represent material A so numbers from 0 to 12 must be assigned to A, 13% of them will represent material B so numbers from 13 to 26 must be assigned to B, etc.
3. Assignment of random number follows cumulative probability distribution of demand as shown in Table 2.

Table 1 Material arrival data

Material	Day 1	Day 2	Day 3	Day 4	Day 5	Day 6	Day 7	Day 8	Day 9	Day 10	Probability
A	●	●	●	●	●	○	○	●	○	○	0.1276
B	○	●	●	●	○	●	●	●	○	●	0.1489
C	○	○	●	○	○	○	●	○	○	○	0.0425
D	○	○	○	○	●	○	○	○	○	○	0.0212
E	●	●	○	○	○	○	○	○	○	○	0.0425
F	○	○	●	○	○	●	●	○	○	●	0.0363
G	●	●	●	○	●	●	○	○	○	○	0.1063
H	○	○	●	○	○	●	○	○	○	○	0.0425
I	○	●	○	○	○	○	○	○	○	●	0.0425
J	○	○	○	●	●	○	○	○	○	○	0.0425
K	●	○	●	●	○	●	○	●	○	○	0.0363
L	●	○	●	●	●	●	○	○	○	○	0.1063
M	○	●	○	○	○	○	○	●	○	●	0.1276
N	○	○	○	○	●	○	○	○	○	○	0.0212
O	○	○	●	○	●	○	○	○	○	○	0.0425

Note ● arrived; ○ not arrived

Table 2 Assigning random number and time

Cumulative probability	Random numbers assigned	Time assigned by most in min for 2 men
0.1276	00–12	26
0.2765	13–26	40
0.319	27–30	26
0.3402	31–32	4
0.3827	33–36	66
0.419	37–39	640
0.5253	40–49	2
0.5678	50–53	6
0.6103	54–57	6
0.6528	58–61	40
0.6891	62–64	10
0.7954	65–74	16
0.923	75–86	32
0.9442	87–88	4
0.9867	89–92	4

3.2 Assigning Time to Do Assembly Using Most Maynard Operation Sequence Technique

1. After assigning random numbers, we assign time to do assembly of material which is calculated using Maynard operation sequence technique.
2. 1TMU = 0.00001 h.
3. 1TMU = 0.0006 min.
4. 1TMU = 0.036 s.

3.3 Generation of Random Numbers Using Microsoft Excel (for 519 Days)

1. Random numbers are generated using excel formula (=rand between (1,92)).
2. After the random numbers are generated, we will assign material using following code (Table 3).

Table 3 Generated random number shown for 25 days

Random numbers	Material	Time loss in minutes
15	B	40
23	B	40
23	B	40
69	L	16
6	A	26
36	E	66
64	K	10
38	F	640
7	A	26
37	F	640
3	A	26
60	J	40
45	G	2
5	A	26
13	B	40
12	A	26
49	G	2
65	L	16
64	K	10
22	B	40
16	B	40
19	B	40
18	B	40
10	A	26
70	L	16

CODE IN EXCEL

```
=IF(M2<=12,$A$2,IF(AND(M2>=13,M2<=26),$A$3,IF(AND(M2>=27,M2<
=30),$A$4,IF(AND(M2>=31,M2<=32),$A$5,IF(AND(M2>=33,M2<=36),$
A$6,IF(AND(M2>=37,M2<=39),$A$7,IF(AND(M2>=40,M2<=49),$A$8,IF
(AND(M2>=50,M2<=53),$A$9,IF(AND(M2>=54,M2<=57),$A$10,IF(AND(
M2>=58,M2<=61),$A$11,IF(AND(M2>=62,M2<=64),$A$12,IF(AND(M2>=
65,M2<=74),$A$13,IF(AND(M2>=75,M2<=86),$A$14,IF(AND(M2>=87,M
2<=88),$A$15,IF(AND(M2>=89,M2<=92),$A$16)))))))))))))))
```

3.4 Result

See Table 4.

Table 4 Simulated results for 519 days

Material	Days	$P(x)$	% of Arrival
A	71	0.137	13.68
B	83	0.160	15.99
C	27	0.052	5.20
D	11	0.021	2.12
E	13	0.025	2.50
F	18	0.035	3.47
G	63	0.121	12.14
H	24	0.046	4.62
I	20	0.039	3.85
J	27	0.052	5.20
K	12	0.023	2.31
L	50	0.096	9.63
M	75	0.145	14.45
N	8	0.015	1.54
O	17	0.033	3.28
Time loss		**44.6628131** min/day	
Total time loss		**56.11650485** min	

3.5 Chi-Square Test

Total number of days $= 519$.

Assuming the arrival of material is uniformly distributed.

The number of days material arrived $= 519/15 = 34.6$ (Table 5).

$$\chi^2 = \Sigma = 277.79$$

Also, degree of freedom $= N - 1 = 150 - 1 = 14$.

$$\chi^2_{0.05} = 23.69$$

$$\chi^2 > \chi^2_{0.05}$$

Therefor material arrival is not uniformly distributed.

Table 5 Chi-square test

Observed frequency (O)	Expected frequency (E)	$(O - E)^2/E$
71	34.6	38.29
83	34.6	67.70
27	34.6	1.67
11	34.6	16.10
13	34.6	13.48
18	34.6	7.96
63	34.6	23.31
24	34.6	3.25
20	34.6	6.16
27	34.6	1.67
12	34.6	14.76
50	34.6	6.85
75	34.6	47.17
8	34.6	20.45
17	34.6	8.95

4 Conclusion

From the above results, we can predict the arrival of material in coming months or days and we can also determine uniformity in arrival of material by chi-square test.

References

1. Operation research by S D Sharma
2. Raychaudhuri, Samik: Introduction to Monte Carlo simulation. Simulation Conference, 2008. WSC 2008. Winter. IEEE, (2008)

Recent Developments in the Field of Rapid Prototyping: An Overview

Umesh Sable and Prashant T. Borlepwar

Abstract New technologies are developed every day in the field of manufacturing for better product accuracy, better quality, improved tolerances, etc. Subtractive manufacturing is gradually becoming obsolete due to new non-conventional methods being introduced. Rapid prototyping is one such method in which we can obtain physical models rapidly. Various researches have been done in this field ever since it was discovered back in the late 1900s. This paper tries to overview some of those recent advances in the field of rapid prototyping.

Keywords Rapid prototyping · Additive manufacturing

1 Introduction

Rapid prototyping originates from two main techniques viz. topography and photo-sculpture. It was developed in the nineteenth century. The first methods were developed in the late 1980s. Earlier the process used to be laborious. Hideo Kodama from Japan and Charles Hull from the USA were the first to introduce this technology. Rapid prototyping is the technology that produces physical models directly from a CAD model. The various technologies of rapid prototyping are stereolithography apparatus (SLA), selective laser sintering (SLS), laminated object manufacturing (LMO), inkjet-based systems and 3-D printing.

Subtractive manufacturing methods are not capable of making complex shapes because of the fact that the tool allowance needs to be considered for manufacturing. But for more complex shapes and intricate parts, additive manufacturing methods are

U. Sable (✉)
Maharashtra Institute of Technology, Aurangabad, Maharashtra, India
e-mail: umeshsable8888@gmail.com

P. T. Borlepwar
Department of Mechanical Engineering, Maharashtra Institute of Technology,
Aurangabad, Maharashtra, India
e-mail: borlepwarprashant@gmail.com

mainly used nowadays. Though, large-scale manufacturing may not be quite possible in AM. The prototypes of exact size, shape or volume can be produced which also aid in testing without having to waste precious materials. Thus, AM is quite trendy and has become a very important part of rapid prototyping in today's world.

The recent developments in RP prove that researchers have favouritized this topic which could reinvent manufacturing on a whole new level and also compel us to scrap the age-old and conventional manufacturing techniques. Various RP technologies have been integrated with computer-based systems so as to automize manufacturing. Thus, also in some non-engineering fields, like biomedical, tissue production, orthopaedics, dentistry, etc., RP has been a revolution. This study intends to review the various developments in the field of RP.

2   Literature Review

Dharipalli et al. [1] have classified and compared rapid prototyping technologies. Rather, the classification was done into three categories:

(1)   Solid-based rapid prototyping
(2)   Liquid-based prototyping
(3)   Powder-based prototyping.

The comparison was studied by Dharipalli et al. on the basis of process parameters like raster width, path speed, slice height and tip dimension.

Alves et al. [2] have given the reasons for 3-D shape recovery and also stated that the shape can be emulated by virtual modelling which can be done by computer-aided technologies like rapid prototyping. A BIOCAD system has been used employing algorithms for three-dimensional shape recovery of digital images. The ciliary calibration algorithm will emulate the human vision.

Monzon et al. [3] have strived for achievement of an innovative mould design mainly with the help of electroforming technology. A mandrel (rapid prototyped) has been achieved. Slow production rate of rotational moulding is a disadvantage but can be converted into an advantage. Nickel chloride can be used to increase the conductivity. The primary advantage is that the geometry of the mould can be changed in a few minutes for another design (Figs. 1 and 2).

Sanna Peltola et al. [4] speak of 3-D scaffolds manufacturing using RP. stereolithography process can be used to produce these scaffolds. Mainly, RP helps in satisfying individual needs, elevated accuracy and leverage to control the pore size. However, some cons definitely raise eyebrows like weak bonds between powder particles, roughened surface, post-processing and restrictions on material selection (Figs. 3 and 4).

Yarlagadda et al. [5] designed, developed and evaluated the performance of mould inserts using powder sintering process where materials like maraging steel powder, sintering acid and other binder materials were used. The testing was done using
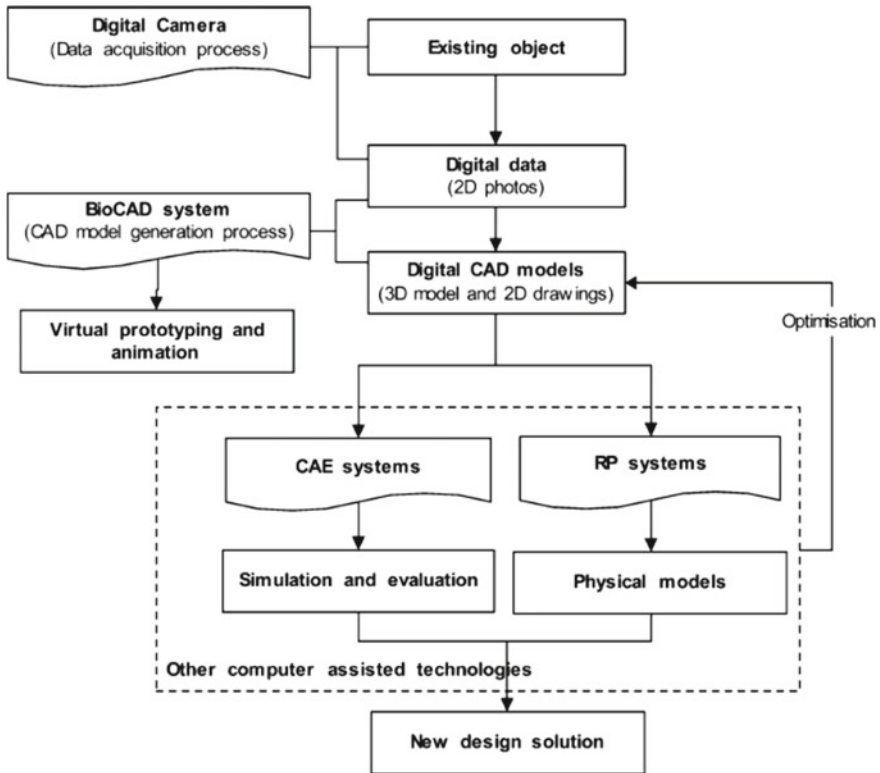
Fig. 1 Representation of a Bio-CAD system [2]

intelligent manufacturing systems for minor changes. IMS specimens were developed. A prototype for the development of IMS stereolithography core model was established. The tolerances of CAD model and functional IMS parts were compared. The other parameters like distortion and shrinkage volumes were also compared and were found to be satisfactory and acceptable. The new IMS specimen showed density more than 95% (Fig. 5).

Laeng et al. [6] speak of laser metal forming process which can produce models directly from a CAD file without the requirement of an intermediate step. The software for rapid metal forming process includes modelling of a 3-D CAD model in standard STL format, generation of layer representation of object and creation of CNC codes for the tool path. Here, a hardware system along with a software system and process parameters were determined (Fig. 6).

Costa et al. [7] studied the degradation of polymer resin through time. The specimens were tested at intervals of 0, 30, 60, 90 and 120 days. Tests like tensile strength test and experimental cantilever beam test were performed. Rapid and virtual prototyping were simultaneously studied. The material used was Veroblue 840. The tensile strain tests were performed on a universal testing machine EMIC DL2000.
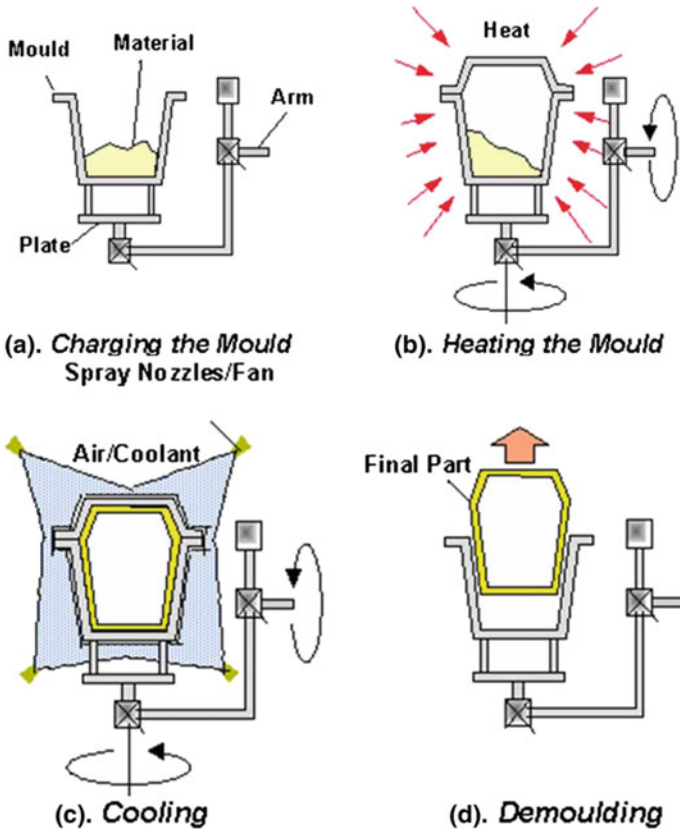
Fig. 2 Rotational moulding [3]
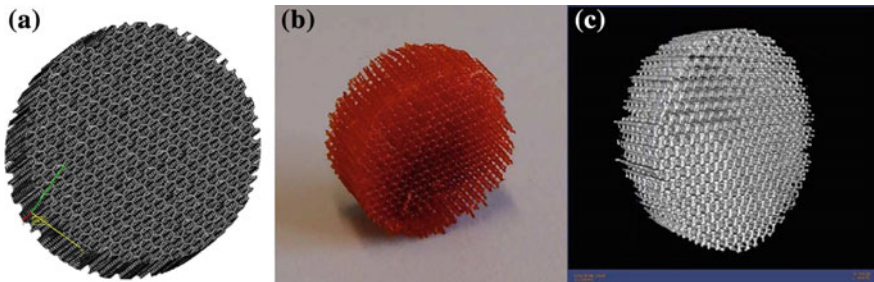
Fig. 3 Example of a scaffold fabricated using stereolithography (SLA). **a** Computer-aided design (CAD) image of the structure. **b** Completed SLA-fabricated scaffold with very regular pore size distribution. **c** Micro-computerized tomography (microCT) image of the scaffold [4]

The value of strength for RP material was observed very near to that proposed by the manufacturer.
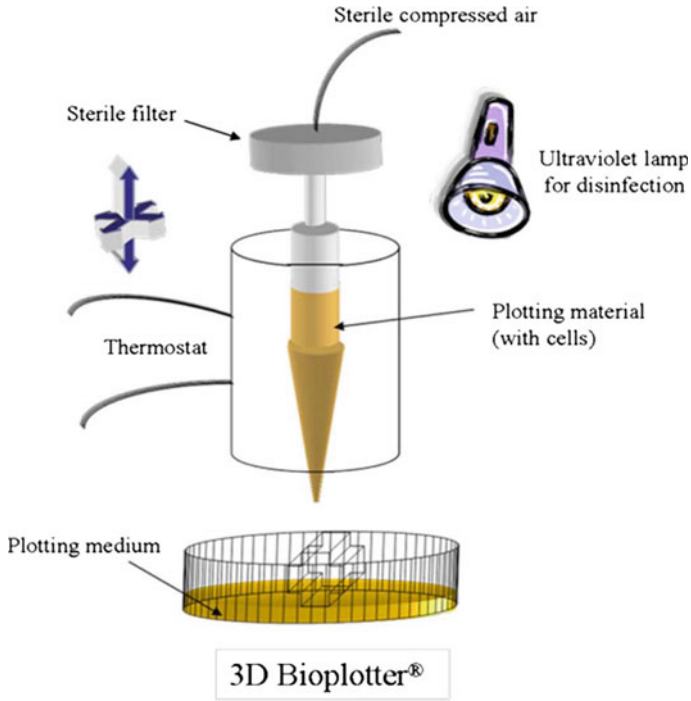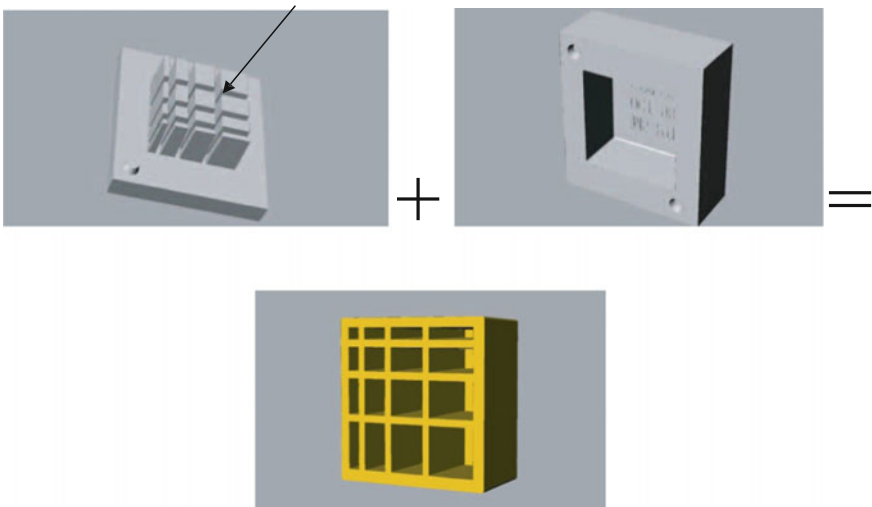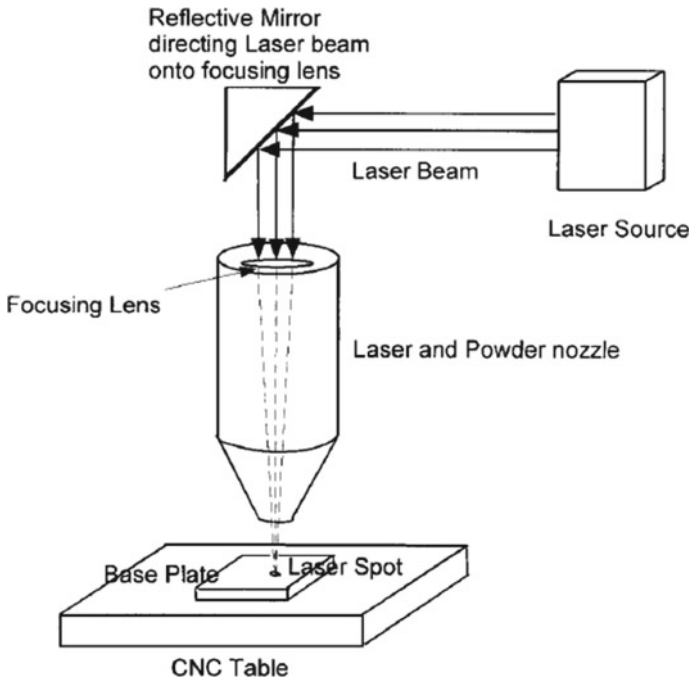
Fig. 4 3-D bioplotter [4]

Fig. 5 Steps involved in IMS part making [5]

Fig. 6 Laser metal forming process [6]

Chaudhary et al. [8] support the RP of high-performance sportswear which plays a rather vital role in deciding various factors like the durability and strength of sportswear. As sports mainly depends on timing, the proper and optimized design of sports accessories play an important role in helping an athlete to win. The process involves 2-D scanning of an athlete's body. Aerodynamic, thermodynamic and hydrodynamic properties are specially taken care of in designing of sportswear. The anthropometric dimensions are used for RP. For the making of a ski jumper, a scanner called NX-16 was used. GRAPHIS software was used for designing the building blocks like zippers and buttons. Wehr et al. [9] have tried to build an experimental set-up by integrating a rolling mill and piezoelectric actuator. A real-time system DS1006 is used as central component. The dynamics of a spindle drive and piezoelectric actuator has to be studied. Thus, a set-up of roll milling and rapid tooling was clubbed and was found to work desirably (Fig. 7).

Kriesi et al. [10] have discussed about a desktop injection moulding machine on which prototypes can be made and tested. The testing was done with the help of a three-point bending test. Some plastic components were prototyped, and four Fs were addressed. Due to some administrative errors, a desktop moulding machine had to be developed. 3-D printers and bench CNC mill were used at TrollLABS. The strength was monitored by a three-point bending test. Firstly, small-sized moulds were produced for surety of strength and then large- and complex-sized moulds
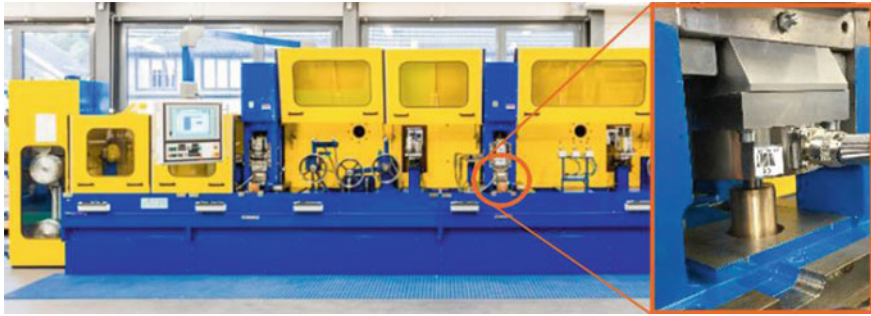
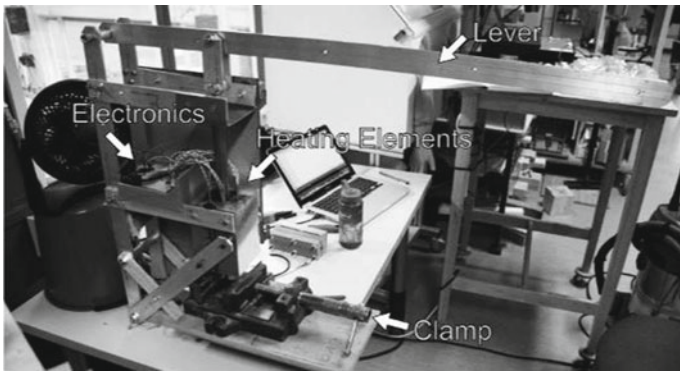**Fig. 7** Integration of rolling mill and piezoelectric actuator [9]

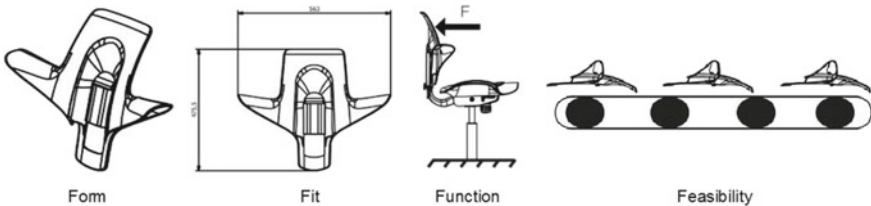**Fig. 8** Desktop injection moulding machine [10]

Fig. 9 The four Fs addressed [10]

were produced. It was observed that the general surface finish of the manufactured part was excellent and a completely intact mould was obtained (Figs. 8 and 9).

Roussi et al. [11] have given the comparative advantages and disadvantages of RP technologies (Table 1).

Sarange et al. [12] have put forth a new idea of biomaterial fabrication which has made it possible to produce scaffolds with mechanical and structural properties similar to bone and teeth. But the problem of balling of nanoparticles was encountered (Fig. 10).

Table 1 Roussi et al. [11] comparison of the basic RP systems

| Technology	Advantages	Disadvantages
SLA	Excellent quality surface, complex geometry, good accuracy	Support structures, parts deform easily, vapours are harmful
SLS	No need for further sintering, no need of supports, high range of materials	The surfaces are rough and porous, Long-time and considerable energy, patterns for precision castings requires, additional processing (infiltration), significant distortions
LOM	Details can be further processed (polished, drilled), ability to manufacture large parts quickly and cheaply	Thin walls have low strength, readily absorb moisture, separation of the parts is difficult
FDM	A wide range of polymeric materials available, machines are easily adjusted and used in an office environment	Support structures, low strength in the vertical direction, process is slow, rough 'textured' outer surface, problematic for tool manufacture
MJM	Suitable for an office environment, build time is short	The supports are removed and leave traces, which limits their use for casting models, strength is low
3D-P	Short deadlines and cheap raw materials, no supporting structures, complex geometry	Delicate details not possible to produce, infiltration is necessary, rough surface
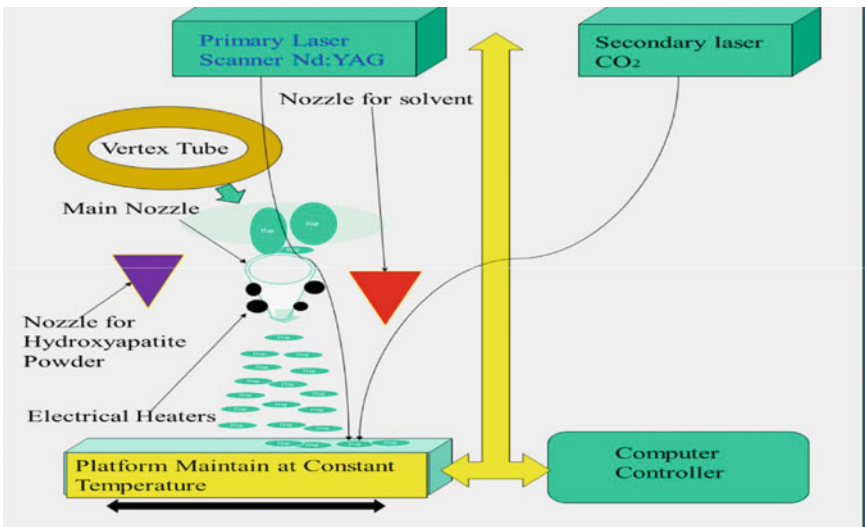
Fig. 10 Experimental set-up given by Sarange et al. [12]

3 Conclusion

Bio-CAD system developed is better for more accuracy in producing the object. The computer-aided process planning (CAPP) will definitely reduce human efforts in RP. The scaffold produced by bioplotter using SLA is definitely a huge leverage in satisfying individual needs. The development of KBRPS ensures faster generation of prototypes at a lower cost. IMS parts prove to be winners with respect to parameters like distortion, shrinkage volume and density. Laser metal forming process can surely eliminate the intermediate step. Also, high-performance sportswear can surely be manufactured using rapid prototyping. We can now emphasize on more research in RP technologies which may stand out. DLRP process can also be thought about because of its flexibility.

References

1. Dharipalli Hyndhavi, S. Bhanu Murthy, Rapid Prototyping Technology- Classification and Comparison, IRJET, Vol. 4, June 2017, 3107–3111
2. Nuno M. F. Alves & Paulo J. S. Bartolo, Automatic 3d shape recovery for Rapid Prototyping, Vol. 3, No 2, June 2008, 123–137
3. Mario Monzon, Maria D. Marrero, Antonio Benitez, Pedro Hernandez & M Kearns, Rapid Prototyping applied to a new development in mould for rotational moulding, Virtual and Physical Prototyping, Vol 2, No 4, Dec 2007, 209–216
4. SannaPeltola, Ferry P. W. Melchels, Dirk W. Grijpma & Minna Kellomaki, A review of rapid prototyping techniques for tissue engineering purposes, Annals of Medicine. 2008; 40: 268–280
5. Prasad K. D. V. Yarlagadda & Lee Kien Wee, Design, Development & evaluation of 3D mold inserts using a rapid prototyping technique & powder sintering process, International Journal of Production Research, Vol 44, No 5, March 2006, 919–935
6. J Laeng, J. G. Stewart & F. W. Liou, Laser Metal forming processes for rapid prototyping—A review, INT. J. PROD. RES, 2000, Vol 38, No 16, 3973–3996
7. Carlos Costa, Paulo Roberto Linzmaier, Felipe M. Pasquali, Rapid Prototyping Material Degradation: A study of Mechanical Properties, IFAC, Management & Control of Production & Logistics, 350–355
8. Harun Chaudhary, FirozAlam, David Mainwaring, Jordi Beneyeto- Ferre, Margaret Tate, Rapid Prototyping of high performance sportswear, Procedia Engineering 34 (2012) 38–43
9. Matthias Wehr, Sven Stockert, Dirk Abel, Gerhard Hert, Rapid control prototyping in cold rolling using piezoelectric actuators, IFAC-Papers Online 49-31 (2016) 55–60
10. Carlo Kriesi, Oystein Bjelland, Martin Steinert, Fast and iterative prototyping for injection moulding- A case study of rapidly prototyping, Procedia Manufacturing 21 (2018) 205–212
11. Roussi Minev, Ekaterin Minev, Technologies for rapid prototyping- basic Concepts, quality issues and modern trends, Scripta Scientifica Medicinae Dentalis, vol. 2, No 1, 2016, pp. 12–22
12. Sarange Shreepad, Warkhedkar Ravi, New Revolutionary Ideas of Material Processing-A Path to Biomaterial Fabrication By Rapid Prototyping, Procedia-Social and Behavioural Sciences 195 (2015) 2761–2768
13. https://en.m.wikipedia.org/wiki/Rapid_prototyping

Performance Study of Stamping Process Using Condition Monitoring: A Review

Tushar Y. Badgujar and Vijay P. Wani

Abstract This paper summarizes activities around the world in the field of stamping machine condition monitoring (CM) and fault diagnosis, in the form of research, development, and application of various tools and techniques. Restricting itself to CM of stamping machine, this paper initially discusses the necessity of condition monitoring, tonnage signature, acoustic signature, vibration signature, and thermal signature as health indicators. Afterward, the acoustic signal is utilized to monitor blanking operation as it is considered most cost-effective and convenient. The acoustic signal power spectral density (PSD) is used to detect variation of sheet thickness. Sheet thickness variation is one of the unavoidable faults associated with the blanking. The paper provides a comprehensive survey of the work done on stamping process CM, expresses the importance of CM and use of CM, fault diagnosis for performance study of the stamping process.

Keywords Stamping machine · Tonnage signature · Acoustic signature Thermal energy signature · FFT · WT · PSD

1 Introduction

Stamping process is used for manufacturing millions of parts of variable size and shape. The various researchers give importance to performance monitoring of stamping system because of its criticalness. In last few decades, condition monitoring experienced evolution regarding the development of sensors, signal processing techniques, and feature extraction. Techniques used for processing is considered to be significant and critical. The various researchers used techniques like fast Fourier transform, wavelet transform, Haar transform, Hilbert Huang transform, power spectral density, fuzzy logic, an artificial neural network for signal processing, feature extraction, and fault diagnosis [1, 2].

T. Y. Badgujar (✉) · V. P. Wani
Department of Mechanical Engineering, MET's Institute of Engineering, Nasik, India
e-mail: tybadgujar@gmail.com

The success of stamping process depends on more than forty associated variables. Faults like blank thickness variation, punch wear, misfeed, binder force variation, misalignment of workpiece/die/punch, and insufficient lubrication encountered while manufacturing products using stamping process. Off-line analyses cannot accurately predict all these faults. Therefore, online monitoring is preferred [3–6].

The present work initially discussed health indicators used for stamping machine CM, data processing and feature extraction techniques. Lastly, the case study detects sheet thickness variation for the blanking process. In stamping operation, clearance between the punch and die is considered as the primary cause of burr formation. The die clearance is set for the particular thickness of the sheet and the material. In the case study, acoustic emission (AE) technique is used to detect variation in the thickness of the blank using power spectral density (PSD).

2 Health Indicators for Stamping Machine

Stamping process is a complicated transient process, which produces non-stationary signals. Several variables influence nature of signal: machine parameters, blank material properties, die design and setup, and process parameters. Critical variables are identified for monitoring, considering failure information, frequency, and associated downtime. Some signatures appreciated by the research are as follows:

2.1 Tonnage Signature

Tonnage signals are rich in feature information and capable of identifying changes in the process variables. The frequency response of the strain gauge is controlled by high inertial of the press structure; it acts as low-pass filter for the signal. Figure 1 shows the tonnage signature of the standard well-performing machine, and different segments are noticeable from it. A fault domain is connected with a particular segment of the signature and fault within a segment identified by an integrated set of signal attribute [7, 8]. Faults like the end of row material, misfeed, slug, variation in sheet thickness, speed variation, and shut height changes are diagnosed using tonnage signature.

2.2 Acoustic Signature

AE is transient stress waves generated by the rapid release of energy in material deformation, crack initiation, propagation, and fracture. AE can be measured using relatively simple instrumentations. The features from suitably processed signals are utilized to characterize the stamping process (material properties of blank, process
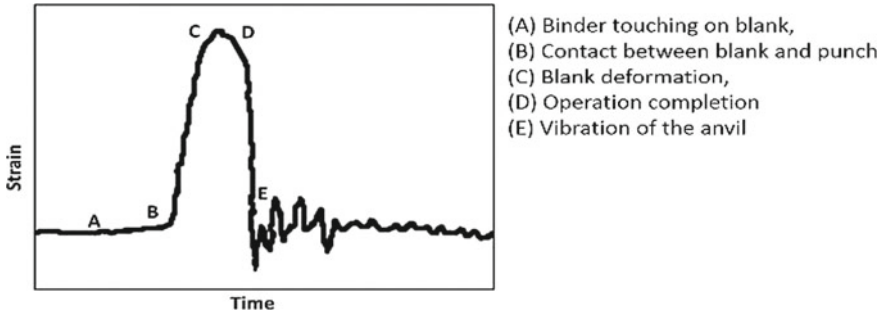
(A) Binder touching on blank,
(B) Contact between blank and punch
(C) Blank deformation,
(D) Operation completion
(E) Vibration of the anvil

Fig. 1 Tonnage signature

variables, etc.). In the feature extraction and diagnosis using AE, transducer and signal transmission path properties have great importance [9, 10].

2.3 Vibration Signature

When faults occur in stamping, it causes variation in dynamic pattern, especially, in the high-frequency band, and the use of vibration is authoritative. The vibration of the press may be caused by many factors. Stamping force is the dominant force that causes the vibration. When the shearing of the blank is completed, operation ends abruptly, and the press attempts to return to its original condition, which also causes vibration. Figure 2 shows the acceleration signal for stamping operation. From the figure, it is interpreted that vibration signal produced in stamping operation is of dynamic nature. The points A, B, C, D, E represent the different phases of operation [11].
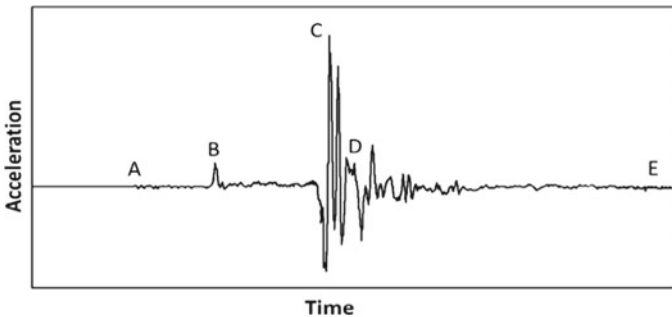
Fig. 2 Vibration signature of press

2.4 Thermal Signature

Understanding strain distribution is significant for die tryout in stamping. The straining of the product can be reconstructed by using the thermal energy distribution. Experimental and analytical studies showing the effect of deformation heating have reported. For strain reconstruction, infrared thermography (IRT) is a non-contact sensing method. In stamping, plastic deformation generates heat energy, which in turn increases the temperature of the surface, especially in deep drawing. The energy conservation principle is used to correlate thermal distribution with a strain in the object. Strain analysis helps in the diagnosis of understressed or overstressed areas of blank to make adjustments in the die and the stamping operations. Thermography is used to capture the thermal image of the object just after processing [12].

3   Signal Processing and Diagnosis

Signal acquired by the sensor is not directly providing information which can be used for diagnosis, but it required processing of it, separation of noise and information, and identification of feature. For the feature extraction and fault diagnosis, various techniques are used by researchers.

3.1 Fast Fourier Transform

Signal data plotted as amplitude versus time are referred as a time domain signature, and used for several types of machinery, to predicting changes in operating conditions. However, time domain data is hard to use. By using fast Fourier transform (FFT), time domain data are converted to Frequency domain. FFT displays signal component of a machine-train as discrete frequency peak. Time domain and frequency domain representations of signal given as:

$$f(t) = e^{j\omega t} = \sin(\omega t) + j\cos(\omega t) \tag{1}$$

$$f(j\omega) = \int\limits_{-\infty}^{+\infty} f(t)e^{-j\omega t}\,dt \tag{2}$$

Frequency domain signals have extensively used in machine condition monitoring [2, 13].

3.2 Wavelet Transform (WT)

Wavelet analysis overcomes the drawbacks of FFT. WT is adaptive time–frequency representation, useful for aperiodic, noisy, periodic signals. WT is sensitive and reliable and can characterize transient components of the signal. It works as a mathematical microscope and benefits in the analysis of localized details [11, 14]. Continuous wavelet transform for signal $f(t)$ is defined as:

$$W_\psi f(s, u) = \frac{1}{\sqrt{s}} \int_{-\infty}^{+\infty} f(t) \psi\left(\frac{t - u}{s}\right) dt \tag{3}$$

3.3 Hilbert Huang Transform (HHT)

To find the instantaneous frequency of the multi-component signal is reasonably tricky. The multi-component signal is decomposed into the mono-component signal using Empirical Mode Decomposition. The multi-component signals may have many similar modes of oscillation at a time. All oscillating modes are designated by an intrinsic mode function (IMF). The IMF is defined in complete multi-component data set, the number of extrema must equal to some of zero crossing, or at the most, it should vary by one. The shifting process is used to obtain the same. First, all local maxima are defined and then by using cubic spline line joined to get an upper envelope. Then, the procedure repeated for local minima to get lower envelop. The Empirical Mode Decomposition (EMD) process of a signal $x(t)$ can be represented as below.

$$x(t) = \sum_{i=1}^{I} c_i + r_I \tag{4}$$

where r_I is residue and $c_i (i = 1, 2, \ldots, I)$ a collection of IMF. The IMFs include different frequency bands [7, 10].

3.4 Artificial Neural Network (ANN)

A primary impetus for the study of neural network (NN) was, how humans understand and learn, based on experiences. Such learning possesses features like sturdiness, gradual degradation, continuous upgrading, distributed intelligence, the accomplishment of significant stability, as well as plasticity in exploring new without losing prior knowledge. NN is comprised of neurons functioning in parallel and can be trained to perform a particular function by adjusting the weights of connections. Commonly,

Fig. 3 Layer arrangement in ANN
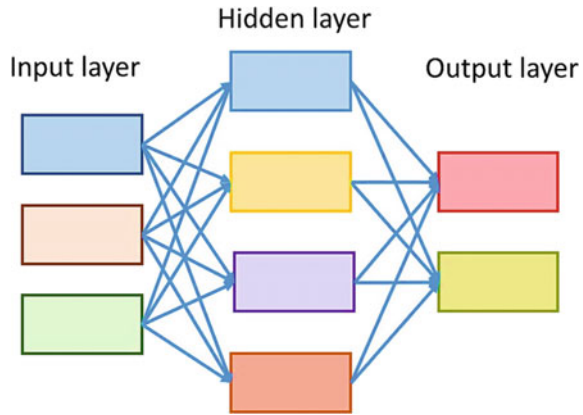
neural networks trained for a particular output, with specific input based on a comparison between output and the target until desired aim achieved. ANN can be learned from experimental data to model the linear as well as the nonlinear relationships with great success. It uses input layer to enter data into the network, ANN-yield output through output layer, and intermittent hidden layers in between. Figure 3 shows the general arrangement of layers in ANN. A newly developed NN is trained first with available data and then tested with a set of data to arrive at an optimum topology and weights. Once trained, the NN can be used for the prediction [15]. Two typical connection architectures are common for NN: feedforward and recurrent networks.

3.5 Hidden Markov Model (HMM)

A HMM uses probability distributions over sequences of observations. It is stochastic and can be used to model time-varying random phenomena. Markov model (MM) can understand as the state-space model. In MM, there are random phenomena that indicate discrete states and transition from one state to the next is random. If the system has distinct states, and each step of the discrete time, it can move to another state at random based on present probability state. In case of autonomous MM process evolves by itself, and in controlled MM actions can be applied to a modeled system to affect the outcomes. In a HMM, the states are not directly observable [5].

4 Case Study

Blanking is metal shearing processes in which the incoming sheet material sheared to the desired shape. In blanking, the removed piece of material is the product. Substantial big metal sheets are used as a raw material for blanking operation. Variation in sheet metal thickness is one of the significant blanking faults [11]. Process parameters are first optimized for the targeted quality of output [16, 17]. Ideally, the thickness of the sheet metal must remain unchanged; but practically it is unavoidable. If the thickness of the sheet metal is less than the planned one, then the clearance between the punch and die will increase compared to optimized clearance and fault-like burr formation is experienced [15, 18]. On the other hand, if the thickness of the sheet metal is more than the specified, then the clearance between the punch and die will decrease which may result in damage to the stamping press. Both the conditions ultimately affect part quality, and productivity as the burr needs to ground before further processing of part.

In the present study, limiting variation in sheet metal thickness is ±8.0% of the specified thickness of 1.0 mm. Figure 4 showing the geometry of the part and the material used is cold roll deep draw steel with tensile strength of 310 MPa.

The experiment is conducted on C-type mechanical power press with tonnage capacity of 20 ton. A microphone was mounted near to the bed of the press to capture AE. Rectangular metal strips are used as raw material of thickness 0.9, 1.0, and 1.1 mm by considering 10% variation in thickness to generate a fault. The ten products for each thickness produced in succession.

The captured signals were filtered to separate useful signal from noise using zero-phase low-pass filter. From the FFT of the filtered signals, it observed that the graph for each thickness is distinguishing. However, this is an indication of the existence of a fault—the FFT not able to capture the dynamic characteristics. Hence, for further analysis, PSD of the signal is calculated. Figure 5 shows power spectral density for various thicknesses.
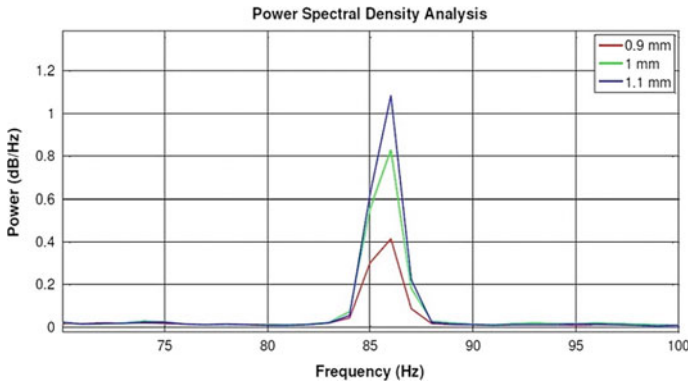
Fig. 4 Part geometry
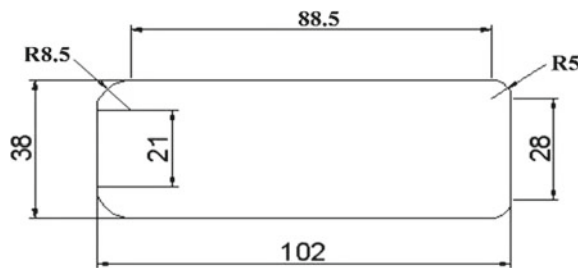
Fig. 5 Power spectral density for various sheet thicknesses

5 Discussion and Conclusion

Stamping process is a particular type of manufacturing process, where the operation is accomplished in short time, and produces transient dynamic signals, and a small improvement in the performance can have a significant influence on the profitability of the organization. All the parameter and techniques discussed above for stamping machine have their advantages and limitations, all are conditional, state-dependent, operation dependent, fault diagnosis through them require historical data of a healthy machine for comparison, signatures are machine dependent. CM technology is maturing at the fast pace, but till industry is expecting the online, cost-effective sensing and data processing technology with the well-established relationship between condition monitoring and organizational goals. There is an excellent scope that acoustic signal can be used to understand the status of the machine with cost-effectiveness. The comprehensive condition monitoring strategy can identify and predict the performance level and time available before machine start producing non-conforming products, reduce the quality checks, provide an opportunity to plan maintenance, and improve productivity.

In blanking process, maintaining proper clearance is very important that it may lead to burr formation. Tool wear and sheet thickness variation are the two major influencing factors related to clearance. PSD of the acoustic signal is used in this paper to predict the variation in the sheet thickness. The thickness characterization using AE is investigated, and AE with PSD is found useful. Further ANN or another advanced tool may improve the accuracy of the material thickness variation prediction.

References

1. Bogue, R.: Sensors for condition monitoring: a review of technologies and applications. Sens. Rev. 33, 295–299 (2013).
2. Roth, J. T., Djurdjanovic, D., Yang, X., Mears, L., Kurfess, T.: Quality and Inspection of Machining Operations: Tool Condition Monitoring. J. Manuf. Sci. Eng. 132, 41015 (2010).
3. Ge, M., Xu, Y., Du, R.: An intelligent online monitoring and diagnostic system for manufacturing automation. IEEE Trans. Autom. Sci. Eng. 5, 127–138 (2008).
4. Klingenberg, W., de Boer, T. W.: Condition-based maintenance in punching/blanking of sheet metal. Int. J. Mach. Tools Manuf. 48, 589–598 (2008).
5. Ge, M., Du, R., Xu, Y.: Hidden Markov model based fault diagnosis for stamping processes. Mech. Syst. Signal Process. 18, 391–408 (2004).
6. Mahayotsanun, N., Sah, S., Cao, J., Peshkin, M., Gao, R.X., Wang, C.T.: Tooling-integrated sensing systems for stamping process monitoring. Int. J. Mach. Tools Manuf. 49, 634–644 (2009).
7. Bassiuny, A. M., Li, X., Du, R.: Fault diagnosis of stamping process based on empirical mode decomposition and learning vector quantization. Int. J. Mach. Tools Manuf. 47, 2298–2306 (2007).
8. Li, X., Bassiuny, A. M.: Transient dynamical analysis of strain signals in sheet metal stamping processes. Int. J. Mach. Tools Manuf. 48, 576–588 (2008).
9. Jayakumar, T., Mukhopadhyay, C. K., Venugopal, S., Mannan, S. L., Raj, B.: A review of the application of acoustic emission techniques for monitoring forming and grinding processes. J. Mater. Process. Technol. 159, 48–61 (2005).
10. Raja, J. E., Lim, W. S., Venkataseshaiah, C.: Emitted Sound Analysis for Tool Flank Wear Monitoring using Hilbert Huang Transform. Int. J. Comput. Electr. Eng. 4, (2012).
11. Ge, M., Zhang, G. C., Du, R., Xu, Y.: Feature Extraction From Energy Distribution of Stamping Processes Using Wavelet Transform. J. Vib. Control. 8, 1023–1032 (2002).
12. Ng, Y. M.H., Yu, M., Huang, Y., Du, R.: Diagnosis of Sheet Metal Stamping Processes Based on 3-D Thermal Energy Distribution. IEEE Trans. Autom. Sci. Eng. 4, 191–196 (2007).
13. Gowid, S., Dixon, R., Ghani, S.: A novel robust automated FFT-based segmentation and features selection algorithm for acoustic emission condition based monitoring systems. Appl. Acoust. 88, 66–74 (2015).
14. Zhu, K. P., Wong, Y. S., Hong, G. S.: Wavelet analysis of sensor signals for tool condition monitoring: A review and some new results. Int. J. Mach. Tools Manuf. 49, 537–553 (2009).
15. Hambli, R.: Prediction of burr height formation in blanking processes using neural network. Int. J. Mech. Sci. 44, 2089–2102 (2002).
16. Badgujar, T. Y., Wani, V. P.: Stamping Process Parameter Optimization with Multiple Regression Analysis Approach. Mater. Today Proc. 5, 4498–4507 (2018).
17. Rote, A. A., Badgujar, T. Y., Mahajan, D.R.: Milling Process Parameter Optimization Using Taguchi Method. Adv. Mater. Manuf. Charact. 7, 92–96 (2017).
18. Lo, S. P., Chang, D. Y., Lin, Y. Y.: Relationship between the punch-die clearance and shearing quality of progressive shearing die. Mater. Manuf. Process. 25, 786–792 (2010).

Application of Discrete-Event Simulation to Increase Throughput of Manufacturing System—A Case Study

Prasad V. Thete and Ramesh R. Lekurwale

Abstract This paper underlines use of discrete-event simulation to increase throughput of a manufacturing facility. The literature survey shows brief information about the recent work done by the various researchers in application of discrete-event simulation in manufacturing industries. The methodology followed while doing study is a stepwise procedure of a simulation study. A case study shows the way to solve the problems in manufacturing by using discrete-event simulation. Alternate possible scenarios are compared, and best scenario is selected as a solution of the problem.

Keywords Discrete-event simulation · Manufacturing · Throughput · FlexSim

1 Introduction

Discrete-event simulation is a process of replicating the physical system in the virtual environment by using computer software program. It is possible to perform number of experiments without disturbing the ongoing process using discrete-event simulation [1].

A case study is performed in which FlexSim (discrete-event simulation software) is used to model the manufacturing system to improve the performance measures of the manufacturing system. Firstly, the current scenario needs to be studied. To understand the current scenario, it is necessary to consider the ongoing process. The company produces various parts of automotive transmission system. For a component, they want to increase their throughput capacity.

The process of producing the component is as follows.

The process flow and layout of the manufacturing facility is shown in Fig. 1.

P. V. Thete (✉) · R. R. Lekurwale
Department of Mechanical Engineering, K. J. Somaiya College of Engineering, Mumbai 400077, India
e-mail: prasad.thete@somaiya.edu

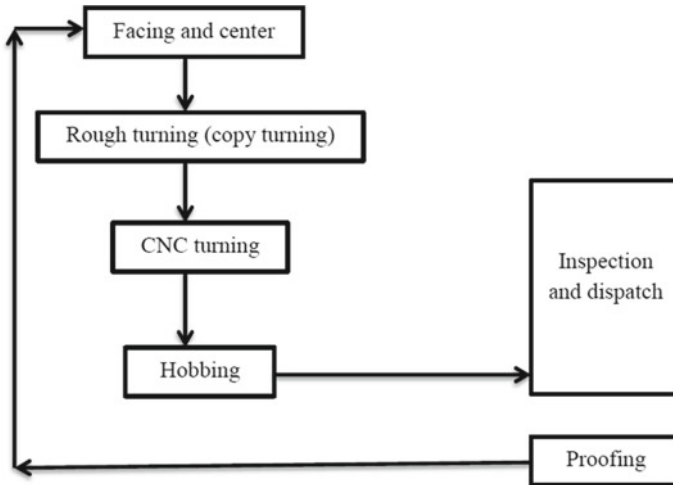R. R. Lekurwale
e-mail: rameshlekurwale@somaiya.edu

Fig. 1 Layout of manufacturing shop

Process flow

- **Proofing**: Proofing is the process in which rough-turning of the collar of component is done. It is necessary to ensure the proper clamping of spline plug on face and center machine. For this operation, a conventional lathe is used. The lathe has hydraulic circuit, customized chuck and mandrel to clamp a job.
- **Facing and Center**: Facing of the job (on either side or both sides) as well as center drilling is done using a special-purpose machine. It is an important operation; because, all the references are taken from the center and face.
- **Rough-turning**: Rough-turning is also known as copy turning. In this process, enough profile is turned using master. This operation is necessary to reduce the cycle time on CNC machine.
- **CNC turning**: In the first cycle, rough-turning is done which is followed by finish turning. Hence, the component is ready for Hobbing.
- **Hobbing**: In this process, splines are cut using a hob cutter. After completing this Hobbing process, splined plug is ready for inspection and dispatch.
- **Inspection and dispatch**: As the machining is completed, the component is inspected for the quality, and then it is dispatched.

Currently, the company produces 48 components per shift (144 components per day). They want to increase their capacity to 300 components per day.

2 Literature Review

Liufang Yao et al. [2] simulated steel production system using FlexSim to solve scheduling problems which are too difficult to solve using analytical methods. Zang Libin et al. [3] made FlexSim model for optimizing the production line completely which enter would reduce the cost involved in maintenance too. Pawel Pawlewski et al. [4] used simulation to solve a problem related to inventory and material handling in automotive industry. Yogesh.Y. Gadinaik et al. [5] modeled the job shop manufacturing system using arena. The experiments were performed to analyze performance measures like inventory management and machine utilization of newly developed system. Rishi H. Singhania et al. [6] used arena to model a manufacturing facility in virtual environment. Alternate plans were analyzed to select the best plan to improve performance measures of the manufacturing system. Sławomir Kukla [7] used arena to model a sports equipment production system to solve issues related to manufacturing. Tomasz Bartkowiak et al. [8] performed simulation investigation into enhancement of floor-board manufacturing to increase material efficiency. Adrian Jakobczyk et al. [9] modeled soap production system using FlexSim and develops alternate system to increase flexibility and to solve other issues of the old system manufacturing planning to improve production rate. Slawomir Klos et al. [10] studied the effect of buffer stock in production line to improve the performance of production process. V. K. Manupati et al. [11] studied sustainable manufacturing system using FlexSim analyzed the effect of work load allocation of multiple components.

3 Methodology

The flow chart of methodology is shown in Fig. 2.

Study starts with problem statement. Then, the objective of study and the overall plan of the study are decided. Then, collection and modeling of data are done. The data consist of information about available resources, process times and location of machines. After modeling the inputs, FlexSim model is built. After that, model is tested for the validation. If model is validated, the process is continued further. If model is not validated, then the data are collected again, and the process is repeated until the model is validated. Once model is validated, alternate scenarios can be model and tested for the desired output. The process is repeated until the system matches the desired output.
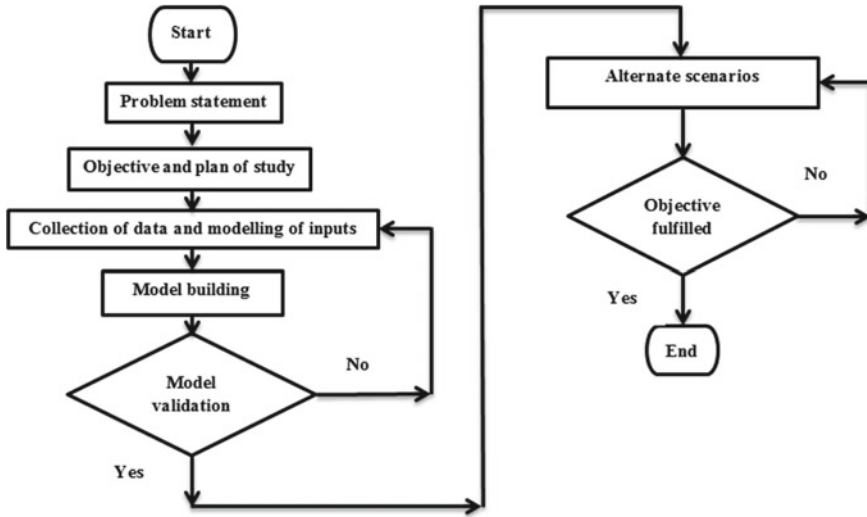
Fig. 2 Flow chart of methodology

4   Case Study

4.1   Problem Definition

The company produces 144 components per day (48 components per shift) on normal days. Now, they have to meet the demand of 300 components per day. To meet this increase in demand, the company wants to increase their capacity.

The problem statement given by the company is as follows:

Develop a strategy to increase the throughput of the manufacturing facility.

4.2   Setting of Objectives and Overall Project Plan

It is decided that the study will be performed to increase the throughput of the system from 144 components per day to 300 components per day.

Following assumptions are made to perform the study:

1. All machines are working (Breakdowns are ignored).
2. All operators are present (Absenteeism is ignored).
3. Raw material is available any time (Shortage is ignored).
4. The operator or worker is considered to be medium-skilled worker.
5. The production line is dedicated for one product.

Table 1 Modeled process time for all operations

| Machines | Process time in seconds | | | | |
	Lathe	Facing center	Copy turning	CNC	Hobbing
Mean	74.44	117	232.4	265.88	531.36
Standard deviation	8.0212	6.3442	21.0178	15.2488	20.0122

Firstly, the current strategy is to be studied. For this, data (like available resources, process time and location of machines) are collected. Current facility will be modeled in FlexSim. Once the model is validated, alternate strategies will be studied using that model.

4.3 Collection and Modeling of Data

After setting the objective of study, the data required to make a complete model are collected and modeling of input data is done. Firstly, the resources allocation (type of machines and number of machines) needs to be considered. Scenario 1 refers to the current facility of the company. The process time considered to be normally distributed. Table 1 shows modeled data of process time (in seconds) for each machine, their mean and standard deviation.

4.4 Making a Model in FlexSim and Its Validation

The model-making process starts with setting the units for the model. The unit for time and distance is set to be seconds and meter, respectively. Then, existing facility is modeled.

4.5 Existing Set-up (Scenario 1)

To model the existing manufacturing facility, the object from the library is dragged and dropped in the 3D space. The raw material is modeled as source. The machines are modeled as processors. The fork lift is modeled as transporter. The operators are also modeled wherever necessary. The output is modeled as sink. The various waiting lines are modeled as queue. The properties such as location and process time are modeled, respectively. The FlexSim model for Scenario 1 is shown in Fig. 3.

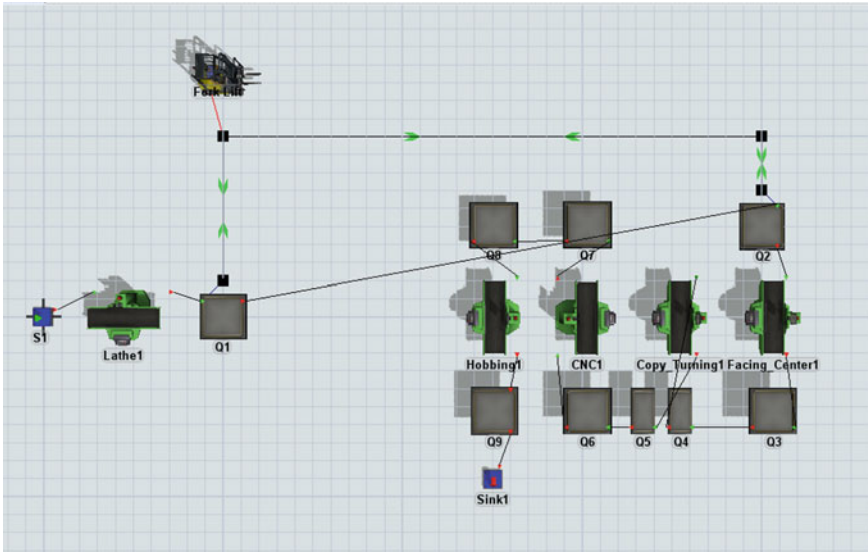After running the model, following outputs are obtained:

Fig. 3 FlexSim model of existing set-up (scenario 1)

The utilization of Lathe1 is 100%, Facing_Center1 and Copy_Turning1 is 92%, CNC1 is 91% and Hobbing1 is 90%.

The throughput of Lathe1 is 373, Facing_Center1 is 228, Copy_Turning1 is 113, CNC1 is 98 and Hobbing1 is 48 components.

The total number of components produced per shift is 48.

4.6 Validation

As stated in problem definition, the company produces 48 components per shift, and the model is producing the same output that is 48 components per shift.

Therefore, the model is said to be validated. And, the model can be used for further experimentation.

4.7 Modeling of Alternate Set-up Scenario 2

As a bottleneck is observed at Hobbing machine, a second-Hobbing machine, Hobbing2 is added to the model. The FlexSim model for Scenario 2 is shown in Fig. 4.

After running the model, following outputs are obtained:

The utilization of Lathe1 is 100%, Facing_Center1 and Copy_Turning1 is 92%, CNC1 is 91%, Hobbing1 is 90% and Hobbing2 is 89%.
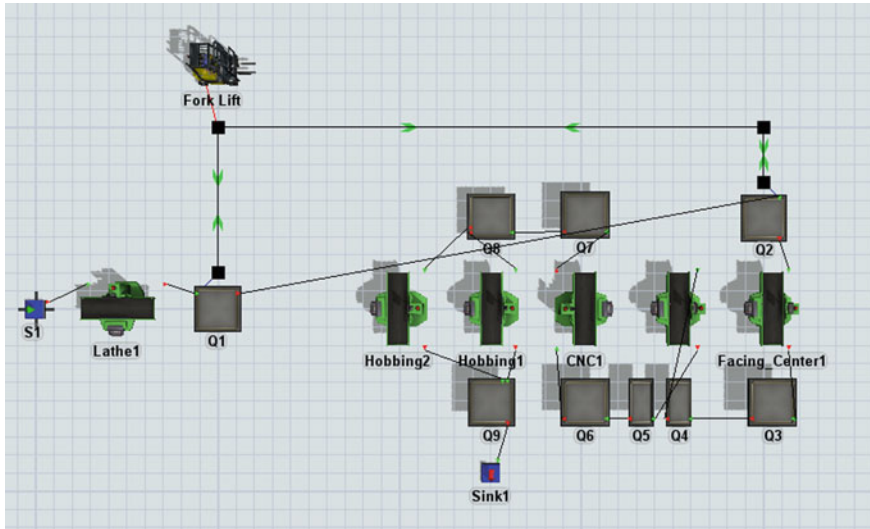
Fig. 4 FlexSim model of alternate set-up scenario 2

The throughput of Lathe1 is 373, Facing_Center1 is 228, Copy_Turning1 is 113, CNC1 is 98 and Hobbing1 and Hobbing2 is 48 components.

The total number of components produced per shift is 96.

By adding a Hobbing machine, the total throughput per shift is increased to 96 components per shift.

4.8 Modeling of Alternate Set-up Scenario 3

As it is seen that, throughput can be increased by adding Hobbing machines. Therefore, more Hobbing machine should be added to increase throughput. As the total output from CNC machine is 98 components and total output from Hobbing machine is 96 components, there is a need to increase the number of CNC machines as well. As per the resource allocation, Hobbing3 and CNC2 are added to the model is shown in Fig. 5.

The utilization of Lathe1 is 100%, Facing_Center1 and Copy_Turning1 is 92%, CNC1 is 54%, CNC2 is 50%, Hobbing1 is 71%, Hobbing2 is 70% and Hobbing2 is 64%.

The throughput of Lathe1 is 373, Facing_Center1 is 228, Copy_Turning1 is 113, CNC1 is 58, CNC2 is 54, Hobbing1and Hobbing2 is 38 and Hobbing3 is 34 components.
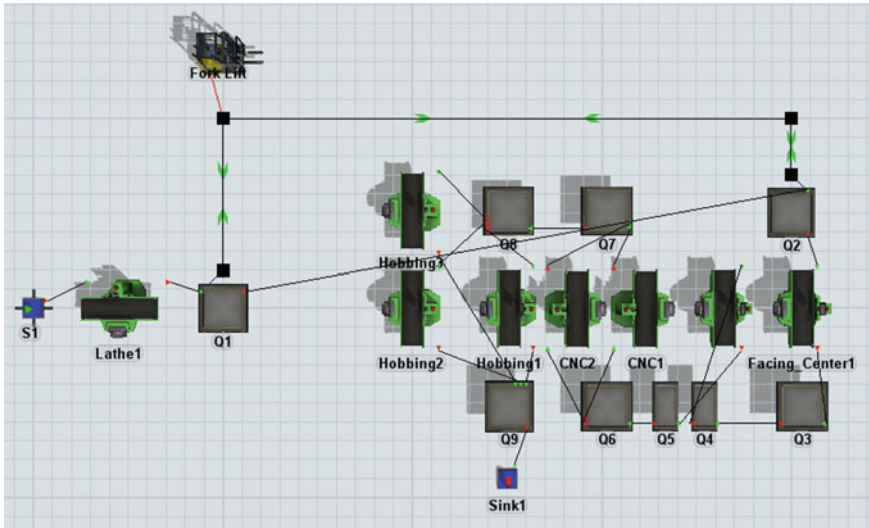
The total number of components produced per shift is 110.

Fig. 5 FlexSim model of alternate set-up scenario 3

By adding a CNC and Hobbing machine, the total throughput per shift is increased to 110 components per shift.

5 Results

The various scenarios and their respective throughputs are given in Table 2.

Table 2 Comparison of scenarios based on throughput

Scenario number	Number of machines					Throughput	
	Lathe machine	Facing and center	Copy turning	CNC machine	Hobbing machine	Per shift	Per day
Scenario 1	1	1	1	1	1	48	144
Scenario 2	1	1	1	1	2	96	288
Scenario 3	1	1	1	2	3	110	330

6 Conclusion

In this paper, manufacturing system is studied. Performance measures of current manufacturing facility are observed. Alternate scenarios are designed, simulated and analyzed in order to improve throughput of the system to a desired value. The FlexSim software is used to model the current and alternative scenarios. By performing this study, not only throughput is increased, but also bottlenecks are avoided. By using discrete-event simulation, the risk associated with physical trials is avoided. It can be seen that some machines are under-utilized. More research can be done to improve resource utilization.

References

1. Jerry, B. (2005). *Discrete event system simulation*. Pearson Education India.
2. Yao, L., & Zhu, W. (2010, September). Visual simulation framework of iron and steel production scheduling based on Flexsim. In *Bio-Inspired Computing: Theories and Applications (BIC-TA), 2010 IEEE Fifth International Conference on* (pp. 54–58). IEEE.
3. Libin, Z., Ling, H., & Shubin, G. (2012, June). Research on simulation of automobile repairing system based on Flexsim. In *World Automation Congress (WAC), 2012* (pp. 1–4). IEEE.
4. Pawlewski, P., Rejmicz, K., Stasiak, K., & Pieprz, M. (2012, December). Just in sequence delivery improvement based on Flexsim simulation experiment. In *Simulation Conference (WSC), Proceedings of the 2012 Winter* (pp. 1–12). IEEE.
5. Yogesh Y. Gadinaik, Vijay S. Bilolikar. (2015). Simulation based analysis of job shop manufacturing planning. Production Operation Management Society 26th Annual Conference, Washington DC, USA.
6. Rishi H. Singhania, Vijay S. Bilolikar (2016). Application of simulation for manufacturing system management - A case study. Production Operation Management Society 27th Annual Conference, Orlando, USA.
7. Kukla, S. (2017, September). Planning and Assessment of Manufacturing Processes Flow Variants Based on a Simulation Experiment. In *International Conference on Information Systems Architecture and Technology* (pp. 369–378). Springer, Cham.
8. Bartkowiak, T., Ciszak, O., Jablonski, P., Myszkowski, A., & Wisniewski, M. (2018). A Simulative Study Approach for Improving the Efficiency of Production Process of Floorboard Middle Layer. In *Advances in Manufacturing* (pp. 13–22). Springer, Cham.
9. Jakobczyk, A., Nogaj, K., Diakun, J., & Davidrajuh, R. (2018). Production Process Analysis in Conditions of Short-Term Raw Materials Expiration Dates and Long Setup Times Using Simulation Method. In *Advances in Manufacturing* (pp. 121–130). Springer, Cham.
10. Klos, S., & Patalas-Maliszewska, J. (2018). The Impact of Buffer Allocation in Assembly-Line Manufacturing Systems on the Effectiveness of Production Processes. In *Advances in Manufacturing* (pp. 33–43). Springer, Cham.
11. Manupati, V. K., Xavior, M. A., Chandra, A., & Ahsan, M. (2018). Workload Assessment for a Sustainable Manufacturing Paradigm Using Social Network Analysis Method. In *Knowledge Computing and Its Applications* (pp. 99–108). Springer, Singapore.

Enhancement in Productivity by Integration of 5S Methodology and Time and Motion Study

Rushank Sangani and Vijaya Kumar N. Kottur

Abstract In the revolutionary age of technology and emergence of global markets, where the customers demand for quality products at a cheaper price, manufacturing sectors need to constantly accelerate their productivity processes by adopting various industrial engineering techniques and lean manufacturing methods. 5S methodology is the foundation step of lean manufacturing system. The domino effects of adopting 5S methodology are organized work areas, standardization, easy sorting of materials, and higher efficiency by reducing waste. The other aspect, time and motion study, helps us to escalate from actual work rate to optimal work rate by keeping in mind the worker's psychology. Time and motion study helps us to understand the problem of low productivity and rectify it. It results in cost minimization, elimination of unessential processes, safe working conditions, and conducive work environment. One of the main challenges, in adopting these methods, is application of these methods by the operational team on a daily basis. A systematic combination of the above methods gives the manufacturer a high productivity in the longer run and an edge over his competitors.

Keywords 5S methodology · Lean manufacturing · Time and motion study
Industrial engineering techniques

1 Introduction

Manufacturing sectors are fast-flowing industries which require constant improvements in the fabrication processes, innovation in assembly line, modified supply chain systems, lean processes that reduce waste, and specialized logistics department which functions effectively. In the current scenario, the manufacturing industries are not utilizing the fullest of their abilities as they are grasping to catch up with the demands

R. Sangani (✉) · V. K. N. Kottur
Mechanical Engineering Department, D. J. Sanghvi College of Engineering,
Mumbai 400056, India
e-mail: rushanksangani@gmail.com

of the market. To provide a regularity in the processes for a longer term and to have an increase in the output of the processes, we have integrated 5S methodology along with time and motion study. 5S methodology first originated in Japan by Hiroyuki Hirano. It is one of the methods of lean manufacturing, which focuses on organizing, keeping the area clean, standardizing. 5S methodology gets its name from the five Japanese words: Seiri, Seiton, Seiso, Seiketsu, and Shitsuke. They mean sort, set in order, shine, standardize, and sustain, respectively. The 5S technique is also considered as "Kaizen" which means "change for the better." Time and motion study was developed and refined by Frederick W. Taylor and his followers which were to determine the "correct time" it takes for a certain task.

The purpose of this paper is to do a small change in a big way by application of 5S and time and motion simultaneously at a grassroots level and measure the changes in the working environment after a certain period. With the integration of the two processes on a daily basis increases, there is an increase in efficiency of the manufacturing plant and workers' safety is prioritized.

1.1 Problem Statement

After the research conducted by Lean Enterprise Research Centre (LERC), UK, it was concluded that for any manufacturing company the ratio of activity is broken down as value-added activity-5%, non-value added(waste)-60%, and necessary non-value added 35% [1]. The results of this research help us to infer that about 60% of the activity at a manufacturing plant can be eliminated [1]. Many businesses have been trying to adopt value-added production system, i.e., adding maximum value while minimizing waste in all production and support area processes. Global companies like BMW have implemented value-added production and support area processes in their companies to maintain flexibility throughout their production processes and improving their productivity and efficiency [2]. The impact of value-added production at BMW is that it has seen an increase of 25% improvement of the operating cost structure, totaling more than 225 million [2]. Therefore to overcome industrial barriers at a general manufacturing plant, we have adopted the 5S method and time and motion study.

2 5S—The Method

2.1 5S—The Process

1. Sort (Seiri): Sorting is the first step of 5S technique, removing all the unneeded items from the shop floor. A red tag is attached to junk items in the workplace.

These items are stored temporarily in an area until further action is taken over them.

2. Set in Order (Seiton): Advantages of this process include clear visibility and identification of missteps. To implement the set in order exercise "2-bin storage system" can be implemented. Figure 1 shows "2-bin storage system" which has been depicted for setting the washers in the order of their sizes at a large-scale automobile industry.

3. Shine (Seizo): This stage of 5S exercise is termed as shine or sweep stage to eliminate the root cause of waste, dirt, and damage as well as clean up the workstation.

4. Standardize (Seiketsu): This stage maintains continuous activities in all areas shift by shift and crew by crew. Therefore, we make use of Kaoru Ishikawa's fishbone diagram of 5M's which allows operational teams to develop their own standards. The 5M's of Ishikawa's fishbone are manpower, methods, materials, machines, and measurements.

5. Sustain (Shitsuke): The benefits of the above four phases will be achieved and can be measured. However, without the cooperation, self-discipline of the operational team at the plant, this cannot be achieved. Continuous efforts should be taken and with continuous dedication, the work should be maintained.

Fig. 1 2-bin storage system

2.2 *Implementation of 5S*

1. Guidelines for practicing sort—The basic steps that are involved in creating a successful red-tagging process begins with introducing the red-tag strategy for creating, holding areas, and planning the disposal of unwanted items. Second, the specific types of items needed for sorting in work areas are identified and followed by determining the items necessary for the processes. Next, the red tag is attached, and methods needed to discard unwanted items are enforced. Lastly, the results of the process are documented which summarizes cost savings and improvements achieved. Unnecessary items identified after applying red-tag strategy are disposed in an eco-friendly way. Items after the process are sold at the best selling price in the market. Potential impacts of the processes are identification and segregation of items, elimination of unwanted items, improved work environment, and maximum utilization of workspace.

2. Guidelines for practicing set in order—It emphasizes effective storage and safety that gradually improves the appearance of the workplace. Set in order begins with introducing names and number on all jigs and tools. The tools that are to be used according to the work operations are stored next to the machine. Any important step is to mark the materials with an oblique line to detect disorder from a distance. Next, slots based on sizes of tools or materials are created and stored. The 2-bin storage system is then implemented, and tool boards are appropriately managed. Potential impacts of this process: Items return to their own address after use, use of first-in–first-out (FIFO) is increased; retrieval time is reduced.

3. Guidelines for practicing shine—Shine ensures a safer, comfortable, and appealing workplace. Steps involved in implementing shine include allocation of cleaning assignments to the employees, setting targets on daily basis, determining what needs to be cleaned in specific amount of time, and the methods to keep the area clean. Faulty and defective machines (equipment) should be repaired. Potential impact of this process: quality products, safe workplace, clear visibility and reduction in retrieval time, economy in cost, and positive impact on inspection officers.

4. Guidelines for practicing standardize—The operation unit must finalize the procedures and maintain a checklist of daily routine practices. The checklist includes the name of the person responsible for the job, what are the prerequisite to get the desired results, actions to be implemented to maintain appropriate standards. These procedures must be followed daily at the workplace. Potential impacts of this process are clear visibility of signposts, determining procedure, and improved operations.

5. Guidelines for practicing sustain—This process maintains the flow and momentum of all the previous 4S' and ensures sustainability. This includes planning, performance, quality check, and actions needed to maintain the consistency in quality procedures. Potential impacts: ideal work practices, effective work environment, better interpersonal relationship, spirit of unity, and feeling of belongingness.

3   Time and Motion

Motion and time study is considered to be the backbone of industrial engineering, industrial technology, and industrial management programs because the information that time studies generate affect many areas including the following:

(1) Cost estimating,
(2) Production and inventory control,
(3) Plant layout,
(4) Materials and processes,
(5) Quality,
(6) Safety.

In an organization which operates without time standards, 60% of performance is typical. When time standards are set, performance improves to an average of 85%. This is a 42% increase in performance.

$$\frac{85\% - 60\%}{60\%} = 42\% \text{ performance increase.}$$

Incentive systems can improve performance even further. It averages 120% that is another 42% increase in performance [3].

$$\frac{120\% - 85\%}{85\%} = 42\% \text{ performance increase}$$

The above results infer that a manufacturing plant with no time and motion standards averages 60% performance, with time and motion standards averages 85% performance, with incentive systems averages 120% performance [3].

3.1   Implementation of Time and Motion Study

To move forward with implementation of this study, it is important to consider the factory parameters like number of orders in a day, amount of operations involved for manufacturing the product, time for fabrication–assembling–logistics in a day's time. Keeping these parameters in mind, the time and motion form sheet is made.

Table below shows the time and motion form sheet that has been designed for a mass production plant of a company which manufactures four-wheeler vehicle.

Assembly Line Analysis using Time and Motion Study

After the chassis has been manufactured by the fabrication department, it is passed forward to the assembly line where the major components of the vehicle are fitted. The time taken by various processes in the assembly department has been noted, and later they are compared with the average time taken by an average worker and

results are inferred. This gives us an idea about how much time has been wasted in the process and areas which need to be improved. Time and motion study for various activities in the assembly line has been performed and for demonstration purpose few of them have been explained below.

(1) LEAF SPRING FITTING

Short coming: (1) No tool, (2) No replacement tools, (3) Unavailability of lifting tool, (4) Minor parts at a distance, (5) Unorganised desk, (6) Unusual breaks, (7) Raw material unavailable, (8) Less space, (9) No supervision FATIGUE FACTOR								
TIME STUDY TOP SHEET								
Factory:					**Date:**		**Operators Bhoir-P**	
Work Station:	**|Leaf Spring Fitting**				**Time:**		**Sunil-C**	
Product Name: Heavy Vehicles **Model No:**			**Product**		**Studied by: Rushank**		**Narine-P**	
Unit of measure: minutes					**Supervisor: Jayesh Patil**			
Time st:		**Time fin:**			**Time Elapsed:**			
ELEMENTS	Done by	Reading >>	1	2	3	4	5	Short fall
(1) Initially pick up the leaf springs and place it on a hand wheel and bring them near the chassis.			2	1	1			
Before attaching leaf spring, shackle plate is inserted on the chassis & connected with leaf spring.			1	1	1			
(2) Shackle bolts are picked up and grease nipple is applied over them			1	3	3			
(3) On the rear side 2 shackle bolts are inserted & leaf springs are aligned properly with the chassis.			1	1	1			
(4) Over the rear side 2 shackle bolts, insert and tighten 2nyloc nuts.			2	2	2			**No tools available for Bolts-5min**
(5) For the front side attachment of the leaf spring a single shackle bolt is inserted and Nyloc Nut is inserted and tightened.			2	2	3			
(4) Same process is carried out to fit other 3 leaf springs			6	5	5			**Work stopped due to absence of leaf springs for 1 week**
(5) After all the above activities, 12 Nyloc Nuts, 12 Shackle Bolts are tightened properly with Nut Runner.			3	2	4			
			18	17	20			

(2) GEARBOX ASSEMBLY

Short coming: (1) No tool, (2) No replacement tools, (3)Unavailability of lifting tool, (4) Minor parts at a distance, (5) Unorganised desk, (6) Unusual breaks, (7) Raw material unavailable, (8) Space less, (9) No supervision								
FATIGUE FACTOR								
TIME STUDY TOP SHEET								
Factory:				Date:				Operators: Shaam
Work Station:		| Gear Box Assembly		Time:				Shaam
Product Name: Heavy Vehicles Product Model No:				Studied by: Rushank				Shaam
Unit of measure: minutes				Supervisor: Jayesh Patil				Shaam
Time st:		Time fin:		Time Elapsed:				Shaam
ELEMENTS	Done by	Reading >>	1	2	3	4	5	Short fall
Initially bring the gear box top and bottom housing, gearbox mounting bracket on the working table.			2	3	2	2	2	
Use a tapper roller bearing. Remove only the cone and press fit in both top and bottom housing			3	3	3	3	4	
Take the output shaft helical gear key. Insert washer at plane end of output shaft keep key in the keyway and press. Insert washer (FW3168415). Press taper roller bearing on both the ends of the output shaft.			8	6	7	8	8	6. Unusual Break- Time lost: 10min
Press the bearing at both ends of the helical shaft.			2	1	1	1	1	
On bottom and rear housing Re-Tapping is performed by the worker.			3	6	6	5	6	The top and bottom housing are not properly finished
Take bottom gear box housing which is already cone pressed and hold it in a bench vice. Put pressed output shaft in the gear box bottom housing which is pressed in the cone closed side after applying grease.			3	2	1	4	2	Filling is performed on rear and top housing for proper finishing- 6min
Insert the pressed helical pinion shaft at open end of the gear box bottom housing			1	1	1	1	2	
Fit the dowel pins on both the machined surface of the gearbox top and bottom housing			2	2	1	3	3	
Apply shaloc on both the machined surface of top and bottom gear box housing			1	1	2	2	2	Unusual Break17min
Keep top housing on bottom housing then hammer it and fit with allen cap screw(51108035-6nos) with spring washer			5	6	4	7	5	

Apply shaloc on input end cover and also on the surface where the input cover will be fitting on top housing. Fit it with hex bolts and spring washers.			4	5	8	6	5	
Press the oil seal in output end cover. Apply shaloc on output end cover and on gear box top housing where the output cover will be fitting. Fit the hex bolts and spring washers.			7	7	8	7	5	
Fit the output flange on the free end of output shaft with key and grub screw and pour a drop on lock tightener on grub screw.			4	6	6	3	8	
Release the gearbox from the bench vice and hold it in reverse direction. Press oil seal on the machined surface and apply shaloc.			3	2	3	2	2	
Keep the gearbox motor mounting bracket (FW3168403) on the gearbox bottom housing at the free end of helical pinion shaft. Fit the hex bolt (M10X25-3) and spring washer.			8	7	8	8	7	
Fit the love joy coupling on the free end of helical pinion shaft with key and allen grub screw. Pour one drop of lock tighener on the grub screw.			2	4	3	5	3	
Release the gearbox from the bench vice and keep it on the working table. Fit the level plug at side of middle on top housing.			2	2	2	2	2	
			60	64	66	69	67	

3.2 Results and Discussion About Time and Motion

OUTCOME OF TIME AND MOTION STUDY AT JOST'S ENGINEERING COMPANY LIMITED

Sr. No.	Activity name (min)	Ideal time (min)	Average time (min)	Unnecessary time (min)
1	Leaf spring fitting	10	18	8
2	Shock absorber fitting	10	12.33	2.33
3	Front axle assembly	40	43.33	3.33
4	Front axle fitting	16	16	0
5	Differential fitting	15	18	3
6	Front and rear wheel fitting	16	21.33	5.33
7	GearBox assembly	45	63.33	18.33
8	Motor and GearBox fitting	15	16.67	1.67
9	Propeller shaft fitment	19	25.33	6.33
10	Steering GearBox assembly	15	17.66	2.66
11	Brake shaft fitment	25	31.33	6.33
12	Brake piping	55	60.67	6.7
13	Platform fitting	40	44.66	4.67

4 Conclusion

Various results of 5S demonstrate that a small change adopted in the right direction, increases productivity along with better working conditions and workers safety is kept in mind. The outcome of time and motion study at a large-scale factory includes the unavailability of nuts and bolts of the required sizes and unavailability of leaf spring material which causes a delay in the assembly line. Analyzing the outcome of time and motion study, we infer that the company should hire a supervisor who will be the link between material handling department and assembly department; this will ensure that product material does not run out of stock. Trolley system should be adopted at various workstations, which will contain all the components and tools of various sizes. This will increase the productivity and reduce the strain on workers.

References

1. Agrahi et al., "Implementation of 5S Methodology in Small Scale Industry" International Journal of Scientific & technology Research Vol 4, Issue 4, pp. 180–187. April 2015.
2. Retrieved from https://www.bmwusfactory.com/manufacturing/building-a-better-bmw/value-added-production-system.
3. Work Systems and the Methods, Measurement, and Management of Work by Mikell P. Groover, ISBN 0-13-140650-7. ©2007 Pearson Education, Inc., Upper Saddle River, NJ.

Decision Support System for Failure and Down Time Reporting: A Tool for Achieving Production Targets from Remote Mining Equipment

V. M. Kalra, Thakur Tilak and B. S. Pabla

Abstract Decision-based maintenance support system is a predictive maintenance management technique that considers the repair or replacement decision to be performed based on the abnormal condition of the expensive heavy earth moving machinery. It stipulates for executing the maintenance based on the condition or performance of the equipment, whereas preventive maintenance is maintenance performed on an item to prevent failure. Condition maintenance helps to detect the hidden faults even when mining equipment is in operation. Performance of the equipment also gets better as overall equipment efficiency improves due to reduction in the small stoppages and finally the improved utilization of the equipment results into better total production. Intelligent system based on CBM techniques has been used to reduce the workshop inventory, breakdown and maintenance time and therefore performs a major role to improve the equipment performance and productivity.

Keywords Availability · Utilization · Global system for mobile
Radio frequency identification device · Condition-based maintenance

1 Introduction

The equipment breakdown and maintenance is the main factor responsible for poor performance and productivity of the equipment. Since maintenance cost in the mining

V. M. Kalra
Department of Electronics and Communication Engineering, S.J.P Polytechnic Damla,
Yamuna Nagar, Haryana 135001, India
e-mail: vmkalra@yahoo.com

T. Tilak (✉)
Department of Electrical Engineering, PEC University of Technology, Chandigarh 160012, India
e-mail: tilak20042005@yahoo.co.in

B. S. Pabla
Department of Mechanical Engineering, NITTTR Sector 26, Chandigarh 160019, India
e-mail: pablabs@yahoo.com

industry is known to be around 30–50% of the total operational cost, it is therefore essential to have a system that could analyze status and decide as when to perform the maintenance [1].

The present paper looks at the vast scope of the CBM in knowing the timely information of the fault before it happens and thus helps in reducing the breakdown time and maintenance cost [2]. Based on the long history of breakdown and maintenance log sheets, parameters that are measurable can be controlled and can improve the production targets set by the company to lower the production cost [3].

Since most of the faults are common, a ready to use solution should be used by the management to reduce the maintenance and downtime cost [4]. Lack of effective maintenance management is due to poor information system. Web-based maintenance management system helps to solve the safety and repair issues effectively [5, 6].

Presently, the information for breakdown is only reported to maintenance force through wireless sets. Expert system has been implemented that can check the faults and send the coded messages to the maintenance crew to reduce the breakdown time to minimum or even nil. The maintenance crew has been tracked by RFID monitoring system for any delay in initiating the maintenance work and therefore helps in reducing the maintenance time and improves the equipment productivity.

2 Role of Condition Monitoring Technology in Maintenance Management

CBM system reduces the breakdown and maintenance time effectively by keeping the equipment working for longer duration of time to achieve the production targets [2, 4]. CBM is well understood as the maintenance carried out according to the need as indicated by automated condition monitoring system [7–9]. CBM technology looked more effective after the availability of intelligent smart sensors and data management softwares [9]. Low-cost fault monitoring and diagnostic system should be developed for old equipment still in use due to high replacement cost, and these underperform due to poor feedback or no equipment monitoring. The time for detection of fault and the faulty stage can be drastically reduced from days to few hours [10]. With the advancement of automation technology, it is now possible to develop system that could issue alerts for risk management and its possible impacts on the system. CBM system is therefore intelligent in nature to identify the faults before any catastrophic failure occurs [11, 12].

3   System Model for Mining Shovel and System Blocks for Signal Acquisition, Processing, and Communication Modules

Based on the system model shown in Fig. 1 [6] and study of system blocks in Fig. 2, the decision support system for maintenance management of hydraulic shovel has been developed.

Intelligent system mainly consists of data acquisition, data analysis, and decision-making system before alerts are issued for any failure [9] as shown in Fig. 2.
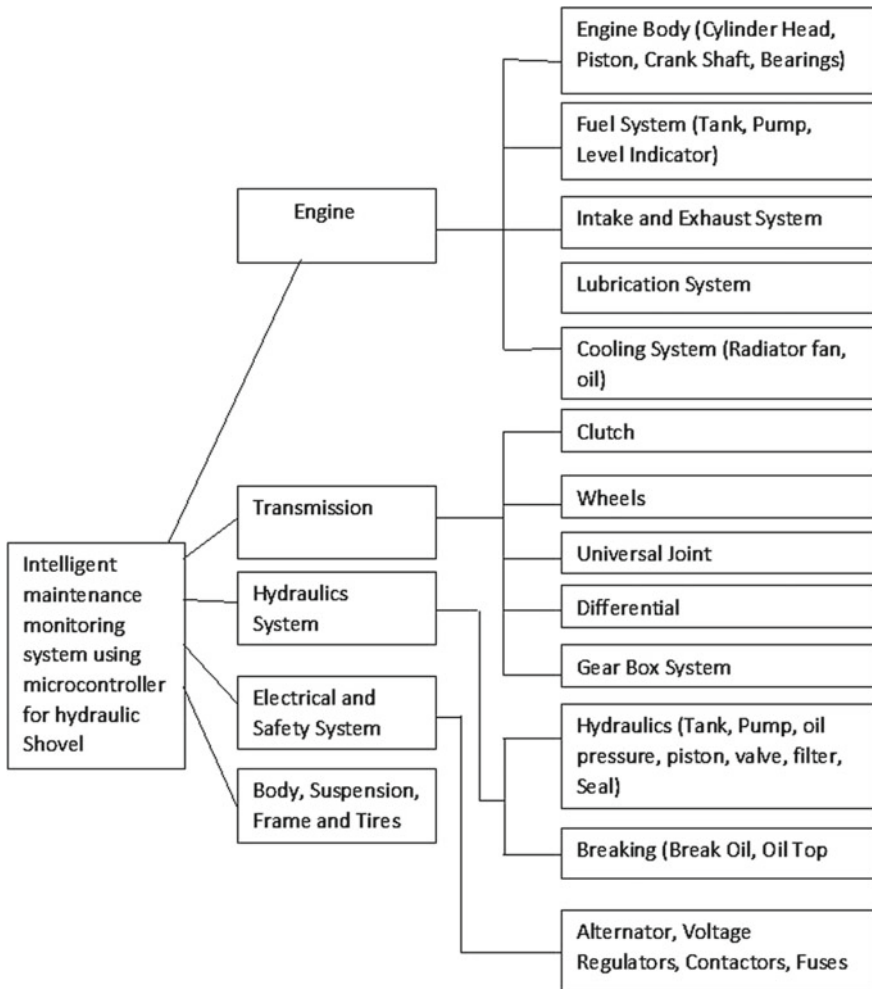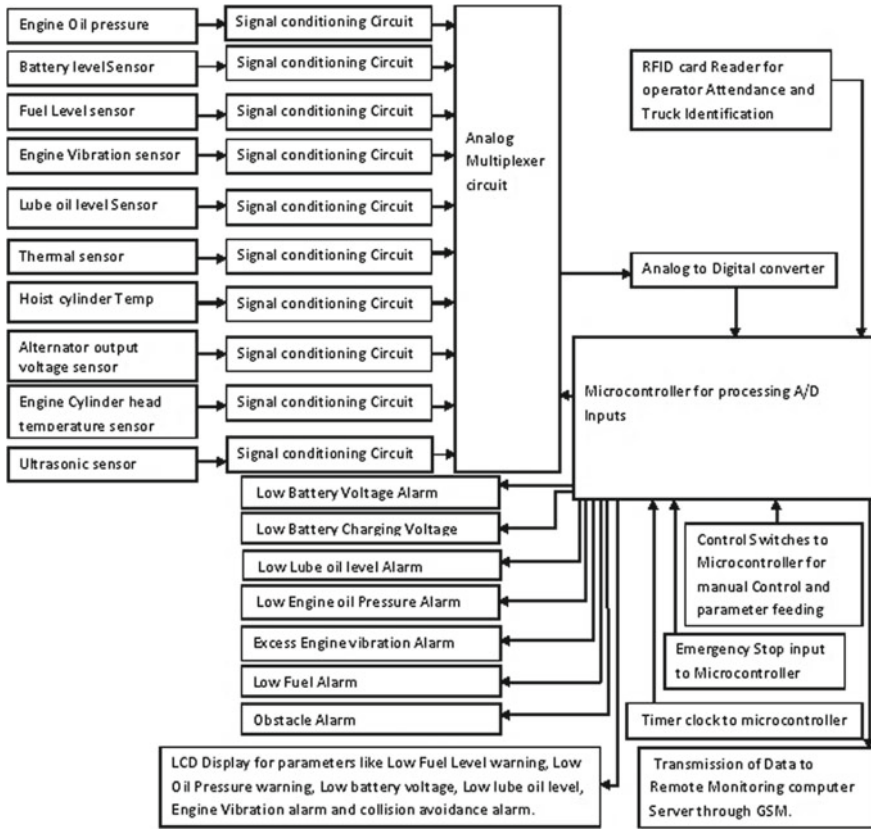

Fig. 1   System model for hydraulic shovel

Fig. 2 Block diagram of the signal acquisition, processing, and communication module

3.1 Expert System for Monitoring and Control of Parameters

The expert system makes use of controller ATMEGA 328 for interfacing with temperature sensor LM35, vibration sensing using sensor SW18020, hydraulic pressure using MPX 2010, battery level and alternator voltage level using resistor networks, and oil level using ultrasonic sensor SR04 as shown in Fig. 3.

3.2 Pressure Sensor (MPX2010GP)

The MPX2010GP series silicon piezo-resistive pressure sensors connected at pin no 27 of controller are used to provide a very accurate and linear voltage output directly proportional to the applied pressure.
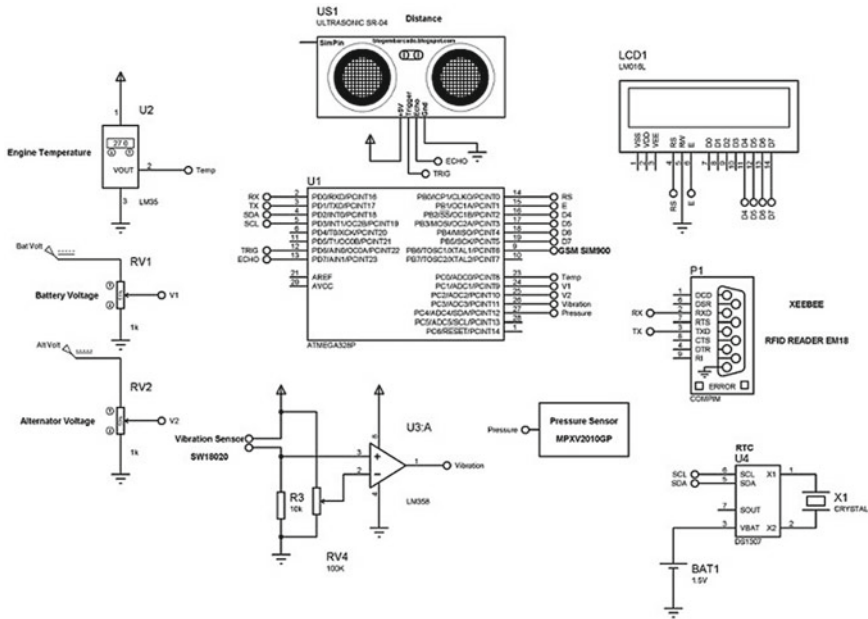
Fig. 3 Hardware for monitoring the machine parameters and maintenance crew

3.3 Real-Time Clock (RTC)

Real-time clock integrated circuit IC DS1307 has been used to supply serial data SDA and serial clock SCL connected at pin 4 and 5 of microcontroller.

3.4 Ultrasonic Sensor for Engine Oil Level Sensor

Ultrasonic sensor SR04 has been used for measuring the engine oil level; the Trig Echo signals from sensor are connected to microcontroller at pin number 12 and 13.

3.5 RFID Module for Maintenance Crew Reporting and GSM Module

RFID, the EM18 card reader module, is connected at pin 2 of the controller. GSM module Simcon900 connected at pin 9 of the controller has been used for transmission of fault information to the maintenance workshop.

3.6   Vibration Sensor for Cabin Jerks

Jerks in the cabin give the sense of insecurity to the machine operator. The cabin jerks are monitored using vibration sensor SW18020.

3.7   Display Module

Any variation in signal acquired is also displayed on the operator console using LCD LM016L at pin numbers 16, 17, 18, 19 of the microcontroller.

4   Software for the Data Acquisition, Signal Processing, and Communication System

The software compares the data acquired from the different sensors with the preset values using conditional statements, and any abnormality is sent to the maintenance staff with the help of GSM module in the form of SMS. The flow chart of the remote monitoring and fault diagnostic system is shown in Fig. 4.

The conditional statements for hydraulic excavators are used in the following manner [14, 15].

(1)   If oil pressure level is low, then mechanics are defective.
(2)   If alternator is defective, then electricity is low.

Fig. 4   Software for parameters monitoring and maintenance workforce
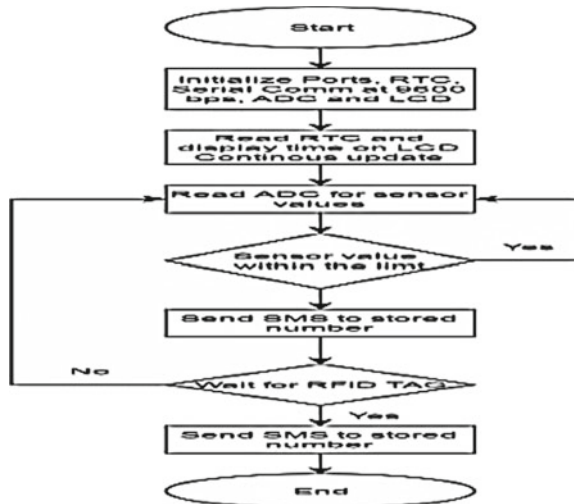
(3) If battery voltage is low, then electricity is low.
(4) If electricity is low, then electronics are unable to work.
(5) If oil level is low, then hydraulic pumps can be faulty.
(6) If hydraulic pumps are unable to work, then hydraulics is defective.
(7) If cylinder head temperature is high, then engine oil level should be low.
(8) If dump hoist pressure is low, then hydraulic oil level should be low due to defective hose or leaking seal.
(9) If charging voltage is low, then alternator is defective.
(10) If battery charging voltage is high, then regulator in alternator is defective.
(11) If engine is difficult to start, then fuel tank can be empty or cylinder head gasket leaking or faulty fuel pump.
(12) If engine noise is excessive, then engine mounts may be broken or restricted air supply.
(13) If engine oil level is low (high consumption), then piston rings may be damaged.
(14) If hoist cylinder temp is high, then hoist holding power is low.
(15) If cabin jerks are greater than set limit, then cabin mounts may be loose.

5 Decision Support System for Maintenance Monitoring and Management

Real-time maintenance monitoring system for maintenance management of hydraulic excavators has been implemented. The XBee on the hardware system communicates with XBee connected with COM port of the central computer for mine manager. LabVIEW is installed on the central computer. LabVIEW program is called as virtual instruments. The data communication established has the following features.

1. Eight data bits.
2. Two stop bits.
3. No parity check bit.
4. Baud rate of 9600 bps (bits per second).
5. Asynchronous communication.

The data transmitted by the hardware installed at the excavators for fault monitoring is captured by the XBee connected at the computer serial port. Sequential data is converted into array form. This array is accessible by indicators, production graphs, performance indicators, parameter monitoring, and production graph windows.

Fig. 5 Decision support system indicators

Fig. 6 Maintenance management system performance indicators

5.1 XCTU Software Configuration for XBee and System Implementation Using LabVIEW Virtual Instruments

XCTU is GUI software to configure XBee for communication between XBee devices. XBee devise on the hardware is configured as router and the other as coordinator on the PC. Initially, the VESA software is installed to access the serial port, LabVIEW software can access data available at the serial port in a particular sequence decided by the microcontroller. The virtual instruments in Fig. 5 show the data captured in the auto mode for battery voltage, alternator voltage output, engine temperature, engine oil level, hydraulic oil pressure, and cabin vibrations.

5.2 Maintenance Management System Performance Indicators

The performance indicator window in Fig. 6 shows the fault due to alternator breakdown. This system measures the maintenance crew reporting time and fault removal time and thus reduces the breakdown time to minimum.

5.3 Data Logging Using Real-Time Parameter Monitoring

The real-time data logs are received serially and displayed in the parameter monitoring window as shown in Fig. 7.

5.4 Manual Data Entry and Productivity Graph Window

Performance and productivity of the system are known in real time to the mine manager by manually entering the data values for shift hours, swing factor, swell factor, bucket fill factor, and shovel cycle time as shown in Fig. 8.

The manual data entered is used by mine manager in the productivity graph window as shown in Fig. 9 to check the performance and productivity of the hydraulic excavator RH90C in the real time for achieving the production targets.

6 Shovel Productivity Evaluations

The effective use of shovel mining is necessary for better equipment performance and productivity and is dependent upon a number of factors as mentioned below [12].

1. Truck size selection.
2. Average swing angle.
3. Truck spotting time.
4. Blasting efficiency.
5. Operator attitude and efficiency.
6. Cycle time.
7. Loading and waiting time.
8. Truck positioning.

Fig. 7 Data logging using parameter monitoring

Fig. 8 Manual data entry

Fig. 9 Productivity graph window

Table 1 Swing factor value for varying swing angle

Swing angle	45°	60°	75°	90°	120°	150°	180°
Swing factor	0.84	0.90	0.93	1	1.1	1.2	1.3

6.1 Shovel Cycle Time and Shovel Swing Factor

Cycle time of the shovel is affected by the bucket swing angle and varies with truck positioning. The cycle time of shovel as loader is expressed in terms of the total time taken to complete one cycle of operation starting from digging to dumping and swinging back to digging face [13]. Productivity of the shovel is directly affected by swing factor (Sf) as this affects the cycle time [13]. Shovel takes different swing angles to fill the truck as shown in Table 1 showing swing factor value for varying swing angle.

6.2 Availability (A)

Availability of the equipment takes into consideration the nonscheduled time, the scheduled maintenance time, the equipment breakdown time, setup and adjustment time [15, 16] for high equipment availability.

$$A = (\text{TSH} - \text{BD} - \text{MH})\big/(\text{TSH}). \tag{1}$$

6.3 Shovel Utilization (U)

Utilization can be calculated using Eq. (2) based on the idle time delays [8, 9, 14, 15].

$$\text{Shovel Utilization } U = (\text{TSH} - \text{BD} - \text{MH} - \text{IT})\big/(\text{TSH} - \text{BD} - \text{MH}). \tag{2}$$

TSH is total shift hours, BD is breakdown hours, MH is maintenance hours, and IT is idle time hours.

6.4 Productivity (P) Evaluation for Hydraulic Shovel Demag H55N 3.3 Cu.M

Productivity of the shovel can be calculated by Eq. (3) as per simple relation [17].

$$P = (\text{Bc} * S * \text{Bf} (3600 * \text{Sf}) * U)\big/\text{CT} \tag{3}$$

where

Bc   bucket capacity (m^3),
S   swell factor (S) of material (1.3),
Bf   bucket fill factor (0.8),
Sf   swing factor (0.9),
CT   shovel cycle time (25 s),
IT   idle time (10 min)

The data known from the NCL records is manually entered from the PC for finding the real-time productivity of the hydraulic excavator as shown in Table 2.

Table 2 Real time productivity estimation of hydraulic shovel demag H55N 3.3 Cu.M

Shovel ID	Breakdown hrs.	Maintenance hrs.	Availability	Utilization	Productivity
DA	0.113	0.09	0.974931	0.9786	1319.04

6.5 *Result and Analysis*

It is observed from the above analysis that to achieve better availability and productivity from the system, it is significant to reduce the breakdown and maintenance time by monitoring the faults before it happens using maintenance monitoring and management system to improve the equipment productivity.

7   Conclusion

Real-time monitoring of the key parameters of the equipment using CBM technology allows the machine operator to find when the machine is going to fail, and the maintenance staff immediately report with the required maintenance tools to rectify the fault, set the equipment in the working order, and hence increase the productive life cycle of the equipment. Implementation of RFID technology helps to keep check on the maintenance personnel for delay in reporting and therefore reduces breakdown time. CBM and communication technologies therefore help to monitor the fault immediately and improve the availability and better productivity of the mine; the proposed technology therefore helps to reduce the downtime cost and requires fewer inventories.

References

1. Imad Alsyouf, "The role of Maintenance in improving company's productivity and Profitability", Science direct, international journal of production Economics, 105 pp. 70–78, 2007.
2. Chris Sellathamby, Brian Moore, Steven Slupsky, "Increased Productivity by Condition based maintenance using Wireless strain measurement system", Memo conference and trade show, Canadian Institute of Mining, Sudbury ON Canada, pp. 24–27, 2010.
3. Piyush Rai, "Performance assessment of Draglines in Opencast mines", International Journal of engineering & material sciences vol. 11, pp. 493–498, 2004.
4. Kumbi Mugwindiri, Charles Mbohwa, "Availability, Performance Improvement by using Autonomous Maintenance – The case of a Developing Country, Zimbabwe." World Congress on Engineering, London, U.K, Vol. 1, 2013.

5. Lifang Tang and Chuanjin Wang "Implementation of Mine Equipment Maintenance management System based on Web", Proceedings of the 2012 2nd International Conference on computer and Information Application (ICCIA), Atlantis Press, Paris, France, 2012.
6. P. Bastos, I. Lopes, and L. Pires, "A maintenance prediction system using data mining techniques", Proceedings of the World Congress on Engineering, Vol. 3, WCE, London, U.K. 2012.
7. Daniela Borissova and Ivan Mustakerov, "An integrated frame work of designing a decision support system for Engineering predictive maintenance", International Journal of information technologies and Knowledge Vol. 6, 2012.
8. R.C.M. Yam, P.W. Tse, L. Liand, P.Tu, "Intelligent Predictive Decision Support System for Condition-Based Maintenance", International Journal of Advanced Manufacturing Technology, 17:383–391 Springer-Verlag London Limited, 2001.
9. Jonathan M Ross, "Condition based maintenance—a tool for improving productivity in shipyards", Journal of ship production, vol. 18, No. 3, pp 175–184, 2002.
10. V.M. Kalra, Tilak Thakur, B.S. Pabla, "Intelligent Equipment Health Monitoring System for improving availability of Remote Mining Equipment", International Journal of Engineering Research and applications (IJERA), ISSN: 2248–9622, National Conference on advances in Engineering and Technology, 2014.
11. Esko K. Juuso and Antti H. Koistinen, "Decision support for risk management in mining industry", Cleen Research report Helsinki, www.cleen.fi.ISBN978-952-5947-87-8, 2015.
12. Prakash Kumar, Srivastava, R.K, "Development of a Condition Based Maintenance architecture for Optimal maintainability of Mine Excavators", IOSR Journal of mechanical and civil engineering (IOSR-JMCE) e-ISSN: 2278–1684, p-ISSN: 2320-334X, vol. 11, Issue 3, Ver. 5, pp. 18–22, 2014.
13. A.Ursenbach, Qun Wang and Ming Rao, "Intelligent maintenance support system for mining truck conditioning monitoring and troubleshooting", International Journal of Surface mining, Mining reclamation and environment, vol. 8, pp. 73–81, 1994.
14. Dal B., Tugwell P. and Great banks R. "Overall equipment effectiveness as a measure of operational Improvement- a Practical Analysis", International Journal of Operations & Production Management, vol. 2 issue 12, pp. 1488, 2000.
15. Abdul Talib Bon, Lim Ping Ping, Berhanuddin Mohd Salleh, Asri Selamat, "Evaluating total productive Maintenance using overall equipment Effectiveness: Fundamental Study" Elixir international Journal, Production Management, pp. 3293–3295, 2011.
16. Elevli, Sermin, and Birol Elevli. "Performance measurement of mining equipment's by utilizing OEE." Acta Montanistica Slovaca, vol. 15, No. 2, pp. 95–101, 2010.
17. Mousa Mohammadi, Piyush Rai, Suprakash Gupta., "Performance Measurement of mining Equipment", International Journal of Emerging Technology and Advanced Engineering, Vol. 5, Issue 7, 2015.

Reviewing the Problem of ELVs in India and Checking Possibilities of Pyrolysis as a Solution

Kaival Rajesh Nayak and Shashikant Auti

Abstract The number of automobiles is rising and so is the amount of end-of-life vehicles in India. With an estimated count of 2,18,95,439 end-of-life vehicles by 2025, the amount of heterogeneous waste in the form of automotive shredder residue is also grave. This paper discusses recycling, and management of end-of-life vehicles. It also discusses automotive shredder residue characteristics. The paper thus focuses on the possibility of pyrolysis as a viable solution to the problem of automotive shredder residue treatment.

Keywords End-of-life vehicles · Automotive shredder residue · Pyrolysis

1 Introduction

1.1 Overview on Automobiles

Since a long time in memorial, mankind has tried to move from one place to another in a manner faster than previous. It was in the mid-1800s when the first automobile of what we know today came into being. Since then, the problem of disposing of the vehicles after their use has been a grave problem. The use of automobiles since their inception has increased exponentially since then. Along with the production and use of automobiles also comes the problem of an environmental deterioration due to increased demands of automobiles, leading to various environmental hazards, polluting the land, air, and soil in various phases of the life of a vehicle. In India, year 2009–2010 witnessed more than 11 crore vehicles that included commercial

K. R. Nayak (✉)
Department of Mechanical Engineering, Dwarkadas J. Sanghvi College of Engineering, Vile Parle, Mumbai, India
e-mail: nayakkaival@gmail.com

S. Auti
Department of Mechanical Engineering, Veermata Jijabai Technological Institute (VJTI), Matunga, Mumbai, India

565

Fig. 1 Market proportions of automobiles in India (%) 2013/2014 (SIAM 2015) [1]

DOMESTIC VEHICLE MARKET SHARE (%)

- 2 Wheelers
- 3 Wheelers
- Personal 4 Wheelers Vehicles
- Official 4 Wheeler Vehicles
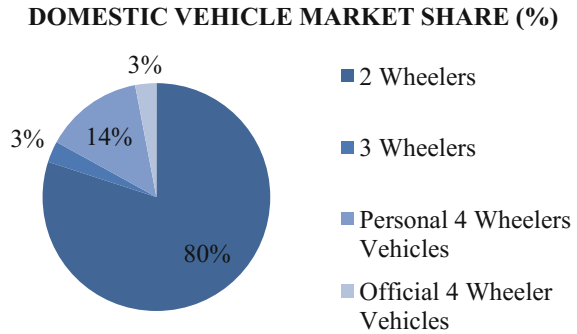
vehicles, passenger vehicles, three-wheeled (3W) and two-wheeled (2W) vehicles; a key observation was that the vehicle ownership has galloped considerably. According to (SIAM) Society of Indian Automobile Manufacturers, during 2014–2015 itself, there were alone 2,33,66,246 automobiles among which 6,97,083 were commercial vehicles, 32,20,172 were passenger vehicles, 9,49,021 were three wheelers, and 1,84,99,970 were two wheelers [1]. The peculiar difference in the automobile sector of any other country like the EU or the USA and India is that the number of 2W is quite high as compared to the 4W which can be seen in the pie diagram (Fig. 1).

1.2 Environmental Considerations

With the increasing pollution across the globe, it becomes imperative to think and enact toward reducing the carbon footprint of automobiles, not only when they are plying on the roads but also when they are not in use or de-registered. The utilization of petroleum products emissions can be brought down by reducing the mass of the car by incorporating more plastics polymers. Despite a small dip in the production of cars in the financial year 2008–2009 due to the global economic recession, the production of cars on a global level has increased manifold in a continuous fashion for about 30–40 years [2]. In the year 2007, about 7.3 crore vehicles were fabricated across the world. When compared to past, it was not more than 3.8 crore in 1980s [3]. The automobile industry in today's world is facing a lot of hurdles as cars and other automobiles have a considerable amount of impact on environment at all the stages of their product life cycle.

1.3 Defining End-of-Life Vehicle (ELVs)

Sometimes due to overuse of vehicles, the life of a vehicle is overstretched, it may undergo many repairs and re-conditioning, and then, over a period of times,

it becomes irreparable and has to be got rid of. Thus, for such vehicles, a new kind of term is used and that is 'end-of-life vehicles' (ELVs). The EU Directive of 2000 has stated that 'end-of-life' means a car or an automobile which is of no use anymore. The final possessor defines a particular automobile as an end-of-life vehicle once it is unsafe to ply on the road or does not comply with the government norms regarding the permissible emission from a vehicle [4]. When one looks into the EU Waste Shipment Regulations, vehicles which are redundant and have become an ELV are not permitted to run on the road or to be sent outside of the EU. Automotive Industry Standards define 'end-of-life vehicle' as a vehicle which by knowledge of its final possessor can be scrapped already [5]. Here, a major attention needs to be drawn toward the point that the number of vehicles de-registered is not the same as the number of ELVs as many vehicles are de-registered and sent as an export or any other purposes. The figure depicts the types of ELVs and their broad description along with their definitions. The population of vehicles in India is ever increasing, and it has been estimated that the count of ELVs has reached more than 87 Lakhs, and among these, about 83% were two wheelers in 2015. Similarly, for the year 2025, it is projected that the number of ELVs will reach to about 2 crores out of which 80% will be 2W.

1.4 Recycling of ELV

Recycling of end-of-life vehicles is not a thing of present; waste cars have been recycled by industries for many years that too before any legislation regarding the same was passed by any nation in the world [6]. The premier industrial level automobile shredder machine was installed and its operation began in the year 1958 (Fig. 2).

As per CPCB of India, it is estimated that the normal consumer vehicles have roughly about 8% aluminum and its alloys, 70% ferrous compounds, and the remaining others consist of glass and other polymers. Sakai et al. states that among the world recycling pattern observed by the institute of recycling, 2014 that recycling of 1 ton of steel consists 635 kg of coal, 1134 kg of ferrous ore, and about 55 kg of limestone. The ever-increasing demands of resources can be fulfilled only if there are changes
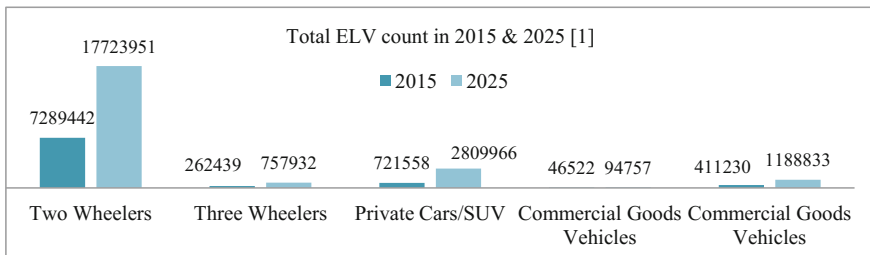
Fig. 2 Total ELV count in 2015 and 2025
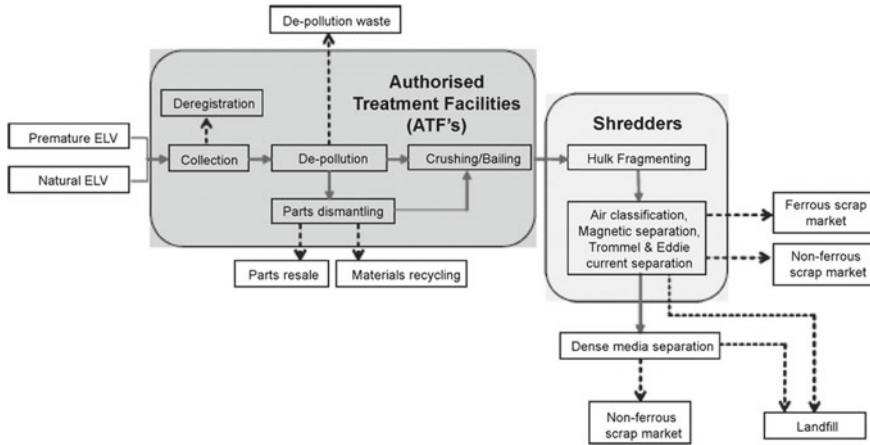
Fig.3 Flow of a vehicle through the different end-of-life operations [21]

in the behavioral pattern of consumption and recycling gets its share of focus. As far as India is concerned, almost all the scrap workshops are managed by the semi- or informal sector which uses very old/ancient methods and tools to extract useful metals from the scrap [1]. The readers are cautioned that the semi-formal recyclers are referred to as informal recycling centers which do not have any compliance or certification from the government or the official governing body. Along with the technological advancements, there can be seen a paradigm shift in the materials that are obtained as recyclables from the car or any automobile for that matter the use of polymers has gone up by 50% over the past 20 years. Figure 3 shows the schematic process of an ELV break down. The 3Rs of recycling play a pivotal role in deter- mining various policies for ELV treatment and management. Reuse, recycling, and recovery are defined as shown below:

- *Recycling*: Processing waste materials again either for their original purpose or for any other purposes, but not energy recovery.
- *Reuse*: Again utilizing parts of an ELV for the same job for which they were designed for.
- *Recovery*: Any of the applicable operations as mentioned in the Annex IIB of the European Directive on ELVs.

2 Management of End-of-Life Vehicle and Automotive Shredder Residue Production

The reusing and recycling of an ELV are economically viable as it is made of about 70% of metals which is much higher than any other consumer product due to the

presence of hazardous substances like heavy metals, lubricating oils, engine and other oils, and POPs better known as persistent organic pollutants. The environment is under an adverse impact because of the fraction of ELV which is not recycled. As a result, even the European Union introduced a stringent regulation regarding the recycling, reusing, and recovery of end-of-life vehicles in 2000 [7]. This helped the governments of various member states of EU to keep a control on the growing stream of waste, and it also introduced a new concept of extended producer responsibility or EPR [8] which makes all the stakeholders responsible in the recycling process of an ELV which is right from collection to shredding. To fulfill the objective of reducing the old and abandoned cars in the EU by 2007, car manufactures had to provide a free service to the last owner that they will collect their cars and treat it accordingly. The car manufactures had to take back about 11% of the total vehicles as in 2000 alone in the UK [9].

2.1 ELV Recycling Activities: De-Pollution and Dismantling

De-pollution: The recycling of as a scrap end-of-life vehicle begins at the dismantling facility where it is initially de-polluted after which it is then dismantled (many a times the two steps are collectively called as 'dismantling'). The definition of de-pollution includes eliminating components and substances that may pose as a possible hazard to the environment like fuel, the battery, any mercury-containing component, other fluids, and airbags [1].

Dismantling: After de-pollution, the next step is to dismantle the vehicle. Dismantling as the name suggests is the process of disassembling the car into its various components like tyres, engine, bumper, etc. [1]. For a developed country and a technologically advanced country, there will be more use of automation and less labor will be required. On the other hand, in economically developing countries like India where labor is easily available, this process is more labor intensive.

2.2 Shredding/ASR

ASR (automotive shredder residue) has a very high degree of heterogeneity in various components like residual metals (5–25%), rubber (3–38%), polymers(20–49%), fibrous material (5–45%), various types of wood (2–5%), and glass (2–18%), most of which can be reprocessed to make fuel substitutes. However, separation from these components to substitutes is very difficult. Thus, it is more commonly either used for recovery of energy or to be directly sent to the landfills [1].

Generally, 7–35% of an end-of-life vehicle's mass is extracted for the purpose of reusing or recycling, which solely depends on the age of the vehicle (premature or natural ELV), on the current market fluctuations, and also on the intensity of labor involved to extract the components. A huge gap persists between the EU countries

(5–10% of ELV mass extraction) and South Korea (up to 35% extraction of ELV) [10–12]. The car bulk that stands after dismantling and de-pollution is then transferred to a shredder machine. As mentioned before, a hammer mill shredder cuts it down to smaller pieces which can even fit in one's hand [10, 12]. Metals are then again extracted from this trash with the help of a chain of mechanical and magnetic separation systems. Up to 65% of the original mass can be achieved by removing ferrous metal portion of an ELV. Metals other than iron are usually removed using the principles of dense media separation or of back emf (eddy currents); about 5% is recovered by this of the original end-of-life vehicles weight. In some parts of the world, some plastic portions (including, e.g., polystyrene, polypropylene, and ABS) although in small numbers are extracted from the system by using mechanical or physical separation methods, making use of the differences in melting point, density or solubility or even boiling points in some cases. After all these process stages as mentioned in Fig. 4, we can say that the residual waste hulk is about 15–25% of the original ELV's weight and this is together collectively termed as 'automotive shredder residue' (ASR). The remaining portion about which we just discussed is believed to increase in the years to come, this is because the quantity of synthetic plastics and other polymers used in vehicles is bound to increase thus decreasing the amount of the ferrous metal portion, and a proper plastic extraction system is yet not a common practice across the globe. Dedicated and appropriate landfill sites are now assigned to extremely heterogeneous materials and classified as hazardous material, ASR [10, 13]. To increase and improvise the existing European policy of reuse and recycling/recovery, two major paths are chalked out: use of ASR processing techniques and systems and more complete dismantling or development of the ELV. Increasing dismantling is at present less feasible on economics aspects as it is a labor-intensive job along with comparatively lesser prices for non-metallic materials [8]. As directed by the European Union, the automobile companies are introducing 'design to disassembly': e.g., welded joints and bonding agents are avoided in order to cause an overall reduction in the time for disassembly; instead, bolded or riveted joints can be used. However, regardless of these changes in design, advancements in the technologies for ASR processing are still needed for processing ELVs, as the average lifetime of an automobile is between 12 and 15 years, depending on the various laws that are practiced in different geographical locations [10, 14, 15] and also the company of the car and the model of the automobile. These advanced technologies for mechanical separation and/or advanced physical separation which keep in mind of recycling, or for thermo-chemical recovery and or energy will gain importance in the near future.

2.3 Characteristics of ASR

Categorization of ASR is imperative to distinguish portions that are potentially combustible so as to choose, optimize, and improvise recovery and recycling methods. Automotive shredder residue is generally considered to be about 10–25% of ELV's
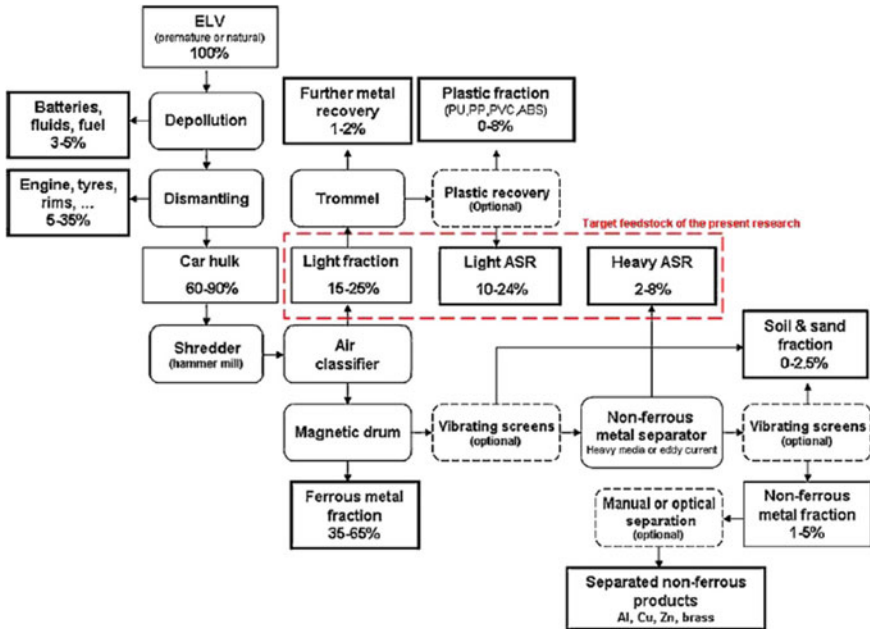
Fig. 4 Diagrammatic representation of the processing of an ELV [21]

mass that remains after all the above-discussed processes (Fig. 4). The author wishes to warn the reader that some authors elucidate ASR as the portion post the process of shredding, yet not considering the extraction of the metal portion that holds for about 65–66% of the actual ELV's mass [11, 16]. Current article accepts the first definition of ASR, which is the residue that remains shredding and after extraction of metals and other alloys along with the chrome. It should also be remembered that the hammer mill shredders are not just used to process ELVs, but also used to process other products which come from various industries, let alone automobile [6, 12, 17]. The properties of ASR depend mainly on a lot of shredder parameters beyond the scope of discussion of this paper [6, 18]. Because of the type of treatment mentioned in Fig. 4, automotive shredder residue can be categorized [6] into light fluff, heavy fluff, and mud fraction.

3 ASR Pyrolysis

Pyrolysis is one of the promising tools used in waste management industry; it is the process in which waste like biowaste or ASR is treated. Pyrolysis is generally operated at temperatures ranging (673–873 K), and in the lack of oxygen, or at very less oxygen, this is done so as the combustion of feedstock does not happen significantly.

The products of combustion are (1) gases, (2) condensable organic vapors named as pyrolytic liquids, and (3) a solid residue [19, 20]. A proportionate outcome of the three products is dependent on the mixture proportion of the feedstock and various other factors like temperature, heat transfer rate to the automotive shredder residue particles, and the time spent by the components in the control volume and also the substances in the reactor. The production of solid char generally lies between 33 and 68 wt%, and thus is seen to exceed the normal char quantities which are seen when paralyzing polymers or biofuel. Fundamental research of ASR pyrolysis mostly uses thermo-gravimetric analysis method and two types of small-scale reactors viz. laboratory-scale pyrolysis reactors and thermo-gravimetric reactors which are always attached in a couple with the characterization and identification of the reaction product.

4 Conclusion

After reviewing research of various authors and publications and also including the current Indian scenario of ELVs and ASR, we can say that the ever-increasing demands of automobiles in India will eventually lead to a generation of a huge amount of automobile wastes and also ELVs. ASR generation and management are also undergoing a paradigm shift as the amount and type of materials being used in the cars are changing from metals to polymers. It is also the need of the hour to consider the environmental factors and find out and optimize various other solutions to generate alternate fuel solutions. By the current review, we can conclude that pyrolysis is a promising solution for the problem of automotive shredder residue treatment.

References

1. Guidelines for environmentally sound management (ESM) of end- of - life vehicles (ELVs) in India by Central pollution control board, ministry of environment, forest & climate change (Government of India), November, 2016.
2. OICA: www.oica.net [production statistics 1998–2009].
3. N. Kanari, J.-L. Pineau, S. Shallari, End-of-life vehicle recycling in the European Union, JOM 8 (2003) 15–19.
4. DIRECTIVE 2000/53/EC OF THE EUROPEAN PARLIAMENT AND OF THE COUNCIL on end-of life vehicles, 18 September 2000.
5. AUTOMOTIVE INDUSTRY STANDARD (AIS – 129) on End-of-Life Vehicles by AUTOMOTIVE RESEARCH ASSOCIATION OF INDIA, central motor vehicle rules – department of road transport & highways (Government of India), March, 2015.
6. M.K. Harder, O.T. Forton, A critical review of developments in the pyrolysis of automotive shredder residue, J. Anal. Appl. Pyrol. 79 (2007) 387–394.
7. European Parliament and the European Council, Directive 2000/53/EC of the European Parliament and of the Council of 18 September 2000 on end-of-life vehicles, ff. J. Eur. Commun. L 269 (2000) 34–42.

8. C. Edwards, G. Coates, P.G. Leaney, S. Rahimifard, Implications of the End-of- Life Vehicles Directive on the vehicle recovery sector, Proc. IMechE, Part B: J. Eng. Manuf. 220 (2006) 1211–1216.
9. S. Kollamthodi, A. Hird, L. Elghali, K. Johnstone, M. Wayman, V. McColl, Data required to monitor compliance with the End of Life Vehicle Directive, TRL Limited Proj. Rep. (2003), SE/483/02.
10. P. Ferrão, P. Nazareth, J. Amaral, Strategies for meeting EU end-of-life vehicle reuse/recovery targets, J. Ind. Ecol. 10 (2006) 77–93.
11. H.-T. Joung, S.-J. Cho, Y.-C. Seo, W.-H. Kim, Status of recycling end-of-life vehicles and efforts to reduce automobile shredder residues in Korea, J. Mater. Cycles Waste Manage. 9 (2007) 159–166.
12. O.T. Forton, M.K. Harder, N.R. Moles, Value from shredder waste: Ongoing limitations in the UK, Resour. Conserv. Recycl. 46 (2006) 104–113.
13. C.A. Ambrose, R. Hooper, A.K. Potter, M.M. Singh, Diversion from landfill: quality products from valuable plastics, Resour. Conserv. Recycl. 36 (2002) 309–318.
14. F. Andersen, H. Larsen, M. Skovgaard, Projection of end-of-life vehicles: development of a projection model and estimates for ELVs for 2005–2030, ETC/RWM working paper 2008/2, Copenhagen, 2008.
15. J. Staudinger, G.A. Keoleian, Management of End-of-life Vehicles (ELVs) in the US, Rep. of the Center for Sustainable Systems, Michigan, USA (2001) No. CSS01–01.
16. OVAM, Validatie van de recyclagepercentagesvoorafgedanktevoertuigenbij shredder-en flottatiebedrijven, H. De Baets, Mechelen, Belgium (2008) D/2008/5024/39.
17. L. Börjeson, G. Löfvenius, M. Hjelt, Characterisation of automotive shredder residues from two shredding facilities with different refining processes in Sweden, Waste Manage. Res. 18 (2000) 358–366.
18. G. Mancini, R. Tamma, P. Viotti, Thermal process of fluff: preliminary tests on a full scale treatment plant, Waste Manage. 30 (2010) 1670–1682.
19. Murillo, R., et al. "The Application of Thermal Processes to Valorise Waste Tyre." Fuel Processing Technology, vol. 87, no. 2, 2006, pp. 143–147, doi: https://doi.org/10.1016/j.fuproc.2005.07.005.
20. Aylón, E., et al. "Valorisation of Waste Tyre by Pyrolysis in a Moving Bed Reactor." Waste Management, Pergamon, 6 Nov. 2009, www.sciencedirect.com/science/article/pii/S0956053X09004231.
21. Vermeulen, J. Van Caneghem, C. Block, J. Baeyens, and C. Vandecasteelea "Automotive shredder residue (ASR): Reviewing its production from end-of-life vehicles (ELVs) and its recycling, energy or chemicals' valorization" Journal of Hazardous Materials 190 (2011) 8–27.

Effect of Process Parameters While Machining Using Abrasive Jet Machine (AJM)

Shaishav M. Jadav and Ramesh R. Lekurwale

Abstract Abrasive jet machine (AJM) uses air jet velocity for to guide abrasive particle and to erode material of workpiece. Amount of material removed depends on various process parameters such as nozzle bore diameter, operating pressure, standoff distance, etc. While drilling micro hole it is very kin to get required amount of bore diameter on workpiece. For such condition it is very important to observe kerf taper. This paper gives us brief review about recent work done by various researchers regarding effect of process parameters on output i.e. hole diameter and also mention value to keep for process parameter to get better result. Experiments were conducted using experimental setup and drilling was performed and results are discussed.

Keywords AJM · Kerf taper · Standoff distance · Pressure · Nozzle · Sea sand

1 Introduction

Abrasive jet machining using (AJM) compressed air force, which is further converted into velocity (air jet), for material removal. This air jet is accompanied by fine abrasive particles. This abrasive particles impact on surface of work material and develop fracture. These fractured particles of work material get detached from material due to continuous impact of abrasive jet and hence material is removed. AJM is similar to that of sand blasting but particles used in AJM are finer. Air which carries abrasive material acts coolant and hence heating of work material does not occur. Comparing other non conventional machining approaches, the investment on AJM setup is low. And also operational and maintenance cost is low. AJM has wide application in manufacturing of electronic devices, tribo-elements and MEMS (Micro-Electro-Mechanical Systems). Recent development of special purpose parts, such as semiconductor and sensors for micro-machine has been expanded [1] (Fig. 1).

S. M. Jadav (✉) · R. R. Lekurwale
Department of Mechanical Engineering, K. J. Somaiya College of Engineering, Mumbai, India
e-mail: shaishav.j@somaiya.edu
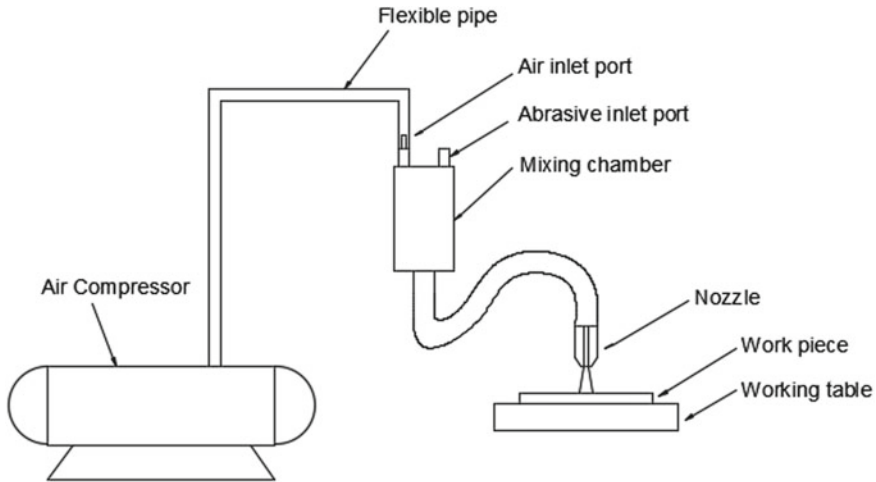
Fig. 1 Components of abrasive air jet machine

Recent study by Nassef et al. [2] used axial feeding mechanism to reduce taper effect of varying stand-off distance across thickness, in drilling of glass plate. With this method stand of distance remains constant through the thickness of work material. Li et al. [3] studied evolution of blind hole on glass using abrasive jet machining. Particle flow rate has key role in hole bottom forming i.e. concave, flat or convex. Srikanth and Sreenivasa Rao [4] conducted experiments to determine machinablity under different control parameter to find out optimal level of performance and listed them. Wang et al. [5] worked on effect of process parameters on grooving performance on quartz crystal. Groove width, depth, surface roughness and kerf taper were inspected.

2 Literature Review

Literature review has been carried out effect of process parameters (such as stand-off distance, air pressure, abrasive grain size and nozzle diameter) on machining using abrasive jet machine.

2.1 Li et al. [3]

Particle flow rate and air pressure were set which resulted in profile variation and hence it indicated that the particles distribution density across the cross section of cylindrical nozzle also varied with the setting parameters. A 3-d laser microscope

Table 1 Process parameters for drilling [2]

Parameters	Levels
Pressure (MPa)	0.3,0.6,0.9
Nozzle diameter (mm)	4, 5, 6
Standoff distance (mm)	4, 6, 10
Abrasive grain size (μm)	150, 300, 600

Fig. 2 Kerf taper comparison with and without axial feed [2]
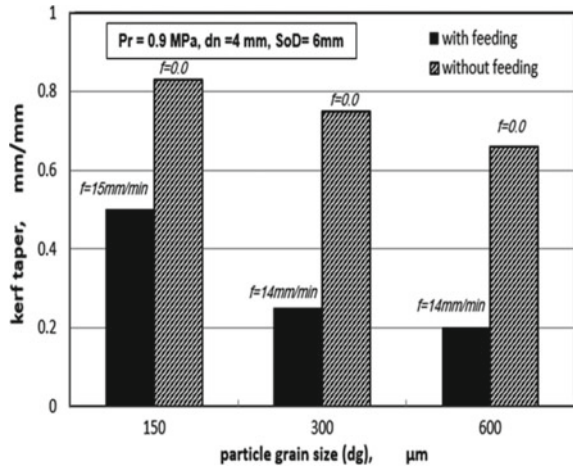
was used to measure depth and curvature of hole bottom surface. At low flow rate, hole bottom was formed with convex shape and with increase in flow rate, hole bottom become flat or even concave. Graph plotted for particle flow rate and cutting time versus air pressure.

2.2 Nassef et al. [2]

3 mm soda lime glass was drilled using AJM. Air pressure, nozzle diameter, SoD and abrasive grain size were considered as process parameters while performing experiments. Experimental results were used to create an ANN predictive model of kerf taper as a function of process parameters and GA was used to optimize process parameters (Table 1).

Secondly an Axial feed setup was used to maintain Standoff distance as erosion takes place and as result kerf taper was reduced (Fig. 2).

Table 2 For better MRR [4]

Pressure	8 kg/cm^2
Standoff distance	10 mm
Nozzle diameter	4 mm

Table 3 For better kerf i.e. smaller width [4]

Pressure	6 kg/cm^2
Standoff distance	9 mm
Nozzle diameter	3 mm

2.3   Srikanth and Sreenivasa Rao [4]

Al_2O_3 and SiC grain were used as abrasive and nozzle made of tungsten carbide with different bore diameter of 1, 2, 3 mm. Glass sheet was used as work piece due to its homogenous nature. Glass was drilled carried out by setting process parameters such as Pressure, SOD and Nozzle diameter. Different readings were taken based on the level of Taguchi Analysis and by changing values different process parameters. Results were then inspected by Taguchi method and compared with ANOVA. Results were obtained as, (Tables 2 and 3).

2.4   Vanmore and Dabade [6]

Laval Type nozzle was developed and used to machine stainless steel ANSI 316 plate. Experiments were conducted by drilling hole on S.S. plate of thickness 0.6 mm, by varying guiding pressure from 1 to 2 bar with 0.5 bar increment. Results shows, the flow of jet exit was convergent for some distance than start diverging. NTD was performed and diameter of hole was measured along depth of hole to check concentricity of hole machined.

2.5   Madhu and Balasubramanian [7]

An internal threaded nozzle was introduced for imparting swirling motion to abrasive particle, for drilling in 3 mm thick carbon fibre reinforced polymer (CFRP). Comparative study for nozzle with internal thread and without internal thread was made through experiments with different settings. Result shows, at same process parameter, machining time was less for internal threaded nozzle when compared to nozzle without internal thread. Material removal rate was better with improved cutting precision for internal threaded nozzle. And also internal thread of nozzle reduces the kerf angle for machining of CFRP.
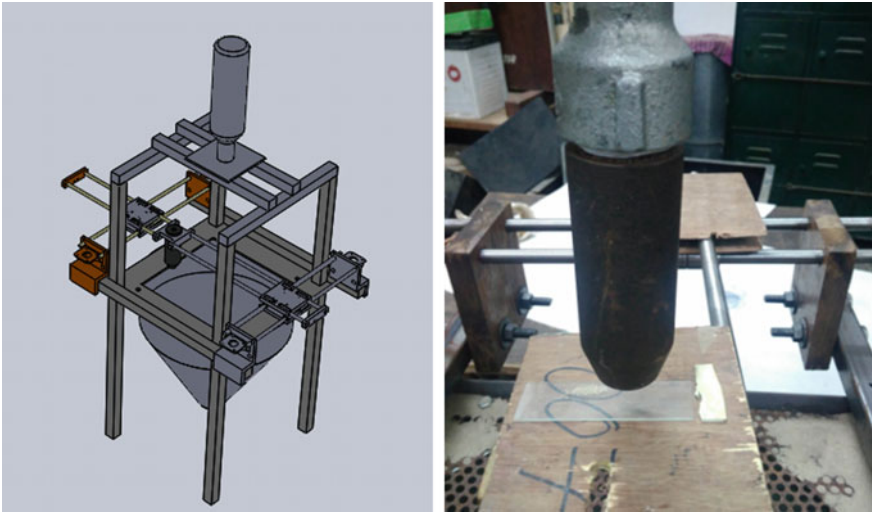
Fig. 3 Experimental setup used for experimentation

2.6 Gupta et al. [8]

AWJM was used for cutting of marble sheet. Experiments were conducted according to taguchi design of experiments. ANOVA was used to evaluate data obtained. Predicted value using ANOVA and actual value showed error less than 5% for kerf taper and width. For top kerf width, nozzle transverse speed is most significant than followed by water pressure. For minimum top kerf width, pressure = 340 MPa and transverse speed = 100 mm/min. For min kerf taper angle pressure = 200 MPa and speed = 50 mm/min.

3 Experimental Setup

Experiments were performed using experimental setup which designed and fabricated. Figure 3 shows experimental setup used for drilling of hole. Nozzle made of tungsten carbide was used and workpiece material is 1.5 mm thick glass. Input parameters to consider while working with abrasive air jet machining are air pressure, abrasive (material and size), nozzle (material and bore diameter), standoff distance, impact angle.

Drilling was done using above specification and output such as upper and lower diameter observed and results are discussed.

Table 4 Specification of Experimentation

Medium	Air
Abrasive	Sea sand
Workpiece material	Glass
Pressure	6.5–7.5 kg/cm^2
Nozzle diameter	1.5 mm
Standoff distance	6–8 mm

4 Results and Discussion

4.1 Effect of Pressure

Pressure was varied and other parameters such as standoff distance and nozzle diameter were kept constant. Results of effect of pressure while standoff distance is kept constant are mentioned in Table 4.

Hole diameter increases with increase in pressure. Also upper diameter has greater value than lower diameter.

4.2 Effect of Standoff Distance

Standoff distance was varied and other parameters such as pressure and nozzle diameter were kept constant. Results of effect of standoff distance while standoff distance is kept constant are mentioned in Table 5.

Hole diameter increases with increase in standoff distance. Also large change in hole diameter with increase standoff distance.

5 Conclusion

Recently lot of work have been done on selection of process parameter, by various researchers. A review of recent research has been conducted in this paper. Changing

Table 5 Effect of pressure

Sr. No.	Pressure (kg/cm^2)	Standoff distance (mm)	Upper diameter (mm)	Lower diameter (mm)
1	6.5	6	2.63	2.54
2	7.0	6	2.74	2.66
3	7.5	6	2.82	2.74

Table 6 Effect of standoff distance

Sr. No.	Pressure (kg/cm^2)	Standoff distance (mm)	Upper diameter (mm)	Lower diameter (mm)
1	6.5	6	2.16	1.90
2	6.5	7	2.34	2.12
3	6.5	8	2.52	2.34

impact angle and axial feed setup as used by Nassef et al. [2] can help for further changes that can improve results. Experimental results shows that hole diameter increases with increasing pressure and standoff distance (Tables 5 and 6).

References

1. S. Rajendra Prasad, Dr. K. Ravindranath, Dr. M.L.S Devakumar (2016), "A Research Review on Advance Approaches in Abrasive Jet Machining", International Conference on Recent Innovations in Civil & Mechanical Engineering, pp. 57–62.
2. Nassef, A., Elkaseer, A., Abdelnasser, E. S., Negm, M., & Qudeiri, J. A. (2018). Abrasive jet drilling of glass sheets: Effect and optimisation of process parameters on kerf taper. Advances in Mechanical Engineering, 10(1), 1687814017748435.
3. Li, H., Wang, J., Kwok, N., Nguyen, T., & Yeoh, G. H. (2018). A study of the micro-hole geometry evolution on glass by abrasive air-jet micromachining. Journal of Manufacturing Processes, 31, 156–161.
4. Srikanth, D. V., & SreenivasaRao, M. (2014). Metal removal and kerf analysis in abrasive jet drilling of glass sheets. Procedia Materials Science, 6, 1303–1311.
5. Wang, J., Moridi, A., & Mathew, P. (2011). Micro-grooving on quartz crystals by an abrasive air jet. Proceedings of the Institution of Mechanical Engineers, Part C: Journal of Mechanical Engineering Science, 225(9), 2161–2173.
6. Vanmore, V. V., & Dabade, U. A. (2018). Development of Laval Nozzle for Micro Abrasive Jet Machining [MAJM] Processes. Procedia Manufacturing, 20, 181–186.
7. Madhu, S., & Balasubramanian, M. (2018). Effect of swirling abrasives induced by a novel threaded nozzle in machining of CFRP composites. The International Journal of Advanced Manufacturing Technology, 1–15.
8. Gupta, V., Pandey, P. M., Garg, M. P., Khanna, R., & Batra, N. K. (2014). Minimization of kerf taper angle and kerf width using Taguchi's method in abrasive water jet machining of marble. Procedia Materials Science, 6, 140–149.

Identifying Key Success Factors of Sustainability in Supply Chain Management for Industry 4.0 Using DEMATEL Method

Malleshappa T. Bhagawati, E. Manavalan, K. Jayakrishna and P. Venkumar

Abstract There is an increase in demand for industrial systems to be more competitive to expand their product reach and streamline their supply chain processes. The vision of sustainable supply chain is becoming reality as rapid advancements are happening in digital technologies. With the emerging fourth industrial revolution industry 4.0, the supply chain environment is compactly interconnected with the devices, equipment, and human that allows accessing and analyzing the real-time information. Based on the literature survey, a framework model with main perspectives and performance factors are developed to assess the sustainability of an automotive organization. Importance of performance factors and their relations are analyzed through DEMATEL technique. The result shows that Internet of Things and environment-friendly practices are the two major influential performance factors in order to become a more sustainable organization to meet industry 4.0 requirements.

Keywords Sustainable supply chain · Industry 4.0 · DEMATEL method

Abbreviations

SSC	Sustainable Supply Chain
SCM	Supply Chain Management
SSCM	Sustainable Supply Chain Management
IoT	Internet of Things
CPS	Cyber-Physical System
DEMATEL	Decision-Making Trial and Evaluation Laboratory

M. T. Bhagawati (✉) · P. Venkumar
Department of Mechanical Engineering, Kalasalingam University,
Krishnankoil, Virudhunagar, Tamil Nadu, India
e-mail: malleshbhagawati@gmail.com

E. Manavalan · K. Jayakrishna
School of Mechanical Engineering, VIT University, Vellore, India
e-mail: mail2jaikrish@gmail.com

MCDM   Multi Criteria Decision-Making
NIDR   Normalized Initial Direct Relation

1 Introduction

Organizations started bringing innovative solutions to stay ahead of the competition and transform customer expectations into reality with the help of digital technology industry 4.0 leverages digital technologies so that interaction happens among components-machines-human to bring personalized items within mass manufacturing process [1].

In this article, the investigation on perspectives and performance factors that affects sustainability of an organization has been studied in the context of industry 4.0. The objective of this research is to study the preparedness of an automotive organization to become a more sustainable organization in industry 4.0 era. The flow of the article is framed as follows. Section 2 presents the literature on industry 4.0 and sustainable performance factors. Section 3 identifies the dominant performance factors using DEMATEL method. Section 4 discusses the importance of sustainability in SCM from industry 4.0, followed by concluding remarks in Sect. 5.

2 Literature Review

The literature has been reviewed from different perspectives of SSCM. Based on the literature, the focus on sustainability of SCM from industry 4.0 perspective has not been reported by researchers. The study is conducted for analyzing the various perspectives of sustainable supply chain organization to meet industry 4.0 requirements. A framework model is developed for assessing sustainability in an organization as presented in Table 1. The framework has two levels. The first level contains five sustainability perspectives represented as "P_x", which influences the sustainability; the second level contains 13 sustainability performance factor represented as "PF_x".

3 Methodology

A model for SSC perspectives and performance factors is formulated based on the literature. An organization to carry out the case study is identified. Later, the causal relations among performance factors are analyzed using DEMATEL, and recommendations based on the relations are suggested.

Table 1 Framework for evaluating sustainability of supply chain

Perspective (P_x)	Performance factor (PF_x)
Business perspective (P_1)	Operational management (PF_1) [2]
	Supplier management (PF_2) [3]
	Strategic sourcing (PF_3) [3]
	Services management (PF_4) [4]
Technology perspective (P_2)	IoT (PF_5) [5]
	CPS (PF_6) [6]
Sustainable development perspective (P_3)	Economic (PF_7) [7]
	Social (PF_8) [8]
	Environment (PF_9) [9]
Collaboration perspective (P_4)	Logistics integration (PF_{10}) [10]
	Customer response adoption (PF_{11}) [11]
Management strategy perspective (P_5)	Cost management (PF_{12}) [12]
	Time management (PF_{13}) [12]

3.1 Case Study

The case study is performed in a leading automotive organization located in India (henceforth referred as ABC). ABC manufactures disk pads, brake linings, and clutch facings. ABC is the suitable organization to perform this study, as the management is optimistic and look forward in becoming a sustainable firm.

3.2 Use DEMATEL Method on Performance Factors

The process of DEMATEL method is summarized with the following steps [13].

Stage 1. Collection of feedback from subject matter specialists, and computation of average matrix

Each subject matter specialist (m) is requested to provide the feedback as per the questionnaire prepared. The feedback received are in the scale of 0–4 where 0 implies no impact, 1 implies low impact, 2 implies moderate impact, 3 implies severe impact, and 4 implies very severe impact, respectively, denoting the effect of a factor on another factor.

For each subject matter specialist, a matrix is calculated by $X^k = \left[x_{ij}^k\right]$, where k represents number of participants.

Consolidating all scores from specialists (m), average matrix $Z = \left[z_{ij}\right]$ is mentioned as follows.

$$z_{ij} = \frac{1}{m} \sum_{i=1}^{m} x_{ij}^{k} \tag{1}$$

Stage 2. Computation of NIDR matrix (*D*)

A NIDR matrix, $D = [d_{ij}]$, wherein every constituent in the matrix is in the range of zero to one. Equation (2) is presented below.

$$D = \lambda \times Z. \tag{2}$$

where

$$\lambda = \text{Min} \left[\frac{1}{\max 1 \leq i \leq n \sum_{j=1}^{n} |z_{ij}|}, \frac{1}{\max 1 \leq i \leq n \sum_{i=1}^{n} |z_{ij}|} \right]$$

Stage 3. Computation of influence matrix (*T*)

Below is the influence matrix *T*.

$$T = D(I - D)^{-1} \tag{3}$$

where *I* represents identity matrix.

Using pair-wise comparisons, scores of subject matter specialists are computed to form average matrix *Z* with reference to Eq. (1). The NIDR matrix *D* is calculated by applying Eq. (2). The overall relation matrix *T* is calculated with reference to Eq. (3) as illustrated in Table 2.

Stage 4. Summation of columns and rows

In this matrix, the summation of columns and rows is denoted through variables *c* and *r* correspondingly.

$$r = [r_i]_{n \times 1} = \left(\sum_{j=1}^{n} t_{ij} \right)_{n \times 1} \tag{4}$$

$$c = [c_j]'_{1 \times n} = \left(\sum_{j=1}^{n} t_{ij} \right)'_{1 \times n} \tag{5}$$

where $[c_j]'$ is denoted as transposition matrix.

The summation of rows as well as the columns of matrix *T* is computed with reference to Eqs. (4) and (5) as mentioned in Table 3.

Stage 5. Computation of threshold value

Table 2 Total influence of performance factors

	PF$_1$	PF$_2$	PF$_3$	PF$_4$	PF$_5$	PF$_6$	PF$_7$	PF$_8$	PF$_9$	PF$_{10}$	PF$_{11}$	PF$_{12}$	PF$_{13}$
PF$_1$	0.271	0.352	0.352	0.319	0.298	0.330	0.324	0.311	0.203	0.352	0.289	0.208	0.314
PF$_2$	0.337	0.252	0.310	0.288	0.269	0.293	0.293	0.281	0.274	0.312	0.267	0.278	0.283
PF$_3$	0.197	0.195	0.152	0.178	0.159	0.173	0.189	0.173	0.169	0.212	0.160	0.170	0.183
PF$_4$	0.218	0.217	0.109	0.155	0.178	0.102	0.102	0.194	0.189	0.101	0.180	0.184	0.195
PF$_5$	0.366	0.363	0.364	0.346	0.248	0.344	0.359	0.337	0.328	0.372	0.331	0.334	0.348
PF$_6$	0.291	0.289	0.282	0.267	0.242	0.212	0.271	0.261	0.246	0.281	0.256	0.240	0.255
PF$_7$	0.294	0.292	0.292	0.278	0.267	0.280	0.222	0.260	0.264	0.290	0.266	0.266	0.265
PF$_8$	0.282	0.270	0.272	0.258	0.242	0.271	0.260	0.190	0.253	0.288	0.255	0.249	0.262
PF$_9$	0.373	0.360	0.362	0.344	0.322	0.340	0.349	0.335	0.251	0.362	0.321	0.330	0.338
PF$_{10}$	0.297	0.287	0.296	0.281	0.255	0.286	0.277	0.258	0.252	0.227	0.261	0.256	0.268
PF$_{11}$	0.289	0.287	0.296	0.273	0.248	0.286	0.286	0.258	0.250	0.287	0.102	0.272	0.250
PF$_{12}$	0.285	0.283	0.283	0.269	0.244	0.282	0.274	0.263	0.256	0.275	0.258	0.101	0.265
PF$_{13}$	0.277	0.275	0.267	0.254	0.245	0.258	0.266	0.255	0.241	0.275	0.251	0.245	0.198

Table 3 Results on performance factors significance

Performance factors	r_i	c_i	$r_i + c_i$	$r_i - c_i$
Operational management (PF$_1$)	3.923	3.777	7.7	0.146
Supplier management (PF$_2$)	3.737	3.722	7.459	0.015
Strategic sourcing (PF$_3$)	2.31	3.637	5.947	−1.327
Services management (PF$_4$)	2.124	3.51	5.634	−1.386
IoT (PF$_5$)	4.44	3.217	7.657	1.223
CPS (PF$_6$)	3.393	3.457	6.85	−0.064
Economic (PF$_7$)	3.536	3.472	7.008	0.064
Social (PF$_8$)	3.352	3.376	6.728	−0.024
Environment (PF$_9$)	4.387	3.176	7.563	1.211
Logistics integration (PF$_{10}$)	3.501	3.634	7.135	−0.133
Customer response adoption (PF$_{11}$)	3.384	3.197	6.581	0.187
Cost management (PF$_{12}$)	3.338	3.133	6.471	0.205
Time management (PF$_{13}$)	3.307	3.424	6.731	−0.117

Threshold value referred as α is derived as follows.

$$\alpha = \frac{\sum_{i=1}^{n} \sum_{j=1}^{n} \left[t_{ij} \right]}{N} \qquad (6)$$

where N represents all number of constituent as per matrix T.

The threshold value α is calculated from Eq. (6).

$$\alpha = \frac{44.732}{169} = 0.265$$

Stage 6. Construction of interrelationship graph
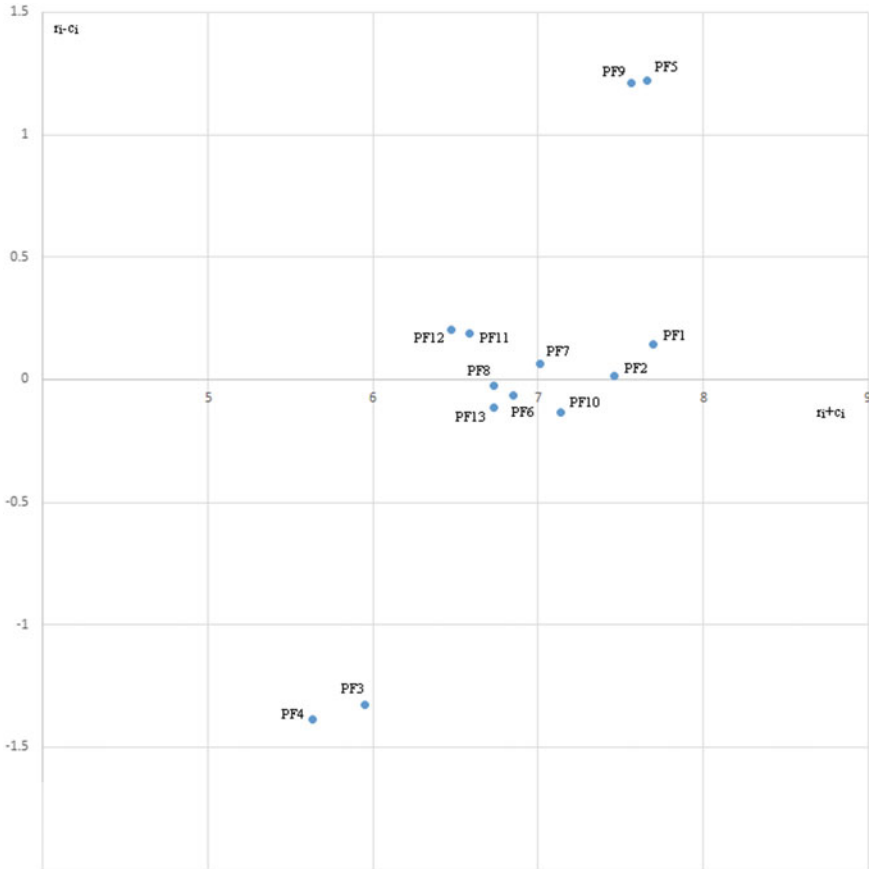
Fig. 1 Cause and effect graph for performance factors

The graph is plotted with the calculated data $(r_i + c_i, r_i - c_i)$ to understand the interrelationship. This graph helps to analyze the critical performance factors and understand how it influences other performance factors. The values that are greater than threshold value α (0.265) in Table 2 are considered for cause and effect analysis. The dominant performance factors are IoT (PF_5) and environment (PF_9) from the interrelationship graph as illustrated in Fig. 1.

4   Results and Discussion

As illustrated in Table 3, the importance of sustainability in SCM from industry 4.0 perspective are found as $PF_5 > PF_9 > PF_1 > PF_2 > PF_7 > PF_{10} > PF_6 > PF_{11} > PF_8 > PF_{12} > PF_{13} > PF_3 > PF_4$ with reference to performance factors importance $(r_i + c_i)$.

From Table 3, the major influential factors are IoT (PF$_5$), environment (PF$_9$), and operational management (PF$_1$) having values 4.44, 4.387, 3.923 respectively. Similarly, the less influential factors are services management (PF$_4$) and strategic sourcing (PF$_3$) having the values 2.124 and 2.31 correspondingly. On discussing the findings with management, they are more interested to implement the dominant performance factors, which influence other performance factors. Management have taken few initiatives to use IoT and working on environment protection measures to move closer toward industry 4.0.

5 Conclusion

The future trend of supply chain will be investing in self-sustainable systems with the help of industry 4.0. The evaluated performance factors will help the organization to move toward digitalization from a sustainability perspective. A framework model has been developed with five perspectives and 13 performance factors. Using DEMATEL method, the influencing performance factors are identified, and cause and effect relationship among them are analyzed. The outcome of the analysis suggests that the management need to adopt IoT and environment-friendly practices, as these are the two most important performance factors to fulfill the industry 4.0 requirements. Focus on IoT influences the transformation of preventive to predictive maintenance and improves the overall operational efficiency. Further, emphasis on environment-friendly practices develops awareness among supply chain partners and enriches overall competitiveness and profitability.

References

1. Cisneros-Cabrera, S., Ramzan, A., Sampaio, P., Mehandjiev, N.: Digital Marketplaces for Industry 4.0: A Survey and Gap Analysis. In Working Conference on Virtual Enterprises, Springer, Cham (2017) 18–27
2. Corbett, CJ., Kleindorfer, PR.: Environmental management and operations management: introduction to the third special issue. Production and Operations Management (2003) 287–289
3. Jayaram, J., Xu, K., Nicolae, M.: The direct and contingency effects of supplier coordination and customer coordination on quality and flexibility performance. International Journal of Production Research (2011) 59–85
4. Balsmeier, P., Voisin, WJ.: Supply chain management: a time-based strategy. Industrial management-Chicago then Atlanta (1996) 24–27
5. Tu, M., Chung, WH., Chiu, CK., Chung, W., Tzeng, Y.: A novel IoT-based dynamic carbon footprint approach to reducing uncertainties in carbon footprint assessment of a solar PV supply chain. In Industrial Engineering and Applications (ICIEA), 2017 4th International Conference, IEEE (2017) 249–254
6. Monostori, L., Kádár, B., Bauernhansl, T., Kondoh, S., Kumara, S., Reinhart, G., Sauer, O., Schuh, G., Sihn, W., Ueda, K.: Cyber-physical systems in manufacturing. CIRP Annals (2016) 621–641

7. Genovese, A., Acquaye, AA., Figueroa, A., Koh, SL.: Sustainable supply chain management and the transition towards a circular economy: Evidence and some applications. Omega (2017) 344–357
8. Wu, Z., Pagell, M.: Balancing priorities: Decision-making in sustainable supply chain management. Journal of Operations Management (2011) 577–590
9. Andersen, MS.: An introductory note on the environmental economics of the circular economy. Sustainability Science (2007) 133–140
10. Qaiser, FH., Ahmed, K., Sykora, M., Choudhary, A., Simpson, M.: Decision support systems for sustainable logistics: a review and bibliometric analysis. Industrial Management & Data Systems (2017) 1376–1388
11. Barratt, M.: Understanding the meaning of collaboration in the supply chain. Supply Chain Management: an international journal (2004) 30–42
12. Um, J., Lyons, A., Lam, HK., Cheng, TC., Dominguez-Pery, C.: Product variety management and supply chain performance: A capability perspective on their relationships and competitiveness implications. International Journal of Production Economics (2017) 15–26
13. Sumrit, D., Anuntavoranich, P.: Using DEMATEL method to analyze the causal relations on technological innovation capability evaluation factors in Thai technology-based firms. International Transaction Journal of Engineering, Management, & Applied Sciences & Technologies (2013) 81–103

Supplier Selection in Plastic Products Manufacturing MSMEs Using a Combined Traditional and Green Criteria Based on AHP and Fuzzy AHP

Ashish J. Deshmukh and Hari Vasudevan

Abstract The concept of green supply chain management looks renewed concept and attracted a lot of interest in the context of current manufacturing practices worldwide. The core attempt is to find an optimum path between industrialization and conservational protection. The initial phase in completing this task is to reconsider the basic form of supplier assessment in supply chain and correspondingly include the environmental worries related with reduction of waste and use of other natural resources. The purpose of this study was to detect the traditional and green supplier evaluation criteria taken together, which are considered vital across the plastic products manufacturing MSMEs in India. The study employed a combined traditional and green supplier selection model, using AHP and fuzzy AHP approaches. In this study, eight main criteria and 40 sub-criteria were used for supplier selection. Results show that the plastic manufacturing companies focus more on cost, quality, and environmental manufacturing management as part of traditional and green supplier selection criteria in selection of supplier.

1 Introduction

Traditional supply chain management always deals with only one purpose, i.e., to lower the cost and enhance the efficiency of supply chain companies, so as to boost the economic gain. Green supply chain management (GSCM), on the other hand,

A. J. Deshmukh
SVKM's NMIMS Mukesh Patel School of Technology Management and Engineering,
Mumbai, India
e-mail: ashish.deshmukh@nmims.edu

H. Vasudevan (✉)
D. J. Sanghvi College of Engineering, Mumbai, India
e-mail: principaldjs@gmail.com

takes into consideration, the crucial aspect of environmental science (reduce the utilization of raw materials, energy, and curtail the secretion of pollutants) as along with various aspects related to maximize economic benefits [1]. Traditional supply chain management thinks more on regulating the end product; no matter how harmful its effects are to the environment during manufacturing and delivery, whereas in GSCM, eco-friendly requirements are considered as key criteria for both manufacturing and the end product [2].

Supplier selection criterion often involves multicriteria decision-making problems, which is affected by several conflicting factors. Multicriteria decision-making techniques support the decision-maker in evaluating a set of alternatives available to the firm. Many researchers have identified different dimensions and factors for application in traditional and green criteria in their studies. The current paper explains the practices and issues related to the implementation of a combined approach involving traditional and green supplier selection criteria in the case of plastic products manufacturing MSMEs, based in India. A total of eight criteria, namely cost, quality, service performance, environmental manufacturing management, risk, environmental performance assessment, delivery, and innovation and learning were considered along with 40 other subfactors. To establish the link between traditional and green supplier selection criteria in supply chain management, relevant review of literature was done and is given in Sect. 2. Section 3 contains the reasons for the selection of plastic products manufacturing MSMEs for supplier selection. Complete research methodology is given in Sect. 4 and the results and comparative analyses of various factors of the combined traditional and green supply chain management are presented in Sect. 5. Finally, the conclusion is presented in Sect. 6.

2   Literature Review

Business demands and other regulatory requirements in the twenty-first century have confirmed that the Government of India promoted the necessities of green product in supply chain, and it is also one of the biggest prevalent fields being discussed in today's businesses [3]. Deshmukh and Vasudevan [2] examined an efficient and combined approach for selection of supplier and pointed that a more serious apprehension is required to be put in toward environmental protection. Deshmukh and Chaudhari [4] ranked, reviewed, and compared various supplier selection criteria from the year 1992–2007. The authors collected 49 articles on traditional criteria and observed that cost, quality, and delivery are crucial criteria used for selection of suppliers. Many of the researchers referred in these articles have used green purchasing, green design, green production, environmental design, life cycle analysis, green manufacturing, minimizing waste, decreased consumption of hazardous and toxic material, minimizing waste green image, etc., as few green criteria in their supplier selection [5, 6].

Analytic hierarchy process (AHP), as an analytical tool, also used in areas such as supply chain management was evolved by Thomas L. Saaty in 1980 [7]. It includes

an eigenvalue way and is used to analyze the substitute (alternatives) with analogous to various criteria. It is noted that the use of tools, such as AHP for supplier selection, increases the company's strength and profitability. AHP was used for pair-wise comparison to make the trade-off between tangible and intangible factors and also to use it to calculate the scores of the suppliers [8]. An AHP-based model is used to help investors to rate and select the suppliers [9]. AHP can also show a very essential role in supplier selection process, because the rate of basic resources and auxiliary parts constitute the main cost of products, and in such a situation decision-making of actual supplier is vital for the manufacturing organizations [10]. AHP model is also used in electronics manufacturing to attract the loyal customers by providing a wide range of choices and to establish a long-term relationship [11].

Zadeh [12] proposed a fuzzy set theory in the year 1965 to tackle the vagueness in human judgment, and since then, many authors have used the fuzzy set theory to deal with ambiguity in supplier choice. Chang (1996) evolve a new way for handling fuzzy AHP by presenting a triangular fuzzy numbers for pair-wise comparison and used an extent analysis for the fake values of pair-wise comparison [13]. Triangular fuzzy number is used to assess and advance decisions for supplier selection in uncertain situations [14]. Integrated fuzzy AHP and quality function deployment are also used for selection of nonconventional machining processes in engineering industries [15]. Extended fuzzy AHP was also used to calculate the risk factors involved in the supplier selection [16].

3 Reasons for Selection of Plastic Manufacturing Sector

Ever since the year 1957, plastic products manufacturing MSMEs in India have made significant progress and advancements. Fastest developing industries in India are plastic products manufacturing companies; Indian plastic manufacturing companies today comprises of over 3000 units involved in manufacturing a diversity of plastic items [17]. The Indian plastic products manufacturing industries have taken big steps, and in the last two decades, these companies have grown up into a position of being the important sector in the country with a substantial base. The fast replacement of typical traditional material with plastic material is because of continuous advancements and development in plastic technology, processing machineries, expertise, and cost-effective manufacturing. Commodity plastics include polyethylene, polypropylene, polyvinyl chloride, and polystyrene. Indian manufacturing plastic industries largely use polyethylene as a plastic material for manufacturing of plastic products [17].

Plastic industry is a vital contributor to the economy of India as well as worldwide business. However, at the same time, according to the extant literature, they are one of the main contamination creators in India. In the context of this serious concern, the suppliers for plastic industry could play a significant role, and the supplier selection is extremely serious and is significant affair for plastic products manufacturing companies. Therefore, the territory of plastic industry was taken up as very pertinent for consideration in this study in the crucial area of supplier selection.

Table 1 Main criteria matrix for comparison

Main criteria	Cost	Quality	SP	EMM	Risk	Delivery	EPA	I&L	L.W.
Cost	1	3	5	4	6	3	6	5	0.466
Quality	0.33	1	2	1	3	1	3	2	0.112
SP	0.20	0.50	1	0.50	1	0.50	1	1	0.079
EMM	0.25	1	2	1	2	0.50	0.50	1	0.066
Risk	0.16	0.33	1	0.50	1	0.33	1	0.50	0.066
Delivery	0.33	1	2	2	3	1	3	2	0.091
EPA	0.16	0.33	1	2	1	0.33	1	0.50	0.077
I&L	0.20	0.50	1	1	2	0.50	2	1	0.044

4   Research Methodology

This section covers the methods of data collection and how AHP and fuzzy AHP are applied in the plastic products manufacturing industries as well as the illustration of the applicability of both methods. Data required for both the AHP and fuzzy AHP from the plastic products manufacturing sector have been collected from the judgment of the professionals and administrator by accepting their opinion and contacting them personally. A hierarchy was formed in the next step with its topmost goal (best supplier selection) followed by the main criteria, sub-criteria, and alternatives. The main criteria included the service performance, cost, quality, environmental manufacturing management, delivery, risk, environmental performance assessment, and innovation and learning. Sub-criteria contributing to the decision were represented at the intermediate levels.

Managers were asked to give their opinion for every hierarchical level, comprise main criteria, sub-criteria, and suppliers. Table 1 exhibits the correlation matrix for main criteria, and the rank specified by the managers using Satty's scale for the AHP matrix. After obtaining the opinion from the managers, the next step was to calculate the local weights (LW) of each element of matrix. In terms of matrix calculations, this comprises computing the eigenvector or local weights of the matrix by totaling the adherent of every column to determine the total. In the later step, in order to normalize every column to the sum to 1, element of the column values was divided by the total of the column and then summed up. At last, the components in every subsequent row were added, and this summation was divided by the number of component in the row to find the average presented in Table 1 in the last column.

Similarly for fuzzy AHP, the matrix of pair-wise comparison was built for a specific level of hierarchy, same as in AHP, but different values are given by the managers. But, the values are given according to the triangular fuzzy numbers (TFN), which contain three levels of evaluation values. Table 2 shows the scale of these values.

Table 2 Satty's and Chang's scale used for pair-wise comparison in AHP and fuzzy AHP

Input values for AHP	Input values for FAHP	Input reciprocal values for AHP	Input reciprocal values for AHP
1	(1,1,1)	1/1	(1/1,1/1,1/1)
2	(1,2,4)	1/2	(1/4,1/2,1/4)
3	(1,3,5)	1/3	(1/5,1/3,1/1)
4	(2,4,6)	1/4	(1/6,1/4,1/2)
5	(3,5,7)	1/5	(1/7, 1/5, 1/3)
6	(4,6,8)	1/6	(1/8, 1/6,1/4)
7	(5,7,9)	1/7	(1/9, 1/7, 1/5)
8	(6,8,10)	1/8	(1/10,1/8 1/6)
9	(7,9,11)	1/9	(1/11, 1/9,1/7)

5 Results and Comparative Analysis Using AHP and Fuzzy AHP

During the initial phase, when both the criteria were combined together, it was observed that in the Indian plastic manufacturing MSME sector, along with quality and cost, eco-friendly criterion was also showing its rank in selection of the supplier. It verified that the selection of supplier by using only traditional criterion or by green criterion will not give complete fairness for the process of selection of supplier. In many of the studies, where AHP is used for selection of supplier, the main criteria and its sub-criteria, whose rankings are got to be greater, are used in fuzzy AHP, and the leftover criteria and sub-criteria are ignored, whereas, in few studies, it is said that it will never provide complete fairness to fuzzy AHP computation. In this study, a comparison of both AHP and fuzzy AHP was made for plastic products manufacturing MSMEs, and hence, it clarifies the usefulness of both the approaches.

Table 3 and Fig. 1 for main criteria illustrates that the cost has maximum preference with its local weight 0.2823 and 0.2620 in plastic product producing MSMEs, even though applying both AHP and fuzzy AHP. It shows that the cost is considered the main import criterion even today for selection of supplier in Indian plastic products producing MSMEs, followed by quality and environmental manufacturing management with its weights 0.191, 0.1992, 0.1228, and 0.1098 using both AHP and fuzzy AHP. It shows that the green (eco-friendly) concept is slowly gaining importance in plastic products manufacturing MSMEs.

Cost has been recognized as a significant evaluation for choice of supplier from a long time. Based on the level of attention and implication, traditional and green costs are reflected the main criterion for effective supplier selection and assessment in supply chain management for plastic products manufacturing MSMEs. Decision below in the matrix of cost include purchase cost (PC), cost for fright (FC), discount for earlier payment (DEFP), tax & custom duties (T&C), cost for recycling (RC), and cost of componenet disposal (COCD) as shown in Table 4 and Fig. 2. It can

Table 3 Comparison of main criteria using AHP and FAHP

Goal	AHP results	FAHP results
Cost	0.2823	0.2620
Quality	0.1915	0.1992
SP	0.0656	0.0592
EMM	0.1228	0.1098
Risk	0.0647	0.0658
Delivery	0.0859	0.0807
EPA	0.0868	0.1276
I&L	0.1073	0.0957

Fig. 1 Comparison of plastic products manufacturing MSMEs using AHP and FAHP for main criteria
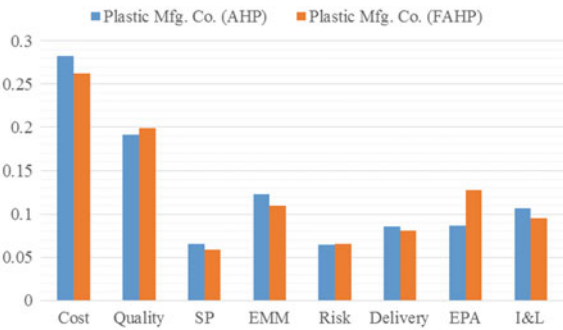
Table 4 Comparison for sub-criteria (cost) using AHP and FAHP

Cost	AHP results	FAHP results
PC	0.3374	0.2997
FC	0.1301	0.1475
DEFP	0.1049	0.0929
T&C	0.0909	0.0805
RC	0.1623	0.1416
COCD	0.1744	0.2379
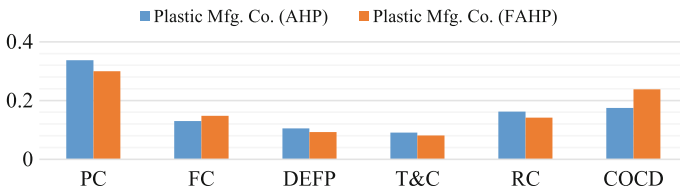
Fig. 2 Comparison of plastic products manufacturing MSMEs using AHP and FAHP for sub-criteria cost

be observed that along with cost of purchase, cost of recycling and component disposal cost are also showing their importance, when it is related in AHP and FAHP approaches (when combined result is calculated for 50 companies in this sector).
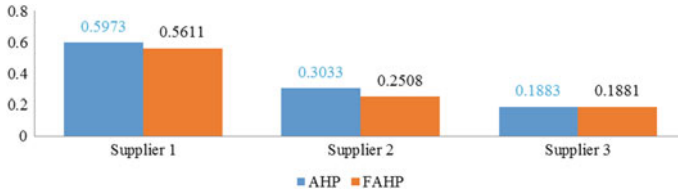
Fig. 3 Overall ranking of the supplier using AHP and FAHP

Similarly weights for all sub-criteria were evaluated and compared. Lastly, it was witnessed that the identical results were found using AHP and FAHP for all the 50 plastic products manufacturing MSMEs. Results prove that in the supplier selection process, traditional criteria show their relevance and pertinence in Indian plastic products manufacturing MSMEs. However, the inclinations also show that the industries are also thinking for acknowledgment of green criteria for supplier selection in supplier selection process. It also shows that consideration of only traditional or green criteria is not sufficient for selection of supplier's in the Indian manufacturing context, particularly in plastic products manufacturing MSMEs.

Supplier's pair-wise assessment matrix was also molded for all main and sub-criteria. Supplier 1 has shown the rating with weight 0.5973 using AHP and 0.5611 using fuzzy AHP, and hence, Supplier 1 is the perfect supplier amid the three. Thereafter, Supplier 2 with weights 0.3033 and 0.1883 and supplier 3 with weights 0.2508 and 0.1881 applying AHP and FAHP. Final rating of all the three suppliers is shown in Fig. 3.

6 Conclusion

In this study, a combined traditional and green supplier selection criteria with analytic hierarchy process (AHP) and fuzzy analytic hierarchy process (FAHP) was employed with respect to the matrix method for weighing the criteria in plastic products manufacturing MSMEs for their comparative judgment and valuation. The perceptions from the cases have assisted to recognize and relate the importance of supplier's performance assessment factors in the Indian plastic products manufacturing MSMEs.

The results involved the analyses of supplier selection in plastic products manufacturing MSMEs. Conferring to the extent of works, traditional supply chain emphases only on cost, quality, and delivery in supply chain and does not reflect the effect on environment and people, natural resources, recycling, and waste disposal. In recent times, many researchers have given considerable stress and importance on traditional criteria or green criteria. In this study, both the traditional and green supplier selection criteria were combine together, and its importance was measured using AHP and FAHP. Results show that cost is the main criteria for supplier selection, followed by quality. But the same inclinations also confirm that the plastic manufac-

turing industries in India are also accepting green criteria for their supplier selection, such as environmental manufacturing management in supply chain management, to encourage enterprises and natural atmosphere. Finally suppliers ranking using AHP and FAHP found the same and outstanding supplier for each plastic product manufacturing company is determined.

References

1. A. Deshmukh and H. Vasudevan: Analysis of Supplier Selection Criterion in Traditional as well as Green Supply Chain Management in Indian MSMEs. International Journal of Business Quantitative Economics and Applied Management Research. Vol. 3, No. 3, 73–85, (2016).
2. A. Deshmukh and H. Vasudevan: Emerging supplier selection criterion in the context of traditional and green supply chain management. International Journal of Managing value and Supply Chain. Vol. 5, No. 1, 19–33 (2014).
3. Jayaram J. and Avittathur B. Green supply chain: A perspective from emerging economy. Internal Journal of Production Economics. Vol. 164, 234–244, (2015).
4. A. Deshmukh and A. Chaudhari: A Review for Supplier Selection Criteria and Methods. Technology Systems and Management. Springer. 145, 283–291, (2011).
5. Sanjeev Kumar, Somnath Chattopadhyay and Vinay Sharma: Green Supply Chain Management: A case study from Indian Electrical and Electronics Industry. Vol. 1, No. 6, 275–281, (2012).
6. Sarkis J. and Talluri S.: A model for strategic supplier selection. Journal of Supply Chain Management. Vol. 38, No. 1, 18–28, (2002).
7. Saaty T.L.: The Analytic Hierarchy Process: planning, priority sett allocations. McGraw Hill, New York (1980).
8. A. Deshmukh and G. Bagle: Develop a model to select best supplier in SCM. Globalization: Opportunities & Challenges, Wisdom Publications, Delhi. 175–188, (2007).
9. Mani V., Rajat Agarwal, and Vinay Sharma: Supplier selection using social sustainability: AHP based approach in India. International Strategic Management Review. Elsevier. 2, 98–112, (2014).
10. A. Deshmukh and H. Vasudevan: Decision criteria and methods for supplier selection. Proceedings of the International conference (SPICON) organized by Sardar Patel College of Engineering, Mumbai (2012).
11. Hui-Feng Chiu, Tzong-Ru Lee and Ching-Kuei Kao: The key factors for selecting electronics manufacturing service suppliers-An example of company in Taiwan. Management and Production Engineering review. Vol. 6, No. 4, 4–14, (2015).
12. Zadeh L.: Fuzzy Sets. Information and Control. Vol. 8, No. 3, 338–353, (1965).
13. Chang D.Y.: Applications of the extent analysis method on FAHP. European Journal of Operation Research. Vol. 95, No. 3, 649–655, (1996).
14. Mukherjee S. and Kar S.: Multi attribute decision making on fuzzy logic and its application in supplier selection problem. Operations and Supply Chain Management. Vol. 5, No. 2, 76–83, (2012).
15. Roy M.K., Ray A. and Pradhan B.B.: Non-traditional machining process selection using integrated fuzzy AHP and QFD techniques: A customer prospective. Production & Manufacturing Research. Vol. 2, 530–549, (2014).
16. Chan F.T.S. and Kumar N.: Global supplier development considering risk factors using fuzzy extended AHP-based approach. International Journal of Management Science. Omega. Vol. 35, No. 4, 417–431, (2007).
17. Potential of Plastic Industry in Northern India with special focus on Plasti-culture and Food Processing, A report on Plastic Industry, FICCI, 2014–15.

Green Supply Chain Management Practices and Its Impact on Business Performance

Meeta Gandhi and Hari Vasudevan

Abstract This study is an attempt to contribute to the empirical investigations related to the impact of green supply chain management practices (GSCM) on business performance in SME manufacturing industries in Western part of India. A comprehensive GSCM performance model was proposed, which considers government initiatives as the mediating variable to increase GSCM practices in small- and medium-sized industries. A survey questionnaire was developed to capture the GSCM practices and their implications on environmental, economic, and organizational performance. Descriptive statistics was used to analyze the survey instrument deployed. Even as most researchers so far have reported that adoption of GSCM practices leads to better business performance, this study concludes that though the SMEs in India are aware of GSCM practices, it is still in its infancy stage and has, thus, reported a mediocre response to business performance.

Keywords Green supply chain management · Economic performance Environmental performance · Operational performance · Government initiatives

1 Introduction

Manufacturing industries these days are forced to improve the quality of their products, while at the same time, reduce cost and delivery time, as the competition has become cutthroat at the marketplace. This compels them to narrow down their focus on sustainability, resulting in less focus on environmental concerns. Implementa-

---

M. Gandhi (✉)
Department of Production Engineering, D. J. Sanghvi College of Engineering, University of Mumbai, Mumbai, India
e-mail: meeta_7405@yahoo.co.in

H. Vasudevan
Department of Mechanical Engineering, D. J. Sanghvi College of Engineering, University of Mumbai, Mumbai, India
e-mail: harivasudevan@iitb.ac.in

tion of green supply chain management (GSCM) practices in these industries is also restrained due to various economic factors. However, it is known that the environmental pollution is a serious problem, and one of the major sources of emission is toxic gases from the manufacturing industries. This has led to new customer requirements, which are beyond the quality and cost, but as to how products are made, how long they last, and how they can be disposed of [1]. This compels the manufacturing industries to incorporate the concept of "green" in their supply chain, which means to develop products that can be reused, recycled, or reclaimed at the end of their life cycle, making supply chain green and sustainable. Thus, GSCM means to incorporate environmental thinking, starting from product design, material selection and sourcing, manufacturing processes, delivering products to customers as well as end of life management of the product [2]. The goal of GSCM practices is to continuously improve products and processes and to prevent air, water, and land pollution [3]. Environmental impact, in fact, leads to greening of supply chain; hence, this should be perceived as a potential source of competition rather than a burden.

India has announced the National Action Plan on Climate Change (NAPCC) in June 2010 to take the extra mile on the path of green. India is also a signatory to the association of Kyoto Protocol and consideration of carbon credit system by various industries. Thus, the change is inevitable, and sooner the industries realize the importance of adapting green business practices, better will they be equipped to compete in global markets. Though various researchers have highlighted on the penetration of GSCM practices in large-scale manufacturing industries, the present study is aimed at exploring the penetration of these practices in Small and Medium Scale Enterprises (SMEs) and also provide a concise framework of GSCM practices on business performance in them. In India, SMEs account for about 45% of manufacturing output and 40% of exports. It has been found from the extant literature that the major barriers to GSCM implementation are the unwillingness to change and the threat of incurring huge costs without getting proper returns. In this specific context, the authors have made an attempt to measure the performance of GSCM practices in SMEs in India. It shall additionally throw light on the level of maturity of GSCM practices and setting up of environmental goals. Authors expect that the feeling of burden of GSCM implementation can be eased by establishing clearly and communicating the benefits, cost, and risk reduction to the top management or decision-makers of SMEs in India.

2 Literature Review

Kudroli [4] described three major practices of GSCM to account for the development of a country's economy. They include:

1. Use of less power and paper termed as internal environmental management practice.
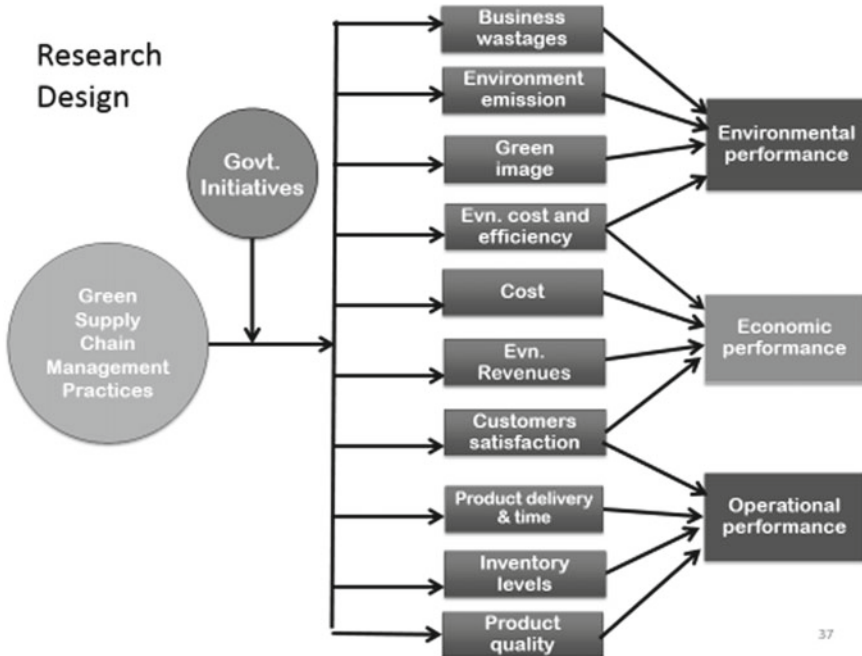
Fig. 1 Conceptualized research design

2. Helping suppliers to practice green purchasing termed as external GSCM practice.
3. Waste minimization, investment recovery, and environmental requirements after cooperating with the customers.

Thus, an energy saving measure is considered a green measure. According to Sambarani [5], manufacturing industries have a key role in the use of waste-free and emission-free energy sources through which they can provide green products to green consumers, who respond better to environmental challenges like global warming and climate change.

Based on the reported studies and extant literature, parameters for exploring the impact of GSCM practices on business performance, in terms of environmental performance, economic performance, and operational performance, are selected in this study and are shown in Table 1.

As a result of the extant literature review and analysis, a research design is conceptualized and is given in Fig. 1.

Table 1 Performance measures

Abbreviation	Measure	Source
ENV1	Air emission	Zhu et al. [9], Vijayvargy and Agarwal [10], Kudroli [4], Shaw et al. [11]
ENV2	Liquid waste	Zhu et al. [9], Kumar et al. [12], Kudroli [4], Rao et al. [13]
ENV3	Solid waste	Zhu et al. [9], Kumar et al. [12], Kudroli [4], Rao et al. [13]
ENV4	Energy consumption	Zhu et al. [9], Lokesh and Agarwal [10], Kudroli [4], Shaw et al. [11]
ENV5	Hazardous and toxic material consumption	Zhu et al. [9], Kumar et al. [12], Kudroli [4], Rao et al. [13]
ENV6	Total flow quantity of scrap	Zhu et al. [9], Kumar et al. [12], Kudroli [4], Rao et al. [13]
ENV7	Frequency of environmental accidents	Green et al. [14]
ENV8	Company's environmental image	Vijayvargy and Agarwal [10]
EP1	Cost per operating hour	Zhu et al. [9], Vijayvargy and Agarwal [10], Kudroli [4], Green et al. [14], Rao et al. [13]
EP2	Manufacturing cost	Zhu et al. [9], Vijayvargy and Agarwal [10], Kudroli [4], Green et al. [14], Rao et al. [13]
EP3	Operating expenses	Zhu et al. [9], Vijayvargy and Agarwal [10], Kudroli [4], Green et al. [14], Rao et al. [13]
EP4	Overhead expenses	Zhu et al. [9], Vijayvargy and Agarwal [10], Kudroli [4], Green et al. [14], Rao et al. [13]
EP5	Costs for purchasing environmentally friendly materials	Zhu et al. [9], Vijayvargy and Agarwal [10], Kudroli [4], Green et al. [14], Rao et al. [13]
EP6	Cost of scrap/rework	Zhu et al. [9], Vijayvargy and Agarwal [10], Kudroli [4], Green et al. [14], Rao et al. [13]
EP7	Disposal costs	Zhu et al. [9], Vijayvargy and Agarwal [10], Kudroli [4], Green et al. [14], Rao et al. [13]
EP8	Fines and penalties	Zhu et al. [9], Vijayvargy and Agarwal [10], Kudroli [4], Green et al. [14], Rao et al. [13]
EP9	Recycling cost	Zhu et al. [9], Vijayvargy and Agarwal [10], Kudroli [4], Green et al. [14], Rao et al. [13]
EP10	Transport cost	Zhu et al. [9], Vijayvargy and Agarwal [10], Kudroli [4], Green et al. [14], Rao et al. [13]
EP11	Revenues from "green" products	Zhu et al. [9], Vijayvargy and Agarwal [10], Shaw et al. [11], Green et al. [14]
EP12	Cost avoidance from environmental action	Zhu et al. [9], Vijayvargy and Agarwal [10], Shaw et al. [11], Green et al. [14]

Table 1 (continued)

Abbreviation	Measure	Source
EP13	Cash rewards/subsidy for using renewable energy sources	Freshly proposed and included in the study
OP1	On time delivery	Zhu et al. [9], Vijayvargy and Agarwal [10], Kumar et al. [12], Kudroli [4]
OP2	Rates of customer complaints	Kumar et al. [12], Pochampally [15]
OP3	After-sales service efficiency	Kumar et al. [12], Pochampally [15]
OP4	Responsiveness to urgent deliveries	Zhu et al. [9], Vijayvargy and Agarwal [10], Kumar et al. [12], Kudroli [4]
OP5	Inventory levels	Green et al. [14]
OP6	Enhanced product quality	Zhu et al. [9], Vijayvargy and Agarwal [10], Kudroli [4], Rao et al. [13]
OP7	Customer reject rate	Zhu et al. [9], Vijayvargy and Agarwal [10], Kudroli [4], Rao et al. [13]
OP8	In plant defect fallow rate	Zhu et al. [9], Vijayvargy and Agarwal [10], Kudroli [4], Rao et al. [13]
OP9	Cycle times	Zhu et al. [9], Vijayvargy and Agarwal [10], Kumar et al. [12], Kudroli [4]
OP10	Delivery lead time	Zhu et al. [9], Vijayvargy and Agarwal [10], Kumar et al. [12], Kudroli [4]
OP11	Increased product line	Green et al. [14]
OP12	Capacity utilization	Green et al. [14]
GI1	Reward for buying renewable energy	Freshly proposed and included in the study
GI2	Relief in Tax	Freshly proposed and included in the study
GI3	Technical assistance	Lee [16]
GI4	Low-interest loans for waste disposal	Lee [16]
GI5	Awards for greening the process	Freshly proposed and included in the study
GI6	Heavy fines/penalties for wrong disposal of waste	Hervani et al. [17]
GI7	Heavy fines for excess use of energy	Freshly proposed and included in the study
GI8	Popularize knowledge of environmental management	Lee [16]
GI9	Build infrastructure for facilitating GSC initiatives	Lee [16]

3   Research Methodology

As part of the analysis, a pilot study was planned during January–March 2018. The research instrument in the form of a questionnaire was administered directly to the Director/Proprietor/Chief Operating Officer/Chief executive Officer/Chief Financial Officer of SMEs in Western part of India. They were chosen, because they are in "a critical position to influence the size of overall environmental footprint of the industry."

SME manufacturing industries were chosen in the study, because they represent the invisible link in the supply chain, and therefore, their lack of environmental management capability could have a negative impact on financial performance and brand image of the customer firm [6–8].

Chemical, textile, and rubber/plastic industries from India were selected for this study. The reason for selecting these industries was that these industries are changing rapidly due to globalization and current technological advances. Consequently, environmental issues, and concerns develop fast, and many significant regulatory acts will be enforced globally for these industries.

To investigate GSCM practices, the structured questionnaire was developed with clear focus on environmental performance, economic performance, operational performance, and government initiatives. The questionnaire was divided into three sections: Sect. 1 captures the general information of the industry, Sect. 2 includes the importance of GSCM practices in the industry, and Sect. 3 measures the business performance in light of GSCM practices and government initiatives. The proposed model has considered government initiatives as the mediating variable. All the questions were rated on a five point Likert scale. Questions were rated as follows: 1 = No, 2 = little, 3 = Moderate, 4 = Very Much, and 5 = Greatly.

4   Results and Discussion

The survey in this study was conducted on a stratified sample of 25 SMEs (seven chemical industries, eight textile industries, and ten rubber/plastic industries). There is likely to be no significant difference in company characteristics in terms of number of employees as 80% of them have employees less than 100. Therefore, the results are expected to be representative of the large sample size.

It was found that at least 40% of the industries had one of the certifications: ISO9000, ISO 14000, or environmental management system. Twenty-eight percentage of them had either ISO 14000 or an environmental management system. As shown in Figs. 2 and 3, 72% of the firms have green supply chain as their strategic priority and 48% have already intensified their efforts in greening the supply chain. 56% of industries (Figs. 4 and 5) were willing to undertake investments in environmental protection, but only 12% have reported to have already invested, while 48% of the industries say that the investment in environmental efforts has not been paid

Fig. 2 GSCM a strategic priority
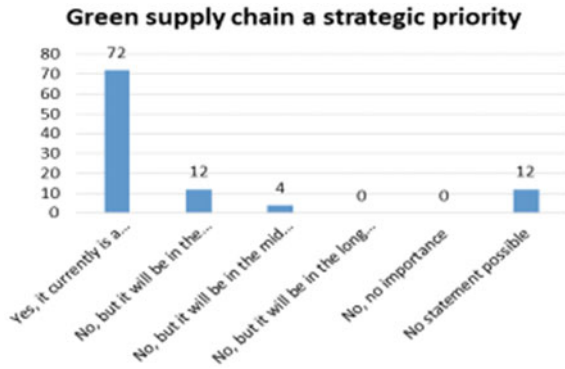
Fig. 3 Efforts made by an organisation in adopting GSCM practices over the past three years
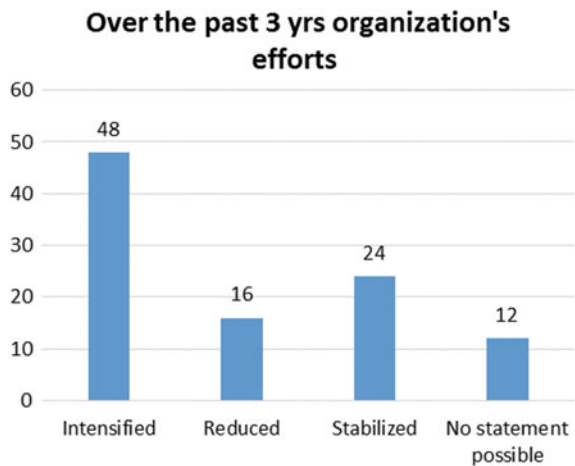
off (Fig. 6). Also, 92% of industries say that the customer does not require carbon emission data (Fig. 4). Figure 7 depicts the rating of an organization for business performance. It can be clearly concluded that at least SMEs are aware of GSCM practices and have rated their business performance to be better with greening the supply chain (Fig. 8).

Table 2 shows the average of all aspects on environmental performance (average is below the median value of 3) to be less than the median value. Values of skewness and kurtosis indicate that the data is normally distributed. Industries have reported reduction in solid waste and air emission to be most useful. Disposal costs, fines, and penalties have a significant impact on economic performance than rest of the parameters, whereas the operating expenses impacts the least (Fig. 9). In operational performance parameters, enhanced product quality, increased product line, and better capacity utilization were found significant (Fig. 10). Most industries believe that the relief in tax and low-interest loans for waste disposal along with heavy penalties for wrong disposal of waste will help greening their supply chain (Fig. 11).

Customer request carbon emission
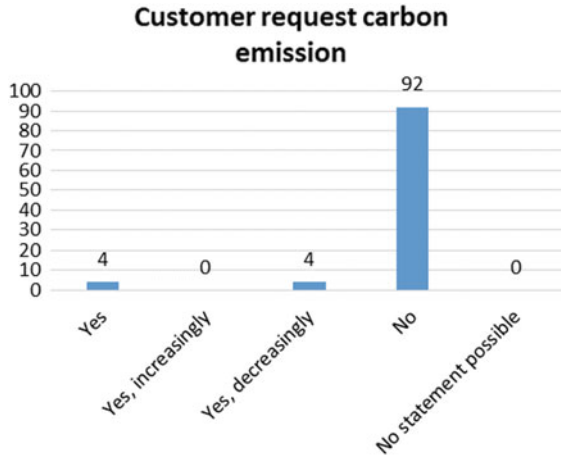
Fig. 4 Customer requesting for carbon emmision data

Undertake investments in environmental protection
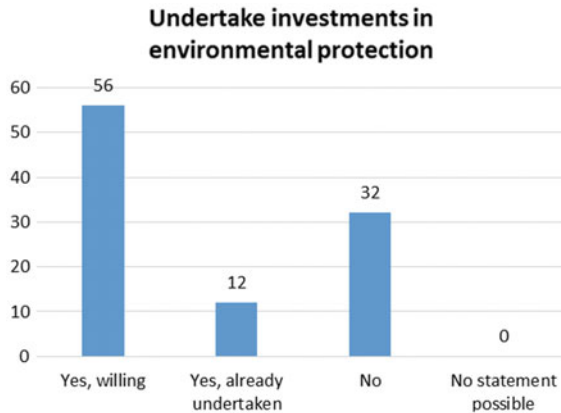
Fig. 5 Investments undertaken in environmental protection

5 Conclusion

The results of the study reveal that SMEs in India are not only aware but have made greening the supply chain as their strategic priority. Many of them have intensified their efforts and are willing to undertake investments in environmental protection, but most of them have reported a very low return on investments. Their customers also do not ask for carbon emission data.

Further, in terms of GSCM performance, SMEs have to focus on economic performance. They need to work on reducing cost of environmentally friendly materials, manufacturing cost, and overhead expenses. Most of the industries believe that government initiatives, in terms of providing technical know how on what to measure,

Fig. 6 Duration of pay-off for investments done in GSCM practices adoption

How fast did they pay off

(bar chart showing: Less than 1 year = 16, Between 1 and 3 years = 20, More than 3 years = 8, Not at all = 48, No statement possible = 8)
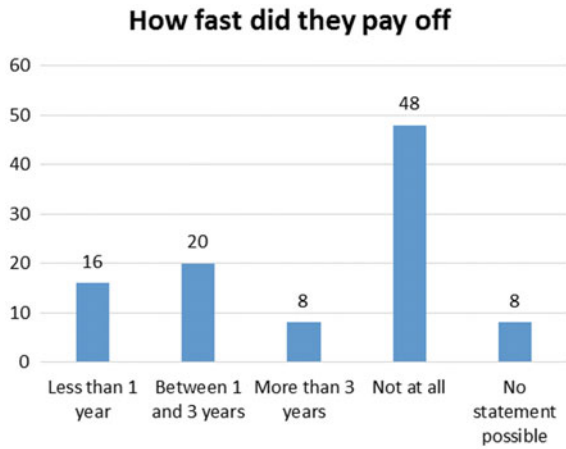
Fig. 7 Rating given by an organisation for its performance

Rating the organisation

(grouped bar chart — Environmental Performance, Economic Performance, Operational Performance — Lowest = 0, 0, 0; 2 = 1, 2, 4; Medium = 4, 9, 4; 4 = 9, 9, 13; Highest = 11, 5, 4)

■ Environmental Performance   ■ Economic Performance
■ Operational Performance

Fig. 8 Environmental performance

Environmental Performance

(bar chart showing Mean and Standard Deviation for ENV1 through ENV8)

■ Mean   ■ Standard Deviation
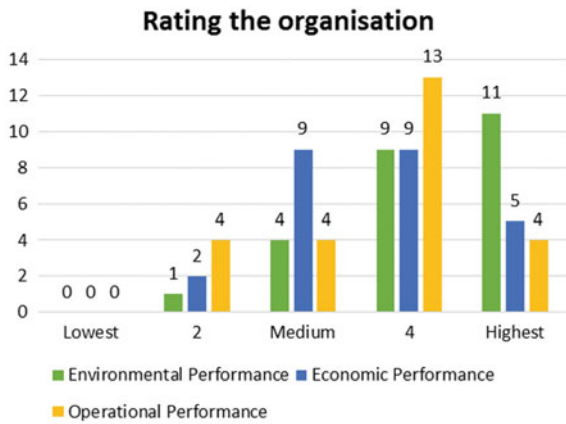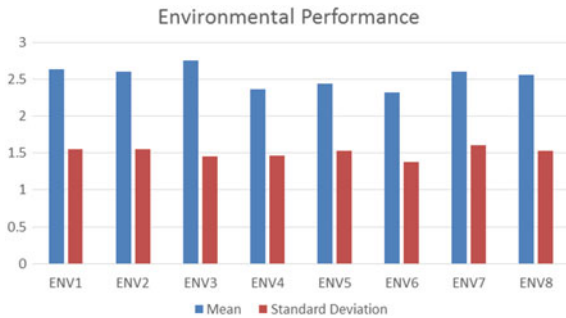
how to measure, providing financial assistance like relief in tax and low-interest rate loans, issuing heavy penalties for using more energy and improper disposal of waste

Table 2 Environmental performance

ENV	Min	Max	Mean	Standard deviation	Kurtosis	Skewness
ENV1	1	5	2.64	1.55134	−1.471	0.22499
ENV2	1	5	2.6	1.55456	−1.4538	0.30379
ENV3	1	5	2.76	1.45144	−1.1848	0.09996
ENV4	1	5	2.36	1.46856	−1.3599	0.51383
ENV5	1	5	2.44	1.52971	−1.3997	0.46484
ENV6	1	5	2.32	1.37598	−1.4192	0.40955
ENV7	1	5	2.6	1.60728	−1.4433	0.32723
ENV8	1	5	2.56	1.52971	−1.5405	0.29431

Fig. 9 Economic performance
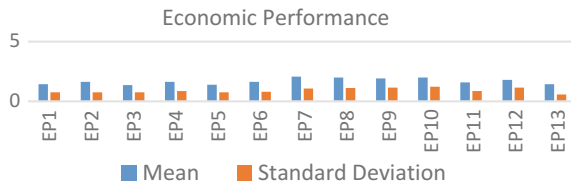
Fig. 10 Operational performance
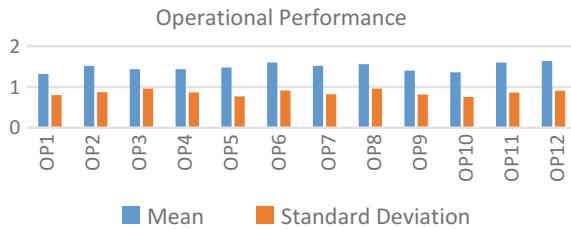
Fig. 11 Suggestion given by firms for the intiatives to be taken by government to strengthen the adoption of GSCM practices
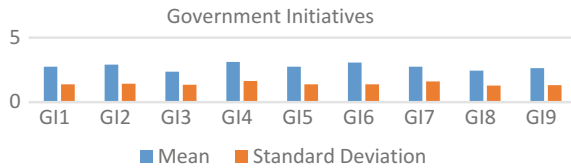
can better the adoption of GSCM practices. This can inturn improve the business performance.

From the results of the study it can be concluded that the average of all aspects of business performance is less than the median value, which means that the SMEs do not perceive GSCM practices to have a positive impact on business performance. Thus, it can further be concluded that though some measures are taken to green the supply chain, it is still in its nascent stage of implementation as industries do not perceive it to be a profitable measure. Educating the SMEs and helping them to realize profit by implementing green practices are the needs of the hour.

References

1. Peattie K.1999. "Trappings versus substance in the greening of marketing planning", Journal of Strategic Marketing, Vol 7, pp. 131–148.
2. S.K. Srivastava, (2007) " Green supply-chain management: A state of the art literature review", International Journal of Management Reviews, vol. 9, no. 1, pp. 53–80.
3. Winroth M, Johansson G (2009), "Lean vs Green Manufacturing: Similarities and Differences" Proceedings of 16th International Annual Euro OMA conference, Implementation Realizing Operations Management Knowledge, June 14–17, Goteborg, Sweden.
4. Karthik Kudroli, (2014), "Green Supply Chain Management: Operation and Environmental Impact at different stages of the supply chain", International J. Conceptions on Management & Social Sciences, Vol 2, No.2, pp 128–132.
5. Vinod Sambrani & Naveen Pol, (2016), "Green Supply Chain Management: A Literature Review", The IUP Journal of Supply Chain Management, Vol. 13, No. 4, pp 7–16.
6. Sarkis, J. and Dijkshoorn, J. (2007), "Relationships between solid waste management performance and environmental practice adoption in Welsh small and medium-sized enterprises (SMEs)", International Journal of Production Research, Vol. 45 No. 21, pp. 4989–5015.
7. Shearlock, C., Hooper, P. and Millington, S. (2000), "Environmental improvement in small and medium-sized enterprises: a role for the business-support network", Greener Management International, No. 30, pp. 50–60.
8. Lee, S.Y. and Klassen, R.D. (2008), "Drivers and enablers that foster environmental management capabilities in small- and medium-sized suppliers in supply chains", Production and Operations.
9. Zhu, Sarkis, Kee-hung Lai, (2007) "Green supply chain management: pressures, practices and performance within the Chinese automobile industry", Journal of Cleaner Production 15, 1041–1052.
10. Lokesh Vijayvargy & Gopal Agarwal, (2013), " A Comparative study of Green Supply Chain management Practices in Indian, Japanese and Chinese Companies", The IUP Journal of Supply Chain, Vol 10, No. 3, pp 7–18.
11. Sarah Shaw, David B Grant, John Mangan, (2010), "Developing environmental supply chain performance measures", Benchmarking: An International Journal, Vol 17, No. 3, pp. 320–339.
12. Bhateja Ashish Kumar, Babbar, Rajesh Singh, Sarbjit Sachdeva, Anish (2011), "Study of Green Supply Chain Management in the Indian Manufacturing Industries: A Literature Review cum an Analytical Approach for the measurement of performance", International Journal, Vol 13, pp 84–89.
13. Purba Rao, Holt Diane, (2005), "Do green supply chains lead to competitiveness and economic performance?", International Journal of Operations & Production Management, Vol 25, no. 9, pp 898–916.
14. Kenneth W. Green Jr et.al. (2012), "Green supply chain management practices: impact on performance", Supply Chain Management: An International Journal, Vol. 17 No. 3, pp. 290–305.
15. Pochampally, (2009), "Metrics for performance measurement of a reverse/closed-loop supply chain", International Journal of Business Performance and Supply Chain Modelling, Vol. 1 No. 1, pp. 8–32.
16. Su-Yol Lee (2008), "Drivers for the participation of small and medium-sized suppliers in green supply chain initiatives", Supply Chain Management: An International Journal, Vol 13, No. 3, pp 185–198.
17. Hervani, Arefa. Helms, Marilyn M. Sarkis, Joseph (2005), "Performance measurement for green supply chain management", Benchmarking: An International Journal, Vol 12, No. 4, pp 330–353.

Part IV
Automation

Reliability Assessment of Seals Used in Propulsion Module of an Autonomous Unmanned Vehicle Using Markov Chains

Prathamesh Mohite, Elroy Rodrigues and Shivani Vartak

Abstract For the successful operation of an autonomous unmanned vehicle, also known as AUV, it is imperative to have an apt design of its hull and other components such as seals and housings to prevent all possible failures due to increasing atmospheric pressure at greater depths below sea level. Thus, each phase, right from the design to the termination phase, involves a series of crucial steps. These steps are sequentially arranged by implementing a mathematical model known as Markov chains. Based on heuristic and experimental data, we analyzed the reliability of the seals used in the propulsion module of the vehicle, by assigning transition probabilities to each step whether recurring, non-recurring, or terminating. The proposed model consists of a total of seven states. These states are then plotted in a square matrix also known as the "distribution matrix". Successive iterations are then obtained based on an initial probability vector. This quantitative analysis of the iterations explores the pattern in which the entire procedure unfolds with time and predicts the success rate and the risk involved in the process when the system attains a steady-state vector.

Keywords Iterations · Risk · Transition · Discrete · Stochastic · Reliability
Corrosive · Terminal · Material

1 Introduction

Modern-day vehicles used for the purpose of marine surveillance deploy complex control systems and mechanisms to prevent all possible failure modes. Prior to the deployment of these systems involves a series of several tests to check for any potential failures. Thus, each phase in the process is accompanied with a measurable amount of risk or uncertainty. Risk analysis tools such as the failure modes and effects analysis fail to provide sufficient information on the behavioral pattern of the

P. Mohite (✉) · E. Rodrigues · S. Vartak
Fr. Conceicao Rodrigues College of Engineering,
Bandra Bandstand, Mumbai 400050, Maharashtra, India
e-mail: mohiteprathamesh77@yahoo.com

615

failure. Thus, we put forward a stochastic model that enables us to better analyze the risks for different phases in the system, known as the "Markov chains". It was observed that the implementation of the Markov model facilitates the analysis of the operation and how the process behaves under different conditions. Markov chains being a highly versatile stochastic model can be implemented in any industrial or non-industrial operations that involve risks or uncertainties such as aerospace, supply chain [1], defense logistics, bioinformatics, kinetic theory of gases [2], astrophysics, and in complex medical procedures like surgery [3]. In this paper the concept of Markov chains was implemented to analyze the reliability of seals used in propulsion module of an underwater marine vehicle when it is subjected to varying pressures and environmental conditions at increasing depths below the sea level.

1.1 Research Background and Motivation

A similar research work was done by Brito, Mario Paulo, and Gwyn Griffiths in the paper titled "A Markov chain state transition approach to establishing critical phases for AUV reliability." published in the IEEE Journal of Oceanic Engineering 36.1 (2011): 139–149. Our research primarily focuses on the selection of seals that are best suited to withstand the pressure and atmospheric conditions when the AUV is submerged in the sea.

2 The Concept of Markov Chains

The Markov chain is a mathematical model named in the honor of Andrey Markov (1856–1922), a Russian mathematician. According to the Markovian property, the past and present states of a system are independent of each other, when the present state is clearly defined; i.e., the future state of a system can be predicted based on the present state. This largely reduces the number of parameters under consideration, thereby simplifying the process of computation. Markov chains help in computing the probability of an event which changes from one state to the other. There are two types of Markov chains, namely "discrete" type Markov chains and "continuous" type Markov chains. In discrete type, the changes in a system occur at regular intervals. In continuous type, the changes in a system occur continuously. This research is of a "discrete" type [4].

3 Experiments Conducted

The quality of seals can be tested by subjecting the seals under pressure. The pressure tests that were conducted helped us to determine any leakage, either due to friction

between motor shaft and housing [5] or due to changes in material properties [6] of the seals due to external environmental conditions [7].

3.1 Test Procedure

Initially the test is conducted at a pressure of 12 bar (atmospheric pressure at 20 m depth below sea level). The propulsion motors, along with the attached seals under consideration, are mounted on a fixture designed as per the internal and external dimensions of the seals. The entire apparatus is then externally pressurized using a hydraulic pressure pump. Specific arrangements can be made to pressurize the seal externally or internally. The test is conducted in two stages; static pressure test and dynamic pressure test, each for a period of thirty minutes. Observations for any drop in the pressure were recorded from the dial indicator mounted on the test pump. Similar tests were conducted for increasing depths, i.e., 22 bar (200 m depth), 32 bar (300 m depth), and 42 bar (400 m depth). The final pressure test 52 bar (500 m depth) is conducted at the test site under actual conditions of temperature and pressure.

3.2 Initial Observation

Leakage due to failure of the seals was evident from the observed drop in pressure. Necessary corrections in the design and material were then made to mitigate these failures. Closer tolerances ensured that the manufactured seals met the required dimensional specifications. The material of the seals was hardened to ensure minimum wear out due to friction. Seawater being highly corrosive in nature, the material properties of the seals were altered as per the chemical properties of it's operating surroundings.

4 Realization of the Markov Chain

The test procedure described earlier is represented as a flowchart of independent states. Our model comprises a total of seven states from S_1 to S_7.

As per the flowchart in Fig. 1, the process starts with the design phase represented by the symbol S_1. Here the seals are designed as per the dimensions of the housings. Changes in the design can be done if the seals fail during any of the tests [8]. These changes may include changes in the dimensions [9], material property of the seals, or the operational parameters [10]. The transition probabilities are assigned based on the experience, skill, and overall efficiency of the design team. Thereafter, we conduct the necessary pressure tests (stages S_2 to S_7) to test the reliability of the designed seals as discussed in Sect. 3.1. Upon failure of any of the tests, the system reverts
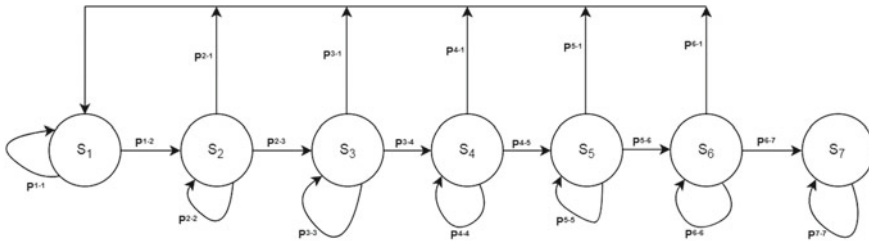
Fig. 1 Markov model to illustrate the sequence of activities

back to the design phase (S_1). The final stage S_7 is the terminal stage which marks the completion of the critical activity. The conditions for each transition are presented in Table 1. The values for recurring transition probabilities, i.e., P^{1-1}, P^{2-2}, P^{3-3}, P^{4-4}, P^{5-5}, P^{6-6} and P^{7-7} have been obtained based on experimental data and by consulting research scholars and industrial experts who have been actively involved in the design team for more than a decade [11]. The results of the Markov chain iterations and graphical analysis were obtained using the computational software MATLAB version 9.1 R 2016 b.

5 The Distribution Matrix

On the basis of the transitions as seen in Fig. 1, the distribution matrix is represented below. States having no transitional relation between them are assigned a probability of zero.

We have,

$$
M = \left\{
\begin{array}{ccccccc}
0.70 & 0.30 & 0.00 & 0.00 & 0.00 & 0.00 & 0.00 \\
0.35 & 0.40 & 0.25 & 0.00 & 0.00 & 0.00 & 0.00 \\
0.30 & 0.00 & 0.35 & 0.35 & 0.00 & 0.00 & 0.00 \\
0.25 & 0.00 & 0.00 & 0.30 & 0.45 & 0.00 & 0.00 \\
0.20 & 0.00 & 0.00 & 0.00 & 0.25 & 0.55 & 0.00 \\
0.15 & 0.00 & 0.00 & 0.00 & 0.00 & 0.20 & 0.65 \\
0.00 & 0.00 & 0.00 & 0.00 & 0.00 & 0.00 & 1.00
\end{array}
\right\}
$$

Since the critical activity initiates with the design phase, we represent the initial probability vector as

$$
\Pi_0 = \left\{ 1.00 \ 0.00 \ 0.00 \ 0.00 \ 0.00 \ 0.00 \ 0.00 \right\}
$$

According to Markov rule, the probability that the system will reach state S_n after "n" iterations is represented by the formula.

Table 1 Summary of experiments

Stages		Symbol	Probability of transition	Corrections in design	
Predecessor	Successor			Dimensional changes	Changes in material property
S_1	S_1	P^{1-1}	0.7	NA	NA
(Design/redesign)	S_2	P^{1-2}	0.3	NA	NA
S_2	S_1	P^{2-1}	0.35	Tighter tolerances	NA
(Pressure test 1)	S_2	P^{2-2}	0.4	NA	NA
	S_3	P^{2-3}	0.25	NA	NA
S_3	S_1	P^{3-1}	0.3	NA	Increase in hardness
(Pressure test 2)	S_3	P^{3-3}	0.35	NA	NA
	S_4	P^{3-4}	0.35	NA	NA
S_4	S_1	P^{4-1}	0.25	NA	Improvement in thermal properties
(Pressure test 3)	S_4	P^{4-4}	0.3	NA	NA
	S_5	P^{4-5}	0.45	NA	NA
S_5	S_1	P^{5-1}	0.2	Introduction of compression seals	NA
(Pressure test 4)	S_5	P^{5-5}	0.25	NA	NA
	S_6	P^{5-6}	0.55	NA	NA
S_6	S_1	P^{6-1}	0.15	NA	Improvement in abrasive properties
(Pressure test 5)	S_6	P^{6-6}	0.2	NA	NA
	S_7	P^{6-7}	0.65	NA	NA
S_7 (Project termination)	S_7	P^{7-7}	1	NA	NA

In our case we take, $n =$ the number of days required to complete the critical activity.

$$\Pi_n = \Pi_{0.} M^n$$

6 The Steady-State Vector ($\prod_N$)

The initial probability vector ($\prod_0$) is multiplied by the n-th power of initial probability matrix (P). The obtained vector from the previous iteration is then multiplied again with the matrix 'P'. Eventually the vector attains a stady state i.e all the subsequent vectors have the same values. Here, 'n' is the number of days required for attaining the steady state [12].

We have,

$$\Pi_0 = \left\{ 0.700 \; 0.300 \; 0.000 \; 0.000 \; 0.000 \; 0.000 \; 0.000 \right\}$$

$$\Pi_{10} = \left\{ 0.490 \; 0.251 \; 0.098 \; 0.051 \; 0.032 \; 0.022 \; 0.055 \right\}$$

$$\Pi_{100} = \left\{ 0.126 \; 0.065 \; 0.026 \; 0.013 \; 0.008 \; 0.006 \; 0.756 \right\}$$

$$\Pi_{100} = \left\{ 0.020 \; 0.011 \; 0.004 \; 0.002 \; 0.001 \; 0.001 \; 0.950 \right\}$$

$$\Pi_{100} = \left\{ 0.020 \; 0.011 \; 0.004 \; 0.002 \; 0.001 \; 0.001 \; 0.950 \right\}$$

At the 220th iteration, we obtain a steady-state vector. The vector $\prod_{220}$ indicates that the entire activity can be completed with a success rate of 95% in a time frame of 220 days. These results may vary depending on several conditions such as the efficiency of workforce and logistics, availability of raw materials and spare components, and timely completion of scheduled tasks. The above iterations can be graphically shown in Fig. 2. It indicates that the process reaches its terminal phase (probability of success) with an initial high rate of failure which decreases as we make the necessary corrections in the design of the seal.

7 Conclusion

The Markov process discussed in this paper is a useful tool for the project management team to analyze the uncertainties in the process of selecting the appropriate seals in order to prevent the risk of leakage in the underwater marine vehicle. The graphical results further reveal the how the system unfolds with time and help us to identify any scope of improvement. Several parameters such as operating time, battery life, environmental conditions, safety measures in case of an emergency which
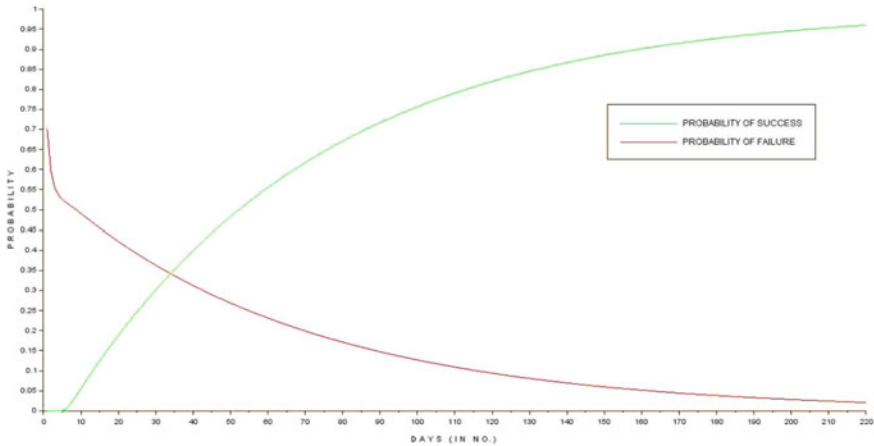
Fig. 2 Graphical representation of success and failure rate

were not discussed earlier can be incorporated in the system to obtain a more detailed analysis in the future.

References

1. Abedi, Sadegh, Morteza Mousakhani, and Naser Hamidi. "Using Markov chain to analyse production lines systems with layout constraints." (2009): 15–23.
2. Li, Lihong, et al. "Mathematical model based on the product sales market forecast of Markov forecasting and application." *Journal of Chemical and Pharmaceutical Research* 6.6 (2014): 1359–1365.
3. Beck, J. Robert, and Stephen G. Pauker. "The Markov process in medical prognosis." Medical decision making 3.4 (1983): 419–458.
4. Karlin, Samuel. *A first course in stochastic processes*. Academic press, 2014.
5. Yu, X. Q., S. He, and R. L. Cai. "Frictional characteristics of mechanical seals with a laser-textured seal face." *Journal of Materials Processing Technology* 129.1 (2002): 463–466.
6. Etsion, Izhak, Y. Kligerman, and G. Halperin. "Analytical and experimental investigation of laser-textured mechanical seal faces." *Tribology Transactions* 42.3 (1999): 511–516.
7. Brito, Mario Paulo, and Gwyn Griffiths. "A Markov chain state transition approach to establishing critical phases for AUV reliability." *IEEE Journal of Oceanic Engineering* 36.1 (2011): 139–149.
8. Etsion, Izhak. "Improving tribological performance of mechanical seals by laser surface texturing." In *PROCEEDINGS OF THE INTERNATIONAL PUMP USERS SYMPOSIUM,* pp. 17–22. 2000.
9. Wittig, S. L. K., L. Dorr, and S. Kim. "Scaling effects on leakage losses in labyrinth seals." *Journal of Engineering for Power* 105.2 (1983): 305–309.
10. Smee, Gregory, et al. "A comparative leakage study of P-30 resin bonded ceramic, Teflon, amalgam, and IRM as retrofilling seals." *Journal of endodontics* 13.3 (1987): 117–121.
11. Larsen and Toubro Lip Seal Failure Case Report.
12. Ramaswami, V. "A stable recursion for the steady state vector in Markov chains of M/G/1 type." *Stochastic Models* 4.1 (1988): 183–188.

Elitist Non-dominated Sorting Genetic Algorithm-Based Heuristic for Optimizing Rail Freight Transportation

Vinay V. Panicker, C. S. Aryadutt and K. P. Anoop

Abstract Transportation services are crucial for any supply chain as these services deliver raw and intermediate materials to manufacturers and deliver finished goods to retailers and end customers. The present work focuses on the freight transportation adopted by an Indian food grain supply chain. The problem can be considered as a single-source multiple-destination distribution-allocation problem. Three penalty factors have been introduced to quantitatively represent the risk of incurrence of demurrage cost, to match time of supply and release of food grains and to maintain uniform capacity utilization throughout the network of depots. A multi-objective model is formulated with an objective to minimize these penalty factors. The model is solved using elitist non-dominated sorting genetic algorithm (NSGA II)-based heuristic. The solutions obtained prove the fast-converging nature of NSGA II algorithm.

Keywords Food grain supply chain · Multi-objective optimization
Non-dominated sorting genetic algorithm (NSGA II)

1 Introduction

Freight transport is crucial for the economic growth and development of a country. Transportation services are very much needed for any supply chain as the point of production and point of consumption rarely coincides. It is a fact that the cost of logistics is very high in India. The improvement in transportation sector and better

V. V. Panicker (✉) · C. S. Aryadutt · K. P. Anoop
Department of Mechanical Engineering, National Institute of Technology Calicut,
Campus P.O, Kozhikode, Kerala, India
e-mail: vinay@nitc.ac.in

C. S. Aryadutt
e-mail: aryadutt93@gmail.com

K. P. Anoop
e-mail: kpanoop05@gmail.com

coordinated development of railways, roads and waterways are the strategies to be adopted to reduce the cost.

As rail transportation is more energy efficient than road, movement of freight via the rail could reduce logistics costs considerably. This work focuses on the freight transportation of food grains by an Indian food grain supply chain. The organization considered in this study owns depots at different states. Since these depots are horizontally collaborated, excess grains are stored at different locations. Since the food grains are moved from one source depot (consignor) to different destination storage depots (consignee), the problem can be considered as a single-source multiple-destination distribution-allocation problem.

Recently, few studies have been done in the food grain supply chain under consideration to optimize the freight transportation. A mathematical model for the determination of the optimal freight rate and the corresponding intermodal terminal location is proposed in [1]. A mathematical model for intra-state transportation of food grains incorporating flexibility in choosing economic mode of transport is developed in [2]. A mixed integer non-linear programming model to minimize the total cost which includes transportation, inventory and operational costs was developed and solved in [3].

Most of the works have considered single grain transportation problem. To overcome this drawback, a mixed integer linear programming model is developed in [4] to minimize the inventory holding cost and transportation cost for multiple food grains. Reference [5] proposed an integer non- linear programming and solved using exact method to formulate a monthly distribution-allocation plan for food grains by minimizing the total penalty value. In this work, a single-objective model priority was given for various penalty factors considered.

Further, a multi-objective model was developed for freight optimization of food grain supply chain and solved using multi-objective simulated annealing (MOSA)-based meta-heuristic in [6]. MOSA is applied to obtain a set of non-dominated plans for the distribution and allocation of food grains. The present work is an extension of this work by using NSGA-based meta-heuristic to solve the problem.

2 Problem Description

Food grains transported from a distant-source depot which is to be distributed and allocated to the set of destination storage depots under consideration. The distant sources are treated as a single source. Hence, the problem type considered can be called as a single-source multiple-destination distribution-allocation problem.

The food grain organization in this study has to distribute the allocated quantity from the source to the warehouses by meeting their demand. As per the provisions of Indian Railway, this organization can combine the demands of its two warehouses and order a full-train load. But Indian railway has put restrictions on the possible combinations of the warehouses based on the distance between them. So the food grains arrive at destination in full rake or half rake depending on warehouse demand.

It is the responsibility of this consignee organization to free the wagons within the allotted free time. For the extra time taken to unload the food grains, penalty (demurrage cost) have to be paid to Indian Railway by the consignee.

In order to quantify the problem, penalty-based approach is adopted in this work. The three penalty factors introduced are, namely rake penalty factor, weekly penalty factor and capacity utilization penalty factor.

- Rake penalty factor

Quantifies the relative risk in allotting a full rake to a depot over a half rake in terms of the incurrence of demurrage cost.

- Weekly penalty factor

Quantifies the priority of a particular week in a month over others. It is defined as the ratio of the outflow in a month to the outflow during a particular week in that month. So, the week with relatively more outflow will be served so as to minimize the weekly penalty factor.

- Capacity utilization penalty factor

The distribution of food grains across the storage depots is made uniform by incorporating capacity utilization penalty factor. It is the ratio of the storage capacity of a depot to the existing stock level there. By minimizing capacity utilization penalty factor, the depots with minimum capacity utilization can be given preference.

These penalty factors quantify the three objectives of the project. The project focuses on obtaining a monthly rake allocation plan for eight warehouses under consideration by minimizing the three penalty factors. The consignee organization has to allocate the food grains in such a way that it should meet demand at all warehouses and should not exceed the storage capacity of the warehouses. In a month, four weeks are considered, and in each week, only one allocation is possible. In some situations, the food grains shipped from source may exceed the demand; hence, the model should be flexible to accommodate that. By approaching the problem as multi-objective optimization problem, the expected result is Pareto-optimal solutions. So the organization can choose from a set of solutions depending on the priority of the objectives.

3 Solution Methodology

A method to solve multi-objective optimization problems and find multiple Pareto-optimal solutions is proposed in [7] named as non-dominated sorting algorithm (NSGA I). NSGA I algorithm is faster compared to other evolutionary algorithms for obtaining multiple Pareto–optimal solutions. Later, modified NSGA I, called as NSGA II, was proposed as in [8] which is computationally faster than NSGA I. NSGA II is based on a non-dominated sorting approach which uses an explicit mechanism to preserve diversity among solutions. NSGA II-based heuristic is proposed

to minimize the supply chain cost and to improve responsiveness of supply chain in [9]. NSGA II algorithm is applied to multi-objective parallel machine scheduling problem in [10]. A NSGA II-based heuristic is developed to solve the problem under consideration.

3.1 Steps Involved in the Heuristic

The steps involved in NSGA II algorithm are given below:

Step 1: Initially, a random population P_0 of size N is created

Step 2: The population is sorted into different domination levels (F_i) and calculate the crowding distance for each solution in various fronts.

Step 3: Solutions are randomly grouped to N pairs in such a way no pair have same solutions. Crowded tournament selection operation is carried out in each pair to get the best solution.

Step 4: Crossover and mutation operations are carried out on resulting population to generate offspring population Q_0.

Step 5: Combine parent and offspring population to create R_t and perform non-dominated sorting and crowding distance calculation on R_t.

Step 6: Set new population $P_{t+1} = \Phi$, and set a counter $i = 1$. Until (abs (P_{t+1}) + abs $(F_i))<N$, perform $P_{t+1} = P_{t+1} \cup F_i$ and $i = i+1$.

Step 7: When (abs (P_{t+1}) + abs $(F_i))>N$, fill the remaining slots based on crowding distance to obtain population P_1.

Step 8: Pair the population and perform crowded tournament selection, crossover and mutation operations on the obtained population to get population Q_1.

Step 9: Repeat steps 5, 6, 7 and 8 till the stopping criteria is met.

3.2 Solution Representation

The solution for the problem considered is represented by 8×4 matrix, where 8 rows denote the eight warehouses, and 4 columns denote the four allocations possible for the month. Hence, the solution is considered as a matrix as in [11] of dimension 8×4. Table 1 represents a sample solution. It is assumed that in a week, only one allocation is possible, and hence in a month, four allocations are possible. Allocations are done in terms of half rakes.

In Table 1, each cell in matrix can be filled by 0, 1 or 2, where 0 represents no allocation, 1 represents half-rake allocation and 2 represents full-rake allocation for a particular warehouse in a particular week. The total quantity transported from the source must be allocated meeting demand of a warehouse subject to storage capacity limitations. Half-rake allocation occurs as a combination.

Table 1 Solution representation

Warehouse	Week 1	Week 2	Week 3	Week 4
WH1	1	2	2	0
WH2	2	1	2	0
WH3	0	0	0	2
WH4	0	0	2	0
WH5	0	1	0	0
WH6	1	0	0	0
WH7	0	2	2	1
WH8	0	2	0	1

3.3 Operators Used

The NSGA II algorithm-based heuristic mainly uses the following six operators such as non-dominated sorting, crowding distance calculation, crowded tournament selection, crossover, mutation and divorce operators.

The above-stated operators are explained below:

Non-Dominated Sorting. This operator classifies the solutions in the population to various non-domination levels. The solutions in the population that are not dominated by any other solutions are put in front one, solutions that are dominated by one solution is put in front two, and so on. No solution is better than any other solution in that front. We calculate two entities to find non-dominated fronts:

 (i) n_i, the number of solutions which dominate the solution i, and
(ii) S_i, a set of solutions which the solution i dominates.

Identify the solutions with n_i value equal to 0 which forms the first non-dominated front is put in list F_1. For each solution in the current front, visit each member (j) in its set S_i and reduce its n_j count by one. After this, again check for the solutions with n_i value zero and put this in list F_2. Then, continue this process using the newly identified front as our current front till all the solutions are classified into non-dominated fronts.

Crowding Distance. The crowding distance for a particular solution gives an estimate of the density of solutions surrounding it.

This quantity can be considered as the size of largest cuboid enclosing a point i without including any other point in the population. It is identified as the largest rectangle in case of two-objective optimization problem. Figure 1 shows the case of a two-objective optimization problem, where $f1$ and $f2$ represent two objectives, and j represents the point for which crowding distance is calculated. Arrange all the solutions in a front F in ascending or descending order for each objective. For the boundary solutions, the crowding distance value is assigned as infinity. For rest of the solutions, crowding distance is calculated using the following formula:

$$d_{i_j^m} = d_{i_j^m} + \frac{f_m^{j+1} - f_m^{j-1}}{f_m^{\max} - f_m^{\min}} \tag{1}$$

Fig. 1 Crowding distance representation for two-objective optimization problem
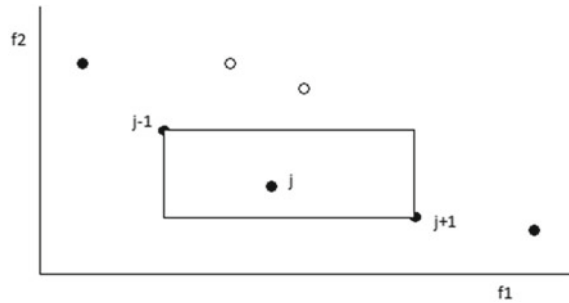
where $d_{i_j^m}$ represents the crowding distance for solution i, and j denotes the position of solution i in the sorted array for objective m; f_m^j represents the objective value of solution in position j in sorted array for objective m and $f_m^{\max}$ and $f_m^{\min}$ represents the maximum and minimum values of objective function value for objective m, respectively.

The distance for solution i is sum of the values calculated using the above formula for each objective.

Crowded Tournament Selection. The crowded comparison operator ($\angle_c$) helps in the selection process at various stages of the algorithm to obtain a uniformly spread out Pareto-optimal front. For every individual solution i in the population, the following two attributes are calculated—(1) Non-domination rank (i_{rank}) and (2) Local crowding distance (i_{distance}). A solution i wins a tournament with another solution j: If ($i_{\text{rank}} < j_{\text{rank}}$) or (($i_{\text{rank}} = j_{\text{rank}}$) and ($i_{\text{distance}} > j_{\text{distance}}$)).

CrossOver. The crossover operation is carried out based on crossover probability. Random numbers are generated for each solution. If the generated random number is within the crossover probability, then that solution enters the mating pool. The solutions are paired, and crossover operation is performed on each pair. Seven cases of crossover are performed on each pair of parents.

Case (1): The first column of parents is interchanged.
Case (2): The first two columns of parents are interchanged.
Case (3): The first three columns of parents are interchanged.
Case (4): The second column of parents is interchanged.
Case (5): The third column of parents is interchanged.
Case (6): The second and third columns of parents are interchanged.
Case (7): The second and fourth columns of parents are interchanged.

Each pair of parents results in seven pair of children after crossover which may be feasible or not. If feasible solutions are obtained in any case, then that case of crossover is chosen, and in case of no feasible solutions in any of seven cases, the case in which the solutions can be made feasible with less complexity is chosen.

Divorce Operator. When two parents are not able to give feasible solutions in any of the cases of crossover, the divorce operator removes this pair of parents from mating pool and selects two other parents randomly.

Mutation. The mutation operation is carried out to incorporate the genetic changes that may occur over generations. So mutation probability is taken as a very low value. Random numbers are generated for each solution, and based on mutation probability, the solutions to undergo mutation are selected. In the selected solution, one cell is selected randomly and change is made into the selected cell in such a way that the solution remains feasible even after the change is made.

4   Results and Conclusion

The proposed heuristic was coded using MATLAB R2015b in a computer with Intel core i5 3.2 GHz processor and 8 GB RAM.

An initial population size of 8 and total allocated quantity of 24 is considered. The monthly demand, initial stock level and storage capacity are shown in Table 2. Table 3 shows the weekly penalty factor matrix. The number of iterations is set at 1000. The value of objective functions of the resulting population after iterations is shown in Table 4.

The solutions in the resulting populations show that some of the solutions are repeated. This is because of the fast-converging nature of the NSGA II algorithm.

Table 2 Problem instance

Warehouse	Demand	Initial stock level	Storage capacity
WH1	3	6	13
WH2	3	17	25
WH3	2	3	6
WH4	2	3	6
WH5	1	12	16
WH6	1	3	5
WH7	3	32	40
WH8	3	2	6

Table 3 Weekly penalty factor

	Week 1	Week 2	Week 3	Week 4
WH1	1	1	10	2
WH2	4	2	2	1
WH3	2	2	3	1
WH4	2	2	3	1
WH5	4	4	3	1
WH6	2	3	4	1
WH7	4	4	3	1
WH8	4	7	3	1

Table 4 Objective function values of solution

Solution No.	Objective 1	Objective 2	Objective 3
1	530	90	37
2	500	86	42
3	510	85	47
4	530	90	37
5	510	85	47
6	540	90	42
7	510	85	47
8	500	86	42

The computational time taken to solve the heuristic is less than ten seconds. A set of non-dominated solutions would provide the manager in the organization with more choice and thus improve the flexibility in decision making. The work can be further extended by considering multiple allocations in a week by incorporating necessary changes for the weekly penalty factor for the further allocations.

References

1. Dandotiya, R, Nath Banerjee, R., Ghodrati, B. and Parida, A.: Optimal pricing and terminal location for a rail–truck intermodal service–a case study, International Journal of Logistics Research and Applications, 14(5), pp. 335–349, 2011.
2. Maiyar, L. M, Thakkar, J. J., Awasthi, A., and Tiwari, M. K.: Development of an effective cost minimization model for food grain shipments, IFAC-PapersOnLine, 48(3), pp. 881–886, 2015.
3. Mogale, D. G., Kumar, S. K. and Tiwari, M. K.: Two stage Indian food grain supply chain network transportation-allocation model, IFAC-PapersOnLine, 49(12), pp. 1767–1772, 2016.
4. Tanksale, A., and Jha, J. K.: An effective heuristic for multi-period multi-foodgrain inventory transportation problem in India, INFOR: Information Systems and Operational Research, 54(4), pp. 355–379, 2016.
5. Manu, N.: Optimization of the movement of food grains in food corporation of India, M.tech Thesis, National Institute of Calicut, 2016.
6. Jerin, S.: Optimization of freight transportation in a food grain supply chain using multi objective simulated annealing based heuristic, M.tech Thesis, National Institute of Calicut, 2017.
7. Srinivas, N. and Deb, K.: Multiobjective optimization using nondominated sorting in genetic algorithms, Evolutionary computation, 2(3), pp. 221–248, 1994.
8. Deb, K ., Agrawal, S., Pratap, A. and Meyarivan, T.: A fast elitist non-dominated sorting genetic algorithm for multi-objective optimization: NSGA-II,In International Conference on Parallel Problem Solving From Nature (pp. 849–858). Springer, Berlin, Heidelber, 2000, September.
9. Chan, F.T ., Jha, A. and Tiwari, M. K.: Bi-objective optimization of three echelon supply chain involving truck selection and loading using NSGA-II with heuristics algorithm, Applied Soft Computing, 38, pp. 978–987, 2016.
10. Bandyopadhyay, . S. and Bhattacharya, R.: Solving multi-objective parallel machine scheduling problem by a modified NSGA-II, Applied Mathematical Modelling, 37(10), pp. 6718–6729, 2013.
11. Jawahar, . N. and Balaji, A. N.: A genetic algorithm for the two-stage supply chain distribution problem associated with a fixed charge, European Journal of Operational Research, 194(2), pp. 496–537, 2009.

Vibration Control of 6 Dof Three-Wheeler Using Pid Controller

Routh Rajesh and S. Srinivasa Rao

Abstract In this paper, a six-DOF three-wheeler is modeled and the dynamic response of the three-wheeler is measured when the vehicle is moving on bump, random, sinusoidal road profiles, by using ADAMS–MATLAB Simulink co-simulation. An active suspension system is developed by applying PID control strategy to this model. The ride comfort of the three wheeler with active suspension system is compared with that of passive suspension system. It has been found that the ride comfort has been improved by applying PID control strategy.

Keywords Three-wheeler · ADAMS–MATLAB co-simulation · Acceleration Ride comfort

1 Introduction

Three-wheelers are used extensively as a mode of transportation in countries like India. In this paper, three-wheeler is modeled in ADAMS software and analysis is done in MATLAB by using ADAMS–MATLAB co-simulation [1]. The three-wheeler has six degrees of freedom. The sprung mass has three degrees of freedom bounce roll and pitch, and the three unsprung masses each have one degree of freedom of bounce. The vertical, roll, and pitch accelerations have been measured. The three-wheeler has been modeled by lumped parameter modeling by which the basic dynamics can be analyzed [2]. A 15-DOF human seat vibratory model has been developed. The dynamic behavior of the model is studied by giving harmonic input.

To improve the ride comfort, we have to decrease the vertical acceleration. This can be achieved by using active suspension system by controlling the suspension system which is not an easy task due to complexity in the components [3]. Experimentally, it is found that a two-DOF active suspension system with hydraulic actuator is better

R. Rajesh (✉)
Pragati Engineering College, Kakinada, India
e-mail: routhrajesh91@gmail.com

S. S. Rao
MVGR College of Engineering, Vizianagaram, India

compared to passive suspension system [4]. PID controller is used as control strategy, and the ride comfort is better than that of passive suspension system [5]. When PID with Genetic Algorithm and FUZZY logic control strategies are better than that of PID, LQR, SKYHOOK, H$_\infty$ are the latest control strategies which are better than PID [6, 7]. LQR control strategy is applied to five-DOF bus system to control the roll stability by giving vehicle speed and front wheel angle as input [8]. The SKYHOOK control strategy is applied to two-DOF system which has better performance than PID [9, 10]. H$_\infty$ active suspension is used for four-DOF active suspension system which ensures better ride comfort.

Lumped parameter model technique is used to model the vibrating systems [1–3], etc., by which the basic dynamics can be analyzed [11]. A hybrid quarter car model has been developed by treating the tire as a continuous ring. The contact force between the tire and the road are defined, and the results have been compared with the conventional model [12, 13]. Different hybrid vibrating systems have been developed where the tire is treated like a flexible ring. Even though designing hybrid model is more complex, the result is more accurate than the conventional model because rotation of the tire is considered.

2   Road Profiles

The road profiles are given as input to the three-wheeler and vertical acceleration, roll acceleration, and pitch acceleration are measured as output. The different road profiles used in this work are bump, random, and harmonic.

2.1   Bump Road Profile

Hongyi et al. [10] the bump on a smooth road is created in MATLAB/Simulink where A and L are the height and length of the bump. The forward velocity of the vehicle $V = 20$ kmph, $A = 0.05$ m, and $L = 2$ m. The bump profile is created by the Eq. (1). The bump profile is shown in Fig. 1 which is created in MATLAB/Simulink.

$$Z_{\mathrm{rf}}(t) = \begin{cases} \frac{A}{2}\left(1 - \cos\left(\frac{2\pi V}{L}t\right)\right), & \text{if } 0 \ \leq \ t \ \leq \ \frac{L}{V} \\ \qquad\quad 0 & \text{if } t \ > \ \frac{L}{V} \end{cases} \tag{1}$$

Fig. 1 Bump road profile
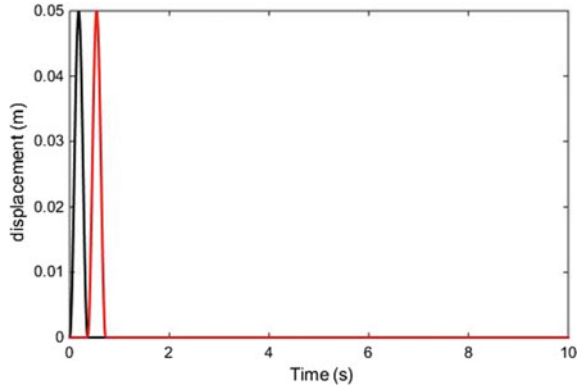
Fig. 2 Harmonic road profile
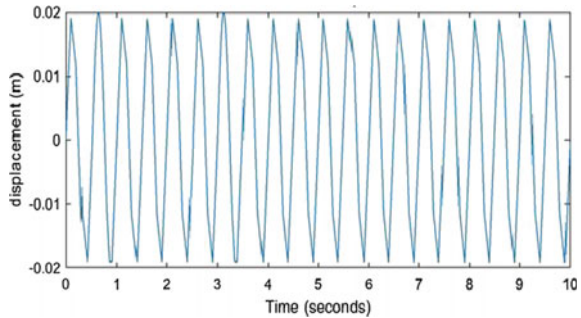
2.2 Harmonic Road Profile

Harmonic road profile is generated with sinusoidal wave in MATLAB/Simulink, amplitude $A = 0.02$ m, frequency $(\omega) = 12.54$ rad/s developed in SIMULINK as depicted in the Fig. 2.

2.3 Random Road Profile [1]

A multi-harmonic input which is closer to an actual road profile can be generated. A possible choice which approximates fairly well a real road profile is a so-called pseudorandom input which results from summing several non-commensurately related sine waves (i.e., the ratio of all possible pairs of frequencies is not a rational number) of decreasing amplitude, so as to provide a discrete approximation of a continuous spectrum of a random input. The trend can be proved to be non-periodic (sometimes referred to as almost periodic) in spite of being a sum of periodic waveforms.

$$S_g(\Omega) = C_{sp}\Omega^{-N}$$
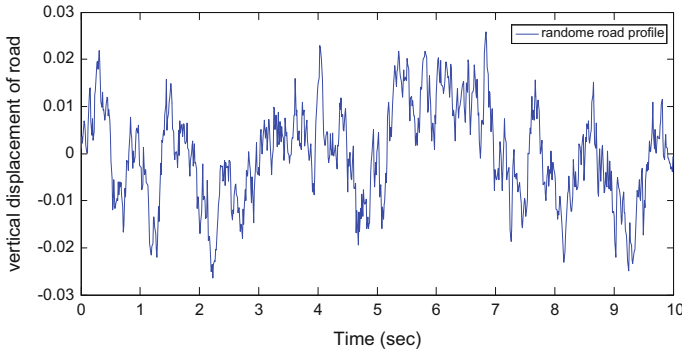
Fig. 3 Random road profile

Table 1 Specifications two-DOF quarter car model

Sl. No.	Parameter	Variable	Units	Value
1	Mass of the sprung system	M_s	Kgs	250
2	Mass of the unsprung system	M_{us}	Kgs	50
3	Suspension stiffness	K_S	N m	18,600
4	Tire stiffness	K_w	N m	19,600
5	Suspension damping coefficient	C_S	N s/m	1000
6	Tire damping coefficient	C_w	N s/m	0

where $S_g(\Omega)$ is the power spectral density function, C_{sp} and N are constants, and Ω is the spatial frequency.

3   Comparison of ADAMS Model and Mathematical Model

The two-DOF quarter car is modeled in ADAMS software and exported to MATLAB/Simulink environment and compared with mathematical model. The mathematical model is developed by motion equations of the two-DOF system on basis of Newton's second law of motion. The two models are compared in time domain for bump, sinusoidal, and random road profiles (Figs. 3, 4 and 5; Tables 1 and 2).

The mathematical equations of two-DOF quartet car model are as follows:
Sprung mass (Z_s) bounce
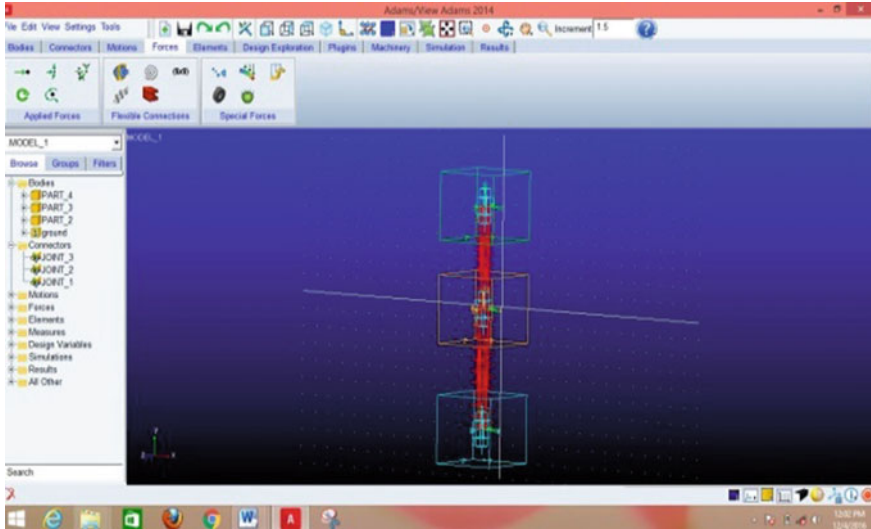
Fig. 4 Adams quarter car model
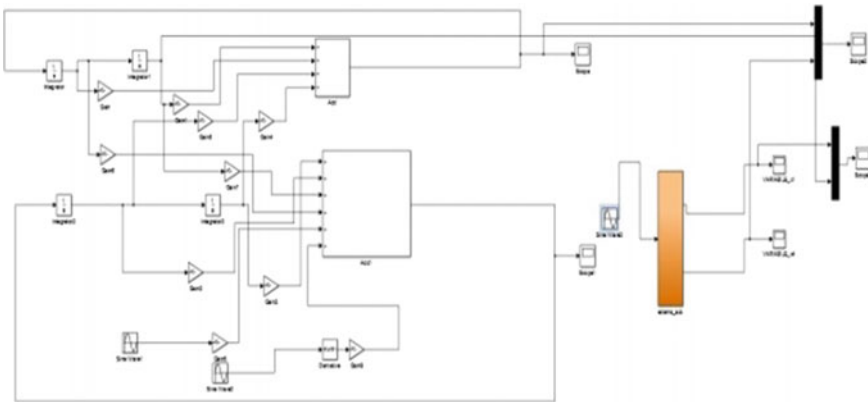
Fig. 5 Comparison of Adams model and mathematical model

$$M_s \ddot{Z}_s + K_S(Z_S - Z_{uS}) + C_S(\dot{Z}_S - \dot{Z}_{uS}) = F$$

Unsprung mass (Z_{us}) bounce

$$M_{us} \ddot{Z}_S - K_S(Z_S - Z_{uS}) - C_S(\dot{Z}_S - \dot{Z}_{uS}) + K_w(Z_{uS} - r) + C_w(\dot{Z}_{uS} - \dot{r}) = F$$

Table 2 Comparison of natural frequencies

Sl. No.	Modes of vibration	Mathematical model (Hz)	Adams model	% error
1	Bounce of sprung mass	1.32	1.31	0.7
2	Bounce of unsprung mass	10.34	10.44	0.9

Fig. 6 Sinusoidal input
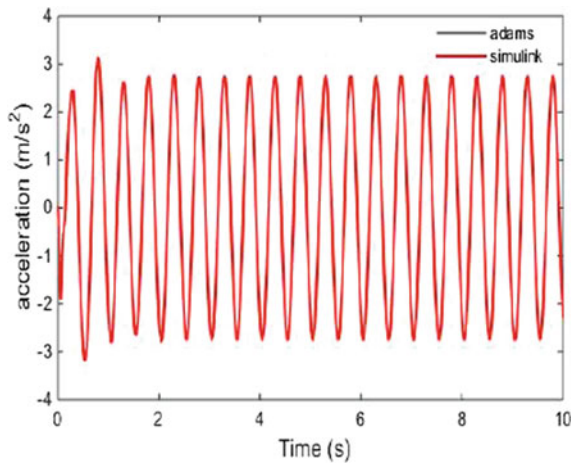
3.1 The Comparison of Dynamic Response of Adams Model and Mathematical Model

The dynamic response of both mathematical model and Adams model are compared in MATLAB/Simulink environment for bump, sinusoidal, and random road profiles in time domain. The modal analysis results of both mathematical and Adams are almost similar with negligible error. The dynamic response from Figs. 6, 7 and 8 was similar from this we can conclude Adams model is very accurate model. By using ADAMS software, we can design complex mechanical systems easily and accurately by avoiding lot of complex mathematical equations. This ADAMS software can be used in the field of Robotics and vehicle dynamics.

4 Modeling of Three-Wheeler

The six-DOF three-wheeler is modeled in ADAMS software and imported to MATLAB/Simulink for analysis. The three-wheeler vertical, roll, and pitch accelerations

Fig. 7 Bump input
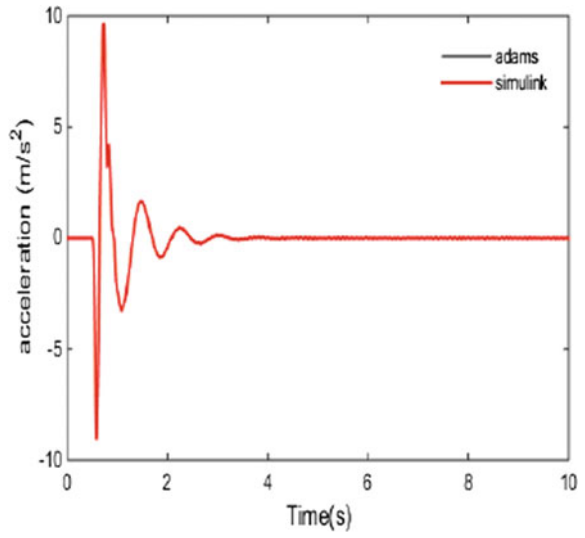
Fig. 8 Random input
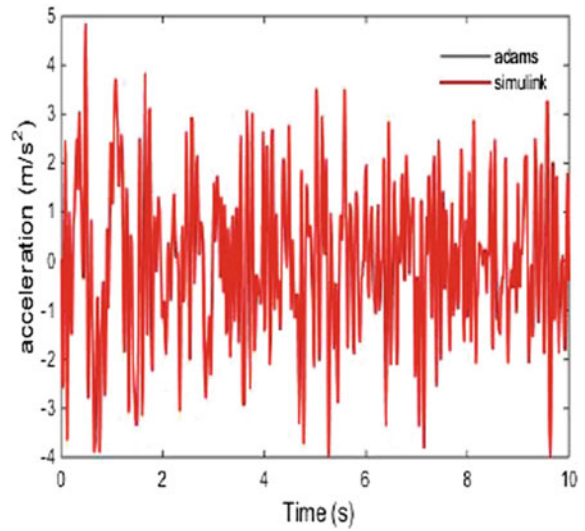
are measured. The suspension and tires are designed as per the specifications [1] of the three given in Table 3.

Table 3 Specifications of three-wheeler

Sl. No.	Parameter	Variable	Units	Value
1	Total mass of sprung system	M_s	Kgs	492.03
2	Mass of front unsprung system	M_{uf}	Kgs	8.5
3	Mass of rear unsprung system	M_{ur}	Kgs	18.0
4	MOI of rear system in x-direction	I_{px}	Kg m^2	182.2
5	MOI of rear system in y-direction	I_{py}	Kg m^2	170
6	Front suspension damping	C_1	N s/m	3500
7	Rear right suspension damping	C_2	N s/m	2207.5
8	Rear left suspension damping	C_3	N s/m	2207.5
9	Front tire damping coefficient	C_4	N s/m	557
10	Rear right tire damping coefficient	C_5	N s/m	436
11	Rear left tire damping coefficient	C_6	N s/m	436
12	Suspension spring stiffness-front	K_1	N m	32,700
13	Suspension spring stiffness-rear right	K_2	N m	50,400
14	Suspension spring stiffness-rear left	K_3	N m	80,000
15	Tire rolling dynamic stiffness-front	K_4	N m	2,38,260
16	Tire rolling dynamic stiffness-rear right	K_5	N m	2.50.490
17	Tire rolling dynamic stiffness-rear left	K_6	N m	2.50.490
18	Half-track width	l_1, l_2	m	0.575
19	Distance of sprung mass CG from the front tire contact point	l_3	m	1.496
20	Distance of sprung mass CG from the rear tire contact point	l_4	m	0.504
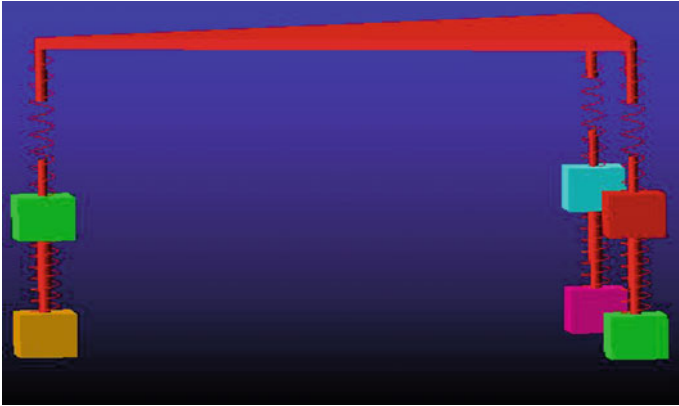
Fig. 9 Sprung mass bounce
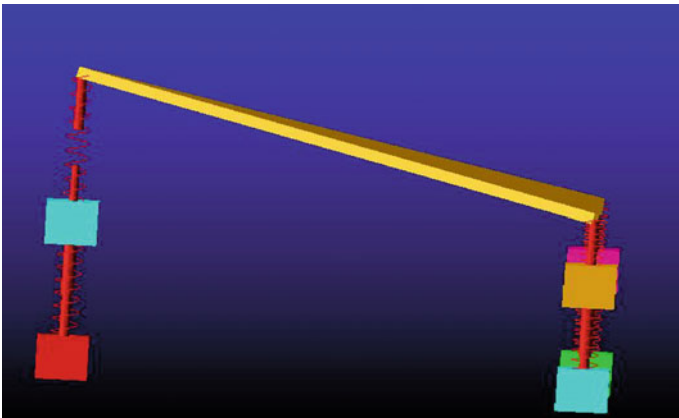
Fig. 10 Sprung mass pitch

4.1   *Model Analysis of Three-Wheeler*

The mode shapes and natural frequencies of the six-DOF are obtained through modal analysis in ADAMS. Here, six degrees of freedom correspond to the sprung mass bounce, pitch, roll, and bounce of unsprung mass of front and rear wheels. The natural frequencies for each mode of vibration calculated by constraining the motions of the sprung mass and unsprung mass and removing the constraint for the motion in the sequential manner such that only one motion is unconstrained for each simulation and observing the natural frequency of unconstrained part. In this way, the mode of vibration is identified with its natural frequency for the six-DOF vehicle model. The different mode shapes of the six-DOF three-wheeler are in Figs. 9, 10, 11, 12, 13 and 14; Tables 4, 5 and 6.
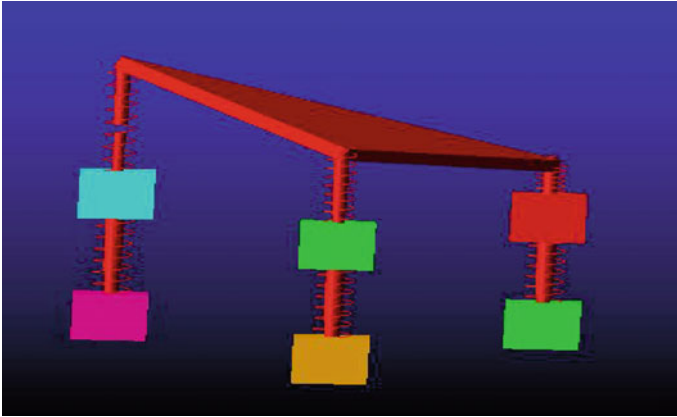
Fig. 11 Sprung mass roll
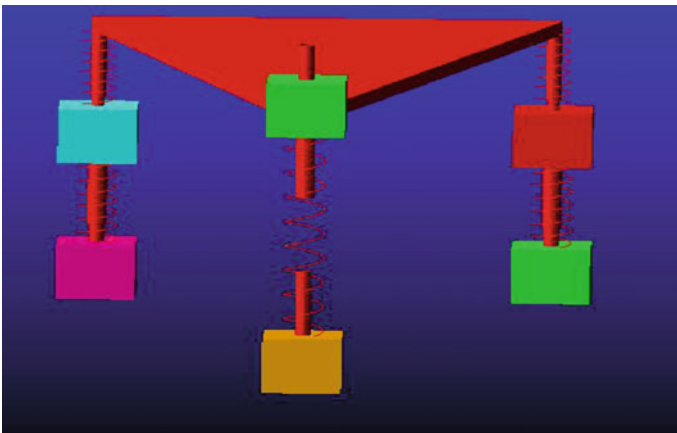
Fig. 12 Front unsprung mass bounce

5 Design of PID Controller

A proportional integral derivative controller (PID) controller is a control loop feedback mechanism commonly used in industrial control systems. A PID controller continuously calculates an error value $e(t)$ as the difference between a desired set point and measured a process variable. The controller attempts to minimize the error over time by adjustment of a control variable $u(t)$.

$$u(t) = K_p e(t) + K_i \int_0^t e(t) \mathrm{d}t + K_d \frac{\mathrm{d}e(t)}{\mathrm{d}x}$$
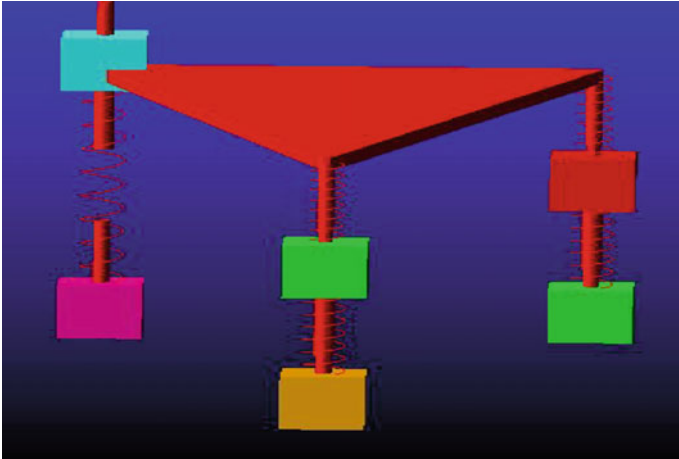
Fig. 13 Left unsprung mass bounce
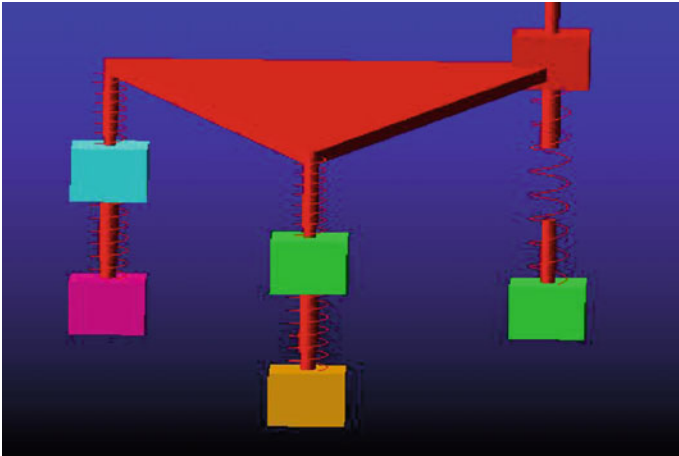
Fig. 14 Right unsprung mass bounce

where K_p, K_i and K_d, all non-negative denote the coefficients for the proportional, integral, and derivative terms, respectively (Fig. 15).

Table 4 Natural frequencies of the three-wheeler

Sl. No.	Modes of vibration	Natural frequency (Hz)
1	Bounce of sprung mass	2.5
2	Pitch of sprung mass	2.3
3	Roll of sprung mass	1.9
4	Bounce of front unsprung mass	12.5
5	Bounce of rear left unsprung mass	28
6	Bounce of rear right unsprung mass	29

Table 5 Comparison of active and passive system for bump input

Sl. No.	Vertical accelerate-on (m/s^2)	Roll acceleration rad/s^2	Pitch acceleration rad/s^2	PSD vertical acceleration $(m/s^2)^2/Hz$	PSD roll acceleration $(rad/s^2)^2/Hz$	PSD pitch acceleration $(rad/s^2)^2/Hz$
Passive	4.5	3.2	18	2.4	0.31	22
Active	4.2	2.8	16	0.4	0.27	17
%Decrease	6	12.5	11.1	83.3	12.9	22.7

Table 6 Comparison of active and passive system for sinusoidal input

Sl. No.	Vertical acceleration m/s^2	Roll acceleration rad/s^2	Pitch acceleration rad/s^2	PSD vertical acceleration $(m/s^2)^2/Hz$	PSD roll acceleration $(rad/s^2)^2/Hz$	PSD pitch acceleration $(rad/s^2)^2/Hz$
Passive	11	2.2	29	2.9	0.7	18
Active	7	2	20	1	0.4	15
% decrease	36.3	9.09	31.03	65.5	42.8	16.6

6 Comparison of Active Suspension with Passive Suspension System for Three-Wheeler

The performance of the PID controller over the passive suspension system is identified. The three-wheeler response for different road profiles bump, random, and sinusoidal is measured. The response of the three-wheeler is taken both in time domain and frequency domain.

6.1 Comparison for Bump Input

Transient analysis with bump excitation is fed as input for the three-wheeler. The sprung body vertical, pitch, and roll acceleration with application of PID controller and passive suspension system are plotted in Figs. 16, 17 and 18 in time domain,
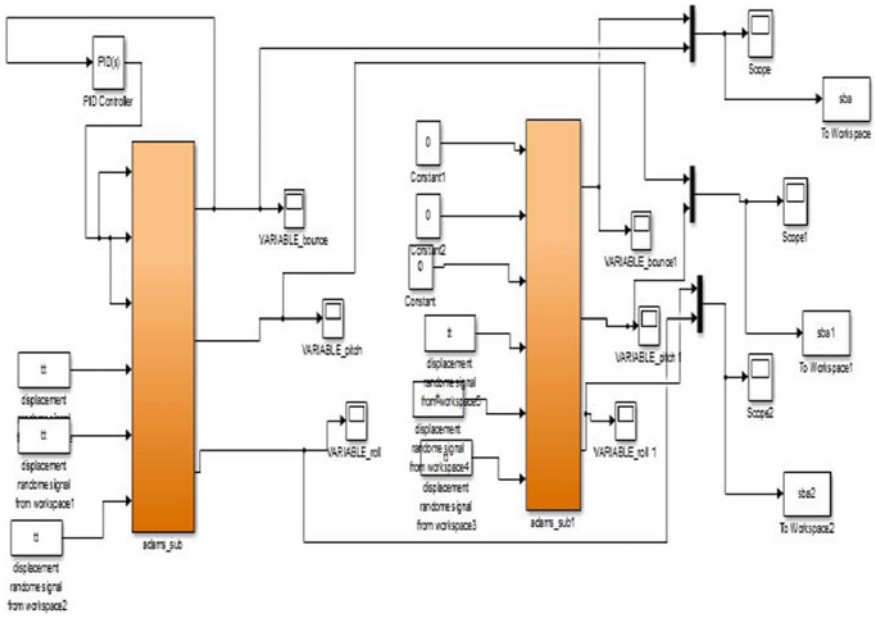
Fig. 15 Three-wheeler block diagram with PID controller

Fig. 16 Vertical acceleration
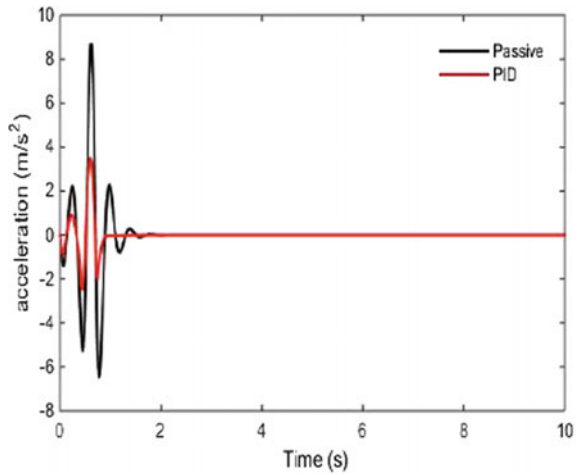
and in Figs. 19, 20 and 21, PSD vertical, PSD roll, and PSD pitch accelerations are plotted in frequency domain.

Fig. 17 Pitch acceleration
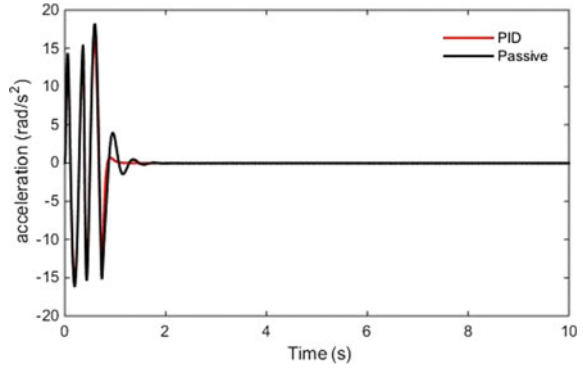
Fig. 18 Roll acceleration
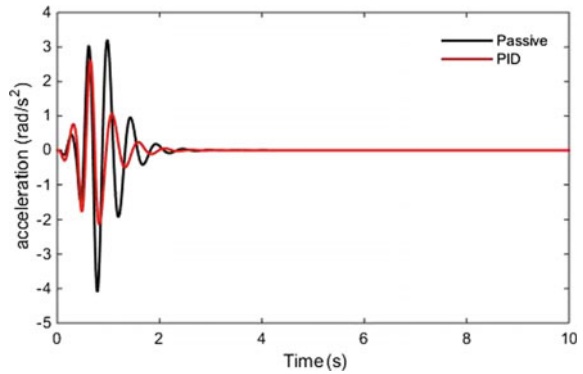
Fig. 19 PSD vertical acceleration
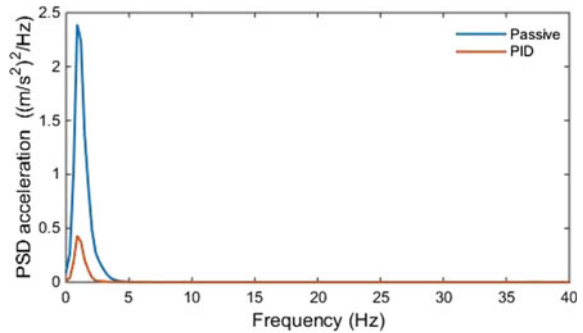
6.2 Comparison for Random Input

Random analysis with random excitation is fed as input for the three-wheeler. The sprung mass vertical, roll, and pitch accelerations with application of PID controller and passive system are plotted in Figs. 22, 23 and 24, and in time domain and in Figs. 25, 26 and 27, PSD vertical acceleration, PSD roll acceleration, PSD pitch

Fig. 20 PSD pitch acceleration
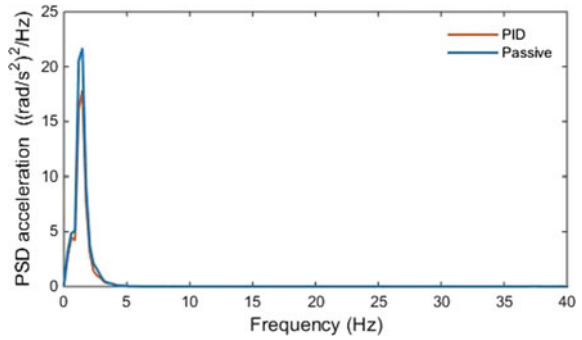
Fig. 21 PSD roll acceleration
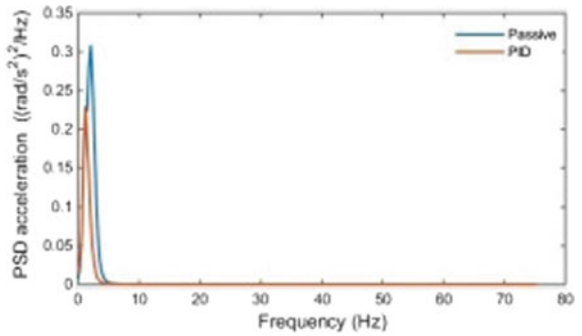
Fig. 22 Vertical acceleration
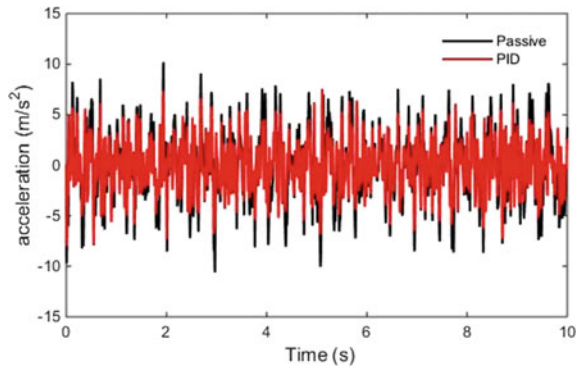
acceleration with application PID controller, and passive system are plotted with respect to frequency.

Fig. 23 Pitch acceleration
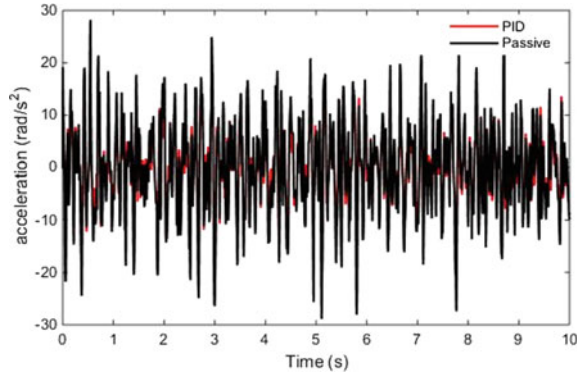
Fig. 24 Roll acceleration of random
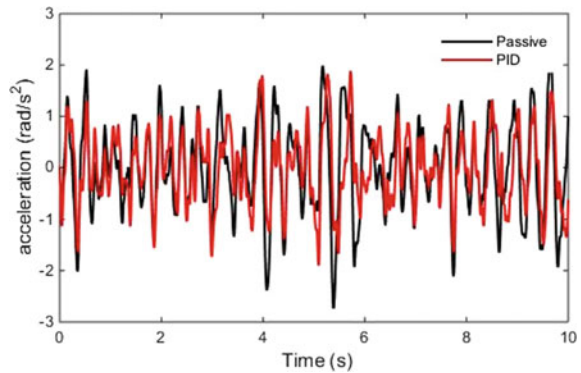
Fig. 25 PSD vertical acceleration
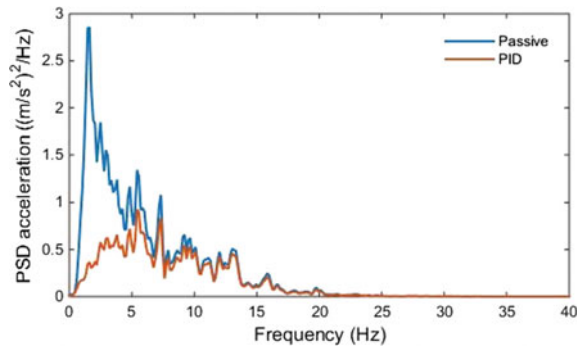
6.3 Comparison for Sinusoidal Input

Harmonic analysis with sinusoidal excitation is fed as input for the three-wheeler. The sprung mass vertical, roll, and pitch acceleration with application of PID controller and passive system are plotted in Figs. 28, 29 and 30 in time domain and in Figs. 31, 32 and 33 PSD vertical acceleration, PSD roll acceleration, PSD pitch acceleration

Fig. 26 PSD pitch acceleration
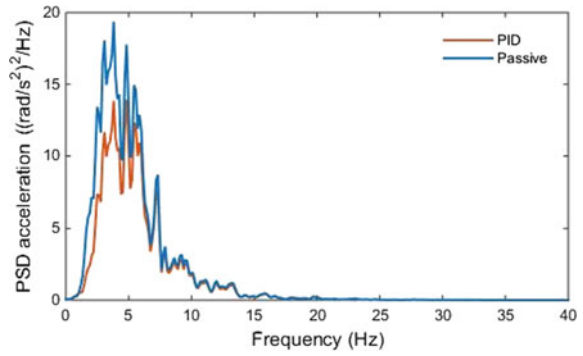
Fig. 27 PSD roll acceleration
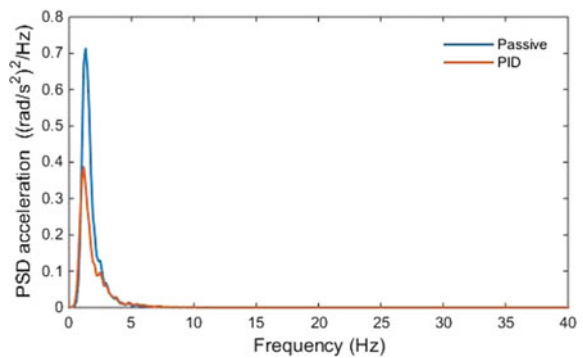
Fig. 28 Vertical acceleration
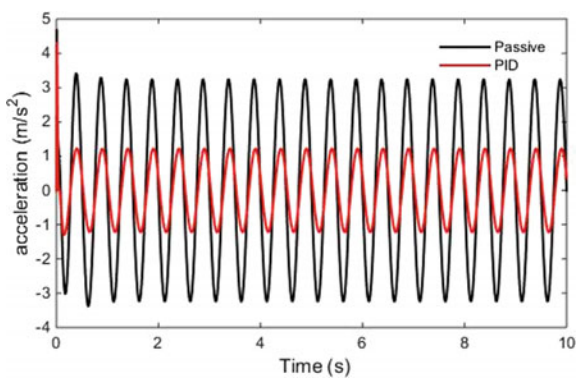
with application of PID controller, and passive system are plotted with respect to frequency.

Fig. 29 Pitch acceleration
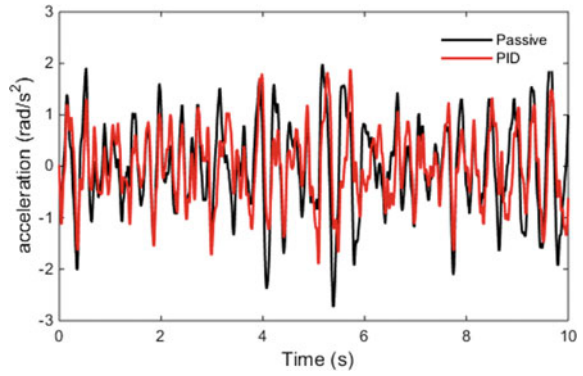
Fig. 30 Roll acceleration
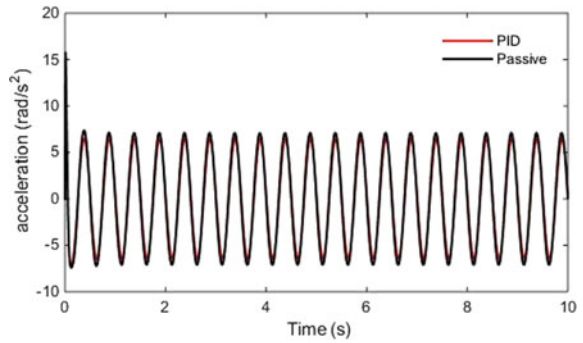
Fig. 31 PSD vertical acceleration
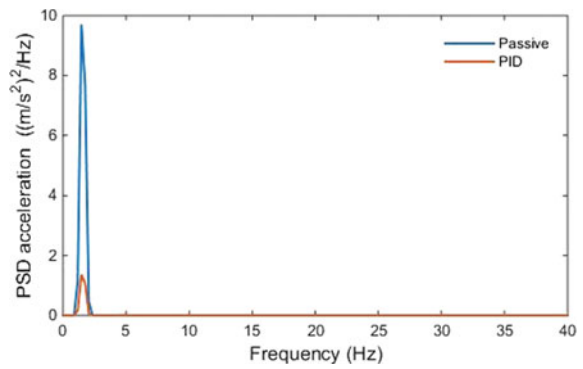
Fig. 32 PSD pitch acceleration
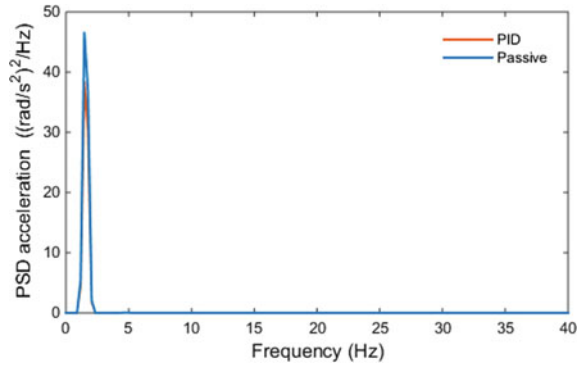
Fig. 33 PSD roll acceleration
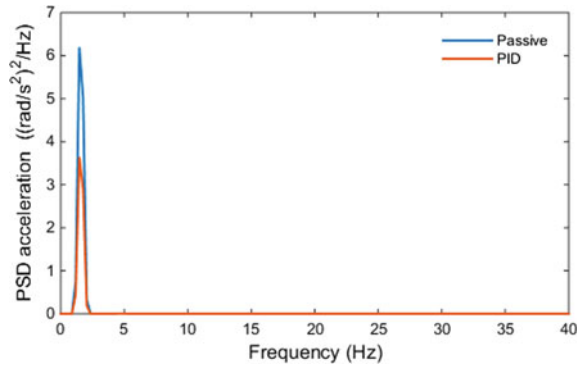
7   Conclusions

From the above analysis, it is concluded that by application of PID controller there is significant improvement in ride comfort. The three-wheeler prototype directly imported to MATLAB/Simulink from ADAMS through the method of co-simulation, and this avoided deriving complex equations and transfer functions. Co-simulation is an effective and accurate method for dynamic modeling.

References

1. M.K.Naidu, S.SrinivasaRao, T.Tejesh: Ride Analysis of Three Wheeled Vehicle UsingMAT-LAB/Simulink . AMAE Int. J. on Manufacturing and Material Science 02, No. 01, May 2012.
2. PantaSrihari Reddy, Avasarala Ramakrishna, KoonaRamji: Study of the dynamic behaviour of ahuman driver coupled with a vehicle. IMechE 2014.
3. Suresh A. Patil & Shridhar G. Joshi: Experimental analysis of 2 DOF quarter-carpassive and hydraulic active suspension systems for ride comfort. Systems Science & Control Engineering, 2014 Vol. 2, 621–631.
4. Abd El-Nasser S. Ahmed, Ahmed S. Ali, Nouby M. Ghazaly, G. T. Abd el- Jaber: Pid Controller Of Active Suspension System For A Quarter Car Model. International Journal of Advances in Engineering & Technology.
5. Amit B Panchal, dr. Jagrut J Gadit, nikunj G Mistry, nirav M Vaghela: Development of Active Suspension System for car using Fuzzy Logic controller, PID& Genetically optimize PID controller. Journal Of Information, Knowledge And Research In Electrical EngineeringISSN: 0975 – 6736| NOV 12 TO OCT 13 | VOLUME – 02.
6. WANG Rui, Sun Yi-ming, Lin Mei-tong, ZHANGHao: Research on Bus Roll Stability Control Based on LQR. 2015 International Conference on Intelligent Transportation, Big Data & Smart City.
7. M Senthil, Svijayrangan: Designe of LQR controller for active suspension system. Indian Journal of Engineering and material science, vol 13, 2006.
8. Rahul N. Sandage, Pranit M. Patil, S.A. Patil: Simulation Analysis of 2dof Quarter Car Semi-Active Suspension System to Improve Ride Comfort—A Review. International Journal of Application or Innovation in Engineering & Management, Volume 2, Issue 12, December 2013.
9. H. Chen, Z. -Y. Liu, P. -Y. Sun: Application of Constrained H_∞ Control to Active Suspension Systems on Half-Car Models Journal of Dynamic Systems, Measurement, and Control, September 2005, Vol. 127.
10. Hongyi Li, Honghai Liu, Chris Hilton and Steve Hand: Non-fragile H_∞ control for half-vehicle active suspension systems with actuator uncertainties. Journal of Vibration and Control, 2012.
11. KhodabakhshSaeedi: Influence of Rotating Tire Dynamics on vehicle System Vibrations. thesis 2012.
12. P.Kindt, P.Sas, W.Desmet: Development and validation of a three-dimensional ring-based structural tyremodel. Journal of Sound and Vibration, 2009.
13. Sakthivel Palanivelu, Narasimha RaoK. VKrishna Kumar Ramarathnam: Determination of rolling tyre modal parameters using Finite Element techniques and Operational Modal Analysis. Mechanical System sand Signal Processing, 2015.

Automation of Stone Feeding on T8 Honing Machine

S. J. Patil, A. S. Suryawanshi, O. R. Choukar and C. R. Deokate

Abstract The process of abrasive machining that produces a precision surface on a work piece by scrubbing an abrasive stone on it is called as honing. The hone is made up of abrasive grains bounded together with an adhesive. It is used for surface finishing outer surface of the inner race and the inner surface of the outer race of taper roller bearings. It is bound to wear and tear. The honing stone is then manually adjusted so that the abrasive surface comes in contact with the material to be machined. Hence, the machine has to be stopped and the operator needs to adjust the stone accordingly. The stopping, adjusting, and restarting of the machine increase the idle time of the machine. Automate process will decrease the idle time and increase the productivity.

Keywords Honing · Bearings · Wear of stone · Automation

1 Introduction

For optimizing the dimension, form and surface of pre-machined specimens, a cutting process is required. This is achieved by using multi-edge tools coated with particles having continuous surface contact between the tool and work piece. The direction between tool and work piece changes with a parallel movement. The finished surfaces are characterized by a cross-hatch pattern on the surface. The honing process includes

S. J. Patil · A. S. Suryawanshi (✉)
Mechanical Department, Dr. Daulatrao Aher College of Engineering, Karad, Maharashtra, India
e-mail: assuryawanshi.mech@dacoe.ac.in

S. J. Patil
e-mail: sjpatil.mech@dacoe.ac.in

O. R. Choukar
Plastic Omniun, Pune, India

C. R. Deokate
GEA Process Engineering Pvt. Ltd. Badodra, Badodra, India
e-mail: omkarchoukar1123@gmail.com

651

both stroke and rotation movement of an expandable honing tool having inserted honing stones or diamond sticks which gives the process a cross-hatch pattern. To achieve rapid smoothing of the surface, the period of the honing is defined by quick cutting of the peaks of the pre-machined bore surface.

2 Selection of Mechanism

After studying about various tool wear compensation techniques and building a basic understanding of the problems related to them, some mechanisms are proposed to automate the existing feeding system. From the past experience, a wear of 2 mm was considered acceptable before the surface finish of bearing race started degrading. The two major steps to be done during this automation are as follows:

1. Detection of 2 mm tool wear.
2. Mechanism for compensation of this 2 mm tool wears.

For the mechanism of compensation of tool, hydraulic system is being finalized its design aspects which are mentioned below.

2.1 Hydraulic System

For designing a hydraulic system, the very first step is to prepare a basic logical circuit. To prepare this circuit, a sequence of operations to be performed is required. Following is the practical sequence of operations to be followed to get the desired motion of tool.

- To sense the tool wear of about 2 mm, this is done by inductive sensor.
- This sensor activates the piston cylinder arrangement, and the piston moves forward such that it touches the tool. This is sensed by another inductive sensor.
- The sensor activates the clamping/declamping mechanism and finally de-clamps the tool.
- After the tool is declamped, the feeding mechanism pushes the tool by 2 mm.
- After the tool is feed by 2 mm, the tool gets clamped.

Based on this sequence, a hydraulic circuit is proposed as shown below.

2.2 Components of Hydraulic Circuit Are as Follows

(a) 1, 2, 5, 6—Tank.
(b) 3, 4—Fixed displacement pumps.
(c) 7—4/2 Direction control valve.

Fig. 1 Proposed hydraulic circuit; **a** feeding circuit; **b** clamping circuit
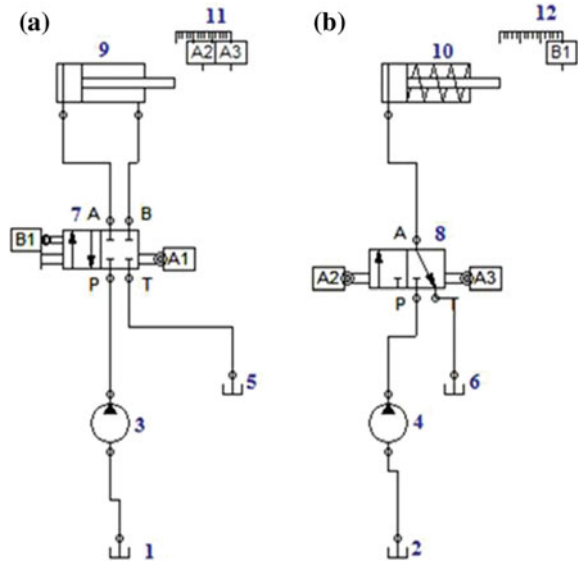
(d) 8—3/2 Direction control valve.
(e) 9—Double action cylinder.
(f) 10—Single acting cylinder (spring retraction)
(g) 11, 12—Displacement rule.
(h) A1, A2, A3, B1—Limit switches or sensors (Fig. 1).

When the honing stone tool wears about by 2 mm, the inductive sensor gets activated. This activation of sensor is linked with direction control valve [1] which allows the flow of fluid from tank to double acting cylinder [3]. Now the piston moves forward until it touches the tool. When it touches the tool, sensors A1 and A2 activate. The spool position of direction control valve [1] is changed by sensor A1, and the spool position of direction control valve [2] is changed by sensor A2. The cylinder gets locked into its current position because of change in position of direction control valve [1]. Due to the change in position of DCV [2], the single acting spring loaded cylinder moves forward and de-clamps the tool. By the time it de-clamps, sensor B1 gets ON. This sensor B1 changes the position of DCV [1], due to which the cylinder [3] moves forward from its present position. The piston of cylinder [3] now moves the tool by 2 mm. This movement of tool by 2 mm is sensed by A3 sensor. Sensor A3 then sends a signal due to which DCV [2] changes the position. Now the piston of cylinder [4] retracts due to the opposite force of spring, which means the tool has being clamped again and the honing cycle can be continued.

Table 1 Designation and its capacity

S. No.	Name of component	Model	Flow capacity
1	Suction strainer	S1	38l pm
2	DCV	D2	38l pm
3	Vane pump	P5	At 35 bar, 37.5l pm
4	Cylinder	A5	Bore = 100 mm
			Rod = 50 mm
5	Oil reservoir	T2	Capacity = 100 L

Table 2 Designation of selected ball screw actuator

DNCE	Company's product code
32	Size
200	Stroke length
BS	Ball screw
"10"	Spindle diameter

2.3 Design of Hydraulic System

The characteristics of all the components and their functioning should be considered while designing the system. Other important aspects which should be considered in design are as follows: safety of operation, performance of desired function, and efficiency of operation.

The factors along with the task have to be considered with a view to arriving at the best possible design. Following are the assumptions made while designing the hydraulic circuit: The maximum force on cylinder piston is about 9.80 kN, the maximum stroke of cylinder is about 300 mm, the maximum velocity of piston is to be about 0.0667, and the maximum working pressure is about 50 bar.

Considering the above assumptions, selection of hydraulic actuator, maximum flow rate, check for maximum pressure, selection of direct control valve, pump, and reservoir were done (Table 1).

2.4 Selection of Ball Screw Actuator

Selection of electric cylinder is based on diameter of spindle and required stroke length. Assuming the required stroke length to be approximately 200 mm. Standard dimension of the honing tool is 13.4 × 12 × 62 mm (Tables 2 and 3).

Table 3 Specifications of selected ball screw

Basic configuration feature	Value
Function	DNCE electrical cylinder
Size	32 mm
Working stroke	200 mm
Variable stroke	200 mm
Drive type	BS ball screw spindle
Secured against rotation	Q non-rotating piston rod
Spindle diameter	10 mm
Piston rod thread	M10*1.25
Motor type	Stepper
Maximum speed	0.5 m/s
Maximum drive torque	0.8 Nm
Weight	1.5 kg

Table 4 Specifications of selected stepper motor

Feature	Values
Holding torque	0.5 Nm
Maximum rotational speed	1740 rpm
Stepper angle	$1.8 \pm 5\%$
Nominal voltage	48 V DC
Nominal current	1.8 A
Weight	0.45 g

2.5 Selection of Stepper Motor

From the specifications of electric cylinder, maximum drive torque is found to be 0.8 Nm. This criterion is considered while selection of stepper motor for ball screws actuator. Based on this maximum torque limit, stepper EMMS-ST-42-S-SE-G2 is selected (Table 4).

3 Block Diagram of Honing Machine Stone Feeding Mechanism

See Fig. 2.
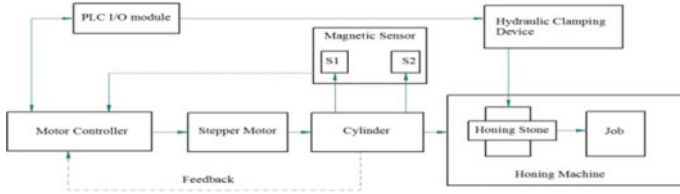
Fig. 2 Block diagram of honing machine stone feeding mechanism
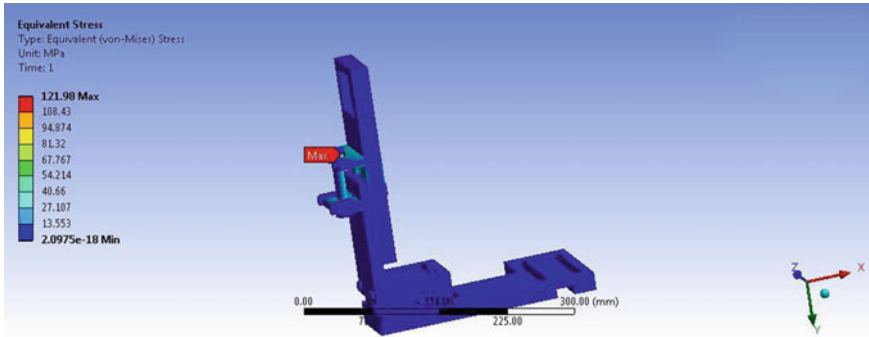
Fig. 3 Equivalent stress

4 Design of Support Structure for Actuator

4.1 Analysis of the Supporting Structure Using ANSYS

Static structural analysis of the designed supporting structure for electric actuator is done using ANSYS Workbench. Following is the results obtained after solving (Fig. 3).

Material is taken as C45, and the yield strength of mild steel is taken as 380 MPa. Considering a factor of safety of 2, we will get the allowable stress which will be $380/2 = 190$ MPa. The equivalent stress obtained was less than the allowable stress.

5 Designing a Hydraulic Clamp

5.1 Parameters to Design Hydraulic Clamping Unit

1. The stone being feed to surface of bearing is pressure controlled.
2. The honing pressure control system requires stone to apply pressure of 2 bar on surface of bearing being honed.
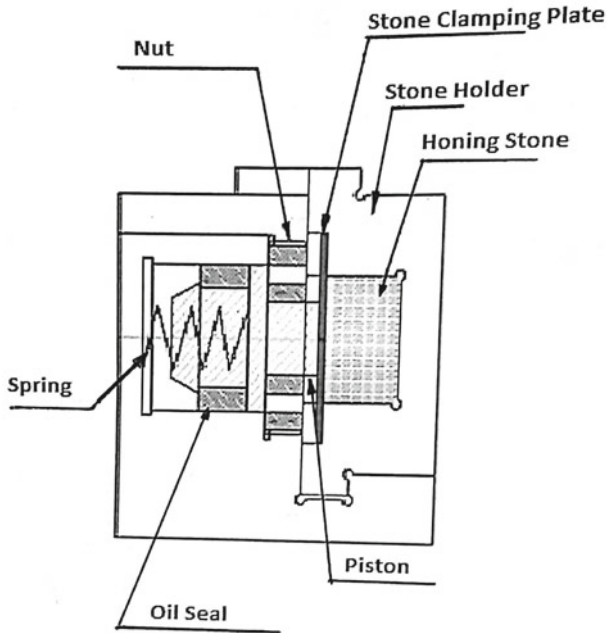
Fig. 4 Front view of hydraulic clamp

3. To maintain pressure of 2 bar at tip of honing stone, clamping unit must put more than 2 bar pressure on stone holder so that it can sustain in honing operation.
4. Hydraulic clamp must hold the stone even after the declamping the stone for moving forward.
5. This states that hydraulic system requires two different pressures at two different conditions, that is one while honing operation is being performed on race of bearing and another when stone is to be moved forward from clamp to match the honing requirement.
6. Two different pressures should be maintained by single clamp.

5.2 Proposed Design for Hydraulic Clamp

See Fig. 4.

Table 5 Record table for stepper motor validation

No.	Type	Target	Start condition	Velocity (mm/s)	Acceleration/deceleration (m/s^2)
1	PA	140 m	Ignore	100.00	1.000
2	FSL	10%	Delay	30.00	1.000
3	PRA	0.00 mm	Ignore	5.80	0.200
4	PRN	2.00 mm	Ignore	10.00	0.200
5	PA	0.00 mm	Ignore	100.00	0.200

PA Positioning to absolute position
FSL Force control–stroke limit active
PRA Positioning relative to actual position
PRN Positioning relative to nominal position

6   Experimental Validation

6.1   Stepper Motor Program Validation

Stepper motor EMMS-ST-42-S-SE-G2 was programmed using software developed by FESTO, Festo Configuration Tool. Following figure shows the record table created using FCT (Table 5).

The above program was validated step by step:

- After initialization of the program, first record was run and the cycle was stopped. The stroke length was measured using Vernier caliper.
- For the second record, the actuator moved forward until it sensed 10% back force due to the presence of tool and it came to rest.
- In the third record, current position of actuator was set as home position by the controller.
- Now the controller moves the actuator and hence the tool by 2 mm from the new home position. This was validated by marking initial position and final position on the tool and measuring it by Vernier caliper.
- The fifth record sends a signal to controller to retract the actuator to absolute home position.

7   Improvements in Production

Before the implementation of new system, the production per shift was 5000 bearing rings. Implementation of the new system has resulted in increase in production by 500 bearing rings per shift. 1 shift consists of 8 h (Table 6).

Table 6 Production and downtime per shift

Parameter	Before	After
Production per shift	5000	5500
Machine downtime per shift	45 min	25 min

8 Conclusion

Earlier the mechanism used for compensating the tool wear was manual, but after implementing the proposed mechanism, it was successfully automated. Various parameters were measured to examine the new system. There was a significant decrease in the surface roughness value. Before implementing the newly automated honing machine stone feeding mechanism, the surface roughness of the inner race of bearing ring was 0.16 µm and now it is found out to be 0.14 µm. The production has been increased by 10%. It can be concluded that the machine downtime per shift earlier was 45 min which has been decreased to 25 min. Thus, the total downtime of honing machine per shift was reduced by 45%.

References

1. C. Scheffer, H. Kratz, P. Heyns and F. Klocke: Development of tool wear-monitoring system for hard turning. International Journal of Machine Tools & Manufacture. pp. 973–985. 2003.
2. E. Aligiri, S. Yeo and P. Tan: A new tool wear compensation method based on real-time estimation of material removal volume in micro-EDM. Journal ofMaterials Processing Technology. pp. 2292–2303. 2010.
3. P. Bleys, J. Kruth, B. Lauwers, A. Zryd, R. Delprettl and C. Tricarico,: Real-time Tool Wear Compensation in Milling EDM.
4. G. Bissacco, G. Tristo, H. Hansen and J. Valentincic,: Reliability of electrode wear compensation based on material removed per discharge in micro EDM milling.CIRP Annals - Manufacturing Technology.pp. 179–182, 2013.

Performance Optimization of Bias Bar-Type Brake System Using Data Acquisition System (DAQ)

Megh Doshi, Suhrid Subramaniam, Sachin Patel and Meet Shah

Abstract The key factor involved in the proper functioning of brake system of a vehicle with dual master cylinder is brake biasing. In order to accomplish this, a bias bar with spherical bearing is used to set correct biasing of the hydraulic system which is actuated with single brake pedal. We have done the practical simulation of bias bar system in our BAJA SAE vehicle by using a self-designed DAQ system to measure the pedal effort and the corresponding brake pressure. The optimal position of the bias bar is experimentally validated based on the various positions of the spherical bearing in the pedal housing to obtain locking of all wheels using minimal pedal effort by using real-time data values.

Keywords Master cylinder · Bias bar · DAQ

1 Introduction

Inhibition of motion of vehicles to avoid collision can be done by using brakes. When brakes are actuated, weight transfer takes place from rear to front of the vehicle. Therefore, brake biasing becomes crucial. The bias bar-based brake system is used in vehicles having dual master cylinders. The bias bar along with the spherical bearing is fabricated for proportioning the brake pressure. The front and the rear brake lines are equipped with brake pressure sensors which are used to measure the front to rear

M. Doshi (✉) · S. Subramaniam
Electronics and Telecommunication Department, DJSCE, Vile Parle(W), Mumbai 400056, India
e-mail: doshimegh@yahoo.co.in

S. Subramaniam
e-mail: suhridsubramaniam@gmail.com

S. Patel · M. Shah
Mechanical Department, DJSCE, Vile Parle(W), Mumbai 400056, India
e-mail: sachinpatel1729@gmail.com

M. Shah
e-mail: shahhmeet.1998@gmail.com

line pressure ratio and calibrate the biasing using the obtained values. A load cell has been used to measure the pedal effort corresponding to the obtained pressure in the brake lines. This data has been stored on an external SD card module for analysis and comparison. Data iterations have been taken for varying positions of the bias bar.

2 Construction of Bias Bar-Based Braking System

The various parts of the bias bar system are shown in the image above. A hardened bar of grade 8.8 and standard thread size of M12 is used as the bias bar. A plain spherical bearing is fitted on the bias bar. The selection of this bearing is done after taking into consideration the nominal diameter of the bias bar and the housing/bush of the brake pedal. This bearing can be press-fit on the bias bar or it can be restricted by using external circlips on both sides. This assembly of bias bar and spherical bearing rests inside the housing of the pedal. The pushrods of the master cylinders are attached to the bias bar via clevises. When brake pedal is actuated, the applied effort is distributed to front and rear master cylinders, ratio of which is governed by the position of the spherical bearing in the housing. This spherical bearing acts a fulcrum/pivot point. As the distance between the two clevises is kept constant, rotating the bias bar leads to corresponding axial movement of the spherical bearing in the housing. For instance, if the bar is rotated and the spherical bearing moves closer to the left clevis, then the left clevis will be subjected to greater force as compared to the right clevis. Hence, by correctly positioning the spherical bearing, proper brake bias can be achieved (Fig. 1) [1, 2, 3].

2.1 Construction of DAQ System

A self-designed DAQ system has been implemented by using an Arduino UNO R3 to acquire and log the fluid pressure and pedal force data. For measurement of the pedal effort, we have used a bar-type load cell having a maximum range of up to 300 kgs which is mounted onto the pad of the brake pedal. The output of the load cell is in the order of a few millivolts, and hence, it is amplified by using an instrumentation amplifier (HX711) (Figs. 2 and 3).

The brake line pressure is measured by using a MEAS 7023 fluid pressure sensor which has a maximum range of up to 120 bar which is sufficient for our use. The pressure sensor is connected to the brake lines by using a four-way *T* connector. A self-designed *I–V* converter circuit is used for determining the brake pressure sensor output signal. We have used a microSD card module in order to store the sensor output data into an external SD card. We have also incorporated digital low-pass filters into the circuit to reduce errors due to noise. We have used the microcontroller Atmega 328 for the purpose of processing and storing the sensor data (Fig. 4) [4].
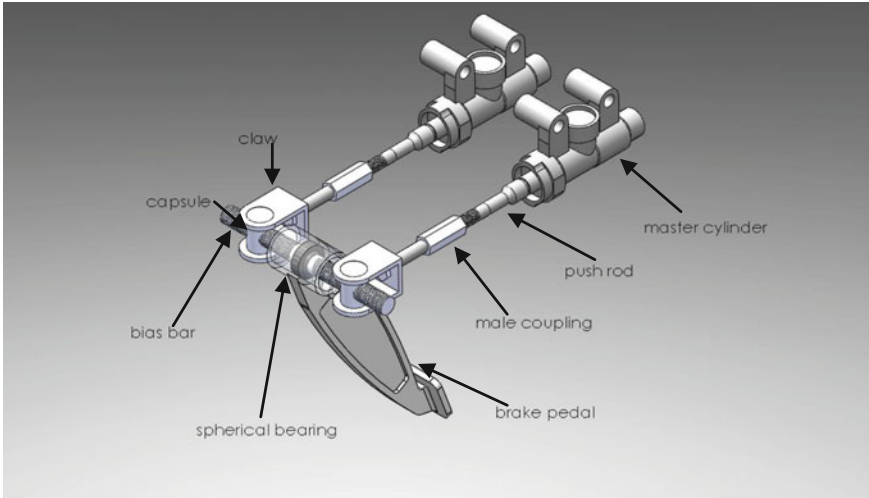
Fig. 1 Bias bar-type brake system

Fig. 2 Designed and practical mounting of load cell

Fig. 3 Brake pressure sensor mounted onto brake circuit

3 Working

Before acquiring data, bleeding of the brake system is done to purge the brake lines of any air bubbles. After bleeding, the brake pedal is pushed by applying force on the
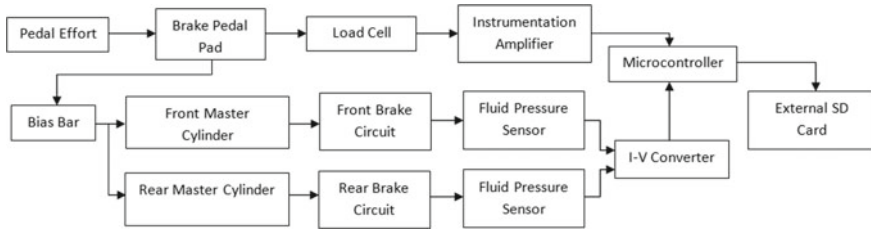
Fig. 4 Block diagram of entire system
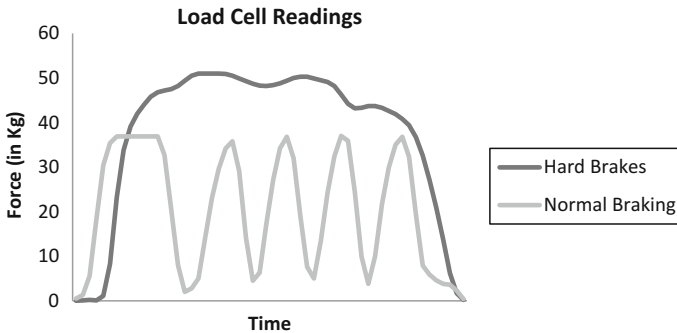
Fig. 5 Pedal effort readings

load cell. The output of the load cell is amplified by HX711, and the output of this amplifier is given to an analog input pin of Arduino which logs the data obtained in an SD card. Simultaneously, pressure in the front and rear brake lines is also measured by taking readings from the fluid pressure sensor by using the I–V converter circuit.

These readings are also in analog form and are stored in the SD card. Measuring the pressure of brake fluid in the brake circuit gives us a measure of the pressure losses in the system. These losses occur due to bends in the brake circuit, air bubbles in the system, or any possible leakages in the system. The position of the spherical bearing on the bias bar is changed, and the newly obtained readings are logged into the data logger. Many such iterations are taken to find out the exact position of the bias bar.

4 Observed Values

We first measured the pedal effort being applied to use the same values in the biasing iterations which are calculated as well as executed; the graphs showing the same are shown in Fig. 5:

Graphs showing pressure in the brake lines for different biasing iterations are shown in Figs. 6, 7 and 8:

Fig. 6 Pressure readings for 50/50 biasing
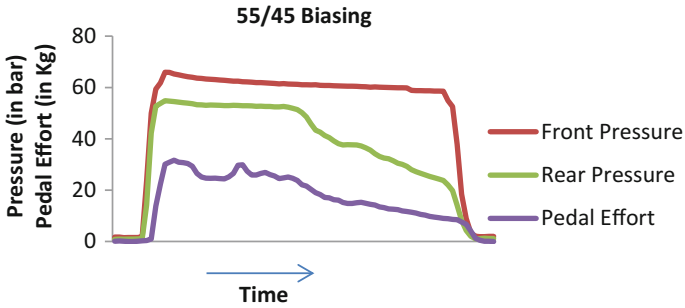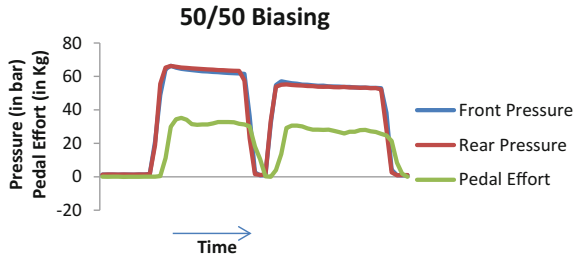
Fig. 7 Pressure readings for 55/45 biasing
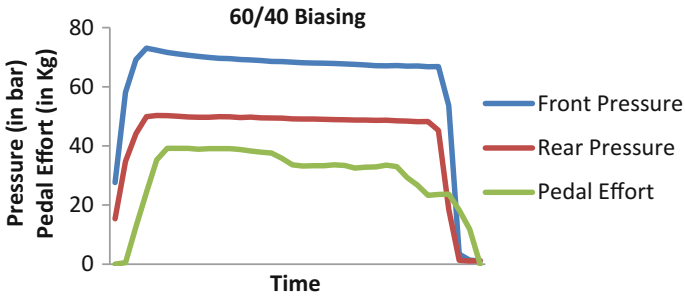
Fig. 8 Pressure readings for 60/40 biasing

For 50:50 biasing position of the bias bar (Fig. 6):
For 55:45 biasing position of the bias bar (Fig. 7):
For 60:40 biasing position of the bias bar (Fig. 8):

5 Comparison Between Theoretical and Practical Values

F_{Rmc} = force on right master cylinder
F_{Lmc} = force on left master cylinder

Table 1 Comparison

Position of spherical bearing	Front pressure (practical)	Rear pressure (practical)	Front pressure (theoretical)	Rear pressure (theoretical)	Biasing
Center	60.9	60.9	62.92	62.92	50:50
6.5 mm to the left	66.81	54.93	69.21	56.288	55:45
13 mm to the left	73.45	48.87	75.755	50.044	60:40

Fig. 9 Important lengths for biasing calculations
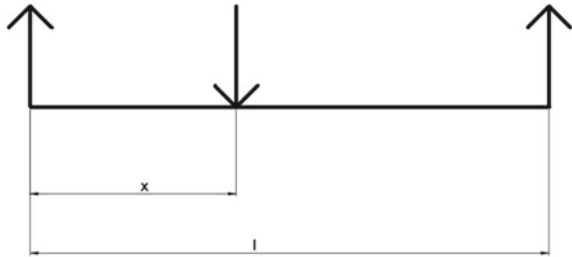
l = effective length of bias bar
x = distance of spherical bearing from left
F = pedal effort
r = pedal ratio

$$F_{\text{Lmc}} = \frac{F \times r \times x}{l} \qquad (1)$$

$$F_{\text{Rmc}} = \frac{F \times r \times (l - x)}{l} \qquad (2)$$

As shown from the free body diagram and force calculations, it can be seen that altering the position of the bearing allows us to obtain various brake bias ratio as required. Table 1 shows the value of pressure obtained and the corresponding position of the spherical bearing with reference taken from the center of the housing for accuracy and ease of measurement (Figs. 9 and 10).

On comparing the observed and calculated values we find that the error percentage for the theoretical and practical values is minimal and is as tabulated in Table 1.

6   Conclusion

We obtained the position of the bias bar corresponding to the required biasing as tested out on our BAJA SAE vehicle; the same method can be used to find out the biasing iterations for any vehicle. We also obtained the pressure losses in the brake

Fig. 10 Top view of pedal system showing lengths
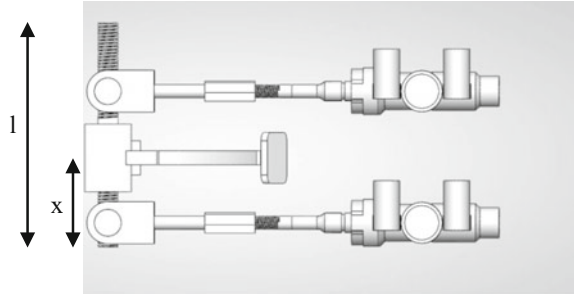
lines and this bias bar positioning is obtained by taking the same into consideration. The pedal effort used for calculations is the measured pedal effort value which we obtained with the help of the load cell; thus, we have also optimized the system taking into account the pedal effort which is being applied practically. Thus, we have found the perfect position of the bias bar to obtain locking of wheels with minimum pedal effort by adjusting the biasing which we got at 60:40 biasing for a front–rear split for our vehicle. Similarly, this technique can be used to optimize as well as validate the braking system of any vehicle with a bias bar-type braking system.

References

1. Puhn, Fred: *Brake Handbook*. HP Books (1985)
2. Ansel, Billavista: "The Largest off Roading Website in the World." *Pirate4x4Com 4x4 And OffRoad Forum RSS*, www.pirate4x4.com/
3. Gillespie, Thomas D.: Fundamentals of Vehicle Dynamics. Society of Automotive Engineers (1994)
4. Suarez, Conor: *Data Acquisition Handbook*. Clanrye Intl (2015)

Simulation for Variable Transmission Using Mono Level Genetic Algorithm

Ritwik Dhar and Niti Doshi

Abstract The simulation is formulated using Genetic Algorithm (GA) for Continuously Variable Transmission (CVT) tuning. The algorithm makes use of the force balance equations to construct the fundamental model for CVT in MATLAB which uses the GA to optimize the parameters for the required output from CVT. The parameters involved for better optimization are the flyweight mass, primary and secondary spring stiffness and primary and secondary cam profiles. The output obtained from the simulation software is then compared to the experimental testing results for validation. The simulation results provide minimal error rate with respect to the engagement and shifting speeds and the results also occur in the constant RPM most of the times.

1 Introduction

Optimization algorithms such as genetic algorithms are popular these days for computational analysis by either maximizing or minimizing fitness functions. The fundamental methodology of genetic algorithm relies on natural biological events such as reproduction, evolution, selection and mutation. This methodology helps in creating an algorithm that is much more powerful and efficient than random permutation and combinational searching algorithms. The genetic algorithm consists of basic components such as a variety of chromosomes which will produce the next generation of chromosomes using crossover, random mutation in a generation using chromosomes

R. Dhar (✉) · N. Doshi
Department of Electronics and Telecommunication,
Dwarkadas J. Sanghvi College of Engineering, Vile Parle (West), Mumbai 400056, India
e-mail: ritwik1798@gmail.com

N. Doshi
e-mail: niti.doshi@live.com

and most importantly, a fitness function which is to be optimized according to the problem.

Continuously Variable Transmissions (CVT) are being used more extensively in commercial automobiles due to their fuel efficiency and uncomplicated mechanism.

The vehicle used to test the simulation results is an All-Terrain Vehicle (ATV) designed and built by the college ATV team which competes in the annually held BAJA SAEINDIA competition which tests the overall performance with equal importance given to every aspect of the vehicle in rough terrain conditions. The components on which the performance of the CVT depends is the flyweight mass, the stiffness of the primary and secondary springs and the cam profiles. Tuning of the variable transmission system is basically changing the tunable components in such a combination so that we get a constant RPM for a range of gear ratio.

2 CVT

2.1 Force Balance Methodology

There are basically two types of approaches towards obtaining the fitness function for the genetic algorithm. Both force balance or energy balance equation methodology can be followed (Fig. 1).

We have used the force balance equation to design the fitness function for tuning.

The clamping force required to use the V-belt slip free is given by the Euler-Grashof theory of V belt. Taking this into consideration, the functional $Z(th, Tv)$ is applied alongside the contacts on the expression depicting the clamping force [1, 2]. The function $Z(th, Tv)$ can be used to calculate both primary and secondary sheaves (Za and Zb).
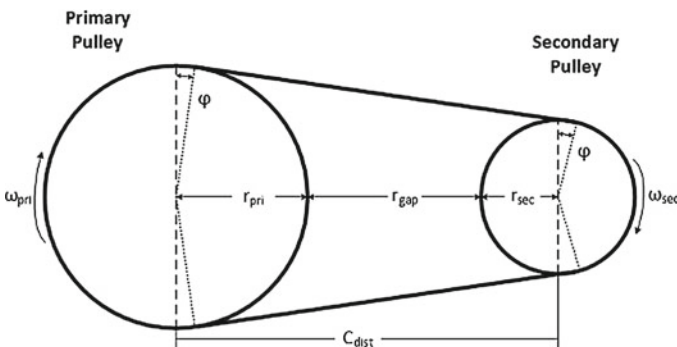
Fig. 1 Geometric parameters for primary and secondary sheaves

The clamping force exerted by the cam on the secondary pulley is given. Here, the torsional stiffness of the spring is denoted by kb and the twist angle is denoted by delb of the secondary spring.

The torque in the primary and secondary sheaves is given by C_a and C_b, respectively. T_1 and T_2 are the tensions on the tight and slack sides of the pulley V-belt, respectively.

The stiffness of primary and secondary springs is given by k_1 and k_2, respectively.

After rearranging the equations to remove belt tension the following relation is obtained for primary sheave speed. The equation obtained below gives us the RPM of the engine in terms of the tuning parameters i.e. weight mass, primary & secondary spring stiffness and cam profiles.

$$Za \approx th_a \tag{1}$$

$$Zb(th_b, Tv) = th_b + \frac{k1 - k2}{p - k2} \times \frac{1}{2\left[\frac{\sinh(\Omega th_b)}{\Omega} - th_b\right]} \tag{2}$$

$$k_1 = k \times \frac{\tan(\alpha + \phi)}{\tan(\alpha)} \tag{3}$$

$$k_2 = k \times \frac{\tan(\alpha - \phi)}{\tan(\alpha)} \tag{4}$$

$$k = 0.8 \times \left(\frac{Rb}{Rb1{:}1}\right)^2 \quad Rb1{:}1 \text{ is } Rb \text{ at } Tv = 1 \tag{5}$$

$$p = \left((1.5 - f \tan\alpha)^2 + 2k\left(1 + \frac{f}{\tan\alpha}\right) - (1.5 - f \tan\alpha)\right) \tag{6}$$

$$\Omega = \frac{\sqrt{(k1 - p) \times (p - k2)} \times \cos(\alpha + \phi) \times \cos(\alpha - \phi)}{p \times \cos\phi} \tag{7}$$

$$C_a = (T1 - T2) \times Ra \tag{8}$$

$$C_b = (T1 - T2) \times Rb \tag{9}$$

$$\omega = \sqrt{\frac{\left\{\frac{[(kb \times \text{delb} \times \tan(\delta)) \times 2 \times \tan_\alpha \times \frac{Za}{Zb} + C_a \times \frac{Za}{Ra}]}{2 \times \tan\alpha} + ka \times xa\right\}}{m \times r \times \tan(\theta)}} \tag{10}$$

3   Procedure

3.1   Shift Starting Range Calculations

The first stage's condition for GA is to obtain shift starting range of 3400 RPM (calculated). The above equation is used as the base for the fitness function and the threshold is set to 3400 RPM.

Table 1 Population range for shift starting range of genetic algorithm

Parameters	Lower limit	Upper limit
Flyweight mass (kg)	0.15	0.22
Primary spring stiffness (N/m)	24,000	28,000
Secondary spring stiffness (N/m)	15,000	19,000

To reduce the error percentage and get more accurate results, the initial population range is set to a certain range of parameters obtained by research on spare parts as shown in Table 1. After successfully obtaining iterations, the number of generations was set to 150 for faster processing and precision. There were no important changes in the output after 150 generations. The population size was adjusted to 50 by the same logic.

3.2   *Constant RPM Calculations*

The second stage condition for GA is to obtain constant RPM during a change in the ratio from low to high. The parameters involved are the cam profiles and the spring stiffness. The fitness function to be obtained is obtained by differentiating the equation with respect to the speed ratio to obtain $d\omega/dTv$ [3, 4]. The limit for the fitness function is kept 0 as we need the differentiated equation equal to 0 for constant RPM alignment.

We are differentiating with every speed ratio (as there will be only one population range of rate of change to be used). By this method, the GA will run through the values and better rates of change are obtained for the parameters in every ratio, simultaneously setting the base for the next set of iterations. The population size is set to 50 and generations used are 150.

4   Results

4.1   *Primary Cam*

The primary cam has the basic function of transferring the force into the dynamic pulleys which are formed by the rotational effect of the weights. This force has to first balance the tension of primary spring and once in the engagement range, it has to balance out the axial thrust from the secondary pulley [5, 1].

From the simulation, it can be said that with the shifting of primary pulley there is a decrease in the transfer of force while moving towards higher speed ratio. Due to

Fig. 2 Primary spring stiffness
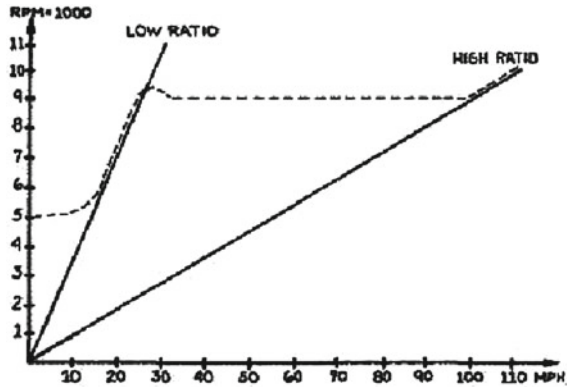
this, same value of torque is given at a high ratio, which results in a lesser requirement of axial thrust.

The profile of the cam for the engagement phase is produced at a constant angle as it is enough to provide sufficient clamping force for an increase in the engine RPM.

4.2 Secondary Cam

From the simulation, it can be said that as the cam rotates, there is a decrease in the angle of side force transfer due to which during longer twists, we get less side force.

4.3 Primary Spring

The stiffness of the primary spring is obtained with the displacement of pulleys as shown in Fig. 2. The force from the flyweights is balanced by the gradual increase in the spring constant. The higher spring constant also provides with better shifting characteristics as it will increase the back force to the pulleys, which will increase the back-shifting rate of the CVT[1, 6].

4.4 Secondary Spring

The spring constant using the genetic algorithm is obtained as 22,800 N-mm.

5   Validation

The results obtained from the simulation using genetic algorithm are then verified by practically using a setup for measurement of the error range and accuracy of the simulation system.

A simple setup using an IR sensor and an Arduino UNO was mounted on the CVT casing which would act as a tachometer for measuring the engagement and shifting phases of the CVT. The practical results for the upshift and downshift have been shown in the table given below (Figs. 3 and 4).

As it can be seen from Table 2, the values from the simulation were very useful in the shift range as RPM would go up to 3423.4 in running conditions during the upshift as the simulation computed a value of 3440 RPM. During the downshift RPM, the value obtained from the simulation is 3440 RPM while in running conditions the RPM was calculated to be 3511.2 RPM.

The engagement phase gave values from the simulation as 1880 RPM during upshift which on running conditions was found out to be 1988.48 RPM. During
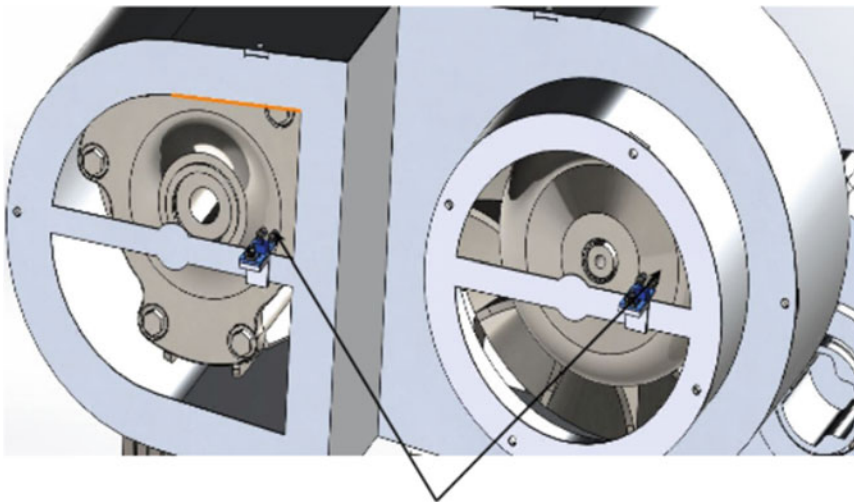
Fig. 3   CAD Model of the IR sensor tachometer on CVT

Table 2   GA simulation results v/s practical experimental results

	Ideal RPM Value	Upshift RPM value(Practical)	Upshift RPM value (Simulation)	Downshift RPM value (Practical)	Downshift RPM value (Simulation)
Engagement range of CVT	2000	1988.48	1880	1976.76	1900
Shift out range of CVT	3400	3423.4	3440	3511.2	3440
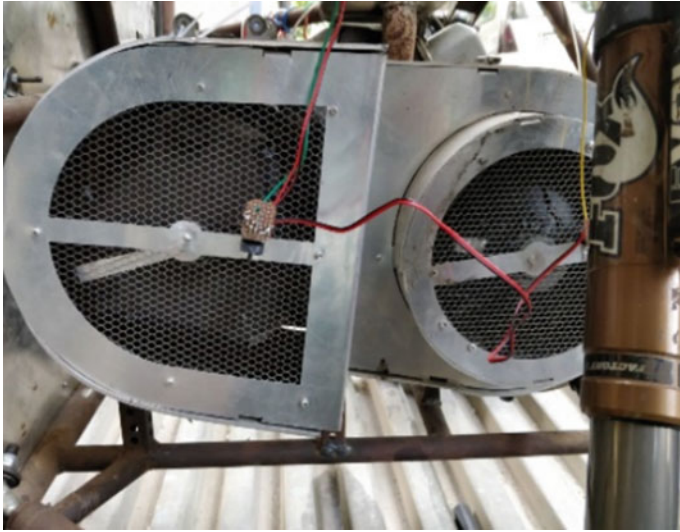
Fig. 4 IR sensor mounting on the CVT casing of Polaris P90

downshift, the value from the simulation was calculated to be 1900 RPM, while in running conditions it was found out to be 1976.76 RPM.

6 Conclusion

The simulation approach towards tuning CVT was implemented using the Genetic Algorithm which was studied in this paper. The simulation values were verified with the vehicle in actual running conditions using a tachometer setup. The simulation showed positive results with the actual values; it can thus be preferred over the traditional trial and error method which is a lot more time-consuming, with a higher probability of not providing estimated results.

The simulation still showed considerable error during downshifting in the shifting range which exhibits further changes in the approach to be made to get a better and more accurate value.

There are also certain aspects which have not yet been included, such as, the deformation of belt and pulleys; they would further add to the accuracy of the values in the future studies.

Appendix

MATLAB code for the simulation

```
% input_func.m
format long
stepin = 1e-5;
rpmint= 2300;
Stop_time  =  1.0;
Cen_dist = 0.5;
prim = 18*pi/180;
mu_a_dr = 0.25;
Dr_torque = 0.01651;
Dn_torque = 0.03265;

% Friction between the element and pulley
% Function 1 paramters
 a = 0.0003;
 b = 0.05;

% Function 2 paramters
mu_b_dr = 0.25;
 a = 7;
 b = 150;
sk_friction= 1.85;

% function 3 parameters
mu_b_sat = 0.25;
 a = 7;
 b = 150;
sk_friction = 1.3;
a_dr = 15;
b_dr = 150;
ff_dr = 1.15;
mu_a_dr = 0.25;

mass = 1.5;
lin_den= 1.65;
rho=(lin_den+mass)/(lin_den*mass);
sheave_int = 0.005;
dn_sheave = 0.005;
const1=(1+(cos(half_sheave))^2)/(sin(half_sheave)*cos(hal
f_sheave));

% Driver pulley loadingconditions
pulleyint = rpmint*rpm2rads;
thetaint = 0.88*pulleyint;
gamint = 0.88*pulleyint;
thetaint=  0.0005;
gamint = 0.00005;
ra = -0.002;
r1 =  -0.002;
rint = 3*in2 m;
r1int= 3.05*in2 m;
Normal = 1000;
```

```
Finput = 1000;
Torqueinput = 200;

% Driven pulley initial conditions
rint2 = 0.001;
r1int2= 0.001;
r2int2 = 4.5*in2 m;
r1_2_int = 4.55*in2 m;
pulley2 = pulley1*r1int/r2int;
theta_dot2int = 0.99*pulley2;
gam_dot2int= 0.88*pulley2;
theta2int = 0.0003;
gam2_int = 0.00025;
Normal2 = 2650;
Force2 = 2350;
TorqueLoad= 250;    % in Nm

% function 3
% Driver initial inlet
Tint = 2819;
Qint = 1321;
% Driven initial condition
Q2int = 149;
T2int = 779;
```

References

1. Aaen, O. (2007). Clutch tuning handbook. Racine, WI: AAEN Performance
2. Seigars, C. M. (1996). Modeling of a continuously variable transmission and clutching of a snowmobile. Honors College, 243
3. Development of simulation approach for CVT tuning using dual level genetic algorithm, Deepinder Jot Singh Aulakh, Cogent Engineering (2017), 4: 1398299
4. Modeling And Simulation Of Friction-Limited Continuously Variable Transmissions, Nilabh Srivastava
5. Willis, C. R. (2006). A kinematic analysis and design of a continuously variable transmission. Blacksburg, VA: Virginia Polytechnic Institute and State University
6. Timothy, R. (2013). The continuously variable transmission: A simulated tuning approach. Worcester Polytechnic Institute. Project Number: Mqp-Dcpfsae-E12-D13
7. Acceleration Simulation of a Vehicle with a Continuously Variable Power Split Transmission, Zhijian Lu

Fuzzy Analytic Hierarchy Process (FAHP) for Green Supplier Selection in Indian Industries

Samadhan Deshmukh and Vivek Sunnapwar

Abstract The supplier selection has a significant impact on the manufacturing industries. Selecting the best green supplier among many alternatives is a multi-criteria decision-making (MCDM) problem. This research aims to survey current green activities in supplier selection in India and to evaluate best green supplier. Various environment factors affecting in the manufacturing sectors are considered in this study. Fuzzy analytic hierarchy process (FAHP) based on Chang's extent analysis, is utilized in order to select best green supplier. The data from pairwise evaluation of all criterions are given in triangular fuzzy numbers. The uncertainties of decision problem can be dealt with, and a more effective decision can be reached. A case study is conducted to illustrate the utilization of the model for the green supplier selection problem.

Keywords Green supplier selection · Multi-criteria decision-making (MCDM)
Fuzzy analytic hierarchy process (FAHP)

1 Introduction

For sustainable supply chain partners, supplier selection using green manufacturing approach is one of the important tasks. The supplier should improve the performance of the supply chain keeping in mind environmental aspects along with social and economic aspects [1]. Green supply chain management (GSCM) is fast changing and growing concept in emerging countries. To address the influence and relation-

S. Deshmukh (✉)
Department of Mechanical Engineering,
Mukesh Patel School of Technology Management and Engineering, NMIMS,
Vile Parle, Mumbai, India
e-mail: Samadhan.Deshmukh@nmims.edu

V. Sunnapwar
Department of Mechanical Engineering, Lokmanya Tilak College of Engineering,
Navi Mumbai, India
e-mail: vivek.sunnapwar@gmail.com

ship between supply chain management and the natural environment, the 'green' dimension is added to supply chain management (SCM). The current awareness in the environmental aspects has made supplier to think and give more emphasis on the environment-friendly criteria [2]. Design for the environment, life-cycle analysis, and total quality environmental management are considered as popular environmentally conscious practices [3]. The fuzzy analytic hierarchy process (FAHP) approach is adopted in this study to develop a supplier selection model. Introduction to fuzzy sets and fuzzy numbers are given initially. In all, seven factors are considered, namely green manufacturing, green design, environment performance assessment, green logistic design, quality, customer co-operation, and green costs with 47 sub-factors.

2 Literature Review on Green Supplier Selection Criteria and Supplier Selection Models

In recent years, various researchers have identified approach toward green supply chain management (GSCM) practice. While the works on the evaluation and/or selection of suppliers are quite a few, those that concern environmental issues are limited. Baskaran et al. [4] assessed various vendors from Indian textile and clothing industry using different green manufacturing measures. For the purpose of metering the performance of the manufacturing sector, Bhateja et al. [5] studied different activities of the supply chain processes of the various Indian manufacturing industries. Deif [6] offered system model for the novel sustainability pattern with an architecture for the designing, planning, and controlling of various green manufacturing undertakings. Kumar et al. [7] explored different practices related to green supply chain management to be adopted by various industries of electrical and electronics products. The environmental performance and green supply chain management practices were studied, and findings were examined using mean score method. Relationships between green supply chain management (GSCM) practices and GSCM driver in Taiwan's textile and apparel manufacturers were investigated thoroughly [8]. The components and elements of green supply chain management were discussed to determine how those components served as a basis for the decision framework [9]. An integrated and fresh look into the area of GSCM was given comprehensively with the state-of-the-art literature review in the study. The literature on GSCM was covered from its conceptualization, primarily taking a reverse logistics angle [10]. Deshmukh and Sunnapwar [11] used factor analysis approach to discuss various environmental performance measures used in different manufacturing organizations. For green supplier selection, different performance measures were validated by mean method [12].

Based on the results of an investigation of 151 respondents, Punniyamoorthy et al. [13] established a new model using structural equation modeling and fuzzy analytic hierarchy process technique. Ataei et al. [14] utilized FAHP for determining the weights of the criteria. The ranking of the sawability of carbonate rocks

was also carried out. Chang [15] presented a methodology for management of fuzzy AHP. Ozdagoglu et al. [16] used analytic hierarchy process (AHP) and fuzzy AHP method. Comparison was made with a case study including the decision-making about employee selection for shop floor of manufacturing platform applied in food industry. To help the industrial specialists in the performance evaluation in a fuzzy environment, Sun [17] developed a model based on the fuzzy analytic hierarchy process (FAHP) and the technique for order performance by similarity to ideal solution (fuzzy TOPSIS). Fuzzy AHP was used by Kahraman et al. [18] for selecting best supplier firm for a white good manufacturer established in Turkey. Deshmukh and Sunnapwar [19] conducted study on use of AHP for green supplier selection in Indian industries.

3 Fuzzy Analytic Hierarchy Process, Fuzzy Sets, Fuzzy Numbers, Algorithm for Fuzzy AHP

To solve multiple-criteria decision-making problems, the analytic hierarchy process (AHP) has been widely used. Because of uncertainty and fuzziness in the individual's judgment, a pairwise comparison with an AHP may not be possible to accurately find the decision-makers' decision. The human preference model is uncertain in many real-world circumstances, and decision-makers might be hesitant to give precise numerical values to the comparison judgments. As human decisions are given with crisp numbers in AHP, there is a necessity to introduce fuzzy logic with pairwise comparison. The fuzzy AHP is based on the fuzzy interval arithmetic with triangular fuzzy numbers and the confidence index with an interval mean approach to determine the weights of evaluative elements. An approach based on fuzzy AHP can benefit to reach an operative decision. By using this method, the uncertainty and fuzziness in the decision process can be dealt with. Fuzzy set theory was introduced by Zadeh in 1965 to solve problems involving the absence of sharply defined criteria [15]. Fuzzy set theory looks a lot like human thinking in its use of estimated information and indecision to generate conclusions. It is designed to mathematically represent uncertainty and fuzziness that is intrinsic to many problems. Fuzzy set theory includes fuzzy logic, fuzzy arithmetic, fuzzy mathematical programming, fuzzy topology, fuzzy graph theory, and fuzzy data analysis; however, the term fuzzy logic is often used to define all of these [18]. Triangular fuzzy numbers are defined by three real numbers, given as (l, m, u). The parameters l, m, and u show the lowest possible value, the middle promising value, and the upper possible value that indicates a fuzzy event. A triangular fuzzy number (TFN), M, is shown in Fig. 1.

The extent FAHP is used in this study, which was introduced by Chang [15]. $X = \{x_1, x_2, x_3, \ldots, x_n\}$ to be considered as an object set, and $G = \{g_1, g_2, g_3, \ldots, g_n\}$ to be a goal set. Every object is considered, and extent analysis is done for each goal as per the method of Chang's extent analysis. M extent analysis values for each object can be obtained, with the signs given as follows:

Fig. 1 A triangular fuzzy
number, M
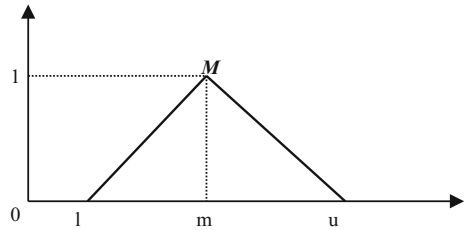
Fig. 2 Intersection between
M_1 and M_2
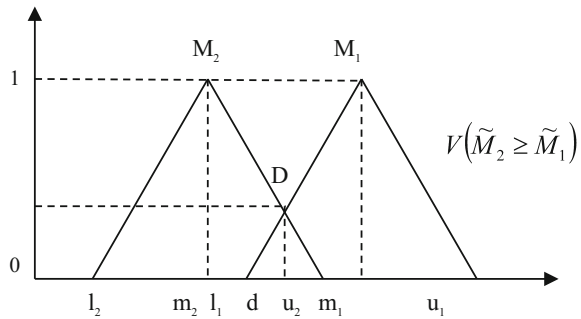
where

$$M_{gi}^1, M_{gi}^2, M_{gi}^j, \quad i = 1, 2 \ldots n,$$

$M_{gi}^j (j = 1, 2, \ldots, m)$ all are triangular fuzzy numbers (TFNs).

Figure 2 illustrates intersection between M_1 and M_2 where D is the ordinate of the maximum juncture point d between μ_{M_1} and μ_{M_2} to associate M_1 and M_2; we need both the values of $V(M_1 \geq M_2)$ and $V(M_2 \geq M_1)$.

4 An Application in Organization (Case Study)

This study focuses on the procurement of various components from three local suppliers Supplier 1, Supplier 2, and Supplier 3, which have been preselected in the approved suppliers' list of one of the leading manufacturing organizations from India. The goal was to find the best supplier taking into account the green manufacturing approach. Figure 3 provides structure for selecting best green supplier. Seven main criteria are selected for assessment are green manufacturing (GM), green design (GD), customer co-operation (CC), green costs (GC), quality (QTY), environment performance assessment (EPA), and green logistics design (GLD). A sample of the questionnaire form is shown in Table 1.

A comparison is made in sub-attributes and main attributes by decision-maker after creating hierarchy. After the information is taken, the pairwise evaluations are
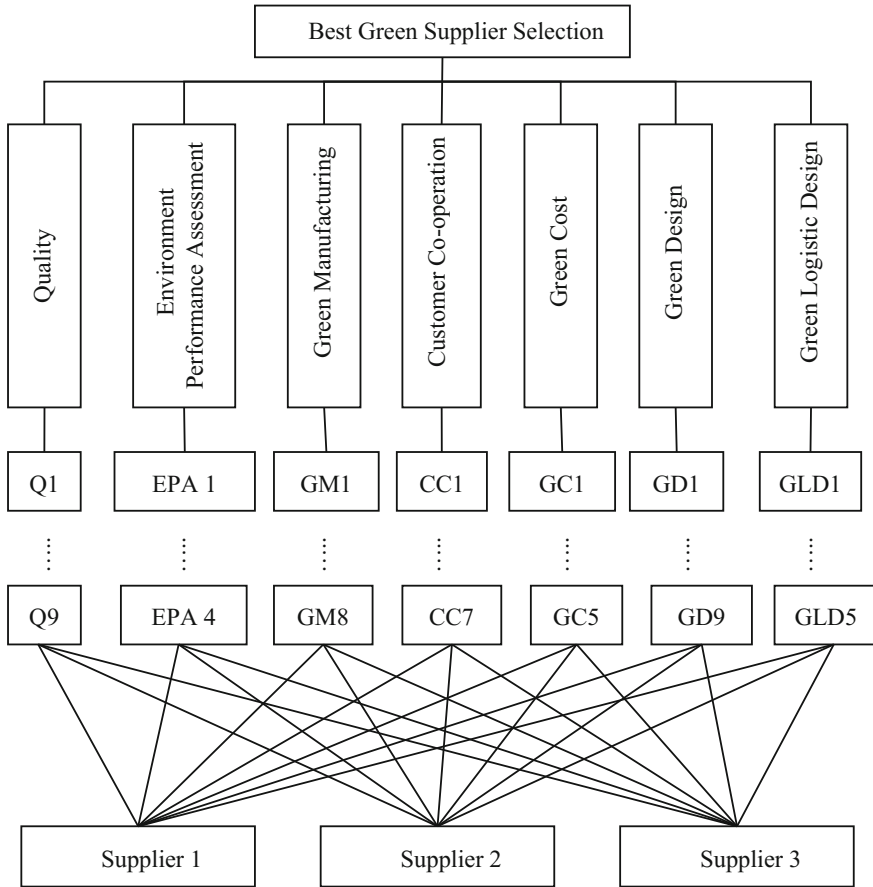
Fig. 3 Structure for the selection of the best green supplier

carried out. It is necessary to represent all pairwise comparison judgements into fuzzy triangular numbers. Table 2 represents relation between fuzzy comparison judgments and the main goal. Calculation is carried out according to fuzzy extent analysis. After the normalization of the values, priority weights with respect to main goal are calculated as—0.3010, 0.2488, 0.0903, 0.0984, 0.0313, 0.1350, 0.0951. It was found that the significant element in the green supplier selection procedure is quality as it is having maximum priority weight value (0.3010).

The same calculations were applied to the other pairwise comparison matrices and the priority weights of each main attribute, sub-attribute, and alternative were calculated. Mentioned priority weights have indicated for each criterion in Table 3. The priority weights of the alternatives with respect to sub-attributes are calculated. The combination of priority weights of main attributes and sub-attributes was done to find priority weights of the different vendors.

Table 1 A sample of the questionnaire form

With respect to GOAL	Importance (or preference) of one of the criteria over another						
	QTY	EPA	GM	CC	GC	GD	GLD
QTY	1	3	2	7	8	4	8
EPA	1/3	1	4	2	7	3	7
GM	½	1/4	1	1	1	1/3	1
CC	1/7	1/2	1	1	3	1	3
GC	1/8	1/7	1	1/3	1	1/5	2
GD	¼	1/3	3	1	5	1	2
GLD	1/8	1/7	1	1/3	1/2	1/2	1

Table 2 Fuzzy evaluation matrix with respect to goal

Goal	QLTY	EPA	GM	CC	GC	GD	GLD
QLTY	(1, 1, 1)	(1, 3, 5)	(1, 2, 4)	(5, 7, 9)	(6, 8, 10)	(2, 4, 6)	(6, 8, 10)
EPA	(1/5, 1/3, 1/1)	(1, 1, 1)	(2, 4, 6)	(1, 2, 4)	(5, 7, 9)	(1, 3, 5)	(5, 7, 9)
GM	(1/4, 1/2, 1/1)	(1/6, 1/4, 1/2)	(1, 1, 1)	(1, 1, 3)	(1, 1, 3)	(1/5, 1/3, 1/1)	(1, 1, 3)
CC	(1/9, 1/7, 1/5)	(1/4, 1/2, 1/1)	(1/3, 1/1, 1/1)	(1, 1, 1)	(1, 3, 5)	(1, 1, 3)	(1, 3, 5)
GC	(1/10, 1/8, 1/6)	(1/9, 1/7, 1/5)	(1/3, 1/1, 1/1)	(1/5, 1/3, 1/1)	(1, 1, 1)	(1/7, 1/5, 1/3)	(1, 2, 4)
GD	(1/6, 1/4, 1/2)	(1/5, 1/3, 1/1)	(1, 3, 5)	(1/3, 1/1, 1/1)	(3, 5, 7)	(1, 1, 1)	(1, 2, 4)
GLD	(1/10, 1/8, 1/6)	(1/9, 1/7, 1/5)	(1/3, 1/1, 1/1)	(1/5, 1/3, 1/1)	(1/4, 1/2, 1/1)	(1/4, 1/2, 1/1)	(1, 1, 1)

Table 3 Priority weights for main criteria

Criteria	Local weights	Global weights
Quality	1.0000	0.3010
Environment performance assessment	0.8266	0.2488
Green manufacturing	0.3000	0.0903
Customer co-operation	0.3269	0.0984
Green cost	0.1041	0.0313
Green design	0.4486	0.1350
Green logistic design	0.3158	0.0951

Table 4 Performance of suppliers with respect to each main criterion

Criteria	Supplier 1	Supplier 2	Supplier 3
Quality (QTY)	0.4626	0.3392	0.1983
Envt. performance assessment (EPA)	0.5585	0.2469	0.1946
Green manufacturing (GM)	0.5066	0.2879	0.2055
Customer co-operation (CC)	0.4869	0.3427	0.1704
Green costs (GC)	0.6209	0.2544	0.1247
Green design (GD)	0.4491	0.2976	0.2533
Green logistics design (GLD)	0.3886	0.3582	0.2532
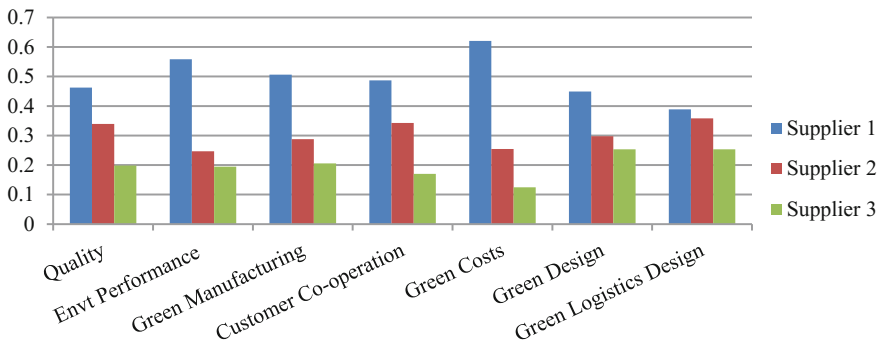
Fig. 4 Performance of suppliers w.r.t. main criterion

Main attributes and sub-attributes weights were used to select best alternative based on the questionnaire forms used. In order to reduce the complex calculations and to calculate the priority weights, macros in Excel were used. The performance of suppliers with respect to each main criterion is shown in Table 4, and corresponding values are shown diagrammatically in Fig. 4. Finally, the weights were calculated keeping into account different alternatives and the main attributes.

The priority weights for the alternatives are found to be 0.4834, 0.3377, and 0.1789.

5 Conclusion

Green supplier selection process plays an important role in today's complex environment. This work provides a scientific approach to the green supplier selection process. It first identifies those green supplier selection criteria which are consid-

ered to be important in Indian manufacturing sector. The extent fuzzy AHP is used in this study for selecting best green supplier. Fuzzy AHP approach appears more effective in decreasing the uncertainty in calculation of relative weights assigned to various criteria. For selecting the most appropriate supplier alternative, preferred degree related to each of the criteria was assessed. The uncertainties involved in the data acquired were efficiently represented and processed by using the extent fuzzy approach to make appropriate decision. Supplier 1, having highest priority weight, is determined as the best green supplier as a result of this study.

References

1. Kannan G., Sarkis J., Sivakumar R., Palaniappan M., Multi criteria decision making approaches for green supplier evaluation and selection: A literature review. Conference on the Greening of Industry Network, GIN 2012 (Linkoping—Sweden, 2012).
2. Lee A. H. I., Kang H. Y., Hsu C. F., Hung H. C., A green supplier selection model for high-tech industry. Expert Systems with Applications (2009) 36: 7917–7927.
3. Nimawat D. and Namdev V., An overview of green supply chain management in India. Research Journal of Recent Sciences (2012) 16:77–82.
4. Baskaran V., Nachiappan S., Rahman S., Indian textile suppliers' sustainability evaluation using the grey approach. Int. J. Production Economics (2012) 135: 647–658.
5. Bhateja A. K., Babbar R., Singh S., Sachdeva A., Study of Green Supply Chain Management in the Indian Manufacturing Industries: A Literature Review cum an Analytical Approach for the measurement of performance. International Journal of Computational Engineering & Management (2011) 13: 84–99.
6. Deif A. M., A system model for green manufacturing. Journal of Cleaner Production (2011), 19: 1553–1559.
7. Kumar S., Chattopadhyaya S., Sharma V., Green Supply Chain Management: A case study from Indian electrical and electronics industry. International Journal of Soft Computing and Engineering (2012) 1: 275–281.
8. Awasthi A., Chauhan S.S., Goyal S., A fuzzy multicriteria approach for evaluating environmental performance of suppliers. Int. J. Production Economics (2010) 126: 370–378.
9. Sarkis J., A strategic decision framework for green supply chain management. Journal of Cleaner Production (2003) 11: 397–409.
10. Srivastava S. K., Green supply-chain management: A state-of the- art literature review. International Journal of Management Reviews (2007) 9: 53–80.
11. Deshmukh S. and Sunnapwar V., Development and validation of performance measures for green supplier selection in Indian industries, International Journal of Engineering and Advanced Technology (2013) 2: 105–109.
12. Deshmukh S. and Sunnapwar V., Validation of performance measures for green supplier selection in Indian industries, International Journal of Modern Engineering Research (2013) 3: 1617–1622.
13. Punniyamoorthy M. and Mathiyalagan P, Parthiban P., A strategic model using structural equation modeling and fuzzy logic in supplier selection. Expert Systems with Applications (2011) 38: 458–474.
14. Ataei M., Mikaeil R., Hoseinie S. H., Hosseini S. M., Fuzzy analytical hierarchy process approach for ranking the sawability of carbonate rock. International Journal of Rock Mechanics & Mining Sciences (2012) 50: 83–93.
15. Chang D. Y., Applications of the extent analysis method on fuzzy AHP. European Journal of Operation Research (1996) 95: 649–655.

16. Ozdagoglu A. and Ozdagoglu G., Comparison of AHP and fuzzy AHP for the multi criteria decision making processes with linguistic evaluations. (2007). www.arastirmax.com/system/files/…/arastirmax_26635_pp_65–85.pdf
17. Sun C.C., A performance evaluation model by integrating fuzzy AHP and fuzzy TOPSIS methods. Expert Systems with Applications (2010) 37: 7745–7754.
18. Kahraman C., Cebeci U., Ruan D., Multi-attribute comparison of catering service companies using fuzzy AHP: The case of Turkey. International Journal of Production Economics (2004) 87: 171–184.
19. Deshmukh S. and Sunnapwar V., Analytic Hierarchy Process (AHP) for green supplier selection in Indian industries, Proceedings of the international conference on Advanced Engineering Optimization through Intelligent Techniques, SVNIT, Surat, July 2013.

Crash Simulation of an Automotive Body to Explore Performance of Different Metallic Materials Using ANSYS

C. M. Choudhari, Jaineel Desai, Shlok Bhavsar and Dharmendra Choudhary

Abstract In case an automobile body moving with a high velocity crashes into a fixed rigid wall, the frontal section of the automotive body will be deformed and it will absorb a lot of energy due to the impact. Hence, there comes a need to select the material for an automotive body, such that, it will protect the occupant in the car during such an incident. In this paper, a car model representing an automotive body is modelled in the three-dimensional modelling software SOLIDWORKS. Furthermore, ANSYS workbench is used for mesh generation and FEM analysis of the three-dimensional geometric model. Aluminium alloy and structural steel are the materials considered for the automotive body. The automotive body is crashed into the fixed rigid wall at a velocity of 35 mph, and the impact energy is calculated based on stresses on the automotive body and Young's Modulus for the materials used. The results are plotted and analysed.

Keywords Crash simulation · FEM · Automobile body · Impact energy

1 Introduction

Safety is the primary consideration while designing the frame of an automotive body. Crash test of an automobile is an important aspect in determining the safety of a vehicle. However, it is a very expensive and time-consuming method to perform crash simulations in reality. Hence, FEM modelling and simulation can be used to virtually perform such crash tests which will be economical and time-saving as well [1]. In addition, selection of materials for the same plays a vital role in deciding the factor of safety during designing of such an automotive body. Different aspects can

C. M. Choudhari · J. Desai (✉) · S. Bhavsar · D. Choudhary
Department of Mechanical Engineering, D. J. Sanghvi College of Engineering,
Mumbai 400756, India
e-mail: jaineeldesai509@gmail.com

C. M. Choudhari
e-mail: c.choudhari75@gmail.com

be considered while selecting the materials for an automotive body. In this paper, we have considered the economical, readily available and feasible aspects of material selection. An extensive literature review has been carried out, and selected papers have been mentioned hereunder:

Hickey et al. [2] conducted quasi-static renderings to imitate automobile crash through finite element method. The simulation was performed on 2002 Ford Explorer modelled in three-dimensional modelling software CREO, and FEM analysis was then performed on importing model into ANSYS. Crash analysis was emulated for dissimilar approaching speeds. It was inferred that when the automobile was approaching at 100 mph, the automobile was damaged beyond repair. The values obtained in numerical simulation agreed with the values obtained on actual examination. Yadav et al. [3] have revaluated finite element modelling approaches used for crash analysis and the consequences of the various criteria on the automobile. The purpose of this paper was to examine the impact of such crash end-points on the dynamic reception of vehicular components via finite element method. An investigation of emergence carried on in the crash renderings of vehicular elements and the related process parameters is presented in this paper. Park et al. [4] documented a different formulation that has a possibility of use for capturing multifariousness in crash count models using finite mixture regression models. The NB retrogression designs are particularly utile where count information is extracted from heterogeneous groups. To solve these designs, Poisson and NB mixture designs were measured through information gathered in Toronto, Ontario. These designs were compared to standard NB retrogression designs measured through the same information. The conclusion of this report highlighted that the data set appeared to be raised from 2 distinct subgroups, each having dissimilar retrogression coefficients and degrees of over-dispersion. Sarwar et al. [5] discussed the development, modification and analysis of a finite element model of car body using high-speed steel. Valayil et al. [6] developed a finite element model of a car in ANSYS and solved it for full frontal impact in ANSYS LS-DYNA explicit code. Computational simulations and numerous conclusions were plotted and analysed. The analysis was limited to an impact of the anterior portion with an inflexible barrier at a speed of 35 mph, corresponding to an NHTSA full-frontal impact. The study showed that composite materials could be used proficiently for their lightweight feature, as its capacity to absorb the energy during an impact was comparable to the metallic materials used for the same purpose.

2 Methodology

2.1 Modelling of Automotive Body

The modelling of the automotive body was performed on three-dimensional modelling software SOLIDWORKS, where the car model and the fixed rigid wall were modelled (Fig. 1).

Fig. 1 Rendered isometric view of car model in SOLIDWORKS
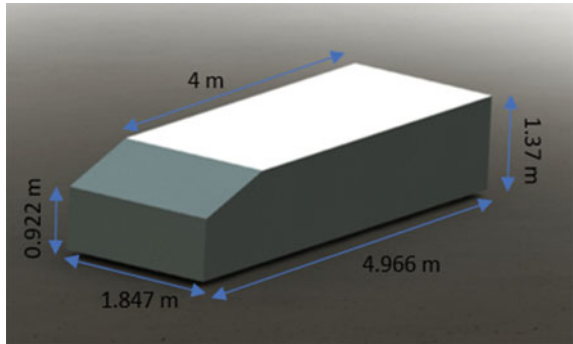
Fig. 2 Empirical relations of different dimensions
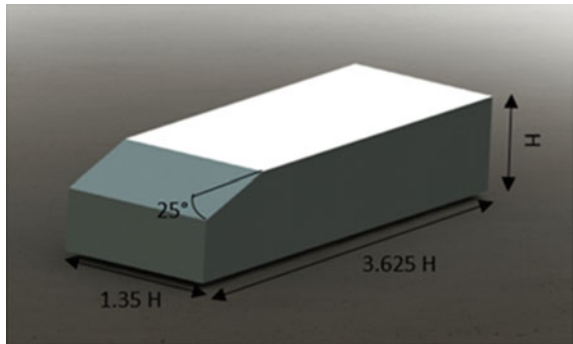
Fig. 3 Set-up for simulation
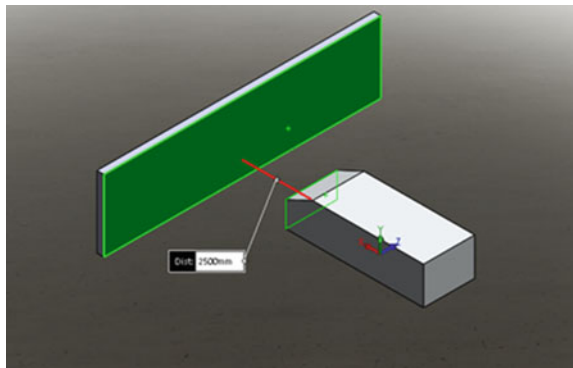
The empirical rules used in selecting the dimensions are as shown in Fig. 2.

After the modelling of the car model, the fixed rigid wall was introduced into the modelling environment. The dimensions of the wall were 10 m × 2.6 m × 0.25 m. The car model was placed at a distance of 2.5 m from the wall (Fig. 3).
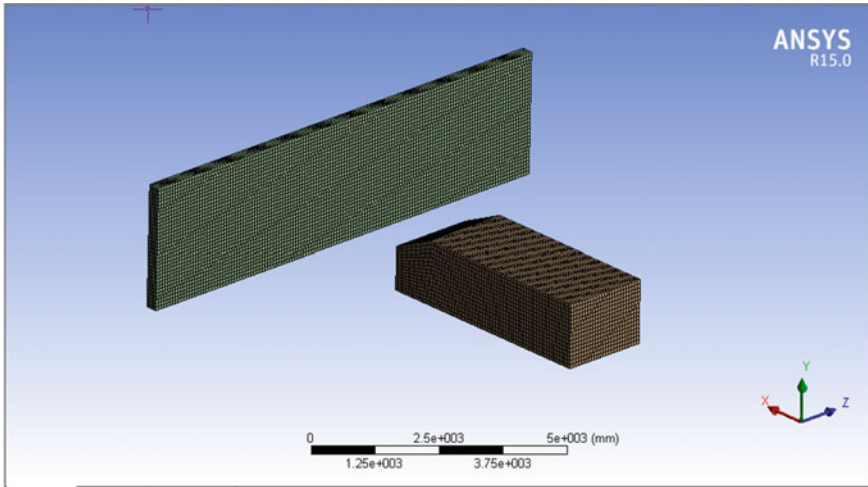
Fig. 4 Mapped quadrilateral mesh

2.2 Meshing

The geometrical set-up was imported into the ANSYS from SOLIDWORKS for mapped mesh generation and for analysing the geometric model using FEM. Before generating the mapped quadrilateral mesh, the materials were specified to the car model as aluminium alloy in the first case and structural steel in the second case. The wall was assigned CONC-35MPA as its material. A mapped quadrilateral mesh was generated on the car model and the rigid wall (Fig. 4). The count of quad-elements and nodal points in the finite element model were 45,960 and 54,798, respectively.

The wall was fixed as per the boundary condition, and the car model was imparted a velocity of 35 mph in the positive x-direction (Fig. 5).

Time taken for the collision to occur is given by the formula:

$$\text{Time at which the collision will take place} = \frac{\text{Distance between Vehicle and Wall}}{\text{Speed of Vehicle}}$$

By using the above formula and substituting the values of distance and speed, the time at which the collision will take place was 0.16 s.
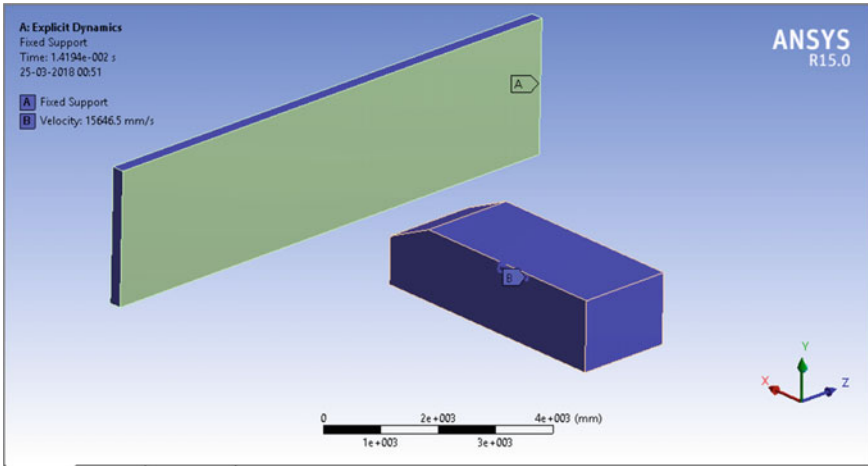
Fig. 5 Boundary condition

Table 1 Material properties

S. no.	Material	Elastic modulus (MPa)
1	Aluminium alloy	71,000
2	Structural steel	200,000

2.3 *Calculating Impact Energy*

The impact energy which will be the total energy stored during elastic deformation is given by:

$$\text{Impact Energy} = \frac{1}{2} \times \frac{(\text{Stress})^2}{\text{Elastic Modulus}} \times \text{Volume}$$

.

The stresses can be calculated at different intervals of time during collision. Moreover, for a material, its elastic modulus was known (Table 1). The volume as calculated by ANSYS solver was 12.173 m^3.

By using these values, the impact energy at different intervals was calculated.

3 Results and Conclusions

The ANSYS solver solved the FEM model for different materials, and the maximum stresses were obtained for the frontal section of the car model as shown in Fig. 6.
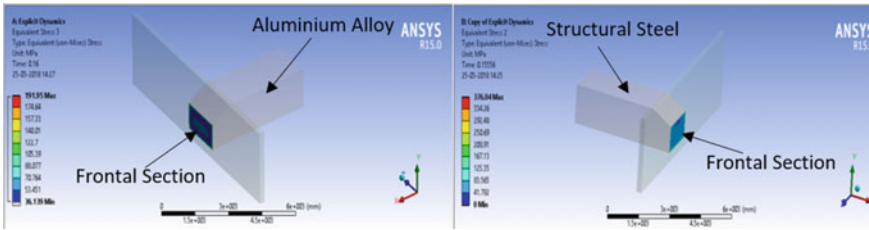
Fig. 6 Stresses developed in frontal area

Table 2 Stress on both materials at different instances

S. no.	Time (s)	Stress (MPa)	
		Aluminium alloy	Structural steel
1.	0.16	191.15	376.04
2.	0.17	21.144	43.835
3.	0.18	22.531	25.304
4.	0.19	25.879	29.853
5.	0.2	20.693	23.319
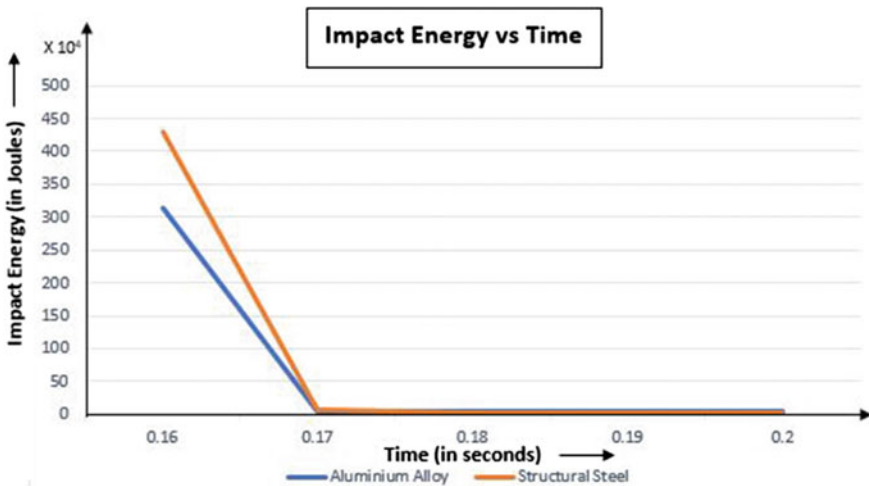
Fig. 7 Graphs of impact energy versus time for steel and aluminium

Using the stresses obtained within the time interval of 0.16–0.2 s (Table 2), the impact energy for both the cases was calculated at each instant and a graph of impact energy vs time was plotted (Fig. 7).

From the graphs, it was evident that the energy absorbed by structural steel car model was more than the energy absorbed by aluminium car model during a crash [6]. Hence, the occupant will be more safer in case of a steel car body as it will absorb

maximum amount of energy from the crash thereby saving the occupant inside the car from the crash.

Since the primary purpose of the study was to compare the impact energy absorbed by an aluminium alloy and a structural steel car body, it was evident from the results that the structural steel car body was more safer as compared to the aluminium alloy car body. It was noticeable during the course of the study, that the lightweight feature of the aluminium alloy could be used prominently, as its capacity to absorb the energy during an impact is comparable to that of structural steel.

References

1. T. Belytschko, W.K. Liu and B. Moran: Nonlinear Finite Elements for Continua and Struc-
   tures. 1st ed. U.S.: Wiley. New York. 2001
2. Andrew Hickey, Shaoping Xiao: Finite Element Modeling and Simulation of Car Crash. Inter-
   national Journal of Modern Studies in Mechanical Engineering (IJMSME). Volume 3. Issue 1.
   2017. PP 1–5
3. Shalabh Yadava, S. K. Pradhanb: Investigations into Dynamic Response of Automobile Com-
   ponents during Crash Simulation. Procedia Eng. 97. 1254–1264. 2014
4. Byung-Jung Park1: Dominique Lord, Application of finite mixture models for vehicle crash data
   analysis, Accident Analysis and Prevention 41. 683–691. 2009
5. Waseem Sarwar and Nasir Hayat: Crash Simulation and Analysis of a Car Body Using ANSYS
   LS- DYNA, MED UET Taxila (2007)
6. Tony Punnoose Valayil, Dr. Jason Cherian Issac: Crash Simulation in ANSYS LS-DYNA to
   explore the Crash Performance of Composite and Metallic Materials. International Journal of
   Scientific & Engineering Research. Volume 4. Issue 8. August 2013

Condition Monitoring of Rolling Element Bearing by Acoustic Analysis Using LabVIEW

Anish Nadar and Rajanarasimha Sangam

Abstract In this paper, it is discussed about the condition monitoring of rolling element bearing as a preventive measure taken so as to do preventive maintenance of bearing. By conducting condition monitoring, it provides us with the present condition of bearing. To do so "Acoustic analysis method" is used, where the acoustic data of bearing is collected on a real-time basis using sensors MAX4466 and MAX9812 with the help of NI-DAQ 9008 and Arduino UNO microcontroller. The acoustic data of the bearing is collected at various shaft speeds by the use of variable speed motor. FFT analysis method is used for the real-time acoustic data analysis by means of LabVIEW software. This paper also focuses on the application of sound pressure and vibration signals to detect the presence of defect in rolling element bearing using acoustic data analysis method and statistical method using kurtosis value analysis.

Keywords Vibration · Acoustic · FFT

1 Introduction

Bearing is an indispensable element of almost any rotating machinery. For various engineering applications, the most basic component used in machinery is ball bearing. Engineering applications with rotary motion of shaft apart from complex engineering mechanisms use these bearings and are used in number of applications such as industrial and automotive gearbox, electric motors, machine tool spindle, small size centrifugal pumps, and automotive front and rear axle.

The fault in ball bearing may occur because of improper design, improper manufacturing, improper mounting, misalignment of bearing races, unequal rolling elements, improper lubrication, overloading, fatigue, uneven wear, etc. Also, the bear-

A. Nadar (✉) · R. Sangam
Department of Mechanical Engineering, K. J. Somaiya College of Engineering, Mumbai, India
e-mail: anish.nadar@somaiya.edu

R. Sangam
e-mail: rajanarasimha.sangam@somaiya.edu

ing may become faulty because of high-speed, heavy dynamic load and also contact forces. So the study of vibration generated by the defect of acoustic analysis plays important role in condition monitoring of rolling contact bearing.

Rate of bearing failure is high in many machines as compared to its other components, and hence, they are often responsible for the machine breakdown. If a bearing failure takes place, malfunction of machine may lead to significant downtime, more maintenance cost, and decrease of productivity. If faults are found at early stage it can prevent such failures [1].

Health of rolling element bearings can be identified by the use of acoustic analysis. Vibration provides important information about fault present within them. For diagnosis of rolling contact bearing, vibration analysis techniques used are motor current analysis, wear debris analysis, noise monitoring, temperature monitoring, and vibration monitoring.

1.1 Literature Survey

Literature survey is done on fault analysis of rolling element bearing which shows that lot of work being carried out to find out the exact fault type, fault location, and fault size. As rolling element bearing is mostly used in machine in industry, it has gained a countless concentration in area of condition monitoring. Examination of vibrations produced due to defects is the main role in quality examination as well as for condition monitoring of the ball bearing machinery [2]. Vibration monitoring technique is widely used to identify health of rolling element because vibration signals discover important characteristics of the defect present inside the bearing. A number of techniques are used to identify defect in a rolling element bearing such as wear debris analysis, motor current analysis, noise monitoring, temperature monitoring, and vibration monitoring [3].

Raghavendra et al. [4] studied statistically the variation of the vibration signals acquired from ball bearings with respect to speed using a setup. He has calculated RMS value and kurtosis value to validate the condition of bearing. The method is simple, quick, and cost-effective method for condition monitoring of ball bearings.

Poddar et al. [5] describe time domain analysis of vibration in ball bearing. Such as peak-to-peak amplitude, root mean square, crest factor, and kurtosis indicate defects in ball bearings. But these factors do not specify the position or the nature of the defects. Each defect produces vibration in ball bearing. Thus, analyzing the vibration spectrum may deliver information on the type of defects. There is no relation between the defect size and the amplitude of the vibration.

Talekar et al. [6] tell how FFT analyser helps to detect various components without disturbing setting of that component. He has purposely made the defect on different elements of bearing and taken out the vibration response of that defective bearing. Every defect excites the system at its characteristic frequency. The defects are located by the FFT frequency domain spectrum. Peak frequency in frequency spectrum

corresponds to the bearing characteristic frequency which can be used to locate the position of bearing defect.

1.2 Theory

The vibration signal obtained from the sensor is difficult to analyze as it contains many signals because of background noise. It is difficult to distinguish the fault information out of it. To overcome this, various vibration techniques, signal analysis techniques, and acoustic techniques are used commonly for the purpose of condition monitoring of rolling contact bearings [7]. The vibration signal discovers significant information of the defect present on the elements of the bearing. Time domain analysis of signals like kurtosis, root mean square, peak-to-peak amplitude, and crest factor can be used to find out faults in ball bearings. But these results are not sufficient to identify the location or position of the defects. To overcome this, frequency domain analysis is used. The defect in bearing will produce the vibration frequency corresponding to the fault frequency which can be seen in frequency spectrum [8].

1.3 Experimental Setup

The setup is designed and fabricated to monitor and find the fault in a deep groove ball bearing at three different running speeds. After turning ON the motor supply, the motor shaft starts rotating. The bearing shaft is connected with the motor shaft by jaw coupling also start rotating. The shaft is supported by the two bearings inside the two bearing housing. The bearing inner race is fixed with the shaft outer surface because of that inner race rotates and outer race remains stationary inside the bearing housing. One bearing is a new bearing, and another support bearing is a used, having inner-race defects.

When the shaft rotates, the vibration develops at the defective bearing. As defective bearing is used, so it will produce more vibration than the new bearing. Acoustic sensor is set on the bearing housing to calculate the amplitude and frequency of the vibration of each bearing. When the bearing vibrates the acoustic sensor acquires the noise created by bearing vibration. The data collected by MAX4466 is then acquired by NI-DAQ (Data Acquisition Card) and Arduino UNO, and it is displayed on the computer screen by using LabVIEW software. The block diagram shown in the figure is used to collect the signal using NI-DAQ (Data Acquisition Card). The NI-DAQ is configured to receive the signal from the accelerometer.

The sampling rate is set as 10,000 Hz and the number of sample kept as 10,000. The spectral measurement palette used for the fast Fourier transform. The amplitude is taken as RMS value, and averaging function is kept as linear averaging. The Hanning window is used and phase plot is kept off. The block diagram shown in the figure is used to collect the signal using Arduino UNO. The signals obtained from
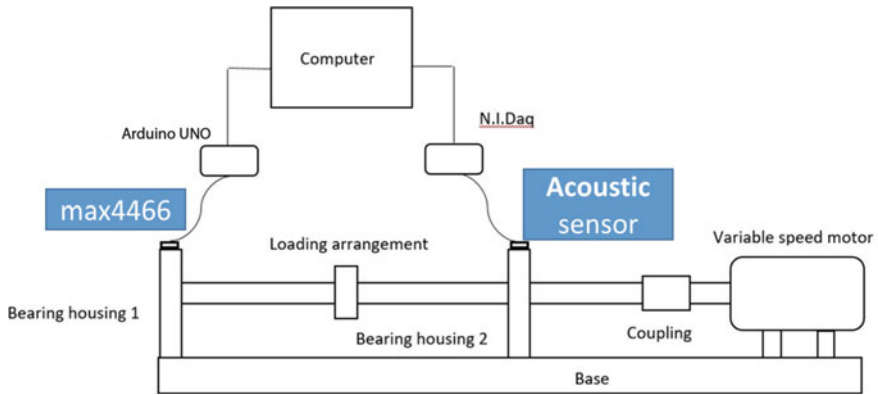
Fig. 1 Block diagram of experimental setup

the Arduino UNO are used to do time domain analysis in LabVIEW software and MATLAB software. The signals obtained from NI-DAQ (Data Acquisition Card) are used to do frequency domain analysis in LabVIEW software. The signals are collected at three different speed 750, 1300, and 1450 RPM, respectively. After collecting signal for inner-race fault bearing and new bearing, the two defective bearings having outer-race and ball faults are mounted in the bearing housing. The signals are collected for them and analyzed in LabVIEW and MATLAB software. The signals obtained from the LabVIEW are compared with the theoretical result for the validation (Fig. 1).

- The following figure shows the various faults in a bearing.

2　Methodology

See Fig. 2.
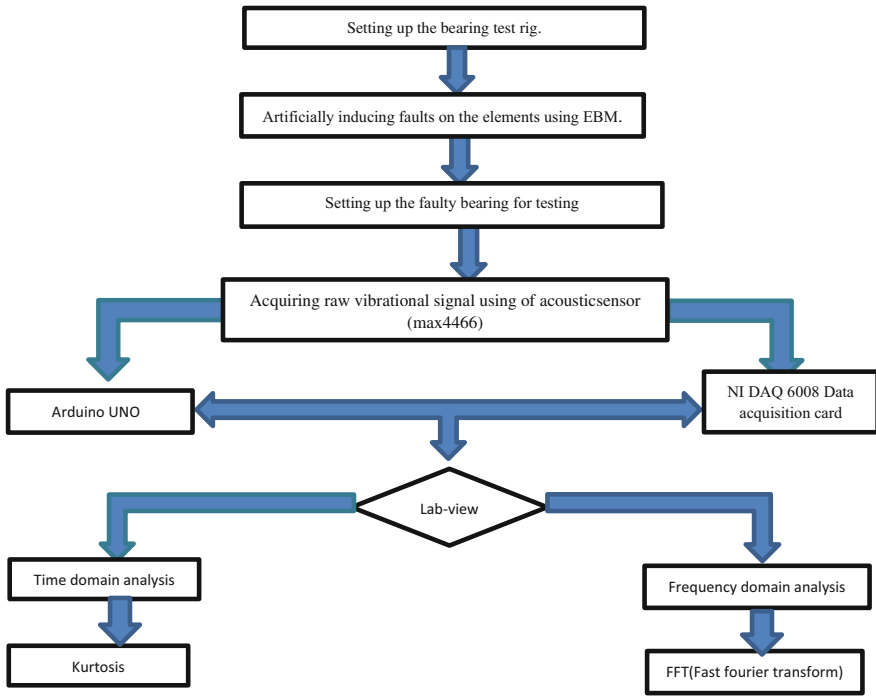
Fig. 2 Methodology flowchart

2.1 Fundamental Characteristics Frequency

The faults in the rolling contact bearing can be categorized according to the damaged elements such as outer-race defect, inner-race defect, ball defect, and combination of all defects. Every bearing has a characteristic defect frequency. This frequency can be calculated using mechanical dimensions of the bearing [9]. The defect frequency of bearing running at given shaft speed is given by product of frequency multipliers with the shaft rotational speed. By finding type of the bearing characteristics frequency, the reason for the defect can be determined. The frequency of bearing multipliers equations gives an approximation of the frequency to be expected when the bearing elements defect takes place. To estimate these frequency multipliers for the REB in which the outer race is stationary and inner race rotates, the following equations are used [10].

FTF—fundamental train frequency (equation of calculating factor for frequency of the defected cage):

$$\text{FTF} = \frac{1}{2}\left[1 - \left(\frac{D_e}{D_p}\right)\cos\beta\right]$$

BPFI—ball pass frequency of inner race (equation of calculating factor for frequency generated when the rolling elements strike with inner-race defect):

$$\text{BPFI} = \frac{Z}{2}\left[1 + \left(\frac{D_e}{D_\text{p}}\right)\cos\beta\right]$$

BPFO—ball pass frequency of outer race (Equation of calculating factor for frequency generated when the rolling elements strike with outer-race defect):

$$\text{BPFO} = \frac{Z}{2}\left[1 - \left(\frac{D_e}{D_\text{p}}\right)\cos\beta\right]$$

BSF—ball spin frequency (equation of calculating factor for rotating frequency of each rolling element as it spins):

$$\text{BSF} = \frac{D_\text{p}}{2D_e}\left[1 - \left(\frac{D_e}{D_\text{p}}\right)\cos\beta\right]^2$$

where D_e = ball diameter; D_p = pitch diameter; β = contact angle; z = number of balls; ω = shaft speed.

2.2   Fast Fourier Transform and Kurtosis

Fast Fourier transform is used in the present study to convert time domain signal into frequency domain signal [11]. This is done using LabVIEW software. The signals obtained from sensor are analyzed in LabVIEW software. The spectral measurement palette which is in build in LabVIEW software is used for this purpose. FFT is a mathematical tool, and its formula is given as follows:

$$h(t)\int_{-\infty}^{\infty} H(f)e^{-2\pi ft}\,\mathrm{d}f$$

Kurtosis is a statistical tool which is used to measure the peakiness of signal with respect to normal distribution. The theoretical value for healthy bearing corresponds to 3. The kurtosis value can be calculated using following formula.

$$K = \sum_{n=1}^{N}\frac{[x(n) - \mu]^4}{N \cdot (s^2)^2}$$

where $x(n)$ represents time series, s represents standard deviation of the data, μ is mean value of the data, and N is the total number of data points.

2.3 LabVIEW

The LabVIEW means "laboratory virtual instrument engineering workbench is a graphically based programming language." It is used to do time and frequency domain analysis in present study. The block diagram is made for time domain analysis. The Arduino UNO is used to collect signal from sensor to LabVIEW. The Arduino UNO programs to send the signal from accelerometer to LabVIEW. The signal from the Arduino UNO is used for time domain analysis in LabVIEW. The signal from the DAQ card is used for frequency domain analysis. The block diagram is made in LabVIEW software for frequency domain analysis.

2.4 LabVIEW Program for Time Domain Analysis
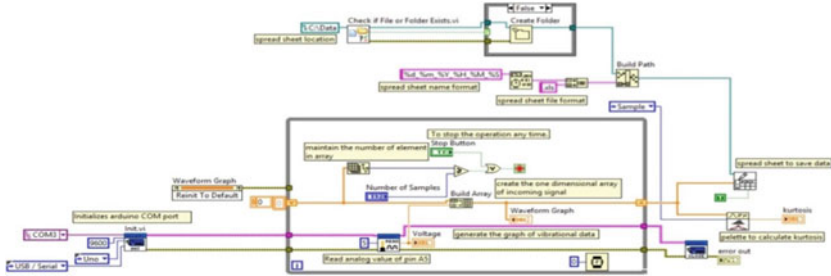
2.5 LabVIEW Program for Frequency Domain Analysis
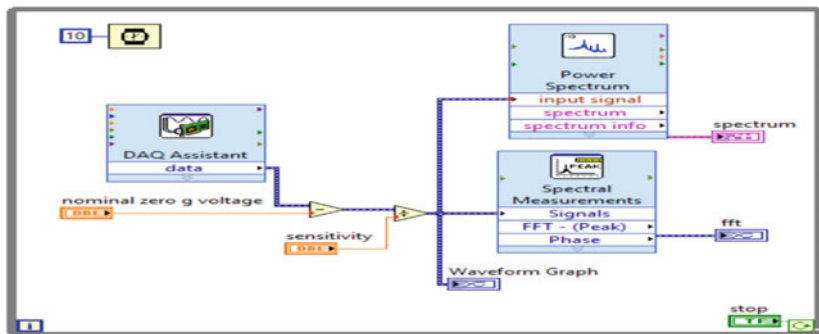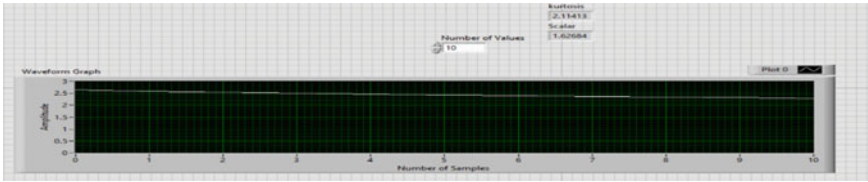
Fig. 3 Kurtosis value calculated for healthy bearing at 750 RPM

Table 1 Kurtosis value for healthy bearing

S. No.	Speed (RPM)	Kurtosis value
1	750	2.11
2	1300	2.11
3	1450	2.14
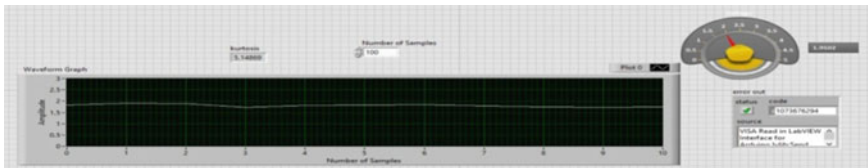
Fig. 4 Kurtosis value calculated for bearing having inner-race fault at 750 RPM

3 Results and Discussions

3.1 *Time Domain Analysis*

The Arduino UNO is specially used to carry out time domain analysis. The data captured using Arduino UNO is analyzed in LabVIEW for calculation of kurtosis.

3.1.1 Kurtosis Value Calculated for Healthy Bearing Using LabVIEW

See Fig. 3; Table 1.

3.1.2 Kurtosis Value Calculated for Inner-Race Fault Using LabVIEW

See Fig. 4; Table 2.

3.1.3 Kurtosis Value Calculated for Outer-Race Fault Using LabVIEW

See Fig. 5; Table 3.

Table 2 Kurtosis value for inner-race fault	S. No.	Speed (RPM)	Kurtosis value
	1	750	5.14
	2	1300	5.51
	3	1450	6.06
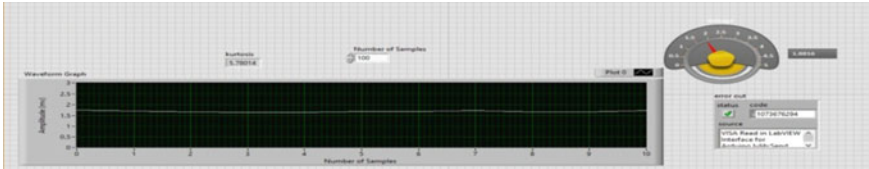
Fig. 5 Kurtosis value calculated for bearing having outer-race fault at 1450 RPM

Table 3 Kurtosis value for outer-race fault	S. No.	Speed (RPM)	Kurtosis value
	1	750	4.29
	2	1300	5.41
	3	1450	5.78
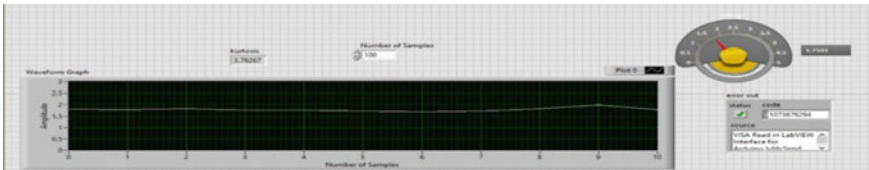
Fig. 6 Kurtosis value calculated for ball fault at 750 RPM

3.1.4 Kurtosis Value Calculated for Ball Fault Using LabVIEW

See Fig. 6; Table 4.

3.1.5 Comparison Between Theoretical and Experimental Kurtosis Value

See Table 5.

Table 4 Kurtosis value for ball fault	S. No.	Speed (RPM)	Kurtosis value
	1	750	3.78
	2	1300	3.91
	3	1450	4.43

Table 5 Comparison between theoretical and experimental kurtosis value

Speed	Hz	Permissible	Inner race	Outer race	Ball	Healthy
750	12	3	5.14	4.29	3.78	2.11
1300	20.8	3	5.51	5.41	3.91	2.11
1450	23.2	3	6.38	5.78	4.43	2.14
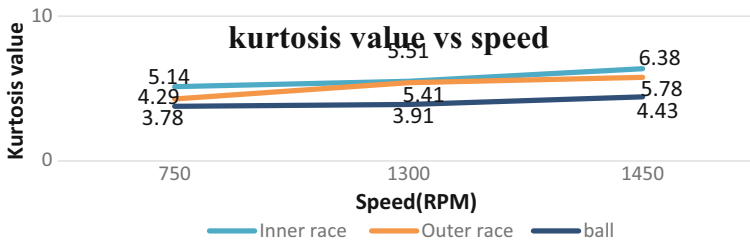
Fig. 7 Kurtosis value comparison

Graph of Kurtosis Value for Faulty Bearing

Form the graph, we can say that all the kurtosis value for faulty bearing at different speed are greater than the permissible value which shows that bearing is faulty. The kurtosis value does not change significantly with increase in speed. Thus, it is found that the bearing is faulty by acoustic analysis (Fig. 7).

3.2 Frequency Domain Analysis

The LabVIEW software converts the time domain signal into the frequency domain signal using FFT tool. The frequency spectrum shows the peak at frequency corresponding to the fundamental fault frequency.

3.2.1 Frequency Calculated for Inner-Race Fault Using LabVIEW

See Figs. 8 and 9.

3.2.2 Frequency Calculated for Outer-Race Fault Using LabVIEW

See Fig. 10.
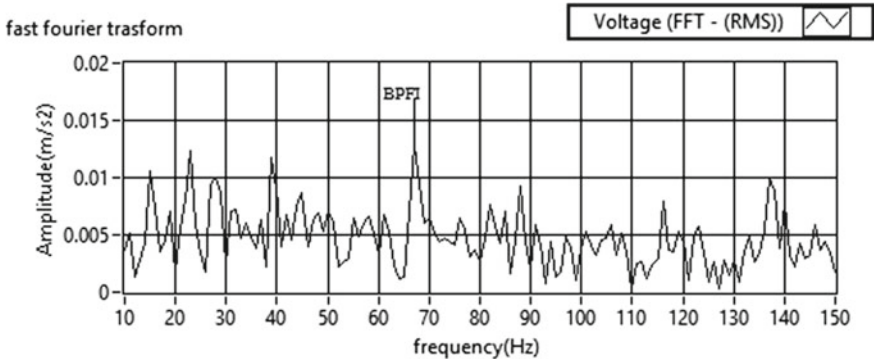
Fig. 8 Frequency spectrum at 750 RPM
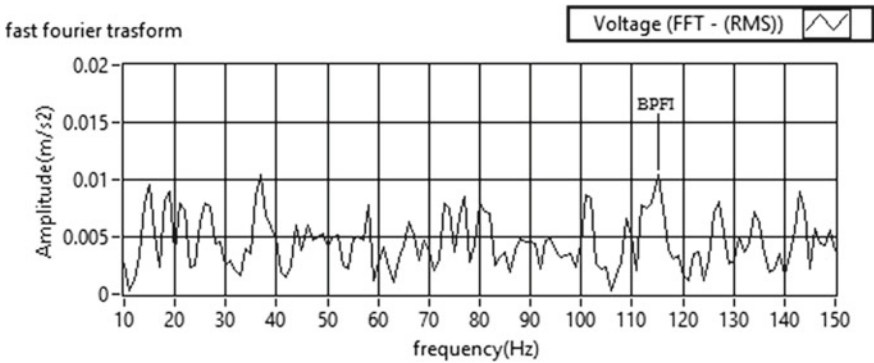
Fig. 9 Frequency spectrum at 1300 RPM
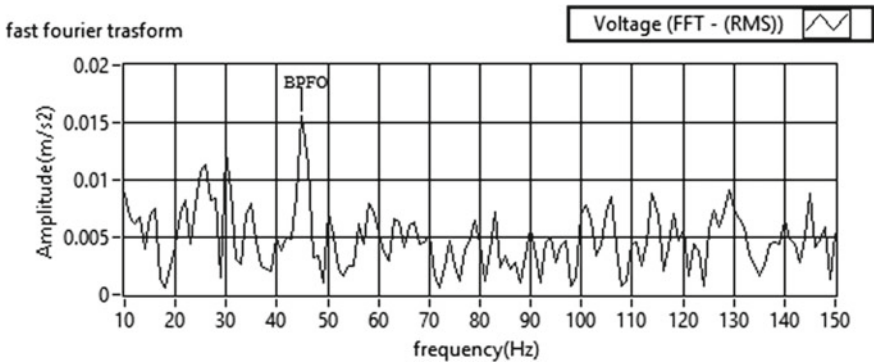
Fig. 10 Frequency spectrum at 750 RPM

fast fourier trasform
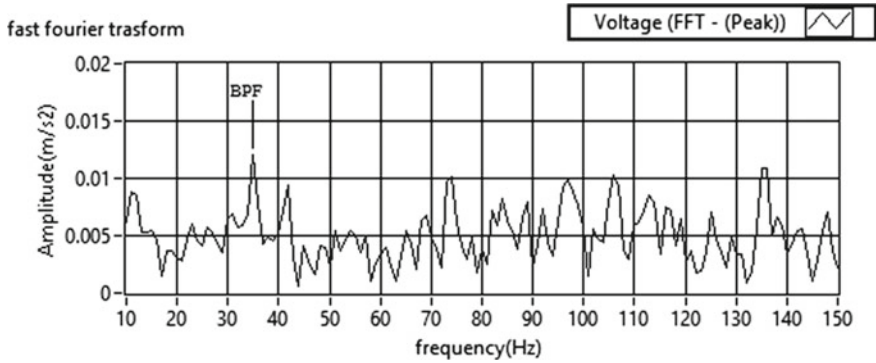
Fig. 11 Frequency spectrum at 750 RPM

Table 6 Comparison between experimental and theoretical frequency

RPM	Hz	Fault frequencies calculated theoretically			Fault frequencies calculated experimentally		
		BPFI	BPFO	BPF	BPFI	BPFO	BPF
750	12.525	68.01075	44.589	37.8255	68	44	37
1300	21.71	117.8853	77.2876	5.5642	118	76	64
1450	24.07	130.7001	85.6892	72.6914	129	85	72

3.2.3 Frequency Calculated for Ball Race Fault Using LabVIEW

See Fig. 11.

3.2.4 Comparison Between Experimental and Theoretical Frequency

Table shows the different value of frequency for different type of fault at three different speeds. The experimental values are corresponding to the theoretical fault frequencies. From the above table, we can say that bearing has inner-race, outer-race, and ball faults (Table 6).

4 Conclusion

The FFT analysis can be done using LabVIEW software. The kurtosis value for bearing is more than 3 which shows the bearing is faulty. The kurtosis value for different speed does not vary much which indicates that it does not change with increase in speed. Experimental test results clearly show the bearing is faulty as the peak frequency in frequency spectrum is closer to the characteristics fault frequencies.

Experimental result shows that frequency response analysis is useful for finding out the location of defect. MAX4466 sensor is useful for condition monitoring and fault identification of a deep groove ball bearing.

References

1. M. Entezami, E. Stewart, J. Tutcher, W. Driscoll, R. Ellis, G. Yeo, Z. Zhang, C. Roberts, T. Kono and S. Bayram "Acoustic Analysis Techniques for Condition Monitoring of Roller Bearings" ©2014
2. P. K. Kankar, Satish C. Sharma, S. P. Harsha "Fault Diagnosis of High Speed Rolling Element Bearings Due to Localized Defects Using Response Surface Method"
3. AkhandRai, S.H. Upadhyay "A review of signal processing techniques utilized in the fault diagnosis of rolling element bearings." Tribology International 96 (2016) 289–306
4. K. Raghavendra, Karabasanagouda.B.N "Frequency Response Analysis of Deep Groove Ball Bearing" (ISSN (Online): 2319–7064)(1)
5. Surojit Poddar, MadanLal Chandravanshi "Ball Bearing Fault Detection Using Vibration Parameters" (IJERT) Vol. 2 Issue 12, December – 2013 IJERT ISSN: 2278-0181
6. VikramTalekar, Prof. L. S. Dhamande "Condition Monitoring of Deep Groove Ball bearing using FFT Analyzer" (IJERT) ISSN: 2278-0181 IJERTV4IS040367 Vol. 4 Issue 04, April-2015)
7. Brandon Van Hecke, Jae Yoon, David He "Low speed bearing fault diagnosis using acoustic emission sensors" © 2016 Published by Elsevier Ltd.
8. Mr. Mahesh. S. Kale, Mr. Vishal, P. Hegana "Vibration Study of Deep Groove Ball Bearing by Considering Single and Multiple Defects In Races" IJIRSE December 2016
9. SuatSarıdemirAdemÇiçek "Vibration Analysis of Rolling Element Bearings Defects" Journal of Applied Research and Technology · June 2014
10. AttelManjunath and D V Girish "Defect Detection In Deep Groove Polymer Ball Bearing Using Vibration Analysis" (IJMECH) Vol.2, No.3, August 2013
11. N Dhanush, G Dinesh, V Perumal, Mohammed Salman R NafeezAhmed. L "Analysis of Deep-Groove Ball Bearing using Vibrational Parameters" Volume 4, Special Issue 3, March 2015

Computational Modeling and Analysis of Artificial Flood Using Automata

Nabamita Deb and Ashiya Noorie

Abstract The study is the effort to analyze the parameters that cause artificial flood in urban areas. Artificial flood is considered a major problem that a place affected by it faces, as it hampers day-to-day life and creates a lot health hazards among aged people and children. The paper tries to contribute in the field of computation by considering the factors which result in an artificial flood. A timed transition automaton is used to depict the behavior of different states over time when there is a heavy rainfall keeping in mind, the rate of cleansing velocity along with it.

Keywords Bharalu basin · Sediment · Timed transition automata

1 Introduction

Assam is occupying about 2.40% of India in landmass and covering an area of 78,438 km^2. Guwahati is situated in between the foothills of the Meghalaya plateau and the southern bank of the river Brahmaputra.

1.1 Climate of Guwahati

The city of Guwahati enjoys a subtropical humid climate; summer from march to june, which is followed by monsoon season from july to august, which gives relief from the humidity of summer. Autumn which succeeds monsoon is favorable for

N. Deb (✉) · A. Noorie
Department of Information Technology, Gauhati University, Jalukbari,
Guwahati, Assam, India
e-mail: deb.nabamita@gmail.com

A. Noorie
e-mail: ashiya.noorie10@gmail.com

tourists having warm and moderate climate. Winters also see light rainfall, and the mornings and afternoons remain moist and foggy.

Other than the various natural calamities that our country is facing like earthquakes, storms, floods and landslides, there is another most frequent problem which the urban population is confronting; it is the artificial flood. 'Artificial'—the name itself depicts that it is not the natural flood that occurs due to the sea-level rise. Artificial flood hampers the lives of the urban areas tremendously causing severe damage to health and property. Artificial flood may occur when there is a heavy rainfall for a short period, or even when there is a continuous rainfall for a longer period. Due to which the water rises in the drains, canals and sewages; if the outlets of the drains and sewers are not open or clean, then the water gets blocked and overflows over the area hence causing an artificial flood [1, 2]. Figure 1 shows the flood effect in the area of Zoo road in the city of Guwahati.

In this research, a major issue of urban flood is discussed; first of all, it is thoroughly studied and tried to compute the relation between the amount of rainfall and artificial flood by a mathematical calculation; which helps to depict, how much amount of rainfall and the associated duration of rainfall that may result in an artificial flood.

Modeling Techniques While talking about the natural hazards due to climate change, there are numerous disastrous events the globe has been facing from time to time. Various modeling techniques and models are designed to cope up with the different types of natural disasters. One of them is the global earthquake model (GEM)'s open-source software OpenQuake [7]. It is a Web-based risk assessment platform which models, views, explores and manages earthquake risk; it has got five main calculators, each one has got its own contribution in the area of seismic risk assessment and mitigation. One of the calculators of the OpenQuake engine is the probabilistic eventbased risk (PEB) which computes the probability of losses and loss statistics for the assets depending upon the probabilistic hazard. The output is thus used to assess the aggregate losses of the collective assets.

The OpenQuake project was initiated by GEM [7] is an open standard for calculating and communicating earthquake risk worldwide.

Flood-inundation modeling using MIKE FLOOD [5] has been used to simulate the flood inundation for the year 2001, and the maximum simulated extent was then compared with the image obtained from the IRS-1D WiFS of the inundated area.

Using the MIKE 11 software, the river flow for the delta region of Mahanadi river basin has been simulated and performed quite satisfactorily [5].

Flood in the urban areas are due to many factors; improper design of the sewer system is one major factor. The drainage system of Guwahati city during monsoon season cannot drain out floodwater. The outlet of the drain is connected to the Bharalu river basin which is connected to the main river Brahmaputra. A study [3] was conducted on artificial flood in Bharalu Basin, Assam focuses on—

(i) The size of the particles in the various parts of the drain of Bharalu is investigated in detailed, and further, the self-cleansing velocity is analyzed.

(ii) An optimal management for proper controlling the flow of sediment and water from hilly watershed is considered after calculation. The channel always carries suspended particles which either floats or suspends due to the flow of the drain water. The design of the channel should be in such a way that no solid particles get deposited at the channel bed. The minimum velocity required to remove the sedimentation and sewage water from the channel is called the self-cleansing velocity. The study [3] highlights the self-cleansing velocity as,

$$V_s = \frac{8K}{f}(S_s - 1)g d_s$$

where V_s = velocity of flow or self-cleansing velocity,

K = characteristics of solid usually which is taken as 0.04–0.06,

f = Dancy's coefficient of friction which is usually taken as 0.03,

S_s = specific gravity of solid which is usually taken as 2.65 and

d_s = effective grain size.

They [3] analyzed the cause of artificial flood which is examined by considering a part of the drainage system and silt samples that were collected from the channel bed, and the data was analyzed to determine the uniformity coefficient, coefficient of curvature and effective particle size of each sample.

2 Methodology

The hourly rainfall data of Guwahati Airport area has been manually collected from the Regional Meteorological Center, Guwahati [6] for the period of 01-01-2016 to 30-06-2017.

The data was then saved in a csv file with the given details:

(i) Start time of the rainfall.
(ii) End time of the rainfall.
(iii) Total duration of rainfall, i.e., End time–Start time.
(iv) Amount of rainfall in millimeter.

Since the data collected here is not considered for a long period of time though, it is kept in a csv file considering the fact that in the future, there might be a possibility of a longer period when there will be a large amount of rainfall data to analyze and study; it can be done at ease. Thus, the rainfall data has been clustered into three different clusters with the help of Weka [9] as discussed below.

2.1 Clustering of the Data

It involves the following steps:

(i) Amount of rainfall in mm, start_time of the rainfall, end_time of the rainfall, total duration of the rainfall is first of all saved in a comma-separated values (csv) file as shown in Fig. 2.

(ii) Since the amount of data collected is not complex, here instead of grouping the data set manually into three different clusters it is decided to use simple K-means algorithm. It is clustered using Euclidean distance (or similarity) function. Here, all the data is clustered considering the mean of their value.

Thus from the rainfall data set, three clusters were formed—cluster0 for low rainfall, cluster1 for medium rainfall and cluster2 for heavy rainfall—using Waikato Environment for Knowledge Analysis (Weka), a software tool for data mining [9].

Clusters are formed using the values of the attributes: Starting Time, Ending Time, Duration and Amt. of rainfall; these clusters which are divided into three: low rainfall, medium rainfall and high rainfall; help us to examine the data which will be relevant for the study intended, since the region often faces rainfall, therefore sparse and low rainfall is not considered.

	Starting Time	Ending Time	Duration	Amt. Of Rainfall(mm)	
1	Starting Time	Ending Time	Duration	Amt. Of Rainfall(mm)	
2	03:00:00	06:45:00	03:45:00	5.2	
3	10:50:00	11:50:00	01:00:00	6.2	
4	20:15:00	22:40:00	02:25:00	7.2	
5	23:00:00	23:24:00	00:24:00	2.4	
6	18:30:00	19:00:00	00:30:00	2.2	
7	18:12:00	20:30:00	02:18:00	2.7	
8	18:50:00	19:05:00	00:15:00	1	
9	01:10:00	01:45:00	00:35:00	7.2	
10	21:30:00	21:43:00	00:13:00	10	
11	21:43:00	23:35:00	01:52:00	10	
12	06:04:00	06:45:00	00:41:00	3.5	
13	03:45:00	05:48:00	02:03:00	0.3	
14	17:45:00	18:00:00	00:15:00	0.5	
15	22:45:00	22:55:00	00:10:00	0.5	
16	01:15:00	03:45:00	02:30:00	4	
17	02:40:00	04:10:00	01:30:00	1.8	
18	01:15:00	02:50:00	01:35:00	4.5	
19	20:00:00	21:00:00	01:00:00	0.5	
20	21:30:00	22:00:00	00:30:00	1.5	
21	23:00:00	23:15:00	00:15:00	7.5	
22	23:15:00	24:30:00	01:15:00	2.8	
23	04:30:00	05:20:00	00:50:00	1.9	
24	06:25:00	06:30:00	00:05:00	5.5	
25	10:20:00	10:30:00	00:10:00	9.7	
26	10:30:00	10:35:00	00:05:00	3.7	
27	11:48:00	12:00:00	00:12:00	9.5	
28	13:43:00	14:15:00	00:32:00	7.3	
29	16:55:00	17:14:00	00:19:00	2	
30	23:30:00	23:35:00	00:05:00	1.5	
31	02:45:00	04:15:00	01:30:00	5	
32	19:30:00	20:20:00	00:05:00	5.4	

Fig. 2 The CSV file where the amount of rainfall data set is kept
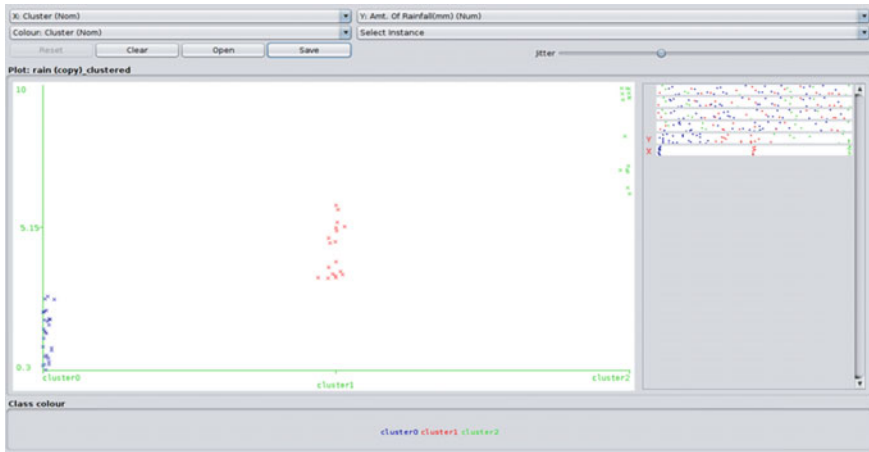
Fig. 3 Three different clusters are shown in the colored dots

Cluster results which can be visualized in the plot as cluster0 shown in blue dots for low rainfall, cluster1 shown in red dots for medium rainfall and cluster2 shown in green dots for excessive rainfall. Figure 3 shows the plot.

Final data after clustering is saved in.attribute-relation file format (arff). From this file, the relevant high rainfall, i.e., cluster2 can be retrieved for further calculation.

After the clustering is done, the next step is to design a model to find whether artificial flood (AF here onwards) is present or not.

3 Computational Model

We use the rainfall data to check whether artificial flood occurs due to the heavy amount of rainfall or any other factor. Here, we have considered AF to be dependent on the following factors:

(i) Rise of water in the road (in meter) which is displaced due to the sediment in the Bharalu basin.
(ii) Amount of rainfall data (in meter) per unit time (in second) and
(iii) Self-cleansing velocity V_s (in m/s) in the basin.

AF thus can be calculated considering the following equation:

$$AF = \text{Rise of water} + \left\{ \frac{\frac{\text{Amount of Rainfall (m)}}{\text{Time duration (sec)}}}{V_s} \right\}$$

where $V_s = \frac{8K}{f}(S_s - 1)gd_s$ [3].

It is assumed that if the value of the AF is more than 0.5 m, then there is a possibility that the particular area is effected by artificial flood, or else not.

4   Results and Discussion

After implementing the above equation in Java, we can insert the different values of the sediment which displaces the amount of water entering into the road and the low-lying areas.

In our study, the cause of artificial flood is examined by considering a part of the drainage system. The drain is considered to be partially full, so when the sediment of a particular volume and height is deposited at the channel bed, then how much amount of water gets displaced from the river basin is calculated. The self-cleansing velocity for the calculation varies between 0.7 and 1.2 m/s. Considering a mathematical formula to calculate AF we see the following:

Case I:

$$\text{AF} = \text{Rise of water} + \left\{ \frac{\frac{\text{Amount of Rainfall (m)}}{\text{Time duration (sec)}}}{V_s \text{ (m/s)}} \right\}$$

Here, rise of water in the road = displaced water from the basin due to the sediment
= Volume of the Sediment

Thus, volume of the sediment (suppose) can be evaluated as

$$\text{Length} = 5.1 \text{ m}   \text{Breadth} = 8 \text{ m}   \text{Height} = 0.65 \text{ m}$$

Then, volume of the sediment $= 26.52 \text{ m}^3$

$$\text{Water in the road in meter} = \frac{\text{volume of the sediment}}{\text{area of the road}}$$

$$\text{Area of the Road} = \text{Length} \times \text{Breadth} = 5.1 \times 10 = 51 \text{ m}^2$$

Therefore, water in the road in meter $= 0.52$ m, amount of rainfall in meter $= 0.0052$ m, time duration in sec $= 13500$ s, self-cleansing velocity $= 0.7$ m/s. So, AF $= 0.52$ m.

Therefore, the value of AF is larger than 0.5, so there is a chance of artificial flood in that area.

We have calculated the value of AF using different ranges of rainfall starting from low to high, but the result is not affected much as the artificial flood depends on the sediment, therefore we tried another case.

Case II:

$$AF = \text{Rainfall in m} + \left\{ \frac{\text{Rate of Deposition of sediment in m/s}}{V_s \text{ in m/s}} \right\}$$

where $V_s = \frac{8K}{f}(S_s - 1)gd_s$ [3]

Therefore, two examples are taken.

Example I: Considering rate of deposition of sediment $= 0.65$ m/s

Amount Of Rainfall in m $= 0.0073$ m

Self-Cleansing Velocity $= 0.7$ m/s

AF $= 0.935$ m (big possibility of artificial flood)

Example II: Now, when self-cleansing velocity is increased manually or mechanically by some suitable method. Considering rate of deposition of sediment $= 0.65$ m/s and amount of rainfall in m $= 0.0073$ m

Self-Cleansing velocity $= 1.2$ m/s

AF $= 0.548$ m

It is obvious that, when the self-cleansing velocity is increased the level of sediment in the drain basin should go down, here if we now consider rate of deposition of sediment $= 0.15$ m/s, amount of rainfall in m $= 0.0073$ m and

self-cleansing velocity $= 1.2$ m/s, therefore, AF $= 0.132$ m

4.1 Program Code

Program commands of the above mathematical calculation for AF is given as:

```
program artificial flood  (Output)
Read rainfallDuration[] and rainfallAmount[] from the csv file
Consider S_Cvelocity;
Calculating volume of sediment, Vsediment;
          Considering the length l_sed, breadth b_sed and
height of sediment h_sed;
Vsediment:= l_sed*b_sed*h_sed;
Calculating the dimension of the road,area_road;
          Considering length of the road l_road, breadth of
the road b_road;
Calculating the dimension of the road,area_road;
Area_road:=l_road*b_road;
Water in the road, water_level:=Vsediment/area_road;
for i=0 to length(rainfallDuration[]);
Af:=water_level+(((rainfallAmount[i]/1000)/(rainfallDuration[i])
)/S_Cvelocity);
end of for loop
```

Thus we see that the value of the artificial flood can be reduced when the self-cleansing velocity in the basin is increased.

A timed automaton over л tuple $A = (\sum Q, T, I, F, X)$, where $\sum$ is a finite alphabet of actions, where Q is a finite set of states, and X a finite set of clocks, $T \subseteq Q \times [C(X) \times \_ \times 2X] \times Q$ is a finite set of transitions, $I \subseteq Q$ is the subset of initial states and $F \subseteq Q$ is the subset of final states [4].
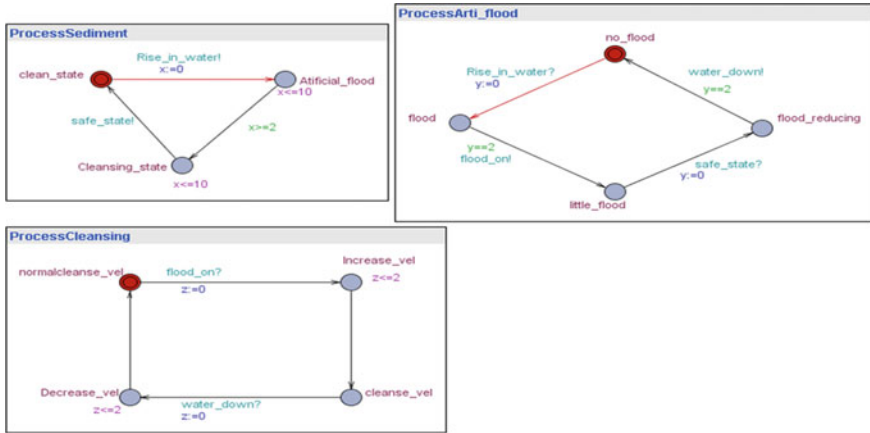
Fig. 4 Processes are shown using Uppaal

This process can be shown by using a timed transition automaton in Uppaal [8]. Uppaal is a tool to model and simulate timed transition models. Here the three different processes are considered each for sediment, artificial flood and self-cleansing velocity which are related to one another, and the transition from one state to another is time oriented. In simple words, when there is an increase in rainfall, the bed of the drain basin is deposited with the sediment collectively with the rainfall water and the debris from the high level areas. Resulting in the increase in the drain water which spread over the area creating artificial flood. If the self-cleansing velocity is increased with the help of manual labor, the blockage in the drain can be cleared, and the natural flow of water in the basin can be generated.

The three process are ProcessSediment, ProcessArti_flood and ProcessCleansing are shown in Fig. 4. Each of the process are dependent on one another. It is clear from the previous mathematical calculation for AF as the deposition of sediment at the bed of the basin plays the vital part in creating an artificial flood. So during excessive rainfall when the sediment gets deposited along with the rain water, garbages, debris etc., it is required to increase the cleansing velocity of the drainage basin.

5 Conclusion

Flood can be considered as the overflowing of water from a river at the adjacent land near to it spreading water all over the low-lying areas, whereas artificial flood or flash flood occurs suddenly due to two components for flood occurrences—one is rainfall intensity and the other is drainage area parameters. It is not always the case that heavy rainfall will cause artificial flood, through this study it has been highlighted that artificial flooding and its causes also depend on certain features of the drainage

basin like the breadth and width of the basin, amount of accumulated sediments or debris flowing from the high level areas play a significant role in obstructing the normal flow of the water through the drainage basin. In this research, we have tried to evaluate the factors resulting to an artificial flood due to the overflow of water from the drainage basin.

The paper depicts the different factors which play a vital role in creating artificial flood in the urban low-lying areas:

i. When there is a continuous rainfall measuring above 0.5 mm for a long duration of time.
ii. The drainage basin through which the sewage water or the outlet flows, at the time of rainfall, should be free of sediment settled at the base.
iii. And lastly during heavy rainfall, the self-cleansing velocity of the drainage basin should be increased to bring back the raised water level to a stable condition, or in other words, removing the blockage caused by the deposited sediment at the bed of the basin can be done by manually increasing the cleansing velocity resulting in the natural flow of rainfall water in the drainage basin.

In the future, if it is possible to detect the amount of sediment in the basin during the rainfall and create mechanical cleanser in the basin, it is possible to speculate the condition and might be possible to find out a clear solution.

Study is further going on to predict the artificial flood due to the deposition of sediments in the drainage basin by comparing the scenarios, considering with the help of a hybrid automata.

References

1. AIDMI (All India Disaster Mitigation Institute) conducted by ASDMA. In "Review of studies on Urban Floods in Guwahati from Flood Knowledge to Urban Action", July, 2014.
2. ASDMA, Govt. of Assam, "Disaster Risk Reduction Including Climate Change Adaptation of Guwahati in Context of Dynamic Growth", Columbia University, September, 2015.
3. Barman P., Sarma B., Sarma A. K., "A study on Flood Hazard Mitigation of Guwahati city", The Asian Review of Civil Engineering, 2012-https://www.iwra.org/.
4. Bouyer, P. (2005). An introduction to timed automata. *Actes École d'été ETR'05*, 79–94.
5. Patro S., Chatterjee C., Mohanty S., Singh R. & Raghuwanshi, N. S.(2009)."Flood Inundation Modelling using MIKE FLOOD and Remote Sensing Data", *Journal of the Indian Society of Remote Sensing* 37(1), 107–118.
6. Regional Meteorological Center, Accessed Annual Rainfall Data, LGBI, Airport, Guwahati.
7. Silva, V., Crowley, H., Pagani, M., Monelli, D., & Pinho, R. (2014). Development of the Open-Quake engine, the Global Earthquake Model's open-source software for seismic risk assessment. *Natural Hazards*, 72(3), 1409–1427.
8. Uppaal. Source: www.uppaal.org.
9. Weka, Waikato Environment for Knowledge Analysis Source: https://machinelearningmastery.com/what-is-the-weka-machine-learning-workbench.

Author Index